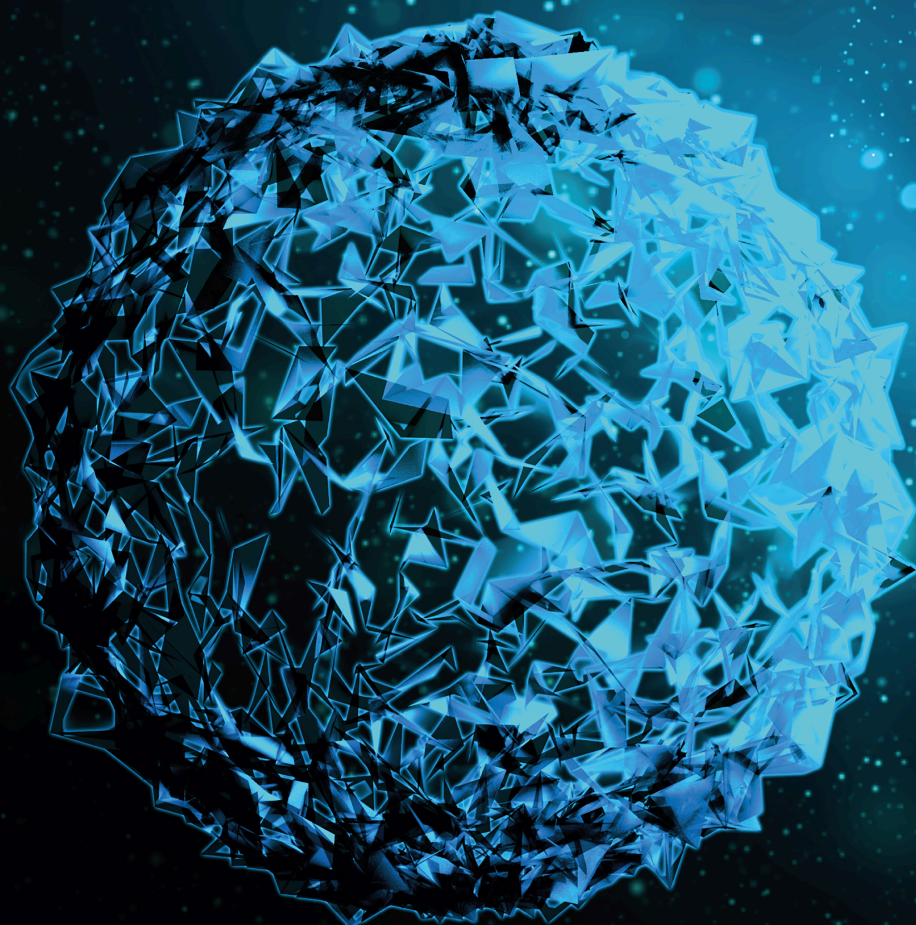# Network Pharmacology and Molecular Docking for Drug Discovery

Lead Guest Editor: Chunpeng Wan
Guest Editors: Tingdong Yan, Muhammad Farrukh Nisar, and Kannan RR Rengasamy

Network Pharmacology and Molecular Docking for Drug Discovery

Network Pharmacology and Molecular Docking for Drug Discovery

Lead Guest Editor: Chunpeng Wan
Guest Editors: Tingdong Yan, Muhammad Farrukh Nisar, and Kannan RR Rengasamy

Contents

Contents

Retraction

Retracted: Intervention Study of Dictyophora Polysaccharides on Arsenic-Induced Liver Fibrosis in SD Rats

BioMed Research International

This article has been retracted by Hindawi following an investigation undertaken by the publisher [1]. This investigation has uncovered evidence of one or more of the following indicators of systematic manipulation of the publication process:

(1) Discrepancies in scope

(2) Discrepancies in the description of the research reported

(3) Discrepancies between the availability of data and the research described

(4) Inappropriate citations

(5) Incoherent, meaningless and/or irrelevant content included in the article

(6) Manipulated or compromised peer review

The presence of these indicators undermines our confidence in the integrity of the article's content and we cannot, therefore, vouch for its reliability. Please note that this notice is intended solely to alert readers that the content of this article is unreliable. We have not investigated whether authors were aware of or involved in the systematic manipulation of the publication process.

Wiley and Hindawi regrets that the usual quality checks did not identify these issues before publication and have since put additional measures in place to safeguard research integrity.

We wish to credit our own Research Integrity and Research Publishing teams and anonymous and named external researchers and research integrity experts for contributing to this investigation.

The corresponding author, as the representative of all authors, has been given the opportunity to register their agreement or disagreement to this retraction. We have kept a record of any response received.

References

[1] G. Wang, P. Zuo, K. Ding et al., "Intervention Study of Dictyophora Polysaccharides on Arsenic-Induced Liver Fibrosis in SD Rats," *BioMed Research International*, vol. 2022, Article ID 7509620, 12 pages, 2022.

Hindawi

Research Article

Cephalosporin as Potent Urease and Tyrosinase Inhibitor: Exploration through Enzyme Inhibition, Kinetic Mechanism, and Molecular Docking Studies

Yahya S. Alqahtani,[1] Bandar A. Alyami,[1] Ali O. Alqarni,[1] Mater H. Mahnashi [ID],[1] Anser Ali,[2] Qamar Javed,[2] Mubashir Hassan,[3] and Muhammad Ehsan[4]

[1]*Department of Pharmaceutical Chemistry, College of Pharmacy, Najran University, Najran, Saudi Arabia*
[2]*Department of Zoology, Mirpur University of Science and Technology (MUST), Mirpur, 10250 AJK, Pakistan*
[3]*The Steve and Cindy Rasmussen Institute for Genomic Medicine, Nationwide Children's Hospital, Columbus, Ohio 43205, USA*
[4]*Department of Chemistry, Mirpur University of Science and Technology (MUST), Mirpur, 10250 AJK, Pakistan*

Correspondence should be addressed to Mater H. Mahnashi; aleen9542@gmail.com

In present study, eleven cephalosporin drugs were selected to explore their new medically important enzyme targets with inherited safety advantage. To this end, selected drugs with active ingredient, cefpodoxime proxetil, ceftazidime, cefepime, ceftriaxone sodium, cefaclor, cefotaxime sodium, cefixime trihydrate, cephalexin, cefadroxil, cephradine, and cefuroxime, were evaluated and found to have significant activity against urease (IC50 = 0.06 ± 0.004 to 0.37 ± 0.046 mM) and tyrosinase (IC50 = 0.01 ± 0.0005 to 0.12 ± 0.017 mM) enzymes. Urease activity was lower than standard thiourea; however, tyrosinase activity of all drugs outperforms (ranging 6 to 18 times) the positive control: hydroquinone (IC50 = 0.18 ± 0.02 mM). Moreover, the kinetic analysis of the most active drugs, ceftriaxone sodium and cefotaxime sodium, revealed that they bind irreversibly with both the enzymes; however, their mode of action was competitive for urease and mixed-type, preferentially competitive for tyrosinase enzyme. Like *in vitro* activity, ceftriaxone sodium and cefotaxime sodium docking analysis showed their considerable binding affinity and significant interactions with both urease and tyrosinase enzymes sufficient for downstream signaling responsible for observed enzyme inhibition *in vitro*, purposing them as potent candidates to control enzyme-rooted obstructions in future.

1. Introduction

The cephalosporins are common antibiotics prescribed in routine for broad range of infections. Lesser toxic and allergic threats along with wide action spectrum make them popular [1]. They possess β-lactam ringed structure similar to penicillin. This interferes with the synthesis of bacterial cell wall showing significant antibacterial properties. Guiseooe Brotzu, Italian scientist, isolated cephalosporin compounds from Cephalosporium acremonium cultures in 1948 [2]. They are classified generation wise, lower generations possess strong activity against gram-positive bacteria, and higher generations possess more activity against gram-negative bacteria; however, cefepime from fourth generation possesses both gram-positive activity (equivalent to first generation) and gram-negative activity (equivalent to third generation) [3]. Third generation cephalosporins are active against gram-negative rods, especially Enterobacter and multiple resistant strains. They are proven helpful in controlling hospital-acquired infections including bacteremia and pneumonia [2]. For present study, eleven drugs from cephalosporin class with single active compound, cefpodoxime proxetil, ceftazidime, cefepime, ceftriaxone sodium, cefaclor, cefotaxime sodium, cefixime trihydrate, cephalexin, cefadroxil, cephradine, and cefuroxime, were purchased aiming

to explore their potential against biologically important two enzymes, urease and tyrosinase.

Urease, a nickel-dependent thiol-rich metalloenzyme is responsible for ammonia and carbamate formation from urea [4]. It is usually present in bacteria, fungi, algae, plants, and invertebrates. It is also present in soil as a soil enzyme [5]. The important components of ureases for catalytic activity are Ni^{2+} ions and the sulfhydryl group (especially the cysteinyl residues in the active site). An important virulence factor of many bacterial species including *Klebsiella pneumoniae*, *Proteus mirabilis*, *Salmonella* species, *Staphylococcus* species, and *Ureaplasma urealyticum* is their ureolytic activity. It is associated with pathogenesis of certain medical conditions, i.e., hepatic coma, pyelonephritis, urinary stone formation, and peptic ulceration [6, 7]. Increased pH (up to 9.2) during hydrolyses of urea is observed [6]. Thus, urease activity helps bacteria to adjust pH allowing them to survive even in originally low pH of stomach causing stomach cancer and peptic ulcers during colonization [8]. Hence, urease inhibitors are the first-line strategy to control infections caused by urease-producing microorganisms.

Tyrosinase, our second study enzyme, is associated with melanin synthesis responsible for hair and skin colour [9, 10]. Melanin is formed from L-tyrosine conversion into 3,4-dihydroxyphenylalanine (L-DOPA) which oxidizes to produce dopaquinone [11]. Thus, the tyrosinase enzyme regulates the melanin content which protects skin from UV radiations and sun burn. However, its overexpression results in hyperpigmentation causing dermatological disorders, i.e., melisma and age spots [12]. Moreover, neuromelanin in the brain and neurodegeneration are known to be linked with Parkinson's disease [13]. Tyrosinase induction produces reactive oxygen species known to cause neurotoxicity [14]. Thus, discovery of tyrosinase inhibitors is important for tyrosinase control and treatment of melanin-related skin complications [15, 16]. Although many tyrosinase inhibitors are identified however, their toxic effects prohibit their commercialization, indicating the need to search new safe and effective alternatives.

Thus, the focus of study is to use already existing safety proven drugs to explore their new therapeutic targets, an effective strategy which not only allow to maximize the use of drug's potential but also help to reduce evaluation time, cost, and risk of failure. Thus, eleven cephalosporin drugs were selected to evaluate their potential against two medically important enzymes. Later, kinetic study of two most potent drugs was executed and evaluated their kinetic parameters and inhibition constants to explore their mechanism of enzyme inhibition. Moreover, a plot among remaining enzyme activity versus various concentrations of respective enzymes in the presence of selected drugs was devised as determinant of reversible or irreversible behaviour of enzyme inhibition. Finally, docking study identifying the binding pattern of drug with enzyme which is important for observed enzyme inhibition was executed.

2. Materials and Methods

2.1. Chemicals. Enzymes, mushroom tyrosinase, and urease were purchased from Sigma. Eleven drugs from cephalosporin class were purchased from local pharmacy, and their active ingredients were summarized in Table 1 and Figure S1 with formula [17–27]. To prepare stock, ground powder was weighted to directly dissolve in DMSO. All items were stored in recommended conditions with shelf life of safe use till all evaluations.

2.2. Urease Inhibitory Assay. To evaluate the urease enzyme activity, assay described by Weatherburn 1967 was performed [28]. In 96-well plate, $10\,\mu l$ of enzyme (jack bean urease, 5 U/ml), $40\,\mu l$ buffer (100 mM urea, 0.01 M K2HPO4, 1 mM EDTA, and 0.01 M LiCl2, pH 8.2), and $20\,\mu l$ of test drug were loaded. Following 15 min incubation at 37°C, $40\,\mu l$ of alkali reagent (0.5%, w/v NaOH and 0.1% active chloride NaOCl) and $40\,\mu l$ of phenol reagents (1%, w/v phenol and 0.005%, w/v sodium nitroprusside) were added. After 35 min incubation at room temperature (RT), OD625 nm was tracked to calculate IC50 values to compare the test drugs result with standard named thiourea.

2.3. Tyrosinase Inhibitory Assay. To evaluate tyrosinase inhibition, assay was performed as described previously [29]. Reaction was started by loading $140\,\mu l$ of phosphate buffer (20 mM, pH 6.8), $20\,\mu l$ of mushroom tyrosinase (30 U/ml), and $20\,\mu l$ of test drug in 96-well plate. After 10 min incubation at RT, $20\,\mu l$ (0.85 mM) L-DOPA (3,4-dihydroxyphenylalanine) was added and incubated again for 20 min at RT. Then, OD475 nm was determined as measure of dopachrome formation by plate reader (BioTek, Elx 800). Kojic acid was used as standard inhibitor for reference. For clear statistical analysis, experiments were performed twice in duplet. First percentage inhibition was determined and then IC50 was calculated using Microsoft excel, and the test drug results were compared with standard.

2.4. Study of Enzyme Kinetics. To evaluate the type of enzyme inhibition, series of kinetic experiments were performed using 2 most active drugs against both enzymes, urease and tyrosinase, following methods reported previously [29, 30]. To this end, the Lineweaver-Burk plots of 1/absorbance versus 1/urea and 1/absorbance versus 1/L-DOPA were plotted. In all kinetic studies, drug concentrations (as indicated in Lineweaver-Burk plot) and respective substrates, urea in buffer (0.063 to 2 mM) for urease and L-DOPA (0.06 to 2 mM) for tyrosinase, were added and plates were incubated for 10 min at 37°C. Later, respective enzymes were added in plates and absorbance (wavelengths same as above) was monitored for 5 min with 1 min interval. The Lineweaver-Burk plot showing type of enzyme inhibition was plotted as inverse of velocities (1/V) versus inverse of substrate concentration 1/[S] Mm^{-1}. Later, inhibition constant (Ki) was evaluated by both the Dixon plot and from Lineweaver-Burk plot, by secondary replot of slope versus concentrations of inhibitor.

2.5. Inhibition Mechanism of Potential Inhibitor. The inhibitory mechanism of both the enzymes, urease and tyrosinase, was determined with two most active drugs following Tahir et al. and Ali et al. [30, 31]. To this end, a plot among remaining enzyme activity versus various concentrations of respective enzymes in the presence of drug concentrations

(as indicated in graph) was devised as determinant of reversible or irreversible behaviour of enzyme inhibition.

2.6. In Silico Study: Repossession of Jack Bean Urease and Mushroom Tyrosinase from PDB.

The crystal structures of jack bean urease and mushroom tyrosinase were retrieved from the Protein Data Bank (PDB) having PDBIDs 4H9M and PDBID 2Y9X (http://www.rcsb.org/), respectively. Furthermore, energy minimization of target, stereochemical properties, Ramachandran graph, and values of urease and mushroom tyrosinase were explored [32, 33].

Moreover, to access architecture of study proteins and occurrence of α-helices, β-sheet and coil tool called VADAR 1.8 was used (http://vadar.wishartlab.com/).

2.7. Designing of Ligands and Molecular Docking Simulation Using Autodock.

The drug molecules cefpodoxime proxetil, ceftazidime, cefepime, ceftriaxone sodium, cefaclor, cefotaxime sodium, cefixime trihydrate, cephalexin, cefadroxil, cephradine, and cefuroxime were sketched in drawing ACD/ChemSketch tool and further minimized by visualizing software UCSF Chimera 1.10.1. PyRx docking tool was used to perform molecular docking experiment for the ligands against urease and tyrosinase enzymes [34]. The grid box center values of urease were adjusted as center_ $X = 18.0279$, $Y = -57.332$ and $Z = -18.5254$, and for tyrosinase, it was fixed as center_ $X = -12.385$, $Y = -18.7636$, and $Z = -46.7393$, respectively, for better conformational position in the active region of target proteins. The selected drugs were docked with default exhaustiveness value = 8, and resultant complexes were evaluated on the basis of lowest binding energy (Kcal/mol) and structure activity relationship (SAR). The three-dimensional (3D) graphical depictions of all the docked complexes were accomplished by Discovery Studio (2.1.0) (https://discover.3ds.com/discovery-studio-visualizer-download) and UCSF Chimera 1.10.1 [32].

3. Results and Discussion

In present study, we selected eleven antibiotics from cephalosporin family aiming to maximize the use of their potential for multiple applications with inherited safety advantages and rooting out their new biological targets such as enzymes, urease and tyrosinase, with possible inhibition mechanism eventually proposing effective and safe alternative for the management of enzyme-associated medical obstructions.

Our results confirmed that drugs with active ingredients, cefpodoxime proxetil, ceftazidime, cefepime, ceftriaxone sodium, cefaclor, cefotaxime sodium, cefixime trihydrate, cephalexin, cefadroxil, cephradine, and cefuroxime, showed excellent activity against urease and tyrosinase enzymes with 50% inhibitory concentration (IC50) ranging from 0.06 ± 0.004 to 0.22 ± 0.006 mM and 0.01 ± 0.0005 to 0.12 ± 0.017 mM, respectively. Urease activity of all drugs was noted lower than positive control thiourea (IC50 = 0.019 ± 0.002 mM); however, tyrosinase activity of all drugs outperforms the positive controls: hydroquinone (IC50 = 0.18 ± 0.02 mM). Cefotaxime sodium and ceftriaxone sodium showed lower IC50 among all test drugs for both urease (IC50 = 0.06 and 0.08 mM, respectively) and for tyrosinase (IC50 = 0.01 and 0.03 mM, respectively).

In other words, ceftriaxone sodium and cefotaxime sodium showed 18 and 6 times better tyrosinase activity than standards hydroquinone.

In biological reactions, enzymes play key role and therefore are considered attractive target in disease control [31, 35]. Likewise tyrosinase, being the rate-limiting player in darkening of skin and fruits, its inhibition is desirable both in cosmetics and food industry. Multiple depigmenting agents called inhibitors such as arbutin [36], azelaic acid [37], retinoids [38], ascorbic acid derivatives [39], kojic acid [40], and hydroquinone [41] are known. However, unwanted side effects including cytotoxicity are observed from many well-known whitening agents such as hydroquinone and kojic acid which minimizes their use. Interestingly, all tested drugs showed activity; however, cefotaxime sodium and ceftriaxone sodium showed multifold better tyrosinase inhibitory effect than standard hydroquinone. Thus, to understand the mechanism of observed enzyme inhibition, study of enzyme kinetics was performed.

3.1. Mechanism of Urease Enzyme Kinetics.

To understand the mechanism of urease inhibition, series of kinetic experiments against two most active drugs, cefotaxime sodium and ceftriaxone sodium, were performed and the respective Lineweaver-Burk and Dixon plots were generated (Figures 1(a1) and 1(a2)). The Lineweaver-Burk plots, $1/V$ versus $1/[S]$, follows Michaelis-Menten kinetics and showed that both drugs behave as competitive inhibitor since increase in their concentration produced a family of straight lines with a common intercept on the ordinate but with different slopes [42]. To obtain insightful pathway, binding affinities of EI and ESI complexes were determined. Analysis revealed competitive mode of urease inhibition (Figures 1(a1) and 1(a2)). The secondary replots of slope versus drug concentration and secondary replots of intercept versus drugs concentration showed EI dissociation constant (Ki) (Figures 1(b1) and 1(b2)) and ESI dissociation constant (Ki') (Figures 1(c1) and 1(c2)). The Ki values for cefotaxime sodium and ceftriaxone sodium were calculated 0.12 and 0.7 mM, respectively, by both the Dixon plot and secondary replot from the Lineweaver-Burk plot of slope. However, Ki' values, 30 mM (cefotaxime sodium) and 6 mM (ceftriaxone sodium), were determined by secondary replot of the Lineweaver-Burk plot of intercept. Comparison showed less Ki compared to Ki' values indicating stronger binding between enzyme and drug [43] justifying preferred competitive mode of inhibition.

3.2. The Inhibitory Effect of Drugs on Urea Hydrolysis Activity of Urease.

To further understand the urease reversible or irreversible inhibitory behaviour by ceftriaxone sodium and cefotaxime sodium, experiments were performed as described in Materials and Methods.

Plots among enzyme activity versus the concentration of enzyme (0.44, 0.88, 1.75, 3.5, 7, and 14 μg/ml) in the presence of drugs produced a group of straight lines (Figure 2). These parallel straight lines with the same slopes indicate irreversible urease inhibition [44, 45]. Thus, our both drugs, ceftriaxone sodium and cefotaxime sodium, are shown to bind effectively with urease active site to inhibit irreversibly.

TABLE 1: Enzyme activity of test drugs and docking energy values.

Selected drugs	Jack bean urease inhibition	Mushroom Tyrosinase inhibition	Jack bean urease docking energy	Mushroom Tyrosinase docking energy
	IC50 ± SEM (mM)		(Kcal/mol)	
Cefpodoxime proxetil	0.1 ± 0.014	0.05 ± 0.0003	-5.10	-5.40
Ceftazidime	0.091 ± 0.007	0.11 ± 0.005	-7.50	-7.90
Cefepime	0.19 ± 0.037	0.09 ± 0.006	-7.50	-8.90
Ceftriaxone sodium	0.08 ± 0.004	0.01 ± 0.0005	-7.90	-8.40
Cefaclor	0.17 ± 0.016	0.03 ± 0.005	-7.20	-7.00
Cefotaxime sodium	0.06 ± 0.004	0.03 ± 0.002	-7.50	-7.60
Cefixime trihydrate	0.18 ± 0.014	0.04 ± 0.002	-6.50	-80
Cephalexin	0.37 ± 0.046	0.12 ± 0.017	-6.30	-7.60
Cefadroxil	0.22 ± 0.006	0.03 ± 0.003	-7.20	-7.70
Cephradine	0.12 ± 0.009	0.07 ± 0.006	-6.50	-6.30
Cefuroxime	0.18 ± 0.009	0.07 ± 0.009	-6.20	-7.10
Standard	0.019 ± 0.002 Thiourea	0.18 ± 0.02 Hydroquinone	—	—

3.3. Mechanism of Tyrosinase Enzyme Kinetics. The mode of tyrosinase inhibition against two most active drugs, ceftriaxone sodium and cefotaxime sodium was determined by tracking oxidation of L-DOPA through the Lineweaver-Burk and Dixon plots. In the Lineweaver-Burk plots, $1/V$ versus $1/[S]$ produced a family of different straight slopes (Figures 3(a1) and 3(a2)). Evaluation showed that $Vmax$ reduces with Km shift and increasing concentrations of ceftriaxone sodium and cefotaxime sodium, revealing their mixed type inhibitory behaviour. This means that drugs can interact with free enzyme (E) and enzyme-substrate (ES) complex [46]. To obtain insightful pathway, binding affinities of EI and ESI complexes were determined. The secondary replots for EI dissociation constant (Ki) (Figures 3(b1) and 3(b2)) and ESI dissociation constant (Ki') (Figures 3(c1) and 3(c2)) extracted. The values of Ki and Ki' were calculated as 0.1 and 0.6 mM (ceftriaxone sodium) and 0.07 and 0.8 mM (cefotaxime sodium), respectively. Comparison showed less Ki compared to Ki' values indicating stronger binding between enzyme and drug [43] that indicate preferentially competitive in mixed type mode of enzyme inhibition.

3.4. The Inhibitory Effect of Drugs on Diphenolase Activity of Tyrosinase. To explore mechanism further and tyrosinase reversible or irreversible inhibitory behaviour, diphenolase activity of both drugs ceftriaxone sodium and cefotaxime sodium was performed. Plots among enzyme activity versus the concentration of enzyme (0.44, 0.88, 1.75, 3.5, 7, and 14 μg/ml) in the presence of different concentrations of drugs a family of straight lines were generated (Figure 4). The parallel straight lines with the same slopes indicate irreversible mode of enzyme inhibition [44, 45]. Thus, like urease, both the most potent drugs, ceftriaxone sodium and cefotaxime sodium ,were irreversible inhibitors of mushroom tyrosinase for oxidation of L-DOPA.

3.5. Structural Assessment of Target Proteins. Urease (Jack bean) have tetra domains with different numbers of residues. Among all, the most important is the domain four due to presence of binding pocket and its catalytic behaviour. It consists 27% α-helices, 31% β-sheets, and 41% coils. The Ramachandran plots showed occurrence of 97.5% residues in favored regions evolving phi (φ) and psi (ψ) angle's good precision among the coordinates of jack bean urease structure (Figure S2).

Second enzyme, mushroom tyrosinase oxidoreductase copper, contains enzyme consisting of 391 amino acids with structural contribution of 39% α-helices (154 residues), 14% β-sheet (57 residues), and 46% coil (180 residues). Its resolution 2.78 Å, R value 0.238, and unit cell length as $a = 103.84$, $b = 104.82$, and $c = 119.36$ with angles 90°, 110.45°, and 90° for all α, β, and γ dimensions were observed, respectively. The Ramachandran plots verified the occurrence of 95.90% residues in favored and 100.0% residues in allowed regions. The Ramachandran graph displayed good accuracy of phi (φ) and psi (ψ) angles among the coordinates of receptor molecules and most of residues plummeted in acceptable region (Figure S2).

3.6. Molecular Docking Analysis. The docked complexes of cefpodoxime proxetil, ceftazidime, cefepime, ceftriaxone sodium, cefaclor, cefotaxime sodium, cefixime trihydrate, cephalexin, cefadroxil, cephradine, and cefuroxime against study enzymes were evaluated based on minimum energy values (Kcal/mol) and ligand interactions pattern. The docking energy values of jack bean urease and mushroom tyrosinase docked complexes have been tabulated in Table 1.

3.6.1. Binding Analyses of Drugs against Jack Bean Urease. Ceftriaxone sodium: the ligand-protein binding analyses showed that ceftriaxone sodium confined in the active binding pocket
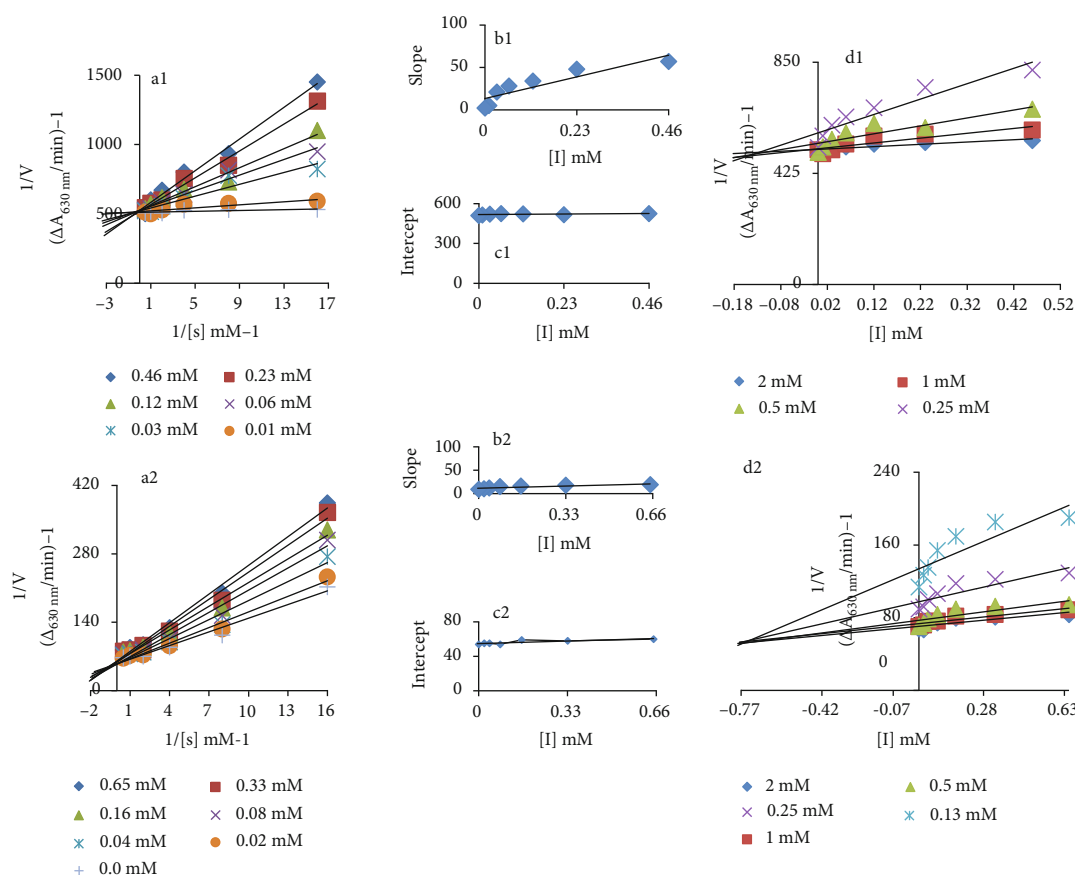
FIGURE 1: (a1 and a2) Lineweaver-Burk plot for inhibition of urease enzyme in the presence of cefotaxime sodium and ceftriaxone sodium. The cefotaxime sodium concentrations 0, 0.01, 0.03, 0.06, 0.12, 0.23, and 0.46 mM and ceftriaxone sodium concentrations 0, 0.02, 0.04, 0.08, 0.16, 0.33, and 0.65 mM; however, urea concentrations ranging from 0.13 to 2 mM were used. (b1 and b2) The insets represent the plot of the slope from the Lineweaver-Burk plot versus inhibitor. (c1 and c2) The secondary replot of the Lineweaver-Burk plot, 1/V (y-intercept) of (a) versus various concentrations of inhibitor. (d1 and d2) The Dixon plot of the reciprocal of the initial velocities versus various concentrations of inhibitor.

of target protein as mentioned in Figures 5(a) and 5(b). The results of ceftriaxone sodium-jack bean urease docked complex showed nine hydrogen bonds. The oxygen atoms of ceftriaxone sodium form hydrogen bond against Arg439 with bonds length 2.76 Å and 3.26 Å, respectively; moreover, the nitrogen atom of drug forms hydrogen bond with Ala636 with the bond distance 3.26 Å. Two oxygen atoms and one nitrogen atom of ceftriaxone sodium make hydrogen bond with Gln635 having bond lengths 3.04 Å, 2.63 Å, and -2.64 Å, respectively. Another hydrogen atom of drug forms hydrogen bond with Gly638 with bond length of 2.75 Å, and two other oxygen atoms form hydrogen bond with Val640 with bond length 2.11 Å and 2.31 Å, respectively.

Cefotaxime sodium: cefotaxime sodium also found to confine in urease active region as mentioned in Figures 5(c) and 5(d). The results of cefotaxime sodium-jack bean urease docked complex showed that five hydrogen bonds depict the stability of drug against target protein. The two hydrogen atoms of cefotaxime sodium formed hydrogen bond against CME592 with bond length 2.44 Å and 1.82 Å, respectively. Another hydrogen was also observed between hydrogen atom

and Ala440 with bond length 3.07 Å. Moreover, oxygen and nitrogen atoms of cefotaxime sodium also formed hydrogen bond with His593 and His519 with bond distances 2.81 Å and 3.05 Å, respectively. The other 2D depiction of urease is shown in Figure S3. The predicted results showed good correlation with published research data which strengthens our work and efficacy [47–49].

3.6.2. Binding Analyses of Drugs against Mushroom Tyrosinase. Ceftriaxone sodium: the binding analyses of ceftriaxone sodium showed that it was confined in the active binding pocket of tyrosinase as indicated (Figures 6(a) and 6(b)). Ceftriaxone sodium-mushroom tyrosinase docked complex showed 5 hydrogen bonds. The oxygen atom of ceftriaxone sodium forms hydrogen bond against Asn81 with bond length 2.94 Å, and the nitrogen and oxygen atoms formed hydrogen bonds with His85 with the bond length of 2.47 Å and 1.97 Å, respectively. Moreover, hydrogen atom of ceftriaxone sodium formed hydrogen bond with Glu322 with bond length of 2.70 Å. Similarly, another oxygen atom of ceftriaxone sodium forms hydrogen bond with Val248 with bond length of 2.70 Å. This shows
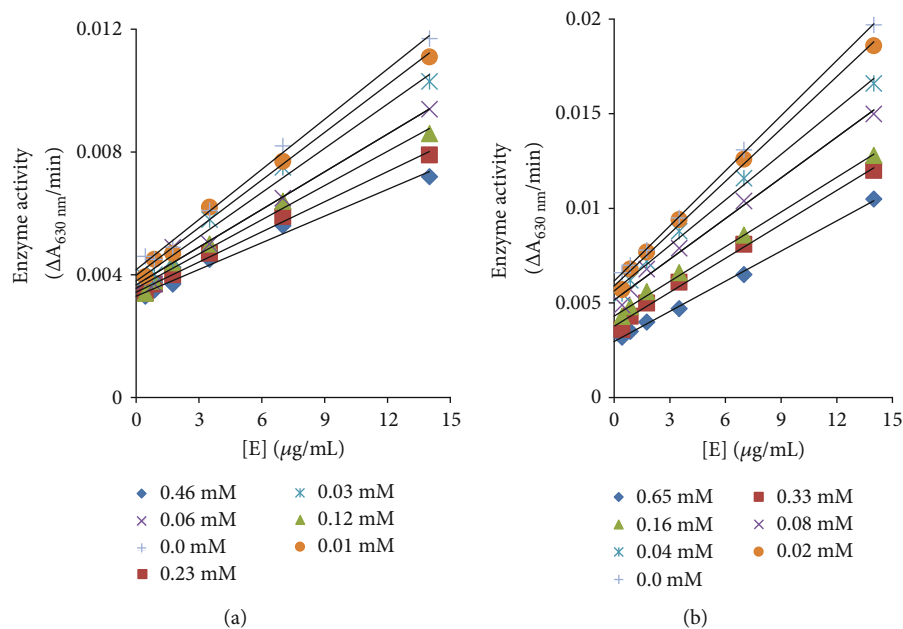
FIGURE 2: Catalytic activity relationship of urease and various concentrations of (a) cefotaxime sodium and (b) ceftriaxone sodium.

good commitment with previous literature [50–52]. Cefotaxime sodium: the ligand-protein binding analyses showed that cefotaxime sodium confined in the active binding pocket of target protein as mentioned in Figures 6(c) and 6(d). The results of cefotaxime sodium-mushroom tyrosinase docked complex showed that 2 hydrogen bonds were observed. An oxygen atom form hydrogen bond with His244 with bond length of 2.97 Å and the nitrogen atom of compound form hydrogen atom with Glu322 with bond length of 2.58 Å. The other 2D depiction of tyrosinase is shown in Figure S3. Our docking results show good correlation with published research which strengthens our work and efficacy [47, 53]. The deep interaction profiles of drugs against urease and mushroom tyrosinase clearly depicted the significance of drugs in the enzyme activity. The binding pocket residues are more important and active key players in the activation of signaling pathways [54]. In our predicted results, drugs directly interact with active site residues of both urease and mushroom tyrosinase which depicts that binding of drugs may affect the activity of enzymes and showed good correlation with *in vitro* results.

Furthermore, rest of all drugs-docking complexes have been mentioned in supporting data. Moreover, Figure S3 confirms drugs binding with urease enzyme through various amino acids; cefaclor interacts through Glu642, Gln649, Arg646, and Phe840, cefadroxil interacts through His492, His519, His593, and Arg439, cefepime interacts through Arg439, Met637, and Asp633, cefixime trihydrate interacts through His519, His492, Ala440, Arg609, and Ala636, cefpodoxime proxetil interacts through Arg439, Asp494, and Met588, and ceftazidime interacts through Ala636 and Arg439; cefuroxime interacts through Leu833, Ser579, Thr578, Arg646, and Phe838; cephalexin interacts through Arg646, Ser645, Thr581, and Phe838; cephradine interacts through Arg639, Arg646, and Glu584. Likewise, Figure S4 represents drugs binding with

tyrosinase enzyme through various amino acids; cefaclor interacts through Asn260, Val283, His244, and Ala286; cefadroxil interacts through His244, His85, Met280, and His263; cefepime interacts through Ala80, Asn81, and His244; cefixime trihydrate interacts through A323, Asn81, His244, and Cys83; cefpodoxime proxetil interacts through Met319, Arg321, His244, Gly86, and Val248; ceftazidime interacts through Asn81, Cys83, His85, Glu322, Val283, and Ala286; cefuroxime interacts through Glu103, Pro329, Cys83, Asn81, and His85; cephalexin interacts through Val283, Asn81, and His85; cephradine interacts through Val283, His244, Ala323, and Asn81. Based on the results, it has been observed that both ceftriaxone sodium and cefotaxime sodium showed highest urease and tyrosinase inhibition, interestingly outperforming tyrosinase positive control, hydroquinone proposing them potential candidates to control enzyme-rooted irregularities in future.

3.7. Structure Activity Relationship (SAR) Analysis. The SAR is the relationship between the chemical structure having different incorporated functional groups (Figure S1) and its biological activities against different enzymes. The cefotaxime sodium, cefixime trihydrate, and cefpodoxime proxetil have basically the same skeleton with different functional groups. Similarly, the other drugs ceftriaxone sodium, cefepime, and ceftazidime correlate with each other in terms of basic structure. Cefaclor, cefadroxil, and cefuroxime are the same, while cephalexin resembles with cephradine. The different drugs showed different inhibition behaviour and docking energy values. All the compounds have potential to block the entry of substrate by binding to amino acid residues lying at the pocket domain. The enzyme/inhibitor complexes are stabilized by number of different interactions such as H-bonding, π-sigma interactions, π-alkyl interactions, π-anion/cation sulphur interactions, polar
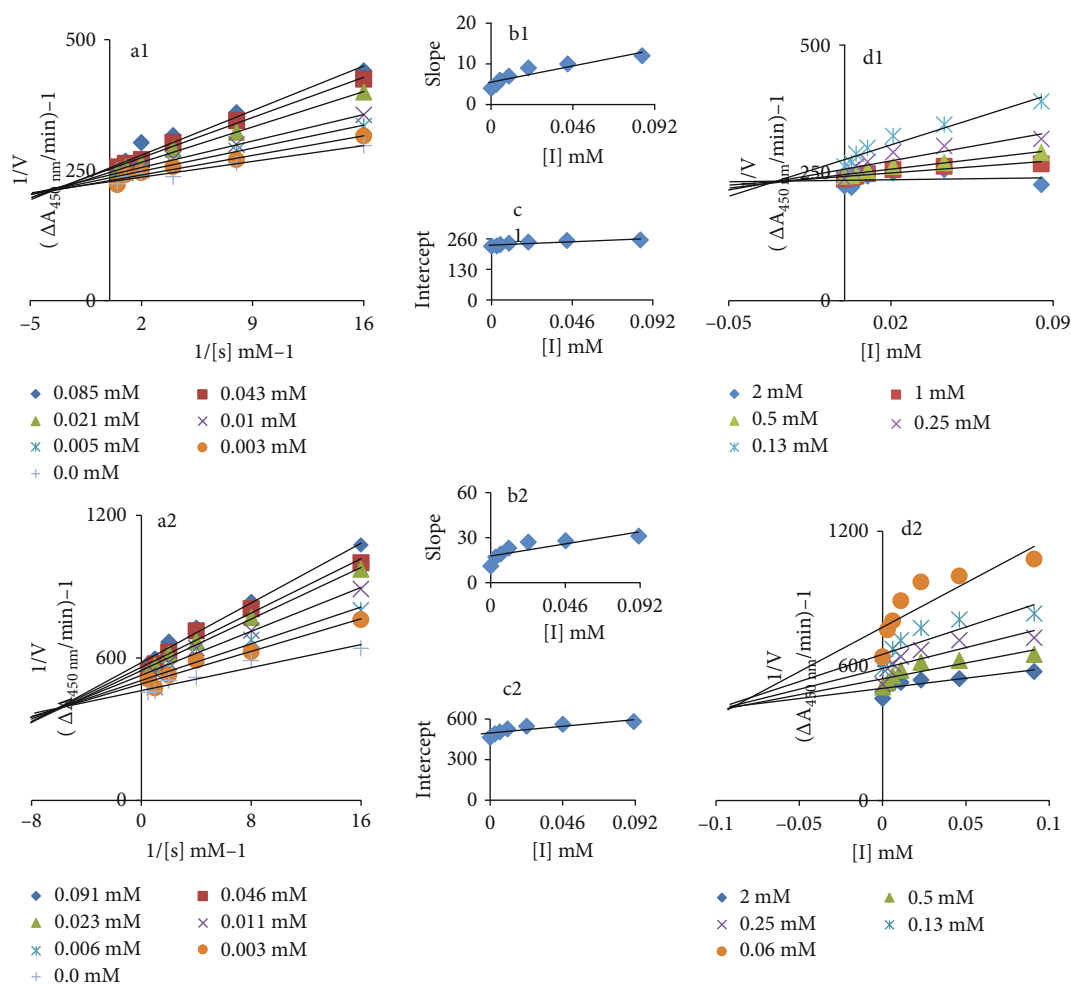
FIGURE 3: (a1 and a2) Lineweaver-Burk plot for inhibition of tyrosinase enzyme in the presence of cefotaxime sodium and ceftriaxone sodium. The cefotaxime sodium concentrations 0, 0.008, 0.02, 0.03, 0.07, 0.14, and 0.27 mM and ceftriaxone sodium concentrations 0, 0.003, 0.006, 0.011, 0.023, 0.046, and 0.091 mM; however, L-DOPA concentrations ranging 0.06 to 2 mM were used. (b1 and b2) The insets represent the plot of the slope from the Lineweaver-Burk plot versus inhibitor. (c1 and c2) The secondary replot of the Lineweaver-Burk plot, 1/V (y-intercept) of (a) versus various concentrations of inhibitor. (d1 and d2) The Dixon plot of the reciprocal of the initial velocities versus various concentrations of inhibitor.

interactions, stacking, and metal-ligand interactions. We discuss the binding mode of two most active compounds (ceftriaxone sodium and cefotaxime sodium) and compare their interactions with the standard ligands. Figures 5 and 6 illustrate the relative positioning of ceftriaxone sodium and cefotaxime sodium in their most stable conformation with minimal energy in the active site of target. Different binding interactions were observed for ceftriaxone sodium and cefotaxime sodium due to structural differences and presence of an additional sodium citrate group in both the drugs. The ceftriaxone sodium showed good inhibition values 0.08 ± 0.004 and 0.01 ± 0.0005 (mM) with binding affinity -7.90 and -8.40 (Kcal/mol) as compared to other selected drugs (Table 1). Ceftriaxone sodium is bulky molecule containing dioxone group at one end and cyclopentane attached with amino group at another end. Moreover, sodium citrate moiety was present at the central region with benzene ring. Similarly,

cefpodoxime proxetil is also a bulky structure composed different moieties such as isopropoxide, couple of methoxy and amino groups at neighboring ends which gave inhibition and docking values against urease (0.1 ± 0.014; -5.10) and mushroom tyrosinase (0.05 ± 0.0003; -5.40), respectively. Both ceftazidime and cefepime possessed acetate ions and amino group which reveals closely related inhibition and docking energy values against urease (0.091 ± 0.007; -7.50 and 0.09 ± 0.006; -7.50) and tyrosinase (0.11 ± 0.005; -7.90 and 0.19 ± 0.037; -8.90). In comparison with all other drugs, most of compounds possessed similar basic skeleton with different functional groups at different positions which depicted different inhibition and docking values against both urease and mushroom tyrosinase, respectively. Therefore, due to the presence of different functional groups in different drugs, it showed different inhibition values and binding affinities (Table 1).

(a)

(b)
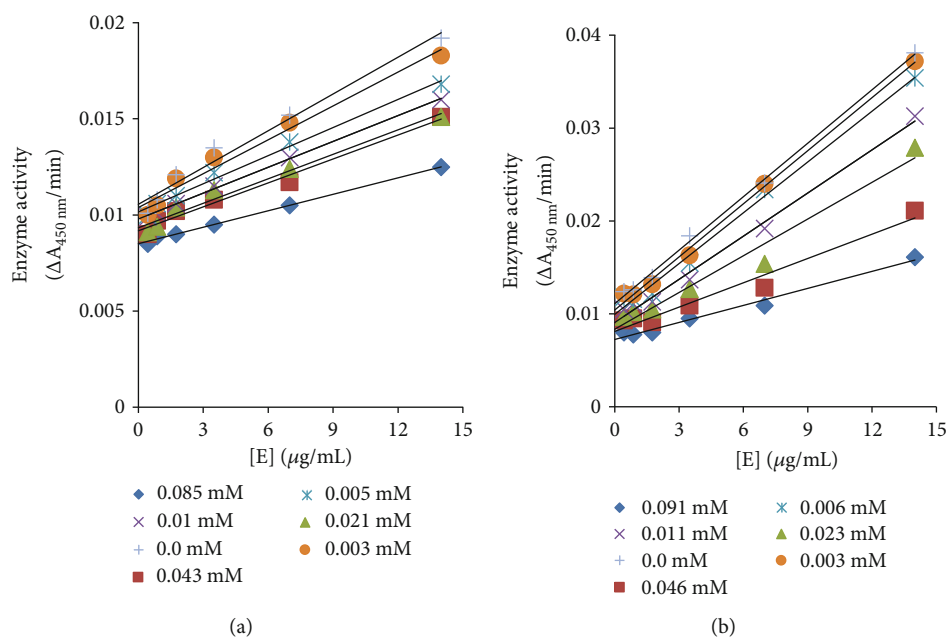
FIGURE 4: Catalytic activity relationship of tyrosinase and various concentrations of (a) cefotaxime sodium and (b) ceftriaxone sodium.

(a)

(b)

(c)

(d)
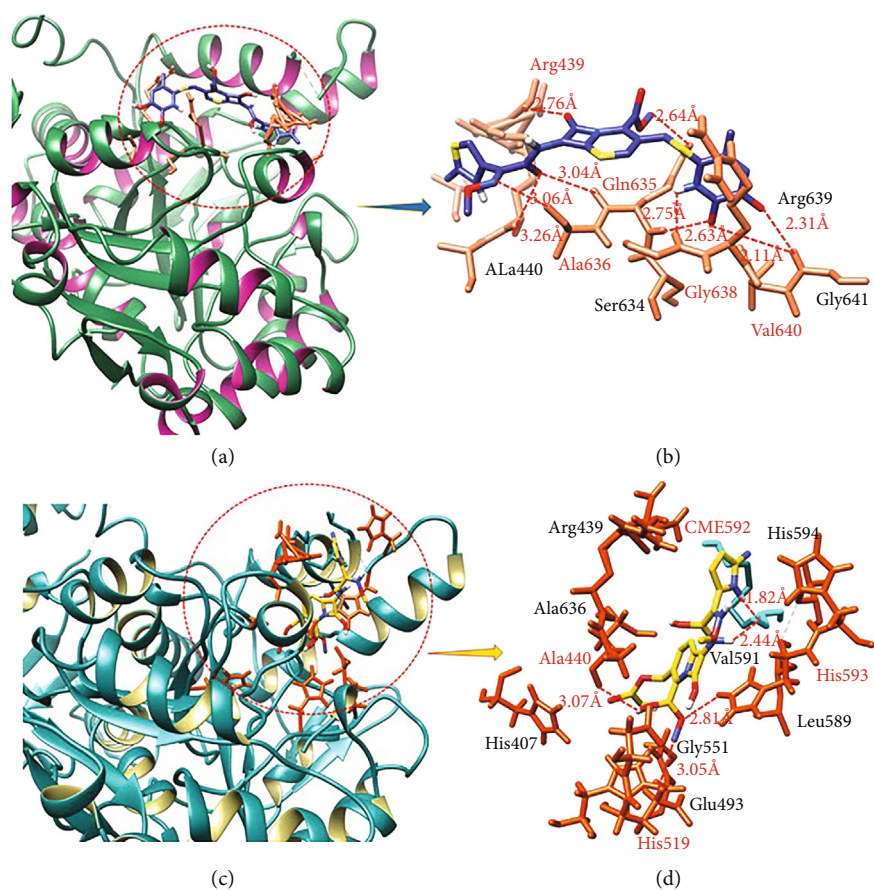
FIGURE 5: Ceftriaxone sodium (a and b) and cefotaxime sodium (c and d) binding analysis against urease.
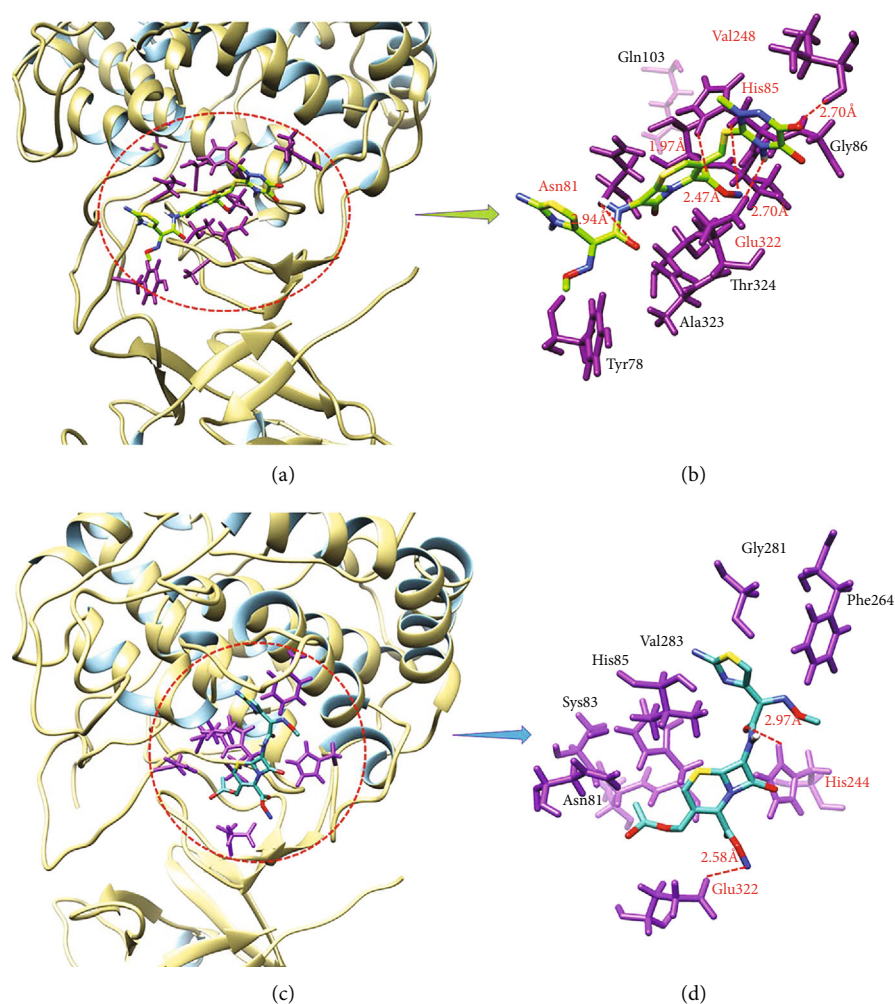
FIGURE 6: Ceftriaxone sodium (a and b) and cefotaxime sodium (c and d) binding analysis with tyrosinase.

4. Conclusion

In present study, eleven cephalosporin drugs with single active ingredient were evaluated and found to inhibit medically important both the enzymes, urease and tyrosinase *in vitro*. All drugs outperform the positive control: hydroquinone for tyrosinase activity. The kinetic analysis of most active drugs, ceftriaxone sodium and cefotaxime sodium, revealed that they bind irreversibly with both enzymes; however, their mode of action was competitive for urease and mixed-type, preferentially competitive for tyrosinase enzyme. In addition, docking study showed their significant bonding with both urease and tyrosinase enzymes purposing them potent candidates to control enzyme-rooted complications in future.

Data Availability

The data used to support the findings of this study are included within the supplementary information file(s).

Conflicts of Interest

Authors show no conflict of interest.

Acknowledgments

Supplementary Materials

Figure S1: chemical structures of test drugs and resemblance of their basic inner structure and different functional groups at different locations. Figure S2: Ramachandran graph of (a) jack

bean urease and (b) mushroom tyrosinase. Figure S3: 2D docking of test drugs with urease enzyme. Figure S4: 2D docking of test drugs with tyrosinase enzyme. *(Supplementary Materials)*

References

[1] S. J. Dancer, "The problem with cephalosporins," *Journal of Antimicrobial Chemotherapy*, vol. 48, no. 4, pp. 463–478, 2001.

[2] M. Jawetz and Adelberg, *Medical Microbiology*, McGraw Hill, New York, 23rd edition, 2004.

[3] C. J. Harrison and D. Bratcher, "Cephalosporins: a review," *Pediatrics in Review*, vol. 29, no. 8, pp. 264–273, 2008.

[4] N. E. Dixon, C. Gazzola, J. J. Watters, R. L. Blakeley, and B. Zerner, "Inhibition of jack bean urease (EC 3.5.1.5) by acetohydroxamic acid and by phosphoramidate. equivalent weight for urease," *Journal of the American Chemical Society*, vol. 97, no. 14, pp. 4130-4131, 1975.

[5] B. Krajewska, "Ureases I. Functional, catalytic and kinetic properties: a review," *Journal of Molecular Catalysis B: Enzymatic*, vol. 59, no. 1-3, pp. 9–21, 2009.

[6] R. A. Burne and Y. Y. M. Chen, "Bacterial ureases in infectious diseases," *Microbes and Infection*, vol. 2, no. 5, pp. 533–542, 2000.

[7] B. Krajewska and W. Zaborska, "Jack bean urease: the effect of active-site binding inhibitors on the reactivity of enzyme thiol groups," *Bioorganic Chemistry*, vol. 35, no. 5, pp. 355–365, 2007.

[8] A. Covacci, J. L. Telford, G. Del Giudice, J. Parsonnet, and R. Rappuoli, "*Helicobacter pylori* virulence and genetic geography," *Science*, vol. 284, no. 5418, pp. 1328–1333, 1999.

[9] S. M. Lee, Y. S. Chen, C. C. Lin, and K. H. Chen, "Hair dyes resorcinol and lawsone reduce production of melanin in melanoma cells by tyrosinase activity inhibition and decreasing tyrosinase and microphthalmia-associated transcription factor (MITF) expression," *International Journal of Molecular Sciences*, vol. 16, no. 1, pp. 1495–1508, 2015.

[10] Z. C. Li, L. H. Chen, X. J. Yu et al., "Inhibition kinetics of chlorobenzaldehyde thiosemicarbazones on mushroom tyrosinase," *Journal of Agricultural and Food Chemistry*, vol. 58, no. 23, pp. 12537–12540, 2010.

[11] N. Ai, W. J. Welsh, U. Santhanam, H. Hu, and J. Lyga, "Novel virtual screening approach for the discovery of human tyrosinase inhibitors," *PLoS One*, vol. 9, no. 11, p. e112788, 2014.

[12] Y. Wang, G. Zhang, J. Yan, and D. Gong, "Inhibitory effect of morin on tyrosinase: insights from spectroscopic and molecular docking studies," *Food Chemistry*, vol. 163, pp. 226–233, 2014.

[13] K. I. Nihei, Y. Yamagiwa, T. Kamikawa, and I. Kubo, "2-Hydroxy-4- isopropylbenzaldehyde, a potent partial tyrosinase inhibitor," *Bioorganic & Medicinal Chemistry Letters*, vol. 14, no. 3, pp. 681–683, 2004.

[14] T. Hasegawa, A. Treis, N. Patenge, F. C. Fiesel, W. Springer, and P. J. Kahle, "Parkin protects against tyrosinase mediated dopamine neurotoxicity by suppressing stress activated protein kinase pathways," *Journal of Neurochemistry*, vol. 105, no. 5, pp. 1700–1715, 2008.

[15] C. F. Chan, C. C. Huang, M. Y. Lee, and Y. S. Lin, "Fermented broth in tyrosinase- and melanogenesis inhibition," *Molecules*, vol. 19, no. 9, pp. 13122–13135, 2014.

[16] X. X. Huang, Q. B. Liu, J. Wu et al., "Antioxidant and tyrosinase inhibitory effects of neolignan glycosides from Crataegus

[17] pinnatifida seeds," *Planta Medica*, vol. 80, no. 18, pp. 1732–1738, 2014.

[17] B. Lin, S. Zheng, J. Liu, and Y. Xu, "Corrosion inhibition effect of cefotaxime sodium on mild steel in acidic and neutral media," *International Journal of Electrochemical Science*, vol. 15, pp. 2335–2353, 2020.

[18] P. Dhara, M. Dhananjay, P. Vandana, P. Devanshi, and P. A. Hiral, "Validated stability indicating RP-HPLC method development and validation for simultaneous estimation of cefixime trihydrate and levofloxacin hemihydrate in pharmaceutical dosage form," *Journal of Analytical Techniques*, vol. 3, no. 1, pp. 1–12, 2017.

[19] A. Chiranjeevi and M. Srinivas, "Simultaneous estimation of cefpodoxime proxetil and ofloxacin in tablet dosage form using RP-HPLC," *Journal of Applied Pharmaceutical Science*, vol. 4, no. 5, p. 46, 2014.

[20] A. Fazli, M. Salouti, G. Ahmadi, F. Mirshojaei, M. Mazidi, and Z. Heydari, "Radiolabeling of ceftriaxone with 99mTc as a targeting radiopharmaceutical for Staphylococcus aureus detection in mouse model," *Iranian Journal of Medical Physics*, vol. 9, no. 2, pp. 103–110, 2012.

[21] A. Endimiani, F. Perez, and R. A. Bonomo, "Cefepime: a reappraisal in an era of increasing antimicrobial resistance," *Expert Review of Anti-Infective Therapy*, vol. 6, no. 6, pp. 805–824, 2008.

[22] R. A. Eid, M. O. Elgendy, A. O. El-Gendy et al., "Efficacy of ceftazidime and cefepime in the management of COVID-19 patients: single center report from Egypt," *Antibiotics*, vol. 10, no. 11, p. 1278, 2021.

[23] C. D. Milagre, L. F. Cabeça, W. F. Almeida, and A. J. Marsaioli, "*β*-Lactam antibiotics epitope mapping with STD NMR spectroscopy: a study of drug-human serum albumin interaction," *Journal of the Brazilian Chemical Society*, vol. 23, no. 3, pp. 403–408, 2012.

[24] H. Salem and E. Samir, "Determination of cefotaxime, cefoperazone, ceftazidime and cefadroxil using surface plasmon resonance band of silver nanoparticles," *Brazilian Journal of Pharmaceutical Sciences*, vol. 54, no. 3, p. e17565, 2018.

[25] C. H. O'Callaghan, R. B. Sykes, A. Griffiths, and J. E. Thornton, "Cefuroxime, a new cephalosporin antibiotic: activity in vitro," *Antimicrobial Agents and Chemotherapy*, vol. 9, no. 3, pp. 511–519, 1976.

[26] J. Anacona, Y. Pineda, A. Bravo, and J. Camus, "Synthesis, characterization and antibacterial activity of a tridentate Schiff base derived from cephalexin and 1,6-hexanediamine and its transition metal complexes," *Medicinal Chemistry (Los Angeles)*, vol. 6, no. 7, pp. 467–473, 2016.

[27] M. Pfeffer, A. Jackson, J. Ximenes, and J. P. De Menezes, "Comparative human oral clinical pharmacology of cefadroxil, cephalexin, and cephradine," *Antimicrobial Agents and Chemotherapy*, vol. 11, no. 2, pp. 331–338, 1977.

[28] M. W. Weatherburn, "Phenol-hypochlorite reaction for determination of ammonia," *Analytical Chemistry*, vol. 39, no. 8, pp. 971–974, 1967.

[29] M. Mojzych, P. Tarasiuk, K. Kotwica-Mojzych et al., "Synthesis of chiral pyrazolo[4,3-e][1,2,4]triazine sulfonamides with tyrosinase and urease inhibitory activity," *Journal of Enzyme Inhibition and Medicinal Chemistry*, vol. 32, no. 1, pp. 99–105, 2017.

[30] T. Tahir, M. I. Shahzad, R. Tabassum et al., "Diaryl azo derivatives as anti-diabetic and antimicrobial agents: synthesis,

in vitro, kinetic and docking studies," *Journal of Enzyme Inhibition and Medicinal Chemistry*, vol. 36, no. 1, pp. 1509–1520, 2021.

[31] A. Ali, Z. Ashraf, M. Rafiq et al., "Novel amide derivatives as potent tyrosinase inhibitors; in-vitro, in-vivo antimelanogenic activity and computational studies," *Medicinal Chemistry*, vol. 15, no. 7, pp. 715–728, 2019.

[32] E. F. Pettersen, T. D. Goddard, C. C. Huang et al., "UCSF Chimera—a visualization system for exploratory research and analysis," *Journal of Computational Chemistry*, vol. 25, no. 13, pp. 1605–1612, 2004.

[33] S. C. Lovell, I. W. Davis, W. B. Arendall III et al., "Structure validation by Cα geometry: φ, ψ and Cβ deviation," *Proteins: Structure, Function, and Bioinformatics*, vol. 50, no. 3, pp. 437–450, 2003.

[34] S. Dallakyan and A. J. Olson, "Small-molecule library screening by docking with PyRx," *Methods in Molecular Biology*, vol. 1263, pp. 243–250, 2015.

[35] M. B. Tufail, M. A. Javed, M. Ikram et al., "Synthesis, pharmacological evaluation and molecular modelling studies of pregnenolone derivatives as inhibitors of human dihydrofolate reductase," *Steroids*, vol. 168, p. 108801, 2021.

[36] M. Nakajima, I. Shinoda, Y. Fukuwatari, and H. Hayasawa, "Arbutin increases the pigmentation of cultured human melanocytes through mechanisms other than the induction of tyrosinase activity," *Pigment Cell Research*, vol. 11, no. 1, pp. 12–17, 1998.

[37] J. F. Hermanns, L. Petit, C. Piérard-Franchimont, P. Paquet, and G. E. Piérard, "Assessment of topical hypopigmenting agents on solar lentigines of Asian women," *Dermatology*, vol. 204, no. 4, pp. 281–286, 2002.

[38] K. Yoshimura, K. Tsukamoto, M. Okazaki et al., "Effects of all-trans retinoic acid on melanogenesis in pigmented skin equivalents and monolayer culture of melanocytes," *Journal of Dermatological Science*, vol. 27, pp. 68–75, 2001.

[39] K. Kameyama, C. Sakai, S. Kondoh et al., "Inhibitory effect of magnesium L-ascorbyl-2-phosphate (VC-PMG) on melanogenesis in vitro and in vivo," *Journal of the American Academy of Dermatology*, vol. 34, no. 1, pp. 29–33, 1996.

[40] J. Cabanes, S. Chazarra, and F. Garcia-Carmona, "Kojic acid, a cosmetic skin whitening agent, is a slow-binding inhibitor of catecholase activity of tyrosinase," *Journal of Pharmacy and Pharmacology*, vol. 46, no. 12, pp. 982–985, 1994.

[41] A. Garcia and J. E. Fulton Jr., "The combination of glycolic acid and hydroquinone or kojic acid for the treatment of melasma and related conditions," *Dermatologic Surgery*, vol. 22, no. 5, pp. 443–447, 1996.

[42] J. X. Zhuang, W. G. Li, L. Qiu, X. Zhong, J. J. Zhou, and Q. X. Chen, "Inhibitory effects of cefazolin and cefodizime on the activity of mushroom tyrosinase," *Journal of Enzyme Inhibition and Medicinal Chemistry*, vol. 24, no. 1, pp. 251–256, 2009.

[43] E. Rattanangkool, P. Kittikhunnatham, T. Damsud, S. Wacharasindhu, and P. Phuwapraisirisan, "Quercitylcinnamates, a new series of antidiabetic bioconjugates possessing α-glucosidase inhibition and antioxidant," *European Journal of Medicinal Chemistry*, vol. 66, pp. 296–304, 2013.

[44] L. Qiu, Q. X. Chen, Q. Wang, H. Huang, and K. K. Song, "Irreversibly inhibitory kinetics of 3, 5-dihydroxyphenyl decanoate on mushroom (*Agaricus bisporus*) tyrosinase," *Bioorganic & Medicinal Chemistry*, vol. 13, no. 22, pp. 6206–6211, 2005.

[45] Z. Chen, D. Cai, D. Mou et al., "Design, synthesis and biological evaluation of hydroxy- or methoxy-substituted 5-benzylidene (thio) barbiturates as novel tyrosinase inhibitors," *Bioorganic & Medicinal Chemistry*, vol. 22, no. 13, pp. 3279–3284, 2014.

[46] W. Yi, X. Wu, R. Cao, H. Song, and L. Ma, "Biological evaluations of novel vitamin C esters as mushroom tyrosinase inhibitors and antioxidants," *Food Chemistry*, vol. 117, no. 3, pp. 381–386, 2009.

[47] M. Hanif, F. Kanwal, M. Rafiq et al., "Symmetrical heterocyclic cage skeleton: synthesis, urease inhibition activity, kinetic mechanistic insight, and molecular docking analyses," *Molecules*, vol. 24, no. 2, p. 312, 2019.

[48] M. A. Abbasi, H. Raza, S. Z. Siddiqui, S. A. A. Shah, M. Hassan, and S. Y. Seo, "Synthesis of novel N-(1, 3-thiazol-2-yl) benzamide clubbed oxadiazole scaffolds: urease inhibition, Lipinski rule and molecular docking analyses," *Bioorganic Chemistry*, vol. 83, pp. 63–75, 2019.

[49] P. A. Channar, A. Saeed, F. Albericio et al., "Sulfonamide-linked ciprofloxacin, sulfadiazine and amantadine derivatives as a novel class of inhibitors of jack bean urease; synthesis, kinetic mechanism and molecular docking," *Molecules*, vol. 22, no. 8, p. 1352, 2017.

[50] M. Hassan, Q. Abbas, Z. Ashraf, A. A. Moustafa, and S. Y. Seo, "Pharmacoinformatics exploration of polyphenol oxidases leading to novel inhibitors by virtual screening and molecular dynamic simulation study," *Computational Biology and Chemistry*, vol. 68, pp. 131–142, 2017.

[51] M. Hassan, Q. Abbas, H. Raza, A. A. Moustafa, and S. Y. Seo, "Computational analysis of histidine mutations on the structural stability of human tyrosinases leading to albinism insurgence," *Molecular BioSystems*, vol. 13, no. 8, pp. 1534–1544, 2017.

[52] M. Hassan, Z. Ashraf, Q. Abbas, H. Raza, and S. Y. Seo, "Exploration of novel human tyrosinase inhibitors by molecular modeling, docking and simulation studies," *Interdisciplinary Sciences: Computational Life Sciences*, vol. 10, no. 1, pp. 68–80, 2018.

[53] F. A. Larik, M. Faisal, A. Saeed et al., "Investigation on the effect of alkyl chain linked mono-thioureas as Jack bean urease inhibitors, SAR, pharmacokinetics ADMET parameters and molecular docking studies," *Bioorganic Chemistry*, vol. 86, pp. 473–481, 2019.

[54] H. Noh, S. J. Lee, H. J. Jo, H. W. Choi, S. Hong, and K. H. Kong, "Histidine residues at the copper-binding site in human tyrosinase are essential for its catalytic activities," *Journal of Enzyme Inhibition and Medicinal Chemistry*, vol. 35, no. 1, pp. 726–732, 2020.

Hindawi

Research Article

Potential Material Basis of Yupingfeng Powder for the Prevention and Treatment of 2019 Novel Coronavirus Pneumonia: A Study Involving Molecular Docking and Molecular Dynamic Simulation Technology

Ying Yu,[1] Gong Zhang,[2] Tao Han,[3] Hongjie Liu [ID],[4] and Hailiang Huang [ID][5]

[1]*Doctor's Degree of Medicine, In Station Post-Doctorate, Innovative Institute of Chinese Medicine and Pharmacy, Shandong University of Traditional Chinese Medicine, Jinan 250355, China*
[2]*Doctor's Degree of Medicine, College of Integrated Traditional Chinese and Western Medicine, Shandong Liming Vocational College of Science and Technology, Tai'an 271000, China*
[3]*Doctor's Degree of Medicine, Graduate Office of Shandong University of Traditional Chinese Medicine, Jinan 250355, China*
[4]*Doctor's Degree of Medicine, School of Traditional Chinese Medicine, Jinan University, Guangzhou 510632, China*
[5]*Doctor's Degree of Medicine, College of Rehabilitation Medicine, Shandong University of Traditional Chinese Medicine, Jinan 250355, China*

Correspondence should be addressed to Hongjie Liu; hongjie_liu@jnu.edu.cn and Hailiang Huang; 06000031@sdutcm.edu.cn

Ying Yu and Gong Zhang contributed equally to this work.

Objective. In this study, we investigated the potential material basis of Yupingfeng powder in the prevention and treatment of 2019 novel coronavirus pneumonia (NCP) by applying molecular docking and molecular dynamic simulation technology. *Design*. The active ingredients and predictive targets of Yupingfeng powder were sourced using the TCMSP, ETCM, and TCMIP traditional Chinese medicine databases. NCP-related targets were then acquired from the DisGeNET and GeneCards databases, and common disease-drug targets were imported into the STRING database, and Cytoscape software was used to generate a protein-protein interaction network following the use of a network topology algorithm to identify key target genes. Gene Ontology (GO) and KEGG pathway enrichment analysis was then performed using the target genes and GOEAST and DAVID online tools. The mechanism of Yupingfeng powder in the prevention and treatment of NCP was analyzed with reference to the relevant literature. AutoDock software was used for molecular docking, the preliminary analysis of binding status, and to identify the best conformation. Desmond software was used to perform molecular dynamic simulations for protein and compound complexes, perform free energy calculations and hydrogen bond analysis, and to further verify the binding mode. *Results*. Overall, 38 main active components and 218 predictive targets of Yupingfeng powder were identified and 298 disease targets related to NCP were retrieved from disease databases. Yupingfeng powder was found to act predominantly on the TNF, Toll-like receptor, HIF-1, NOD-like receptor, cytokine-receptor interaction, MAPK, T cell receptor, and VEGF signaling pathways. Molecular docking of the three selected key active components with the 3CL-like protease (3CL-Pro) of SARS-CoV-2 showed that they each had a strong binding force and good affinity. *Conclusions*. Yupingfeng powder primarily acts on multiple active ingredients and potential targets through multiple action channels and signal pathways. Molecular docking and molecular dynamic simulation technology were used to effectively predict and analyze the potential mechanism by which this Chinese medicine can combat NCP. These results provide a reference for developing new modern Chinese medicine preparations against NCP in the future.

1. Introduction

Novel coronavirus pneumonia (NCP), which the World Health Organization has officially named "coronavirus disease 2019" (COVID-19) [1], is an acute form of infectious pneumonia. The main clinical manifestations in patients are fever, fatigue, and a persistent dry cough. In severe cases, dyspnea (shortness of breath) has been observed to develop within a week, and can, in some instances, rapidly develop into acute respiratory distress syndrome, septic shock, or multiple organ failure, leading to death [2]. The disease is highly infectious and epidemic; the number of new confirmed cases, suspected cases, and mortality rates in most countries and regions is increasing rapidly. Moreover, the daily reports of newly confirmed cases, suspected cases, and deaths around the world have all shown a sharp upward trend. As of the 19th October 2021, the cumulative number of confirmed cases exceeded 241,909,397 worldwide and resulted in outcomes that carries serious consequences for physical and mental health and the quality of life and work; these effects pose significant long-term threats that can exert broad implications on social stability and economic development [3, 4].

The research teams of Zihe Rao and Haitao Yang at Shanghai University of Science and Technology have identified the high-resolution crystal structure (PDB 6LU7) of the 3CL hydrolytic protease of the severe acute respiratory syndrome coronavirus 2 (SARS-CoV-2) virus, thereby providing a basis for screening the active ingredients against the specific viral strain that causes COVID-19 [5, 6]. However, there are many types of respiratory viruses and each can be prone to mutation. As yet, researchers have not been able to elucidate the specific pathogenesis of SARS-CoV-2 and there are no specific treatments available at present. Western medicine is primarily investigated antiviral drugs, such as interferons, lopinavir-ritonavir combinations, and ribavirin, as well as the antimalarial chloroquine phosphate. However, with the prolongation of the medication cycle, patients inevitably experience different degrees of side effects which can reduce compliance and curative effects for patients during the treatment process. Alternatively, traditional Chinese medicine (TCM) offers the distinctive advantages of overall regulation and syndrome differentiation for disease prevention. Not only does TCM have substantial foundation in clinical practice, many classic prescriptions have been generated over time. Furthermore, TCM has historically played a crucial role in the treatment of various respiratory viral diseases and in combating epidemics; consequently, TCM has attracted widespread attention.

In the present study, we reviewed the prescriptions and performed statistical analysis of the prevention schemes of TCM that have demonstrated clinical curative effects in various provinces and cities in China and found that Yupingfeng powder is the basic prescription for clinical prevention in many TCM schemes. The powder consists of *Astragalus* root (*A. membranaceus*; *huangqi* in Chinese), *Atractylodes macrocephala* (*baizhu,* in Chinese), and siler root (*Saposhnikovia divaricata*; *fangfeng* in Chinese). This powder can benefit *qi*, strengthen the surface of the body, and stop perspiration; it has become the classic ancient prescription for strengthening the foundation of life. Modern pharmacological studies have shown that this prescription can play a role in immune regulation and maintain an anti-inflammatory, bacteriostatic, and stable microecological environment. It also exerts antitumor potential, *via* a variety of mechanisms, and has a significant effect on repeated upper-respiratory tract infection, influenza, refractory mycoplasma pneumonia, bronchial asthma, and other respiratory diseases [7, 8].

Given its overall treatment characteristics in relation to multiple targets and the additional and numerous effects of this TCM compound, Yupingfeng powder appears to offer certain advantages and potential for addressing the current pandemic. However, there is a lack of comprehensive and systematic understanding of its active constituents and the molecular mechanisms of action, thus limiting the discovery, application, and promotion of this TCM compound and its preparation for treating NCP. Therefore, in the present study, we identified the key active components and targets of Yupingfeng powder using a combination of molecular docking and molecular dynamic simulation technology. Our aim is to systematically analyze the potential preventive mechanism of the prescription and to further explore potential relationships between the prescription and the disease. Next, we aimed to identify the best matching pattern of drug targets by complementing the spatial structure of active receptor sites. By adopting this approach, we hoped to provide a feasible strategy for basic research, clinical application, and new drug development towards the prevention and treatment of NCP by TCM in the future. Our findings may also advance the promotion of TCM towards globalization, internationalization, and modernization.

2. Methods

2.1. Screening Active Components and Prediction Targets in Yupingfeng Powder. We used analysis platforms, along with TCMSP, ETCM, TCMIP, and other TCM databases and the names of three herbs (*Astragalus membranaceus*, *Atractylodes macrocephala*, and *Saposhnikovia divaricata*) as keywords to retrieve all chemical composition information for each herb. Following the pharmacokinetic ADME (Absorption, Distribution, Metabolism, and Excretion) parameters recommended in relation to the TCMSP platform, the screening parameters of "oral bioavailability" and "drug likeness" were set at ≥30% and ≥0.18, respectively. Information relating to key active ingredients was collated and combined with herbal compound data obtained from the ETCM and TCMIP databases. A final data list for the compounds was obtained by eliminating any duplicated information. Next, we sourced the target protein information corresponding to the predicted compounds in the database, standardized the target protein name by reference to the UniProt platform, and finally summarized the target data for the compounds as the prediction targets of the main active ingredients of Yupingfeng powder.

2.2. Acquisition of a Target for NCP. Using "novel coronavirus pneumonia" as the key search term and "*Homo sapiens*" as the selected species, we searched the DisGeNET and GeneCards disease databases, combined the target genes from each database, deleted duplicated targets, and finally identified NCP-related genes.

2.3. Construction of a Database of Intersecting Drug-Disease Target Genes. We imported the target data for herbs and diseases into the OmicShare online tool to generate a Venn diagram, thus mapping the potential target genes of Yupingfeng powder for the prevention and treatment of NCP. Finally, the intersecting target genes were identified.

2.4. Construction of a Protein-Protein Interaction Network. We uploaded the intersecting targets to the STRING network platform and set the protein species to "*Homo sapiens*" and the minimum interaction threshold to "medium confidence." A protein-protein-interaction (PPI) network was then constructed, and the data list, in the form of a tab-separated value (TSV) file, was saved for further analysis.

2.5. The Screening of Key Active Compounds and Targets. The TSV data list was imported into Cytoscape, a bioinformatics image-processing software package, and a plug-in was used for the network topology analysis in an attempt to construct a direct or indirect compound or target protein network, thus revealing the effect of Yupingfeng powder for the prevention and treatment of NCP. We analyzed topological parameters such as "degree centrality," "closeness centrality," and "betweenness centrality" and selected nodes for which degree centrality was more than twofold higher than the median of the nodes. The selected nodes were then used as key active compounds and targets (hubs).

2.6. Analysis of the Biological Processes of Key Targets. Gene Ontology (GO) functional enrichment analysis was carried out by using the GOEAST analysis tool; this allowed us to describe the biological process, cellular components, and molecular functions of the gene products. In the present study, we evaluated biological process, cellular components, and molecular function according to statistical probability (p) and false discovery rate values. The annotated terms were then used to carry out cluster analysis, thus resulting in cluster scores: the higher the scores, the more important the biological processes regulated by the key genes.

2.7. KEGG Signaling Pathway Enrichment Analysis. Next, we analyzed the enrichment of KEGG signaling pathways for the key target genes using the DAVID tool. This analysis allowed us to identify the key signaling pathways of Yupingfeng powder when used to treat NCP. The DAVID database integrates various database resources, and the gene set was enriched and analyzed using an improved Fisher's exact test algorithm, in which $p < 0.01$ was regarded as the threshold for statistical significance with regard to KEGG pathway enrichment analysis. According to the functional items in the enriched pathway, we were able to identify potential targets for herbal medicine in related signaling pathways.

2.8. Molecular Docking. First, we downloaded mol2 files for kaempferol, quercetin, and wogonin from the PubChem database. After minimizing the energy of the downloaded compounds through Chem3D, the small molecule compounds were imported into MGLTools-1.5.6 software and processed to obtain pdbqt files. The 3CLpro (PDB ID: 6LU7, Resolution: 2.16 Å) crystal structure was downloaded in PDB format from the Protein Data Bank (PDB). After deleting irrelevant small molecules using Pymol2.1 software, the protein molecules were imported into MGLTools-1.5.6 software to delete water molecules, add hydrogen atoms, set the atom type, and calculate the protein charge; data were then saved as pdbqt files. All processed compounds were used as small-molecule ligands, and the protein targets were used as receptors. The center position of the Grid Box was determined according to the site of interaction for the small molecule and the target ($x = -9.87$, $y = 12.982$, $z = 67.654$), along with the length, width, and height ($50 \times 50 \times 50$). Finally, molecular docking was performed with AutoDock 4.2 software. The Lamarckian genetic algorithm was used for molecular docking calculations as follows: a population of 150, a maximum energy evaluation of 25 million, a maximum of 2000, a crossover rate of 0.8, and a mutation rate of 0.02. Independent docking was performed 100 times, and the final docking complex structure was evaluated based on the binding free energy. Molecular docking results were visualized by Pymol2.1 software. The action mode of the compound and the target protein was analyzed to identify the nature of the interaction between the compound and the protein residue, including hydrogen bond interaction, π-π interaction, and hydrophobic interaction. Then, by referring to the docking score of the compounds, we considered whether the compounds screened had similar activities to the positive compound.

2.9. Molecular Dynamic Simulation. Molecular dynamic (MD) simulations of protein and compound complexes were performed using Desmond version 2020. Here, the molecular force field in the MD simulation was selected as OPLS3e, and the TIP3 water model was used to solvate the system. Charges of the system were neutralized by adding ions. Energy minimization for the entire system was achieved using the OPLS3e force field (all-atomic force field). The geometric structure of water molecules, the bond lengths, and bond angles of heavy atoms were constrained by the SHAKE algorithm. The continuous system was simulated by applying periodic boundary conditions, and long-range static electricity was maintained using the particle grid Ewald method. An NPT ensemble with a temperature of 300 k and a pressure of 1.0 bar was used to balance the system. The Berendsen coupling algorithm was used for the coupling of temperature and pressure parameters. During the subsequent preparation of the system, a 100 ns operation was performed with a time step of 1.2 fs and a track record was performed every 10 ps, which recorded a total of 1000 frames. The root-mean-square deviation (RMSD) of the main chain atoms was calculated, and graphical analysis was performed to investigate the nature of the protein-ligand interaction.

TABLE 1: Main active component information of Yuping wind powder.

Herbs	TCMSP ID	Compound	OB	DL	Targets
Fangfeng	MOL011737	Divaricatacid	87	0.32	5
Huangqi	MOL000378	7-O-methylisomucronulatol	74.69	0.3	45
Huangqi	MOL000392	Formononetin	69.67	0.21	39
Huangqi	MOL000433	Folic acid	68.96	0.71	3
Fangfeng	MOL000011	(2R,3R)-3-(4-hydroxy-3-methoxy-phenyl)-5-methoxy-2-methylol-2,3-dihydropyrano[5,6-h][1,4]benzodioxin-9-one	68.83	0.66	18
Huangqi	MOL000380	(6aR,11aR)-9,10-dimethoxy-6a,11a-dihydro-6H-benzofurano[3,2-c]chromen-3-ol	64.26	0.42	22
Baizhu	MOL000022	14-acetyl-12-senecioyl-2E,8Z,10E-atractylentriol	63.37	0.3	1
Fangfeng	MOL011732	Anomalin	59.65	0.66	7
Huangqi	MOL000211	Mairin	55.38	0.78	1
Baizhu	MOL000049	3β-Acetoxyatractylone	54.07	0.22	16
Huangqi	MOL000371	3,9-Di-O-methylnissolin	53.74	0.48	23
Huangqi	MOL000239	Jaranol	50.83	0.29	13
Fangfeng	MOL011730	11-Hydroxy-sec-o-beta-d-glucosylhamaudol_qt	50.24	0.27	7
Huangqi	MOL000354	Isorhamnetin	49.6	0.31	35
Huangqi	MOL000439	Isomucronulatol-7,2$'$-di-O-glucosiole	49.28	0.62	1
Huangqi	MOL000417	Calycosin	47.75	0.24	22
Huangqi	MOL000098	Quercetin	46.43	0.28	151
Fangfeng	MOL001942	Isoimperatorin	45.46	0.23	1
Fangfeng	MOL011749	Phelloptorin	43.39	0.28	5
Fangfeng	MOL001494	Mandenol	42	0.19	3
Huangqi	MOL000422	Kaempferol	41.88	0.24	62
Fangfeng	MOL002644	Phellopterin	40.19	0.28	12
Fangfeng	MOL007514	Methyl icosa-11,14-dienoate	39.67	0.23	1
Fangfeng	MOL013077	Decursin	39.27	0.38	16
Huangqi	MOL000442	1,7-Dihydroxy-3,9-dimethoxy pterocarpene	39.05	0.48	4
Fangfeng	MOL011753	5-O-Methylvisamminol	37.99	0.25	24
Huangqi	MOL000296	Hederagenin	36.91	0.75	22
Fangfeng	MOL000359	Sitosterol	36.91	0.75	3
Fangfeng	MOL000358	Beta-sitosterol	36.91	0.75	37
Huangqi	MOL000379	9,10-Dimethoxypterocarpan-3-O-β-D-glucoside	36.74	0.92	3
Fangfeng	MOL003588	Prangenidin	36.31	0.22	15
Huangqi and Baizhu	MOL000033	(3S,8S,9S,10R,13R,14S,17R)-10,13-Dimethyl-17-[(2R,5S)-5-propan-2-yloctan-2-yl]-2,3,4,7,8,9,11,12,14,15,16,17-Dodecahydro-1H-cyclopenta[a]phenanthren-3-ol	36.23	0.78	1
Baizhu	MOL000072	8β-Ethoxy atractylenolide III	35.95	0.21	5
Fangfeng	MOL001941	Ammidin	34.55	0.22	8
Fangfeng	MOL011747	Ledebouriellol	32.05	0.51	14
Fangfeng	MOL011740	Divaricatol	31.65	0.38	16
Huangqi	MOL000387	Bifendate	31.1	0.67	7
Fangfeng	MOL000173	Wogonin	30.68	0.23	45

3. Results

3.1. The Active Components of Yupingfeng Powder and Target Selection.

The active parameter data, along with the absorption-, distribution-, metabolism-, and excretion-related parameter data pertaining to the herbs, were obtained by the interrogation of several TCM databases; duplicated material was deleted. Ultimately, 38 main active ingredients were identified, encompassing 17 *Astragalus*, 4

Atractylodes macrocephalae, and 18 fangfeng species. Of these, MOL000033 was found to be a common compound for *Astragalus* and *Atractylodes macrocephala*. Furthermore, 714 component-related target protein names were predicted. The names of the target proteins were standardized and corrected using the UniProt platform, and any duplicated information was removed. Following this process, 218 target proteins were identified. In addition, as different active compounds can act on the same target, and different targets may

be associated with the same compound, the multicomponent, multitarget, and multilevel characteristics of the Chinese herbal medicines were fully confirmed, as detailed in Table 1.

3.2. Disease Targets. By retrieving NCP-related target genes from the DisGeNET and GeneCards databases, merging disease target genes from each database, and deleting duplicate targets, 298 NCP-related target genes were obtained.

3.3. A Database for Intersecting Drug-Disease Target Genes. The predicted targets of the herbal medicines and disease target data were imported using the OmicShare online tool to construct a Venn diagram and identify intersections. Through this process, 51 common targets were obtained, comprising related targets of Yupingfeng powder acting on disease. As illustrated in Figure 1, the mapping rate of the target gene for Yupingfeng powder to NCP was 11%, thus suggesting that the prevention prescription would have a significant therapeutic effect in preventing and treating NCP.

3.4. A PPI Network for Shared Targets. To better understand the mechanisms of Yupingfeng powder in relation to NCP, the 51 intersecting targets were imported into the STRING platform to generate a PPI network map and a TSV data list. There were 51 PPI targets in the network, and the 384 edges represent the PPI relationship. The mean node degree value of each node in the network was 15.1, and the mean local clustering coefficient was 0.641, as shown in Figure 2.

3.5. Key Compounds and Targets. The TSV list was imported into Cytoscape software, and network topology analysis was carried out. There were 49 nodes and 384 relationship edges in the network. Network topology analysis showed that the network density value was 0.055, the network concentration was 0.506, the network heterogeneity was 1.519, and the median value was 4.506. Then, we identified the key compounds and targets with nodes larger than 9.012. Note that the core node was used as the connection compounds or targets; thus, core nodes play an important role in the whole network. In our analysis, three key compounds and six key targets were identified, showing that Yupingfeng powder has great potential as a key compound or target and could play an important role in the prevention and control of NCP. Of these, the key compounds were MOL000098 (quercetin), MOL000173 (wogonin), and MOL000422 (kaempferol), which can interact with 62, 151, and 45 target proteins, respectively. The key targets were PTGS2, DPP4, PTGS1, NOS2, PPARG, and NOS3; these could interact with 32, 20, 17, 15, 12, and 10 compounds, respectively. These results indicate that there is synergism between the effective components of Yupingfeng powder and that the key targets also play a certain therapeutic role in the development of NCP, as detailed in Table 2.

3.6. GO Analysis of Biological Function Analysis. The 51 intersecting targets were mapped to the GOEAST platform for enrichment analysis of the related biological processes, cellular components, and molecular functions. Using $p < 0.01$ as the significant enrichment screening standard, 82
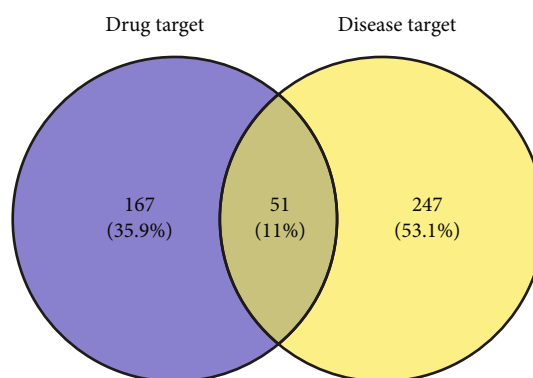
Figure 1: Venn diagram showing the potential NCP targets of Yupingfeng powder.

functional enrichments were identified. Moreover, the first 20 major GO functional enrichment analysis results involved 15 significant enrichments to biological processes, encompassing inflammatory response, cellular response to lipopolysaccharide, extrinsic apoptotic signaling pathways in the absence of a ligand, positive regulation of transcription from the RNA polymerase II promoter, response to drugs, negative regulation of the apoptosis process, immune response, the lipopolysaccharide-mediated signaling pathway, positive regulation of angiogenesis, positive regulation of transcription, DNA-templated, positive regulation of nitric oxide biosynthesis, positive regulation of gene expression, angiogenesis, and cellular response to organic cyclic compounds. Significant enrichment was observed in relation to cell composition, mainly involving extracellular levels. There was also enrichment pertaining to several molecular functions, mainly involving identical protein binding, cytokine activity, enzyme binding, and protein binding. The results of GO enrichment analysis are depicted in Figure 3.

3.7. KEGG Pathway Analysis. Next, the 51 intersecting targets were mapped to the DAVID tool for KEGG pathway analysis. With screening criteria of $p < 0.01$, the top 20 major enrichment signal pathways were encapsulated in a bubble chart. We found that 12 signaling pathways were involved in related diseases, while the other eight signal pathways involved TNF, Toll-like receptor, HIF-1, NOD-like receptor, cytokine–receptor interaction, MAPK, T cell receptor, and VEGF signaling pathways. All signaling pathways overlapped with the key target enrichments related to Yupingfeng powder. These results suggest that the effective components of Yupingfeng powder may act on multiple signaling pathways to treat NCP, a finding that suggests an important direction for future research on Yupingfeng powder in the prevention and treatment of NCP (see Figure 4).

3.8. Molecular Docking. The results of molecular docking are shown in Table 3 [9, 10, 11]. The complex of protein and small molecules was visually analyzed in Pymol2.1, as shown in Figure 5. In this experiment, kaempferol, quercetin, and wogonin were docked with the 3CLpro target protein. Molecular docking results showed that the compound and target protein exhibited good binding and a high degree of
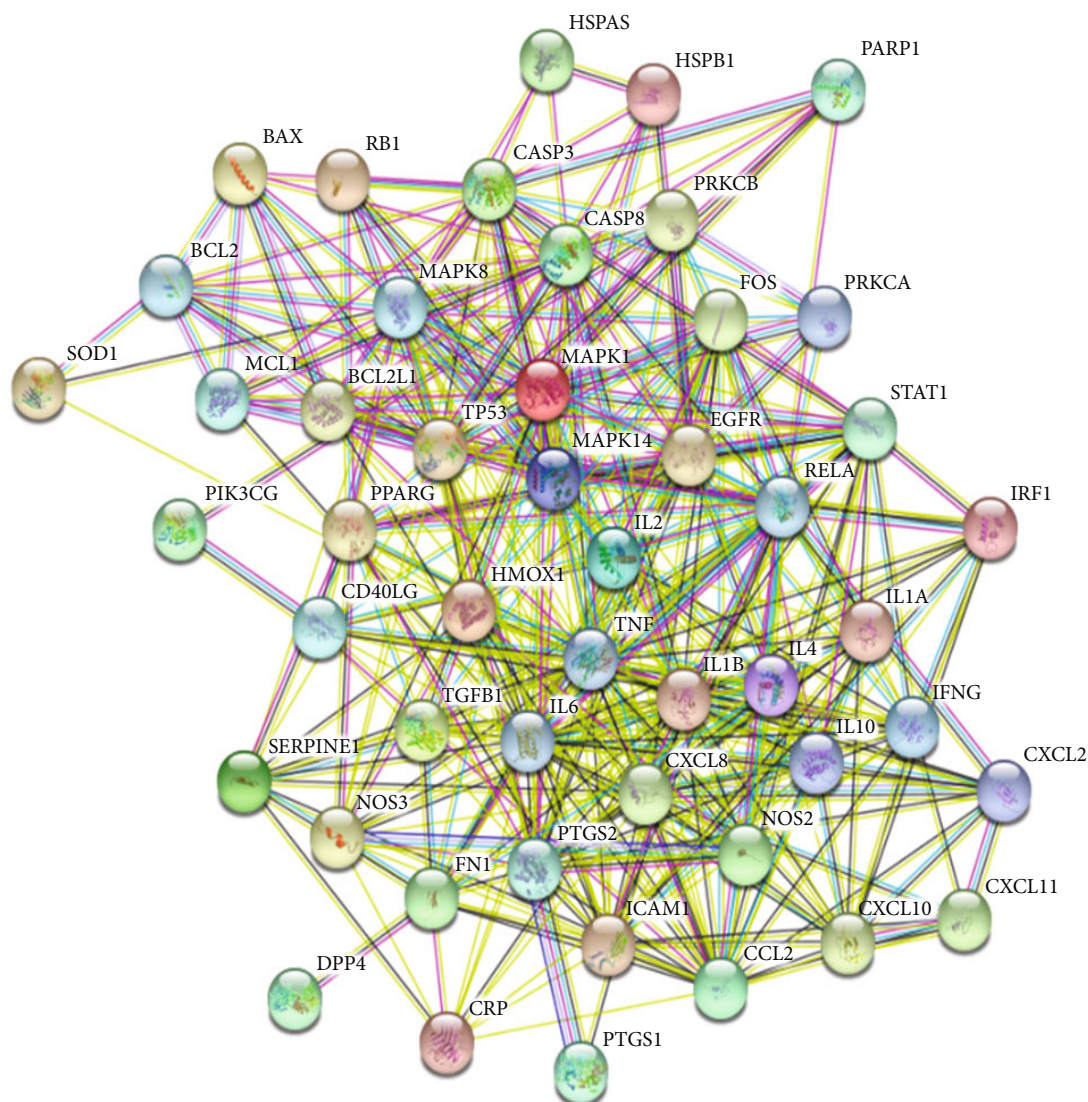
FIGURE 2: Network diagram of the core targets for Yupingfeng powder.

TABLE 2: Network topological characteristics of key compounds and targets.

Node	Node name	Degree centrality	Betweenness centrality	Closeness centrality
C17	Quercetin	47	0.588	0.656
PTGS2	Prostaglandin G/H synthetase 2	32	0.305	0.621
DPP4	Dipeptidyl peptidase IV	20	0.101	0.526
C32	Wogonin	19	0.111	0.463
C13	Kaempferol	18	0.075	0.453
PTGS1	Prostaglandin G/H synthetase 1	17	0.083	0.506
NOS2	Inducible nitric oxide synthetase 2	15	0.025	0.380
PPARG	Peroxisome proliferator activated receptor γ	12	0.026	0.461
NOS3	Endothelial nitric oxide synthetase	10	0.026	0.451

matching (Figures 5(b) and 5(c)). The binding energies were -7.75 kcal/mol, -7.47 kcal/mol, and -7.92 kcal/mol, respectively. Of these, wogonin showed an excellent docking score and binding mode with 3CLpro. The product from the dock-

ing of the compound and the protein was visualized using Pymol2.1 to identify the binding mode. The amino acid residues featured in the pocket of the compound and protein were clearly observed according to the binding mode. The
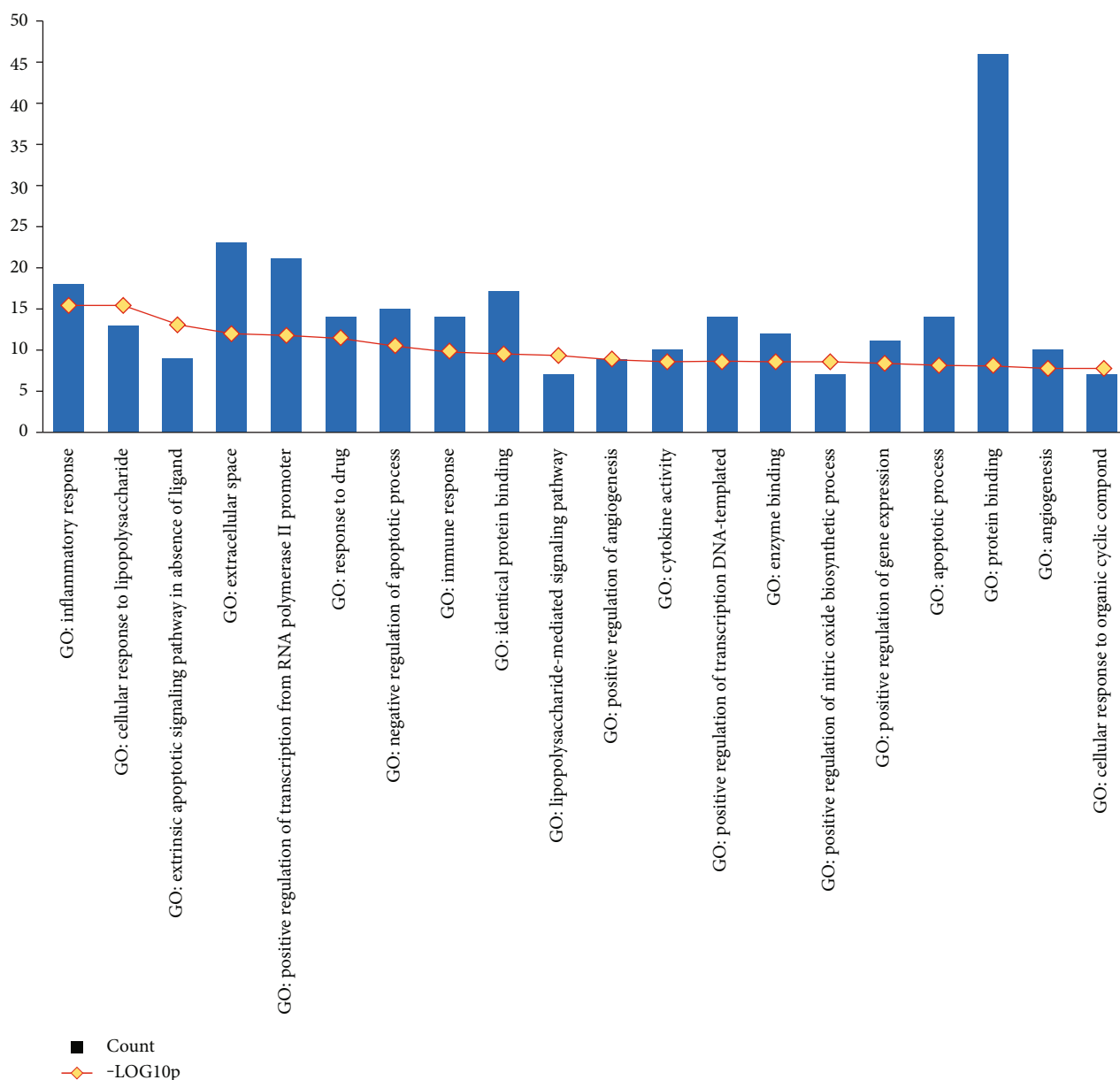
FIGURE 3: GO functional analysis.

active amino acid residues of the three compounds binding to the 3CLpro protein were HIS-41, LEU-141, GLU-166, and THR-190. The kaempferol, quercetin, and wogonin compounds were all flavonoid core compounds with high similarities in terms of binding mode (Figures 5(a)–5(c)). The binding modes of kaempferol and quercetin compounds with the 3CLpro protein were largely identical and formed strong hydrogen bond interactions with active sites in the protein (GLU-166 and THR-190; Figures 5(b) and 5(c)), thus resulting in short hydrogen bond distances and strong binding forces, thereby anchoring the small molecules in protein pockets. The wogonin compound had a slightly different binding mode with the protein, forming strong hydrogen bond interactions with the active site of the protein (GLU-166 and LEU-141; Figure 5(a)). The hydrogen bonds

were shorter than that in the other two compounds and were relatively strong; this may be the main reason for the slightly better score. In addition, the three compounds could form a π-π conjugated interaction with HIS-41; this is important as it stabilized the small molecules in the pocket.

3.9. Molecular Dynamic Simulation Analysis. To further study the interaction between small molecules and proteins, we used molecular dynamic simulations to perform 100 ns molecular dynamic operations on proteins and small molecule complexes. The relationship between RMSD and the stability of the reactive protein and small molecules was analyzed; the larger the RMSD, the more unstable the protein. As shown in Figure 6, small molecules fluctuated at the beginning and tended to stabilize during movement, which
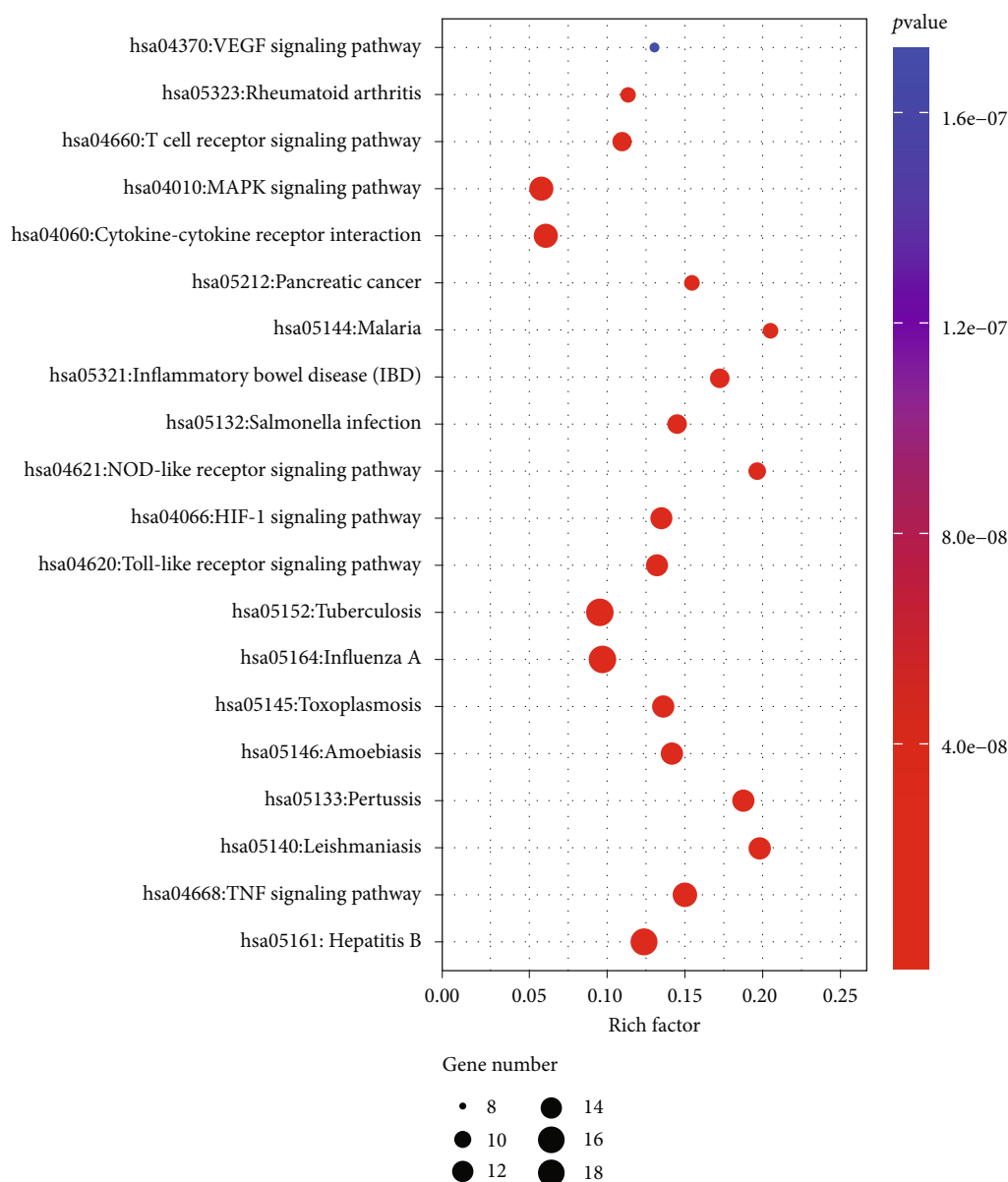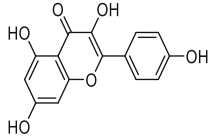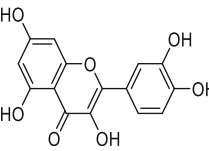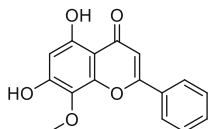
FIGURE 4: Bubble diagram showing the KEGG pathway analysis.

mainly reflected the continuous collisions between small molecules and active sites in the protein pocket. The RMSD of kaempferol, quercetin, wogonin, and the 3CLpro target proteins was small and reached equilibrium at about 15 ns, thus indicating a good combination of small molecules and proteins. Molecular dynamic simulations verified that small molecules could bind to the active sites of the receptor complex (Figures 7(a)–7(c)). During the simulated binding of kaempferol, quercetin, and wogonin to the 3CLpro target protein complex, the total binding free energy was -15.61 kcal/mol, -18.91 kcal/mol, and -15.49 kcal/mol, respectively. The Van der Waals force and electrostatic interactions contributed significantly to the binding process of small molecules and target proteins. The polar solvation energy inhibited the binding process. Wogonin had the largest polar solvation energy, mainly because it contains a methoxy group and significantly

fewer hydroxyl groups than kaempferol and quercetin, thus directly enhancing its hydrophobicity and increasing its polar solvation energy. Comparison between the energy changes of the three compounds revealed that when forming a complex with the protein, the Van der Waals forces of wogonin contributed greater than electrostatic interactions due to its hydrophobicity. The kaempferol and quercetin compounds contained multiple hydroxyl groups and protein sites that could form multiple hydrogen bonds. Thus, electrostatic interaction is dominant. Molecular dynamic simulation of the three compounds also showed that significantly fewer hydrogen bonds were formed by wogonin and the active sites of the protein: only two main hydrogen bonds were formed with GLU-166 and LEU-141. In contrast, kaempferol and quercetin formed three hydrogen bonds with GLU-166, TYR-54, and GLN-192, see Tables 4–7 for details.

TABLE 3: The binding energy of key active compounds in Yupingfeng powder and 2019 ncov 3CL Hydrolase.

Target ID	Compounds	Structure	PubChem CID	CAS number	Docking score (kcal/mol)	Combination type
3CLpro	Kaempferol		5280863	520-18-3	-7.75	Hydrogen bonds, Hydrophobic interactive
3CLpro	Quercetin		5280343	117-39-5	-7.47	Hydrogen bonds, Hydrophobic interactive
3CLpro	Wogonin		5281703	632-85-9	-7.92	Hydrogen bonds, Hydrophobic interactive

Note: Binding energy function [9–11]: $\Delta Gbind = C_{lipo-lipo}\sum f(T \mid r) + C_{hbond-neuto-neut}\sum g(\Delta r)h(\Delta\alpha) + C_{hbond-charged-charged}\sum g(\Delta r)h(\Delta\alpha) + C_{max-metal-ion}\sum f(T \mid m) + C_{rotb}H_{rotb} + C_{polar-phob}V_{polar-phob} + C_{coul}E_{coul} + C_{vdW}E_{vdW} + solvationerms$. $\Delta Gbind$: binding energy function; $C_{lipo-lipo}$: the energy sum of the hydrophobic interaction; $C_{hbond-neuto-neut}$: neutral hydrogen bond interactions; $C_{hbond-charged-charged}$: the energy sum of charged hydrogen bond interactions; $C_{max-metal-ion}$: the energy sum of the coordination action of metal ions; $C_{rotb} H_{rotb}$: rotational bond energy; $C_{polar-phob}V_{polar-phob}$: polar interaction; $C_{coul}E_{coul}$: electrostatic interaction; $C_{vdW}E_{vdW}$: Van der Waals force; solvationerms: solvation energy.

4. Discussion

At present, the world is dealing with the prevention and control of major pandemic. It is therefore particularly important to undertake comprehensive prevention and coordination measures to avoid pathogens, adjust diets, control emotions, strengthen bodies, and apply any other measures as necessary to achieve the optimum preventative effect. Yupingfeng powder is the basis of TCM prevention prescriptions issued in provinces and cities throughout China. Owing to its ability to deal with different syndromes and compatibility considerations, its diagnostic capability, and its flexibility with regard to individual consolations and treatment schemes, TCM has been found to achieve notable clinical outcomes in combating NCP. The first principle of TCM in pandemic prevention is to support and strengthen qi and to strengthen the surface of the body. This approach is not only in line with the underlying theory of TCM to treat a disease before it occurs but can also improve autoimmune function by supporting the healthy qi of the human body, so as to give full opportunity to the unique theoretical, practical, and herbal advantages of TCM. Thereby, TCM can be involved in the whole process of prevention, treatment, and prognosis related to the current pandemic in a multifaceted manner by strengthening the early preventative advantages of the uninfected and carrying out early detection and prognosis in the infected in isolation, thus allowing timely diagnosis and treatment. Thus, when combined with Western medicine, complementary TCM advantages should be provided to comprehensively improve the clinical efficacy of antipandemic strategies.

Through ancient herbal books, critical modern research, and evidence from animal experiments, it has been discovered that Yupingfeng powder has high clinical application value in the prevention of disease, immune regulation, and antiviral application [12, 13, 14]. In the present study, we performed biological enrichment analysis of the key active components and targets of Yupingfeng powder and found that the main enrichments related to the respiratory and immune systems. Our analysis suggested that these enrichments involved signaling pathways related to hepatitis B, pertussis, influenza A, tuberculosis, Salmonella infection, inflammatory bowel disease, rheumatoid arthritis, pancreatic cancer, and other diseases, thus suggesting that this prescription has a certain targeted regulatory role in the treatment of viral or bacterial infectious diseases and therefore has the potential to exert antibacterial and antiviral functionality. Furthermore, we found that the TNF, Toll-like receptor, HIF-1, NOD-like receptor, cytokine receptor interaction, MAPK, T cell receptor, VEGF, and other signaling pathways related to immune and inflammatory responses were all affected by Yupingfeng powder.

Currently, it is thought that TNF is mainly involved in cell apoptosis, cell proliferation, inflammation, and immune regulation. It has also been theorized that Yupingfeng powder may participate in the process of immune activation and regulation through the TNF signal pathway, thus affecting viral replication and persistence [15]. Toll-like receptors and NOD-like receptors not only act as extracellular and intracellular pattern-recognition receptors, respectively, but also stimulate the expression of different effector molecules through the cascade reaction of signal transduction. Moreover, they can jointly act on the innate immune process of infectious diseases, detect the invasion of pathogens, and initiate a protective response [16]. Research has also shown that, when the body is infected, it will induce different types of immune cells to generate physiological and pathological coordinated responses to effectively regulate cell proliferation, migration, differentiation, and other metabolic activities, in which HIF regulates a variety of effector molecules,
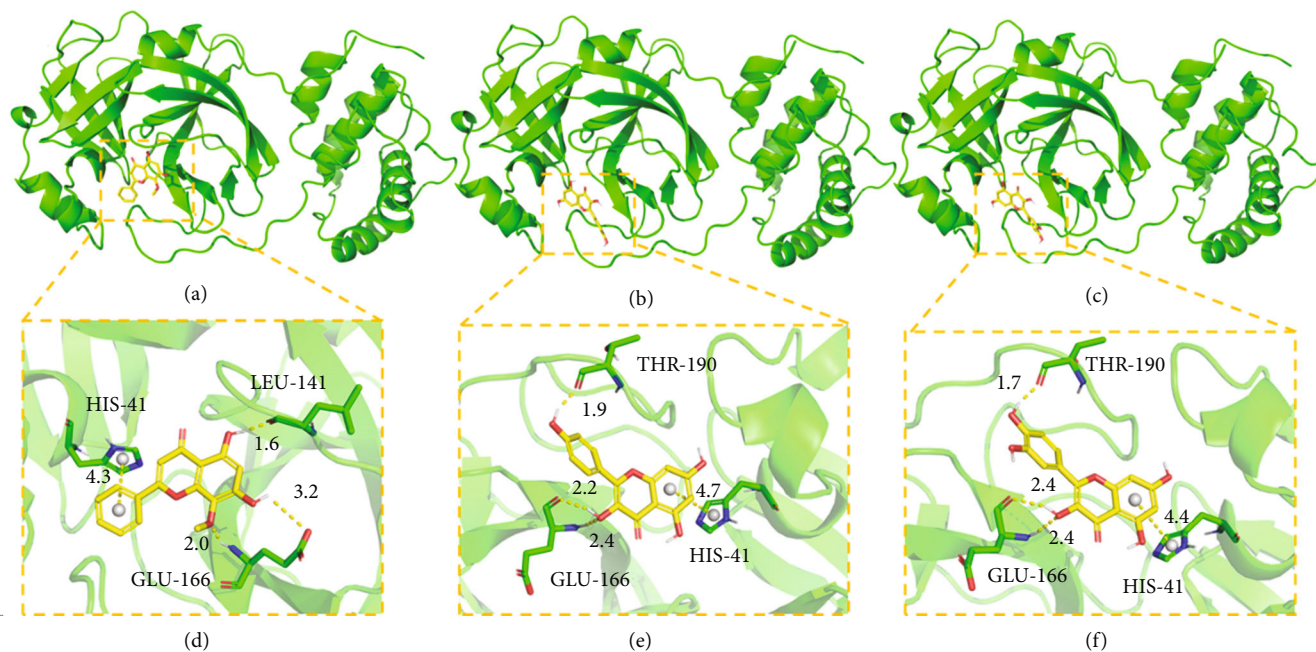
FIGURE 5: The binding mode of protein with compound. (a)–(c) The 3D structure for 3CLpro with wogonin, kaempferol, and quercetin. (d)–(f) The detail binding mode 3CLpro with wogonin, kaempferol, and quercetin. The backbone of protein was rendered in tube and colored in green. Compound is rendering by yellow. Yellow dash represents hydrogen bond distance or π-stacking.
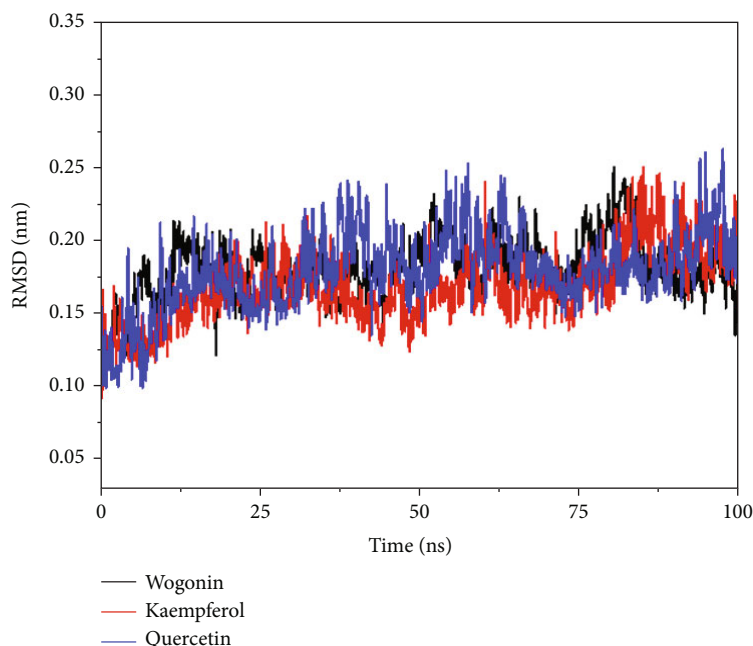
FIGURE 6: RMSD plot of molecular dynamic simulations between the protein and compounds.

signal transduction molecules, and transport molecules of cell metabolism. Consequently, the metabolism, differentiation, and immune function regulation of T cells will also be affected. In addition, the HIF-1α–VEGF-A axis plays an important role in regulating the immune and autoimmune functions of various pathogens. It has been postulated that Yupingfeng powder can build the immune microenvironment of the body, balance the immune system and eliminate

inflammation, regulate the T cell receptor signal pathway, and enhance cell transformation ability to cope with the two-way regulatory mechanism responsible for immune enhancement and immunosuppression [17, 18, 19]. Moreover, the MAPK pathway is the main cell signaling system to be activated by a variety of viruses and also plays a key role in the regulation of cell proliferation, stress, inflammation, differentiation, transformation, apoptosis, and other

(a) (b) (c)
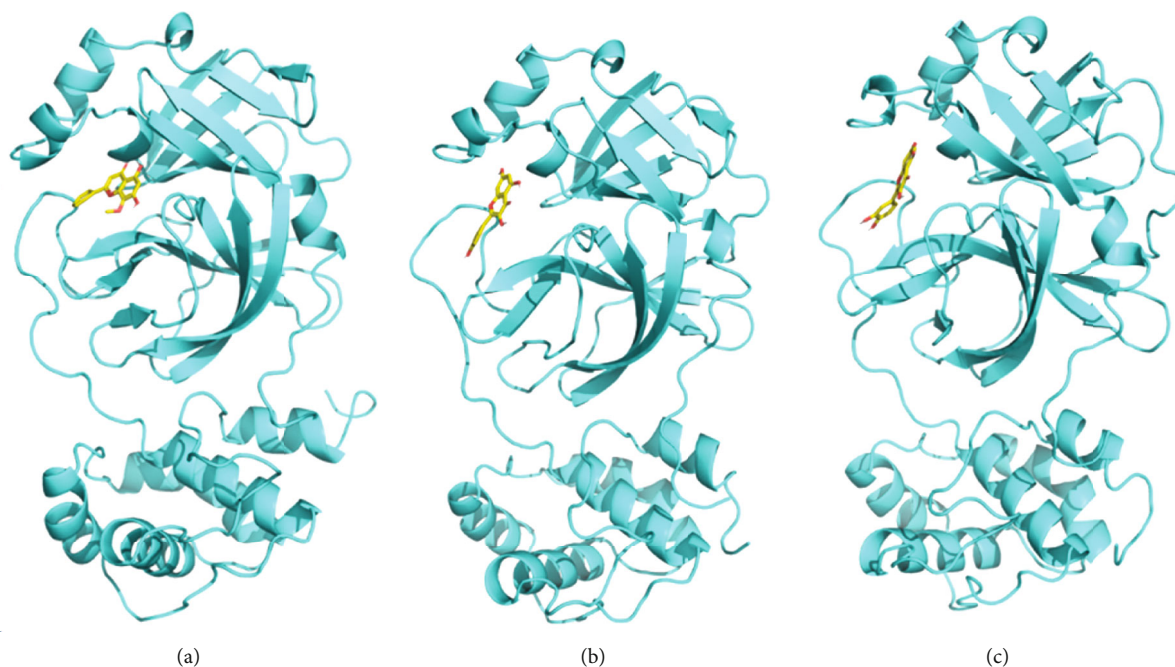
FIGURE 7: The 3D complex structure of the protein with compounds. (a)–(c) represent 3CLpro with wogonin, kaempferol, and quercetin, respectively.

processes. Accordingly, it has been suggested that the MAPK signaling pathway may be activated to induce a cytopathic effect and then play a role in inhibiting viral replication [20].

In this study, we conducted molecular docking experiments involving kaempferol, quercetin, and wogonin with the 3CLpro target protein. Analysis showed that the three compounds bound strongly with the 3CLpro target protein. To further study the mechanism of interaction between small molecules and protein pockets, we performed 100 ns molecular dynamic simulations on the three complexes. The simulation results showed that kaempferol, quercetin, and wogonin could form stable complexes with the 3CLpro protein. The contribution of active sites to the stability of small molecules was also analyzed. Our findings provide reference guidelines for future mechanistic research related to small molecules and proteins. However, our virtual screening results were mainly aimed at the theoretical level, thus warranting experimental pharmacological verification. Therefore, our future work will focus on the design, modification, and transformation of the compounds that bind to 3CLpro based on our knowledge of docking mode, the characteristics of the binding pocket in the receptor's crystal structure, and clinical trials. Collectively, these studies will further enhance the specificities of these medicines in regulating the biological activity of 3CLpro, thus creating new drugs with better specificities.

5. Conclusions

By applying relevant computer simulation calculation methods, we identified three key compounds (kaempferol, quercetin, and wogonin), six key targets (PTGS2, DPP4, PTGS1, NOS2, PPARG, and NOS3), and eight important

TABLE 4: The analysis of binding energy for target with compound.

Energy type	Binding free energy/(kcal/mol)		
	Wogonin	Kaempferol	Quercetin
VDW	-27.15	-26.47	-29.63
Eele	-22.97	-28.28	-31.35
Egb	30.38	23.99	21.62
Esurf	-3.87	-4.11	-4.29
ΔG gas	-36.21	-35.97	-35.4
ΔG solv	25.23	24.23	20.23
ΔG total	-15.49	-15.61	-18.91

TABLE 5: Hydrogen bond interaction parameters for target with wogonin.

Atom	Residues	Bond distance/ (Å)	Bond angle/ (°)	Proportion/ (%)
O3	MET-49	2.92	143.38	1.13
O5	LEU-141	2.90	145.23	36.48
O3	CYS-44	2.88	153.17	1.39
O3	GLN-192	2.87	140.11	0.97
O3	GLU-166	2.84	149.23	41.24
O5	LEU-167	2.71	150.01	1.48
O4	ASP-187	2.65	138.76	1.32

signal pathways (TNF, Toll-like receptor, HIF-1, NOD-like receptor, cytokine receptor interaction, MAPK, T cell receptor, and VEGF signal pathway) involved in the action of Yupingfeng powder on NCP. We also identified that some signaling pathways were enriched and overlapped with the

TABLE 6: Hydrogen bond interaction parameters for target with kaempferol.

Atom	Residues	Bond distance/ (Å)	Bond angle/ (°)	Proportion/ (%)
O5	GLU-166	2.96	140.32	13.25
O3	ASP-187	2.86	148.25	1.20
O2	MET-49	2.85	154.14	1.38
O3	LEU-167	2.74	142.45	0.97
O2	THR-190	2.71	147.21	3.11
O6	CYS-44	2.63	143.52	1.15
O5	LEU-141	2.59	156.47	2.23
O6	TYR-54	2.48	150.59	35.43
O5	GLN-189	2.48	152.43	1.93
O4	GLN-192	2.37	139.78	35.22

TABLE 7: Hydrogen bond interaction parameters for target with quercetin.

Atom	Residues	Bond distance/ (Å)	Bond angle/ (°)	Proportion/ (%)
O6	CYS-44	3.00	156.71	3.13
O7	GLN-189	2.86	153.58	2.78
O2	THR-190	2.84	147.11	3.25
O3	LEU-167	2.81	150.19	1.02
O2	MET-49	2.74	147.25	0.75
O7	LEU-141	2.74	160.24	1.09
O4	GLN-192	2.73	148.29	36.43
O7	ASP-187	2.71	140.32	0.87
O3	TYR-54	2.62	152.65	27.34
O5	GLU-166	2.59	154.21	15.76

key targets related to Yupingfeng powder. Molecular dynamic simulations showed that kaempferol, quercetin, and wogonin could form stable complexes with the 3CLpro protein. This study not only clarified the efficacy of the mechanistic action of Yupingfeng powder; it also revealed the therapeutic effects of prescription drugs on NCP through multichannel and multiple approaches aimed towards intervention and regulation. It is hoped that this study will stimulate additional research concerning new targets and new pathways within the herbal medicine field, as well as further exploration of the mechanistic actions of various herbal medicines in respect of the observed synergistic effect, thereby providing innovation and facilitating the development of TCM. In the present work, the molecular mechanisms of a natural herbal medicine were investigated, and its complex mechanism was revealed at the molecular level, thus providing a theoretical basis for specific research and the development of natural and antiviral Chinese herbal medicines for clinical application. Furthermore, our findings confirm that the clinical application of TCM is recommended as the main entry point for prevention, to benefit from the proven advantages of both Chinese herbal medicine and Western medicine, and as a strategy for multidisciplinary combination therapy towards the prevention and control of NCP.

Abbreviations

BC:	Betweenness centrality
COVID-19:	Coronavirus disease 2019
CC:	Closeness centrality
DC:	Degree centrality
DL:	Drug likeness
ETCM:	The encyclopedia of traditional Chinese medicine database
GO:	Gene Ontology
HIF-1:	Hypoxia-inducible factor 1
KEGG:	The Kyoto Encyclopedia of Genes and Genomes
MAPK3:	Mitogen-activated protein kinase 3
MAPK8:	Mitogen-activated protein kinase 8
NCP:	Novel coronavirus pneumonia
OB:	Oral bioavailability
PPI:	Protein-protein interaction network
SARS-CoV-2:	Severe acute respiratory syndrome coronavirus 2
TCM:	Traditional Chinese medicine
TCMSP:	Traditional Chinese medicine systems pharmacology database and analysis platform
TCMIP:	Integrative pharmacology-based research platform of traditional Chinese medicine
TNF:	Tumor necrosis factor
VEGF:	Vascular endothelial growth factor.

Data Availability

The data used to support this study can be obtained from the corresponding authors, according to the requirements of the journal. The data supporting the relevant research conclusions are openly available. Provided URLs or supplier details for all key software packages are as follows: TCMSP: A traditional Chinese medicine systems pharmacology database and analysis platform, available at http://www.tcmspw.com/tcmsp.php. ETCM: An encyclopedia of traditional Chinese medicine, available at http://www.nrc.ac.cn:9090/ETCM. TCMIP: A traditional Chinese medicine (including prescriptions) data-mining platform, available at http://www.tcmip.cn. UniProt platform: A database of protein sequence and functional information, available at https://www.uniprot.org. DisGeNET: A database of gene–disease associations, available at https://www.disgenet.org. GeneCards: A database of human genes that provides concise genomic-related information on all known and predicted human genes, available at https://www.genecards.org. OmicShare online tool: See https://www.omicshare.com/tools. STRING: STRING (Search Tool for the Retrieval of Interacting Genes/Proteins) is a biological database and web resource of known and predicted protein–protein interactions, available at https://string-db.org. Cytoscape software: See http://www.cytoscape.org/. GOEAST: GOEAST (Gene Ontology Enrichment Analysis Software Toolkit), available

at http://omicslab.genetics.ac.cn/GOEAST. KEGG: KEGG (Kyoto Encyclopedia of Genes and Genomes) is a database resource for understanding high-level functions and utilities of the biological system, such as the cell, the organism, and the ecosystem, from molecular-level information, especially large-scale molecular data sets generated by genome sequencing and other high-throughput experimental technologies, see https://www.kegg.jp. DAVID: DAVID (Database for Annotation, Visualization, and Integrated Discovery) bioinformatic microarray analysis, available at https://david.ncifcrf.gov. PubChem: See https://pubchem.ncbi.nlm.nih.gov. MGL Tool software: Software developed at the Molecular Graphics Laboratory (MGL) of the Scripps Research Institute for visualization and analysis of molecular structures, available at http://mgltools.scripps.edu. PDB: RCSB (Research Collaboratory for Structural Bioinformatics) Protein Data Bank, available at https://www.rcsb.org. AutoDock software: A molecular docking and virtual screening program, available at http://vina.scripps.edu. Pymol software: A molecular visualization system, available at https://pymol.org.

Conflicts of Interest

The authors declare that the research was conducted in the absence of any commercial or financial relationships that could be construed as a potential conflict of interest.

Authors' Contributions

YY and ZG conceived and designed the research. YY and ZG performed the research. YY and ZG were responsible for data curation. YY and ZG wrote this paper, were responsible with the formal analysis, research methods, and software usage analysis, extracted data, and contributed to the writing-original draft and writing review and editing. HT, TJQ and HHL were responsible with the funding, administer the project, provided supervision, and revised the manuscript. LHJ and HHL were primary responsible for final the content, and all of the authors have read, reviewed, and approved to the published version of the final manuscript. Ying Yu and Gong Zhang contributed equally to this work.

Acknowledgments

References

[1] Y. Liu, R. Kuo, and S. Shih, "COVID-19: the first documented coronavirus pandemic in history," *Biomedical Journal*, vol. 43, no. 4, pp. 328–333, 2020.

[2] X. Lan, Y. Long, F. Shao, and Y. Song, "Expert consensus on the safety prevention and control of nuclear medicine diagnosis and treatment during the outbreak of COVID-19 (1st edition): (translated from Chinese version)," *European Journal of Nuclear Medicine and Molecular Imaging*, vol. 48, no. 4, pp. 1134–1143, 2021.

[3] A. Parasher, "COVID-19: current understanding of its pathophysiology, clinical presentation and treatment," *Postgraduate Medical Journal*, vol. 97, no. 1147, pp. 312–320, 2021.

[4] Y. Wu, C. Chen, and Y. Chan, "The outbreak of COVID-19: An overview," *Journal of the Chinese Medical Association*, vol. 83, no. 3, pp. 217–220, 2020.

[5] J. Xiong, E. Hou, Y. Tang, J. Zheng, X. Xu, and F. Luo, "Study on the mechanism of fuzi lizhong decoction in the treatment of advanced gastric cancer based on molecular docking and network pharmacology," *Journal of Acta Chinese Medicine*, vol. 35, no. 1, pp. 164–171, 2020.

[6] M. Niu, R. Wang, Z. Wang et al., "Rapid establishment of traditional Chinese medicine prevention and treatment of 2019-nCoV based on clinical experience and molecular docking," *China Journal of Chinese Materia Medica*, vol. 45, no. 6, pp. 1213–1218, 2020.

[7] M. Mohamadian, H. Chiti, A. Shoghli, S. Biglari, N. Parsamanesh, and A. Esmaeilzadeh, "COVID-19: virology, biology and novel laboratory diagnosis," *Journal of Gene Medicine*, vol. 23, no. 2, article e3303, 2021.

[8] Q. Wang, W. Lv, J. Li, Y. Ni, L. Hu, and R. Zhang, "Advances in the experimental study and application of Yupingfeng powder," *Chinese Archives of Traditional Chinese Medicine*, vol. 38, no. 9, pp. 165–168, 2020.

[9] M. Rajeswari, N. Santhi, and V. Bhuvaneswari, "Pharmacophore and virtual screening of JAK3 inhibitors," *Bioinformation*, vol. 10, no. 3, pp. 157–163, 2014.

[10] R. Fazi, C. Tintori, A. Brai et al., "Homology model-based virtual screening for the identification of human helicase DDX3 inhibitors," *Journal of Chemical Information and Modeling*, vol. 55, no. 11, pp. 2443–2454, 2015.

[11] R. A. Friesner, J. L. Banks, R. B. Murphy et al., "Glide: a new approach for rapid, accurate docking and scoring. 1. Method and assessment of docking accuracy," *Journal of Medicinal Chemistry*, vol. 47, no. 7, pp. 1739–1749, 2004.

[12] L. Zhang, F. Yao, G. Jiang, and G. Liang, "Research on direct inhibition and immunoregulation effects of Yupingfeng powder in hepatic cell carcinoma," *Chinese Archives of Traditional Chinese Medicine*, vol. 32, no. 5, pp. 1046–1050, 2014.

[13] D. Wang, W. Li, L. Ding, S. Zhang, and H. Zhang, "The explanation, classification and origin of Yupingfeng powder," *Journal of Anhui University of Traditional Chinese Medicine*, vol. 34, no. 3, pp. 6–8, 2015.

[14] C. Chen, Q. Wang, Z. Su, L. Peng, J. Li, and T. Wang, "Clinical trial of Yupingfeng granules in recuperation of qi-deficient constitution with recurrent common cold," *Chinese Journal of Experimental Traditional Medical Formulae*, vol. 24, no. 5, pp. 182–187, 2018.

[15] S. Pasquereau, A. Kumar, and G. Herbein, "Targeting TNF and TNF receptor pathway in HIV-1 infection: from immune activation to viral reservoirs," *Viruses*, vol. 9, no. 4, 2017.

[16] S. Tartey and O. Takeuchi, "Pathogen recognition and Toll-like receptor targeted therapeutics in innate immune cells," *International Reviews of Immunology*, vol. 36, no. 2, pp. 57–73, 2017.

[17] A. Palazon, A. W. Goldrath, V. Nizet, and R. S. Johnson, "HIF transcription factors, inflammation, and immunity," *Immunity*, vol. 41, no. 4, pp. 518–528, 2014.

[18] A. Palazon, P. A. Tyrakis, D. Macias et al., "An HIF-1α/VEGF-A axis in cytotoxic T cells regulates tumor progression," *Cancer Cell*, vol. 32, no. 5, pp. 669–683.e5, 2017.

[19] J. Jiang, K. Natarajan, and D. H. Margulies, "MHC molecules, T cell receptors, natural killer cell receptors, and viral immunoevasins–key elements of adaptive and innate immunity," *Advances in Experimental Medicine and Biology*, vol. 1172, pp. 21–62, 2019.

[20] Q. Wang, Y. Su, J. Sheng et al., "Anti-influenza A virus activity of rhein through regulating oxidative stress, TLR4, Akt, MAPK, and NF-κB signal pathways," *PloS One*, vol. 13, no. 1, article 191793, 2018.

Research Article

Molecular Docking and In Silico Simulation of *Trichinella spiralis* Membrane-Associated Progesterone Receptor Component 2 (*Ts-MAPRC2*) and Its Interaction with Human PGRMC1

Muhammad Tahir Aleem [iD],[1] **Asad Khan,**[1] **Zhaohai Wen,**[1] **Zhengqing Yu,**[1] **Kun Li** [iD],[1,2] **Aftab Shaukat,**[3] **Cheng Chen,**[1] **Tauseef-ur -Rehman,**[4] **Mingmin Lu,**[1] **Lixin Xu,**[1] **Xiaokai Song,**[1] **Xiangrui Li,**[1] **and Ruofeng Yan** [iD][1]

[1]*MOE Joint International Research Laboratory of Animal Health and Food Safety, College of Veterinary Medicine, Nanjing Agricultural University, Nanjing, Jiangsu, China 210095*
[2]*Institute of Traditional Chinese Veterinary Medicine, College of Veterinary Medicine, Nanjing Agricultural University, Nanjing 210095, China*
[3]*National Center for International Research on Animal Genetics, Breeding and Reproduction (NCIRAGBR), Huazhong Agricultural University, Wuhan 430070, China*
[4]*Department of Parasitology, Faculty of Veterinary and Animal Sciences, The Islamia University of Bahawalpur, Pakistan*

Correspondence should be addressed to Ruofeng Yan; yanruofeng@njau.edu.cn

Background. *Trichinellosis* is a foodborne zoonotic disease caused by *Trichinella* spp., including *Trichinella spiralis*. This parasitic disease ranks as seven of the most infectious in the world. In this context, it is important to develop a vaccine that can combat *Trichinellosis*, especially for humans and pigs. This would be an important step in preventing transmission. In this study, we focus on homology modelling, binding site prediction, molecular modelling, and simulation techniques used to explore the association between *Trichinella spiralis* membrane-associated progesterone receptor component 2 (*Ts-MAPRC2*) and the human PGRMC1 protein. It was found that the progesterone receptor component 2 of *T. spiralis* has 44.54% sequence identity with human PGRMC1 (PDB ID: 4X8Y). Binding sites predicted for human PGRMC1 are GLU 7, PHE 8, PHE 10, PHE 18, LEU 27, ASP 36, and VAL 104. Molecular docking has six clusters based on *Z* scores. They range from -1.5 to 1.8. It was found that the progesterone receptor component 2 of *T. spiralis* has 44.54% sequence identity with human PGRMC1. During simulation, the average RMSD was 2.44 ± 0.20 Å, which indicated the overall stability of the protein. Based on docking studies and computational simulations, we hypothesized that the interaction of the proteins *Trichinella spiralis* membrane-associated progesterone receptor component 2 and human PGRMC1 formed stable complexes. The discovery of *Ts-MAPRC2* may pave the way for the development of drugs and vaccines to treat *Trichinellosis*.

1. Introduction

The zoonotic disease *Trichinellosis* is caused by a nematode parasite named *Trichinella spiralis* (*T. spiralis*). Among the most contagious parasitic diseases in the world, it ranks seventh [1]. The most common source of *T. spiralis* infection in humans is pork, commonly eaten raw, undercooked, or as a byproduct of pork processing [2–4]. Due to the prevalence of naturalized animal reserves in China, their high morbidity from this disease is becoming an increasingly serious problem due to the consumption of pork and pork products [5–7]. A major feature in the survival of *T. spiralis*

(a)

(b)
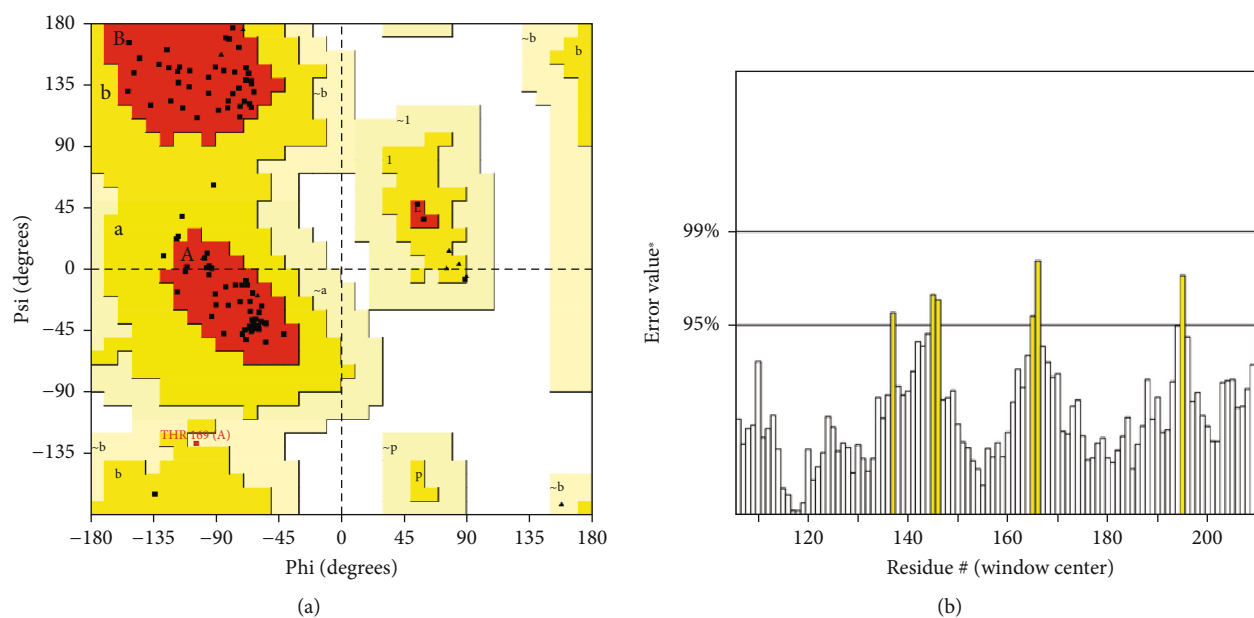
Figure 1: (a) Ramachandran plot. The residues in the red area are lying in the most favorable region (92.1%), while 6.9% of residues lie in additional allowed regions (yellow region). There was no residue in the disallowed region (white area). (b) ERRAT quality chart.
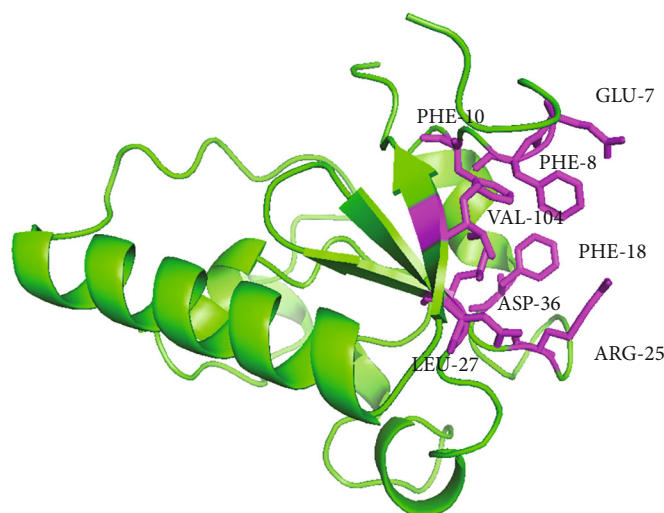
Figure 2: Predicted binding sites of human PGRMC1 shown in magenta sticks.

Table 1: HADDOCK clusters of target protein and human PGRMC1 protein.

Clusters	Haddock score	Size	RMSD	Van der Waals energy	Electrostatic energy	Desolvation energy	Restraint's violation energy	Buried surface area	Z score
4	-49.8 ± 12.3	11	1.1 ± 0.9	-66.6 ± 3.0	-492.9 ± 57.0	-4.0 ± 1.6	1194.0 ± 81.8	2592.6 ± 165.3	-2.2
2	-19.1 ± 8.6	16	9.3 ± 0.1	-60.6 ± 6.6	-386.4 ± 20.9	2.5 ± 4.6	1162.5 ± 47.2	2317.2 ± 132.8	-0.7
9	-16.4 ± 18.1	6	13.4 ± 0.1	-65.6 ± 5.5	-224.1 ± 16.8	-21.5 ± 3.7	1155.6 ± 122.8	2005.8 ± 95.4	-0.6
15	-14.1 ± 19.3	4	11.8 ± 0.2	-54.5 ± 10.1	-348.1 ± 18.6	-14.0 ± 1.7	1240.1 ± 179.0	2317.9 ± 285.9	-0.5
1	-5.6 ± 10.0	26	14.9 ± 0.0	-62.2 ± 1.8	-180.4 ± 31.1	-18.3 ± 1.2	1109.5 ± 118.6	1866.2 ± 19.6	-0.1
8	0.6 ± 9.4	7	11.5 ± 0.1	-56.2 ± 5.1	-209.2 ± 34.9	-14.0 ± 2.7	1125.9 ± 101.5	1919.1 ± 41.5	0.2

nematodes is only through direct host-to-host transmission. It adapts to normal cellular functions and the immune system during all stages of infection [8, 9]. In spite of the wide use of antihelminthic agents against *Trichinellosis*, excessive use causes drug residues in meat, resistance to parasites, and other problems in the environment. In this light, the
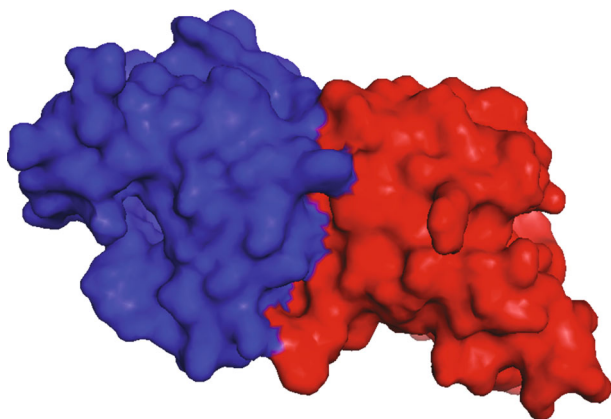
Figure 3: Target protein and human PGRMC1 protein cluster 4. The blue surface shows the human PGRMC1 protein while the red surface shows the target protein.

Table 2: Protein-protein interactions based on KFC.

Chain	Residue	Number	KFC configuration value
A	PHE	8	HS (0.90 and 0.29)
A	PRO	24	HS (0.47)
A	ARG	25	HS (0.27)
A	ILE	26	HS (0.84 and 0.29)
A	ASP	36	HS (0.52)
A	THR	38	HS (1.18)
A	LYS	39	HS (1.20 and 0.28)
A	ARG	41	HS (1.38 and 0.28)
A	LYS	42	HS (0.24)
A	THR	98	HS (0.14)
A	HIS	102	HS (1.68 and 0.19)
A	VAL	104	HS (0.31)
B	ASN	125	HS (0.65)
B	ASP	127	HS (0.54)
B	LEU	173	HS (1.21 and 0.24)
B	ALA	174	HS (0.05)
B	LEU	176	HS (0.49 and 0.14)
B	ILE	181	HS (1.17 and 0.17)
B	LEU	184	HS (0.96 and 0.25)
B	ARG	185	HS (1.60 and 0.35)
B	MET	189	HS (1.23 and 0.21)
B	LYS	205	HS (1.64 and 0.37)
B	LEU	206	HS (0.47 and 0.23)
B	ASP	211	HS (0.19)

development of an effective vaccine to combat *Trichinellosis*, in particular for humans and pigs, would be an important step in preventing the transmission [7, 10]. As a vaccine applicant, a series of proteins have recently been discovered that inhibit host invasion and parasite viability and, thus, produce resistance against parasite infection. In addition, their ability to defend against *T. spiralis* larvae inoculation has been investigated in model animals [11–14]. Most of

these vaccines have shown moderate success against *T. spiralis* infection; however, no comparable vaccine for *T. spiralis* infection is currently available [1]. Membrane-associated progesterone receptor (MAPR) proteins and progesterone receptor membrane component 1 (PGRMC1) and two (PGRMC2) are members of the same family. Porcine smooth muscle PGRMC1 protein of 28 kDa was the first to be collected [15–18]. Additionally, several studies have found that small androgen receptor-interacting proteins are found in cysts such as *S. japonicum* and that PGRMC receptors and progestin-induced proteins are found in helminths such as *S. japonicum* [19, 20]. The previous study focused on the cloning and characterization of the *T. spiralis* membrane-associated progesterone receptor component-2 gene (*Ts-MAPRC2*). A series of experiments throughout the process were performed, including expression, purification, immunoblot assay, binding ability against progesterone antibody, and immunofluorescence assay (IFA). Additionally, we assessed the direct effect of progesterone (P4) and mifepristone (RU486) on *Ts-MAPRC2* gene expression using in vitro cell culture tests that showed different levels of expression during all stages of development (muscle larvae, female adult worm, male adult worm, and newborn larvae). Afterward, mifepristone's in vivo phenotypic and relative mRNA effects on the F-AL stage were evaluated [21]. The current study focuses on the *T. spiralis* membrane-associated progesterone receptor component 2, and its interactions with human PGRMC1 have been docked and simulated in silico. Based on molecular docking and dynamic simulations, the study is now exploring the binding affinity of the membrane-associated progesterone receptor component 2 of *T. spiralis* and its interactions with human PGRMC1 to determine whether the compound has antiparasitic properties against *T. spiralis*.

2. Materials and Methods

2.1. Homology Modelling of T. spiralis Membrane-Associated Progesterone Receptor Component 2 (Ts-MAPRC2). The amino acid sequence of *Trichinella spiralis* membrane-associated progesterone receptor component 2 (target protein) (NCBI accession no. XP_003375934.1) was submitted to the NCBI Blastp server https://blast.ncbi.nlm.nih.gov/Blast.cgi) to find the template protein in Protein Data Bank. The SWISS-MODEL server [22] with default parameters was used to model the three-dimensional structure of *Trichinella spiralis* membrane-associated progesterone receptor component 2. Two parameters were used to estimate the quality of the model: GMQE and QMEAN scoring. Additionally, the quality of the model was verified by the SAVES Server (https://saves.mbi.ucla.edu/). This server contains different algorithms to verify a model such as PROCHECK [23] which calculates the stereochemical quality of the model, ERRAT [24] which checks the interactions of noncovalently bonded amino acids, and VERIFY 3D which assesses compatibility of protein structure.

2.2. Retrieval of Human PGRMC1 Protein and Binding Site Prediction. The crystal structure of human PGRMC1 protein

(a)

(b)

Figure 4: Continued.

(c)
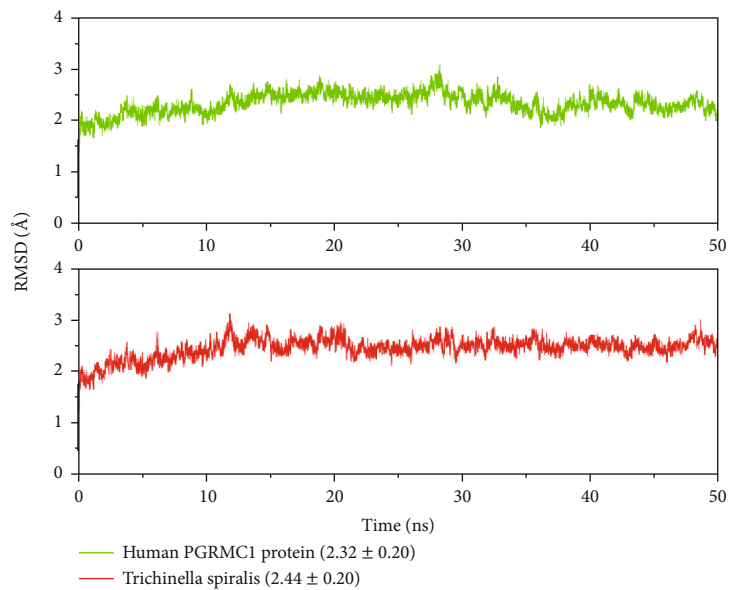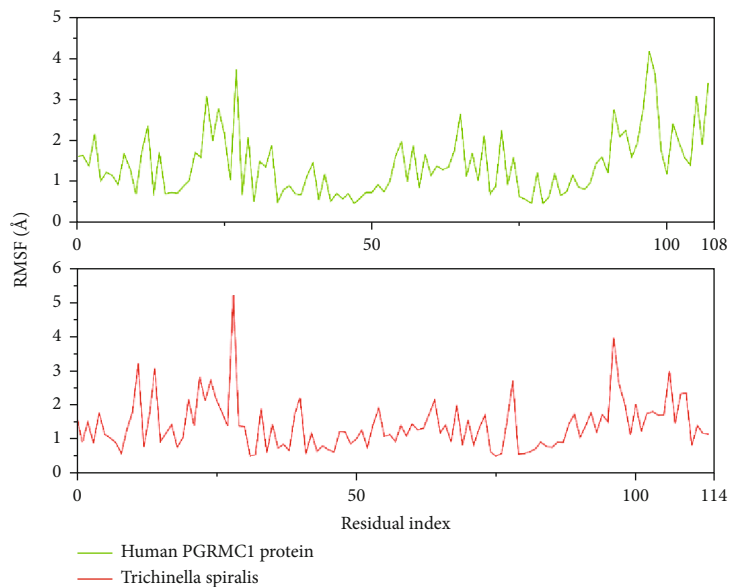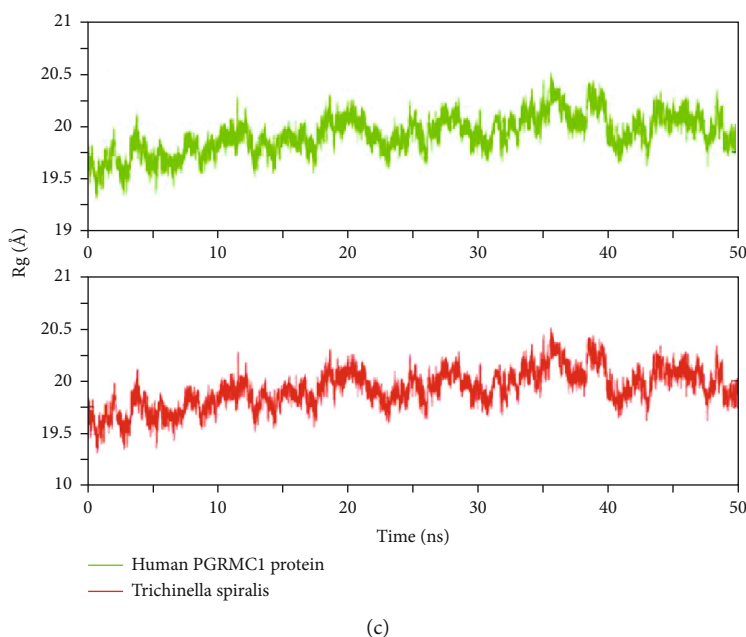
FIGURE 4: Protein-protein complex stability analysis by MD simulation. (a) RMSD plots. (b) RMSF plots. (c) Rg plots.

was retrieved from the Protein Data Bank (PDB ID: 4X8Y) and prepared in the PyMOL tool by removing the protoporphyrin and water molecules. After preparation of the PGRMC1 structure, the protein actives sites were predicted by using the CASTp server [25]. Similarly, the binding site residues of the model were predicted by the same method.

2.3. Molecular Docking.
The molecular docking between the human PGRMC1 protein and *Trichinella spiralis* membrane-associated progesterone receptor component 2 was analyzed by the HADDOCK web server [26]. The resulting clusters were analyzed based on the Z score. The cluster with the best Z score was then selected to test the stability of the complex by using MD simulations. The protein-protein interactions were predicted by the KFC (knowledge-based FADE and contacts) web tool [26].

2.4. MD Simulation.
The MD simulation of the selected cluster was conducted at 50 ns using the VMD [27] and NAMD [28]. The input files were prepared using AMBER21 tools [29]. The LeaP program was used to add missing hydrogen to protein [30]. The solvation of the protein-protein complex was done in a periodic box of 10 Å by using the TIP3P water model [31]. The system was neutralized by adding Na^+ and Cl^- counter ions prior to the minimization step. The ff14SB force field was used for both proteins. To avoid energy clashes, the systems were relaxed by minimization at 10000 steps. After removing the clashes of systems, the solvation system was equilibrated at 310 K. Three additional equilibrations were run by increasing the temperature from 200 K to 250 K and 300 K to maintain the stability of the systems. Then systems were subjected to 50 ns simulation in a production run. The MD trajectories were stored every 2 ps during the production run. The trajectory analysis was carried out by VMD and BIO3D packages of R [32].

3. Results

3.1. Homology Modelling and Validation.
The membrane-associated progesterone receptor component 2 of *T. spiralis* showed a 44.54% sequence identity with the PGRMC1 of human (PDB ID: 4X8Y). The homology model had GMQE and QMEAN values of 0.36 and 0.64, respectively. To evaluate the modelling result, the GMQE combines properties from both the target-template alignment and the template search approach. Its value ranged from 0 to 1, with a greater number suggesting higher reliability of the predicted homology model. The QMEAN around zero suggested that the model structure and experimental structures of similar size were in good agreement, whilst scores of -4.0 or below indicated that the models were of poor quality. The PROCHECK software was used to assess the quality of the three-dimensional (3D) model by the Ramachandran plot (Figure 1(a)). It was observed that 93 amino residues (92.1%) were located in the most favorable region, 7 amino acids (6.9%) were located in the allowed region, and no amino acid was in a disallowed region which indicated the good quality of the model with 93.33 ERRAT quality factor (Figure 1(b)).

3.2. Binding Site Prediction.
The binding sites of both proteins, i.e., human PGRMC1 and target protein, were predicted by the CASTp server. The predicted binding sites of human PGRMC1 were GLU 7, PHE 8, PHE 10, PHE 18, ARG 25, LEU 27, ASP 36, and VAL 104 (Figure 2) while all the residues of the target protein were predicted as binding site residues in during the prediction of the binding site. These predicted binding sites were used in the docking studies.

3.3. Molecular Docking.
The molecular docking of a target protein and human PGRMC1 protein was performed by

(a)

(b)
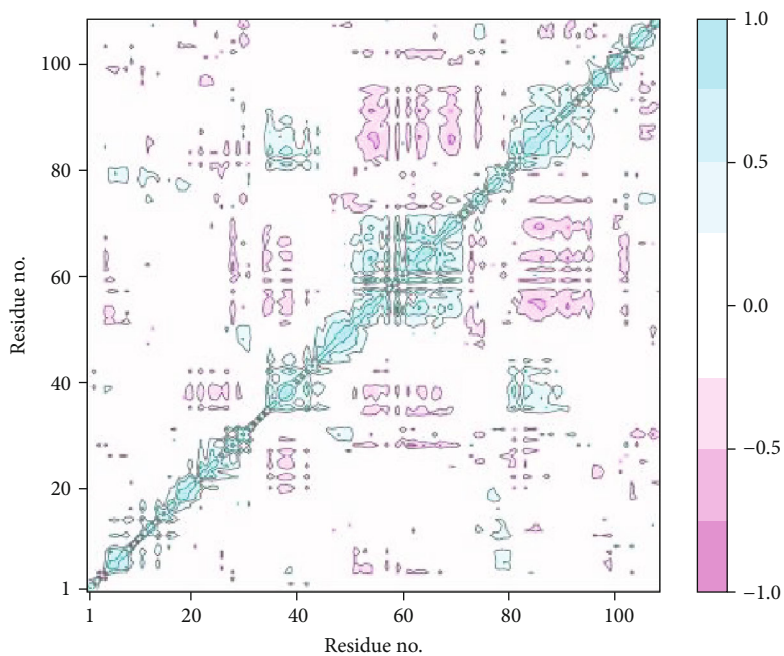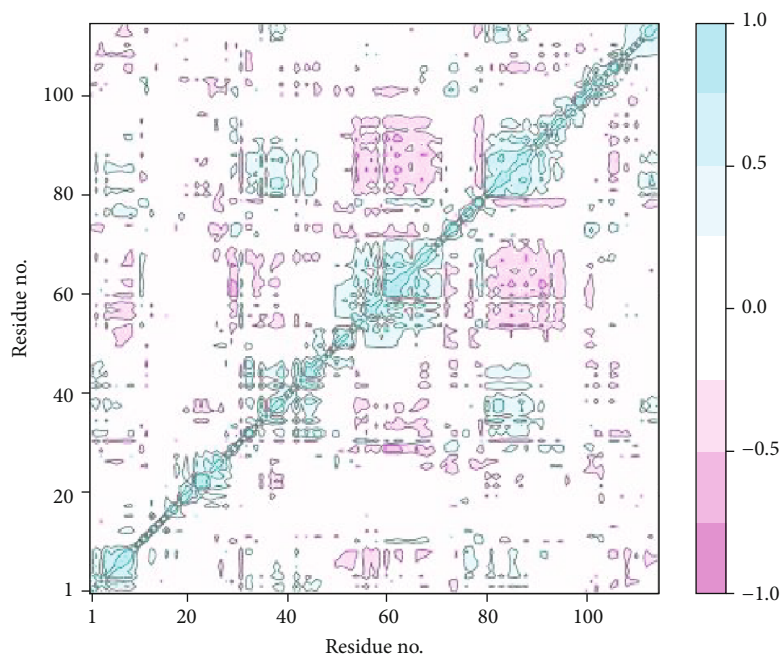
Figure 5: Continued.
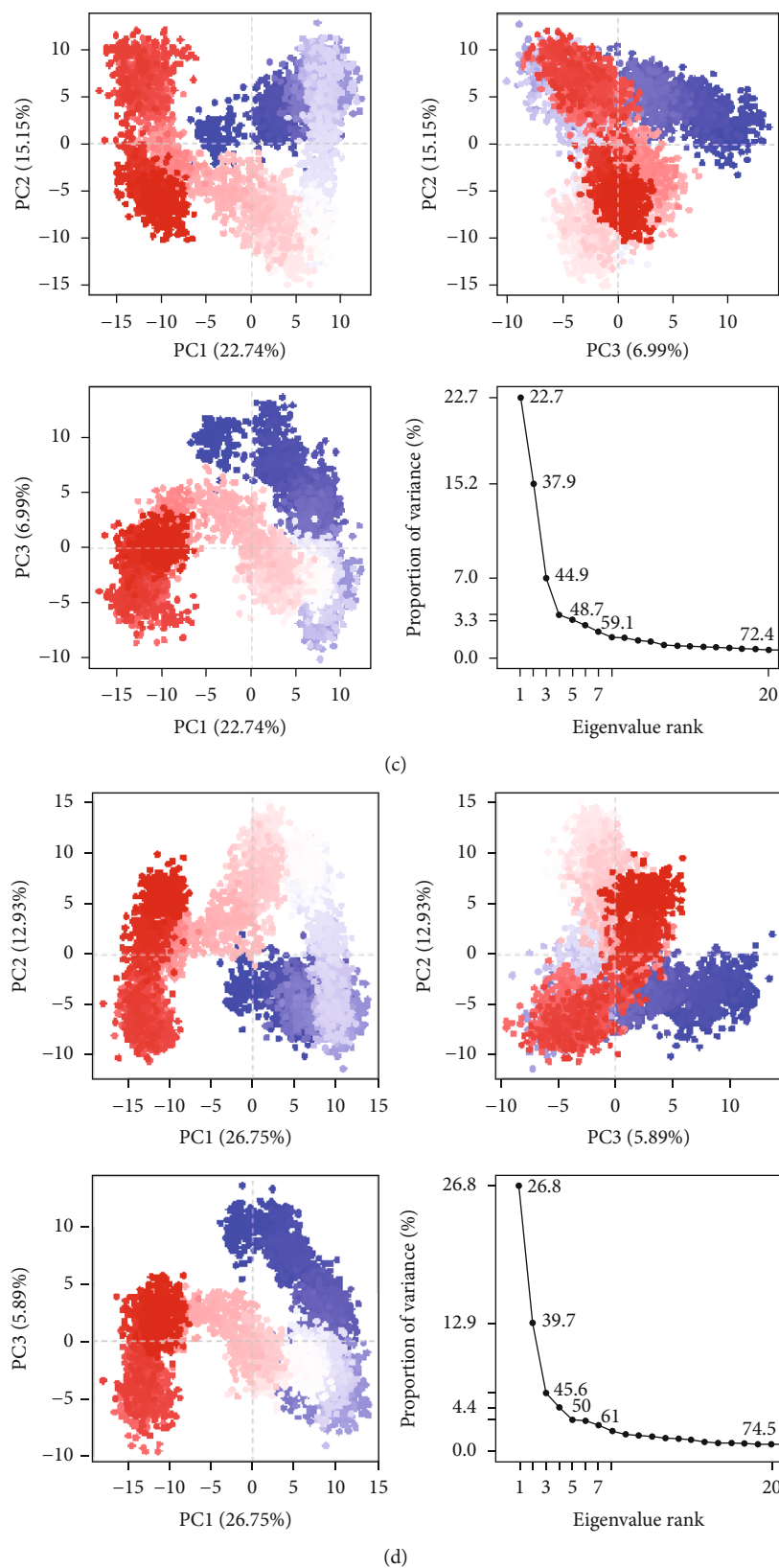
FIGURE 5: The dynamic motions analysis by simulation. (a) Cross-correlation map of human PGRMC1. (b) Cross-correlation map of the target protein. (c) PCA plot of Human PGRMC1. (d) PCA plot of the target protein.

the HADDOCK 2.4 web server. The docking results are shown in (Table 1). There were a total of six clusters based on the Z scores. The Z scores range from -1.5 to 1.8. The cluster with a minimum Z score was selected for further studies. This cluster is shown in (Figure 3). The protein-protein interactions predicted by the KFC server are shown in (Table 2).

3.4. MD Simulation. Cluster 4 was selected to check the binding stability in the complex form by a 50 ns simulation. For this purpose, different analyses, i.e., RMSD, RMSF, radius of gyration (Rg), dynamic cross-correlation, and principal component analysis (PCA), were performed. Figure 4(a) shows the RMSD plots of the human PGRMC1 protein (green) and Trichinella spiralis (red). The RMSD plot of the human PGRMC1 protein showed that the RMSD of initial confirmation was ~2 Å at the start of the simulation. The RMSD remained in the range of ~2 to 2.5 Å till ~30 ns, and a slight increase was observed in value where it reached ~3 Å. The RMSD value attained stability after 30 ns and remained stable till the end of the simulation. The average RMSD value of this protein was 2.32 ± 0.20 Å which showed the overall stability of protein during simulation. Similarly, the RMSD plot of T. spiralis protein showed that the initial conformation of protein had an RMSD value of ~2 Å that increased to ~3 Å near ~12 ns. The RMSD value remained in the range of ~2.5 to 3 Å during 12 to 20 ns. After 20 ns, the RMSD value remained stable in the range of 2.5 to 3 Å till the end of the simulation. The average RMSD value of this protein was 2.44 ± 0.20 Å which showed protein stability. Similarly, the amino acid fluctuations were calculated by RMSF analysis. Figure 4(b) shows the RMSF plots of the human PGRMC1 protein (green) and T. spiralis (red).

The green plot shows that the residues ~20-25 had the highest RMSF value which indicated that these residues showed maximum flexibility during the simulation. The remaining residues showed a lower RMSF value than these residues which showed that those were rigid during simulation except for the residues from ~90-108 as these are at the C-terminal. Similarly, the red plot showed the same behavior, and the residues from ~20-30 showed the flexibility which indicated the loop region in protein while the remaining residues with lower RMSF values showed the rigid part of the protein. The compactness of proteins was calculated by Rg. Rg calculates the protein unfolding events observed during the simulation. Figure 4(c) shows the Rg plots of the human PGRMC1 protein (green) and T. spiralis (red). The Rg plots of both proteins showed the same trend throughout the simulation. The Rg value at the start was ~19.5 Å, increased to ~20.2 Å at 10 ns, and then dropped to ~20 Å after 12 ns. From 10 to 35 ns, the Rg value remained in the range of ~19.75 to 20 Å. After 35 ns, the Rg value increased to ~20.5 Å and remained in this range till 40 ns. The Rg value dropped to ~20 Å at 40 ns and then remained in this range till the end of the simulation. The Rg plots of both proteins showed that there were no unfolding events were observed during the simulation.

The pairwise correlated motions among the residues of human PGRMC1 protein and T. spiralis were obtained from the trajectory. The cross-correlation maps of both proteins are shown in Figures 5(a) and 5(b), respectively. The cyan color showed the motions of correlated residues while the magenta color represented the anticorrelated residues. The solid diagonal cyan line showed the positively correlated residues of the protein during simulation. The dynamic motions of the residues were further investigated by the principal component analysis. In the graphs of both proteins, the eigenvalues of the protein had been plotted against the corresponding eigenvector index for the first twenty modes of motion (Figures 5(c) and 5(d)). The eigenvalues showed eigenvector fluctuations in hyperspace.

The overall movement of the proteins was controlled by eigenvectors with higher eigenvalues. The largest motion of the residues of human PGRMC1 protein was observed in PC1 (22.74%). The second most important direction was PC2 which accounted for a total of 15.15% variance in the protein residues. PC2 was orthogonal to PC1. Similarly, PC3 recorded a 6.99% variance. The total protein variance in the first three PC components was 44.88%. The overall variance in the T. spiralis protein was 45.57%. The highest motions recorded in PC1 were 26.75%, while the variations in PC2 and PC3 were 12.93% and 5.89%, respectively.

4. Discussion

PGRMC1 and PGRMC2 are membrane-associated progesterone receptor (MAPR) proteins that belong to the same family [16, 17]. In this study, we find the association of Trichinella spiralis membrane-associated progesterone receptor component 2 with human PGRMC1 protein by applying molecular modelling and simulation techniques. For this purpose, the homology model of the Trichinella spiralis membrane-associated progesterone receptor component 2 was built by SWISS-MODEL, and the accuracy of the model was validated by the Ramachandran plot and ERRAT quality score [33, 34]. The Ramachandran plot (Figure 1(a)) illustrated that the amino acid residues of the model were in the allowed region and not a single residue was in the disallowed or unfavorable region which explains the better quality of the model. To find the interactions of this protein with human PGRMC1 protein, the binding sites of both proteins were predicted by CASTp web server [35]. As a result, we find that the binding site residues of human PGRMC1 protein were GLU 7, PHE 8, PHE 10, PHE 18, ARG 25, LEU 27, ASP 36, and VAL 104 (Figure 2), while the target protein showed the whole sequence as the binding pocket. Both proteins were docked through the HADDOCK web server [36]. We prioritized the docked clusters based on the HADDOCK analysis and Z scores. We also discovered that the interactions between Trichinella spiralis membrane-associated progesterone receptor component 2 and human PGRMC1 protein had a KFC > 1, indicating that the best protein-protein interactions actually occurred in the conserved region [37]. The docking results showed that the closest distances between these two proteins were located in cluster 4, indicating that interactions are possible.

We further analyzed the details of proteins and their stability in the complex form through molecular dynamics

simulation. Several analyses have been performed to check the stability of both proteins involved; root means square deviations, root means square fluctuations, the radius of gyration studies, dynamic cross-correlation maps, and principal component analysis. The RMSD analysis confirmed the steady confirmation with an average RMSD of 2.32 ± 0.20 and 2.44 ± 0.20 for human PGRMC1 and *Trichinella spiralis* membrane-associated progesterone receptor component 2 proteins, respectively. The residual flexibilities of both proteins were lower which showed that the hydrogen bonds of the systems maintained the integrity of protein structures during the simulation. Additionally, the steady radius of gyration plots of both proteins illustrated that the protein structures remained compact during the simulation. To further validate the complex stability, two additional analyses have been performed that explained the dynamic behavior of proteins throughout the simulation period. The cross-correlation maps of both proteins (Figures 5(a) and 5(b)) described the dynamic motions of proteins; a solid cyan diagonal line explained the positive correlation of residues while the magenta patches showed the negative correlations. The amino acid residues of both proteins were positively correlated throughout the simulation. Similarly, we performed a principal component analysis to calculate the variance in the residues in three hyperspace regions. The overall variance of 44.88% and 45.57% for human PGRMC1 and *Trichinella spiralis* membrane-associated progesterone receptor component 2 proteins, respectively, explained that the proteins were less flexible during simulation [21]. Hence, we assumed that both proteins made stable complexes based on the results of a simulation.

5. Conclusion

To conclude based on docking and simulation results, we assumed that the interaction of both proteins *Trichinella Spiralis* membrane-associated progesterone receptor component 2 and human PGRMC1 formed stable complexes. The discovery of this protein (*Ts-MAPRC2*) may open up new avenues of drug and vaccine development for the treatment of *Trichinellosis* in humans. Further studies are ongoing to determine the antibody effect of this protein (*Ts-MAPRC2*) in vitro and in vivo.

Data Availability

Data is contained within the article.

Conflicts of Interest

The authors declare no conflict of interest.

Acknowledgments

References

[1] Y. Yang, X. Bai, C. Li et al., "Molecular characterization of fructose-1,6-bisphosphate aldolase from *Trichinella spiralis* and its potential in inducing immune protection," *Frontiers in Cellular and Infection Microbiology*, vol. 9, p. 122, 2019.

[2] J. Cui and Z. Wang, "An epidemiological overview of swine trichinellosis in China," *The Veterinary Journal*, vol. 190, no. 3, pp. 323–328, 2011.

[3] K. D. Murrell and E. Pozio, "Worldwide occurrence and impact of human trichinellosis, 1986–2009," *Emerging Infectious Diseases*, vol. 17, no. 12, pp. 2194–2202, 2011.

[4] WHO, *Multicriteria-Based Ranking for Risk Management of Food-Borne Parasites*, WHO, Geneva, Switzerland, 2016.

[5] J. Cui, P. Jiang, L. Na Liu, and Z. Q. Wang, "Survey of *Trichinella* infections in domestic pigs from northern and eastern Henan, China," *Veterinary Parasitology*, vol. 194, no. 2-4, pp. 133–135, 2013.

[6] P. Jiang, X. Zhang, L. A. Wang et al., "Survey of Trichinella infection from domestic pigs in the historical endemic areas of Henan province, Central China," *Parasitology Research*, vol. 115, no. 12, pp. 4707–4709, 2016.

[7] X. Bai, X. Hu, X. Liu, B. Tang, and M. Liu, "Current research of Trichinellosis in China," *Frontiers in Microbiology*, vol. 8, p. 1472, 2017.

[8] X. Wang, L. Li, X. Wei et al., "Proteomic analysis of the response of *Trichinella spiralis* muscle larvae to exogenous nitric oxide," *PLoS One*, vol. 13, no. 6, pp. 1–15, 2018.

[9] R. R. White, S. Miyata, E. Papa, E. Spooner, K. Gounaris, and E. Murray, "Characterisation of the *Trichinella spiralis* deubiquitinating enzyme, TsUCH37, an evolutionarily," *PLoS Neglected Tropical Diseases*, vol. 5, no. 10, p. e1340, 2011.

[10] N. Zhang, W. Li, and B. Fu, "Vaccines against *Trichinella spiralis*: Progress, challenges and future prospects," *Transboundary and Emerging Diseases*, vol. 65, no. 6, pp. 1447–1458, 2018.

[11] S. Feng, X. Wu, X. Wang et al., "Vaccination of mice with an antigenic serine protease-like protein elicits a protective immune response against *Trichinella spiralis* infection," *The Journal of Parasitology*, vol. 99, no. 3, pp. 426–432, 2013.

[12] Y. Gu, X. Sun, B. Li, J. Huang, B. Zhan, and X. Zhu, "Vaccination with a paramyosin-based multi-epitope vaccine elicits significant protective immunity against *Trichinella spiralis* infection in mice," *Frontiers in Microbiology*, vol. 8, p. 1475, 2017.

[13] Y. Y. Song, Y. Zhang, D. Yang et al., "The immune protection induced by a serine protease inhibitor from the foodborne parasite *Trichinella spiralis*," *Frontiers in Microbiology*, vol. 9, p. 1544, 2018.

[14] Z. Yang, W. Li, Z. Yang, A. Pan, W. Liao, and X. Zhou, "A novel antigenic cathepsin B protease induces protective immunity in Trichinella-infected mice," *Vaccine*, vol. 36, pp. 248–255, 2018.

[15] M. A. Cahill, "Progesterone receptor membrane component 1: an integrative review," *The Journal of Steroid Biochemistry and Molecular Biology*, vol. 105, no. 1-5, pp. 16–36, 2007.

[16] R. M. Lösel, D. Besong, J. J. Peluso, and M. Wehling, "Progesterone receptor membrane component 1-many tasks for a versatile protein," *Steroids*, vol. 73, no. 9-10, pp. 929–934, 2008.

[17] E. Falkenstein, C. Meyer, C. Eisen, P. C. Scriba, and M. Wehling, "Full-length cDNA sequence of a progesterone membrane-binding protein from porcine vascular smooth muscle cells," *Biochemical and Biophysical Research Communications*, vol. 229, no. 1, pp. 86–89, 1996.

[18] J. J. Peluso, "Multiplicity of progesterone's actions and receptors in the mammalian ovary," *Biology of Reproduction*, vol. 75, no. 1, pp. 2–8, 2006.

[19] G. Oliveira and D. A. Johnston, "Mining the schistosome DNA sequence database," *Trends in Parasitology*, vol. 17, no. 10, pp. 501–503, 2001.

[20] W. Hu, Q. Yan, D.-K. Shen et al., "Evolutionary and biomedical implications of a Schistosoma japonicum complementary DNA resource," *Nat. Genet.*, vol. 35, pp. 139–147, 2003.

[21] M. T. Aleem, J. Shi, Z. Yu et al., "Characterization of membrane-associated progesterone receptor Component-2 (MAPRC2) from *Trichinella spiralis* and its interaction with progesterone and mifepristone," *Vaccines*, vol. 9, no. 8, 2021.

[22] A. Waterhouse, M. Bertoni, S. Bienert et al., "SWISS-MODEL: homology modelling of protein structures and complexes," *Nucleic Acids Research*, vol. 46, no. W1, pp. W296–W303, 2018.

[23] R. A. Laskowski, M. W. MacArthur, D. S. Moss, and J. M. Thornton, "PROCHECK: a program to check the stereochemical quality of protein structures," *Journal of Applied Crystallography*, vol. 26, no. 2, pp. 283–291, 1993.

[24] O. Dym, D. Eisenberg, and T. Yeates, "ERRAT," *International Tables for Crystallography*, vol. F, pp. 678-679, 2012.

[25] W. Tian, C. Chen, X. Lei, J. Zhao, and J. Liang, "CASTp 3.0: computed atlas of surface topography of proteins," *Nucleic Acids Research*, vol. 46, no. W1, pp. W363–W367, 2018.

[26] S. J. De Vries and M. Van Dijk, "The HADDOCK web server for data-driven biomolecular docking," *Nature Protocols*, vol. 5, no. 5, pp. 883–897, 2010.

[27] X. Zhu and J. C. Mitchell, "KFC2: A knowledge-based hot spot prediction method based on interface solvation, atomic density, and plasticity features," *Proteins: Structure, Function, and Bioinformatics*, vol. 79, no. 9, pp. 2671–2683, 2011.

[28] W. Humphrey, A. Dalke, and K. Schulten, "VMD: Visual molecular dynamics," *Journal of Molecular Graphics*, vol. 14, no. 1, pp. 33–38, 1996.

[29] J. C. Phillips, R. Braun, W. Wang et al., "Scalable molecular dynamics with NAMD," *Journal of Computational Chemistry*, vol. 26, no. 16, pp. 1781–1802, 2005.

[30] D. A. Case, H. M. Aktulga, K. Belfon et al., *Amber 2021: Reference Manual*, University of California, San Francisco, 2021.

[31] D. A. Case, T. A. Darden, T. E. Cheatham III et al., "AMBER 9," vol. 45, University of California, San Francisco, 2006.

[32] D. J. Price and C. L. Brooks III, "A modified TIP3P water potential for simulation with Ewald summation," *The Journal of Chemical Physics*, vol. 121, no. 20, pp. 10096–10103, 2004.

[33] B. J. Grant, A. P. C. Rodrigues, K. M. ElSawy, J. A. McCammon, and L. S. D. Caves, "Bio3d: an R package for the comparative analysis of protein structures," *Bioinformatics*, vol. 22, no. 21, pp. 2695-2696, 2006.

[34] R. W. Hooft, C. Sander, and G. Vriend, "Objectively judging the quality of a protein structure from a Ramachandran plot," *Bioinformatics*, vol. 13, no. 4, pp. 425–430, 1997.

[35] S. A. Sehgal, N. A. Khattak, and A. Mir, "Structural, phylogenetic and docking studies of D-amino acid oxidase activator (DAOA), a candidate schizophrenia gene," *Theoretical Biology and Medical Modelling*, vol. 10, no. 1, pp. 1–13, 2013.

[36] S. Kumar and A. Srikanth, "Structural validation and identification of active site in deadly virus," *International Journal of Novel Trends in Pharmaceutical Sciences*, vol. 9, no. 3, pp. 55–58, 2020.

[37] A. Adji, N. J. Niode, V. V. Memah et al., "Designing an epitope vaccine against *Dermatophagoides pteronyssinus*: An *in silico* study," *Acta Tropica*, vol. 222, article 106028, 2021.

Research Article

Jinlida Granules Reduce Obesity in db/db Mice by Activating Beige Adipocytes

Hong-ru Zhou [ID],[1,2,3] **Tong-xing Wang** [ID],[2,3] **Yuan-yuan Hao** [ID],[2,3,4] **Yun-long Hou,**[2,3]
Cong Wei,[2,3] **Bing Yao,**[2,3] **Xuan Wu,**[1,2,3] **Dan Huang,**[5] **Hui Zhang,**[6] **and Yi-ling Wu** [ID][1,2,3]

[1]*Hebei Medical University, No. 361 Zhongshan Road, Chang'an District, Shijiazhuang, Hebei Province, China*
[2]*National Key Laboratory of Collateral Disease Research and Innovative Chinese Medicine, Shijiazhuang, China*
[3]*Key Laboratory of State Administration of TCM (Cardio-Cerebral Vessel Collateral Diseases), Shijiazhuang, China*
[4]*Hebei University of Chinese Medicine, Shijiazhuang, China*
[5]*Affiliated Hospital of Integrated Traditional Chinese and Western Medicine, Nanjing University of Chinese Medicine,
Nanjing 210028, China*
[6]*The First Affiliated Hospital of Henan University of CM, Zhengzhou, China*

Correspondence should be addressed to Yi-ling Wu; wuyiling68@126.com

Recent studies indicate existence of beige adipocytes in adults. Upon activation, beige adipocytes burn energy for thermogenesis and contribute to regulation of energy balance. In this study, we have analyzed whether Jinlida granules (JLD) could activate beige adipocytes. JLD suspended in 0.5% carboxymethyl cellulose (CMC) was gavage fed to db/db mice at a daily dose of 3.8 g/kg. After 10 weeks, body weight, biochemical, and histological analyses were performed. In situ hybridization, immunofluorescence, and western blotting were conducted to test beige adipocyte activation in mice. X9 cells were induced with induction medium and maintenance medium containing 400 μg/mL of JLD. After completion of induction, cells were analyzed by Nile red staining, time polymerase chain reaction (PCR), western blotting, and immunofluorescence to understand the effect of JLD on the activation of beige adipocytes. A molecular docking method was used to preliminarily identify compounds in JLD, which hold the potential activation effect on uncoupling protein 1 (UCP1). JLD treatment significantly improved obesity in db/db mice. Biochemical results showed that JLD reduced blood glucose (GLU), triglyceride (TG), and low-density lipoprotein cholesterol (LDL) levels as well as liver aspartate aminotransferase (AST) and alanine aminotransferase (ALT) levels in mice. Hematoxylin and eosin staining (H&E) showed that JLD reduced hepatocyte ballooning changes in the liver. Immunofluorescence showed that JLD increased the expression of the thermogenic protein, UCP1, in the beige adipose tissue of mice. JLD also increased the expression of UCP1 and inhibited the expression of miR-27a in X9 cells. Molecular docking results showed that epmedin B, epmedin C, icariin, puerarin, and salvianolic acid B had potential activation effects on UCP1. The results suggest that JLD may activate beige adipocytes by inhibiting miR-27a expression, thereby promoting thermogenesis in beige adipocytes. This study provides a new pharmacological basis for the clinical use of JLD.

1. Introduction

The prevalence of obesity is increasing globally. Assuming an annual growth rate of 2.6%, the number of obese adults in 2025 will be 40% higher than that reported in 2012 [1]. The most striking feature of obesity is the abnormal adipocyte proliferation and hypertrophy. Hypertrophic adipose tissue secretes adipokines that stimulate various organs and cause diseases [2] such as metabolic syndrome, coronary heart disease, diabetes, and nonalcoholic steatohepatitis [3–6]. However, treatment options for obesity are currently limited.

Beige adipocytes are regarded as the third type of adipocyte with an intermediate morphology between white and brown adipocytes (BAT). Although like brown adipocytes in the thermogenic function [7], beige adipocytes sporadically

reside in the areas of white adipose tissue (WAT) depots rather than in the BAT depots. In addition, current research suggests that BAT are derived from myf5+ progenitor cells [8], while beige adipocytes may originate from precursors of white adipocytes [9]. In the inactive state, beige adipocytes resemble WAT with an extremely low basal expression of UCP1 but are stimulated by cold exposure, receptor activation, and exercise, the expression of UCP1 will be regulated, and its function is changed as same as that of classic BAT. Thus, to some extent, beige adipocytes are considered the inducible BAT. Due to the thermogenic function, activated beige adipocytes can alleviate the disorders of blood glucose and lipid metabolism in mice [10]. Although the activation of beige adipocytes is beneficial to energy expenditure, the potential mechanisms for the induction of differentiation remain unclear. Recent research demonstrates that the peroxisome proliferator-activated receptor-gamma (PPARγ) protein can promote the activation of beige adipocyte through activating PPAR coactivator 1-alpha (PGC-1α), by which UCP1 expression increases in the inner mitochondrial membrane of beige adipocyte to stimulate thermogenesis [11]. Therefore, the activation of the PPARγ/PGC-1α pathway may be a potential target for obesity treatment. MicroRNAs (miRNAs) are endogenous noncoding single-stranded RNAs composed of 19-23 nucleotides that may play a critical regulatory role in a variety of biological processes, especially in the posttranscriptional regulation of proteins [12]. miR-27a can inhibit the expression of PPARγ, acting as a negative obesity regulator [13, 14]. Therefore, we hypothesized that the antiobesity effect on inhibiting the expression of miR-27 might depend on the activation of the beige adipocytes.

Jinlida granules (JLD), a traditional Chinese medicine (TCM) prescription produced by Yiling Pharmaceutical Co., Ltd. (Shijiazhuang, Hebei Province, China) are clinically used for the treatment of type 2 diabetes. Previous studies have shown that JLD can maintain glucose and lipid homeostasis, increase insulin sensitivity, inhibit fat accumulation, and promote the expression of brown adipose cell-derived adipokine [15–20]. However, there is no study about the antiobesity effect of JLD associated with the activation of beige adipocytes. The aim of this study was to reveal the antiobesity effect of JLD and explore the potential mechanism by activating the beige adipocytes.

2. Materials and Methods

2.1. Oral Gavage Preparation. JLD, composed of 17 TCMs (ginseng, sealwort, *Rhizoma Atractylodis*, *Sophora flavescens*, *Ophiopogon japonicus*, dried rehmannia root, prepared fleece flower root, dogwood, *Herba Eupatorii, Coptis, Epimedium*, poria, *Anemarrhena*, lychee seed, *Salvia, Pueraria montana Lobata*, and *Cortex Lycii*), was purchased from Shijiazhuang Yiling Pharmaceutical Co., Ltd. (Shijiazhuang, China) and suspended in 0.5% carboxymethyl cellulose (CMC) for intragastric administration to mice at a daily dose of 3.8 g/kg for 10 weeks, as previously reported [19–22]. Rosiglitazone tablets, purchased from Chengdu Ruiheng Pharmaceutical Co., Ltd. (Chengdu, China), were ground

into a powder and suspended in 0.5% CMC for intragastric administration to mice at a daily dose of 4 mg/kg.

2.2. Cellular Drug Preparation. JLD ($3 ± 0.1$ g) was dissolved in $30 ± 1$ mL serum-free DMEM/F12 medium; after ultrasonic solubilization, the mixture was centrifuged at 4000 rpm and the supernatant was filtered through a $0.22 \mu m$ filter (Millipore, USA).

Finally, JLD suspension with concentration of $100 ± 10$ mg/mL was obtained, and the liquid was stored at -20°C.

2.3. Grouping and Feeding Animals. All animal studies were approved by the Ethical Review Board of Hebei Yiling Pharmaceutical Research Company (Shijiazhuang, China). Male db/db mice (4 weeks old, $20 ± 2$ g) were purchased from Jiangsu Jicui Yaokang Biotechnology Co., Ltd. (Nanjing, China) and reared at 22°C, 50% humidity, and 12-hour simulated natural light with adequate diet and water. The mice were acclimatized for one week before being randomly divided into three groups ($n = 20$). The blank group was administered with CMC by oral gavage, while the control group and JLD group mice were administered with rosiglitazone and JLD, respectively, daily for 10 weeks.

The body weight of the mice was measured weekly from the fourth week onward. In the last week of the study, the mice were exposed to 4°C environment to test their ability of cold tolerance, and their anal temperatures were recorded as body temperatures. The mice were anesthetized and euthanized by cervical dislocation. The weight of subcutaneous, inguinal, epididymal adipose and liver tissues was recorded and then stored in liquid nitrogen or with a fixative for future analysis.

2.4. Biochemical Parameter Detection. Total triglyceride (TG), low-density lipoprotein cholesterol (LDL-C), total cholesterol (TC), serum aspartate aminotransferase (AST), alanine aminotransferase (ALT), and glucose (GLU) levels were measured by using an automated biochemical analyzer (Hitachi 7080, Japan) and a commercial kit (Jiuqiang, Beijing, China).

2.5. Pathology and Immunohistochemistry. The fixed, embedded, and sectioned adipose tissue and liver specimens were stained with hematoxylin and eosin (H&E). After staining, morphological tests were performed by conventional histological methods. The adipose tissue sections were deparaffinized and processed using an immunohistochemistry kit (ZSGB-BIO, China). Target proteins were labeled with two antibodies: UCP1 (10983, Abcam) and CD137 (EPR23218-111, Abcam), and fluorescence in situ hybridization (FISH) was performed with an miR-27a probe (-DIG-GCGGAACUUAGCCACUGUGAA-DIG-3′). The slides were observed and photographed by using a fluorescence microscope (Leica DM6000, Germany), and the fluorescence intensity was calculated by using ImageJ (1.53).

2.6. Cell Culture and Induction. The X9 cell line, a beige adipose precursor cell developed by the Harvard Medical School [9], was purchased from the ATCC Cell Bank (CRL-3282, USA) and cultured in DMEM/F12 medium

TABLE 1: Primer sequences used for qRT-PCR in this study.

Primer	Forward	Reverse
PPARγ	CCTGGACCTCTGCTGGTGAT	GCTGGAGAAATCAACCGTGG
PGC-1α	GGCACCTGAACAGAACGAAC	CAACAGGCATCAGCAGTGTC
UCP1	ACGTCCCCTGCCATTTACTG	CCCTTTGAAAAAGGCCGTCG
GAPDH	CTGCGACTTCAACAGCAACT	GAGTTGGGATAGGGCCTCTC
miRNA27a	TGCGCTTCACAGTGGCTAAGT	CCAGTGCAGGGTCCGAGGTATT
U6	CGCTTCGGCAGCACATATAC	AAATATGGAACGCTTCACGA

(ATCC30-2006), 15% fetal bovine serum (FBS), and 2.36 mM L-alanyl-L-glutamine. The appropriate JLD concentration was screened using the MTS method. During cell induction, the blank group was incubated in DMEM/F12 medium containing 10% FBS, which was replaced every 2 days. In the control group, 5 μM dexamethasone, 0.5 μg/mL insulin, 0.5 mM isobutylmethylxanthine q5, 1 μM rosiglitazone, and 1 nM T3 in DMEM/F12 medium containing 10% FBS were added to the cultures on the first day of induction (day 0). This solution was replaced every other day (day 2) until the DMEM/F12 medium containing 10% FBS, 0.5 μg/mL insulin, and 1 nM T3 was added to the cultures (day 4). After 2 days (day 6), cell differentiation was complete, and follow-up experiments were conducted.

2.7. Nile Red Staining. X9 cells were seeded in 96-well plates at a density of no less than 1×10^5/mL. After inducing differentiation and maturation, the medium was discarded, the cells were washed with phosphate-buffered saline, and Nile red dye was added. The cells were observed using a fluorescence microscope to examine the morphology and number of lipid droplets in the cells. The fluorescence intensity was measured using a microplate reader (BioTek, USA).

2.8. Confocal Microscopy. The X9 cells were seeded into 35 mm glass-bottom cell culture dishes with a density no less than 1×10^5/mL and fixed after the induction of differentiation and maturation. UCP1 was observed by using immunofluorescence under a laser confocal microscope (ZEISS, Germany) and images were collected, and the fluorescence intensity was calculated by using ImageJ (1.53).

2.9. Western Blotting. Protein samples were collected, separated on a 12% SurePAGE preformed gel (GenScript, China), and transferred onto polyvinylidene difluoride (PVDF) membranes (Millipore, USA). The membranes were completely sealed with a sealing solution and incubated with primary antibody overnight at 4°C and then incubated with a secondary antibody for 1 h at 4°C. After incubation, an Odyssey infrared laser imaging system (LI-COR, USA) was used for signal detection. Protein quantification was performed using image analysis software. The antibodies used in this experiment include anti-PPARγ (ab45036, Abcam), anti-PGC-1α (ab54481, Abcam), anti-UCP1 (ab10983, Abcam), anti-oxphos (ab110413, Abcam), anti-β-actin (3700, CST), and anti-GAPDH (5174, CST).

2.10. Quantitative Reverse Transcription-Polymerase Chain Reaction (qRT-PCR). X9 cells were seeded in 6-well plates with a density no less than 1×10^5/mL. After induced differentiation and maturation, total RNA was extracted by using the Eastep™ Total RNA Extraction Kit (Promega, China). cDNA was synthesized by using the Prime Script™ synthesis kit (TaKaRa, China), detected by SYBR Green PCR Master Mix (TaKaRa), and analyzed by using an ABI 7900 real-time fluorescent quantitative PCR instrument (ABI, USA). The miRNA was extracted from X9 cells on days 1, 3, and 5 after induction, and cDNA was synthesized by using the Mir-X miRNA First-Strand Synthesis Kit (Takara Bio, USA). The expression level was detected by using SYBR Green PCR Master Mix (TaKaRa) and analyzed by using the ABI 7900 real-time fluorescent quantitative PCR instrument. The primer sequence is shown in Table 1.

2.11. Molecular Docking Evaluation. In the previous study, nine compounds were identified in the established ultraperformance liquid chromatography (UPLC) fingerprints of JLD, including danshensu sodium, puerarin, salvianolic acid B, epmedin B, epmedin C, icariin, ginsenoside Rb1, ginsenoside Rb2, and ginsenoside Rc [23]. In order to preliminarily identify the molecules with the potential activating effect on UCP1, a molecular docking method was taken to evaluate the binding affinity. AutoDock Vina 1.1.2 was used to conduct the docking task [24]. Through literature search, we obtained five small molecular compounds (berberine [25], thiazolidinedione [26], rhein [27], formononetin [28], and fluvastatin sodium [29]), which can activate UCP1 as the control. The compound structures were downloaded from the PubChem database in SDF format [30]. Three-dimensional structures of UCP1 (P25874) were obtained from the AlphaFold database (https://alphafold.ebi.ac.uk) [31, 32], which is an openly accessible and extensive database of high-accuracy protein-structure predictions. ProteinsPLUS (https://proteins.plus/) was used to predict the active pockets. The ligands and receptors were prepared according to the tutorial of AutoDock Vina. If the docking score of compounds in JLD is higher than that of all control molecules and have good binding activity in more than one site, they are more likely to have potential activation effect on UCP1. The conformation with the lowest affinity was used as the best docking conformation, and PLIP was taken to visualize the interaction mode [33].

(a)

(b)

(c)

(d)

(e)

(f)
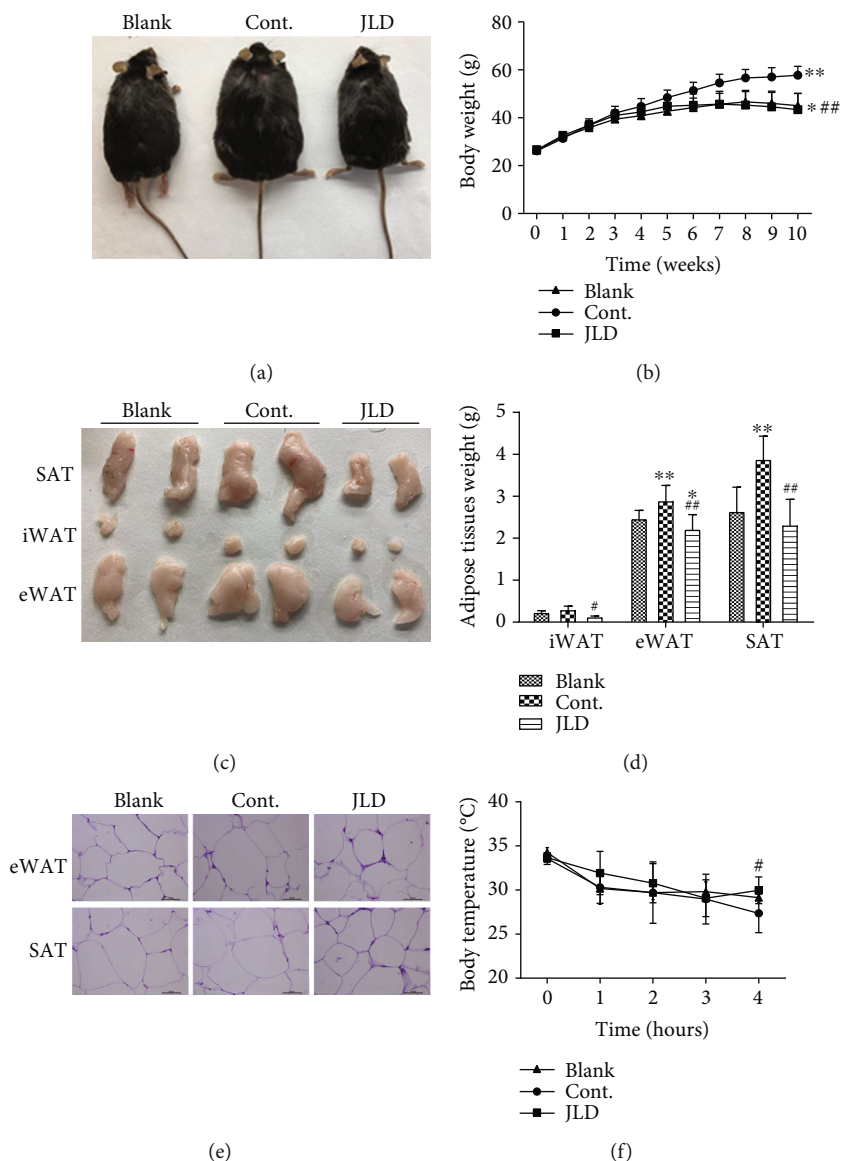
FIGURE 1: JLD reduces fat content and maintains body temperature in db/db mice. (a) Representative pictures of the weight in mice after 10 weeks of intervention and body weight-time curve ($n = 15$-20). (b) Body weight-time curve ($n = 15$-20). (c) Representative pictures of SAT, iWAT, and eWAT. (d) SAT, iWAT, and eWAT weights ($n = 8$-10). (e) Representative H&E staining of iWAT and eWAT (400x). (f) Body temperature-time curve ($n = 5$-6). Data are shown as the mean ± SD. $^{*}P < 0.05$, $^{**}P < 0.01$ vs. blank group, $^{#}P < 0.05$, $^{##}P < 0.01$ vs. control group. All graphs are done through GraphPad Prism (V.5.01).

2.12. Statistics. All experimental data were expressed as the mean ± standard deviation. SPSS19.0 software was used for statistical analysis. One-way analysis of variance (ANOVA) was used for comparison among groups, and $P < 0.05$ was considered statistically significant. All graphs are done through GraphPad Prism (V.5.01).

3. Results

3.1. JLD Reduced Adipose Content and Maintained Body Temperature in db/db Mice. The fat accumulation in mice can be observed intuitively through the body weight, so we observed the body shape, adipose morphology, body weight, and adipose weight of mice to understand the situation of fat

accumulation and metabolism in mice. In addition, the maintenance of body temperature was also observed under 4°C environment. The results showed that JLD significantly reduced body weight in db/db mice. The body weight became different from the third week of taking JLD (Figures 1(a) and 1(b)). The mice in the control group gained weight significantly faster than the mice in the JLD-treated group, and the same results were observed in the blank group (Figure 1(b)). Epididymal white adipose tissue (eWAT) was reduced in the JLD-treated group compared with the blank group (Figures 1(c) and 1(d)). Compared with mice in the control group, JLD-treated mice had reduced subcutaneous white adipose tissue (SAT), eWAT, and inguinal subcutaneous white adipose tissue (iWAT)
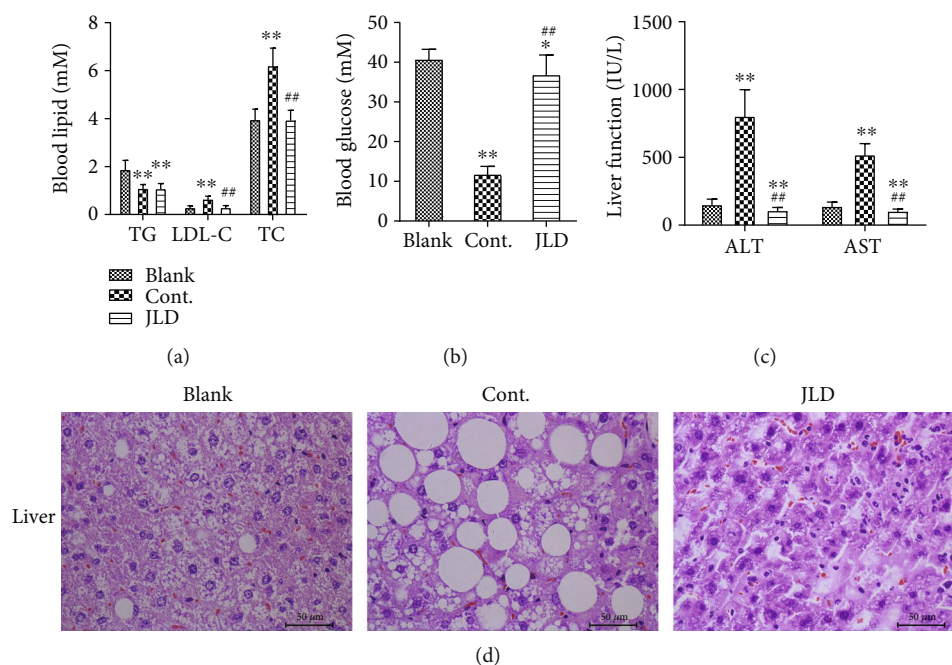
FIGURE 2: JLD maintained glucose and lipid homeostasis in db/db mice. (a, b) Fasting serum lipid levels of TG, LDL-C, TC, and GLU ($n = 14$-16). (c) Serum AST and ALT concentrations ($n = 10$-12). (d) Representative H&E staining of the liver (400x). Data are shown as the mean ± SD. $^*P < 0.05$, $^{**}P < 0.01$ vs. blank group, $^{\#\#}P < 0.01$ vs. control group. All graphs are done through GraphPad Prism (V.5.01).

(Figures 1(c) and 1(d)). Additionally, compared with the control group, the morphology of fat cells in the JLD treatment group was significantly different, with more complete cell structure and smaller cell morphology (Figure 1(e)). Interestingly, the data showed that the body temperature of mice in the JLD-treated group was more stable at 4°C environment and was significantly higher than that of control mice after 4 h exposure to 4°C (Figure 1(f)). The above data suggest that JLD could reduce the lipid accumulation in mice and maintained the body temperature.

3.2. JLD Maintained Glucose and Lipid Homeostasis in db/db Mice.

In order to further understand the effects of JLD on glucose and lipid metabolism, we observed the blood lipid, blood glucose, liver function, and lipid deposition in the liver of mice. Spontaneous obesity occurred in db/db mice, leading to disorders of glucose and lipid. JLD also plays an important role in improving lipid metabolism disorders. In the JLD-treated group, serum TG levels were lower than those in the blank group, and LDL-C and TC levels were significantly lower than those in the control group (Figure 2(a)). Additionally, GLU levels were significantly lower than those in the blank group (Figure 2(b)). JLD reduced liver damage caused by high lipid levels, indicated by significantly lower ALT and AST levels in the JLD-treated mice than those in the control group (Figure 2(c)). H&E staining result showed that hepatocyte ballooning in the JLD-treated group was significantly reduced compared to that in the other groups (Figure 2(d)). These results indicated that JLD could regulate glucose and lipid metabolism in db/db mice and improve liver injury caused by high lipid levels.

3.3. JLD Activated Beige Adipocytes in db/db Mice.

To understand the change of WAT after JLD treatment, we observed the activation of WAT by immunofluorescence, in situ hybridization, and western blot. However, UCP1 expression increased in WAT of db/db mice treated with JLD compared to the control group, although no increase was observed in beige adipocytes (Figures 3(a) and 3(b)), indicating that JLD induces the activity of beige adipocyte. To identify beige fat, CD137 was specifically labeled, which is a member of the tumor necrosis factor receptor superfamily and has recently been identified as one of the marker proteins of beige fat [9]. Western blotting results showed that UCP1 expression was significantly increased in the JLD-treated group compared with the control group (Figures 3(c) and 3(d), Supplementary Figure S1A). The inhibition of WAT is closely related to the expression of miRNA27a. Therefore, we further investigated the expression of miR-27a using fluorescence in situ hybridization, and the results showed that JLD inhibited miR-27a expression. The high expression of miR-27a in the control group may be due to the gain of adipose and weight (Figures 4(a) and 4(b)).

3.4. JLD Reduced Lipid Deposition in X9 Cells.

We verified the results of animal experiments at the cellular level to observe whether JLD could activate beige adipocytes and increase the expression of UCP1 in beige adipocytes. We used the MTS assay to examine the effect of different concentrations of JLD on the activity of X9 cells (Figure 5(a)), and 400 μg/mL was selected as the dose. We found that JLD could markedly reduce the lipid droplet content (Figures 5(b) and 5(c)) and increase the expression of UCP1 in X9 cells (Figures 5(d) and 5(e)) compared with

(a)

(b)

(c)

(d)
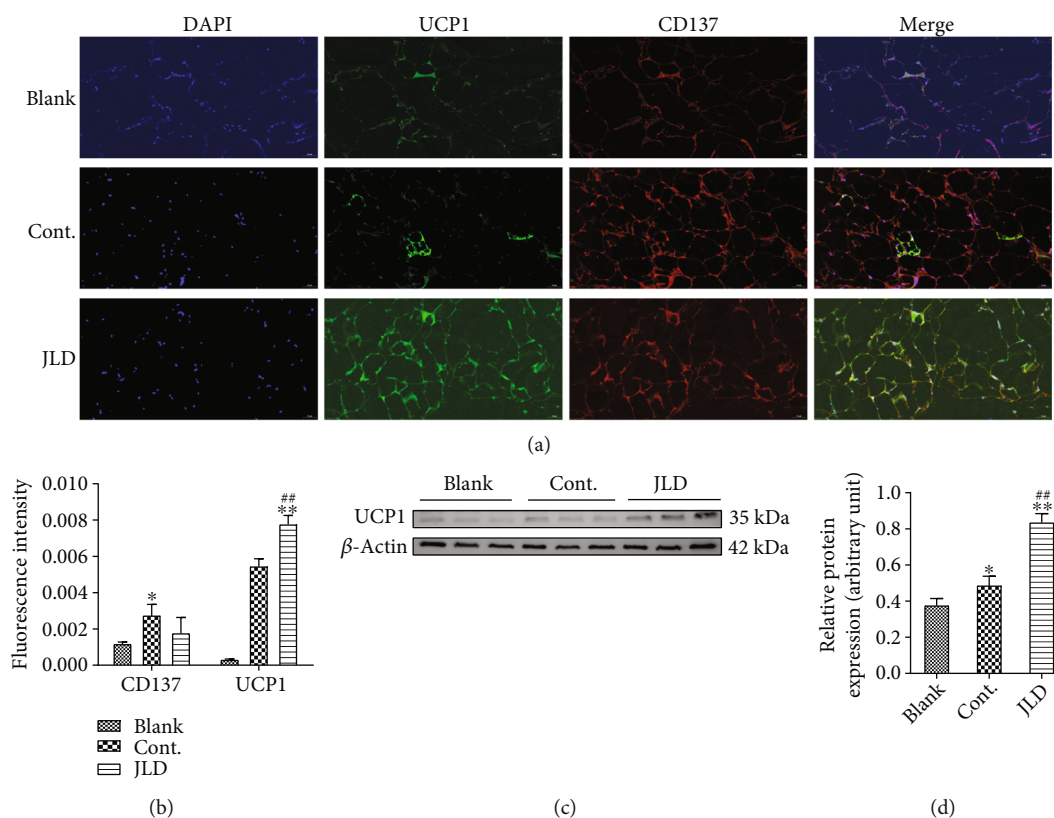
FIGURE 3: JLD activates the activity of beige adipocytes in db/db mice. (a) Fluorescence images of UCP1 and CD137 in the subcutaneous fat tissue of db/db mice (200x). (b) Fluorescence intensity of UCP1 and CD137 in the subcutaneous fat tissue of db/db mice. (c) Western blot analysis of thermogenic-related protein UCP1 expression in subcutaneous fat tissue of db/db mice and (d) quantitative measurement of relative protein expression ($n = 4$-5). Data are shown as the mean ± SD. $^*P < 0.05$, $^{**}P < 0.01$ vs. blank group, $^{##}P < 0.01$ vs. control group. The samples derive from the same experiment, and gels/blots were processed in parallel. Full-length gels/blots are presented in Supplementary Figure S1B. All graphs are done through GraphPad Prism (V.5.01).

(a)

(b)
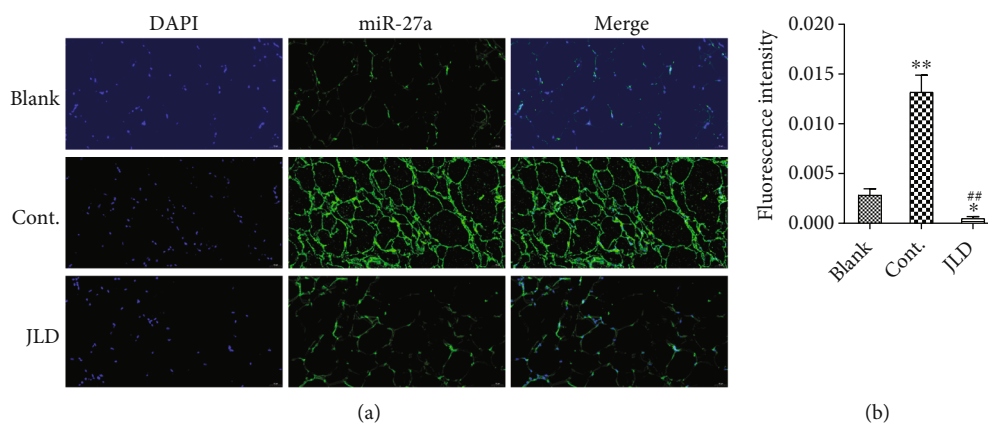
FIGURE 4: JLD inhibits the expression of miR-27a in the subcutaneous fat tissue of db/db mice. (a) Fluorescence images of miR-27a in the subcutaneous fat tissue of db/db mice (200x). (b) Fluorescence intensity of miR-27a in the subcutaneous fat tissue of db/db mice. Data are shown as the mean ± SD. $^*P < 0.05$, $^{**}P < 0.01$ vs. blank group, $^{##}P < 0.01$ vs. control group. All graphs are done through GraphPad Prism (V.5.01).

the control group. These data suggest that JLD can enhance the expression of UCP1, a thermogenesis-related protein, reducing intracellular lipid deposition.

3.5. JLD Inhibited the Expression of miR-27a to Promote the Activation of Beige Adipocyte. To understand how JLD activates beige adipose, we used western blot, PCR, and confocal
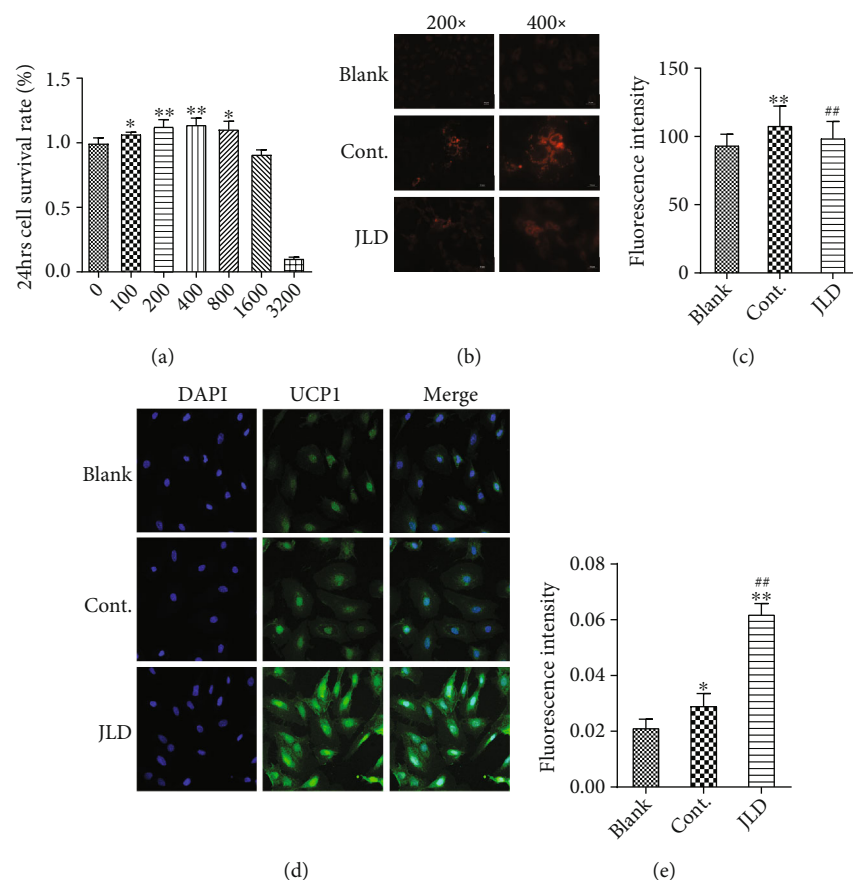
FIGURE 5: JLD reduces lipid deposition in X9 cells. (a) The correlations of JLD concentration with X9 cell density. (b) Nile red staining of blank, control, and JLD-treated X9 cells. (c) Fluorescence intensity of Nile red-stained lipid droplet. (d) Fluorescence images of UCP1 (400x) and fluorescence intensity of UCP1 in the X9 cells. (e) Fluorescence intensity of UCP1 in the X9 cells. Data are shown as the mean ± SD. $^*P < 0.05$, $^{**}P < 0.01$ vs. blank group, $^{\#\#}P < 0.01$ vs. control group. All graphs are done through GraphPad Prism (V.5.01).

microscopy methods to observe the expression of UCP1, PPARγ, PGC-1α, and miR-27a. JLD increased mRNA expression of thermogenic genes such as PPARγ, PGC-1α, and UCP1 (Figure 6(a)). Simultaneously, JLD also increased the expression of PGC-1α, UCP1, and oxidation-related proteins, ATP5A and SDHB (Figures 6(b) and 6(c), Supplementary Figure S1B), and significantly inhibited the expression of miR-27a (Figure 6(d)).

3.6. Small Molecules Potentially Activating UCP1 in JLD. Based on the "drug score" obtained by ProteinsPLUS, we have chosen the top three active pockets for UCP1. The docking results of 5 control molecules and 9 compounds in JLD with three sites of UCP1 are shown in Table S1. In UCP1_site1, epmedin C and icariin got the lowest binding affinity (-8.8 kcal/mol). In UCP1_site2, salvianolic acid B obtained the lowest binding affinity (-9.3 kcal/mol). Epmedin B and epmedin C showed good binding activity at all three sites. Secondly, salvianolic acid B, icariin, and puerarin have good binding activities to more than one sites. The interaction mode between five core components and three UCP1 sites is shown in Figure 7.

4. Discussion

The study proved that JLD treatment significantly ameliorated HFD-induced obesity and adipose accumulation, maintained glucose and lipid homeostasis, and improved hepatic steatosis and inflammation.

Beige adipocytes, found in white adipose depots, are inducible to express the UCP1 in cold or drug stimulation [34, 35]. In contrast to white adipocytes, beige adipocytes can increase energy metabolism and reduce adipose accumulation in the activated state [36]; thus, beige adipocytes are considered therapeutic targets for the treatment of obesity and its complications, such as metabolic syndrome, diabetes, and nonalcoholic steatohepatitis.

In this study, we used db/db mice, a model of spontaneous obesity due to the leptin receptor deficiency [37], to explore the antiobesity effect of JLD. Consistent with the previous study [20], our study also confirmed this point. We also observed the alleviating effect of JLD on lipid deposition in the liver. Compelling evidence suggests that adipokines released by hypertrophic adipocytes affect multiple organs and biological processes [38], especially in chronic system inflammation and glucose metabolism dysfunction [39–42].
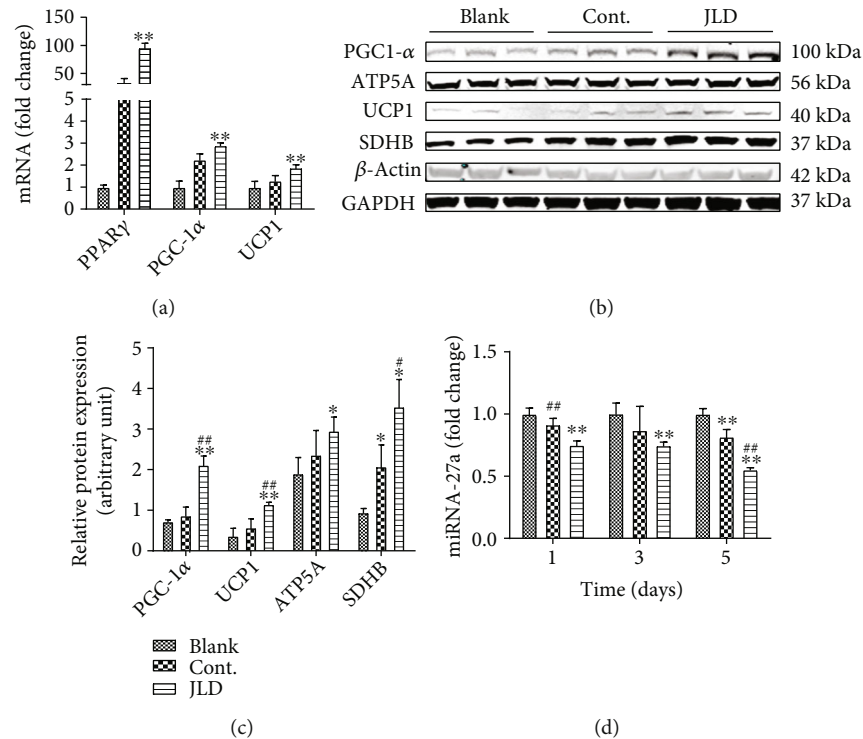
FIGURE 6: JLD inhibits the expression of miR-27a to promote the activation of beige adipocytes. (a) Western blot analysis of thermogenic-related protein UCP1 and PGC-1α oxidation-related protein ATP5A and SDHB expression in X9 cells treated with inducer or inducer and JLD. (b) Quantitative measurement of relative protein expression. (c) qRT-PCR analysis of thermogenic and fatty acid oxidation-related gene expression from X9 cells treated with inducer or inducer and JLD. (d) Relative expressions of miR-27a in X9 cells treated with inducer or inducer and JLD at 1, 3, and 5 days. Data are shown as the mean $\pm$ SD. $^{*}P < 0.05$, $^{**}P < 0.01$ vs. blank group, $^{#}P < 0.05$, $^{##}P < 0.01$ vs. control group. The samples derive from the same experiment, and gels/blots were processed in parallel. Full-length blots/gels are presented in Supplementary Figure S1B. All graphs are done through GraphPad Prism (V.5.01).

We found that JLD improved the glucose metabolism by reducing GLU, consistent with previous reports [16, 20]. We considered that JLD has a great potential to improve the disorders of glucose and lipid metabolism as well as concomitant inflammatory responses.

Activation of beige adipocytes is characterized by upregulated expression of UCP1, which has been identified as a thermogenic gene that releases energy in the form of heat in adipose tissue [43]. To investigate whether the antiobesity effect of JLD depended on the activation of beige adipocytes, the cold tolerance test showed that the body temperature of mice in the JLD-treated group was more stable than that of mice in other groups. Using immunofluorescence, we found a significant increase in UCP1 expression, suggesting that the increased heat release in JLD-treated mice might be due to the differentiation of beige adipocytes in the white adipose depots. To explore whether JLD plays a direct role in the differentiation of beige adipocytes, we induced the differentiation of the beige adipocyte precursor (X9 cell line) in vitro, and JLD intervention was given in this process [9, 44, 45]. The result showed that JLD increased the thermogenesis of beige adipocytes. In addition, we found that JLD also increased the expression level of ATP5A and SDHB protein, which may promote the energy metabolism through oxidative phosphorylation. This suggests that JLD can activate beige adipocytes and increase their energy metabolism.

Previous studies have shown that miR-27a could inhibit the expression of PPARγ, which promotes the differentiation of beige adipocytes in the white adipose depots [13, 46, 47]. The prediction assay for the miRNAs binding to the PPARγ mRNA also confirmed the binding site of miR-27a. Therefore, we performed fluorescence in situ hybridization on mouse adipose sections and found that miR-27a expression in the JLD-treated group was lower than that in untreated mice. In subsequent qPCR assays, we revealed that JLD inhibited the expression level of miR-27a in the postdifferentiated X9 cells. All these results indicate that the potential mechanism of JLD-induced activation of beige adipocytes may depend on inhibiting miR27a expression, which could inhibit PPARγ expression, to activate beige fat.

Through molecular docking, we obtained five potential candidate compounds in JLD with potential activation effect on UCP1. The binding affinity between icariin and UCP1 sites 1 and 3 was -8.8 and -7.4 kcal/mol, respectively, indicating good potential activity. One study showed that icariin can increase UCP1 expression in white adipocytes by increasing the expression of PGC-1α [48]. The binding affinity between salvianolic acid B and UCP1 sites 1 and 2 was -8.6 and -9.3 kcal/mol, respectively. And it may be involved in lipid metabolism and energy metabolism in mice, playing an antiobesity role by regulated energy metabolism [49]. Puerarin can increase the expression of PPARγ in bovine
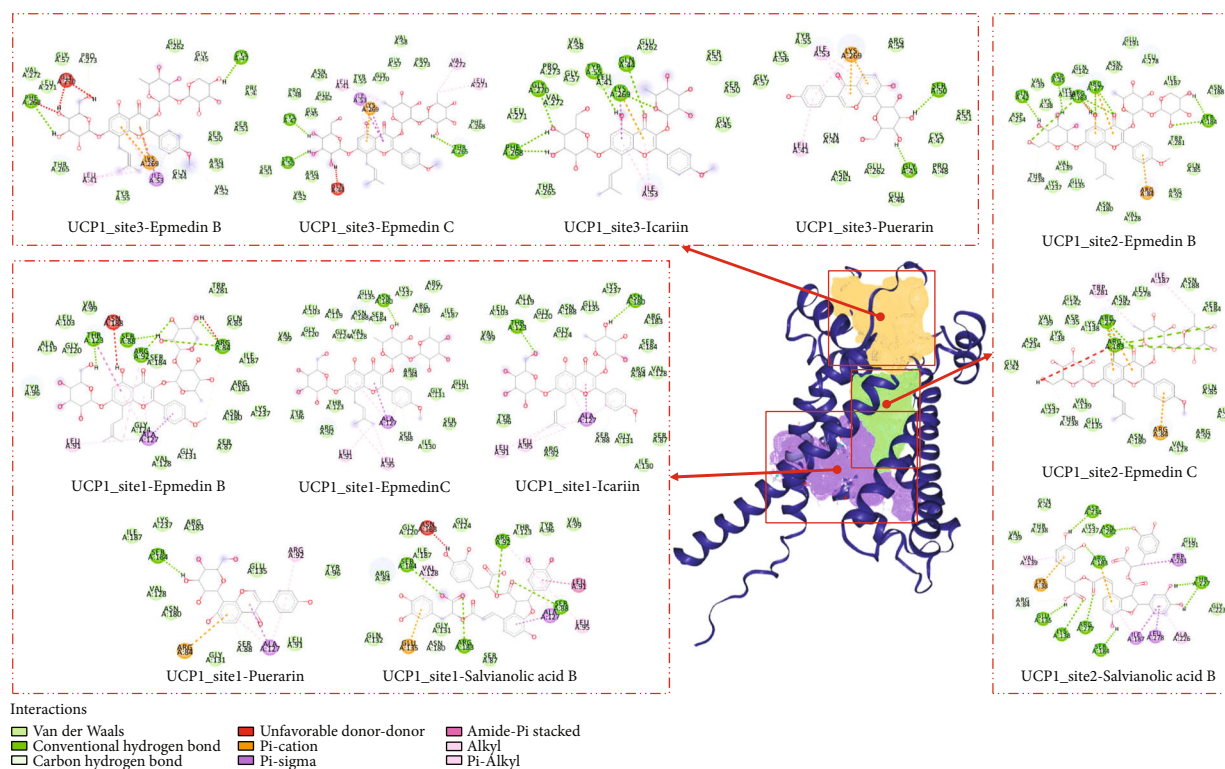
FIGURE 7: The interaction mode between five core components and three UCP1 sites. The UCP1 active sites were predicted by ProteinsPLUS. Purple is site 1 (drug score = 0.82), green is site 2 (drug score = 0.81), and yellow is site 3 (drug score = 0.8).

preadipocytes [50]. In this study, puerarin showed good binding activity with UCP1, with binding affinity of -7.9 and -7.8 kcal/mol to site 1 and site 2, respectively. Although ginsenoside Rb1, ginsenoside Rb2, and ginsenoside Rc were not screened by the strict screening criteria, they still had certain binding activity on UCP1 sites 1 or 2. Ginsenoside Rb1 can promote browning effect by enhancing protein expression of PR domain containing 16 (PRDM16), PGC-1α, and UCP1 [51]. Ginsenoside Rb2 can ameliorate obesity and metabolic disorders by inducing gene expression of PGC-1α and UCP1 [52]. In addition, ginsenoside Rc can resist obesity by inhibiting the expression of PPARγ and CCAAT/enhancer binding protein (C/EBP) [53]. Notably, no association between epmedin B or epmedin C and obesity, metabolic disorder, or UCP1 targets has been reported. However, the results showed that epmedin B and epmedin C had good binding affinity for all three UCP1 sites, indicating good verifiability. In short, JLD activates the beige adipocytes through its multiple active ingredients, and further experiments are needed to confirm the activity.

5. Conclusions

Our data show that JLD has an antiobesity effect in the db/db mouse model of spontaneous obesity, while improving maintained glucose and lipid homeostasis and hepatic steatosis. This study for the first time demonstrates that JLD may induce the activation of beige adipocytes by suppressing the expression of miR-27a. Epmedin B, epmedin C, icariin, puerarin, and salvianolic acid B may be the pharmacodynamic material basis of JLD that plays an important role in regulating UCP1. These findings suggest that JLD has great potential in maintained glucose and lipid homeostasis, making it useful for controlling the body weight and alleviating the glucose and lipid homeostasis dysfunction caused by obesity.

Abbreviations

JLD:	Jinlida granules
PCR:	Polymerase chain reaction
UCP1:	Uncoupling protein 1
WAT:	White adipose tissue
PPARγ:	Peroxisome proliferator-activated receptor-gamma
PGC-1α:	PPAR coactivator 1-alpha
TCM:	Traditional Chinese medicine
TG:	Total triglyceride
LDL-C:	Low-density lipoprotein cholesterol
TC:	Total cholesterol
AST:	Serum aspartate aminotransferase
ALT:	Alanine aminotransferase
GLU:	Glucose
eWAT:	Epididymal white adipose tissue
iWAT:	Inguinal subcutaneous white adipose tissue
PRDM16:	PR domain containing 16
C/EBP:	CCAAT/enhancer binding protein.

Data Availability

The data used to support the findings of this study are included within the article.

Conflicts of Interest

The authors declare that they have no conflicts of interest.

Authors' Contributions

Hong-ru Zhou, Tong-xing Wang, Yuan-yuan Hao, Yun-long Hou, Cong Wei, Bing Yao, Xuan Wu, Dan Huang, Hui Zhang, and Yi-ling Wu were responsible for the conceptualization. Hong-ru Zhou, Tong-xing Wang, Yuan-yuan Hao, Yun-long Hou, and Cong Wei were responsible for the data curation. Hong-ru Zhou, Yuan-yuan Hao, Bing Yao, Xuan Wu, Dan Huang, and Hui Zhang were responsible for the formal analysis. Hong-ru Zhou, Tong-xing Wang, Yuan-yuan Hao, Yun-long Hou, Cong Wei, Bing Yao, Xuan Wu, Dan Huang, Hui Zhang, and Yi-ling Wu were responsible for the investigation. Hong-ru Zhou was responsible for the methodology. Tong-xing Wang, Yun-long Hou, Cong Wei, and Yi-ling Wu were responsible for the project administration. Tong-xing Wang, Yun-long Hou, Cong Wei, and Yi-ling Wu were responsible for the supervision. Hong-ru Zhou wrote the original draft. Hong-ru Zhou, Tong-xing Wang, Yuan-yuan Hao, Yun-long Hou, Cong Wei, Bing Yao, Xuan Wu, Dan Huang, Hui Zhang, and Yi-ling Wu reviewed and edited the paper.

Acknowledgments

Supplementary Materials

Table S1: docking scores of 5 control molecules and 9 compounds in JLD with three active sites of UCP1. Fig S1_raw_ images. (Supplementary Materials)

References

[1] Nations FaAOotU, The State of Food Security and Nutrition in the World 2020, Nations FaAOotU, 2020.

[2] D.-V. Pham and P.-H. Park, "Recent insights on modulation of inflammasomes by adipokines: a critical event for the pathogenesis of obesity and metabolism-associated diseases," Archives of Pharmacal Research, vol. 43, no. 10, pp. 997–1016, 2020.

[3] G. Heyn, L. H. Corrêa, and K. G. Magalhaes, "The impact of adipose tissue–derived miRNAs in metabolic syndrome, obesity, and cancer," Frontiers in Endocrinology, vol. 11, article 563816, 2020.

[4] N. Katta, T. Loethen, C. J. Lavie, and M. A. Alpert, "Obesity and coronary heart disease: epidemiology, pathology, and coronary artery imaging," Current Problems in Cardiology, vol. 46, no. 3, article 100655, 2021.

[5] Y. T. Wondmkun, "Obesity, insulin resistance, and type 2 diabetes: associations and therapeutic Implications," Targets and Therapy, vol. 13, pp. 3611–3616, 2020.

[6] I. Hazer, H. O. Kabukçu, M. Yağcı, Z. Ertürk, G. K. Yıldırım, and B. Kirel, "The association of lipid metabolism and nonalcoholic fatty liver disease in children with obesity," Türk Pediatri Arşivi, vol. 55, no. 3, pp. 263–269, 2020.

[7] B. Cousin, S. Cinti, M. Morroni et al., "Occurrence of brown adipocytes in rat white adipose tissue: molecular and morphological characterization," Journal of Cell Science, vol. 103, no. 4, pp. 931–942, 1992.

[8] P. Seale, B. Bjork, W. Yang et al., "PRDM16 controls a brown fat/skeletal muscle switch," Nature, vol. 454, no. 7207, pp. 961–967, 2008.

[9] J. Wu, P. Boström, L. M. Sparks et al., "Beige adipocytes are a distinct type of thermogenic fat cell in mouse and human," Cell, vol. 150, no. 2, pp. 366–376, 2012.

[10] M. Shao, Q. A. Wang, A. Song et al., "Cellular origins of beige fat cells revisited," Diabetes, vol. 68, no. 10, pp. 1874–1885, 2019.

[11] Á. Klusóczki, Z. Veréb, A. Vámos et al., "Differentiating SGBS adipocytes respond to PPARγ stimulation, irisin and BMP7 by functional browning and beige characteristics," Scientific Reports, vol. 9, no. 1, 2019.

[12] H. Dong, J. Lei, L. Ding, Y. Wen, H. Ju, and X. Zhang, "MicroRNA: function, detection, and bioanalysis," Chemical Reviews, vol. 113, no. 8, pp. 6207–6233, 2013.

[13] L. Sun and M. Trajkovski, "MiR-27 orchestrates the transcriptional regulation of brown adipogenesis," Metabolism, vol. 63, no. 2, pp. 272–282, 2014.

[14] F. Yao, F. Yu, L. Feng et al., "Adipogenic miR-27a in adipose tissue upregulates macrophage activation via inhibiting PPARγ of insulin resistance induced by high-fat diet-associated obesity," Experimental Cell Research, vol. 355, no. 2, pp. 105–112, 2017.

[15] Y. Liu, A. Song, S. Zang et al., "Jinlida reduces insulin resistance and ameliorates liver oxidative stress in high-fat fed rats," Journal of Ethnopharmacology, vol. 162, pp. 244–252, 2015.

[16] C. Wang, X. Dai, D. Zhang, Z. Liu, and Q. Huang, "Jinlida granules improve dysfunction of hypothalamic-pituitary-thyroid axis in diabetic rats induced by STZ," BioMed Research International, vol. 2018, 9 pages, 2018.

[17] D. Wang, M. Tian, Y. Qi et al., "Jinlida granule inhibits palmitic acid induced-intracellular lipid accumulation and enhances autophagy in NIT-1 pancreatic β cells through AMPK activation," Journal of Ethnopharmacology, vol. 161, pp. 99–107, 2015.

[18] J. Tian, F. Lian, L. Yang, and X. Tong, "Evaluation of the Chinese herbal medicine Jinlida in type 2 diabetes patients based on stratification: results of subgroup analysis from a 12-week trial," Journal of Diabetes, vol. 10, no. 2, pp. 112–120, 2018.

[19] X. Jin, H. Zhang, W. Cui et al., "Effect of Jinlida on MAPK signaling pathways in skeletal muscle in ApoE~(-/-) mice with fat-induced insulin resistance," Chinese Journal of New Drugs, vol. 24, pp. 1648–1653, 2015.

[20] H. Zhang, Y. Hao, C. Wei et al., "Chinese medicine Jinlida granules improve high-fat-diet induced metabolic disorders via activation of brown adipose tissue in mice," Biomedicine & Pharmacotherapy, vol. 114, p. 108781, 2019.

[21] F. Liu, R. Song, Y. Feng et al., "Upregulation of MG53 induces diabetic cardiomyopathy through transcriptional activation of peroxisome proliferation-activated receptor α," Circulation, vol. 131, no. 9, pp. 795–804, 2015.

[22] X. Jin, H. Zhang, and W. Cui, "Effect of Jinlida on DGAT1 in skeletal muscle in fat-induced insulin resistance ApoE -/- mice," Chinese Pharmacological Bulletin, vol. 38, p. 1237, 2014.

[23] J. Xin-Gang, J. Ji-Ming, and L. I. Ye-Shuang, "UPLC finger-prints of Jinlida granule," *Chinese Journal of Experimental Traditional Medical Formulae*, vol. 1, pp. 126–129, 2013.

[24] N. T. Nguyen, T. H. Nguyen, T. N. H. Pham et al., "Autodock Vina adopts more accurate binding poses but Autodock4 forms better binding affinity," *Journal of Chemical Information and Modeling*, vol. 60, no. 1, pp. 204–211, 2020.

[25] Z. Zhang, H. Zhang, B. Li et al., "Berberine activates thermogenesis in white and brown adipose tissue," *Nature Communications*, vol. 5, no. 1, p. 5493, 2014.

[26] J. E. Digby, C. T. Montague, C. P. Sewter et al., "Thiazolidinedione exposure increases the expression of uncoupling protein 1 in cultured human preadipocytes," *Diabetes*, vol. 47, no. 1, pp. 138–141, 1998.

[27] X. Sheng, X. Zhu, Y. Zhang et al., "Rhein protects against obesity and related metabolic disorders through liver X receptor-mediated uncoupling protein 1 upregulation in brown adipose tissue," *International Journal of Biological Sciences*, vol. 8, no. 10, pp. 1375–1384, 2012.

[28] T. Nie, S. Zhao, L. Mao et al., "The natural compound, formononetin, extracted from Astragalus membranaceus increases adipocyte thermogenesis by modulating PPARγ activity," *British Journal of Pharmacology*, vol. 175, no. 9, pp. 1439–1450, 2018.

[29] N. Yin, H. Zhang, R. Ye et al., "Fluvastatin sodium ameliorates obesity through brown fat activation," *International Journal of Molecular Sciences*, vol. 20, no. 7, p. 1622, 2019.

[30] S. Kim, P. A. Thiessen, E. E. Bolton et al., "PubChem substance and compound databases," *Nucleic Acids Research*, vol. 44, no. D1, pp. D1202–D1213, 2016.

[31] M. Varadi, S. Anyango, M. Deshpande et al., "AlphaFold protein structure database: massively expanding the structural coverage of protein-sequence space with high-accuracy models," *Nucleic Acids Research*, vol. 50, no. D1, pp. D439–D444, 2022.

[32] J. Jumper, R. Evans, A. Pritzel et al., "Highly accurate protein structure prediction with AlphaFold," *Nature*, vol. 596, no. 7873, pp. 583–589, 2021.

[33] S. Salentin, S. Schreiber, V. J. Haupt, M. F. Adasme, and M. Schroeder, "PLIP: fully automated protein-ligand interaction profiler," *Nucleic Acids Research*, vol. 43, no. W1, pp. W443–W447, 2015.

[34] F. Norheim, T. M. Langleite, M. Hjorth et al., "The effects of acute and chronic exercise on PGC-1α, irisin and browning of subcutaneous adipose tissue in humans," *FEBS Journal*, vol. 281, no. 3, pp. 739–749, 2014.

[35] J. Chi, Z. Wu, C. H. J. Choi et al., "Three-dimensional adipose tissue imaging reveals regional variation in beige fat biogenesis and PRDM16-dependent sympathetic neurite density," *Cell Metabolism*, vol. 27, no. 1, article e223, pp. 226–236.e3, 2018.

[36] K. Klepac, A. Georgiadi, M. Tschöp, and S. Herzig, "The role of brown and beige adipose tissue in glycaemic control," *Molecular Aspects of Medicine*, vol. 68, pp. 90–100, 2019.

[37] A. M. Ingalls, M. M. Dickie, and G. D. Snell, "Obese, a new mutation in the house mouse," *The Journal of Heredity*, vol. 41, no. 12, pp. 317-318, 1950.

[38] S. Ludger and H. Joerg, "The endocrine function of adipose tissues in health and cardiometabolic disease," *Nature Reviews Endocrinology*, vol. 15, no. 9, pp. 507–524, 2019.

[39] Y. Cyr, S. Bissonnette, V. Lamantia et al., "White adipose tissue surface expression of LDLR and CD36 is associated with risk factors for type 2 diabetes in adults with obesity," *Obesity*, vol. 28, no. 12, pp. 2357–2367, 2020.

[40] S. Michurina, I. Stafeev, N. Podkuychenko et al., "Decreased UCP-1 expression in beige adipocytes from adipose-derived stem cells of type 2 diabetes patients associates with mitochondrial ROS accumulation during obesity," *Diabetes Research and Clinical Practice*, vol. 169, p. 1084, 2020.

[41] C. S. M. Fonseca, J. E. Basford, D. G. Kuhel et al., "Distinct influence of hypercaloric diets predominant with fat or fat and sucrose on adipose tissue and liver inflammation in mice," *Molecules*, vol. 25, no. 19, p. 4369.2020/09/27, 2020.

[42] S. A. Polyzos, J. Kountouras, and C. S. Mantzoros, "Adipose tissue, obesity and non-alcoholic fatty liver disease," *Minerva Endocrinology*, vol. 42, no. 2, pp. 92–108, 2017.

[43] K. Ikeda and T. Yamada, "UCP1 dependent and independent thermogenesis in brown and beige adipocytes," *Frontiers in Endocrinology*, vol. 11, p. 498, 2020.

[44] D. L. Barbato, G. Tatulli, K. Aquilano, and M. R. Ciriolo, "Mitochondrial hormesis links nutrient restriction to improved metabolism in fat cell," *Aging*, vol. 7, no. 10, pp. 869–881, 2015.

[45] L. Ye, J. Wu, P. Cohen et al., "Fat cells directly sense temperature to activate thermogenesis," *Proceedings of the National Academy of Sciences*, vol. 110, no. 30, pp. 12480–12485, 2013.

[46] Y.-Y. Wu, X.-M. Huang, J. Liu et al., "Functional study of the upregulation of miRNA-27a and miRNA-27b in 3T3-L1 cells in response to berberine," *Molecular Medicine Reports*, vol. 14, no. 3, pp. 2725–2731, 2016.

[47] B. Zou, Z. Ge, W. Zhu, Z. Xu, and C. Li, "Persimmon tannin represses 3T3-L1 preadipocyte differentiation via up-regulating expression of miR-27 and down-regulating expression of peroxisome proliferator-activated receptor-γ in the early phase of adipogenesis," *European Journal of Nutrition*, vol. 54, no. 8, pp. 1333–1343, 2015.

[48] S. Q. Chen, L. N. Ding, N. X. Zeng et al., "Icariin induces irisin/FNDC5 expression in C2C12 cells via the AMPK pathway," *Biomedicine & Pharmacotherapy*, vol. 115, p. 108930, 2019.

[49] B. Lv, Y. Wu, J. Lian et al., "Effects of salvianolic acid B on RNA expression and co-expression network of lncRNAs in brown adipose tissue of obese mice," *Journal of Ethnopharmacology*, vol. 278, p. 114289, 2021.

[50] D. X. Xu, X. X. Guo, Z. Zeng, Y. Wang, and J. Qiu, "Puerarin improves hepatic glucose and lipid homeostasis in vitro and in vivo by regulating the AMPK pathway," *Food & Function*, vol. 12, no. 6, pp. 2726–2740, 2021.

[51] S. J. Park, M. Park, A. Sharma, K. Kim, and H. J. Lee, "Black ginseng and ginsenoside Rb1 promote browning by inducing UCP1 expression in 3T3-L1 and primary white adipocytes," *Nutrients*, vol. 11, no. 11, p. 2747, 2019.

[52] Y. Hong, Y. Lin, Q. Si, L. Yang, W. Dong, and X. Gu, "Ginsenoside Rb2 alleviates obesity by activation of brown fat and induction of browning of white fat," *Frontiers in Endocrinology*, vol. 10, pp. 1–11, 2019.

[53] J. W. Yang and S. S. Kim, "Ginsenoside Rc promotes anti-adipogenic activity on 3T3-L1 adipocytes by down-regulating C/EBPα and PPARγ," *Molecules*, vol. 20, no. 1, pp. 1293–1303, 2015.

Research Article

GC-MS Profile, Antioxidant Activity, and In Silico Study of the Essential Oil from *Schinus molle* L. Leaves in the Presence of Mosquito Juvenile Hormone-Binding Protein (mJHBP) from *Aedes aegypti*

Oscar Herrera-Calderon [iD],[1] Haydee Chavez [iD],[2] Edwin Carlos Enciso-Roca [iD],[3] Pablo Williams Común-Ventura [iD],[3] Renan Dilton Hañari-Quispe [iD],[4] Linder Figueroa-Salvador [iD],[5] Eddie Loyola-Gonzales [iD],[6] Josefa Bertha Pari-Olarte [iD],[2] Nada H. Aljarba [iD],[7] Saad Alkahtani [iD],[8] and Gaber El-Saber Batiha [iD][9]

[1]*Department of Pharmacology, Bromatology and Toxicology, Faculty of Pharmacy and Biochemistry, Universidad Nacional Mayor de San Marcos, Lima, Peru*

[2]*Department of Pharmaceutical Chemistry, Faculty of Pharmacy and Biochemistry, Universidad Nacional San Luis Gonzaga, Ica 11001, Peru*

[3]*Department of Human Medicine, Faculty of Health Sciences, Universidad Nacional de San Cristobal de Huamanga, Portal Independencia 57, Ayacucho 05003, Peru*

[4]*Clinical Pathology Laboratory, Faculty of Veterinary Medicine and Zootechnics, Universidad Nacional del Altiplano, Av Floral 1153, Puno 21001, Peru*

[5]*School of Medicine, Faculty of Health Sciences, Universidad Peruana de Ciencias Aplicadas, Prolongación Primavera 2390, Lima 15023, Peru*

[6]*Department of Pharmaceutical Science, Faculty of Pharmacy and Biochemistry, Universidad Nacional San Luis Gonzaga, Ica 11001, Peru*

[7]*Department of Biology, College of Science, Princess Nourah bint Abdulrahman University, P. O. Box 84428, Riyadh 11671, Saudi Arabia*

[8]*Department of Zoology, College of Science, King Saud University, P. O. Box 2455, Riyadh 11451, Saudi Arabia*

[9]*Department of Pharmacology and Therapeutics, Faculty of Veterinary Medicine, Damanhour University, Damanhur, 22511 El-Beheira, Egypt*

Correspondence should be addressed to Oscar Herrera-Calderon; oherreraca@unmsm.edu.pe

Schinus molle is a medicinal plant used as an anti-inflammatory and for rheumatic pain in the traditional medicine of Peru. On the other hand, *Aedes aegypti* is the main vector of several tropical diseases and the transmitter of yellow fever, chikungunya, malaria, dengue, and Zika virus. In this study, the aim was to investigate the antioxidant activity in vitro and the insecticidal activity in silico, in the presence of the mosquito juvenile hormone-binding protein (mJHBP) from *Aedes aegypti*, of the essential oil from *S. molle* leaves. The volatile phytochemicals were analyzed by gas chromatography-mass spectrometry (GC-MS), and the profile antioxidants were examined by DPPH, ABTS, and FRAP assays. The evaluation in silico was carried out on mJHBP (PDB: 5V13) with an insecticidal approach. The results revealed that EO presented as the main volatile components to alpha-phellandrene (32.68%), D-limonene (12.59%), and beta-phellandrene (12.24%). The antioxidant activity showed values for DPPH = 11.42 ± 0.08 μmol ET/g, ABTS = 134.88 ± 4.37 μmol ET/g, and FRAP = 65.16 ± 1.46 μmol ET/g. Regarding the insecticidal approach in silico,

alpha-muurolene and gamma-cadinene had the best biding energy on mJHBP ($\Delta G = -9.7$ kcal/mol), followed by beta-cadinene ($\Delta G = -9.5$ kcal/mol). Additionally, the volatile components did not reveal antioxidant activity, and its potential insecticidal effect would be acting on mJHBP from *A. aegypti*.

1. Introduction

Essential oils (EOs) are a class of natural products characterized by their volatile components, especially terpenes and sesquiterpenes [1]. EOs are obtained by several methods such as hydrodistillation, supercritical fluids, microwaves, and ultrasound [2]. Although the yield rate is very low, a majority are used in perfumery [3], aromatherapy [4], and the pharmaceutical [5] and food industries [6]. Their biological activities have been reported as insecticidal, antiviral, antibacterial, antifungal, antimalarial, antidepressive, anticancer, antimutagenic, hepatoprotective, anti-inflammatory, antioxidant, analgesic, and antipyretic [5, 7]. *Schinus molle* L., internationally commonly known as peruvian pepper, false pepper, American pepper, or pink pepper, is a perennial tree belonging to the Anacardiaceae family, which is native to subtropical regions of South and Central America [8]. In Peru, it is popularly known as molle (in Spanish) and its leaves and fruits exhibit anti-inflammatory, analgesic, antirheumatic, antibacterial, antiseptic, and repellent activity [9]. The essential oil of *S. molle* (leaves and fruits) exhibits biological activities such as antibacterial (gram-positive and gram-negative bacteria), antifungal, insecticidal, repellent, and cytotoxic activities [10]. Locally, the plant is used as a rheumatic reliever, analgesic, antiseptic, purgative, stomach cramp reliever, and diuretic. Moreover, leaves, fruits, and latex are used for many conditions, including menstrual, respiratory, and urinary disorders, and as an antidepressant, digestive stimulant, and astringent [11].

Regarding insecticidal activity, several synthetized chemicals are used as repellents, vector control, or insecticides, but during the last year, some of them have been retired due to their carcinogenic, genotoxic, or harmful-to-the-environment effects by bioaccumulation [12]. The application of natural products as insecticides might be highly effective, less expensive, biodegradable, and safer than that of synthetic insecticides [13]. The harmful effect of essential oils or their isolated compounds against insects can be manifested in various ways, including mortality, toxicity, inhibiting growth, the suppression of reproductive behavior, and reducing fertility and fecundity [14]. Hence, the use of bioinsecticides based on natural products might be a powerful tool to combat some insects who are responsible for several tropical diseases (Zika, malaria, dengue, and yellow fever) transmitted mainly by the mosquito *Aedes aegypti* [15].

Recently, a group of salivary D7 proteins known as mosquito juvenile hormone-binding protein (mJHBP) has been identified in *A. aegypti*, which consist of two modified odorant-binding protein domains with its respective ligand in the N-terminal domain named JH-III [16]. This hormone is found in pupae and adults; furthermore, it regulates the larval development in the mosquito. On the other hand, the juvenile hormone (JH) plays an essential role in adult female promoting the ovary maturation before blood feeding; additionally, it is involved with the nutritional state and its relationship with blood meal-dependent reproductive development [17]. In recent years, a class of insecticides named JH analogues have been designed to disrupt this endocrine process and affect the normal development in mosquitoes. A synthetic JH analogue is pyriproxyfen, which is a phenyl carbonyl derivative, and its main effect is to produce an imbalance in the mosquito hormonal system, inhibiting the embryogenesis, adult metamorphosis, and development of the adult mosquito [18].

Although the insecticidal activity of *S. molle* EO was evaluated in several species such as *Trogoderma granarium*, *Tribolium castaneum* [19], *Sitophilus oryzae* [20], *Haematobia irritans* [21], *Ctenocephalides felis felis* [22], and *Gonipterus platensis* [23], currently, there is not scientific literature on *A. aegypti*. Thus, we investigated the potential insecticidal effect in silico of the volatile components of *S. molle* EO to find any responsible molecule as a JH analogue, which might combat the presence of mosquitoes in tropical regions and reduce the prevalence of diseases transmitted by them. The aim in this study was (1) to determine the total volatile component of the EO from *S. molle* leaves by gas chromatography-mass spectrometry (GC-MS), (2) to evaluate the antioxidant activity using the DPPH, ABTS, and FRAP methods, and (3) to determine the insecticidal activity using a virtual screening of the EO from *S. molle* leaves on the mosquito juvenile hormone-binding protein from *Aedes aegypti*.

2. Materials and Methods

2.1. Chemicals. All the solvents (dichloromethane, chloroform, methanol, and hydrogen peroxide), of analytical grade (99.5%), were purchased from Merck (Darmstadt, Germany). 2,2-Diphenyl-1-picrylhydrazyl (DPPH), 2,2′-azinobis(3-ethylbenzothiazoline-6-sulfonic acid) (ABTS), 2,4,6-tri(2-pyridyl)-s-triazine (TPTZ), and Trolox were purchased from Sigma-Aldrich (St. Louis, MO, USA).

2.2. Plant Material. A quantity of 4700 g of *Schinus molle* (leaves) cultivated in Tinguiña, Ica Region, Peru (406 m.a.s.l.) in December 2020 was received. Leaves were cleaned and peeled to be incorporated in a Clevenger equipment and to obtain essential oil by hydrodistillation for 2 h [24]. The essential oil was separated by decantation; then, anhydrous Na_2SO_4 was added to eliminate any water drops. Finally, the EO was stored in a sealed amber vial until further use.

2.3. Identification of Volatile Compounds by Gas Chromatography-Mass Spectrometry (GC-MS). Volatile chemicals were determined with a GC-MS system (Agilent Technologies 7890 Gas Detector and Agilent Technologies
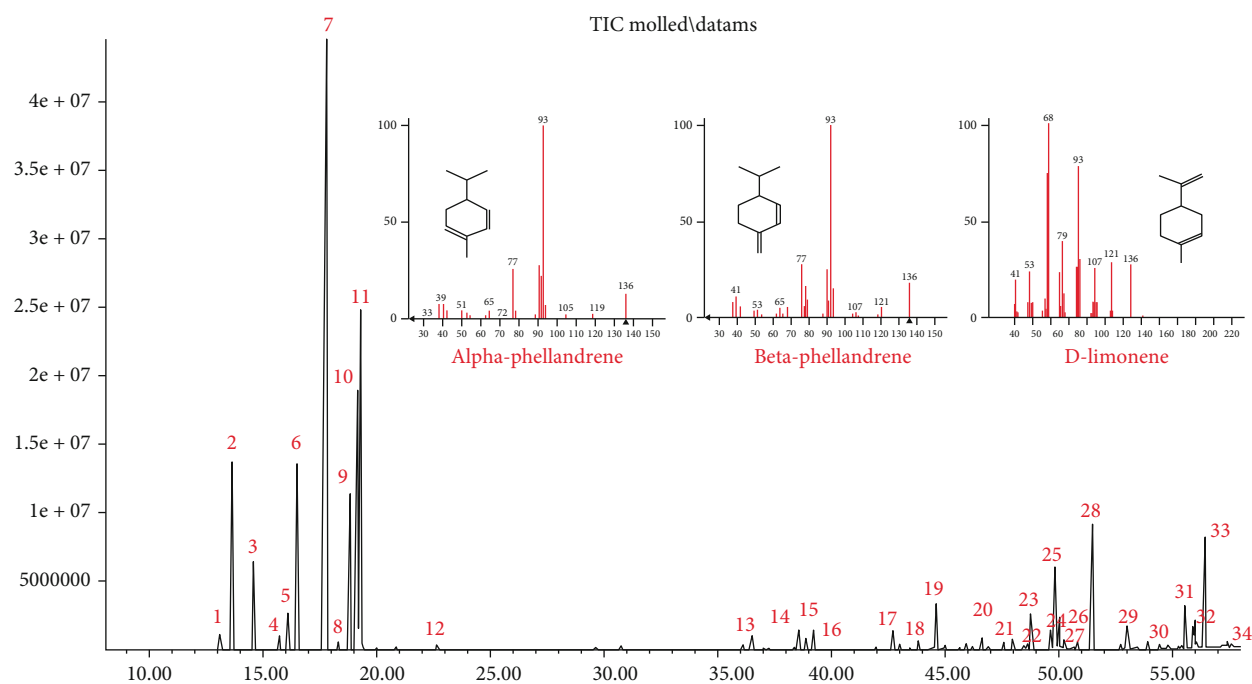
FIGURE 1: Chromatographic profile of the essential oil from *S. molle* leaves by GC-MS.

5975C Mass Spectrometer Detector, Santa Clara, CA, USA). Then, 20 μL of EO was mixed with 1.0 mL of dichloromethane. Next, 1.0 μL of the working solution was injected into the equipment in splitless mode (split: 20 : 1). The EO was run on a J&W 122-1545.67659 DB-5 ms column, (60 m × 250 μm × 0.25 μm) (Agilent Technologies, Santa Clara, CA, USA). The working conditions were as follows: the temperature program was 40°C, starting with increments of 5°C/min up to 180°C, followed by increases of 2.5°C/min up to 200°C for 5 min, and finally 10°C/min up to 300°C, remaining for 3 min. The helium flow rate was at 1 mL/min. Volatile components' identification was based on a comparison of relative retention indices (RIs) and mass spectra data with the NIST20 library data and the published literature [25]. Each RI was calculated compared with a homologous series of n-alkanes C9–C25 (C9, BHD purity 99%; C10–C25, Fluka purity 99%). The relative amount (expressed as a percentage) of each compound identified in the EO was calculated by comparing the area of the corresponding peak in the chromatogram with the total area of identified peaks.

2.4. Determination of the Antioxidant Capacity by the Free Radical 2,2-Diphenyl-1-picrylhydrazyl (DPPH).

A 150 μL of EO (10 mg/mL) was mixed with 2850 μL of a methanolic solution of DPPH (20 mg/L) with an absorbance adjusted to 1.1 ± 0.02 nm. After mixing, it was incubated in the dark for 30 minutes, and the absorbance reading was carried out at 515 nm. The standard curve was elaborated with Trolox at concentrations of 0 to 800 μmol/mL. The Trolox equivalent antioxidant capacity (TEAC) was expressed as μmol TE/g of essential oil [26]. To calculate the half inhibitory concentration (IC50), a linear regression method was used based on the different concentrations of the EO.

2.5. Determination of the Antioxidant Capacity by the Method of the Radical 2,2'-Azinobis-(3-ethylbenzothiazoline)-6-sulfonic Acid (ABTS^{+}).

To carry out the antioxidant activity using the ABTS radical, a solution was prepared using the mixing of 10 mL of ABTS (4.06 mg/mL) and 10 mL of potassium persulfate (0.7 mg/mL), both reacted for 16 hours. Then, 150 μL of the EO (5 mg/mL, diluted with methanol) was mixed with 2850 μL of ABTS radical and incubated for 7 min, the same procedure was used with Trolox standard ranging between 0 and 400 μmol/mL. The absorbance was read to 0.7 ± 0.02 at a wavelength of 734 nm. The Trolox equivalent antioxidant capacity (TEAC) was expressed as μmol TE/g of essential oil [27]. To calculate the half inhibitory concentration (IC$_{50}$), a linear regression method was used based on the different concentrations of the EO.

2.6. Determination of Antioxidant Capacity by the Ferric Reducing/Antioxidant Power (FRAP).

In the determination of FRAP of EO, a reagent battery was made using 25 mL of acetate buffer pH 3.6; 2.5 mL of 20 mM TPTZ was dissolved in 40 mM HCl and 2.5 mL of 20 mM ferric chloride hexahydrate. The mixing of this reagents constituted the FRAP solution which reacted with the EO at different concentrations as well as Trolox standard. 150 μL of EO (1 mg/mL) was mixed with 2850 μL of FRAP reagent and reacted for 4 min at room temperature. The absorbance reading was carried out at 593 nm. A standard curve was prepared with Trolox (50-800 μM). The results were expressed as μmol equivalents of Trolox per gram of essential oil (μmol TE/g EO) [28]. To calculate the half inhibitory concentration (IC$_{50}$), the linear regression method was used based on the different concentrations of the EO.

TABLE 1: Chemical composition of the volatile oil of *Schinus molle* leaves.
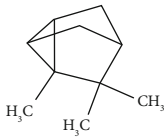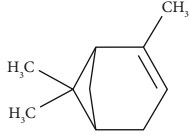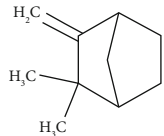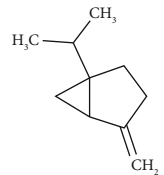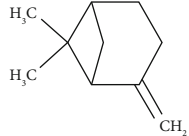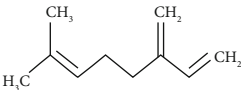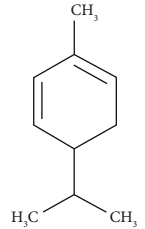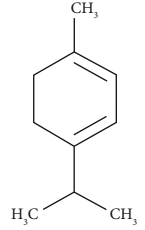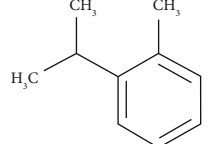
Compound name	Rt (min)	Molecular formula/ molecular mass	%	LRI Exp	LRI Ref	Chemical structure	Chemical group
Tricyclene	13.13	$C_{10}H_{16}$ (136.23)	0.49	926	926		Monoterpene hydrocarbon
Alpha-pinene	13.65	$C_{10}H_{16}$ (136.23)	5.27	930	932		Monoterpene hydrocarbon
Camphene	14.58	$C_{10}H_{16}$ (136.23)	2.50	938	946		Monoterpene hydrocarbon
Sabinene	15.72	$C_{10}H_{16}$ (136.23)	0.40	973	974		Monoterpene hydrocarbon
Beta-pinene	16.10	$C_{10}H_{16}$ (136.23)	1.11	976	975		Monoterpene hydrocarbon
Beta-myrcene	16.51	$C_{10}H_{16}$ (136.23)	5.94	988	988		Monoterpene hydrocarbon
Alpha-phellandrene	17.80	$C_{10}H_{16}$ (136.23)	32.68	1006	1006		Monoterpene hydrocarbon
Alpha-terpinene	18.31	$C_{10}H_{16}$ (136.23)	0.26	1019	1020		Monoterpene hydrocarbon
o-Cymene	18.82	$C_{10}H_{14}$ (136.22)	5.58	1022	1022		Aromatic monoterpene hydrocarbon
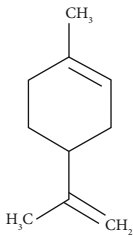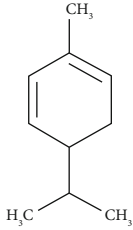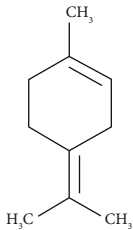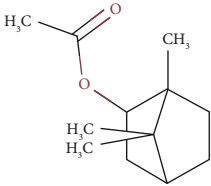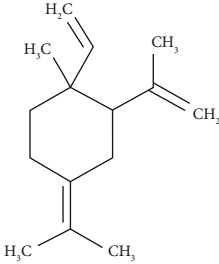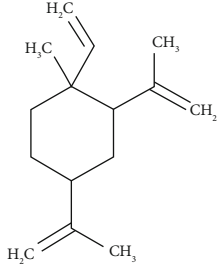
TABLE 1: Continued.

Compound name	Rt (min)	Molecular formula/ molecular mass	%	LRI Exp	LRI Ref	Chemical structure	Chemical group
D-Limonene	19.16	$C_{10}H_{16}$ (136.23)	12.59	1027	1024		Monoterpene hydrocarbon
Beta-phellandrene	19.32	$C_{10}H_{16}$ (136.23)	12.24	1029	1025		Monoterpene hydrocarbon
Terpinolene	22.65	$C_{10}H_{16}$ (136.23)	0.21	1082	1086		Monoterpene hydrocarbon
Bornyl acetate	36.12	$C_{12}H_{20}O_2$ (196.29)	0.20	1277	1284		Oxygenated monoterpene
Gamma-elemene	39.20	$C_{15}H_{24}$ (204.35)	0.68	1650	1651		Sesquiterpene hydrocarbon
Beta-elemene	42.71	$C_{15}H_{24}$ (204.35)	0.72	1382	1389		Sesquiterpene hydrocarbon
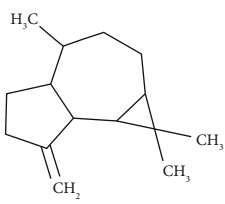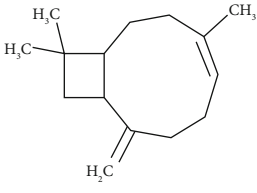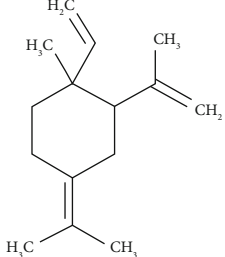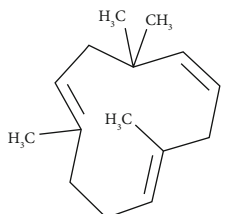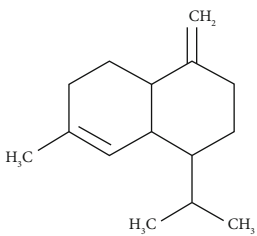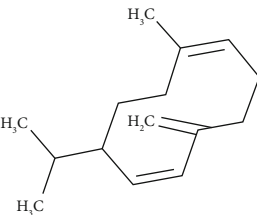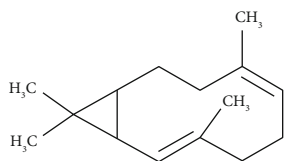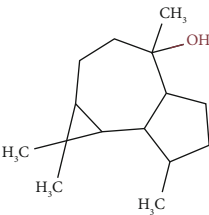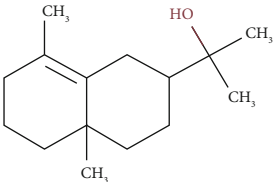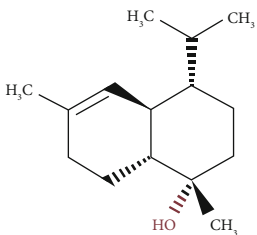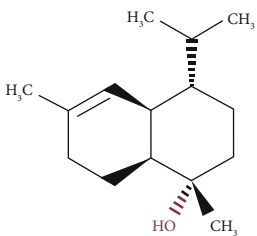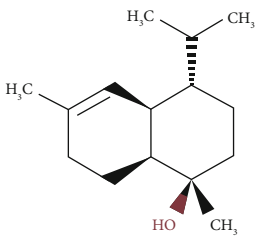
TABLE 1: Continued.

Compound name	Rt (min)	Molecular formula/ molecular mass	%	LRI Exp	LRI Ref	Chemical structure	Chemical group
Beta-gurjunene	43.83	$C_{15}H_{24}$ (204.35)	0.30	1402	1409		Sesquiterpene hydrocarbon
Beta-caryophyllene	44.60	$C_{15}H_{24}$ (204.35)	0.30	1416	1417		Sesquiterpene hydrocarbon
Elixene	44.99	$C_{15}H_{24}$ (204.35)	0.26	1441	1445		Sesquiterpene hydrocarbon
Humulene	46.62	$C_{15}H_{24}$ (204.35)	0.39	1450	1452		Sesquiterpene hydrocarbon
Gamma-muurolene	47.58	$C_{15}H_{24}$ (204.35)	0.21	1452	1451		Sesquiterpene hydrocarbon
Germacrene D	47.99	$C_{15}H_{24}$ (204.35)	0.38	1471	1480		Sesquiterpene hydrocarbon
Bicyclogermacrene	48.77	$C_{15}H_{24}$ (204.35)	1.30	1492	1500		Sesquiterpene hydrocarbon

TABLE 1: Continued.

Compound name	Rt (min)	Molecular formula/ molecular mass	%	LRI Exp	LRI Ref	Chemical structure	Chemical group
Alpha-muurolene	48.83	$C_{15}H_{24}$ (204.35)	0.60	1509	1510		Sesquiterpene hydrocarbon
γ-Cadinene	49.66	$C_{15}H_{24}$ (204.35)	0.62	1514	1513		Sesquiterpene hydrocarbon
Beta-cadinene	49.87	$C_{15}H_{24}$ (204.35)	2.95	1515	1522		Sesquiterpene hydrocarbon
Shyobunol	50.03	$C_{15}H_{26}O$ (222.37)	1.11	1541	1542		Oxygenated sesquiterpene
Unknown I	50.27	$C_{15}H_{26}O$ (222.37)	0.67	1600		n.d.	Oxygenated sesquiterpene
Elemol	51.48	$C_{15}H_{26}O$ (222.37)	4.53	1610	1610		Oxygenated sesquiterpene
Unknown II	52.97	$C_{15}H_{26}O$ (222.37)	1.13	1623		n.d.	Oxygenated sesquiterpene

TABLE 1: Continued.

Compound name	Rt (min)	Molecular formula/ molecular mass	%	LRI Exp	LRI Ref	Chemical structure	Chemical group
Viridiflorol	53.91	$C_{15}H_{26}O$ (222.37)	0.31	1625	1627		Oxygenated sesquiterpene
Gamma-eudesmol	55.59	$C_{15}H_{26}O$ (222.37)	1.22	1636	1630		Oxygenated sesquiterpene
τ-Cadinol	55.93	$C_{15}H_{26}O$ (222.37)	0.61	1648	1652		Oxygenated sesquiterpene
τ-Muurolol	55.99	$C_{15}H_{26}O$ (222.37)	1.71	1641	1643		Oxygenated sesquiterpene
Delta-cadinol	56.08	$C_{15}H_{26}O$ (222.37)	0.23	1655	1656		Oxygenated sesquiterpene
Aromatic monoterpene hydrocarbons			5.58%				
Monoterpene hydrocarbons			73.69%				
Oxygenated monoterpenes			0.20%				
Sesquiterpene hydrocarbons			8.71%				
Oxygenated sesquiterpenes			11.52%				
Total identified			99.7%				

Rt: retention time; n.d.: not determined; LRI [Ref]: linear retention index obtained from the literature [25]; LRI [Exp]: linear retention index calculated against n-alkanes C9–C24. [a]Mean of three determinations.

2.7. Molecular Docking Studies. The molecules isolated from phytochemicals of essential oil were docked against the mosquito juvenile hormone-binding protein (PDB id: 5V13). In order to validate the docking, the crystal structures were docked with the native ligand pyriproxifen and JH3 bound to X-ray structures of mosquito juvenile hormone-binding protein. In addition to the former for comparison, better validation of docking at the binding cavity of mosquito juvenile

TABLE 2: Antioxidant profile of the essential oil of S. molle.

Method	Mean ± SD
TEAC DPPH (μmol TE/g)	11.42 ± 0.08
IC$_{50}$ DPPH (mg/mL)	41.84 ± 0.31
TEAC ABTS (μmol TE/g)	134.88 ± 4.37
IC$_{50}$ ABTS (mg/mL)	2.05 ± 0.07
TEAC FRAP (μmol TE/g)	65.16 ± 1.46
IC$_{50}$ FRAP (mg/mL)	1.50 ± 0.02

TABLE 3: Ligand interaction energies and inhibitory concentrations with mosquito juvenile hormone-binding protein in the molecular docking study.

Ligand	Binding free energy (ΔG, kcal/mol)	Ki (μM)
Alpha-phellandrene	-7	14.6
Alpha-terpinene	-6.5	58.46
Beta-caryophyllene	-8.3	1.22
Beta-myrcene	-6.5	58.46
Beta-elemene	-8.3	1.22
Bicyclogermacrene	-7.6	7.46
Camphene	-7.2	13.06
D-Limonene	-7.3	12.57
Elixene	-9	0.398
Germacrene D	-9.5	0.226
Alpha-muurolene	-9.7	0.134
Alpha-pinene	-7.5	8.19
Beta-cadinene	-9.6	0.176
Beta-gurjunene	-8.2	1.67
Beta-phellandrene	-7.5	8.19
Beta-pinene	-7.5	8.19
Elemol	-7.7	6.15
γ-Cadinene	-9.7	0.134
Gamma-muurolene	-9.5	0.226
Bornyl acetate	-7.8	5.56
Humulene	-9.2	0.319
o-Cymene	-7	14.6
Sabinene	-7.3	12.57
t-Cadinol	-7.8	5.56
Terpinolene	-7.5	8.19
Tricyclene	-7	14.6
Gamma-Elemene	-7.6	7.46
Shyobunol	-9.1	0.332
Gamma-eudesmol	-8.9	0.913
Delta-cadinol	-7.8	5.56
τ-Muurolol	-8.4	1.01
Viridiflorol	-7.7	6.15
Pyriproxyfen (synthetic insecticide)	-9.9	0.099
Juvenile hormone III (JH3)	-9.2	0.319

hormone-binding protein was determined surrounding the 3 Å distance from the bound ligand JH3 using the DoGSiteScorer server. The binding cavity residues comprised mainly TYR33, LEU37, TRP50, AL51, TRP53, TYR64, SER69, TYR129, TYR133, ILE140, PHE269, TRP278, and ALA281. Protein and ligand preparations were performed using AutoDock Tools (v. 1.5.6) (Forli et al., 2016). Gasteiger charges were added to the ligand molecules prior to converting to PDBQT format. The online server DoGSiteScorer and the information about the binding site residues of the native ligand were used to construct the grid box. The grid box of dimensions $25 \times 25 \times 14$ Å for the mosquito juvenile hormone-binding protein with 0.375 Å grid spacing was constructed using AutoGrid 4.2. Semiflexible docking was performed keeping the receptor molecule rigid and ligands flexible. AutoDock 4.2 using the Lamarckian genetic algorithm (LGA) scoring function with number of GA runs = 100, population size = 500, and maximum number of evaluations = 25,000,000 was used to develop the molecular docking of all volatile components of EO. Then, the RMSD clustering maps were obtained by a reclustering command with a clustering tolerance of 0.25 Å, 0.5 Å, and 1 Å, respectively, in order to obtain the best cluster having the lowest energy score with a high number of populations [18].

2.8. Molecular Dynamics Simulation (MD). This evaluation was carried on the dock complexes for α-phellandrene (the most abundant in GC-MS analysis) and α-muurolene (the most active in molecular docking analysis) with the mosquito juvenile hormone-binding protein (mJHBP) using the Desmond 2020.1 from Schrödinger, LLC. The reproducibility was completed using three replicates for each MD run. The OPLS-2005 force field and explicit solvent model with the SPC water molecules were used in this system. To neutralize and simulate the physiological conditions, the charge Na+ ions and 0.15 M NaCl were added, respectively. The system was equilibrated using constant-temperature and constant-volume ensemble (NVT) for 100 ps. This was followed by a short run equilibration and minimization using constant-temperature and constant-pressure ensemble (NPT) for 12 ps and was set up using the Nose-Hoover chain coupling scheme with temperature 27°C, the relaxation time of 1.0 ps, pressure 1 bar, and a time of 2 fs. The Martyna-Tuckerman-Klein chain coupling scheme barostat method was used for pressure control using a relaxation time of 2 ps. The particle mesh Ewald method was used for calculating long-range electrostatic interactions with a radius of 9 Å for the coulomb interactions. Bonded forces were calculated using a RESPA integrator with a time step of 2 fs for each trajectory. The root mean square deviation (RMSD), radius of gyration (Rg), root mean square fluctuation (RMSF), and solvent accessible surface area (SAS area) were calculated to monitor the stability of the MD simulation.

2.9. Statistical Analysis. In the analysis of the antioxidant profile of essential oil from S. molle, the IC$_{50}$ values were estimated by linear regression statistics. A Spearman's Rho coefficient was calculated to establish a correlation
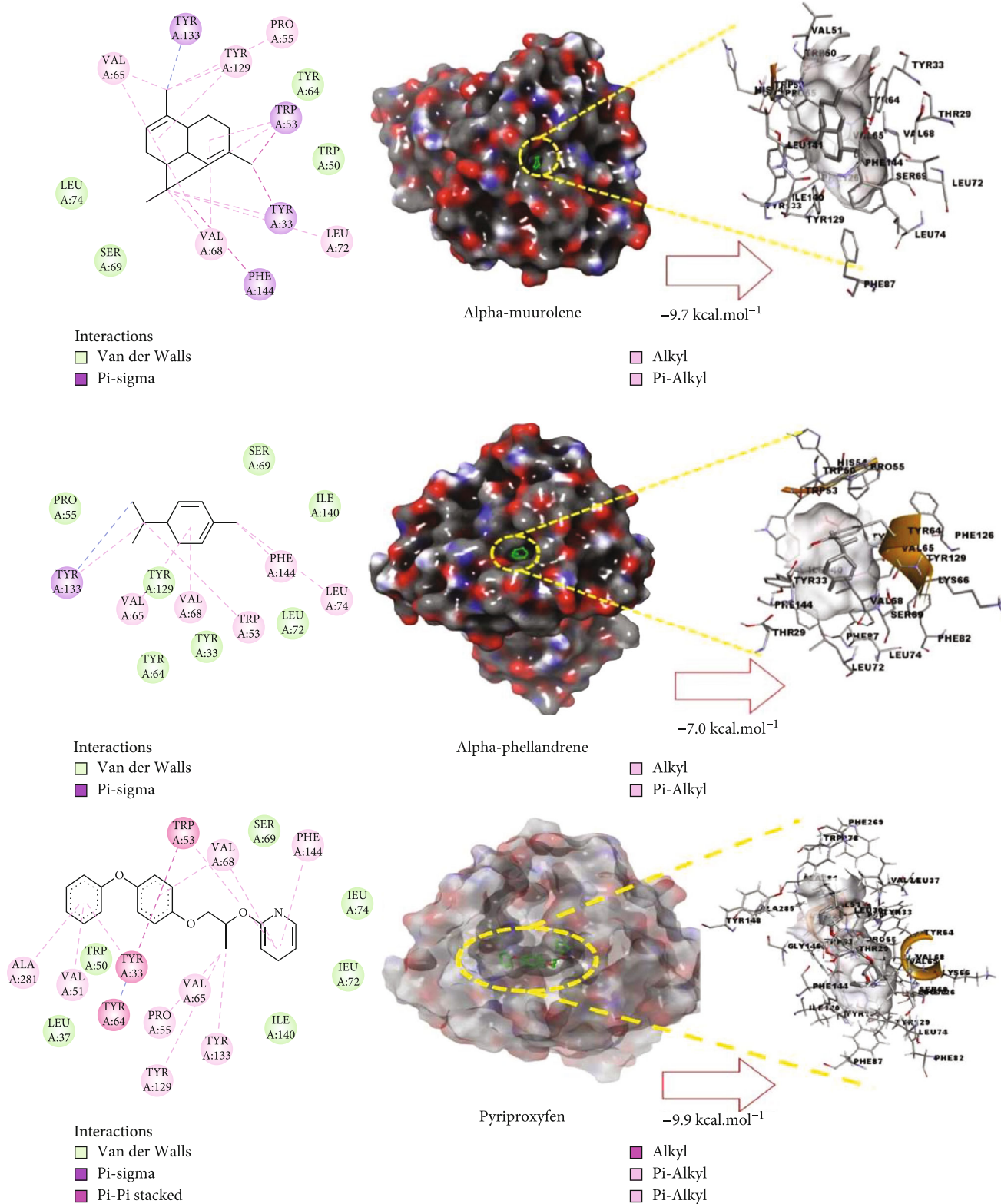
FIGURE 2: Molecular studies of the interaction of volatile constituents of *S. molle* essential oil (alpha-muurolene, alpha-phellandrene) and synthetic insecticide (pyriproxyfen) with mosquito juvenile hormone-binding protein (PDB ID: 5V13): surface view (right) and 2D (left) interactions.

(a)

(b)

(c)

(d)

(e)

FIGURE 3: Continued.

(f)

(g)

(h)

(i)

Receptor unbound
Receptor bound

H-bonds   Ionic
Hydrophobic   Water bridges

(j)
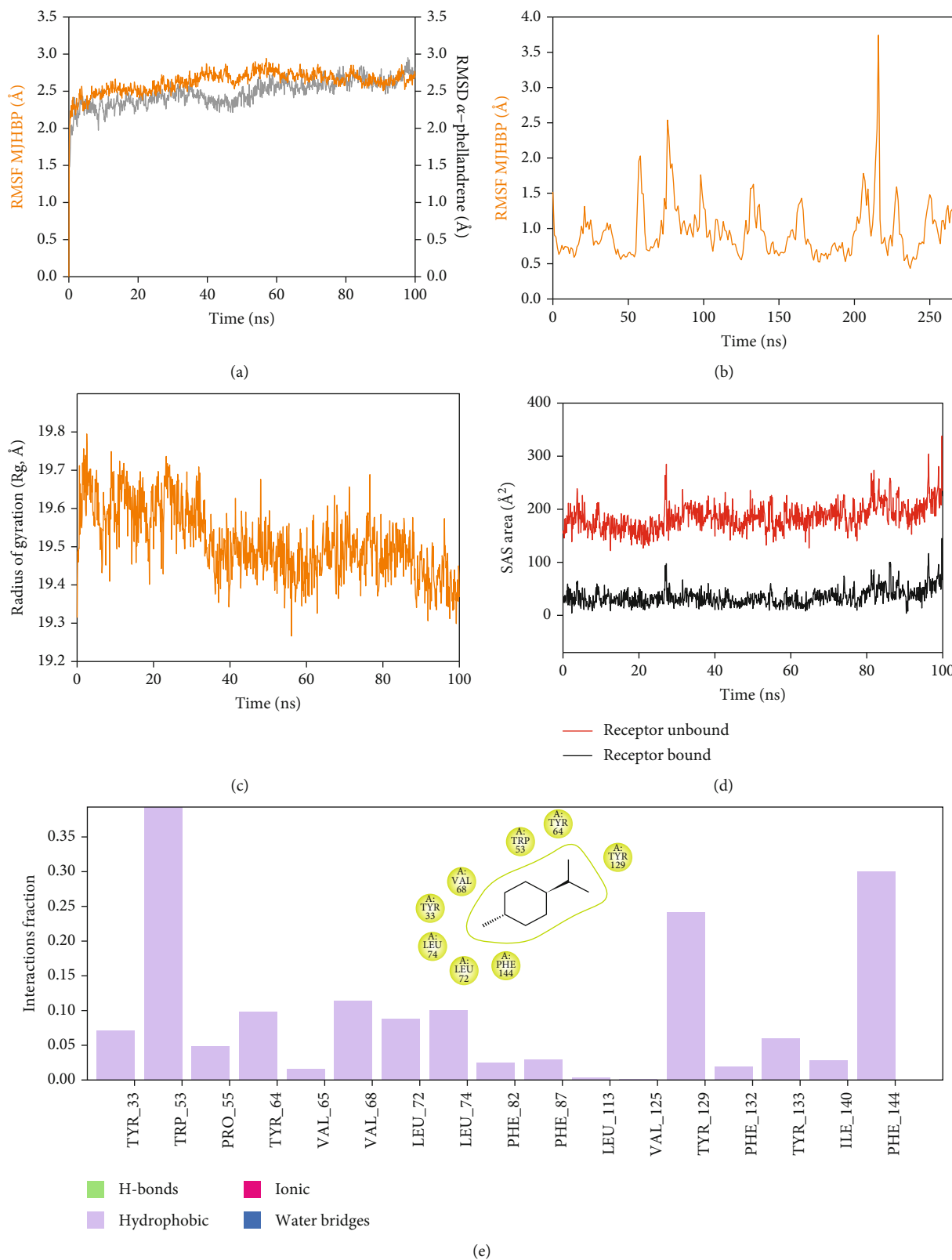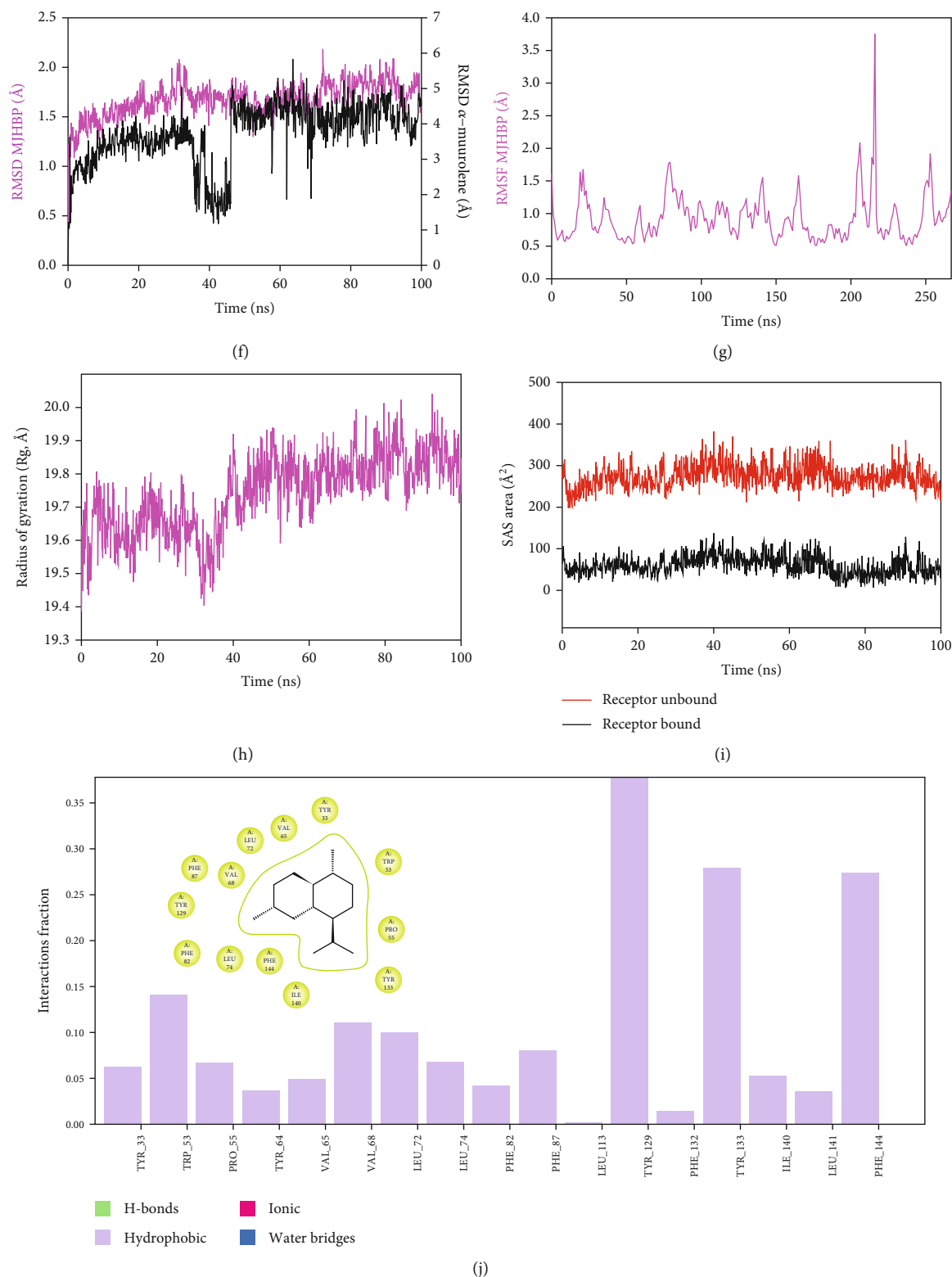
FIGURE 3: Analysis of MD simulation trajectories for 100 ns. RMSD plots displaying the molecular vibrations of Cα backbone of (a) mJHBP+α-phellandrene and (f) mJHBP+α-muurolene. RMSF plots showing the fluctuations of respective amino acids throughout the simulation time 100 ns for (b) mJHBP+α-phellandrene and (g) mJHBP+α-muurolene. Radius of gyration plots for the deduction of compactness of protein (c) mJHBP+α-phellandrene and (h) mJHBP+α-muurolene. Solvent accessible surface area (SAS area) displaying the ligand-bound and ligand-unbound area at the binding pocket (d) mJHBP+α-phellandrene and (i) mJHBP+α-muurolene. Interaction fractions displaying the predominant hydrophobic interactions of the binding cavity residues of mJHBP with (e) α-phellandrene and (j) α-muurolene.

between the evaluated concentrations and the antioxidant response. *P* values less than 0.01 were considered statistically significant. GraphPad Prism program version 6.0 (La Jolla, CA, USA) was used to carry out the statistical analysis.

3. Results and Discussion

3.1. Chemical Profile of the Essential Oil of S. molle. The obtained EO of fresh leaves showed a light-yellow color, a density of 0.873 ± 0.02 g/mL at 20°C, and an extraction yield of 0.73% during 2 hours of distillation. The profiles of volatile constituents of *S. molle* essential oil were analyzed by GC-MS and are presented in Figure 1 and Table 1. Regarding the chemical profile, the EO showed 34 compounds (Figure 1), two of which are of unknown structures (compounds 27 and 29), which accounted for 99.7% of the total composition. Those unknown chemical structures were classified as oxygenated sesquiterpenes with the following formula $C_{15}H_{26}O$ and a molecular weight of 222.37 g/mol. The analysis identified alpha-phellandrene as the main volatile chemical with 32.68%, followed by D-limonene (12.59%) and beta-phellandrene (12.24%). According to Figure 1, the retention time at 17.80 min corresponded to the major component in the EO (compound 7).

In the phytochemical analysis, our results differed from those of other investigations and could be explained by different types of factor such as type of extraction, temperature conditions, storage conditions, edaphic conditions, plant part extracted, ecosystem, environmental, harvesting time, and the presence of environmental pollution [29]. In this study, the most representative molecule was alpha-phellandrene with 32.68%. However, in recent studies, as reported by Morales-Rabanales et al., β-phellandrene (15.7%) and α-phellandrene (12.1%) were the main components of the EO from *S. molle* leaves cultivated in Tepetitla de Lardizábal, Mexico [30]. In an analysis of *S. molle* EO obtained of dried leaves from Seropédica, Rio de Janeiro, Brazil, epi-α-cadinol (22.85%) was the major component [31]. Additionally, in *S. molle* from Caxias do Sul, Brazil, alpha-pinene (60.04 ± 0.07%) was the most abundant constituent [32]. In Naviraí-MS, Brazil, the major component was epi-α-cadinol with 21.0 ± 1.1%, followed by myrcene (16.7 ± 1.1) and sabinene (14.5 ± 0.8) [33]. *S. molle* from North Cyprus showed values of alpha-phellandrene, limonene, and beta-phellandrene equivalent to 31.5%, 10.1%, and 9.9%, respectively [34]. On the other hand, *S. molle* from Sonora, Mexico, revealed 60.8% of D-limonene (17.8%), o-cymene (16.4%), β-phellandrene (12.6%), δ-cadinene (7.5%), and caryophyllene (6.5%) [35]. However, in Jordan and Turkey, alpha-phellandrene was the most abundant constituent with 48.2% and 29.0%, respectively.

3.2. Antioxidant Profile of S. molle Essential Oil. *S. molle* EO exhibited a low antioxidant activity, as is shown in Table 2. On the other hand, there was a significant difference between the different methods used in the antioxidant activity ($P = 0.0004$). Other reports have shown different values; according to Eryigit et al., EO showed a TEAC (ABTS) = 4.7 ± 1.2 mM Trolox of *S. molle* grown in Turkey [36]. EO

from Portugal reported an inhibition value of 4.8% at 16 mg/mL and was obtained by hydrodistillation. Although alpha-phellandrene, myrcene, limonene, and beta-phellandrene were the main components in this EO, its low antioxidant activity could be associated with the low ability of monoterpene hydrocarbons for DPPH scavenging activity. However, in other methods, such as beta-carotene bleaching, the antioxidant activity was high and might be justified by the presence of the monoterpenes α and β-phellandrene, α-pinene, sabinene, limonene, β-myrcene, and others [10]. In this study, the IC_{50} against DPPH was 41.84 μg/mL, which was higher compared to the findings of the EO from southeast Portugal [10]. In another study, *S. molle* from Egypt showed an IC_{50} at DPPH of 172.45 μg/mL and a high percentage of oxygenated sesquiterpene (17.73%) [37]. According to Table 2, the best effect was found in the FRAP assay, followed by ABTS and DPPH. It is known that DPPH and ABTS methods are based on electron and H atom transfer reaction, while the FRAP method is based on electron transfer reaction. Thus, the volatile phytochemicals from *S. molle* EO could be acted by electron transfer to reduce the free radicals.

3.3. Molecular Docking of the Essential Oil from S. molle in the Presence of the Mosquito Juvenile Hormone-Binding Protein (mJHBP) from Aedes aegypti. The virtual screening of the 32 chemical components, additionally JH3 and the pyriproxyfen (synthetic insecticide), was carried out in order to understand the interaction profile of various volatile compounds present in *S. molle* EO leaves with mJHBP from *A. aegypti*. Out of 32 specific compounds found abundantly in chromatography, gamma-cadinene and alpha-muurolene displayed a lower binding energy (ΔG) of -9.7 kcal/mol and predicted inhibitory concentration (Ki) of 0.134 μM (Table 3). Although the major component (alpha-phellandrene) had a high binding free energy ($\Delta G = -7$ kcal/mol), compared to alpha-muurolene, the total components might be synergizing the insecticidal effect.

The principal residues of mJHBP, TYR133, TRP53, TYR33, and PHE144 were involved in Pi-Sigma bond formation with alpha-muurolene (Figure 2). We observed that TYR133 was the main residue of mJHBP in which the molecules of the EO established a Pi-sigma, Van der Walls, and Pi-alkyl bonds (Supplementary Materials S1–S32). Interestingly, elixene, germacrene D, beta-cadinene, gamma-muurolene, germacrene-D, humulene, and gamma-eludesmol exhibited activity and binding energies close to those of the known insecticide pyriproxyfen and the cocrystallized ligand JH3. Alpha-phellandrene, beta-caryophyllene, beta-elemene, alpha-pinene, beta-phellandrene, beta-pinene, elemol, etc. have exhibited significant binding and inhibition of the mosquito juvenile hormone-binding protein. Therefore, from the docking study, it can be predicted that the molecules from this essential oil have great potential as inhibitors of the mosquito juvenile hormone-binding protein. The interactions of JH3 in this study are according to the results of Ramos et al., which the epoxy group forms a conventional hydrogen bond with the phenolic hydroxyl of Tyr-129, and other interactions showed on the isoprenoid chain were Val65, Val68, Pro55, Phe144, Tyr64, Tyr33, Ala281, Trp53, and Phe269 [18].

Furthermore, the low binding free energy ($\Delta G > -9$ kcal/mol) of some volatile components was evidenced in those interactions with the Tyr133, Trp53, Tyr33, and Phe144 residues as shown in Supplementary Materials Figures S1–S32. These could infer that the insecticidal activity is related to these residues mentioned above.

3.4. Molecular Dynamics of the Phytoconstituents of the Essential Oil from S. molle. Molecular dynamics and simulation (MD) studies were carried out in order to determine the stability and convergence of mJHBP+α-phellandrene and mJHBP+α-muurolene complexes. Each simulation of 100 ns displayed stable conformation comparing the root mean square deviation (RMSD) values. The Cα backbone of mJHBP bound to α-phellandrene exhibited a deviation of 0.5 Å (Figure 3(a)), while mJHBP bound to α-muurolene exhibited a deviation of 1.0 Å (Figure 3(f)). RMSD plots are within the acceptable range signifying the stability of mJHBP in the ligand-bound state before and after simulation, and it can also be suggested that ligand α-phellandrene and α-muurolene-bound mJHBP are quite stable in complex due to the higher affinity of the ligand. The plots for root mean square fluctuations (mMSF) displayed a significant spike in fluctuation (3.5 Å) at amino acid residue 220 in mJHBP, while the rest of the residues fluctuated less during the entire 100 ns simulation (Figures 3(b) and 3(g)) indicating the stable amino acid conformations during the simulation time. Therefore, from the RMSF plots, it can be suggested that the structures of mJHBP were stable during simulation in α-phellandrene- and α-muurolene-bound conformations. The radius of gyration is the measure of compactness of the protein. In this study, the mJHBP Cα backbone displayed a lowering of the radius of gyration (Rg) from 19.6 Å to 19.4 Å, and the lowering of the Rg indicates the compactness of the complex (Figure 3(c)). On the other hand, the lowering of Rg was observed for the mJHBP+α-muurolene complex till 35 ns, and a later increment of the peak was observed. This indicates the less stable conformation of mJHBP+α-muurolene as compared to mJHBP+α-phellandrene. However, the stable Rg peak confirmed the significant compactness of the protein in the α-muurolene-bound state (Figure 3(h)). The overall quality analysis from RMSD and Rg suggests that α-phellandrene and α-muurolene bound to the protein targets posthumously in the binding cavities and played a significant role in stability of the proteins. Solvent accessible surface area provides the information about the compactness of protein complex with the ligand. The lowering of SASA in the case of α-phellandrene and α-muurolene bound to mJHBP as compared to the unbound state signifies the achievement of stable converged structures due to the high compactness of both the systems (Figures 3(d) and 3(i)). The interaction plots of both α-phellandrene and α-muurolene bound to mJHBP displayed no involvement of conventional hydrogen bonds, while hydrophobic interactions played a major role in ligand stabilization at the binding cavity of mJHBP (Figures 3(e) and 3(j)).

4. Conclusions

The essential oil of *S. molle* leaves presented 34 volatile constituents determined by gas chromatography-mass spectrometry (GC-MS). Alpha-phellandrene was the major component, which represented 32.68% of the total composition; furthermore, beta-phellandrene and D-limonene were the following more abundant metabolites with 12.24% and 12.59%, respectively. Additionally, the antioxidant activity was evaluated in order to determine the antioxidant profile of EO using the three methods of DPPH, ABTS, and FRAP. According to the results, the EO showed better affinity and a good effect on FRAP assay and IC$_{50}$ equivalent to 1.50 ± 0.02 mg/mL. However, this study revealed that *S. molle* EO is not a good antioxidant. Regarding the insecticidal activity in silico based on a virtual screening on mosquito juvenile hormone-binding protein, several volatile compounds were active against this target such as alpha-muurolene and gamma-cadinene, being similar to pyriproxyfen, which is a synthetic insecticide analogue of JH. The molecular dynamics carried out for alpha muurolene (the best result in molecular docking) and alpha-phellandrene (the most abundant molecule) were very stable during 100 ns of evaluation. In the future, *S. molle* EO might be used as bioinsecticide on *A aegypti*, but an in vitro and in vivo assay has to be evaluated to validate our findings.

Data Availability

The data used to support the findings of this study are included within the supplementary information file.

Conflicts of Interest

The authors declare no conflicts of interest.

Authors' Contributions

Conceptualization was supervised by O.H.-C., H.C., G.E.-S. B., and N.H.A. Methodology was supervised by S.A. and H.C. Formal analysis was supervised by E.C.E.-R. Investigation was supervised by O.H.-C., P.W.C.-V., and R.D.H.-Q. Writing the original draft preparation was supervised by O. H.-C., J.B.P.-O., and E.L.G. Writing the review and editing was supervised by O.H.-C. and L.F.-S. Funding acquisition was supervised by N.H.A. and S.A.

Acknowledgments

Supplementary Materials

Figures S1–S32: molecular interaction studies of the phytochemical components from *S. molle* and mosquito juvenile hormone-binding protein (mJHBP) from *Aedes aegypti*. (*Supplementary Materials*)

References

[1] Z. A. A. Aziz, A. Ahmad, S. H. M. Setapar et al., "Essential oils: extraction techniques, pharmaceutical and therapeutic potential - a review," *Current Drug Metabolism*, vol. 19, no. 13, pp. 1100–1110, 2018.

[2] P. Tongnuanchan and S. Benjakul, "Essential oils: extraction, bioactivities, and their uses for food preservation," *Journal of Food Science*, vol. 79, no. 7, p. R1231, 2014.

[3] J. B. Sharmeen, F. M. Mahomoodally, G. Zengin, and F. Maggi, "Essential oils as natural sources of fragrance compounds for cosmetics and cosmeceuticals," *Molecules*, vol. 26, no. 3, 2021.

[4] B. Ali, N. A. Al-Wabel, S. Shams, A. Ahamad, S. A. Khan, and F. Anwar, "Essential oils used in aromatherapy: a systemic review," *Asian Pacific Journal of Tropical Biomedicine*, vol. 5, no. 8, pp. 601–611, 2015.

[5] G. León-Méndez, N. Pájaro-Castro, E. Pájaro-Castro et al., "Essential oils as a source of bioactive molecules," *Revista Colombiana de Ciencias Químico - Farmacéuticas*, vol. 48, no. 1, pp. 80–93, 2019.

[6] M. Perricone, E. Arace, M. R. Corbo, M. Sinigaglia, and A. Bevilacqua, "Bioactivity of essential oils: a review on their interaction with food components," *Frontiers in Microbiology*, vol. 6, p. 76, 2015.

[7] J. Sharifi-Rad, A. Sureda, G. C. Tenore et al., "Biological activities of essential oils: from plant chemoecology to traditional healing systems," *Molecules : A Journal of Synthetic Chemistry and Natural Product Chemistry*, vol. 22, no. 1, p. 70, 2017.

[8] M. J. Kim, D. W. Kim, J. G. Kim, Y. Shin, S. K. Jung, and Y. J. Kim, "Analysis of the chemical, antioxidant, and anti-inflammatory properties of pink pepper (Schinus molle l.)," *Antioxidants*, vol. 10, no. 7, p. 1062, 2021.

[9] G. Turchetti, S. Garzoli, V. L. Masci et al., "Antimicrobial testing of Schinus molle (L.) leaf extracts and fractions followed by GC-MS investigation of biological active fractions," *Molecules*, vol. 25, no. 8, p. 1977, 2020.

[10] M. D. R. Martins, S. Arantes, F. Candeias, M. T. Tinoco, and J. Cruz-Morais, "Antioxidant, antimicrobial and toxicological properties of Schinus molle L. essential oils," *Journal of Ethnopharmacology*, vol. 151, no. 1, pp. 485–492, 2014.

[11] C. D. Machado, V. Raman, J. U. Rehman et al., "Schinus molle: anatomy of leaves and stems, chemical composition and insecticidal activities of volatile oil against bed bug (Cimex lectularius)," *Revista Brasileira de Farmaco*, vol. 29, no. 1, pp. 1–10, 2019.

[12] A. T. H. Mossa, S. M. M. Mohafrash, and N. Chandrasekaran, "Safety of natural insecticides: toxic effects on experimental animals," *Bio Med Research International*, vol. 2018, article 4308054, pp. 1–17, 2018.

[13] M. B. Isman, "Bioinsecticides based on plant essential oils: a short overview," *Zeitschrift fur Naturforschung - Section C Journal of Biosciences*, vol. 75, no. 7-8, pp. 179–182, 2020.

[14] X. Liu, A. Cao, D. Yan, C. Ouyang, Q. Wang, and Y. Li, "Overview of mechanisms and uses of biopesticides," *International Journal of Pest Management*, vol. 67, no. 1, pp. 65–72, 2019.

[15] J. L. Martin, C. A. Lippi, A. M. Stewart-Ibarra et al., "Household and climate factors influence Aedes aegypti presence in the arid city of Huaquillas, Ecuador," *PLOS Neglected Tropical Diseases*, vol. 15, no. 11, article e0009931, 2021.

[16] W. Jablonka, I. H. Kim, P. H. Alvarenga, J. G. Valenzuela, J. M. C. Ribeiro, and J. F. Andersen, "Functional and structural similarities of D7 proteins in the independently-evolved salivary secretions of sand flies and mosquitoes," *Scientific Reports*, vol. 9, no. 1, pp. 1–12, 2019.

[17] I. H. Kim, J. C. Castillo, A. Aryan et al., "A mosquito juvenile hormone binding protein (mJHBP) regulates the activation of innate immune defenses and hemocyte development," *PLOS Pathogens*, vol. 16, no. 1, article e1008288, 2020.

[18] R. D. S. Ramos, J. D. S. Costa, R. C. Silva et al., "Identification of potential inhibitors from pyriproxyfen with insecticidal activity by virtual screening," *Pharmaceuticals*, vol. 12, no. 1, p. 20, 2019.

[19] E. Abdel-Sattar, A. A. Zaitoun, M. A. Farag, S. H. el Gayed, and F. M. H. Harraz, "Chemical composition, insecticidal and insect repellent activity of Schinus molle L. leaf and fruit essential oils against Trogoderma granarium and Tribolium castaneum," *Natural Product Research*, vol. 24, no. 3, pp. 226–235, 2009.

[20] V. Benzi, N. Stefanazzi, and A. A. Ferrero, "Biological activity of essential oils from leaves and fruits of pepper tree (Schinus molle L.) to control rice weevil (Sitophilus oryzae L.)," *Chilean Journal of Agricultural Research*, vol. 69, no. 2, pp. 154–159, 2009.

[21] A. López, S. Castro, M. J. Andina et al., "Insecticidal activity of microencapsulated Schinus molle essential oil," *Industrial Crops and Products*, vol. 53, pp. 209–216, 2014.

[22] L. C. S. O. de Batista, Y. P. Cid, A. P. de Almeida et al., "In vitro efficacy of essential oils and extracts of Schinus molle L. against Ctenocephalides felis felis," *Parasitology*, vol. 143, no. 5, pp. 627–638, 2016.

[23] Í. Chiffelle, A. Huerta, C. A. Sandoval et al., "Insecticide effect of leaf extracts from Schinus molle on larvae of Gonipterus platensis," *Revista Facultad Nacional de Agronomía Medellín*, vol. 70, no. 3, pp. 8263–8270, 2017.

[24] O. Herrera-Calderon, L. J. Chacaltana-Ramos, I. C. Huayanca-Gutiérrez, M. A. Algarni, M. Alqarni, and G. E. S. Batiha, "Chemical constituents, in vitro antioxidant activity and in silico study on NADPH oxidase of Allium sativum L. (garlic) essential oil," *Antioxidants*, vol. 10, no. 11, p. 1844, 2021.

[25] R. P. Adams, *Identification of essential oil components by gas chromatography/mass spectrometry*, Allured Publishing, Carol Stream, IL, USA, 2017.

[26] V. Kumar, C. S. Mathela, M. Kumar, and G. Tewari, "Antioxidant potential of essential oils from some Himalayan Asteraceae and Lamiaceae species," *Medicine in Drug Discovery*, vol. 1, article 100004, 2019.

[27] M. Kokina, A. Salevic, A. Kaluševic et al., "Characterization, antioxidant and antibacterial activity of essential oils and their encapsulation into biodegradable material followed by freeze drying," *Food Technology and Biotechnology*, vol. 57, no. 2, pp. 282–289, 2019.

[28] A. C. Moller, C. Parra, B. Said et al., "Antioxidant and anti-proliferative activity of essential oil and main components from leaves of Aloysia polystachya harvested in Central Chile," *Molecules*, vol. 26, no. 1, 2021.

[29] M. Moghaddam and L. Mehdizadeh, "Chemistry of essential oils and factors influencing their constituents," *Soft Chemistry and Food Fermentation*, pp. 379–419, 2017.

[30] Q. N. Morales-Rabanales, W. A. Coyotl-Pérez, E. Rubio-Rosas, G. S. Cortes-Ramírez, J. F. Sánchez Ramírez, and N. Villa-Ruano, "Antifungal properties of hybrid films containing the essential oil of Schinus molle : protective effect against postharvest rot of tomato," *Food Control*, vol. 134, article 108766, 2022.

[31] R. C. D. S. S. da Silveira, A. L. Guedes, F. S. Frattani, N. M. M. Epifânio, M. A. A. de Souza, and D. S. D. A. Chaves, "Chemical profile of schinus molle L. essential oil and its antihemostatic properties," *Natural Volatiles and Essential Oils*, vol. 7, no. 1, pp. 1–8, 2020.

[32] C. B. Vicenço, W. P. Silvestre, V. T. da Silva et al., "Bioactivity of Schinus molle L. and Schinus terebinthifolia Raddi. Essential oils on Anticarsia gemmatalis (Hübner 1818)," *Brazilian Archives of Biology and Technology*, vol. 63, pp. 1–12, 2020.

[33] A. F. N. Volpini-Klein, S. E. Lima Júnior, C. A. L. Cardoso et al., "Chemical composition of essential oils from leaves and fruits of Schinus molle obtained by different extraction methods hydrodistillation, fractional hydrodistillation and steam distillation and seasonal variations," vol. 24, no. 2, pp. 228–242, 2021.

[34] H. Alnawari, B. Demirci, A. Hanoğlu, D. Hanoğlu, İ. Çalış, and K. H. C. Başer, "Chemical characterization of Schinus molle L. essential oils from North Cyprus," *Natural Volatiles and Essential Oils*, vol. 5, no. 3, pp. 7–12, 2018.

[35] A. K. López-Meneses, M. Plascencia-Jatomea, J. Lizardi-Mendoza et al., "Schinus molle L. essential oil-loaded chitosan nanoparticles: preparation, characterization, antifungal and anti-aflatoxigenic properties," *LWT*, vol. 96, pp. 597–603, 2018.

[36] T. Eryigit, B. Yildirim, K. Ekici, and M. Çirka, "Chemical composition, antimicrobial and antioxidant properties of Schinus molle L. essential oil from Turkey," *Journal of Essential Oil Bearing Plants*, vol. 20, no. 2, pp. 570–577, 2017.

[37] R. M. Romeilah, S. A. Fayed, and G. I. Mahmoud, "Antioxidant and antiviral activities of essential oils from Callistemon viminalis and Schinus molle L," *Research Journal of Pharmaceutical, Biological and Chemical Sciences*, vol. 7, no. 1, pp. 1982–1993, 2016.

Research Article

Potential Small Molecules for Therapy of Lupus Nephritis Based on Genetic Effect and Immune Infiltration

Jianbo Qing [ID],[1] **Wenzhu Song** [ID],[2] **Lingling Tian** [ID],[3] **Sonia Biju Samuel** [ID],[4] **and Yafeng Li** [ID][5,6,7,8]

[1]*The Fifth Clinical Medical College of Shanxi Medical University, Taiyuan, Shanxi 030001, China*
[2]*School of Public Health, Shanxi Medical University, Taiyuan, Shanxi 030001, China*
[3]*Shanxi University of Traditional Chinese Medicine, Taiyuan, Shanxi 030000, China*
[4]*Department of Medicine, Albany Medical Center. 43 New Scotland Ave, Albany, New York 12208, USA*
[5]*Department of Nephrology, Shanxi Provincial People's Hospital (Fifth Hospital) of Shanxi Medical University, Taiyuan, Shanxi 030012, China*
[6]*Core Laboratory, Shanxi Provincial People's Hospital (Fifth Hospital) of Shanxi Medical University, Taiyuan, Shanxi 030012, China*
[7]*Shanxi Provincial Key Laboratory of Kidney Disease, Shanxi Provincial People's Hospital (Fifth Hospital) of Shanxi Medical University, Taiyuan, Shanxi 030012, China*
[8]*Academy of Microbial Ecology, Shanxi Medical University, Taiyuan, Shanxi 030000, China*

Correspondence should be addressed to Yafeng Li; dr.yafengli@gmail.com

Lupus nephritis (LN) is the most common and significant complication of systemic lupus erythematosus (SLE) due to its poor prognosis and mortality rates in SLE patients. There is a critical need for new drugs as the pathogenesis of LN remains to be elucidated and immunosuppressive therapy comes with many deficiencies. In this study, 23 hub genes (IFI6, PLSCR1, XAF1, IFI16, IFI44, MX1, IFI44L, IFIT3, IFIT2, IFI27, DDX58, EIF2AK2, IFITM1, RTP4, IFITM3, TRIM22, PARP12, IFIH1, OAS1, HERC6, RSAD2, DDX60, and MX2) were identified through bioinformatics and network analysis and are closely related to interferon production and function. Interestingly, immune cell infiltration analysis and correlation analysis demonstrate a positive correlation between the expression of 23 hub genes and monocyte infiltration in glomeruli and M2 macrophage infiltration in the tubulointerstitium of LN patients. Additionally, the CTD database, DsigDB database, and DREIMT database were used to explore the bridging role of genes in chemicals and LN as well as the potential influence of these chemicals on immune cells. After comparison and discussion, six small molecules (Acetohexamide, Suloctidil, Terfenadine, Prochlorperazine, Mefloquine, and Triprolidine) were selected for their potential ability in treating lupus nephritis.

1. Introduction

The pathogenesis of systemic lupus erythematosus (SLE) and lupus nephritis (LN) is generally caused by multiple factors including genetics, immune abnormalities, ultraviolet radiation, drugs, estrogen [1, 2], and viral infections [3, 4]. LN is characterized by glomeruli and tubulointerstitium inflammation [5], which are mediated by a variety of immune cells and cytokines [6]. This leads to a series of clin-ical presentations including hematuria, proteinuria, and impaired glomerular filtration rate [7].

At present, immunosuppressants, glucocorticoids (GC), and biological agents are mainly available for the treatment of LN worldwide. Various drug regimens have also been proposed based on the stage of the disease [8]. Since 1980, GC, mycophe-nolate (MPA), mofetil (MMF), calcineurin inhibitors (CNI), hydroxychloroquine (HCQ), rituximab (RTX), and others have been gradually explored in clinical practice and achieved

(a)

(b)

(c)

(d)
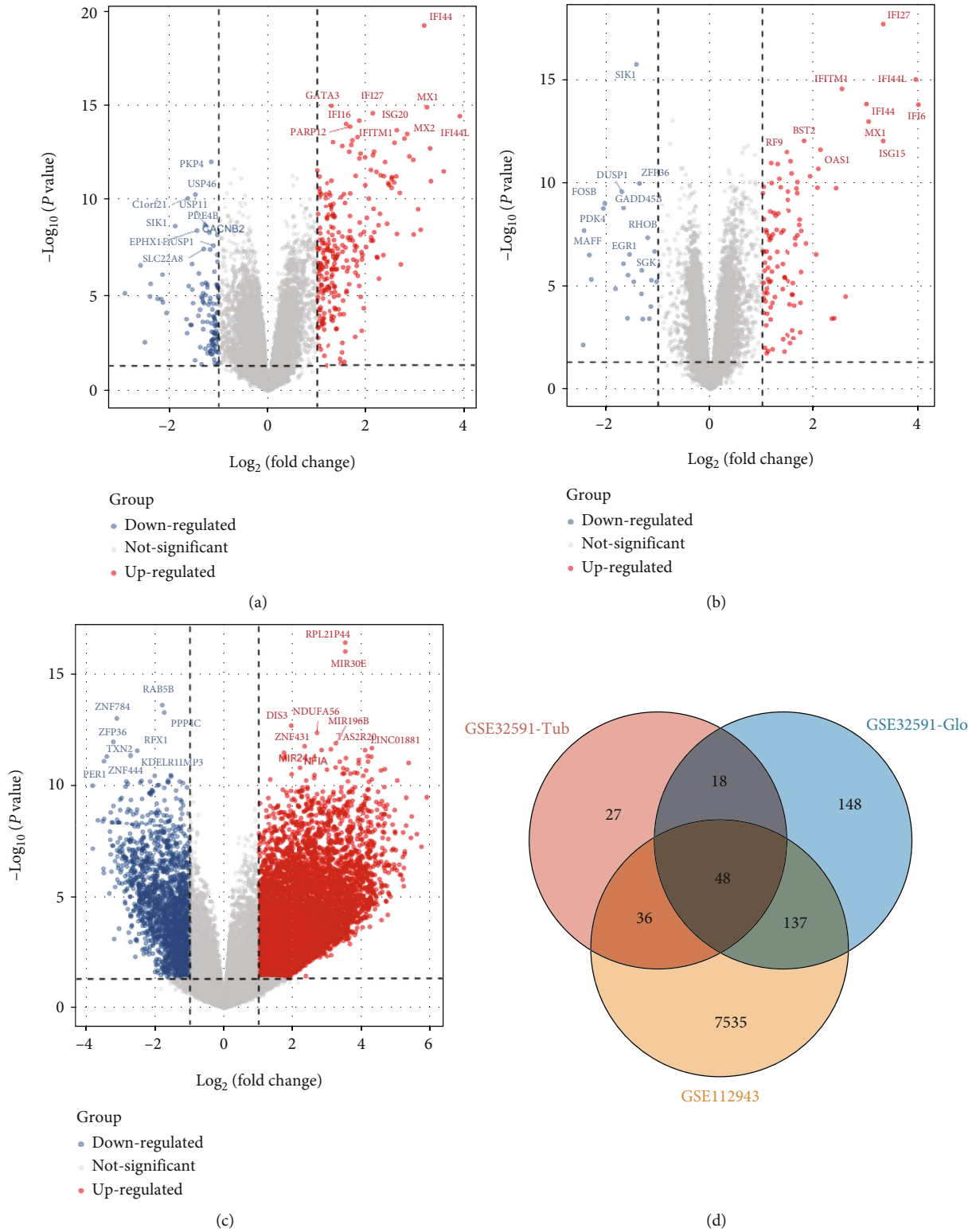
Figure 1: Identification of DEGs of kidney tissues from LN and control samples in GSE32591 and GSE112943. (a) The volcano map of all DEGs of the 46 glomeruli samples in GSE32591. (b) The volcano map of all DEGs of the 47 tubulointerstitium samples in GSE32591. (c) The volcano map of all DEGs of the 21 kidney samples in GSE112943. (d) The Venn diagram of GSE32591 and GSE112943.

(a)

(b)
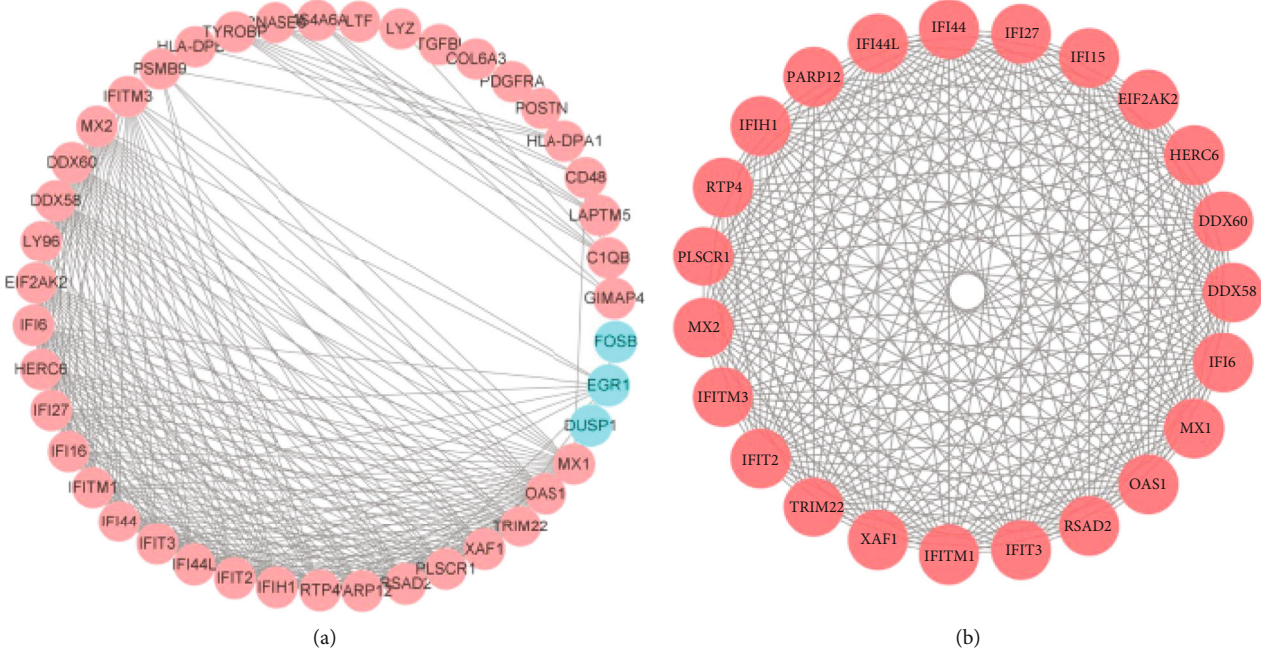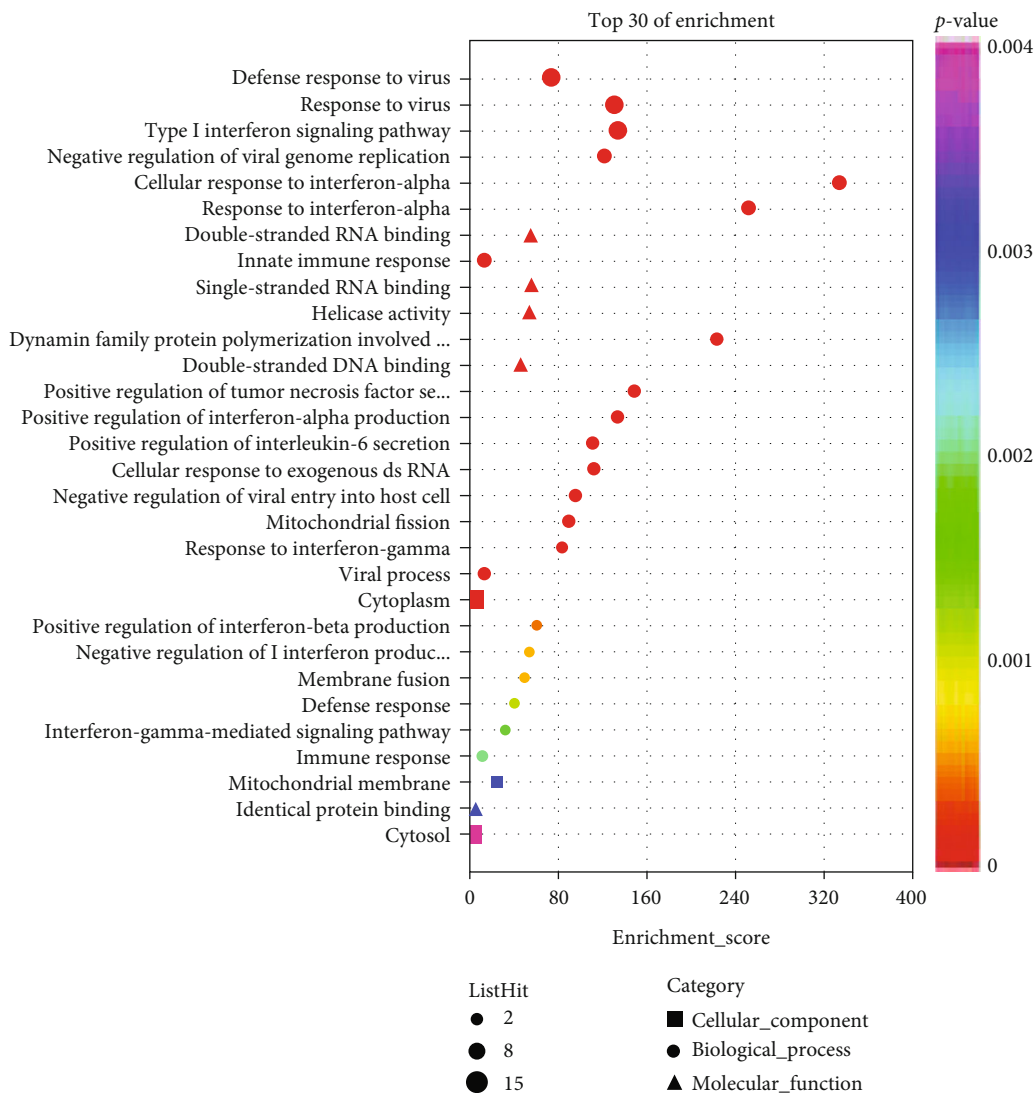
Figure 2: Continued.

(c)

Figure 2: Continued.

(d)
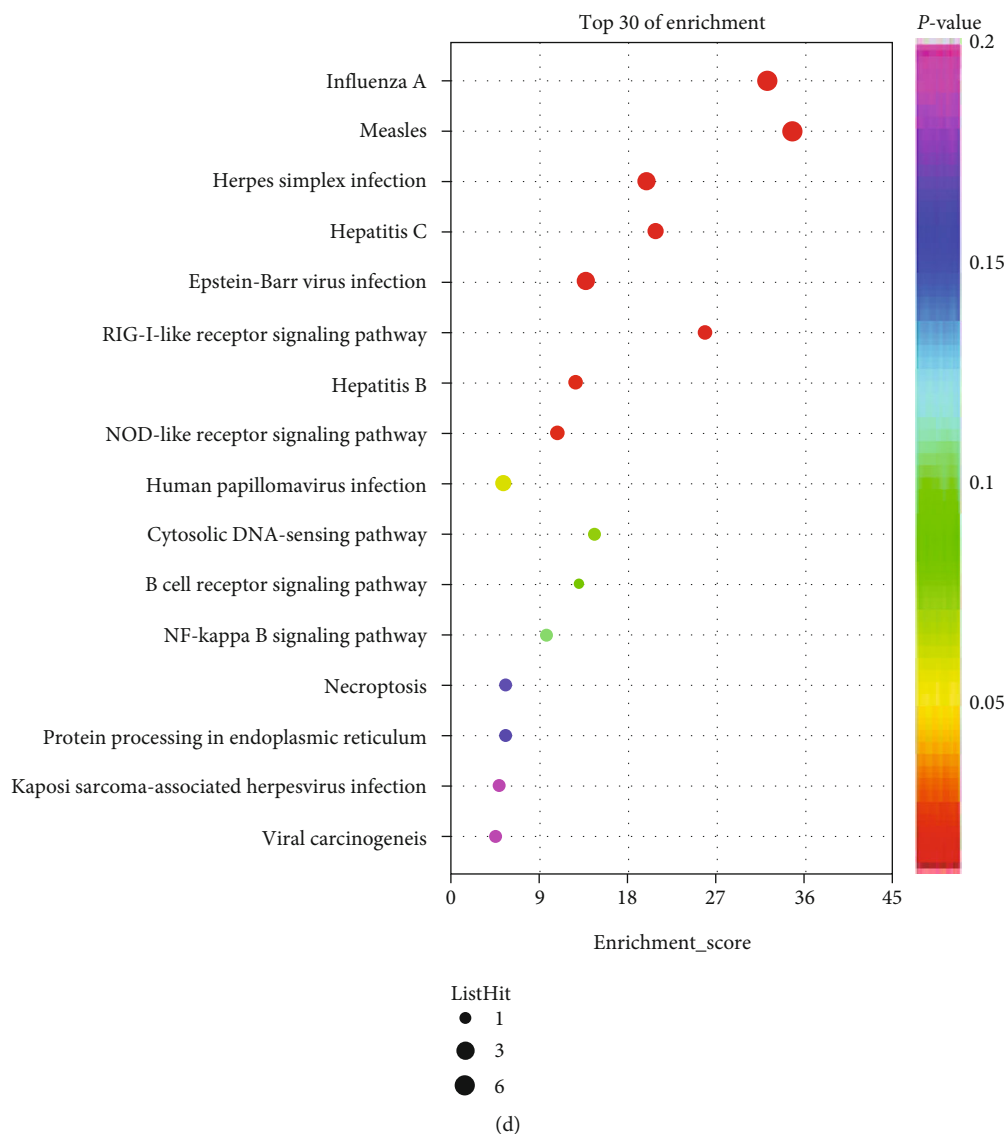
Figure 2: Protein–protein interaction (PPI) network and identification of hub genes. (a) Protein–protein interaction (PPI) network of 48 common genes in GSE32591 and GSE112943. Nodes in pink represent coupregulated genes while nodes in blue represent codownregulation of genes. The analyzed network holds 43 nodes and 296 edges. (b) Protein–protein interaction (PPI) network of 23 hub genes identified by MCODE in Cytoscape. The analyzed network holds 23 nodes and 240 edges. (c) Top 30 GO functional enrichment of the 23 hub genes. (c) 16 KEGG signaling pathway enrichment of the 23 hub genes.

promising results [9]. However, emerging studies are identifying their high side effect profile and toxicity. Some of them even fail to prevent disease recurrence in more than half of the patients [10]. Therefore, the discovery of new drugs for LN is of great urgency and importance to reduce mortality rates.

Currently, drug selection is primarily based on three principles: immunosuppression, immunomodulation, and symptomatic treatment [11]. Meanwhile, more studies are identifying genes that are implicated in the development and progression of LN [12], and researchers have sequenced kidney tissue from LN and documented them in the GEO database. Drug-gene relationships are continuously being enriched by further research and exploration.

In the present study, we focus on existing small molecules. First, we identify the core pathogenic genes of LN

and then detect the association between chemicals, genes and LN through various reliable databases to screen potential small molecules for the treatment of LN. Finally, the potential mechanism of these small molecules was evaluated according to the immune signatures.

2. Materials and Methods

2.1. Microarray Data and Identification of Differently Expressed Genes (DEGs). The screening criteria of datasets are as follows: First, the datasets must include cases and controls. Second, the organization used for sequencing should be the kidney of human. Third, the number of samples in each group should not be less than 10. Thus, GSE32591 [13] and GSE112943 [14] were downloaded from the GEO
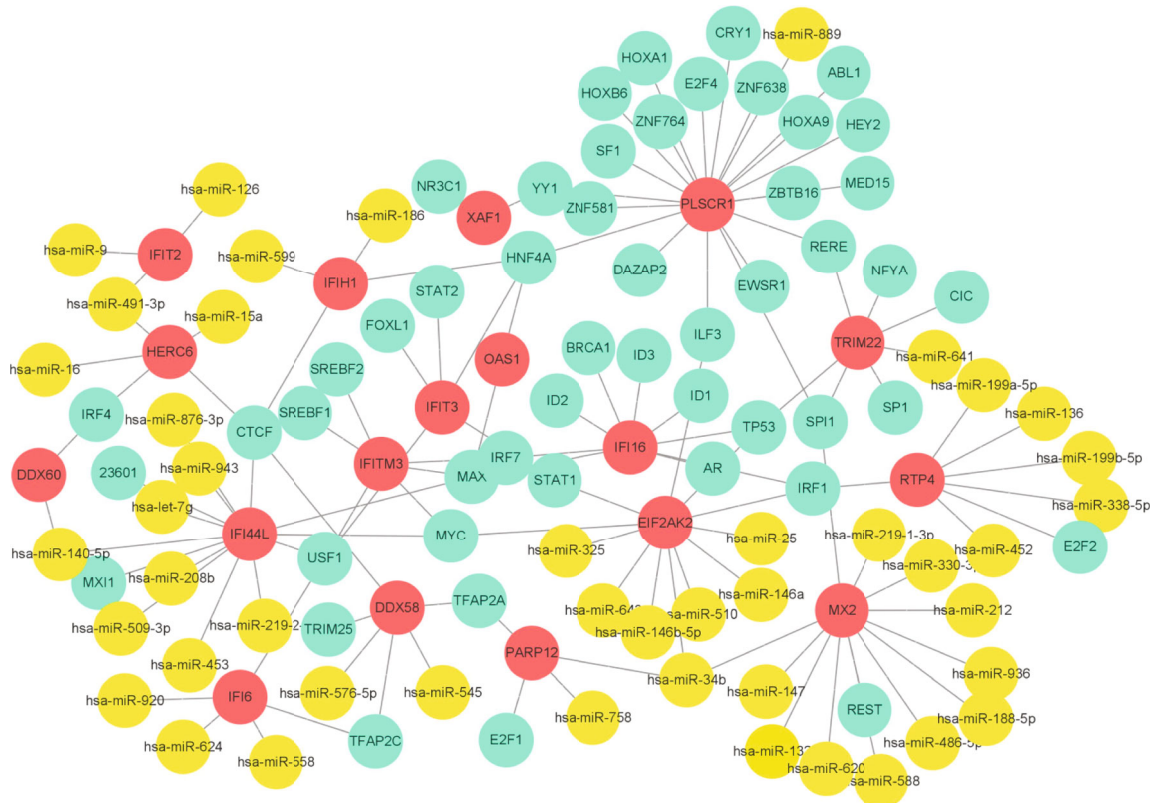
FIGURE 3: The network of TF-miRNA coregulatory. Nodes in red color represent the hub genes, nodes in blue color represent the TF-genes, and nodes in yellow color represent the miRNAs. The analyzed network holds 113 nodes and 127 edges. 55 miRNAs and 50 TF-genes have interacted with the 18 hub genes

database [15]. Quality control was made to ensure our analysis accuracy. 46 glomeruli samples (32 disease samples and 14 control samples) and 47 tubulointerstitium samples (32 disease samples and 15 control samples) were obtained in the GSE32591 dataset. 21 kidney samples (14 disease samples and 7 control samples) were obtained in the GSE112943 dataset. We removed and/or averaged the probe sets which did not match the gene symbols or genes with multiple probe sets. Probes were transformed into the corresponding gene symbols under platform annotation information.

Differentially expressed genes between the LN and control groups in the GSE32591 and GSE112943 datasets were identified using the Limma R package [16]. Adjusted "-

$P < 0.05$ and Log (fold change) > 1 or Log (Fold Change) $< −$ 1" were defined as the thresholds for screening of the differential expression of mRNAs. The results of the two datasets are able to be combined into a more accurate target.

2.2. PPI Network and Identification of Hub Genes. The protein–protein interaction (PPI) network is an important means to identify protein functions and to understand system biology [17]. Search Tool for the Retrieval of Interacting Genes (STRING) (https://string-db.org/) was utilized to generate the PPI network of the common genes [18]. Analysis of functional interactions between proteins was performed to discover the mechanism of the occurrence and development

of LN. Cytoscape (3.8.1) was developed for the visualization of molecular interaction networks [19] and better visualization of PPI network and identification of hub genes. Furthermore, we used the plug-in MCODE to perform PPIs network of hub genes and our selection criteria were as follows: MCODE scores > 5, node score cut-off = 0.2, degree cut-off = 2, k-score = 2, and max depth = 100.

2.3. Gene Ontology and Kyoto Encyclopedia of Genes and Genomes Analysis. Visualization and Integrated Discovery (DAVID, http://david.ncifcrf.gov) [20] was employed to conduct Gene Ontology (GO), Kyoto Encyclopedia of Genes and Genomes (KEGG) pathway analysis to gain further insights into the biological pathways of the hub genes.

2.4. TF-miRNA Coregulatory Network. TF-miRNA coregulatory network analysis was performed to discover the potential expression mechanism of hub genes. Transcription factors (TFs) could act as both activators and repressors of gene expression at the transcriptional level, while miRNAs usually downregulated the expression of genes at the post-transcriptional level. TFs and miRNAs could regulate each other and coregulate a common target gene to form a forward loop (FFL) [21]. FFLs participated in many important cellular processes by regulating the expression of genes [22].

We used NetworkAnalyst (https://www.networkanalyst .ca/), a visual analytics platform for comprehensive gene expression profiling and meta-analysis [23], to identify TF-

(a)

(b)

(c)
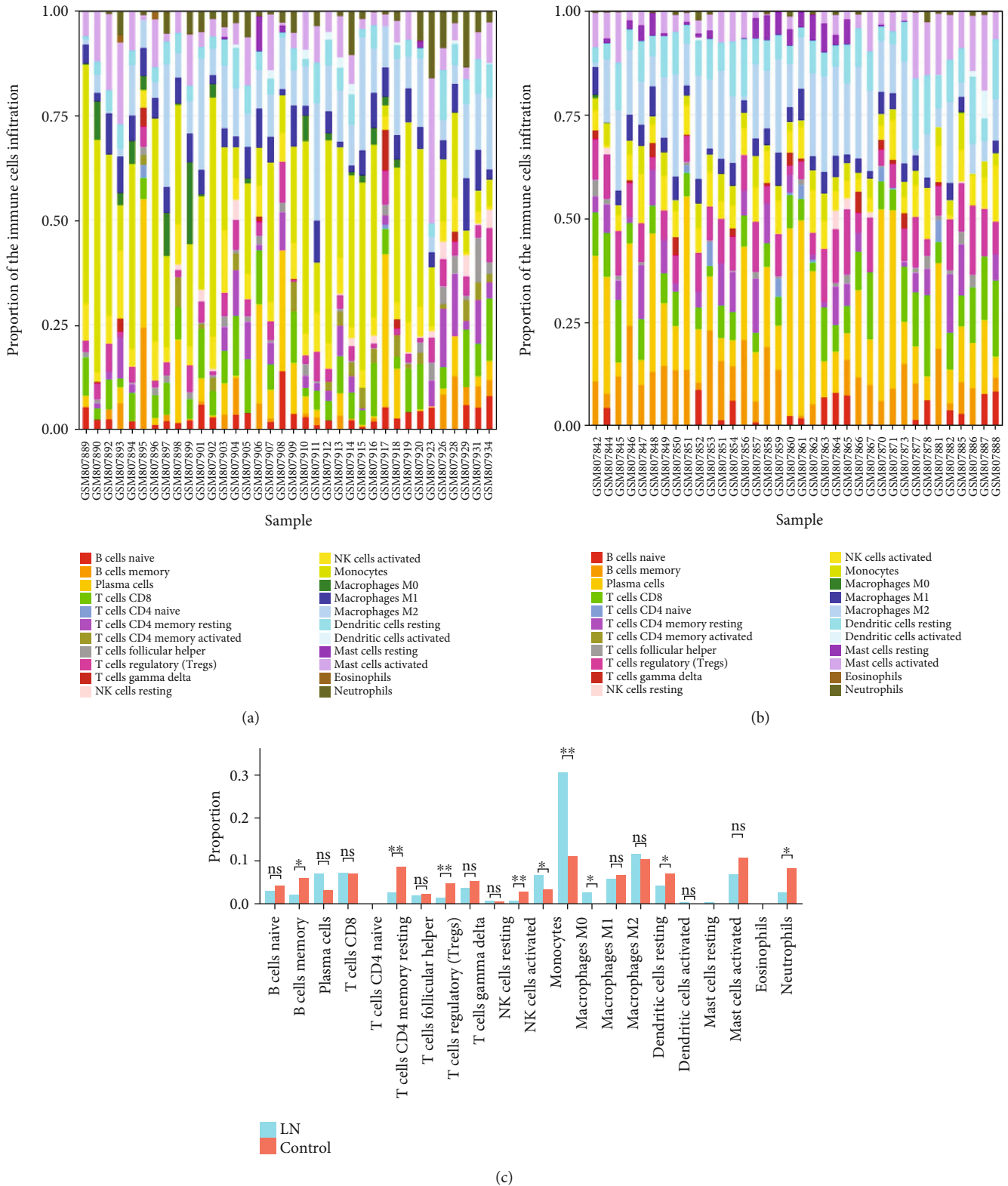
Figure 4: Continued.
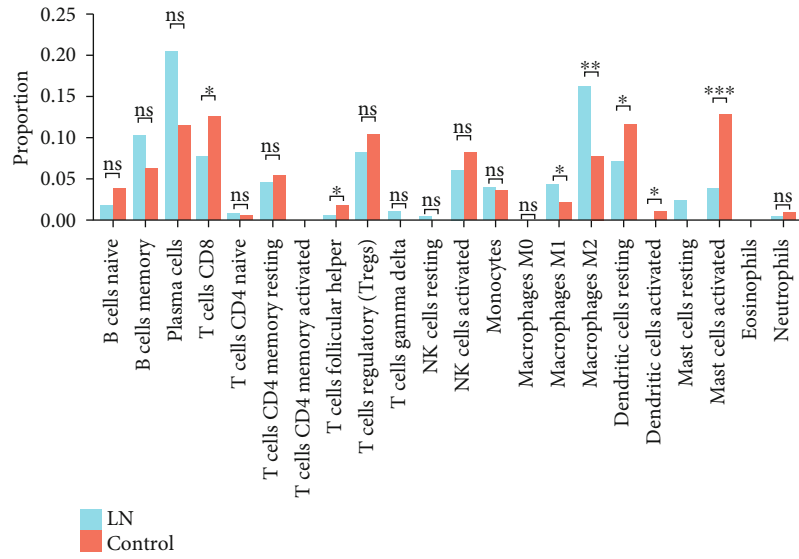
(d)

FIGURE 4: The landscape of immune infiltration in LN. (a) Bar charts of 22 immune cell proportions in LN and normal glomeruli tissues. (b) Bar charts of 22 immune cell proportions in LN and normal tubulointerstitium tissues. (c) Differential expression of different types of immune cells between LN and normal glomeruli tissues. (d) Differential expression of different types of immune cells between LN and normal tubulointerstitium tissues.

(a)

(b)
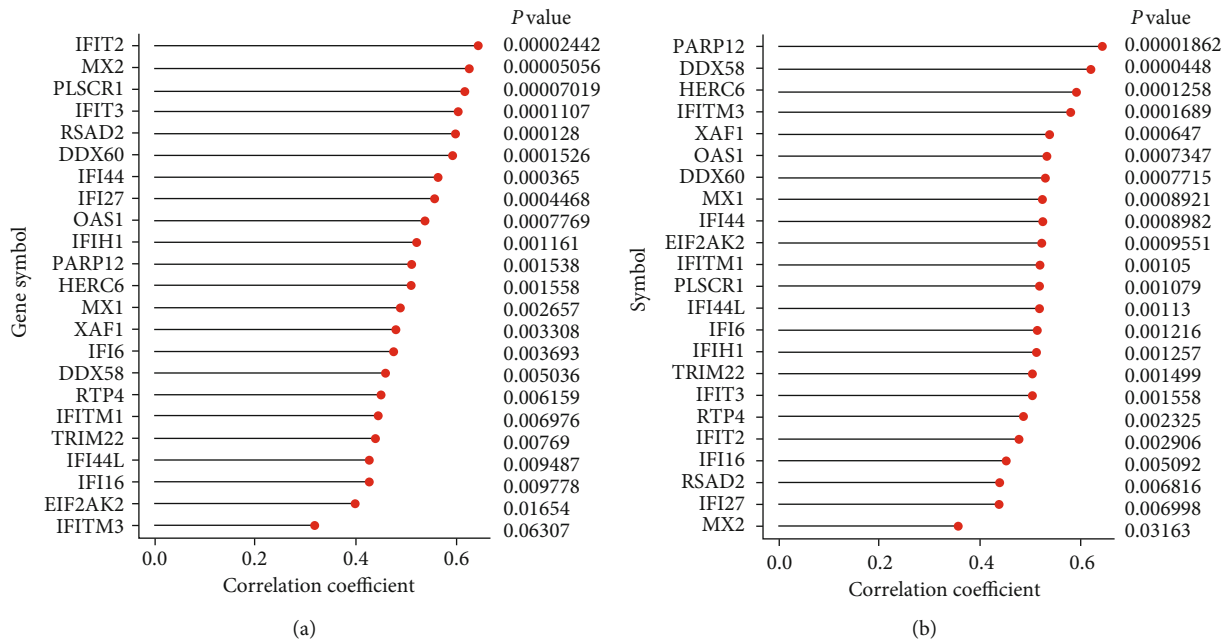
FIGURE 5: Correlation analysis between hub genes and infiltrating immune cells in glomeruli tissues (a) and tubulointerstitium tissues (b) of GSE32591.

miRNA coregulatory interactions with identified hub genes. Interactions for TF-miRNA coregulation were collected from the RegNetwork repository, which is an integrated database of transcriptional and posttranscriptional regulatory networks in humans and mice [24]. Afterwards, TF-miRNA coregulatory network was visualized using Cytoscape.

2.5. Correlation Analysis between Hub Genes and Infiltrating Immune Cells. To further explore the correlation between hub genes and inflammation of the kidneys in LN patients, we uploaded the gene expression matrix data of GSE32591 to CIBERSORT. Immune cell infiltration analysis was performed on 46 glomeruli and 47 tubulointerstitium samples from the GSE32591 dataset and selected only samples with
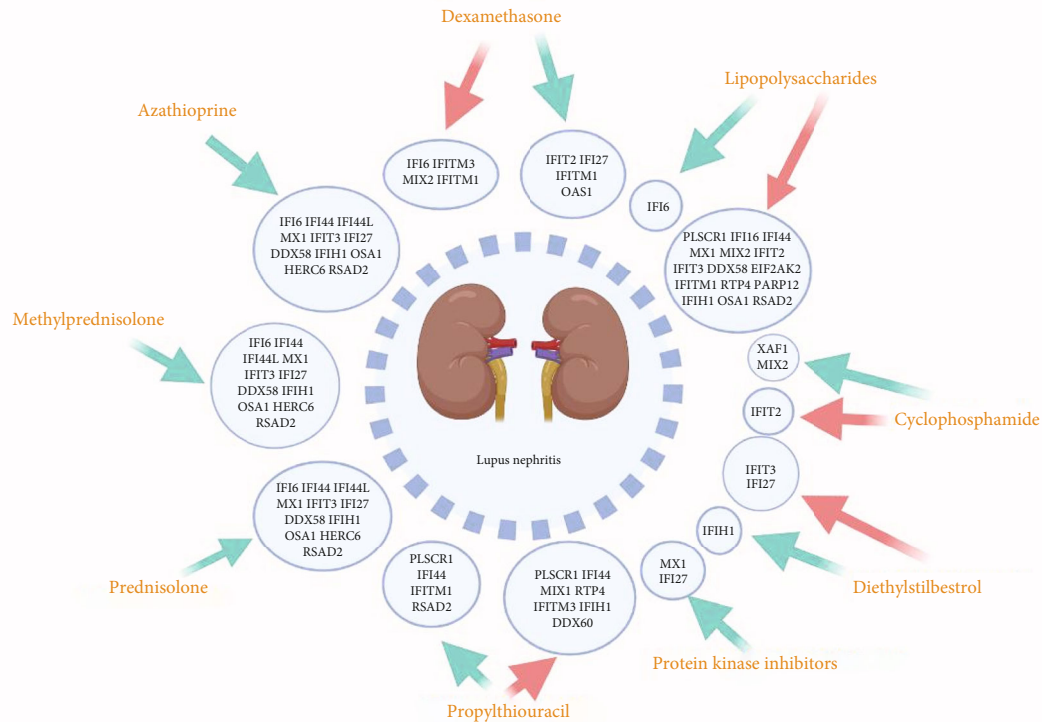
FIGURE 6: Chemical-gene-disease interactions. Nine common chemicals were identified through the CTD database that could affect LN by regulating the expression of 23 hub genes. The red arrows represent upregulated gene expression while the green arrows represent downregulated gene expression.

$P < 0.05$. R package "ggplot2" was used to draw the bar charts of 22 types of infiltrating immune cells and to visualize the differences in immune cell infiltration. Moreover, Spearman's correlation analysis on hub genes and infiltrating immune cells were performed using the OECloud tools at https://cloud.oebiotech.cn, and dot-chart was used to visualize the results.

2.6. Chemical-Gene-Disease Interactions. Understanding chemical-gene interactions could provide insight into the mechanisms of disease susceptibility of chemical actions and therapeutic drug interactions [25]. We obtained the interaction data between common chemicals, 23 hub genes, and LN from the Comparative Toxicogenomics Database (CTD, http://ctd.mdibl.org). CTD is a curated database that offers chemical-gene interactions, chemical-disease relationships, and gene-disease relationships from the literature for studying the effects of environmental chemicals on human health [26]. It is worth mentioning that chemicals in the CTD database include large and small molecules, as well as drugs and harmful substances. The figure was created with BioRender (https://biorender.com) [27] to help us visually understand and evaluate which common compounds may affect LN through identified hub genes. In addition, we used Cytoscape to create the network of small molecules and genes and calculate the degree of each gene and obtained the functions of 23 core genes from STRING.

2.7. Identification of Potential Small Molecules for LN. Identifying potential small molecules for LN is the ultimate target of our hub-gene screening. Drug Signatures database (DSigDB) which contains 22527 gene sets [28] was used to generate the small molecules which could downregulate the expression of hub genes. The access to the DSigDB database is acquired through Enrichr (https://amp.pharm.mssm.edu/Enrichr/) platform, an interactive and collaborative HTML5 gene list enrichment analysis tool [29].

Furthermore, DREIMT (http://www.dreimt.org.) is a bioinformatics tool for hypothesis generation and prioritization of drugs capable of modulating immune cell activity from transcriptomics data [30]. We used it to understand the immunological mechanisms by which the small molecules we predicted can affect LN patients. Meanwhile, we collected the immune signatures of seven drugs that have been shown to be effective in LN. Immune signatures can be widely used to better identify which small molecules are more reliable. BioRender was used to create the figure of immune signatures of potential small molecules.

3. Results

3.1. Identification of DEGs. Since three types of kidney tissues (Supplementary Table 1&2) are included in GSE32591 (glomeruli and tubulointerstitium) and GSE112943 (formalin-fixed paraffin-embedded kidney), we performed the DEGs of the three types of samples, respectively; 351 DEGs were identified in the glomeruli samples of GSE32591, with 250 upregulated genes and 101 downregulated genes (Figure 1(a)). Similarly, 129 DEGs were identified in the tubulointerstitial samples of
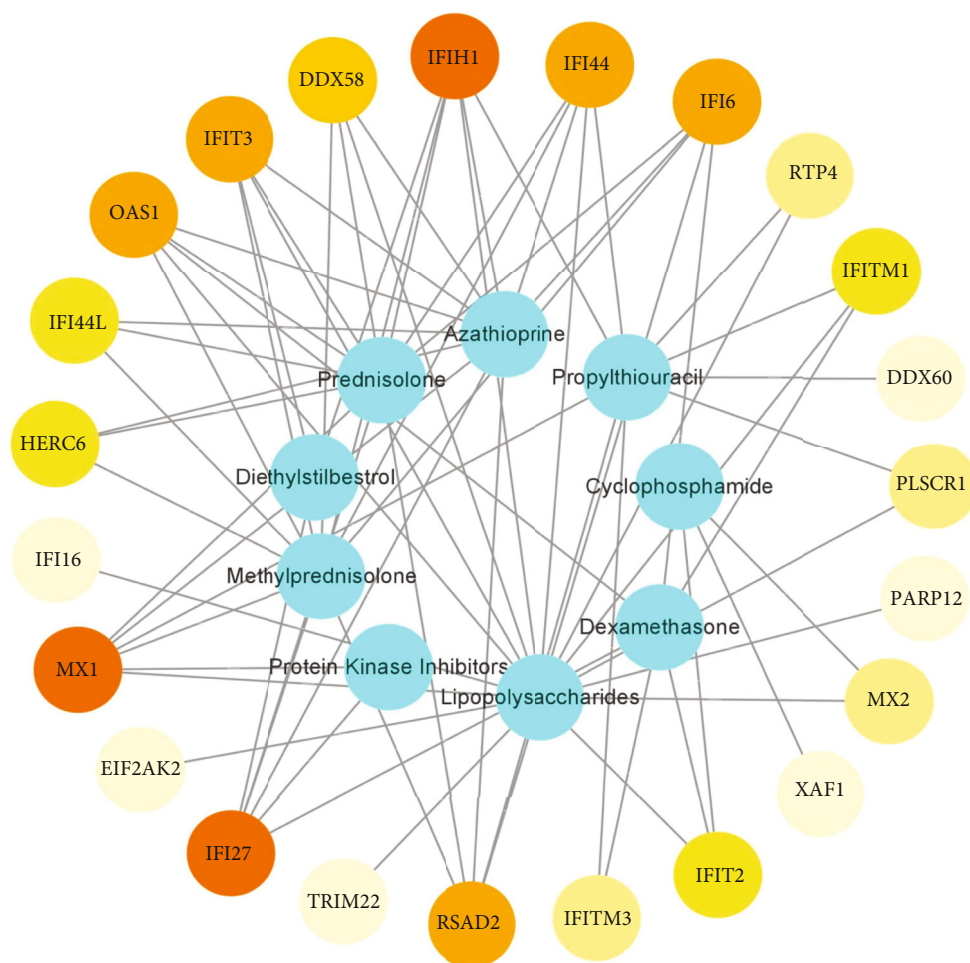
FIGURE 7: The network between chemicals and genes. Blue for chemicals; red for genes; the color depth of genes represents the level of degree.

TABLE 1: Suggested top 10 small molecules for the Lupus nephritis.

Small molecules	Odds ratio	P value	Category
Acetohexamide	2595.71	$9.91E-35$	K-ATP inhibitors [31]
Suloctidil	1737.4875	$3.40E-44$	Calcium channel blockers [32]
Prenylamine	1626.684783	$3.01E-37$	Calcium channel blockers [33]
Terfenadine	673.9951691	$7.41E-31$	H1 receptor blockers [34]
Chlorophyllin	293.4264706	$6.63E-13$	Antioxidant [35]
Prochlorperazine	261.4460641	$5.99E-18$	Dopamine receptor antagonists [36]
Propofol	231.084058	$7.80E-16$	GABA receptor enhancer [37]
Benfluorex	230.9375	$1.47E-10$	RNA polymerase II activator [38]
Mefloquine	168.0168421	$3.10E-08$	Antimalarial [39]
Triprolidine	157.5631579	$2.02E-06$	H1 receptor blockers [40]

GSE32591 (Figure 1(b)) of which 104 were upregulated and 25 were downregulated genes. Furthermore, a total of 7759 DEGs consisting of 6143 upregulated and 1616 downregulated genes were identified as significantly different in expression between the disease and control samples of GSE112943 (Figure 1(c)). Additionally, a total of 48 DEGs which comprises 45 common upregulated genes and 3 common downregulated genes were identified from the three types of samples (Figure 1(d)).

3.2. PPI Network and Identification of Hub Genes. The PPI network of common DEGs and most densely connected
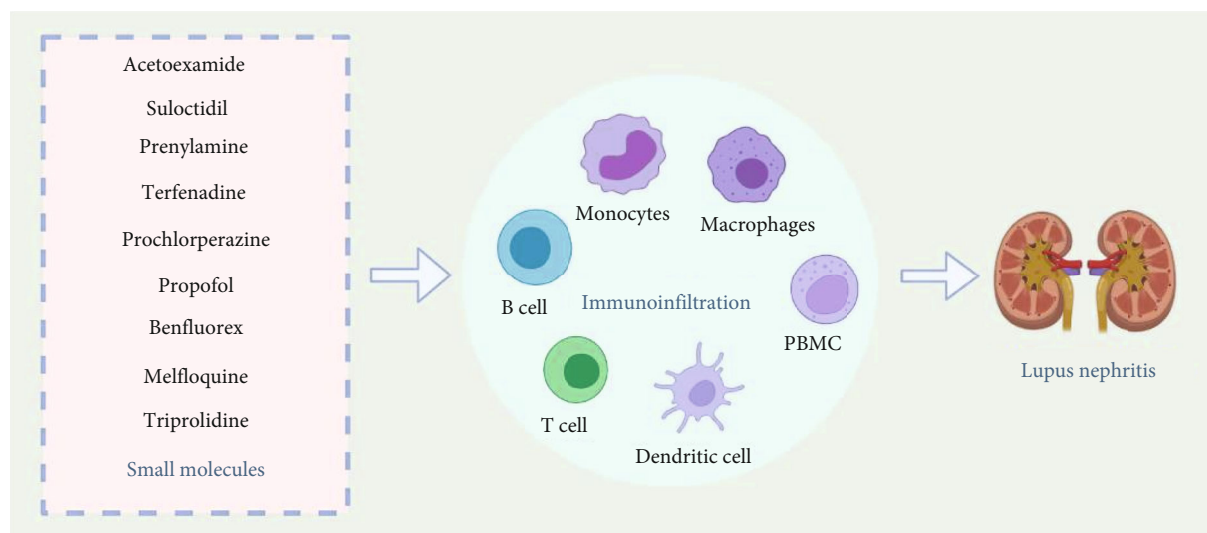
FIGURE 8: Immune signatures of potential small molecules. Nine small molecules may impact LN by altering immune cell infiltration including monocytes, macrophages, B cells, T cells, dendritic cells, and PBMC.

TABLE 2: Immune signatures of 9 potential small molecules and 7 common effective drugs.

	Small molecules	Inhibited cells
Potential small molecules	Acetohexamide	Bn, DC, macrophage, monocyte, PBMC, Pre-B2 cell, Th, Tn
	Suloctidil	Bm, Bn, DC, PBMC, Th1, Tm, Tn, Treg
	Prenylamine	DC, macrophage, CTL, PBMC, Th1, Tm, Treg
	Terfenadine	Bn, DC, Th1, Th2, Tm, Treg
	Prochlorperazine	B1 cell, Bm, Bn, DC, macrophage, PBMC, Th1, Th2, Tm, Treg
	Propofol	Bn, DC, monocyte, PBMC, Tm
	Benfluorex	Macrophage, PBMC, Tn, Tm
	Mefloquine	Bm, Bn, DC, PBMC, Th1, Treg
	Triprolidine	B1 cell, Bn, DC, macrophage, PBMC, Pre-B1 cell, CTL, Th1, Th17, Tm, Treg
Common Drugs	Methylprednisolone	B cell, Pre-B2 cell, DC, macrophage, monocyte, neutrophil, NK cell, Tm, Tn, Treg
	Cyclophosphamide	Bm, DC, macrophage, monocyte, NK cell, PBMC, Th1, Th17, Tm, Tn
	Mycophenolate-mofetil	B cell, DC, neutrophil, NK cell, PBMC, Treg, Th1, Th2, Tm
	Azathioprine	B cell, DC, macrophage, monocyte, neutrophil, PBMC, Th1, Th2, Tm, Treg
	Hydroxychloroquine	Plasma cell, CD21B cell, Bms, Bn, macrophage, monocyte, neutrophil, NK cell, PBMC, CTL, Th, Tm, Tn
	Tacrolimus	Bm, Pre-B1 cell, Pre-B2 cell, DC, macrophage, monocyte, PBMC, CTL, Th1, Th2, Tm, Treg
	Cyclosporin-a	Bm, B1 cell, Pre-B2cell, DC, macrophage, monocyte, neutrophil, PBMC, CTL, Th1, Th2

Bn: naive B cell; Bm: memory B cell; Pre-B cell: precursor B cell; Tn: naive T cell: Th: helper T cell; Tm: memory T cell; Treg: regulatory T cell; CTL: cytotoxic T lymphocyte; DC: dendritic cell; PBMC: peripheral blood mononuclear cell; NK cell: natural killer cell.

regions (43 nodes, 296 edges) were obtained from Cytoscape (Figure 2(a)). 23 genes (IFI6, PLSCR1, XAF1, IFI16, IFI44, MX1, IFI44L, IFIT3, IFIT2, IFI27, DDX58, EIF2AK2, IFITM1, RTP4, IFITM3, TRIM22, PARP12, IFIH1, OAS1, HERC6, RSAD2, DDX60, and MX2) were identified as hub genes using the plug-in MCODE in Cytoscape (Figure 2(b)). Since the products of genes were at the core of the PPI network, these hub genes were considered potential therapeutic targets.

3.3. Gene Ontology and Kyoto Encyclopedia of Genes and Genomes Analysis. To analyze the biological classification of DEGs, we performed a functional enrichment analysis of 23 hub genes. Functional enrichment analysis identified 101 GO terms in the biological process (BP) category and 33 GO terms in the cellular component (CC) category. Regarding BP, the hub genes were involved in viral defense response, type I interferon(IFN) signaling pathway, interferon-α (IFN-⊠) response and positive regulation of tumor

necrosis factor (TNF) secretion, and IFN-α production. In terms of MF, the DEGs were mainly associated with double-stranded RNA binding, single-stranded RNA binding, double-stranded DNA binding, and helicase activity. The cellular components of the DEGs were cytoplasm, mitochondrial membrane, cytosol, mitochondria, and mitochondrial outer membrane. The top 30 of GO enrichment were shown in Figure 2(c). Moreover, 16 KEGG pathway analysis indicates hub genes were mainly enriched in viral infections (Figure 2(d)).

3.4. TF-miRNA Coregulatory Network. A TF-miRNA coregulatory network was generated using NetworkAnalyst, and better visualization was seen through Cytoscape. The analysis of the TF-miRNA coregulatory network showed miRNA-TF interaction with the hub genes. The network created for TF-miRNA coregulatory network was performed in Figure 3, which contains 113 nodes and 127 edges. 45 miRNAs and 50 TF-genes have interacted with 18 hub genes. This network could provide us with reasonable regulatory mechanisms for the expression of the DEGs.

3.5. Correlation Analysis between Hub Genes and Infiltrating Immune Cells. Thirty-six glomeruli samples (30 disease samples and 6 control samples) and 36 tubulointerstitium samples (28 disease samples and 8 control samples) were maintained with P value < 0. 05. Figures 4(a) and 4(b) show the proportions of 22 immune cells in 36 glomeruli tissues and 36 tubulointerstitium tissues. Monocyte infiltration was predominant in the glomeruli (Figure 4(c)) with a statistically significant difference ($P = 0.0065$). Although the most infiltrated cell in tubulointerstitium was plasma cells, there was no statistically significant difference. Moreover, there was an abundant infiltration of M2 macrophages cells in the tubulointerstitium ($P = 0.0042$) (Figure 4(d)). Correlation analysis demonstrated a positive correlation between 23 hub genes and monocyte infiltration in the glomeruli and M2 macrophage infiltration in the tubulointerstitium (Figures 5(a) and 5(b)). The gene expression of LN was converted to infiltrating immune cells through CIBERSORT and after verification; the expression of 23 hub genes screened was positively correlated with the proportion of the most typical infiltrated immune cells in the glomeruli and tubulointerstitium of LN. This indicates that the 23 hub genes not only are representatives of the characteristic genetic effect but also signify the immune characteristics of LN.

3.6. Chemical-Gene-Disease Interactions. Nine chemicals that affect LN by regulating the expression of 23 hub genes were identified through the CTD database (Supplementary Table 3), and their interactions are shown in Figure 6. Azathioprine, Lipopolysaccharides, Dexamethasone, Methylprednisolone, Cyclophosphamide, Prednisolone, Propylthiouracil, Diethylstilbestrol, and Protein Kinase Inhibitors were associated with LN by affecting the expression of hub genes. Among them, Azathioprine, Dexamethasone, Methylprednisolone, Cyclophosphamide, and Prednisolone could relieve LN by downregulating hub gene expression. It is noteworthy that the effects of

Propylthiouracil on hub gene expression might be as complex as their duality. The data recorded in this database are mainly derived from experiments, and many of them consist of classical and common chemicals; many of the potential relationships are still being explored. Therefore, some chemicals closely related to LN may be unavailable, but we should not ignore their influence on the expression of hub genes. In addition, the network between chemicals and genes is shown in Figure 7. The color depth of genes represents the level of degree and their degree and function are available in Supplementary Table 4.

3.7. Identification of Potential Small Molecules. Enrichr platform is used to identify potential molecules for 23 hub DEGs. The small molecules which could downregulate the expression of hub genes were collected from the DSigDB database (Supplementary Table 5). The results from the potential small molecules were generated based on the odds ratio, which is automatically generated by the DSigDB database and represents the closeness between the small molecules and genes. Table 1 points out the top 10 potential small molecules from the DSigDB database for hub genes.

The DREIMT database provided an abundance of data between the relationship of potential small molecules and various immune cells (Supplementary Table 6). Nine of ten potential small molecules and 7 common effective drugs were found in the DREIMT database, and they mainly affect monocytes, macrophages, T cells, B cells, dendritic cells, and PBMC, which may be involved in the potential mechanism for the treatment of LN (Figure 8). The inhibition of immune cells by 9 potential and 7 common effective drugs is shown in Table 2.

4. Discussion

Approximately 70% of SLE patients have clinical manifestations of renal damage while 100% were found to have renal involvement when immunofluorescence and electron microscopy were performed on renal biopsy [41]. LN represents the most common complication of SLE, and renal involvement is significant in the prognosis of LN patients [42]. Accordingly, effective prevention and treatment of LN are of great importance and urgency.

23 common differential genes in tissue samples were identified in both datasets, making our results significant. The pathways of GO enrichment mainly involve the IFN signaling pathway, IFN-α cellular response, innate immune response, and positive regulation of TNF and IFN-α production. IFN is a primary pathogenic factor of LN [43] while TNF is a major player in the development of LN by inducing renal IgG deposition [44]. In addition, KEGG enrichment analysis showed that hub genes are enriched in viral infections such as influenza A, Epstein-Barr virus, and hepatitis B. These results suggest that the immune response to LN is similar to the human response towards viral infections. The results of the enrichment analysis demonstrated that drug prediction using 23 hub genes is reliable.

There are 50 TF-genes and 45 miRNAs in the TF-miRNA coregulatory network. Among the most interacted TFs, USF1, MAX, HNF4A, and CTCF have 4 edges. USF1 is associated with macrophage inflammation [45], and HNF4A is a major regulator of the renal proximal tubule [46]. Additionally, hsa-mir-34b, with 3 edges, is the most frequently reported epigenetically abnormal miRNAs in SLE [47]. Furthermore, researches have shown that FFL could affect the development of certain diseases, including cancer [48], by altering biological processes such as cell differentiation and cytokine production [49]. FFLs may affect the activity of IFN-related pathways in SLE through altered the expression of hub genes, which revealed the possibility of FFLs as novel biomarkers and therapeutic targets in LN.

The immune infiltration results suggest that the glomeruli of LN patients are dominated by monocyte infiltration in addition to a large amount of macrophage M2 cell infiltration in the tubulointerstitium, which was positively correlated with the expression of 23 hub genes. Monocytes are major players in both innate and adaptive immunities [50]. Their role in the inflammatory response is closely associated with glomerulopathy of LN [51] while macrophage M2 cells could promote kidney fibrosis [52]. It is worth noting that infections may increase monocytes [53] and that the widespread use of immunosuppression and steroid therapy in LN makes patients more susceptible to infections [11]. In addition, recent discoveries have demonstrated the importance of tubulointerstitial inflammation in LN. Both M1 and M2 macrophages are involved in the inflammation of tubulointerstitium. M1 macrophages are increased in LN compared to controls, and their histotoxicity leads to tubulointerstitial damage. Also, podocytes, mesangial cells, tubular epithelial cells, kidney resident macrophages, and stromal cells cause the produce cytokines and chemokines together which lead to their injury and damage of the kidney.

It is worth mentioning that the 23 hub genes obtained from three types of kidney tissue samples represent not only the genetic effect but also the emblematic immune signature of LN. The above results demonstrate they may be biomarkers and novel drug targets for the diagnosis and treatment of LN.

The result of chemical-gene-disease interactions demonstrated that nine chemicals could affect LN by regulating the expression of hub genes. Azathioprine, Cyclophosphamide, Dexamethasone, Methylprednisolone, and Prednisolone downregulate hub gene expression to treat LN. They are widely used in clinical therapy for LN and are proven safe and efficacious [54]. Moreover, Protein Kinase Inhibitors downregulate the expression of several hub genes, which could play an important anti-inflammatory role in autoimmune diseases [55].

In addition, natural diethylstilbestrol is a key player that not only affects the reproductive system but also markedly influences the immune system [56]. Estrogen is implicated in the pathogenic pathways in LN [57], and diethylstilbestrol may cause or worsen LN through the upregulation of hub genes, necessitating attention to the adverse effects of diethylstilbestrol. There has also been a report of LN occurring after treatment with Propylthiouracil suggesting that attention should be paid to Propylthiouracil in the clinical treatment of LN patients with hyperthyroidism.

Microbial studies have shown that many autoimmune diseases are infectious and lipopolysaccharides play a key role in host-pathogen interactions with the natural immune system [58]. Altered immune function induced by lipopolysaccharide could lead to enhanced immune responses in the kidney leading to renal insufficiency [59]. Lipopolysaccharide-gene-LN interactions may provide new mechanisms for the prevention and treatment of LN. Many chemicals are closely associated with LN, such as tacrolimus and hydroxychloroquine [60], and a few have been documented in the CTD database. It is important to note and explore their influence on the expression of hub genes in LN.

The mechanism of chemicals in the occurrence and development of diseases has long been a mystery, but genes may be a bridge between them. The function of 23 hub genes is closely related to the synthesis, secretion, and biological function of IFN. The presence of IFN-α in the serum of SLE patients can induce differentiation of normal monocytes into dendritic cells (DCS). This can capture apoptotic cells and nucleosomes and perform antigen presentation ultimately leading to the destruction of immune tolerance in LN. The occurrence of autoimmunity and a feedback loop of interaction centered around antigen-presenting cell-IFN-nuclear antigen plays an important link in the pathogenesis of SLE [43]. Chemicals may affect this pathway by regulating the expression of hub genes and ultimately contribute to LN. Azathioprine, Cyclophosphamide, Dexamethasone, Methylprednisolone, and Prednisolone are expected to downregulate the expression of hub genes to improve the abnormal immune state mediated by IFN. Other chemicals such as LPS may adversely affect LN by upregulating the expression of hub genes. Genes may be the language of conversation between chemicals and disease, and we should use them to predict potentially therapeutic small molecules for LN.

Small molecules which could downregulate the expression of 23 hub genes were found from the DSigDB database. Among all candidate small molecules, the current study highlights the top 10 key players: Acetohexamide, Suloctidil, Prenylamine, Terfenadine, Chlorophyllin, Prochlorperazine, Propofol, Benfluorex, Mefloquine, and Triprolidine.

Abnormal activation of immune cells is the most important feature of LN. Continuous activation of antigen-presenting cells (APC), imbalances of regulatory and effector CD4+T cells, and high proliferation and activity of B cells which secrete a lot of antibodies combined with autoantigen ultimately lead to autoimmunity of LN [61]. The immune signature of seven drugs commonly used to treat LN is due to their inhibition of B cell activation as well as helper T cells (Ths), regulatory T cells (Tregs), memory T cells (Tms), and APCs. Among them, hydroxychloroquine has inhibitory effects on plasma cells, memory B cells (Bms), naive B cells (Bns), NK cells, cytotoxic T cells (CTLs), Ths, Tms, naive T cells (Tns), APCs, and PBMCs, which may contribute to its central role in treating LN. A series of interactions between immune cells culminates in an increase in antibody secretion by B cells. Therefore, B cells play an indispensable role in LN, corresponding to the inhibition of B cells by common drugs. The nine small molecules we identified also show inhibitory effects on the relevant immune cells. Nevertheless, Prenylamine and Benfluorex are

less effective due to their inability to inhibit B cell activity. Triprolidine displays an immune signature similar to that of HCQ which can inhibit T cell proliferation [62] demonstrating essential roles in the pathogenesis of LN. Other small molecules also show inhibition of relevant immune cells which signifies potential evidence for treating LN.

SLE is a systemic disease and the involvement of the nervous and circulatory systems may also change when LN occurs. Meanwhile, the occurrence of LN is accompanied by changes in blood glucose, lipids, and other physiological indicators [63]. Nevertheless, the current drugs for LN are mainly immunosuppressants, which can achieve straightforward effects, but can also cause many complications such as bone myelosuppression and liver damage. Therefore, there is a need to identify small molecules which may improve other symptoms of LN with fewer adverse effects. Acetohexamide could be effective in treating LN patients with diabetes on account of its hypoglycemic effects [31, 38]. Additionally, suloctidil may play a significant role in improving circulation and blood vessel function to benefit LN. Moreover, Propofol and Prochlorperazine may demonstrate unique effects in patients with Neurolupus, but Propofol is unlikely to be used, for it is a type of anesthetic. Also, the superior antioxidant and anti-mutational effects of chlorophyllin [35] may protect against kidney damage in LN. It is worth mentioning that mefloquine may have great therapeutic potential for LN as its analogue hydroxychloroquine plays an important role in the treatment of LN.

In conclusion, six small molecules (Acetohexamide, Suloctidil, Terfenadine, Prochlorperazine, Mefloquine, and Triprolidine) were considered meaningful to be validated in future trials as our current results have shown their rich potential in treating LN.

The GEO database provides little clinical information on the types of pathogenesis and disease activity of LN which is a limitation of our study. Further detailed information could make our conclusions more precise.

5. Conclusions

We identified six small molecules (Acetohexamide, Suloctidil, Terfenadine, Prochlorperazine, Mefloquine, and Triprolidine) that might have potential therapeutic effects for LN through the exploration of hub genes and immune characteristics of LN. The six small molecules can affect the immune signatures of LN by downregulating hub genes because 23 hub genes (IFI6, PLSCR1, XAF1, IFI16, IFI44, MX1, IFI44L, IFIT3, IFIT2, IFI27, DDX58, EIF2AK2, IFITM1, RTP4, IFITM3, TRIM22, PARP12, IFIH1, OAS1, HERC6, RSAD2, DDX60, and MX2) could emerge as the biomarkers and novel drug targets for the diagnosis and treatment of LN.

Data Availability

The raw data supporting the conclusions of this article will be made available in GEO database. All data generated or analyzed during this study are included in this article and its supplementary information files.

Conflicts of Interest

The authors declare that they have no conflicts of interest.

Authors' Contributions

Jianbo Qing collected and processed the data and drafted the paper. Yafeng Li and Lingling Tian gave constructive suggestions for the manuscript. Wenzhu Song and Sonia Biju Samuel helped polish the manuscript. All authors approved the final version.

Acknowledgments

Supplementary Materials

Supplementary Materials Supplementary Table1: the expression data of GSE32591, which contains 32 glomeruli and tubulointerstitum tissues of LN patients and 14 glomeruli tissues and 15 tubulointerstitum tissues of healthy controls. Supplementary Table2: the expression data of GSE112943 consists of formalin fixed paraffin-embedded kidneys (14 lupus nephritis and 7 control kidney). Supplementary Table3: the data of the relationships between Nine chemicals, 23 hub genes and lupus nephritis. Supplementary Table4: the degree of 23 hub genes in the network between small molecules and genes and the description and function of 23 hub genes. Supplementary Table5: all the data of small molecules based on the 23 hub genes from the DSigDB database. Supplementary Table6: the relationship of nine potential small molecules and 7 common effective drugs for LN were found in the DREIMT database. (*Supplementary Materials*)

References

[1] T. Dörner and R. Furie, "Novel paradigms in systemic lupus erythematosus," *Lancet*, vol. 393, no. 10188, pp. 2344–2358, 2019.

[2] M. Teruel and M. E. Alarcón-Riquelme, "The genetic basis of systemic lupus erythematosus: What are the risk factors and what have we learned," *Journal of autoimmunity*, vol. 74, pp. 161–175, 2016.

[3] R. Illescas-Montes, C. C. Corona-Castro, L. Melguizo-Rodríguez, C. Ruiz, and V. J. Costela-Ruiz, "Infectious processes and systemic lupus erythematosus," *Immunology*, vol. 158, no. 3, pp. 153–160, 2019.

[4] G. Houen and N. Trier, "Epstein-Barr virus and systemic autoimmune diseases," *Frontiers in immunology*, vol. 11, p. 587380, 2021.

[5] S. A. de Zubiria and C. Herrera-Diaz, "Lupus nephritis: an overview of recent findings," *Autoimmune diseases*, vol. 2012, Article ID 849684, 21 pages, 2012.

[6] A. Arazi, D. Rao, C. Berthier et al., "The immune cell landscape in kidneys of patients with lupus nephritis," *Nature Immunology*, vol. 20, no. 7, pp. 902–914, 2019.

[7] F. Yu, M. Haas, R. Glassock, and M. Zhao, "Redefining lupus nephritis: clinical implications of pathophysiologic subtypes," *Nature reviews Nephrology*, vol. 13, no. 8, pp. 483–495, 2017.

[8] A. Hoi and E. Morand, "Treatment update in systemic lupus erythematous," *Rheumatic diseases clinics of North America*, vol. 47, no. 3, pp. 513–530, 2021.

[9] M. Gasparotto, M. Gatto, V. Binda, A. Doria, and G. Moroni, "Lupus nephritis: clinical presentations and outcomes in the 21st century," *Rheumatology (Oxford, England)*, vol. 59, Supplement_5, pp. v39–v51, 2020.

[10] W. Li, W. Chen, and L. Sun, "An update for mesenchymal stem cell therapy in lupus nephritis," *Kidney diseases (Basel, Switzerland)*, vol. 7, no. 2, pp. 79–89, 2021.

[11] E. Morales, M. Galindo, H. Trujillo, and M. Praga, "Update on lupus nephritis: looking for a new vision," *Nephron*, vol. 145, no. 1, pp. 1–13, 2021.

[12] R. Dias, U. Hasparyk, M. Peres, J. de Barros, E. Simões, and A. Silva, "Novel biomarkers for lupus nephritis in the "OMICS" era," *Current medicinal chemistry*, vol. 28, no. 29, pp. 6011–6044, 2021.

[13] C. C. Berthier, R. Bethunaickan, T. Gonzalez-Rivera et al., "Cross-species transcriptional network analysis defines shared inflammatory responses in murine and human lupus nephritis," *Journal of immunology*, vol. 189, no. 2, pp. 988–1001, 2012.

[14] W. Ko, L. Li, T. Young et al., "Gene expression profiling in the skin reveals strong similarities between subacute and chronic cutaneous lupus that are distinct from lupus nephritis," *The Journal of investigative dermatology*, vol. 141, no. 12, pp. 2808–2819, 2021.

[15] E. Clough and T. Barrett, "The Gene Expression Omnibus Database," *Methods in molecular biology*, vol. 1418, pp. 93–110, 2016.

[16] M. E. Ritchie, B. Phipson, D. I. Wu et al., "limma powers differential expression analyses for RNA-sequencing and microarray studies," *Nucleic acids research*, vol. 43, no. 7, p. e47, 2015.

[17] R. M. Ewing, P. Chu, F. Elisma et al., "Large-scale mapping of human protein–protein interactions by mass spectrometry," *Molecular systems biology.*, vol. 3, no. 1, p. 89, 2007.

[18] D. Szklarczyk, A. Franceschini, S. Wyder et al., "STRING v10: protein-protein interaction networks, integrated over the tree of life," *Nucleic acids research*, vol. 43, no. D1, pp. D447–D452, 2015.

[19] B. Demchak, T. Hull, M. Reich et al., "Cytoscape: the network visualization tool for GenomeSpace workflows," *F1000Research*, vol. 3, p. 151, 2014.

[20] D. W. Huang, B. Sherman, and R. Lempicki, "Systematic and integrative analysis of large gene lists using DAVID bioinformatics resources," *Nature protocols*, vol. 4, no. 1, pp. 44–57, 2009.

[21] G. Qin, S. Mallik, R. Mitra et al., "MicroRNA and transcription factor co-regulatory networks and subtype classification of seminoma and non-seminoma in testicular germ cell tumors," *Scientific Reports*, vol. 10, no. 1, p. 852, 2020.

[22] O. Hobert, "Gene regulation by transcription factors and microRNAs," *Science*, vol. 319, no. 5871, pp. 1785-1786, 2008.

[23] G. Zhou, O. Soufan, J. Ewald, R. Hancock, N. Basu, and J. Xia, "NetworkAnalyst 3.0: a visual analytics platform for comprehensive gene expression profiling and meta-analysis," *Nucleic acids research*, vol. 47, no. W1, pp. W234–W241, 2019.

[24] Z. Liu, C. Wu, H. Miao, and H. Wu, "RegNetwork: an integrated database of transcriptional and post-transcriptional regulatory networks in human and mouse," *Database : the journal of biological databases and curation*, vol. 2015, 2015.

[25] A. P. Davis, C. G. Murphy, M. C. Rosenstein, T. C. Wiegers, and C. J. Mattingly, "The comparative Toxicogenomics database facilitates identification and understanding of chemical-gene-disease associations: arsenic as a case study," *BMC Medical Genomics*, vol. 1, no. 1, p. 48, 2008.

[26] A. P. Davis, C. G. Murphy, C. A. Saraceni-Richards, M. C. Rosenstein, T. C. Wiegers, and C. J. Mattingly, "Comparative Toxicogenomics database: a knowledgebase and discovery tool for chemical-gene-disease networks," *Nucleic acids research*, vol. 37, pp. D786–D792, 2009.

[27] R. Mohseni, S. M. Alavian, Z. A. Sadeghabadi, and M. Heiat, "Therapeutic effects of Chlorella vulgaris on carbon tetrachloride induced liver fibrosis by targeting hippo signaling pathway and AMPK/FOXO1 axis," *Molecular biology reports*, vol. 48, no. 1, pp. 117–126, 2021.

[28] M. Yoo, J. Shin, J. Kim et al., "DSigDB: drug signatures database for gene set analysis," *Bioinformatics*, vol. 31, no. 18, pp. 3069–3071, 2015.

[29] E. Chen, C. Tan, Y. Kou et al., "Enrichr: interactive and collaborative HTML5 gene list enrichment analysis tool," *BMC Bioinformatics*, vol. 14, no. 1, p. 128, 2013.

[30] K. Troulé, H. López-Fernández, S. García-Martín et al., "DREIMT: a drug repositioning database and prioritization tool for immunomodulation," *Bioinformatics*, vol. 37, no. 4, pp. 578-579, 2021.

[31] T. Skillman and J. Feldman, "The pharmacology of sulfonylureas," *The American journal of medicine*, vol. 70, no. 2, pp. 361–372, 1981.

[32] P. Calderon, W. van Dorsser, K. Geöcze von Szendroi, J. G. de Mey, and J. Roba, "in vitro vasorelaxing activity of suloctidil," *Archives internationales de pharmacodynamie et de therapie*, vol. 284, no. 1, pp. 101–113, 1986.

[33] J. Lamers, K. Cysouw, and P. Verdouw, "Slow calcium channel blockers and calmodulin: Effect of felodipine, nifedipine, prenylamine and bepridil on cardiac sarcolemmal calcium pumping atpase," *Biochemical Pharmacology*, vol. 34, no. 21, pp. 3837–3843, 1985.

[34] F. Simons, K. Simons, M. Chung, and J. Yeh, "The comparative pharmacokinetics of H1-receptor antagonists," *Annals of allergy*, vol. 59, pp. 20–24, 1987.

[35] A. Patar, A. Sharma, D. Syiem, and S. Bhan, "Chlorophyllin supplementation modulates hyperglycemia-induced oxidative stress and apoptosis in liver of streptozotocin-administered mice," *BioFactors*, vol. 44, no. 5, pp. 418–430, 2018.

[36] A. Einarson and R. Boskovic, "Use and safety of antipsychotic drugs during pregnancy," *Journal of psychiatric practice*, vol. 15, no. 3, pp. 183–192, 2009.

[37] M. Sahinovic, M. Struys, and A. Absalom, "Clinical pharmacokinetics and pharmacodynamics of propofol," *Clinical Pharmacokinetics*, vol. 57, no. 12, pp. 1539–1558, 2018.

[38] D. Ravel and N. Laudignon, "Research prospects with benfluorex," *Journal of diabetes and its complications*, vol. 10, no. 5, pp. 246–254, 1996.

[39] P. Schlagenhauf, M. Adamcova, L. Regep, M. Schaerer, and H. Rhein, "The position of mefloquine as a 21st century malaria chemoprophylaxis," *Malaria journal*, vol. 9, no. 1, p. 357, 2010.

[40] F. Estelle and R. Simons, "H_1-receptor antagonists: safety issues," *Annals of allergy, asthma & immunology : official publication of the American College of Allergy, Asthma, & Immunology*, vol. 83, no. 5, pp. 481–488, 1999.

[41] A. Kolios and G. Tsokos, "Skin-kidney crosstalk in SLE," *Nature reviews Rheumatology*, vol. 17, no. 5, pp. 253-254, 2021.

[42] A. Ugarte and G. Ruiz-Irastorza, "SLE: the changing prognosis," *Lupus*, vol. 25, no. 12, pp. 1285–1287, 2016.

[43] M. Postal, J. Vivaldo, R. Fernandez-Ruiz, J. Paredes, S. Appenzeller, and T. Niewold, "Type I interferon in the pathogenesis of systemic lupus erythematosus," *Current opinion in immunology*, vol. 67, pp. 87–94, 2020.

[44] Z. Liu and Q. Zhou, "Tumor necrosis factor-like weak inducer of apoptosis and its potential roles in lupus nephritis," *Inflammation research : official journal of the European Histamine Research Society*, vol. 61, no. 4, pp. 277–284, 2012.

[45] M. Ruuth, J. Soronen, E. Kaiharju et al., "USF1 deficiency alleviates inflammation, enhances cholesterol efflux and prevents cholesterol accumulation in macrophages," *Lipids in health and disease*, vol. 17, no. 1, p. 285, 2018.

[46] S. S. Marable, E. Chung, and J. S. Park, "Hnf4a is required for the development of Cdh6-expressing progenitors into proximal tubules in the mouse kidney," *Journal of the American Society of Nephrology : JASN*, vol. 31, no. 11, pp. 2543–2558, 2020.

[47] K. Piletič and T. Kunej, "MicroRNA epigenetic signatures in human disease," *Archives of Toxicology*, vol. 90, no. 10, pp. 2405–2419, 2016.

[48] R. Mitra, M. Edmonds, J. Sun et al., "Reproducible combinatorial regulatory networks elucidate novel oncogenic microRNAs in non-small cell lung cancer," *RNA*, vol. 20, no. 9, pp. 1356–1368, 2014.

[49] C. Bo, H. Zhang, Y. Cao et al., "Construction of a TF-miRNA-gene feed-forward loop network predicts biomarkers and potential drugs for myasthenia gravis," *Scientific reports*, vol. 11, no. 1, p. 2416, 2021.

[50] R. Kratofil, P. Kubes, and J. Deniset, "Monocyte conversion during inflammation and injury," *Arteriosclerosis, thrombosis, and vascular biology*, vol. 37, no. 1, pp. 35–42, 2017.

[51] Y. Ding, Y. Tan, Z. Qu, and F. Yu, "Renal microvascular lesions in lupus nephritis," *Renal failure*, vol. 42, no. 1, pp. 19–29, 2020.

[52] Y. Ikezumi, T. Kondoh, Y. Matsumoto et al., "Steroid treatment promotes an M2 anti-inflammatory macrophage phenotype in childhood lupus nephritis," *Pediatric nephrology*, vol. 36, no. 2, pp. 349–359, 2021.

[53] E. Nikitina, I. Larionova, E. Choinzonov, and J. Kzhyshkowska, "Monocytes and macrophages as viral targets and reservoirs," *International journal of molecular sciences*, vol. 19, no. 9, p. 2821, 2018.

[54] M. Kostopoulou, A. Fanouriakis, K. Cheema et al., "Management of lupus nephritis: a systematic literature review informing the 2019 update of the joint EULAR and European Renal Association-European Dialysis and Transplant Association (EULAR/ERA-EDTA) recommendations," *RMD open*, vol. 6, no. 2, 2020.

[55] R. Roskoski, "Properties of FDA-approved small molecule protein kinase inhibitors: A 2021 update," *Pharmacological Research*, vol. 165, p. 105463, 2021.

[56] S. Ahmed, "The immune system as a potential target for environmental estrogens (endocrine disrupters): a new emerging field," *Toxicology*, vol. 150, no. 1-3, pp. 191–206, 2000.

[57] M. Cunningham, M. Richard, J. Wirth et al., "Novel mechanism for estrogen receptor alpha modulation of murine lupus," *Journal of autoimmunity.*, vol. 97, pp. 59–69, 2019.

[58] T. Vatanen, A. D. Kostic, E. d'Hennezel et al., "Variation in microbiome LPS immunogenicity contributes to autoimmunity in humans," *Cell*, vol. 165, no. 4, pp. 842–853, 2016.

[59] L. P. Whittall-García, J. Torres-Ruiz, A. Zentella-Dehesa et al., "Neutrophil extracellular traps are a source of extracellular HMGB1 in lupus nephritis: associations with clinical and histopathological features," *Lupus*, vol. 28, no. 13, pp. 1549–1557, 2019.

[60] A. Fanouriakis, M. Kostopoulou, K. Cheema et al., "2019 update of the Joint European League Against Rheumatism and European Renal Association-European Dialysis and Transplant Association (EULAR/ERA-EDTA) recommendations for the management of lupus nephritis," *Annals of the rheumatic diseases*, vol. 79, no. 6, pp. 713–723, 2020.

[61] S. Parikh, S. Almaani, S. Brodsky, and B. Rovin, "Update on lupus nephritis: core curriculum 2020," *American journal of kidney diseases: the official journal of the National Kidney Foundation*, vol. 76, no. 2, pp. 265–281, 2020.

[62] Z. Radvány, Z. Darvas, K. Kerekes et al., "H1 histamine receptor antagonist inhibits constitutive growth of Jurkat T cells and antigen-specific proliferation of ovalbumin-specific murine T cells," *Seminars in cancer biology*, vol. 10, no. 1, pp. 41–45, 2000.

[63] L. Jin, M. Tao, J. Zhou et al., "Metabolic syndrome in systemic lupus erythematosus was closely related to body mass index, blood pressure, blood sugar, blood lipids, and arthritis," *Pakistan journal of medical sciences*, vol. 36, no. 6, pp. 1220–1227, 2020.

Research Article

Trigonella foenum-graecum Methanolic Extract on Isolated Smooth Muscles and Acetylcholinesterase Enzyme: An In Vitro and Mechanistic In Silico Investigation

Muhammad Nabeel Ghayur [ID],[1,2] **Mohnad Abdalla** [ID],[3] **Asaad Khalid** [ID],[4,5] **Saeed Ahmad**,[2] **and Anwarul Hassan Gilani** [ID][2,6]

[1]*Kentucky College of Osteopathic Medicine, University of Pikeville, Pikeville, 41501 Kentucky, USA*
[2]*Department of Biological and Biomedical Sciences, Aga Khan University, Karachi, 74800 Sind, Pakistan*
[3]*Key Laboratory of Chemical Biology (Ministry of Education), Department of Pharmaceutics, School of Pharmaceutical Sciences, Cheeloo College of Medicine, Shandong University, 44 Cultural West Road, Shandong Province 250012, China*
[4]*Substance Abuse & Toxicology Research Center, Jazan University, Jazan 45142, Saudi Arabia*
[5]*Medicinal and Aromatic Plants and Traditional Medicine Research Institute, National Center for Research, Khartoum 11111, Sudan*
[6]*Dept of Public Health and Nutrition, The University of Haripur, Haripur 22620, Khyber Pakhtunkhwa, Pakistan*

Correspondence should be addressed to Muhammad Nabeel Ghayur; nabeelghayur@yahoo.com

Background and Objective. Trigonella foenum-graecum Linn., also called fenugreek, is a popular medicinal plant cultivated all over the globe. Fenugreek seeds are known for their many medicinal properties. We present our findings on the effect of a 70% aqueous methanolic fenugreek seed extract (Tfg.Cr) on isolated GI smooth muscles (rabbit jejunum and rat ileum) and the effect of extract and its constituent diosgenin on acetylcholinesterase (AChE) enzyme. *Results*. When tested on the baseline of isolated tissues, Tfg.Cr was devoid of any activity (stimulant or relaxant) till 10 mg/ml. This is an interesting finding, keeping in mind that the fenugreek seeds are used to alleviate constipation and diarrhoea. When Tfg.Cr was tried for any potential AChE inhibitory activity, it did show an inhibitory effect in increasing concentrations (47-380 μg/ml). This inhibitory effect was comparable to the effect produced by a standard AChE inhibitor physostigmine. One of the known fenugreek constituents, diosgenin, was also tested, and it also showed an AChE inhibitory effect in a concentration-dependent manner (11-190 μg/ml). Interaction between diosgenin and AChE was further investigated by molecular docking and molecular dynamics simulations for 100 ns, which showed that diosgenin interacted with the active-site gorge of AChE through hydrophobic, pi-pi stacking, and hydrogen bonds with various amino acids of the AChE enzyme. *Conclusion*. The results show that the fenugreek extract does not possess any GI stimulant or relaxant activity even though it is used traditionally in GI motility disorders. The extract and diosgenin could inhibit the AChE enzyme pointing towards their benefit to enhance the memory.

1. Introduction

Trigonella foenum-graecum Linn. (family: Fabaceae or Leguminosae), or "fenugreek" as commonly known in English, is a widely used medicinal plant. In Urdu or Hindi, it is called "methi." An annual herb [1, 2], fenugreek is orig-

inally from southeast Europe (the Mediterranean region) and West Asia [3, 4], but today, it is cultivated in many areas of the globe, including South Asia [2], Northern Africa, and even in North America [3]. It is a known and often consumed condiment all over the world [3]. In terms of its traditional use, the whole plant, leaves, and seeds are employed

for medicinal benefits [1, 2]. The active medicinal compounds and the most potent activity are concentrated in the oblong, yellow to yellowish brown seeds [3, 4].

For centuries, fenugreek has popularly been used by herbalists and traditional healers of China and South Asia in several medical conditions, specifically for gastrointestinal (GI) and neurological issues. The seeds are consumed as is or processed (boiled or roasted) for their benefit in dyspepsia, colic, flatulence, diarrhoea, dysentery, anorexia [1, 2, 4], gastritis, constipation [4], chronic cough, and bronchitis [2, 3]. It is also used as a stimulant and tonic of the central nervous system (CNS) [1] and is known to enhance memory [5]. There are also claims for its activity in the treatment of all kinds of skin infections and inflammatory conditions (leg ulcers, wounds, abscess, cellulitis, boils, and carbuncles), myalgia, arthritis, kidney, and liver problems [1–4] and as a galactagogue [1, 6]. Despite the popularity of fenugreek, most of these above-mentioned claims await verification and scientific proof [4]. Some of the studies done on fenugreek report that it has galactagogue [7, 8], anti-inflammatory [9, 10], antidiabetic [10], anticholesterolemic [11, 12], antihypertensive, kidney and liver protective [13], androgenic/anabolic [14], antibacterial, and anticancer [15] properties. All these medicinal uses and properties show how popular and beneficial this herb is in such a broad spectrum of disease conditions.

Many of the benefits of this plant are linked to the chemicals that have been isolated from it. Fenugreek is known to contain steroidal saponins like diosgenin, tigogenin, trigogenin, and fenugreekine; alkaloids like choline and trigonelline; amino acids like histidine, arginine, tryptophan, and lysine; and vitamins like nicotinic acid [1, 2, 4, 16]. The steroidal saponins are responsible for most of the medicinal benefits of fenugreek [3].

As noted above, several experimental and clinical studies on fenugreek scientifically elucidate its traditional uses. But still, a lot more work needs to be done to discover the many hidden benefits of this herb. This was the idea behind undertaking this endeavour. A 70% aqueous methanolic crude extract was prepared. This extract was tested pharmacologically on gastrointestinal (GI) smooth muscle preparations from rabbits and rats to see if there is any smooth muscle tone modulatory activity in the GI system, a potential acetylcholine- (ACh-) like effect that would lead us to believe in its memory-enhancing effects too. A substance acting like ACh can potentially have both GI stimulant and memory-enhancing effects due to an action similar to ACh on the cholinergic receptors in the GI tract and CNS. The extract was also tested for activity against the acetylcholinesterase (AChE) enzyme in vitro. This is because fenugreek is used to enhance the memory. Although the extract did not exhibit any effect on GI smooth muscle preparations, it did show an inhibitory effect on the AChE enzyme. The AChE inhibitory activity was traced back to its known chemical ingredient, diosgenin (Figure 1). Interaction between diosgenin and AChE was further investigated by molecular docking and molecular dynamics simulations for 100 ns.
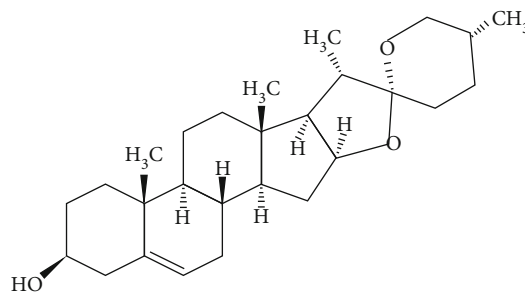
FIGURE 1: The chemical structure of fenugreek active constituent, a steroidal sapogenin, diosgenin (European Pharmacopoeia (EP) Reference Standard, structure taken from website of source of the chemical: https://www.sigmaaldrich.com).

2. Methodology

2.1. Animals. Care was taken to avoid any suffering to the animals used in this study. Experiments were performed ethically in strict accordance with lab animal handling specifications of European Community guidelines, EEC Directive 86/609/EEC. Local rabbits (either sex, around 1 kg) and Sprague-Dawley rats (either sex, 170-200 g) were used in this project. These were kept in the animal quarter at the Aga Khan University. The air was pathogen-free, and the temperature was controlled at around 23°C. The rabbits and rats had free access to water, although the food was withheld a day before the experiments. Food given to the animals was made of the following: fiber, table salt, white flour, sweetener, Nutri-vet L, potassium metabisulfite, grease, seafood, and powdered milk.

2.2. Chemicals. Standard chemicals and reagents were obtained from Sigma Company, USA. These included acetylcholine (ACh), acetylthiocholine (ATCh), 5,5-dithiobis (2-nitro), benzoic acid (DTNB), diosgenin, electric eel AChE (type VI-S), histamine, nicotine, and physostigmine. The solutions and dilutions of these were made on the day of the experiment. To make Tyrode's physiological salt solution, chemicals were purchased from Sigma, USA, and Merck, Germany. Tyrode's was constituted as follows (mM): 2.68 KCl, 136.90 NaCl, 1.05 $MgCl_2$, 11.90 $NaHCO_3$, 0.42 NaH_2PO_4, 1.80 $CaCl_2$, and 5.55 glucose.

2.3. Fenugreek Seeds and the Process of Extract Making. Fenugreek seeds (around a kg) were acquired from a supplier in Karachi, Pakistan. This was botanically identified by Mr. S. Ahmad. A specimen was kept in the herbarium of Natural Products Research Unit, Aga Khan University, for identification and cataloguing (# TF-SE-05-04-59). For making the crude extract, methodology described previously [17] was used (Figure 2). Briefly, seeds were washed with water and then lightly mashed. The seeds were then kept dipped for 3 days in a couple of litres of 70% aqueous methanol at 23°C. After the 3 days, the seeds and methanol were passed through a fabric filter. Later, the plant material was immersed again in a new batch of aqueous methanol for 72 hours, twice. Finally, filtrates were filtered using
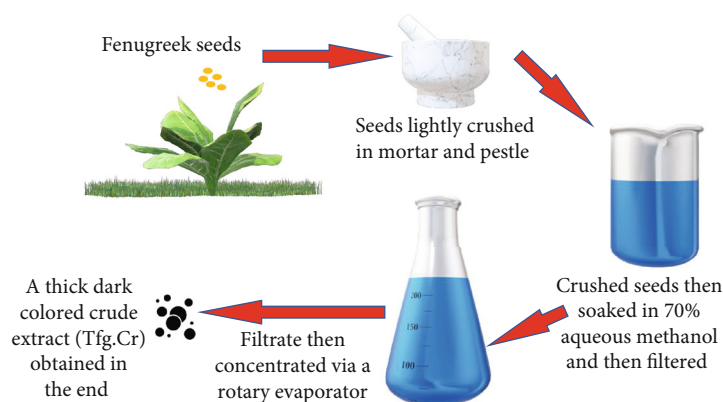
FIGURE 2: Schematic representation of the plant material (fenugreek seeds) and the crude extract preparation. All pictures in the scheme were taken from 3D models, Online Sources, Microsoft PowerPoint 2019.

Whatman-qualitative grade-1 filters. A rotary evaporator (Rotavapor, BUCHI Labortechnik AG, Switzerland) was used to obtain a crude extract, labelled as Tfg.Cr. We kept this extract stored at -4°C until use.

2.4. Experiments on Isolated Smooth Muscle Tissue Preparations

2.4.1. Isolated Rabbit Jejunum.
We have described and worked with isolated intestinal smooth muscles before. Detailed descriptions can be found in our previous communication [17]. Portions of the jejunum (around 2 cm long) were obtained from rabbits. These were hung in tissue baths with a thread. The tissue baths were filled with the physiologic salt solution, aerated with a mixture of 95% O_2 and 5% CO_2 at physiologic temperature. All changes in contractility were noted isotonically using Harvard equipment (oscillographs and force transducers). The tissues were left to stabilize for half an hour. The advantage of using rabbit jejunum is its ability to contract spontaneously (Figure 3(a)). This permits to test the spasmolytic and spasmogenic potential of a drug being investigated. The spasmolytic effect is calculated as the % change in contractility of the tissue, while the spasmogenic effect is quantified while comparing with the action of a standard spasmogenic agent like ACh 10 μM and nicotine 10 μM (Figure 3(a)).

2.4.2. Isolated Rat Ileum.
We have previously described the use of isolated smooth muscle preparations [17]. Small intestinal sections of the ileum (about 2 cm long) were obtained from rats. These pieces of the tissue were hung in baths as described above. Changes in contractility of the tissue were captured isotonically using Harvard equipment. The tension kept on the tissue was 1 g. Unlike rabbit jejunum, rat ileum does not exhibit baseline contractions; instead, it has a flat baseline (Figure 3(b)). The tissue was left to normalize for half an hour, following which repeated contractions were obtained from standard drugs like ACh 10 μM and histamine 10 μM (Figure 3(b)). Drugs were permitted to stay in contact with tissue for around 20 s while a gap of 3 min was given between concentrations of ligands.

2.5. Enzyme Assay for AChE Inhibition.
AChE inhibitory activity of the extract and diosgenin was determined via the standard spectrophotometric method [18]. Certain modifications to the process were introduced, as described before [17]. Electric eel AChE (type VI-S) was utilized as an enzyme source, while ATCh iodide worked as the substrate. Ellman's reagent (DTNB) behaved as the chromogenic marker for determining enzyme inhibitory activity. For the working enzyme solution, sodium phosphate buffer (1 mM) was used. Enzyme concentrates were made and kept at -70°C; the substances under study were diluted on the test day.

The enzyme inhibitory tests were done in 96-well microtiter plates. Briefly, sodium phosphate buffer (140 μl and 0.1 mM at pH 8.0), Tfg.Cr extract (20 μl and diluted in 5% ethanol), and AChE (20 μl) were dissolved and kept for 15 min at 25°C. Then, DTNB (10 μl) was added. The interaction of chemicals initiated with the addition of 10 μl of ATCh (0.71 mM). Breakdown of ATCh was quantified by determining synthesis of 5-thio-2-nitrobenzoate anion (yellow in color, formed due to interaction of DTNB and thiocholine) using SpectraMax microplate spectrophotometer (Molecular Devices, USA). The test for the substances under study was performed at least thrice. The preliminary difference was calculated as the difference in optical density/min and used in the following determination. The test reaction contained test samples, while the control lacked test substance. For comparison, the standard AChE inhibitor was physostigmine.

2.6. Molecular Docking and Dynamics Simulation

2.6.1. Molecular Docking Protocol.
The ligand diosgenin, a phytosteroid sapogenin (Figure 1), was considered with flexibility of a defined ligand-specific torsion tree. Torpedo californica acetylcholinesterase (TcAChE) structure retrieved from Protein data bank accession I.D. 7B2W was downloaded, protonated, and minimized prior to docking. AutoDock docking setup for TcAChE was asserted as rigid, and the grid spacing was applied onto the whole 3-dimensional protein structure to explore the putative binding sites.
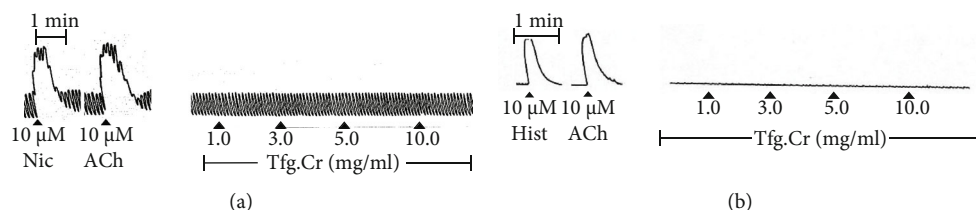
Figure 3: Tracings showing the effect of fenugreek crude extract (Tfg.Cr) on isolated intestinal tissue preparations. (a) Activity of Tfg.Cr on resting spontaneous contractions of rabbit jejunum tissues in comparison to standard drugs like acetylcholine (ACh) and nicotine (Nic). (b) Activity of Tfg.Cr on resting baseline of isolated rat ileum tissues in comparison to standard drugs like acetylcholine (ACh) and histamine (Hist).

Auto-Dock algorithm having precalculated maps of each atom of the ligand with the pre-defined electrostatic potential was utilized. The autogrid algorithm implemented in Auto-Dock predicts the binding energy via the ligand conformation and contribution of each atom of a specified element with the specified grid point in the vicinity of the receptor. The grid box is generated around the active site of the TcAChE enzyme, allowing the docking software to look for all possible interactions between the ligands and the receptor. Other configurational settings were set as the default. Auto-Dock examined the intact 3D structure of AChE and ligand diosgenin in the prescribed grid spacing to search the space for docking. 2D and 3D molecular interactions of the protein-ligand complex was visualized to interpret the binding mode.

2.6.2. Molecular Dynamics Simulation Setup. The investigated docked AChE-diosgenin complex was further expedited to spurt molecular dynamics (MD) production run via the Desmond simulation package. MD simulations of the AChE-diosgenin docked complex were accomplished to reveal the capability of the diosgenin inhibition in the acetylcholinesterase. Receptor topology was generated, and the SPC water model with the specified periodic boundary conditions at a distance of 1.0 nm was set to create an aqueous environment. Furthermore, the solvated receptor charges were neutralized by the addition of required Na^+ or Cl^- ions. Subsequently, the default value of pressure and temperature was maintained as per the Parrinello-Rahman algorithm and Nose-Hoover temperature coupling method. The NPT ensemble was used for minimization and relaxation. The 100 ns production MD simulation run was executed with the interval record of 100 ps. Furthermore, simulated trajectories were analyzed and visualized via simulation interaction diagram (SID) module implemented in Desmond Schrödinger package to record the protein deviation, fluctuation, compactness, and hydrogen bond contacts with their occupancies, while ligand root means square deviation (RMSD), the radius of gyration (rGyr), torsional angle, molecular surface area (MolSA), solvent accessible surface area (SASA), and polar surface area (PSA) were also calculated during the production run of MD simulated time.

2.7. Result Representation. Data are shown as mean ± standard error of the mean (SEM; "n" is observations) and the effective concentration producing 50% inhibition

(EC_{50}) with 95% confidence intervals (CI). The graphs were constructed and analyzed utilizing the GraphPad program (GraphPad, USA). Statistical comparisons were made via two-way analysis of variance (ANOVA), and unpaired Student's t-test ($p < 0.05$) was taken as statistically different (GraphPad program).

3. Results and Discussion

This project was aimed at looking into some of the pharmacological activities of fenugreek seed extract. Fenugreek seeds are traditionally used in multiple GI conditions [1, 2, 4] while also regarded as useful as a CNS tonic to enhance memory [1, 5].

3.1. Effect of Tfg.Cr on Isolated Smooth Muscle Tissue Preparations. The 70% aqueous methanolic extract was investigated on the isolated rabbit and rat GI smooth muscle tissue preparations. The reason for selecting these tissue preparations was that rabbit jejunum, once isolated in a tissue bath under controlled conditions, elicits spontaneous contractions, and it is ideal for testing for potential GI spasmolytic agents [19, 20]. However, spasmogenic effects can also be investigated on rabbit jejunum. Tfg.Cr (0.1-10 mg/ml) did not exhibit a response when evaluated on spontaneous contractions of rabbit jejunum tissue preparations ($n = 3$; Figure 3(a)). There was neither a stimulant nor a relaxant effect seen with the extract (Figure 3(a)). This could be due to a number of reasons. The simplest reason could be that the plant extract just does not have any GI-active components which is why it did not exhibit any activity in this preparation. Other reasons are discussed below. In comparison to the extract, standard GI stimulants like ACh (10 μM) and nicotine (10 μM) both elicited an immediate stimulant effect on the resting spontaneous contractions (Figure 3(a)). The rat ileum, on the contrary, maintains a flat baseline and is ideal for screening spasmogenic activity [21]. When tried on this tissue, Tfg.Cr (0.1-10 mg/ml), similar to how it acted in rabbit jejunum, did not exhibit any effect ($n = 3$; Figure 3(b)). There was neither a stimulant nor a relaxant effect seen from Tfg.Cr (Figure 3(b)). On the contrary, standard gut spasmogenics like ACh (10 μM) and histamine (10 μM) both exhibited a sharp spasmogenic response on the baseline of rat ileum tissues (Figure 3(b)). These results are worth mentioning, keeping in mind that fenugreek seeds are used traditionally in constipation

(spasmogenics help in constipation to increase the muscular tone) and diarrhoea (spasmolytics help to relax muscular tone in diarrhoea). The traditional use was an indication that the seed extract should have either spasmolytic or spasmogenic or even both activities, as we have shown so often from our studies [17]. The seeds are also known to contain choline, a quaternary ammonium compound that forms ACh in the body [22]. ACh is a major neurotransmitter in the biological systems as a modulator of GI motility and memory [22]. As to why we did not see any muscular tone modulatory effect of the extract in the isolated preparations, it could be that multiple chemical components in the seed extract balanced out a final effect due to their presence or maybe the GI-active component did not concentrate out in the 70% aqueous methanolic solvent that we used. There could even be a species-specific effect. We have shown, in the past, that plant extracts exhibit different effects in tissues from different species [21, 23, 24]. Whatever the reason may be, although negative, these findings help rule out several different variables for any future studies other researchers might decide to perform to further investigate the GI effects of this very popularly used herb.

3.2. Effect of Tfg.Cr and Diosgenin on Enzyme Assay for AChE Inhibition. Another reason for using the isolated tissue preparations was to see if the extract can show an ACh-like spasmogenic effect. This is because ACh is a GI stimulant and a major neurotransmitter implicated in the pathophysiology of Alzheimer's disease [25]. Chemicals with an ACh-like effect can help patients with memory disorders like Alzheimer's [22]. We have reported several ACh-like GI stimulant extracts with additional AChE inhibitory pharmacology [20, 26]. But as discussed, the extract did not exhibit any effect on the isolated tissues. Although when tested against the in vitro AChE enzyme assay, Tfg.Cr, in increasing concentrations (47-380 μg/ml), inhibited the ACh-degrading enzyme AChE (Figure 4). The EC_{50} for this effect was 196.0 μg/ml (152.6-251.9, $n = 4$). Tfg.Cr showed a maximum of $48.8 \pm 1.3\%$ ($n = 4$) inhibition of the enzyme (Figure 4). This inhibitory effect was like the effect exhibited by physostigmine, a standard AChE inhibitor, that showed its inhibitory effect with EC_{50} of 0.04 μg/ml (0.04-0.04, 3 observations; data not shown). This action of fenugreek aligns with its folkloric consumption to enhance memory [1, 5]. AChE inhibitors are the mainstay of therapy for Alzheimer's disease, and currently, three out of the four clinically used Alzheimer's medications are AChE inhibitors [27]. One study in the literature [28] reports the AChE inhibitory effect of fenugreek but that study used an ethanolic standardized extract compared to our methanolic crude extract. This shows the widespread presence of AChE inhibitory constituents in fenugreek seeds. Recently, a couple of in vivo studies reported the positive effect of fenugreek on memory [29] and cognition [30].

To determine the responsible compound for this AChE inhibitory action, we tested diosgenin (Figure 1), a steroidal sapogenin reported in fenugreek [1, 2, 4]. Diosgenin, in increasing concentrations (11-190 μg/ml), inhibited the AChE enzyme (Figure 4). This activity of diosgenin was sig-
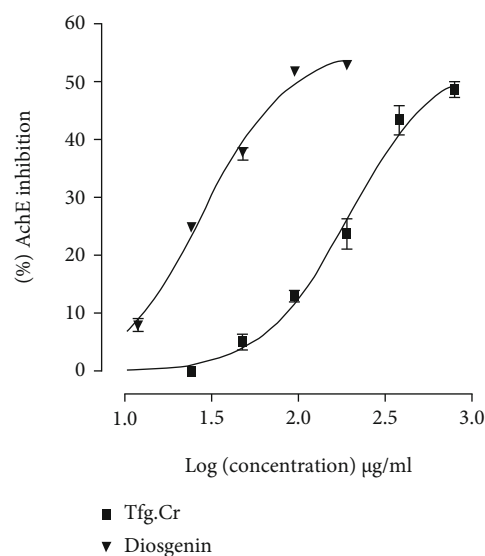
Figure 4: Curves showing the response of fenugreek crude extract (Tfg.Cr) and diosgenin on the in vitro enzyme assay for acetylcholinesterase (AChE) inhibition. Data presented are mean $\pm$ SEM, four observations; the two curves are statistically different ($p < 0.001$), two-way ANOVA.

nificantly more potent than that of the extract ($p < 0.001$, two-way ANOVA). The EC_{50} of the suppressive action of diosgenin was 27.9 μg/ml (24.9-31.1, $n = 4$). Diosgenin showed a maximum of $53.0 \pm 0.4\%$ ($n = 4$) inhibition of the AChE enzyme (Figure 4). The maximum inhibition of the AChE enzyme by diosgenin was significantly different from that of the crude extract ($p < 0.01$, unpaired t-test). We have earlier reported this AChE inhibitory effect of diosgenin [31], so in that sense, this finding regarding diosgenin is not novel. However, this shows that diosgenin is likely behind the AChE inhibitory effect observed with Tfg.Cr.

3.3. Molecular Docking Interpretation of Diosgenin Interactions with TcAChE. A molecular modelling study was executed to interpret the binding mode analysis of diosgenin into the possible binding cavity of the TcAChE receptor 7B2W. The docking output with putative interaction site with the highest ΔG binding energy threshold of -10.7 kcal/mol was observed among all the ranked poses based on the estimated interaction energy. The top ranked conformation of diosgenin according to the highest ΔG binding energy was elected for molecular investigation. Auto-Dock Vina top most ranked pose output revealed that diosgenin established hydrogen-mediated, hydrophobic, and pi-pi stacking contacts with the aromatic amino acid residues of TcAChE of the peripheral anionic site (Tyr70, Tyr121, Trp279, and Tyr334), an anionic subsite (Phe330), catalytic site (Phe331), and acyl pocket residues (Phe288 and Phe290) as illustrated in Figure 5. PAS anionic site and anionic subsite residues have been previously reported for the CNS activity. These amino acids Tyr70, Tyr121, Trp279, Phe288, Phe290, Phe331, and Tyr334 which directly involve in mediating hydrophobic interactions were discovered in case of diosgenin which were reported for CNS activity in literature.

Torpedo californica acetylcholinesterase
PDB ID 7B2W
Diosgenin

(a)

(b)

Figure 5: Continued.

(c)
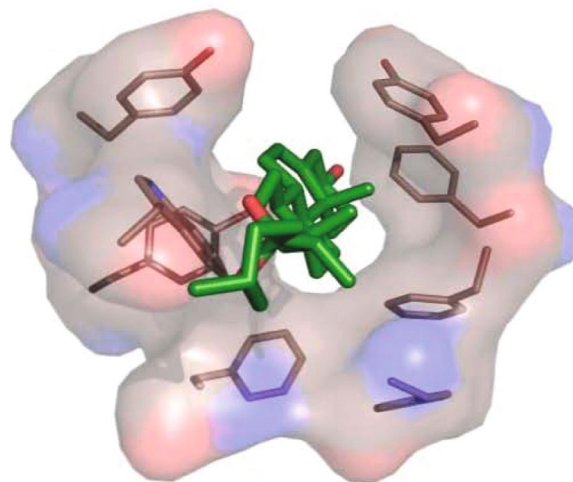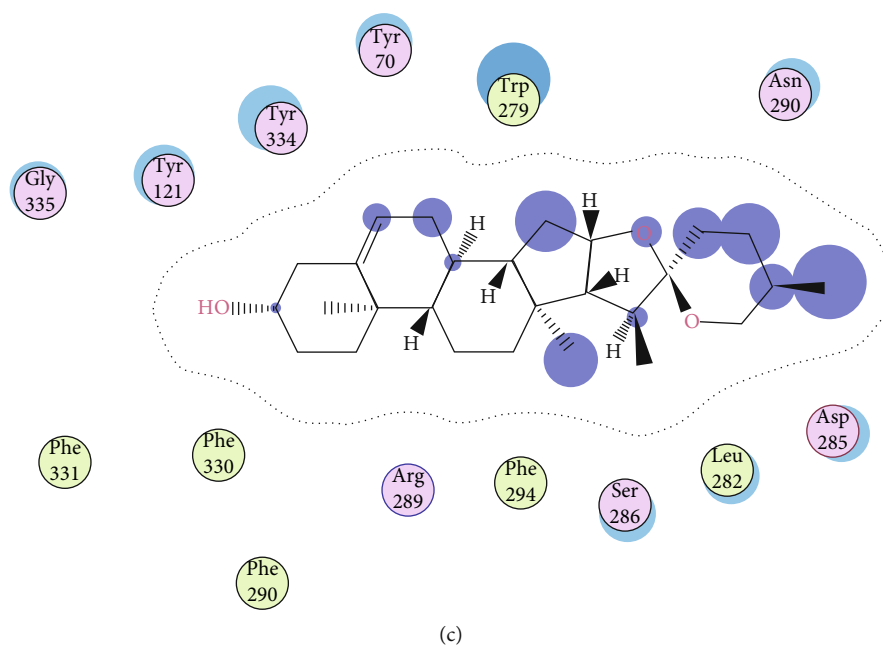
FIGURE 5: Postdocking analysis of Torpedo californica acetylcholinesterase with diosgenin. The green color represents ligand, while brown represents protein atoms.

3.4. MD Analysis. Molecular dynamic simulation data analysis is the basic quantitative evaluation parameter to analyze the stability, instability, deviations, fluctuations, compactness, and molecular interaction contact analysis of the protein and ligand via conformational geometries and dynamic vibrations and motions.

3.4.1. AChE-Diosgenin Complex Deviation and Fluctuation. RMSD was used to record the dislocation of the atoms present within the protein and ligand during MD simulated time with the initially generated frame of the pre-MD production run. RMSD plot analyzed for the protein backbone carbon-alpha atoms and the heavy atoms of the ligand during 100 ns of MD executed production runs. RMSD plot of TcAChE receptor 7B2W-diosgenin complex as depicted in Figure 6(a) demonstrated that AChE receptor deviations were noted within the range of 1.2 Å to 1.75 Å during the 100 ns of the trajectories record. In contrast, more deviations were observed between 65 ns and 75 ns with the deviation of ±2 Å. In the case of ligand fitting, RMSD with the heavy atoms of diosgenin in the 7B2W receptor showed more distortions in the initial 5 to 25 ns of the production run within the range of 1.6 Å to 6.4 Å. In comparison, the stability was almost attained after 25 ns to 100 ns near to ±4 Å. A slight or minor deviation was noted at 65 ns as the same noted in the protein RMSD. Lig fit Prot plot revealed that ligand had been slightly diffused away from its binding pocket. Root mean square fluctuation of the protein-ligand complex of 537 amino acid residues was also analyzed during 100 ns of MD run. The influence of residue fluctuations was also noted for this 7B2W-diosgenin complex with Tyr70, Trp84, Trp279, and Phe288-Tyr334. Significant fluctuation at Tyr70 amino acid residue within the PAS region was observed. Minor fluctuations were observed with the other interacting PAS and an anionic subsite residue. The low deviation via RMSD and less fluctuation via RMSF results suggested that TcAChE, when complexed with the diosgenin, showed stability with the respective protein and its binding cavity.

3.4.2. Protein-Ligand Interaction Contact Analyses. The stability of the TcAChE-diosgenin was estimated via a protein-ligand contact histogram plot to check the overall protein-ligand contacts with the active-site residues in terms of interaction fraction pattern. These protein-ligand contacts were also inspected on the simulated trajectories of 100 ns of the production run. The interaction patterns follow H-bonds, hydrophobic, ionic, and water bridging-mediated interactions. H-bonding interactions play a crucial role in drug designing, but in this contrast, hydrogen bonding occurred as 0.74% with Asp72 and <0.1% with the Tyr121 and Tyr334. Hydrophobic contacts were established with Tyr70, Phe75, Trp279, Phe331, and Tyr334 while 0.55% hydrophobic contact with Trp279 and 0.3% and 0.35% fraction contact with Phe331 and Tyr334 were noted. Trp84, Tyr121, and Tyr334 possessed weak hydrogen bonding interactions. Asp72 showed maximum H-bond occupancy throughout the simulation, but in the last 25 ns, MD run. Its contact with diosgenin was diminished and converge into the water-mediated bridging interactions. At the same time, other residues which are mediating interactions with negligible hydrogen bond occupancies were observed negligible as implemented in Figure 7. 2D protein-ligand interaction pattern was also checked for further explanation as depicted in Figure 8. It is also evident by the 2D protein-ligand contact diagram, which was also showing that hydroxyl moiety of

(a)

(b)
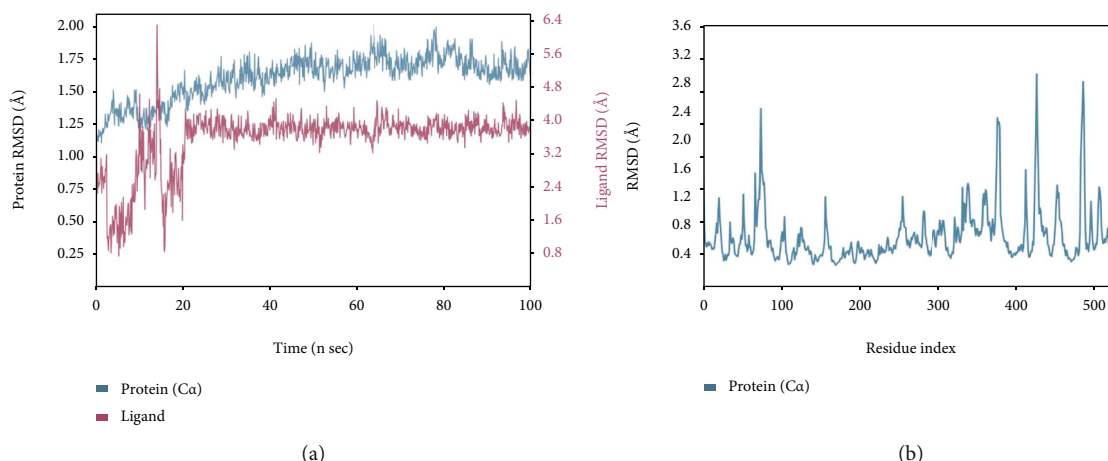
FIGURE 6: Deviation and fluctuation analysis in the TcAChE-diosgenin complex. (a) RMSF plot of the protein-ligand complex. Blue color indicates the alpha-carbon backbone of the protein, while maroon color indicates RMSD upon ligand fitting. (b) RMSD of the backbone carbon-alpha atoms of protein and heavy atom ligand.
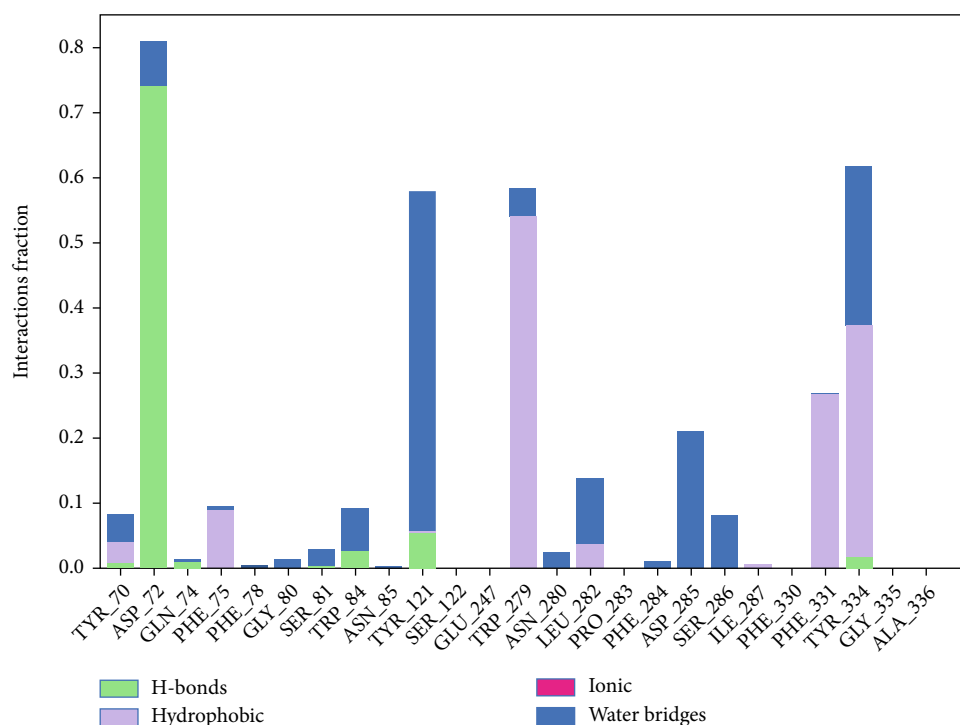
FIGURE 7: Histogram analysis of the interacted fraction pattern of amino acid residues with the ligand.

the diosgenin-mediated H-bond with Asp72 persists to 74% during simulation while the water-bridge interaction with the Tyr121 persisted 44%.

A timeline representation of the above-mentioned receptor-ligand histogram was further analyzed to check the total number of interaction or molecular contacts in each trajectory record frame of all amino acid residues of the TcAChE, further clarified by the timeline exhibit of active-site residues of the TcAChE-diosgenin complex. The top panel of the timeline representation, as depicted in Figure 9(a), demonstrated the total number of exhibited

molecular contacts in each trajectory record frame. Throughout the 100 ns of the production run, almost 05 intermolecular contacts persisted while the increase in molecular contacts was noted at 30 and 80 ns. During this phase of the MD run, it showed variation in establishing any molecular interactions that raised from 5 to 9. Furthermore, we noted which amino acid residues mediated intermolecular contacts in each trajectory throughout the simulation, as mentioned in Figure 9(b). Asp72, Tyr121, Trp279, Phe331, and Phe334, the peripheral active-site gorge residues, interacted throughout the simulation, while Tyr70,
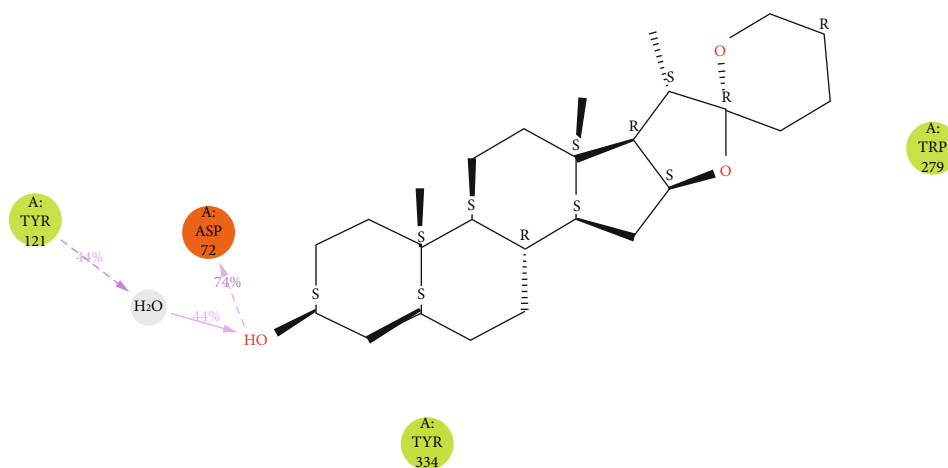
FIGURE 8: 2-dimensional interaction pattern observed during 100 ns of MD production run.
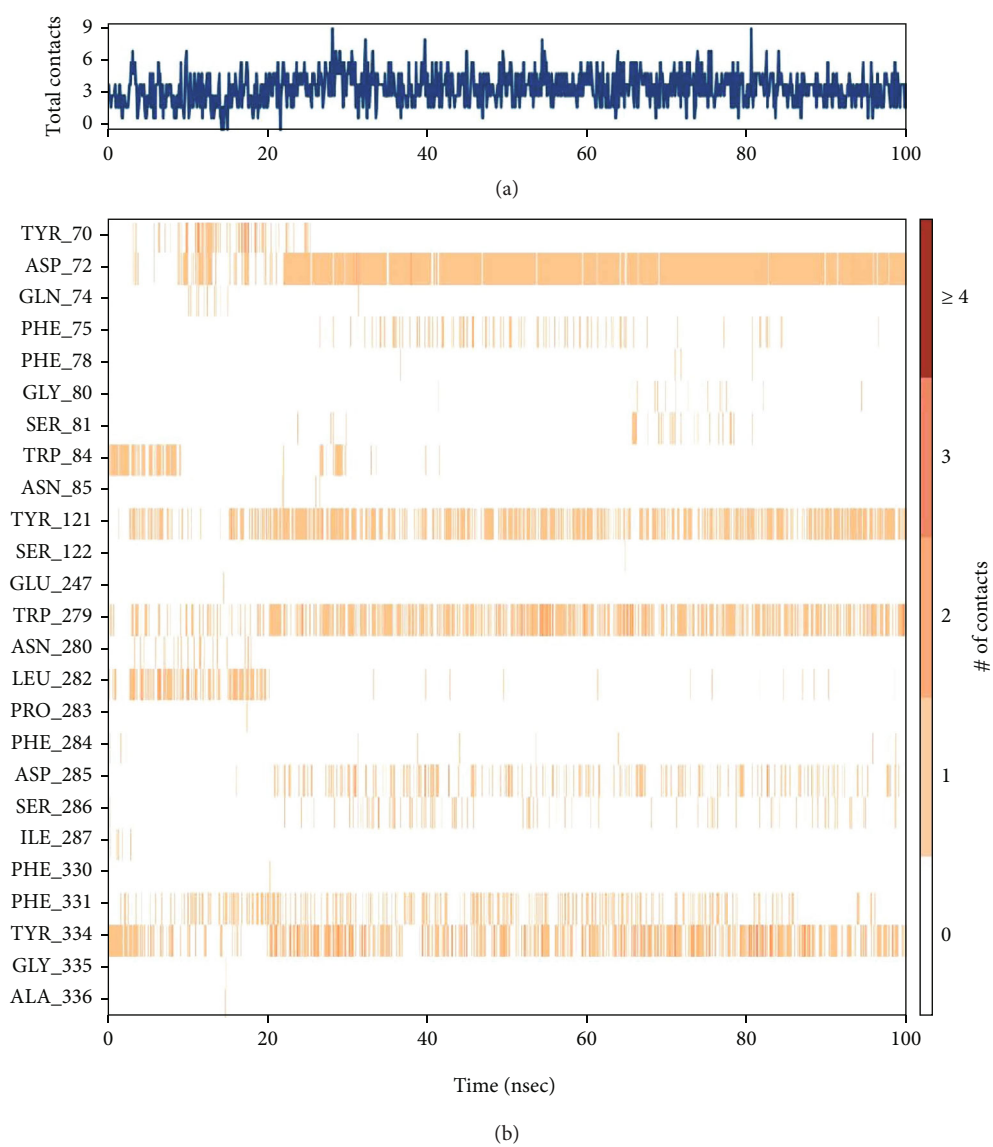
FIGURE 9: (a) Timeline representation of the total number of molecular interaction contacts in each trajectory frame. (b) The number of interactions with the active-site residues in each frame of the simulated 100 trajectory frames.
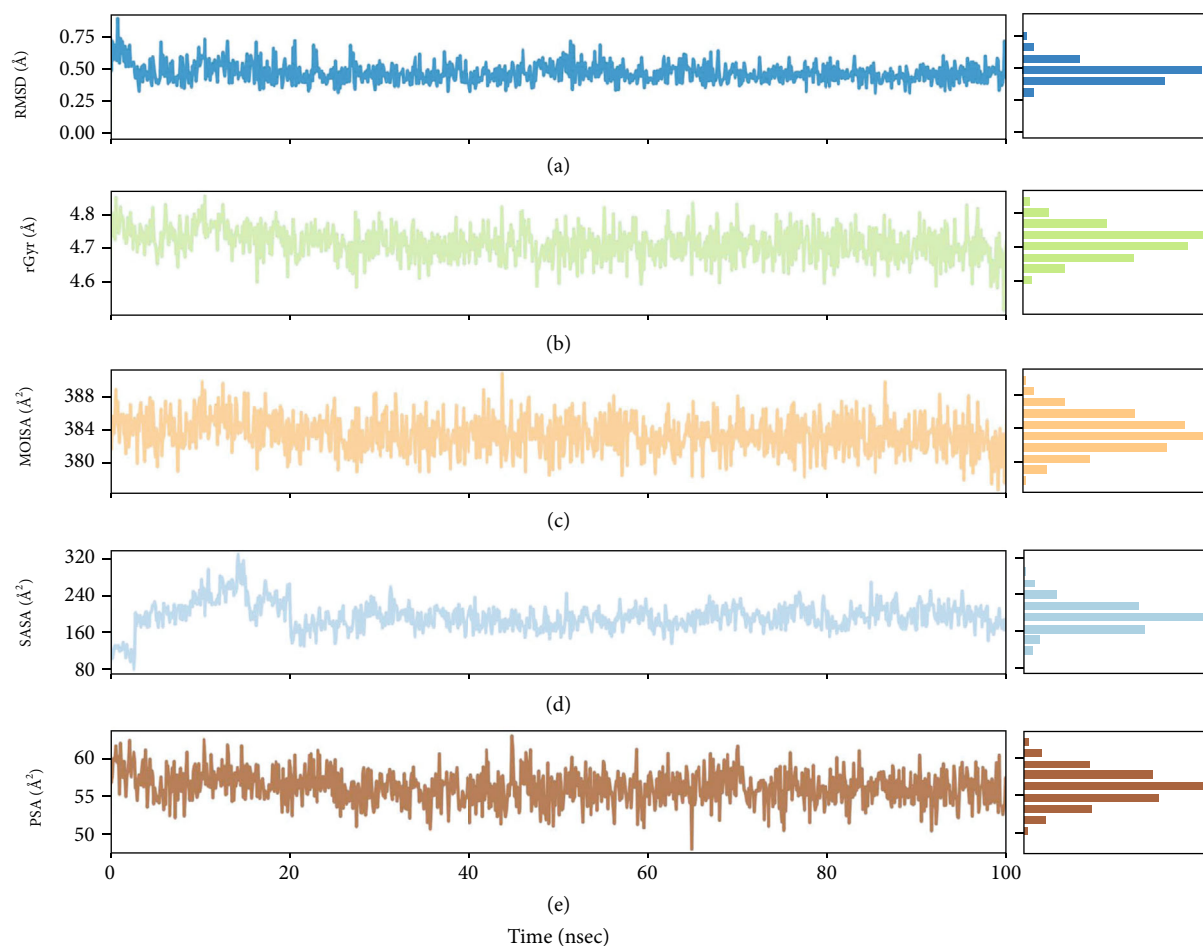
Figure 10: The ligand property analyses of 7B2W-diosgenin complex throughout the trajectory of 100 ns simulation run. (a) Ligand root means square deviation (RMSD), (b) radius of gyration (rGyr), (c) molecular surface area (MolSA), (d) solvent accessible surface area (SASA), and (e) polar surface area (PSA).

Phe75, Gly80, Ser81, Trp84, Leu282, Asp285, Ser286 interacted very few or showed inconsistent molecular interaction as indicated by light orange color, which means a single contact obtained during simulation. Subsequently, Asp72 showed a dark band of orange color, showing that it interacted in high occupancy with more molecular contacts throughout the simulation, which validates that the crucial active-site amino acid residues have more interactions with diosgenin. It verified that approximately all probable positional geometries were achieved during this highly occupied H-bonds as described in the aforementioned histogram plot. Despite Asp72, Tyr121, Trp279, Phe331, and Phe334 showed variation sometimes single or more contacts throughout the simulation, these molecular contacts showed inconsistency during 100 ns of MD production run each frame trajectory record.

3.4.3. Detailed Analyses of the Diosgenin Properties throughout the Simulation.
The ligand properties were studied carefully to understand the conformational repositions utilizing the reference of pre-MD production data. For this purpose, all atoms of the diosgenin used for the detailed analysis such as RMSD, compactness or extendedness,

MolSA determination via 1.4 Å probe radius, SASA, the PSA were estimated as shown in Figure 10, and the torsional angle profile of the rotatable bonds present in the diosgenin was also critically analyzed as explained in Figure 11.

The RMSD of the ligand showed stability throughout the simulation, while minor fluctuations were seen at 50-55 ns after reaching the equilibrium position after 5 ns. The ligand RMSD lay around 0.25 Å to 0.8 Å, while RMSD attained around 0.6 Å during the whole simulation shown in Figure 10(a). The rGyr was also measured by which the compactness of the ligand was analyzed. The rGyr of the diosgenin slightly fluctuated to 40 ns simulation, later slowly attained equilibrium. The ligand showed an rGyr range of about 4.6 Å to 4.8 Å, and the equilibria attained around $\pm$ 4.7 Å (Figure 10(b)). Another property MolSA was also determined with a 1.4 Å probe radius. MolSA of ligand seemed stable during simulation, although there was a little less variation in 45 ns and 85 ns trajectory records. The range of MolSA is around 380Å^2 to 388Å^2, and the equilibrium achieved around 385Å^2 is visualized in Figure 10(c). The SASA by H_2O solvent was also noted. The SASA denoted that the raised value from 80 to 320 Å^2 until 20 ns simulation and then afterward became persistent until the end of the
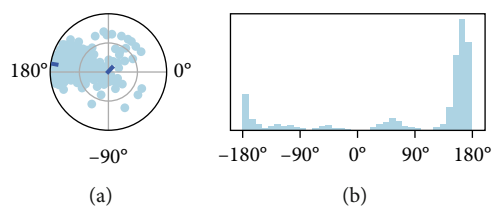
FIGURE 11: Ligand torsional profile of the rotatable bonds present in diosgenin during simulation. (a) The conformation of torsion during simulation. (b) The bar plot demonstrating the probable density of the torsions present in the ligand.

simulation with the range of 200Å^2 (Figure 10(d)). The PSA was also estimated for diosgenin molecules influenced by the polar O_2 and N atoms. The PSA was in the range of 50Å^2-60Å^2 throughout the simulation, but there were visible fluctuations occurred at 46 ns to 65 ns simulation period, while the equilibrium attained around 56Å^2 inspected in Figure 10(e). The above-mentioned studied ligand properties show that there were some fluctuations in the initial or intermediate recorded trajectory frames, which gradually achieved equilibrium till the completion of the simulation, which demonstrated the stability of diosgenin in the active site of the gorge region TcAChE.

Dial plot illustrated that the torsion angle variations persisted throughout the whole MD production runs. The bar plot emphasized the dial plots by indicating the probable density of the torsions via utilizing each rotatable bond present in the ligand, as depicted in Figure 11. It showed that the torsional angle of the rotatable bond lay between 160 to 180 degrees of angular rotation, while the occupancy showed at 170 degrees of angular rotation. Histogram and torsion interactions may reflect conformational strain that ligand faces to sustain a protein-bound conformation.

3.5. Pre- and Post-MD Binding Mode Analysis of TcAChE-Diosgenin Complex. Molecular docking and post-MD results revealed that diosgenin penetrated in the active-site gorge region of TcAChE and showed almost similar molecular interactions in the static and dynamic mode. The peripheral anionic site aromatic residues Trp279 and Tyr334 showed hydrophobic or pi-pi stacking contacts with diosgenin in both pre- and post-MD stages. Subsequently, new molecular interactions were also observed and mediated hydrogen bond during 100 ns MD run with the hydroxyl moiety of diosgenin via Asp72 with the distances of 1.68 Å and 2.84 Å and Ser81 with the distances of 2.93 Å. The OH group interacted with Asp72- and Ser81-mediated H-bonding interactions could be the reason for enhancing the binding affinity of diosgenin in TcAChE.

4. Conclusion

These results show that although fenugreek is so popularly used traditionally in GI disorders, it exhibited neither a stimulant nor a relaxant effect on the GI smooth muscles. This is an important finding as it rules out several variables and gives valid information to other researchers to try either a different solvent system for the extraction or different ani-

mal species to investigate any potential GI effects of this herb. Isolated smooth muscle preparations not only help to elucidate GI effects but also help look for ACh-like effects, which are also relevant in Alzheimer's disease pharmacology. Although it did not affect the isolated tissues, the extract did exhibit an inhibitory effect on the AChE enzyme assay, providing a rationale for its traditional consumption in memory loss. Diosgenin, a known chemical component of fenugreek, also showed a much more potent inhibitory effect on the AChE enzyme assay, indicating that it must be the responsible compound in fenugreek for this effect. After applying in silico approaches, we concluded that diosgenin permeated the active-site gorge of TcAChE and displayed substantially identical molecular interactions in the static and dynamic states obtained from molecular docking and post-MD findings.

Data Availability

All data is provided in the study.

Conflicts of Interest

The authors declare that they have no conflicts of interest.

Authors' Contributions

Muhammad Nabeel Ghayur and Mohnad Abdalla contributed equally to the work.

References

[1] A. K. Nadkarni, *Indian Materia Medica*, Popular Prakashan, Bombay, 2000.

[2] L. D. Kapoor, *CRC Handbook of Ayurvedic Medicinal Plants*, CRC Press Inc., Boca Raton, 2000.

[3] S. Lininger, J. Wright, S. Austin, D. Brown, and A. Gaby, *The Natural Pharmacy*, Prima Health, Rocklin, 1998.

[4] C. W. Fetrow and J. R. Avila, *Professional's Handbook of Complementary and Alternative Medicines*, Lippincott Williams and Wilkins, Philadelphia, 2004.

[5] S. Kaviarasan, G. H. Naik, R. Gangabhagirathi, C. V. Anuradha, and K. I. Priyadarsini, "In vitro studies on antiradical and antioxidant activities of fenugreek (Trigonella foenum graecum) seeds," *Food Chemistry*, vol. 103, no. 1, pp. 31–37, 2007.

[6] E. B. Claflin and E. A. Treamblay, *1801 Home Remedies*, Reader's Digest Association, Montreal, 2007.

[7] F. S. Yuliani, S. Purwono, A. H. Sadewa, E. Damayanti, and D. S. Heriyanto, "Polyherbal formula (ASILACT®) induces milk production in lactating rats through upregulation of α-lactalbumin and aquaporin expression," *BMC Complementary Medicine and Therapies*, vol. 20, no. 1, p. 368, 2020.

[8] S. C. Foong, M. L. Tan, W. C. Foong, L. A. Marasco, J. J. Ho, and J. H. Ong, "Oral galactagogues (natural therapies or drugs) for increasing breast milk production in mothers of non-hospitalised term infants," *Cochrane Database of Systematic Reviews*, vol. 5, article CD011505, 2020.

[9] M. Asif, H. M. Yousaf, M. Saleem et al., "Trigonella foenum-graecum seeds oil attenuated inflammation and angiogenesis in vivo through down-regulation of TNF-alpha," *Anti-Cancer*

Agents in Medicinal Chemistry (Formerly Current Medicinal Chemistry-Anti-Cancer Agents), vol. 21, no. 11, pp. 1460–1471, 2021.

[10] C. Zhou, Y. Qin, R. Chen, F. Gao, J. Zhang, and F. Lu, "Fenugreek attenuates obesity-induced inflammation and improves insulin resistance through downregulation of iRhom2/TACE," Life Sciences, vol. 258, article 118222, 2020.

[11] K. Heshmat-Ghahdarijani, N. Mashayekhiasl, A. Amerizadeh, Z. Teimouri Jervekani, and M. Sadeghi, "Effect of fenugreek consumption on serum lipid profile: a systematic review and meta-analysis," Phytotherapy Research, vol. 34, no. 9, pp. 2230–2245, 2020.

[12] M. Askarpour, F. Alami, M. S. Campbell, K. Venkatakrishnan, A. Hadi, and E. Ghaedi, "Effect of fenugreek supplementation on blood lipids and body weight: a systematic review and meta-analysis of randomized controlled trials," Journal of Ethnopharmacology, vol. 253, article 112538, 2020.

[13] A. Hadi, A. Arab, H. Hajianfar et al., "The effect of fenugreek seed supplementation on serum irisin levels, blood pressure, and liver and kidney function in patients with type 2 diabetes mellitus: a parallel randomized clinical trial," Complementary Therapies in Medicine, vol. 49, article 102315, 2020.

[14] A. Mansoori, S. Hosseini, M. Zilaee, R. Hormoznejad, and M. Fathi, "Effect of fenugreek extract supplement on testosterone levels in male: a meta-analysis of clinical trials," Phytotherapy Research, vol. 34, no. 7, pp. 1550–1555, 2020.

[15] L. A. N. Al-Timimi, "Antibacterial and anticancer activities of fenugreek seed extract," Asian Pacific Journal of Cancer Prevention, vol. 20, no. 12, pp. 3771–3776, 2019.

[16] B. Cai, Y. Zhang, Z. Wang et al., "Therapeutic potential of diosgenin and its major derivatives against neurological diseases: recent advances," Oxidative Medicine and Cellular Longevity, vol. 2020, Article ID 3153082, 16 pages, 2020.

[17] A. H. Gliani, A. H. Ghayur, and A. Khalid, "Presence of antispasmodic, antidiarrheal, antisecretory, calcium antagonist and acetylcholinesterase inhibitory steroidal alkaloids in Sarcococca saligna," Planta Medica, vol. 71, no. 2, pp. 120–125, 2005.

[18] G. L. Ellman, K. D. Courtney, V. Andres, and R. M. Featherstone, "A new and rapid colorimetric determination of acetylcholinesterase activity," Biochemical Pharmacology, vol. 7, no. 2, pp. 88–95, 1961.

[19] R. Blattner, H. G. Classen, H. Dehnert, and H. J. Doring, Experiments on Isolated Smooth Muscle Preparations, Hugo Sachs Elektronik KG, Freiburg, 1978.

[20] A. H. Gilani, M. N. Ghayur, Z. S. Saify, S. P. Ahmed, M. I. Choudhary, and A. Khalid, "Presence of cholinomimetic and acetylcholinesterase inhibitory constituents in betel nut," Life Sciences, vol. 75, no. 20, pp. 2377–2389, 2004.

[21] M. N. Ghayur and A. H. Gilani, "Gastrointestinal stimulatory and uterotonic activities of dietary radish leaves extract are mediated through multiple pathways," Phytotherapy Research, vol. 19, no. 9, pp. 750–755, 2005.

[22] H. P. Rang, M. M. Dale, J. M. Ritter, and P. K. Moore, Pharmacology, Churchill Livingstone, New Delhi, 2003.

[23] M. N. Ghayur, A. H. Gilani, and P. J. Houghton, "Species differences in the gut stimulatory effects of radish seeds," The Journal of Pharmacy and Pharmacology, vol. 57, no. 11, pp. 1493–1501, 2005.

[24] M. N. Ghayur and A. H. Gilani, "Species differences in the prokinetic effects of ginger," International Journal of Food Sciences and Nutrition, vol. 57, no. 1-2, pp. 65–73, 2006.

[25] R. A. Bekdash, "The cholinergic system, the adrenergic system and the neuropathology of Alzheimer's disease," International Journal of Molecular Sciences, vol. 22, no. 3, p. 1273, 2021.

[26] M. N. Ghayur, A. H. Gilani, T. Ahmed et al., "Muscarinic, Ca(++) antagonist and specific butyrylcholinesterase inhibitory activity of dried ginger extract might explain its use in dementia," The Journal of Pharmacy and Pharmacology, vol. 60, no. 10, pp. 1375–1383, 2008.

[27] M. Vaz and S. Silvestre, "Alzheimer's disease: recent treatment strategies," European Journal of Pharmacology, vol. 887, article 173554, 2020.

[28] N. Satheeshkumar, P. K. Mukherjee, S. Bhadra, and B. P. Saha, "Acetylcholinesterase enzyme inhibitory potential of standardized extract of Trigonella foenum graecum L and its constituents," Phytomedicine, vol. 17, no. 3-4, pp. 292–295, 2010.

[29] A. Konuri, K. M. R. Bhat, K. S. Rai, K. Gourishetti, and M. Y. S. Phaneendra, "Supplementation of fenugreek with choline-docosahexaenoic acid attenuates menopause induced memory loss, BDNF and dendritic arborization in ovariectomized rats," Anatomical Science International, vol. 96, no. 2, pp. 197–211, 2021.

[30] P. K. Kodumuri, C. Thomas, R. Jetti, and A. K. Pandey, "Fenugreek seed extract ameliorates cognitive deficits in streptozotocin-induced diabetic rats," Journal of Basic and Clinical Physiology and Pharmacology, vol. 30, no. 4, 2019.

[31] M. N. Ghayur, S. F. Kazim, H. Rasheed et al., "Identification of antiplatelet and acetylcholinesterase inhibitory constituents in betel nut," Zhong Xi Yi Jie He Xue Bao, vol. 9, no. 6, pp. 619–625, 2011.

Retraction

Retracted: Intervention Study of Dictyophora Polysaccharides on Arsenic-Induced Liver Fibrosis in SD Rats

BioMed Research International

This article has been retracted by Hindawi following an investigation undertaken by the publisher [1]. This investigation has uncovered evidence of one or more of the following indicators of systematic manipulation of the publication process:

(1) Discrepancies in scope

(2) Discrepancies in the description of the research reported

(3) Discrepancies between the availability of data and the research described

(4) Inappropriate citations

(5) Incoherent, meaningless and/or irrelevant content included in the article

(6) Manipulated or compromised peer review

The presence of these indicators undermines our confidence in the integrity of the article's content and we cannot, therefore, vouch for its reliability. Please note that this notice is intended solely to alert readers that the content of this article is unreliable. We have not investigated whether authors were aware of or involved in the systematic manipulation of the publication process.

Wiley and Hindawi regrets that the usual quality checks did not identify these issues before publication and have since put additional measures in place to safeguard research integrity.

We wish to credit our own Research Integrity and Research Publishing teams and anonymous and named external researchers and research integrity experts for contributing to this investigation.

The corresponding author, as the representative of all authors, has been given the opportunity to register their agreement or disagreement to this retraction. We have kept a record of any response received.

References

[1] G. Wang, P. Zuo, K. Ding et al., "Intervention Study of Dictyophora Polysaccharides on Arsenic-Induced Liver Fibrosis in SD Rats," *BioMed Research International*, vol. 2022, Article ID 7509620, 12 pages, 2022.

Research Article

Intervention Study of Dictyophora Polysaccharides on Arsenic-Induced Liver Fibrosis in SD Rats

Guoze Wang [1,2,3] **Peipei Zuo,** [1,2,3] **Kai Ding,** [1] **Qibing Zeng,** [1,2,3] **Ting Hu,** [1,2,3] **Shaofeng Wei** [1,2,3] **and Peng Luo** [1,2,3]

[1]*The Key Laboratory of Environmental Pollution Monitoring and Disease Control, Ministry of Education & Affiliated Hospital of Guizhou Medical University & School of Public Health, Guizhou Medical University, Guiyang 550025, China*
[2]*State Key Laboratory of Functions and Applications of Medicinal Plants, Guizhou Medical University, Guiyang 550014, China*
[3]*Guizhou Provincial Engineering Research Center of Food Nutrition and Health, Guiyang, 550025 Guizhou, China*

Correspondence should be addressed to Peng Luo; luopeng@gmc.edu.cn

Long-term arsenic (As) exposure can cause liver injury, hepatic cirrhosis, and cancer. Meanwhile, Dictyophora polysaccharides (DIP) have excellent antioxidation, anti-inflammation, and immune protection effects. There are currently few reports on the protection effects of DIP on As-induced hepatotoxicity and its pharmacological value. Therefore, this study was aimed at elucidating the protection of DIP on As-induced hepatotoxicity and exploring its preventive role in antifibrosis. In our study, the SD rat As poisoning model was established by the feeding method to explore the influence of As exposure on liver fibrosis. Then, DIP treatment was applied to the rats with As-induced liver fibrosis, and the changes of serum biochemical indexes and liver tissue pathology were observed. And the expression of fibrosis-related proteins TGF-β1, CTGF, and α-SMA levels was then determined to explore the DIP intervention function. The results demonstrated that through reduced pathological changes of hepatic and increased serum AST, ALT, TP, ALB, and A/G levels, DIP ameliorated liver fibrosis induced by As as reflected. And the administration of DIP decreased the concentration of HA, LN, PCIII, CIV, TBIL, and DBIL. In addition, the synthesis of TGF-β1 inhibited by DIP might regulate the expression of CTGF and decrease the proliferation of fibrinogen and fibroblasts, which reduced the synthesis of fibroblasts to transform into myofibroblasts. And a decrease of myofibroblasts downregulated the expression of α-SMA, which affected the synthesis and precipitation of ECM and alleviated the liver fibrosis caused by exposure to As. In conclusion, based on the pathological changes of liver tissue, serum biochemical indexes, and related protein expression, DIP can improve the As-induced liver fibrosis in rats and has strong medicinal value.

1. Introduction

Arsenic (As) is a metallic element widely found in the natural environment, including the earth's crust, soil, groundwater, ambient air, and living organisms [1]. The different forms of As can migrate and accumulate in the atmosphere, soil, and water. Generally, As has different physical and chemical factors that result in various degrees of environmental toxicity [2]. The primary sources of As include natural sources and artificial sources (industrial and agricultural release). With the rapid development of modern agriculture and industry, arsenide compounds are widely used in nonferrous metals, pigments, fuels, glass, and pesticides.

However, they cause various environmental pollutions, including air, soil, groundwater, and food [3]. As is a serious threat to human health; therefore, studies have increasingly focused on how to treat and prevent As poisoning.

Long-term exposure to As or arsenide compounds and consumption of As-exposed food cause severe harm to humans and animals, including diabetes, neurological diseases, various forms of cancer, cardiovascular diseases, and peripheral vascular diseases [4, 5]. Previous epidemiological investigations and animal experiments have confirmed that As is correlated with liver damage. Research has shown that the occurrence and development of liver diseases caused by acute and chronic As poisoning are associated with the

synthesis and metabolism of cytokine regulatory networks composed of many proinflammatory and anti-inflammatory cytokines [6]. Meanwhile, As and its metabolites are toxic to hepatocytes, cause DNA damage, and produce several free radicals. The free radicals subsequently induce lipid peroxidation, which can cause cell dysfunction or directly attack the cells, triggering their damage [7]. Hepatocytes are repeatedly damaged and repaired, resulting in hepatic fibrosis [8]. Some studies also found that liver fibrosis is a reversible pathological process, and it is necessary that hepatic stellate cells reverse to their static state during liver fibrosis [9]. At present, research on As and arsenide compounds poisoning is limited.

Recently, numerous studies have confirmed that chronic As poisoning could induce liver injury. The effect of "As expulsion therapy" in managing chronic As poisoning is effective but has certain limitations. Research has established that the pectic polysaccharides of Momordica charantia could inhibit the oxidative stress of liver cells induced by sodium arsenite [10]. Besides, numerous studies have demonstrated that polysaccharides regulate immunity and protect the liver [11, 12]. Hence, our study explored effective and side effect-free hepatoprotective regimens from natural active products to manage chronic As poisoning.

Dictyophora is a cryptophytic root-parasitic fungus on withered bamboo. In Guizhou Province, five different types of Dictyophora are edible and medicinal. Dictyophora is rich in nutrition and fragrance and has a delicious taste. Generally, it is known as "flower of fungi" or "queen of fungi" [13]. In addition, some research has shown that Dictyophora is rich in amino acids, vitamins, polysaccharides, and inorganic salts. The dried Dictyophora contains protein, fat, total carbohydrate, bacterial sugar, crude fiber, and ash at concentrations of 19.4%, 2.6%, 60.4%, 4.2%, 8.4%, and 9.3%, respectively [14]. Among them, polysaccharide is a polyhydroxy aldehyde ketone polymer formed by ten or more monosaccharides through glycosidic bonds. It widely exists in higher plants, animal cell membranes, and microbial cell walls [15]. Furthermore, polysaccharides have many biological activities such as antioxidation, enhancing immunity, antitumor, neuroprotection, and antiaging [16]. In particular, studies have discovered that DIP have positive effects on liver damage [17]. The results of animal experiment in vivo showed that treatment with DIP could improve the excessive level of lipid profiles in liver injury caused by hyperlipidemia, as well as strengthen antioxidant status [18]. Meanwhile, DIP administration could improve obesity-associated hepatic metabolic impairment and ameliorate oxidative stress of liver by downregulating serum enzyme activities [19]. At present, many scientists have turned their attention to fungus polysaccharides, because they are natural and free of harmful side effects and have highly effective antioxidant properties. Moreover, their extraction process is relatively simple with minimal toxicity and side effects.

This study used rats whose metabolism mimics that of humans to comprehensively evaluate the relative efficacy function of DIP on As-induced liver injury. It has used the feeding method to establish an As poisoning model, which explores the influence of As on liver damage and evaluates the degree of liver fibrosis. Subsequently, after the intervention of DIP, we observed changes in serum biochemical indexes and pathological liver tissues. Taken together, our research has established that DIP have functional protective effects on As-induced liver injury in rats, and this function may regulate the expression of fibrosis-related proteins. Furthermore, this is the first study to explore the efficacy of different DIP levels on As-induced liver injury, providing new natural drug treatment insights for chronic As poisoning. Lastly, it gives a theoretical basis to advance the medicinal value of DIP.

2. Materials and Methods

2.1. Ethics Statement. This study was approved by the Guizhou Medical University experimental animal operation regulations and welfare management committee. All methods used herein were performed in accordance with the relevant guidelines.

2.2. Animal Grouping and Treatment. The study rats were randomly allocated into four groups and exposed to sodium arsenite (Sigma, USA, serial number: C1386-50G, purity: 98.9%) by feeding for three months at doses of 0, 25, 50, and 100 mg/kg. Subsequently, forty SD rats in the medium As group were randomly divided into four groups ($n = 10$ in each group, half male and half female) and exposed to DIP. Water extraction and alcohol precipitation methods were applied to extract DIP from Dictyophora, and the extraction rate was 13.016%. The detailed extraction steps and structure of DIP were reported in previous research by our research group [20]. DIP administration was by gavage once a day for 30 d, at a dose of 0, 2.5, 5, and 10 mg/ml (20 ml/kg BW). All rats were fed with a normal diet and free water.

2.3. Organization of Sample Collection. The experiment endpoint was fasting rats for 12 h, after which the weight of each group was measured. Cardiac blood was collected by an EDTA tube, centrifuged at 3000 rpm for 10 min, and stored at -80°C. After the rats were killed, the livers were separated, and the livers in each group were weighed. The liver weight of each group was calculated as liver weight/rat weight, using the unit grams per 100 g BW.

2.4. Analysis of Total As Content. The As content in the sample was determined by incomplete digestion flame atomic absorption spectrometry (AF-630A, Beijing Rayleigh Analytical Instrument Co, Ltd, China). Firstly, the 200 mg liver tissue was put in a clean 2 ml EP tube and ground with an electronic homogenizer. Then, a 7 ml nitric acid solution was added, and the tissue was fully digested in a microwave digester for 3 h. The samples were then stored for further determination.

2.5. Serum Biochemistry. The blood samples were collected from the cardiac apex, and plasma samples were obtained by centrifugation at 3000 rpm for 10 min, then used to obtain serum samples. The serum was used for measurement of alanine aminotransferase (ALT), aspartate aminotransferase

(AST), total protein (TP), albumin (ALB), total bilirubin (TBIL), and direct bilirubin (DBIL) by an automatic biochemical analyzer (AU400, Olympus Co, Ltd, Japan). Subsequently, four indexes of serum liver fibrosis, including hyaluronic acid (HA), laminin (LN), type III collagen (PC), and type IV collagen (CIV), were detected by ELISA Kits (Wuhan bode Bioengineering Co, Ltd, China).

2.6. H&E and Masson Staining. For each experimental group, a small piece of liver tissue was sampled from the left liver lobe and fixed in 4% formalin. After 24 h, the tissues were dehydrated in 70%, 80%, 90%, 95%, and 100% ethanol series and embedded in paraffin; then, 5-micron serial sections were sliced on a microtome. The sections were in turn dehydrated by graded ethanol (95%, 75%, 45%, and 25%), vitrificated by dimethylbenzene and wax immersion, and subjected to routine HE staining. After dehydration in ethyl alcohol, the sections were stained with a nuclear dye solution for 2 min, followed by cytoplasmic dye for 1 min. Afterward, the sections were stained with color separation solution and redyeing solution for 5 min at room temperature. The sections were then observed under a light microscope (BX51, Olympus, Japan, 400x). Histopathological scores were calculated with reference to Additional Table 1 and Additional Table 2.

2.7. Immunohistochemistry Analyses of TGF-β1, CTGF, and α-SMA. Immunohistochemistry staining was performed using the previously prepared paraffin sections. The stained sections were observed under the light microscope (BX51, Olympus, Japan, 400x). The integrated optical density (IOD) and area of all the collected images were measured by an Image-Pro Plus 6.0 image analysis system.

2.8. Statistical Analysis. The data are presented as the mean ± SEM. The comparisons among several groups were performed by one-way ANOVA using SPSS 17.0. Pairwise comparison and analysis of homogeneous variance were conducted using LSD, while uneven variance was analyzed by the Games-Howell method. $P < 0.05$ was considered statistically significant.

3. Results

3.1. Basic Information of Rats. All 80 SD rats survived. Compared with the control group, the low and medium As groups demonstrated slower weight gain, had medium body shape, and slightly sparse hair. Meanwhile, the high As group had very slow growth, extremely dim and sparse hair, and obvious depilation on the back and buttocks. The high As group rats demonstrated poor spirit, normal walking, and reduced activity. With time increment, the food intake of the control group increased significantly ($P < 0.05$). However, the food intake of rats in the high As group showed a significant ($P < 0.05$) downward trend with the increase of exposure dose and time (Figures 1(a) and 1(b)). Weekly evaluation of the rodent weights in the As poisoning group showed a slow increase with the increase of dose and time (Figures 1(c)).

3.2. DIP Ameliorates Liver Coefficient and As Content by As-Induced Liver Injury in Rats. This study evaluated the liver coefficient and As contents to assess the protective effects of DIP against As-induced injury in rats. As shown in Figure 2(a), the liver coefficient increased significantly with an increase in the As exposure dose ($P < 0.05$). Furthermore, the As content in the liver also increased significantly with an increase of exposure dose, relative to the control group ($P < 0.05$) (Figure 2(b)). Intervention with DIP resulted in a significant decrease ($P < 0.05$) of the liver coefficient of the treatment group (Figure 2(c)); the change was more substantial with increase in the polysaccharide dose. Meanwhile, the As content decreased with increase in the DIP concentration; there were significant differences between the As high-dose group and its control group ($P < 0.05$) (Figure 2(d)).

3.3. DIP Ameliorates As-Induced Liver Injury in Rats. In order to investigate the protective effect of DIP in As-induced liver injury, we assessed the liver histopathological changes; the serum ALT, AST, TP, A/G, and ALB; and bilirubin metabolism levels of TBIL and DBIL. Histological analysis by H&E staining in the low As group showed an increase in the volume of hepatocytes; the cytoplasm stained lightly and loosely than the control group (Figures 3(a)–3(d)). Meanwhile, hepatic edema and vacuolar degeneration could be observed. The results of the medium As group suggested that the volume of hepatocytes expanded further due to hepatocyte hydrodenaturation. Also, the hepatocytes showed varying degrees of edema and vacuolar degeneration and inflammatory cell infiltration in the stroma; hepatocyte liquefaction and necrosis were apparent. The results showed that hemangiectasis was more obvious in the high As group than in the medium-dose group. Besides, cell swelling, inflammatory cell infiltration, fiber hyperplasia, and other unique cell trauma characteristics were more apparent in the high As group. The As groups demonstrated a dose-dependent remarkable increase in the levels of serum ALT and AST ($P < 0.05$) (Figure 4(a)) and the bilirubin metabolism of TBIL and DBIL ($P > 0.05$) (Figures 4(c)); however, the TP, A/G, and ALB levels of As groups decreased to varying degrees, relative to the control ($P < 0.05$) (Figure 4(e)). Administering DIP significantly diminished the levels of ALT, AST, TBIL, and DBIL and increased the levels of TP, A/G, and ALB in the serum ($P < 0.05$) (Figures 4(b), 4(d), and 4(f)). Increasing the DIP dose decreased the collagen fibers around the hepatic lobule and the portal area, and inflammatory cell infiltration also decreased (Figures 3(e)–3(g)). These results suggest that DIP plays a protective role in mitigating As-induced liver injury in rats.

3.4. DIP Ameliorates As-Induced Liver Fibrosis in Rats. We detected four markers of liver fibrosis in serum to further evaluate the degree of liver fibrosis in rats. The results showed that the concentrations of LN, HA, PCIII, and CIV had a significant increasing trend relative to the control group ($P < 0.05$) (Figure 5(a)). We also performed Masson staining to precisely confirm the results of liver fibrosis. In turn, we observed a few blue-stained collagen fibers around
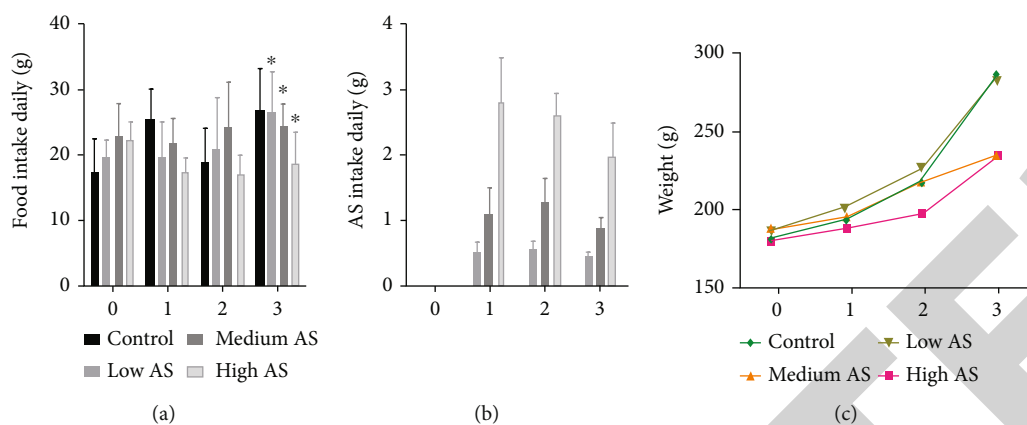
Figure 1: General situation of rats by sodium arsenic: (a) As group rats of changes in food intake; (b) As group rats of average daily taken As content; (c) As group rats of weight trend chart. Values are mean ± standard deviation, and $n = 10$. *$P < 0.05$.
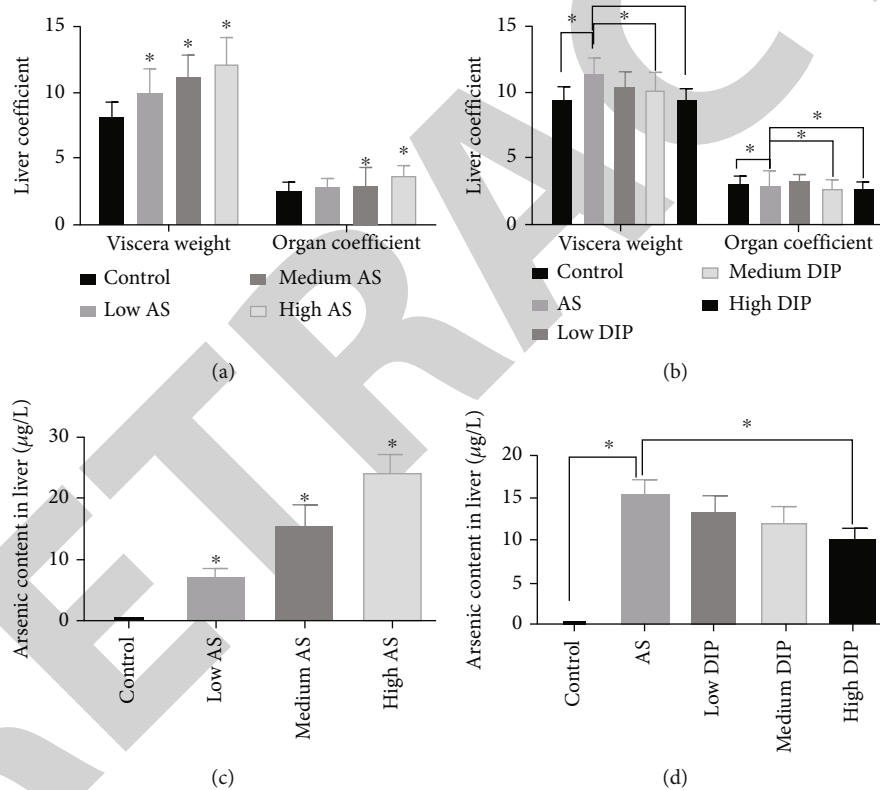
Figure 2: Organ coefficient and As content in liver of rats: (a, b) changes of the rat liver coefficient and the As content in the liver in the model group; (c, d) changes of the rat liver coefficient and the As content in the liver in the DIP group. Values were mean ± standard deviation, and $n = 10$. *$P < 0.05$.

the hepatic lobule and portal area, and the collagen fibers around the hepatic lobule were slightly proliferated in the low As group (Figure 6(b)). The results of the medium As group revealed significant inflammatory cell infiltration in the interstitium, with moderate hyperplasia of collagen fibers around liver lobules (Figure 6(c)). Moreover, a large number of fibrous septa formed in the peripheral area of the lobules, and there was obvious inflammatory cell infiltration in the interstitium of the high As group. Meanwhile, the collagen

fibers around the hepatic lobules were moderately and severely proliferated (Figure 6(d)). According to the image analysis system, the area of proliferative fiber in the liver of rats increased with increasing exposure dose. There were statistically significant differences in the area of collagen fiber deposition in the low, medium, and high As groups, compared with the control group ($P < 0.05$) (Figure 6(h)). In brief, degeneration and liver fibrosis demonstrated an inevitable surge with increasing concentration of sodium arsenite.
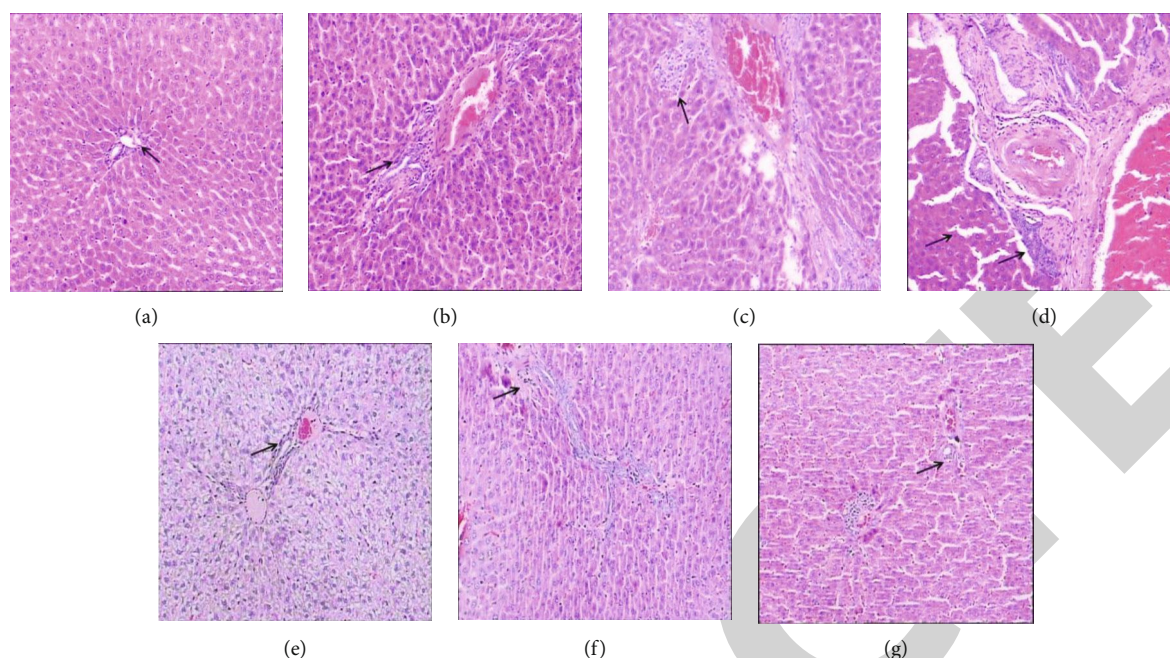
Figure 3: HE staining of the liver: (a) the control group; (b) the low As group; (c) the medium As group; (d) the high As group; (e) the low DIP group; (f) the medium DIP group; (g) the high DIP group (HE ×100).

DIP treatment reversed the levels of LN, HA, PCIII, and CIV caused by chronic As exposure (Figures 5(b)). Subsequently, fibrous tissue hyperplasia of hepatocytes in the treatment group was significantly less than that in the As poisoning group (Figures 6(e)–6(g)). Meanwhile, the area of proliferative fiber in the liver of rats decreased after the administration of DIP; there were statistically significant differences among the low-, medium-, and high-dose polysaccharide groups relative to the As poisoning control group ($P < 0.05$) (Figure 6(i)).

3.5. DIP Inhibits the Expression of Fibrosis-Related Protein TGF-β1, CTGF, and α-SMA Levels. To further determine the antifibrosis function of DIP-triggered inhibition of TGF-β1, CTGF, and α-SMA expression, we evaluated the expression levels of these proteins in rat livers. TGF-β1 was only slightly expressed in the portal area and the wall of the central lobular vein in the control group; however, its expression increased with an increase in the As dose. The TGF-β1-positive cells were mostly concentrated in the portal area and proliferative collagen fibers, with a clear contour (Figures 7(a)–7(d)). The optical densities of TGF-β1 proteins from the livers of As-treated rats were significantly higher than those from control livers ($P < 0.05$) (Table 1). In addition, CTGF was expressed in liver parenchymal cells and stromal cells of the portal area, as demonstrated by a brownish-yellow coloration in positive regions. The expression of CTGF increased with increase in the exposure dose, and the positive cells were mostly concentrated in the interstitial cells of the portal area, with a clear contour (Figures 8(a)–8(d)). We also found that the optical density of CTGF protein expression increased significantly ($P < 0.05$) with increase in exposure dose (Table 1). α-SMA

was expressed in the cell membrane or cytoplasm, and its positive products were yellow and brown. In the medium and high As groups, α-SMA had high expression in the cell membrane and cytoplasm. The expression of α-SMA showed an increased response in a dose-dependent manner according to the As concentration (Figures 9(a)–9(d)). The optical density of the α-SMA protein was also significantly higher than that of the control group ($P < 0.05$) (Table 1). However, DIP posttreatment decreased the expression of TGF-β1, CTGF, and α-SMA proteins in the liver of rats, and the optical densities showed statistically significant decrease with increase in the DIP dose ($P < 0.05$) (Figures 7–9(e)–9(g), Table 2). These data indicate that DIP intervention could inhibit the expression of TGF-β1, CTGF, and α-SMA proteins, combined with the results of four indicators of fibrosis LN, HA, PCIII, and CIV concentration; DIP has the function of antifibrosis and liver protection.

4. Discussion

The liver is one of the main detoxification organs in the human body. In long-term chronic As poisoning, substantial amounts of organic As can be oxidized (III)As to (V)As by metabolizing the liver and reduced (V)As to (III)As or As methylation [21, 22]. Dictyophora contains a variety of trace elements and nutrients. And its polysaccharide is a high bioactivity macromolecule with high curative effects in lowering blood pressure, blood sugar, antitumor, and immune stimulation [23]. Our previous studies have shown that DIP intervention on As-induced L-02 cells alleviates the changes in cell viability, apoptosis, and oxidation stress [24]. Meanwhile, DIP could reduce arsenic content in the liver, increase

(a)

(b)

(c)

(d)

(e)

(f)
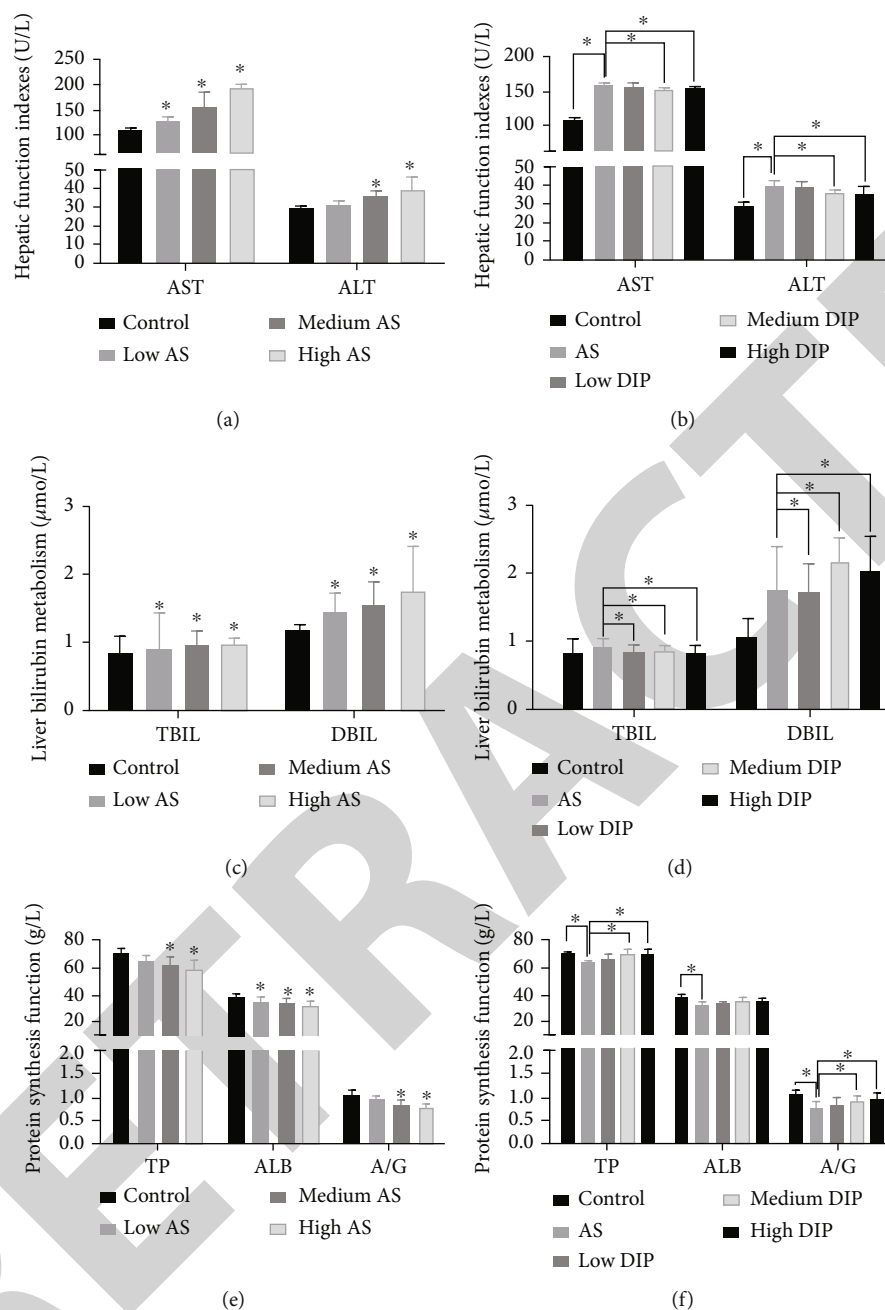
Figure 4: Serum-related indexes of liver injury in rats: (a) changes of the rat liver damage index of serum enzymology in the model group; (b) changes of the rat liver damage index of serum enzymology in the DIP group; (c) changes of bilirubin metabolism in the model group; (d) changes of bilirubin metabolism in the DIP group; (e) changes of protein synthesis function in the model group; (f) changes of protein synthesis function in the DIP group. Values are mean ± standard deviation, and $n = 10$. *$P < 0.05$.

As in blood and urine, and inhibit liver tissue damage caused by sodium arsenite [25, 26], suggesting that DIP could inhibit As toxicity at cellular and whole-organism levels and protect liver function. Therefore, on the basis of the previous, we explored the DIP that had a substantial protective effect on the occurrence and development of As-induced liver fibrosis in the present study.

We established a rat model of As poisoning by the feeding method, the research results showed that As contents and organ coefficient of the liver increase in each As-

exposed group of rats, and the trend of weight gained slowly. The serum hepatic enzyme indexes of ALT and AST and metabolic levels of TBIL and DBIL in bilirubin increased, while the TP, A/G, and ALB levels decreased at varying degrees. These results indicated that the rats in each exposure group had different degrees of liver damage. (III)As exposure significantly increased the levels of serum biochemical indexes, which is consistent with previous study findings [27]. The DIP was entered intervention treatment after three months. Compared with the As poisoning control

(a)

(b)
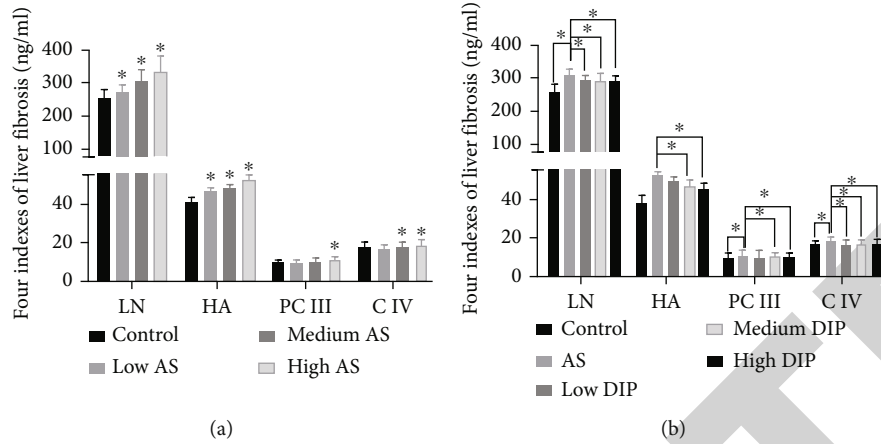
FIGURE 5: Changes of four indexes of liver fibrosis in rats. (a) Changes of four indexes of liver fibrosis in the model group. (b) Changes of four indexes of liver fibrosis in the DIP group. Values are mean ± standard deviation, and $n = 10$. $^{*}P < 0.05$.

(a)

(b)

(c)

(d)

(e)

(f)

(g)

(h)

(i)
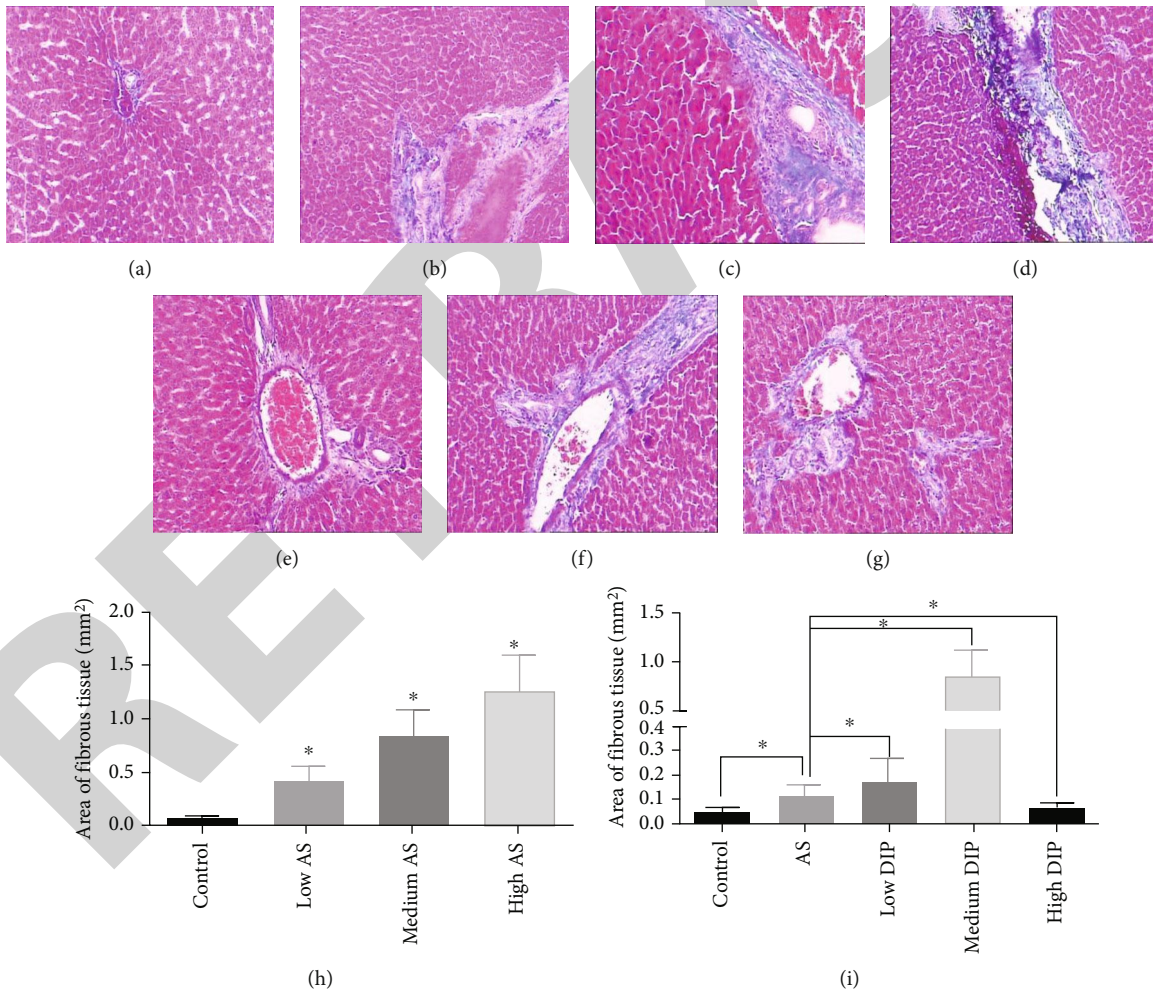
FIGURE 6: Masson staining of the liver: (a) the control group; (b) the low As group; (c) the medium As group; (d) the high As group; (e) the low DIP group; (f) the medium DIP group; (g) the high DIP group (Masson ×100); (h) the rat liver hyperplasia of fibrous tissue area measurement in the model group; (i) the rat liver hyperplasia of fibrous tissue area measurement in the DIP intervention group. Values are mean ± standard deviation, and $n = 10$. $^{*}P < 0.05$.
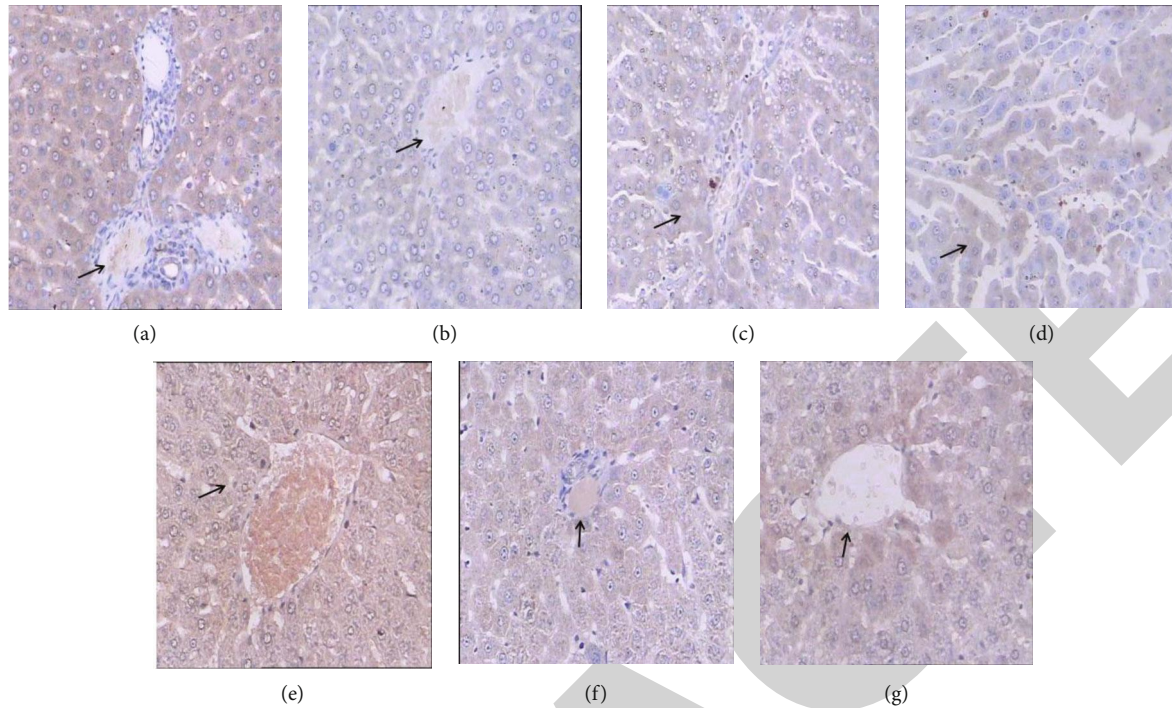
FIGURE 7: Immunohistochemical staining of TGF-β1: (a) the control group; (b) the low As group; (c) the medium As group; (d) the high As group; (e) the low DIP group; (f) the medium DIP group; (g) the high DIP group (×400).

TABLE 1: TGF-β1-, CTGF-, and α-SMA-positive color intensity and density value in the As model group ($n = 10$, $\bar{x} \pm s$).

Group	TGF-β1		CTGF		α-SMA	
	Immune intensity	Density value	Immune intensity	Density value	Immune intensity	Density value
Control	+	150.45 ± 3.14	+	118.48 ± 9.52	+	123.63 ± 7.42
The low AS group	+~++	157.23 ± 2.29^a	+~++	135.23 ± 10.13^a	+	130.56 ± 9.15
The medium AS group	+~++	160.67 ± 1.24^a	++~+++	156.47 ± 11.24^a	+~++	155.85 ± 8.84^a
The high AS group	++~+++	166.76 ± 3.34^a	++~+++	164.25 ± 9.34^a	+~+++	168.25 ± 11.34^a

Note: [a]compared with the normal group, $P < 0.05$. [b]Compared with the As control group, $P < 0.05$.

group, the protective effect on the liver injury was more obvious with increasing dose of DIP, suggesting that DIP has antagonistic effects on As-induced liver injury in rats.

Liver fibrosis refers to the pathological process of inflammation and necrosis of hepatocytes caused by various factors, which lead to the deposition of extracellular matrix (ECM), cytokine imbalance, and generation of liver fibroblasts [28]. Hence, liver fibrosis induced by sodium arsenite is a slow disease process in which many cellular and inflammatory factors participate, including hepatocyte hydrodegeneration, hepatocyte ballooning, hepatocyte necrosis (inflammatory infiltration), hepatocyte regeneration, fibrous tissue proliferation, and liver fibrosis [29]. There are four serum indicators for liver fibrosis, LN, HA, PCIII, and CIV. HA is a matrix component synthesized by stromal cells; it can accurately and sensitively reflect the amount of fiber produced in the liver and the damage extent of liver cells, which is a sensitive index of liver fibrosis and cirrhosis [30]. CIV is the standard of collagen synthesis and the primary component of basement membrane reticular structure.

In the initial stage of liver fibrosis, CIV proliferates and transforms rapidly and finally forms an extensive basement membrane with the precipitation of LN [31]. In this study, the concentrations of LN, HA, PCIII, and CIV in As-exposed groups increased with increase in the exposure dose; there was a positive correlation. This finding suggests that long-term As exposure can induce hepatic fibrosis. These findings are consistent with Tao et al.'s results that long-term exposure to sodium arsenite can induce hepatic stellate cell (HSC) activation and hepatic fibrosis in SD rats [32]. Combined HE and Masson staining can accurately determine the level of tissue fibrosis. The current study showed that liver fibrosis aggravates the degeneration and necrosis of liver cells and inflammatory cell infiltration with prolonged As exposure time. A large number of fibrous septa and moderately to severely proliferated collagen fibers formed around the hepatic lobules. Meanwhile, the structure of liver lobules was abnormal, and the cell lines had a disordered arrangement. It is obvious that inflammatory cells infiltrate the interstitial tissues, accompanied by a
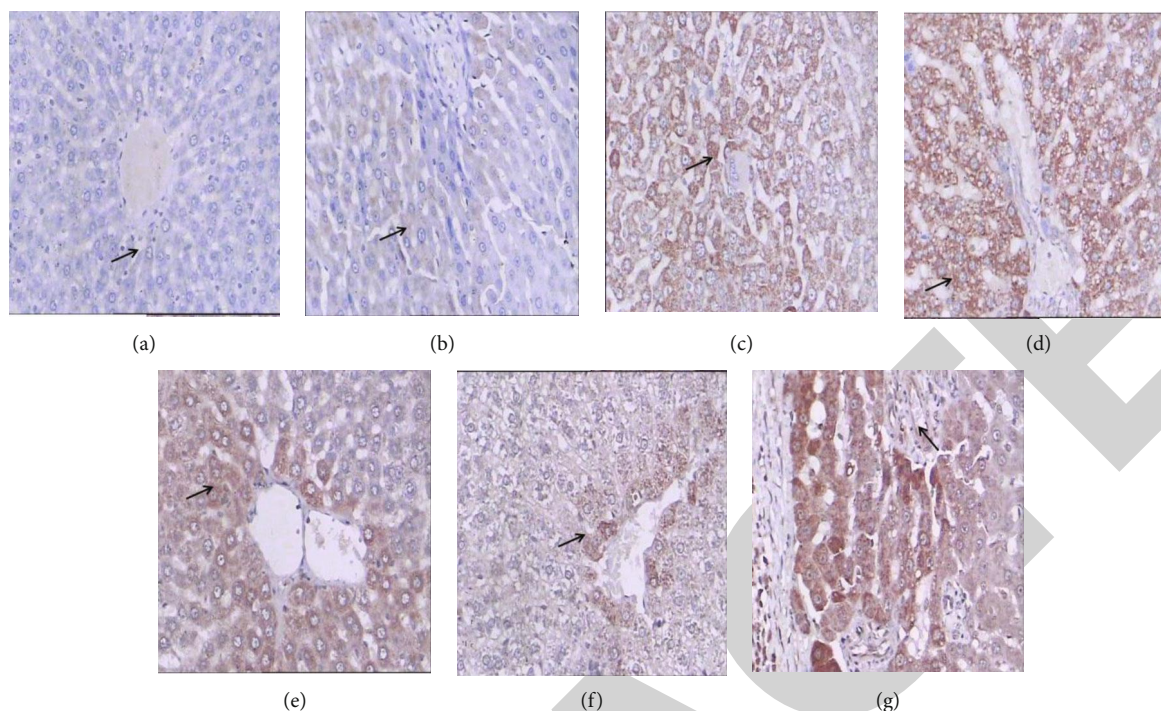
FIGURE 8: Immunohistochemical staining of CTGF: (a) the control group; (b) the low As group; (c) the medium As group; (d) the high As group; (e) the low DIP group; (f) the medium DIP group; (g) the high DIP group (×400).
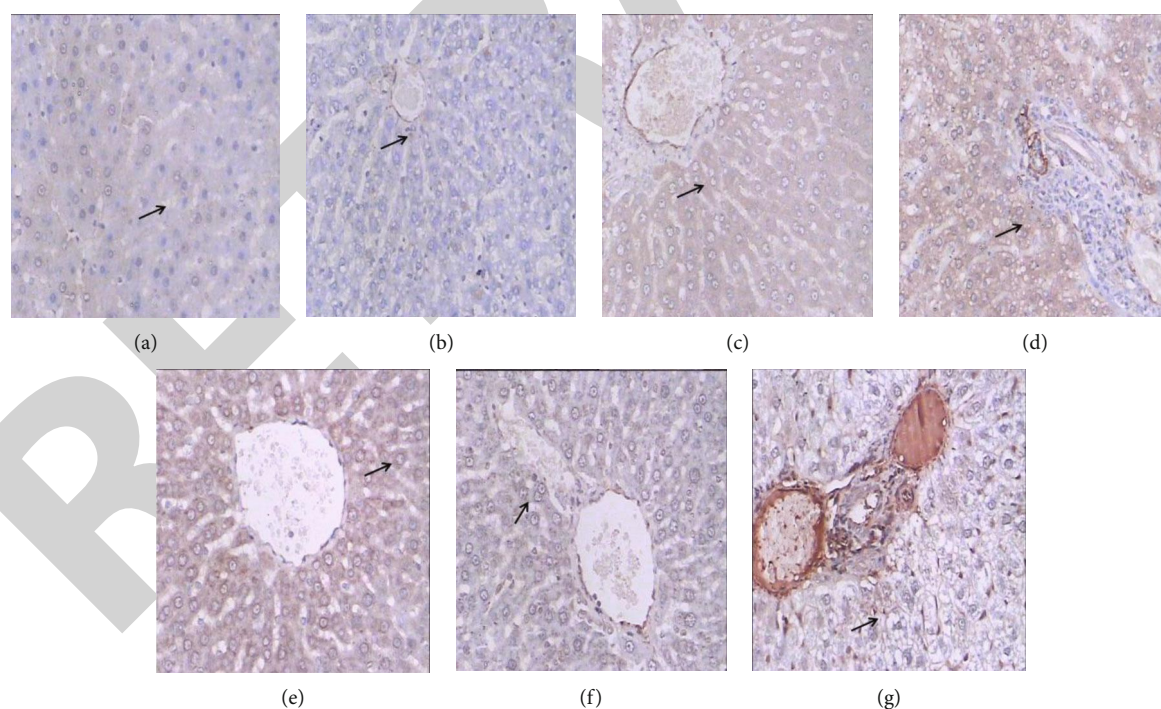
FIGURE 9: Immunohistochemical staining of α-SMA: (a) the control group; (b) the low As group; (c) the medium As group; (d) the high As group; (e) the low DIP group; (f) the medium DIP group; (g) the high DIP group (×400).

progressive increase of fibrous tissue proliferation. This result suggested that As exposure could cause liver injury in rats, and the degree of liver fibrosis was aggravated with increase in dose and time. Intervention with DIP decreased the con-

centrations of LN, HA, PCIII, and CIV with increasing polysaccharide doses. Following intervention, the collagen fibers in the peripheral and portal areas of the liver lobule and inflammatory cells decreased, and the area of hyperplastic

Table 2: TGF-β1-, CTGF-, and α-SMA-positive color intensity and density value in the DIP group ($n = 10$, $\bar{x} \pm s$).

Group	TGF-β1		CTGF		α-SMA	
	Immune intensity	Density value	Immune intensity	Density value	Immune intensity	Density value
Control	+	149.34 ± 2.42	+	110.07 ± 11.02	—	131.19 ± 10.57
AS control group	+~+++	161.49 ± 1.13[a]	++~+++	149.34 ± 10.13[a]	++	159.36 ± 11.13[a]
The low DIP group	+~+++	158.67 ± 1.07	+~+++	141.22 ± 13.82	+~++	155.03 ± 9.88
The medium DIP group	+~++	154.44 ± 2.24[b]	+~++	132.29 ± 10.24[b]	+~++	137.55 ± 10.24[b]
The high DIP group	+~++	151.82 ± 2.82[b]	+~++	128.01 ± 11.34[b]	+	127.25 ± 12.18[b]

Note: [a]compared with the normal group, $P < 0.05$. [b]Compared with the As control group, $P < 0.05$.
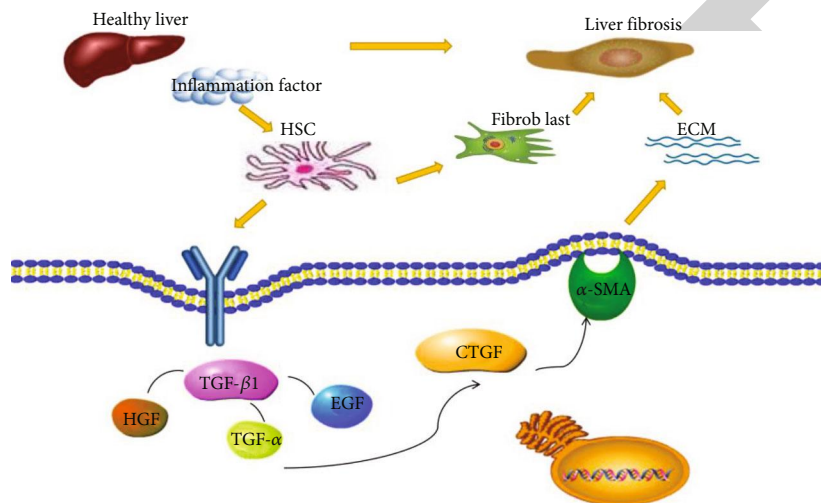
Figure 10: Schematic diagram of hepatic fibrosis-related proteins. The inflammatory cells and damage factors can activate HSC in liver tissue and increase the synthesis of TGF-β1, which led to proliferation of fibrous connective tissue and upregulated the expression of CTGF. And the synthesis and transformation of fibroblasts into myofibroblasts, thereby regulating the expression of α-SMA, were increased the synthesis of ECM and caused liver fibrosis finally.

fiber demonstrated a reducing trend, suggesting that DIP has antagonistic effects on the progression of liver fibrosis.

When the damage of inflammatory cells and damage factors (alcohol, virus, drugs, poisons, parasites, etc.) to the liver exceeds the compensatory capacity of the body, it releases various inflammatory factors, activating HSC to transform into myofibroblast cells, further leading to substantial precipitation of ECM and proliferation of fibrous connective tissue. And the reconstructed hepatic lobules and formed pseudolobules or nodules develop into liver fibrosis, cirrhosis, and liver cancer, eventually leading to liver failure and death. However, synthesis and degradation of ECM are mainly controlled by TGF-β1. When liver injury occurs, activation of hepatocyte leads to the increase of TGF-β1 synthesis, with aggravating degree of fibrosis; CTGF was found to be overproduced in liver tissue. CTGF is an important downstream factor that mediates the profibrotic effect of TGF-β1 and regulates the growth of fibroblasts and the secretion of ECM. Both TGF-β1 and CTGF can stimulate the synthesis of fibroblasts to transform into myofibroblasts, thus upregulating the expression of α-SMA and increasing the synthesis of ECM [33, 34] (Figure 10). As an important fibrosis cytokine, TGF-β1 is an initiating factor of liver fibrosis [35]. The protein expression was located in

the cell cytoplasm, and the positive products were brown-yellow. Since TGF-β1 plasma concentrations can be significantly increased and are closely related to ALT and AST levels in severe liver injury, the protein TGF-β1 is a marker of liver inflammation and necrosis [36]. Our results showed that the expression of TGF-β1 increased with increasing exposure dose in the liver tissue of rats. The TGF-β1-positive cells were mostly concentrated in the portal area and proliferative collagen fibers with a clear outline. CTGF is a strong, sensitive index for expression, mainly expressed in the liver parenchymal cells and interstitial cells in the portal area. The CTGF-positive product is brown-yellow, while strongly positive is brown. We found high expression in the portal area and cytoplasm in the moderate and high As-exposed group, and the positive cells were mainly concentrated in the interstitial cells. The expression of α-SMA was located in the cell membrane or cytoplasm; its positive products are yellow and brown. We found high α-SMA expression in the membrane and cytoplasm of medium and high As-exposed groups. The expression level of α-SMA in the liver of rats increased with increasing exposure dose. DIP intervention decreased the expression of TGF-β1, CTGF, and α-SMA protein in rat liver. The combined results of the four serum liver fibrosis indexes, LN, HA,

PCIII, and CIV, suggested the synthesis of TGF-β1 inhibited by DIP might regulate the expression of CTGF and decrease the proliferation of fibrinogen and fibroblasts, which reduced the synthesis of fibroblasts to transform into myofibroblasts. And a decrease of myofibroblasts downregulated the expression of α-SMA, which affected the synthesis and precipitation of ECM and alleviated the liver fibrosis caused by exposure to As. The activation of cytokines may relate to the regulation of relevant pathways, which needs further study.

Taken together, long-term exposure of SD rats to sodium arsenite by the feeding method can cause liver damage, and the degree of harmful effects is positively correlated with the concentration of As. The current study results demonstrated that DIP mitigated the serum AST, ALT, TP, ALB, A/G, TBIL, and DBIL levels and the concentrations of HA, LN, PCIII, and CIV. Thus, DIP alleviates the liver histopathological changes caused by exposure to As. Further study indicated that DIP significantly inhibited As-induced liver fibrosis by decreasing the expressions of fibrosis-related proteins TGF-β1, CTGF, and α-SMA. This finding suggests that DIP could regulate the synthesis and degradation of ECM and inhibit fibroblast proliferation, which alleviated the liver fibrosis caused by exposure to As. Combined with the results of our previous research, the current study findings suggest that DIP has excellent prospects for application in protecting the liver.

Data Availability

The data presented in this study are available on request from the corresponding author.

Ethical Approval

The protocol of this study was approved by the Guizhou Medical University experimental animal operation regulations and welfare management committee. Animal handling and care were carried out throughout the experiment according to Chinese National Guidelines for Experimental Animal Welfare.

Conflicts of Interest

The authors declare that the research was conducted in the absence of any commercial or financial relationships that could be construed as a potential conflict of interest.

Authors' Contributions

Guoze Wang and Peipei Zuo contributed equally to this work.

Acknowledgments

Supplementary Materials

Supplementary 1. Supplementary Table 1: the histopathological scoring system in the As model group. Supplementary 2. Supplementary Table 2: the histopathological scoring system in DIP intervention. *(Supplementary Materials)*

References

[1] Y. Z. Shao, H. J. Zhao, Y. Wang et al., "The apoptosis in arsenic-induced oxidative stress is associated with autophagy in the testis tissues of chicken," *Poultry science*, vol. 97, no. 9, pp. 3248–3257, 2018.

[2] M. E. Schreiber and I. M. Cozzarelli, "Arsenic release to the environment from hydrocarbon production, storage, transportation, use and waste management," *Journal of Hazardous Materials*, vol. 411, p. 125013, 2021.

[3] I. D. Rae, "Arsenic: its chemistry, its occurrence in the earth and its release into industry and the environment," *ChemTexts*, vol. 6, no. 4, 2020.

[4] C. Li, S. Zhang, L. Li, Q. Hu, and S. Ji, "Ursodeoxycholic acid protects against arsenic induced hepatotoxicity by the Nrf2 signaling pathway," *Frontiers in Pharmacology*, vol. 11, article 594496, 2020.

[5] U. Okereafor, M. Makhatha, L. Mekuto, N. Uche-Okereafor, T. Sebola, and V. Mavumengwana, "Toxic metal implications on agricultural soils, plants, animals, aquatic life and human health," *International journal of environmental research and public health*, vol. 17, no. 7, p. 2204, 2020.

[6] J. Liu, H. Zhao, Y. Wang, Y. Shao, J. Li, and M. Xing, "Alterations of antioxidant indexes and inflammatory cytokine expression aggravated hepatocellular apoptosis through mitochondrial and death receptor-dependent pathways in Gallus gallus exposed to arsenic and copper," *Environmental Science and Pollution Research*, vol. 25, no. 16, pp. 15462–15473, 2018.

[7] D. Ezhilarasan, "Oxidative stress is bane in chronic liver diseases: clinical and experimental perspective," *Arab Journal of Gastroenterology*, vol. 19, no. 2, pp. 56–64, 2018.

[8] S. J. Flora, "Arsenic-induced oxidative stress and its reversibility," *Free Radical Biology and Medicine*, vol. 51, no. 2, pp. 257–281, 2011.

[9] F. Alegre, P. Pelegrin, and A. E. Feldstein, "Inflammasomes in liver fibrosis," *Seminars in Liver Disease*, vol. 37, no. 2, pp. 119–127, 2017.

[10] H. Perveen, M. Dash, S. Khatun, M. Maity, S. S. Islam, and S. Chattopadhyay, "Electrozymographic evaluation of the attenuation of arsenic induced degradation of hepatic SOD, catalase in an in vitro assay system by pectic polysaccharides of _Momordica charantia_ in combination with curcumin," *BB Reports*, vol. 11, pp. 64–71, 2017.

[11] Z. E. Rashed, E. Grasselli, H. Khalifeh, L. Canesi, and I. Demori, "Brown-algae polysaccharides as active constituents against nonalcoholic fatty liver disease," *Planta Medica*, vol. 88, pp. 9–19, 2022.

Research Article

In Silico and *In Vitro* Screening of Natural Compounds as Broad-Spectrum β-Lactamase Inhibitors against *Acinetobacter baumannii* New Delhi Metallo-β-lactamase-1 (NDM-1)

Aparna Vasudevan [iD],[1,2] **Dinesh Kumar Kesavan** [iD],[1,2] **Liang Wu** [iD],[2] **Zhaoliang Su** [iD],[1,2] **Shengjun Wang** [iD],[2] **Mohan Kumar Ramasamy** [iD],[3] **Waheeta Hopper** [iD],[4] and **Huaxi Xu** [iD][1,2]

[1]*International Genomics Research Center (IGRC), Jiangsu University, Zhenjiang 212013, China*
[2]*Department of Immunology, School of Medicine, Jiangsu University, Zhenjiang 212013, China*
[3]*Interdisciplinary Institute of Indian System of Medicine, SRM Institute of Science and Technology, Tamil Nadu, India*
[4]*Department of Biotechnology, School of Bioengineering, Faculty of Engineering & Technology, Kattankulathur Campus, SRM Institute of Science & Technology, India*

Correspondence should be addressed to Huaxi Xu; xuhx@ujs.edu.cn

Antibiotic resistance is one of the significant problems globally; there is an increase in resistance with introducing every new class of antibiotics. Further, this has become one of the reasons for arising of new resistance mechanisms in *Acinetobacter baumannii*. In this study, we have screened natural compounds as a possible inhibitor against the NDM-1 β-lactamase enzyme from *A. baumannii* using a combination of *in silico* methods and *in vitro* evaluation. The database of natural compounds was screened against NDM-1 protein, using Glide docking, followed by QM-polarised ligand docking (QPLD). When the screened hits were validated *in vitro*, withaferin A and mangiferin had good IC$_{50}$ values in reducing the activity of NDM-1 enzymes, and their fractional inhibitory concentration index (FICI) was ascertained in combination with imipenem. The withaferin A and mangiferin-NDM-1 docking complexes were analyzed for structural stability by molecular dynamic simulation analysis using GROMACS for 100 ns. The molecular properties of the natural compounds were then calculated using density functional theory (DFT). Withaferin A and mangiferin showed promising inhibitory activity and can be a natural compound candidate inhibitor synergistically used along with carbapenems against NDM-1 producing *A. baumannii*.

1. Introduction

The worldwide increase in carbapenem resistance among Gram-negative bacteria has become a significant clinical concern. *Acinetobacter* is one such species that showed high resistance after just four years of its identification in 1971 and as early as the 1990s. They were resistant to imipenem, the trusted drug of choice [1] [2]. Resistance to carbapenems in *A. baumannii* (carbapenem-resistant *A. baumannii* (CRAB)) can itself make them highly resistant. Apart from the intrinsic resistance determinants, oxacillinases (Ambler Class D) and Metallo β-lactamases (Ambler Class B) are major contributors to resistance against carbapenems [3].

There are three subclasses under the Metallo β-lactamases, B1, B2, and B3; the New Delhi Metallo-β-lactamase 1 (NDM-1) belongs to B1. NDM-1 is an emerging concern among the heterogeneous group of carbapenemases, first described from *Klebsiella pneumoniae*, *Escherichia coli*, *Pseudomonas aeruginosa*, *A. baumannii*, and, more recently, Enterobacteriaceae [4] [5] [6].

NDM-1-positive strains have been rapidly and widely spreading in many countries among *A. baumannii* strains [7]. NDM-1-positive strains are resistant to fluoroquinolones, aminoglycosides, and β-lactams (especially carbapenems) while being susceptible to colistin and sometimes to tigecycline. NDM-1 resistance dissemination occurs by

transferring resistance plasmids with the bla_{NDM-1} gene, making them a severe clinical and public health concern [7].

The crystal structure of NDM-1 reveals two zinc ions, which are essential for cleaving the C-N bond in the β-lactam ring of the antibiotic, thereby inactivating them. NDM-1 structure comprises lysine-rich residues that help protonate lactam nitrogen in β-lactam antibiotics [8]. MBLs are resistant to commercially available β-lactamase inhibitors, such as clavulanic acid, sulbactam, tazobactam, and avibactam, and there are no commercially available MBL inhibitors meant for clinical use [9]. Increased resistance to carbapenem in *A. baumannii* is often seen with a high mortality rate. The current management of infections and outbreaks due to MDR *A. baumannii* requires a combination of medical interventions, antibiotic stewardship, environmental, and prevention of resistance dissemination. There is an urgent need for newer ways to combat the infections; one is to synergistically enhance the bioactivity of the available drugs with inhibitors of resistance determinants [10]. The purpose of this research is to search for natural compounds that can inhibit acquired β-lactamases, which contribute to carbapenem resistance in *A. baumannii*, specifically NDM-1 Metallo-lactamase. The workflow for the study is given as in Figure 1. A preliminary computational method was used to identify a subset of compounds from a database of natural compounds by predicting their binding mode against the target proteins from *in silico* molecular docking experiments and density functional theory (DFT). The top hits were validated by molecular dynamic simulation studies and *in vitro* enzyme inhibition assay, and fractional inhibitory concentration and *in silico* ADME properties were predicted.

2. Materials and Methods

2.1. Protein and Ligand Preparation. The protein sequence information of NDM-1 from *A. baumannii* was retrieved from NCBI (accession number: ALD19783). The 3D structure of NDM-1 protein was modeled using Swiss Prot 3D modeling server [11]. Homology modeling commonly results in unfavourable bond lengths, bond angles, torsion angles, and contacts in protein models. As a result, it was critical to minimize energy to standardize local bond and angle geometry and relax near contacts in the geometric chain. The 3D model of NDM-1 was validated after optimization using PROCHECK [12], ERRAT [13], and VERIFY3D [14] programs from the Structural Analysis and Verification Server (SAVES). PROCHECK was used to assess the stereochemical consistency of the protein structure, and the VERIFY3D program was used to evaluate the 3D protein structure by analyzing the compatibility of an atomic model (3D) with its amino acid sequence (1D).

All analyses were performed using Schrödinger LLC-Maestro version 10.2. The modeled 3D protein and PDB structures were minimized with OPLS-2005 force field using protein preparation wizard in Maestro. Using OPLS-3e force field in Prime program, missing hydrogens atoms, missing side chain atoms, and missing loops were inserted. Restrained minimization was used to minimize hydrogen

atoms and heavy atoms, and a receptor grid generation module was used to generate a grid using the binding site residues of modeled NDM-1. The natural compounds collected with known antibacterial bioactivity from plants were obtained from literature and Dr. Duke's Phytochemical and Ethnobotanical Database [15]. The structures of the compounds were retrieved from the PubChem database and subjected to ligand preparation. LigPrep module assigns proper bond orders and corrects the protonation and ionization states of the compounds; after that, each ligand's tautomeric and ionization states were formed. Default values were used for pre- and postprocess minimization; a maximum of 100 conformers were generated per structure. Each minimized conformer was filtered through an 11.4 kcal/mol (50 kJ/mol) relative energy window with a maximum atom deviation of 2.00 Å.

2.2. Glide XP Docking. XP Glide module was used to perform molecular docking studies with the natural compound database against NDM-1. The XP docking score was enhanced by several factors such as the addition of large desolvation penalties to both ligand and receptor; a specific structural motif that contributes to binding affinity; and sample and an algorithm for scoring functions. The XP docking scoring functions include Ecoul (Coulomb energy), EvdW (van de Waals energy), Ebind (components favouring binding), and Epenalty (components impeding binding) [16]. The top-ranking poses were chosen based on the Glide ratings for further analysis. Finally, the top eight compounds were selected for further investigation.

2.3. QPLD Docking. QM-polarised ligand docking (QPLD) method was used to dock all ligand molecules with modeled NDM-1 protein. QPLD docking method is used to improve docking scores by calculating quantum mechanics and molecular mechanics (QM/MM) approach using QSITE program coupled with Jaguar for QM region and the IMPACT molecular modeling code for MM region [17]. The QM/MM energy is calculated as the complex's Coulomb–van der Waals force, calculated from the ligand's electrostatic potential energy. This is derived from a single-point calculation for the QM region using density functional theory using the 6-31G∗/LACVP∗ basis set, B3LYP density functional, and "Ultrafine" SCF accuracy level (iacc = 1 and iacscf = 2) [18]. Briefly, three steps were included in the protocol: first, generating the best pose for ligand docking using standard precision (SP) scoring mode followed by XP refinement; second, initial partial charges on ligand atoms were removed, and QM-ESP charges were calculated from the electrostatic potential energy surface of the ligand, generated from a single-point calculation using B3LYP/6-31G∗ level within the protein environment and density function for the QM region; and third, the ligands were redocked in the most energetically favourable pose using Glide standard docking for QPLD refinement, and then, the level of quantum–mechanical treatment was set at Fast mode [19].

2.4. DFT Calculations. The density functional theory (DFT) analysis was performed for the natural compounds. The
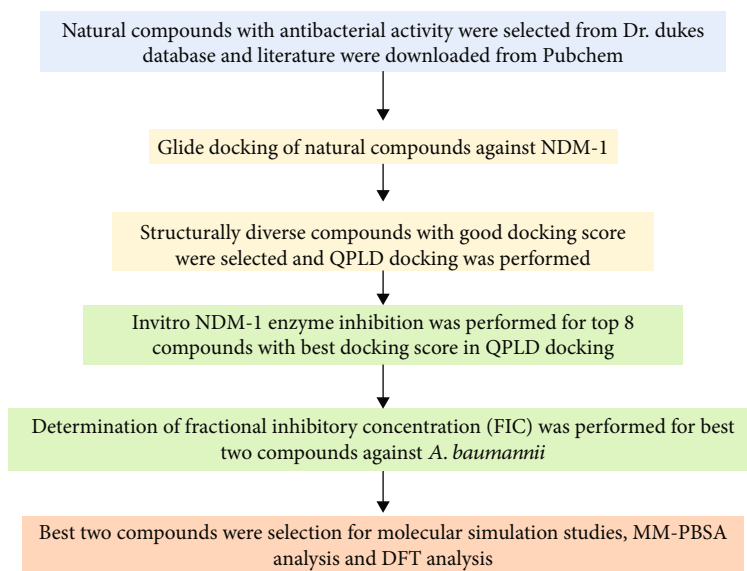
FIGURE 1: Flow chart of virtual screening, filtering, and experimental screening strategy for identifying NDM-1 inhibitors.

minimized ligands obtained from LigPrep were used for DFT calculations using the Jaguar panel of Maestro Schrödinger. Recognized conformers were studied by DFT using the Jaguar module in Maestro. DFT calculations were performed to determine the electronic molecular properties, such as electron density, molecular electrostatic map, and frontier molecular orbital density fields, revealing biological activity and molecular characteristics (lowest and highest occupied molecular orbital). These compounds were measured using DFT using a Jaguar module depending on the solvation condition. Using the 491 6-31G** basis set standard, the conformers were analyzed using the Lee-Yang–Parr correlation functional (B3LYP) and Becke's three-parameter exchange potential [20]. With single-point calculations, the implicit redemption model of the Poisson–Boltzmann Finite (PBF) was calculated. Dipole moment, highest occupied molecular orbital (HOMO), lowest unoccupied molecular orbital (LUMO) energy, and lowest unoccupied molecular orbital (MESP) were used to calculate the molecular electrostatic properties. The electrostatic potentials were calculated using the molecule's van der Waals (vdW) contact surface region. The colour-coded surface values showed the positive electrostatic potentials and total molecular size. The most positive electrostatic potential regions are indicated by the darkest blue colour, whereas the most negative electrostatic potential regions are indicated by the deepest red colour [19, 21].

2.5. ADME Analysis.

Absorption, distribution, metabolism, and excretion (ADME) properties of natural compounds were calculated using the QikProp module in Maestro. QikProp module predicts the several pharmaceutically relevant properties and other physically significant ADME property descriptors for the ligand. The essential properties for drug-likeness, like log P, human oral absorption, and Lipinski's rule of 5, were calculated in the QikProp module [22].

2.6. Molecular Simulation.

The docked protein-ligand complex of apoproteins and ligand complexed NDM-1 were simulated to study the stability using molecular dynamic simulation analysis software GROMACS 5.16 [23]. Apo proteins and protein-ligand complexes were simulated for a 100 ns time scale to get an insight into the conformational changes of atoms in protein-ligand complexes in the dynamic environment. Using the PRODRG server and GROMACS tools, the topologies were generated for all the ligands in the complexes. The structure of protein complexes was relaxed and hydrated using simple point charge (SPC) water with periodic boundary conditions. Genion tool in GROMACS was used to add Na+ and Cl– to the system to neutralize the system. The Verlet cut-off scheme was used to perform an energy minimization iteration. The Ewald method was used to calculate the long-range electrostatic and van der Waals interactions with a cut-off of 1.0 and 1.2 nm. The simulation was performed after equilibrating the system to the room temperature, pressure, and constant number of particles (NPT), and a simulation of 100 ns was performed [24]. The trajectories were used for various dynamic analyses, such as root mean square deviation (RMSD), root mean square fluctuation (RMSF), and the radius of gyration (Rg); a number of hydrogen bonds and SASA by different inbuilt scripts of GROMACS after the 100 ns MD simulation were completed. MM-PBSA binding free energy of receptor-ligand complexes was calculated using the molecular mechanics/Poisson–Boltzmann surface area (MM/PBSA) process, which uses MD simulation trajectories and is one of the most widely used methods in this field [25].

2.7. Molecular Docking of Natural Compounds with Other Types of β-Lactamases.

The natural compounds were taken for Glide docking analysis against other different types of β-lactamases from various organisms. The study was done to analyze the binding efficiency of these compounds against non-NDM-1 β-lactamases. The β-lactamase, ADC-7 (PDB

ID: 6PWL, *A. baumannii*), AmpC (PDB ID: 1KDW, *E. coli*), CTX-M-15 (PDB ID: 4HBT, *E. coli*), KPC-2 (PDB ID: 3RXX, *K. pneumoniae*), SHV-1 (PDB ID: 3MXR, *K. pneumoniae*), TEM-1 (PDB ID: 1TEM, *E. coli*), OXA-24/40 (PDB ID: 6MPQ, *A. baumannii*), and VIM-2 (PDB ID: 2YZ3, *Pseudomonas putida*) were selected for the Glide docking studies. The previously used protein preparation and Glide protocol in Sections 2.1 and 2.7 were followed for β-lactamase protein and the four natural compounds.

2.8. In Vitro NDM-1 Enzyme Inhibition Assay. The NDM-1 enzyme inhibition assay was carried out spectrophotometrically using nitrocefin as a chromogenic substrate as described previously [26] [27]. Briefly, the known inhibitors (EDTA (Aladdin, China, E299201) and substrate (nitrocefin (Aladdin, China, N163020)) and natural compounds were dissolved in DMSO. Recombinant NDM-1 enzyme (RayBiotech Life ID: 230-00554-500, Georgia) at a concentration of 1 nM was supplemented with $10\,\mu M$ ZnSO4, incubated with various concentrations (10-$100\,\mu M$) of shortlisted compounds from computational screening ($10\,\mu L$ of DMSO as negative control) for 10 min at 30°C temperature. Nitrocefin was then added at a final concentration of $60\,\mu m$, and the absorbance was measured at 490 nm at 30°C temperature using a multimode reader (BioTek Synergy, United States). The IC_{50} values were determined thrice by fitting the concentration dependence of residual enzyme activity to the nonlinear regression using GraphPad Prism 5.03.

2.8.1. Determination of Fractional Inhibitory Concentration (FIC). The combined effect of the natural compounds and imipenem (Zhejiang Hisun Pharmaceutical, China) was done using the checkerboard synergy titration assay in a 96-well microtitre plate [28]. Imipenem was tested at concentrations of eight dilutions lower than their MIC and two dilutions higher than the MIC. MIC concentration of imipenem (4x) was added in all wells under column 1 of the 96-well checkerboard panel for each concentration of natural compounds (one each row). The compounds were serially diluted at different subinhibitory concentrations, and each concentration was added to the corresponding rows. The bacterial strain (PAN resistance *A. baumannii* clinical isolate (strain number: P-29) was adjusted to 0.5 McFarland's standard and added to each well. The plates were incubated at 35°C and read at 600 nm using a BioTek microplate reader. The compound's fractional inhibitory concentration (FIC) index was calculated as given by the formula (MIC of A in combination with B/MIC of A alone) + (MIC of B in combination with A/MIC of B alone).

A FIC = 0.5 for a compound was taken as synergistic, FIC > 0.5 – 4 was additive/indifferent, and FIC > 4 was taken as antagonistic.

3. Results and Discussion

3.1. Homology Modeling of NDM-1. The Ramachandran plot was used to evaluate the reliability of the NDM-1 3D model using PROCHECK software (Suppl. Figure 1). The predicted 3D model's Ramachandran plot showed that

89.7% of residues were in the most favourable region, while 9.8% were in the allowed region, suggesting that the predicted model is of good quality. The "overall quality factor" for nonbonded atomic interactions is given by ERRAT scoring; the higher the scores, the better the quality. The commonly accepted range for a high-quality model is >50. The overall quality factor predicted by the ERRAT server for the current 3D model was 84.40, and the VERIFY3D server predicted that 96.68% of the residues in NDM-1 had an average 3D-1D score > 0.2, indicating that the model was valid.

The active site of NDM-1 includes residues ILE35, MET67, VAL73, TRP93, HIS120, GLN123, HIS122, ASP124, ASN220, GLY219, LYS211, LEU218, HIS189, and HIS250, as shown in (Figure 2) [5]. Crucial for bioactivity of Class B β-lactamases are zinc ions; there are two zinc ions surrounded by HIS120, HIS 122, ASP124, HIS189, CYS208, and HIS250 in the NDM-1 protein. The β-lactam ring interacts with two zinc ions, LYS211, a conserved residue ASN 220, ASP123, and ASP124, contributing to binding and orientation [6].

3.2. Molecular Docking Analysis. The literature and Dr. Dukes database selected the natural compounds with only antibacterial activity, and a database was created for this study. A total of 168 phytochemicals were shortlisted using Glide docking against NDM-1 protein. The natural compounds with the maximum docking score and binding mode in the active sites of the proteins were prioritized, and the top eight compounds interacting with active site residues of NDM-1 were chosen for further analysis (Table 1).

The results of molecular docking and molecular interactions provide additional insights into selective interactions of natural compounds with NDM-1, as shown in Figure 3 and Suppl. Figure 2. The natural compound database was docked into the active site of NDM-1 based on the docking score priorities; compounds were selected for further studies. Based on the hydrogen-bonding interactions and docking score, the top 8 compounds with structural diversities and binding mode were chosen. Figure 3 shows the protein-ligand complexes and their hydrogen bond interactions.

The enzyme inhibition assay with β-lactamase and NDM-1 enzyme was performed with 8 compounds, mentioned in Table 1. Of the eight, only two compounds (withaferin and mangiferin) showed the highest activity, and two compounds showed moderate activity (rutin and mangostin) (explained in Section 3.5). The four compounds were further analyzed for docking interaction with NDM-1. Four compounds, rutin, mangiferin, withaferin A, and mangostin, were found to have good Glide score for NDM-1 (-9.44, -9.12, -5.12, and -6.54 kcal/mol, respectively) and the Glide score for the known inhibitor D-captopril (-5.52), respectively. Molecular docking analysis showed that all four selected compounds interacted with NDM-1 catalytic amino acid residues through hydrogen bonding and hydrophobic interactions.

Withaferin A, a terpenoid containing four cycloalkane ring structures, three cyclohexane rings, and one cyclopentane ring, is isolated from *Acnistus arborescens* and

(a) (b)
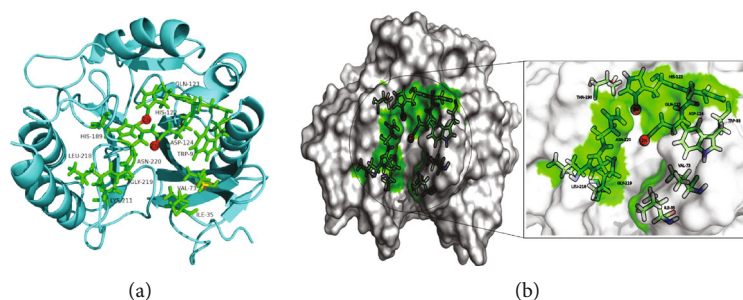
FIGURE 2: The active site region of NDM-1 protein. Panel (a) gives the cartoon model representation of NMD-1, and panel (b) shows the active site amino acid residues in the cavity of NDM-1 receptor. The active site amino acids are shown as green carbon atom stick and surface representation and Zn ions shown as red color sphere, whereas the protein is depicted in grey color surface.

TABLE 1: Molecular docking results of natural compounds with NDM-1 protein.

| | | | XP Glide docking | | | QPLD docking | |
S. no	Compounds	Molecular formula	Glide score	Glide energy	Amino acid interaction	Glide score	Glide energy	Amino acid interaction
1	Rutin	$C_{27}H_{30}O_{16}$	-9.44	-59.59	GLU152, Zn	-9.31	-88.67	HIS250 (PI-PI), LYN211, ASP124, GLU152, ASP223, and Zn
2	Mangiferin	$C_{19}H_{18}O_{11}$	-9.12	-57.25	ASP223, GLU152, ASP124, and Zn	-10.62	-52.76	GLU152, GLN123, ASN220
3	Phytic acid	$C_6H_{18}O_{24}P_6$	-7.64	-45.94	Zn, ASP223	-9.24	-59.19	ASN220, ASP124, and Zn
4	Chlorogenic acid methyl ester	$C_{17}H_{20}O_9$	-8.22	-46.44	ASP212, ASN220	-11.01	-58.38	ASP212, LYN211, LYS216, SER217, and ASN220
5	Naringin	$C_{27}H_{32}O_{14}$	-6.97	-55.64	GLU152, ASP223, and GLN123	-10.87	-68.81	GLN123, TRP93 (PI-PI), LYN211, SER217, and HIS250
6	Quercetrin	$C_{21}H_{20}O_{11}$	-7.74	-51.90	GLU152	-8.72	-49.49	LYN211
7	Withaferin A	$C_{28}H_{38}O_6$	-5.12	-36.50	ASP124, Zn	-6.21	-43.02	ASP124, Zn
8	Mangostin	$C_{24}H_{26}O_6$	-6.54	-40.17	GLU152, Zn	-7.76	-44.45	ASN220, HIE122 (PI-PI), GLU152, and Zn
9	D-captopril	$C_9H_{15}NO_3S$	-5.52	-31.72	Zn, ASN220	-6.28	-42.22	LYS211 (SALT BI), ASP124, ASN220, and Zn
10	Meropenem	$C_{17}H_{25}N_3O_5S$	-8.77	-41.51	GLU152, ASP223, and Zn	-11.11	-53.66	GLU152, ASP223, and Zn

Withania somnifera [29]. Recent research has shown that withaferin A has anticancer, adaptogenic, antistress, anticonvulsant, immunomodulatory, and neurological effects. It is a natural proteasome inhibitor, an apoptosis inducer by inhibiting the topoisomerase-I DNA complex, and a mitotic poison with antiangiogenic properties [30]. Withaferin A showed a Glide score of -5.12 and -6.21 kcal/mol and Glide energy of -36.50.15 and -43.02 kcal/mol from QPLD, respectively, and binding affinity with NDM-1. In both XP and QPLD docking analyses, withaferin interacted strongly with ASP124 (1.8 Å) and Zn+ and formed hydrophobic interactions with ILE35, VAL73, MET67, and TRP93 (Figure 3 and Suppl. Figure 2). A pharmacophore of withaferin A involves the 4-hydroxy-5,6-epoxy-22-en-1-one moiety, and its unsaturated lactone has been identified as essential for cytotoxic activity by structure-activity relationship studies [31]. In this study, we found that (6S)-6-ethyl-3-(hydroxymethyl)-4-methyl-5,6-dihydropyran-2-one region of withaferin A formed hydrogen bond with active site

amino acids in NDM-1. This showed that (6S)-6-ethyl-3-(hydroxymethyl)-4-methyl-5,6-dihydropyran-2-one region might be important in the biological activity of the withaferin A against β-lactamase (Figure 4).

Mangiferin is a xanthone found in higher plants and various parts of the mango crop, including the peel, stalks, leaves, barks, kernel, and stone. It is a promising antioxidant with a long list of health benefits, including antiviral, anticancer, antidiabetic, antioxidative, antiaging, immunomodulatory, hepatoprotective, and analgesic properties [32].

Mangiferin docked with NDM-1 protein gave a Glide score of -9.12 and -10.62 kcal/mol, and Glide energy of -57.25 and -52.76 kcal/mol was observed by XP and QPLD analysis. Mangiferin formed hydrogen bond between 9H-xanthen-9-one and D-glucitol region and active site amino acids ASP223 (2.0 Å), GLU152 (2.4 Å), ASP124 (2.5 Å), and Zn+ in XP docking and GLU152 (1.9 Å), GLN123 (1.9 Å), and ASN220 (2.0 Å) in QPLD docking (Figure 3
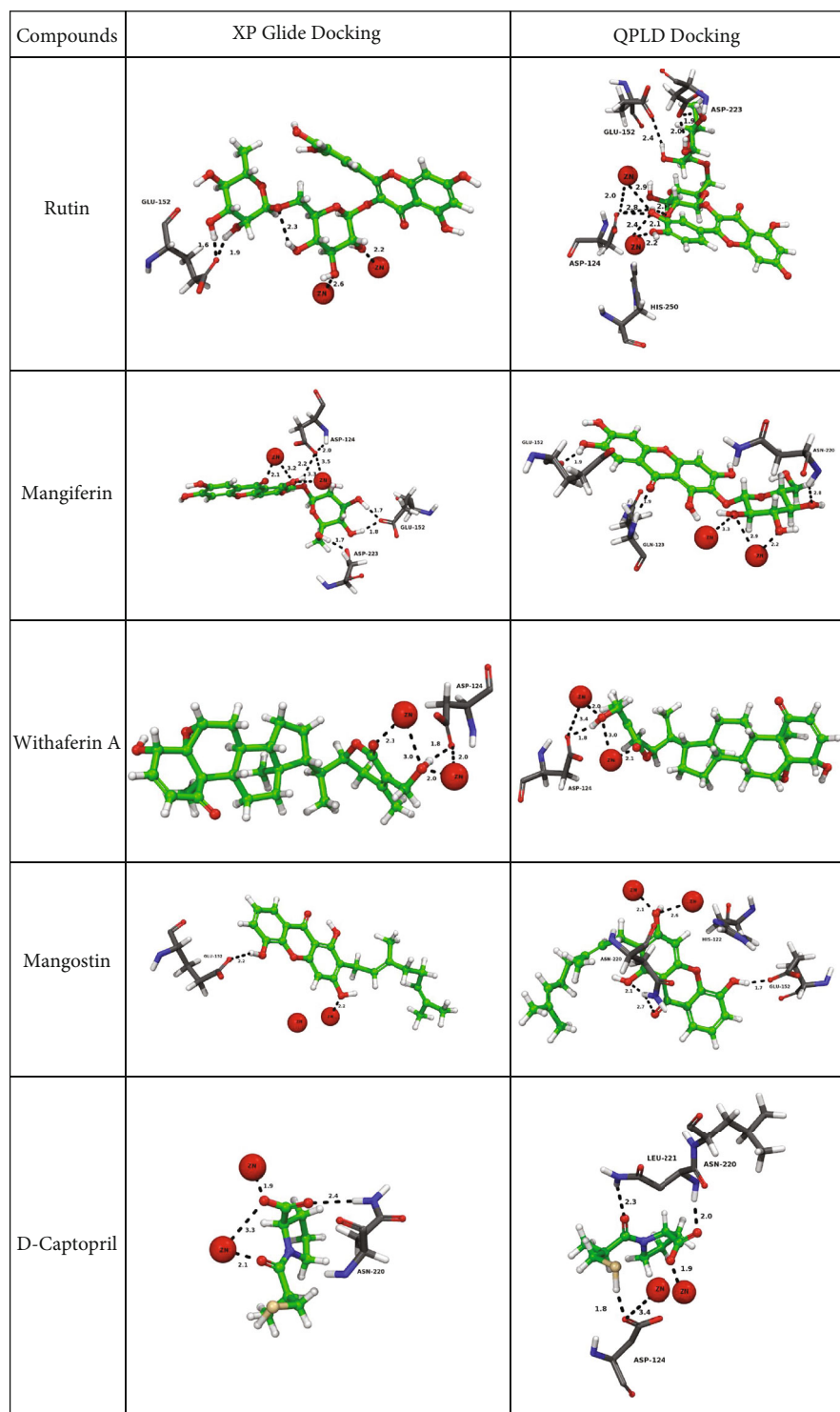
FIGURE 3: Docking interactions of natural compounds with active site residues of NDM-1 protein. Residues lining in the active site are shown as grey colour capped sticks. Ligands are green-coloured. Zn atoms are represented in red colour spheres. Hydrogen bonds are represented by black dashed lines.

and Suppl. Figure 2). The 1,5-anhydroglucitol region of mangiferin formed hydrogen bonds with active site amino acids of NDM-1, indicating the possible biological activity of mangiferin (Figure 4).

Mangostin is a significant xanthone found in the *Garcinia mangostana* Linn (mangosteen tree's) fruit pericarps, bark, and dried sap. Mangostin has a wide range of pharmacological effects, including antioxidant, anticancer, and anti-
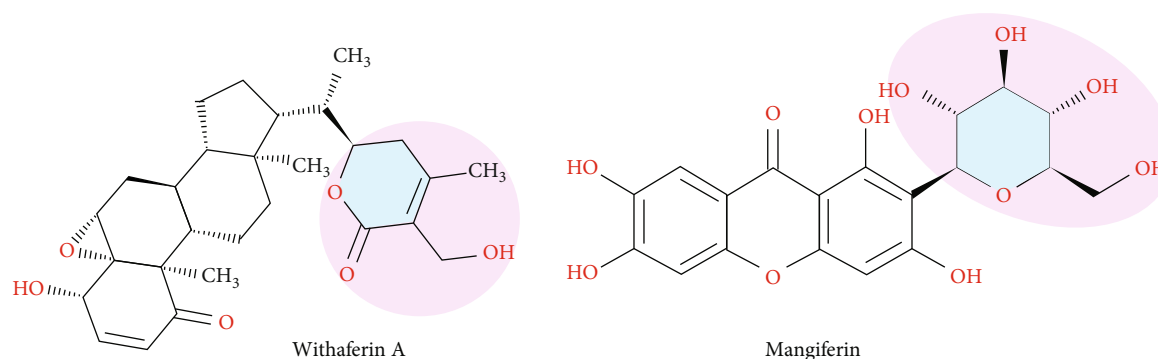
FIGURE 4: Structure representing the bioactive moiety of withaferin A and mangiferin against β-lactamase.

inflammatory effects [33]. From docking analysis with NDM-1, Glide scores of -6.54 and -7.76 kcal/mol and Glide energy of -40.17 and -44.45 kcal/mol were observed in the XP and QPLD. The hydrogen bonds were formed between 9H-xanthene region of mangostin and active site amino acids GLU152 (2.2 Å) in XP docking and ASN220 (2.1 Å) and GLU152 (1.7 Å) in QPLD docking (Figure 3). In QPLD docking, 9H-xanthene region of mangostin formed PI–PI cation interaction with HIE122 and a strong interaction between Zn+ in the active site (Figure 3 and Suppl. Figure 2).

A flavonol glycoside, rutin (quercetin-3-rutinoside), is between quercetin and α-l-rhamnopyranosyl-(16)—d-gluco-pyranose [34]. Rutin contains flavonolic aglycone quercetin and disaccharide rutinose [35], the hydroxy (-OH) groups in the sugar moiety aid in the formation of H-bond interactions between amino acid residues. Docking results of NDM-1 and rutin are shown in Table 1 and (Figure 3 and Suppl. Figure 2). Rutin with NDM-1 showed a Glide score of -9.44 and -9.31 kcal/mol and Glide energy of -59.59 and -88.67 kcal/mol in XP docking and QPLD docking methods. In XP docking, rutin interacted with GLU152 (1.6 Å), ASP124 (2.4 Å), GLU152 (2.4 Å), ASP223 (2.0 Å), and Zn+ ions in QPLD. In both docking methods, rutin strongly binds to the two Zn+ ions. And it also formed PI–PI interaction between its quercetin region and HIS250 residue in the active site.

The Structural Interaction Fingerprints (SIFt) algorithm helps find the types of interactions in a binding site by locating amino acids around bound ligands and residue types. SIFt was analyzed using residue features such as backbone, side chain, hydrophobic, aromatic, acceptor, donor, polar, and charged groups in the neighbourhood of the ligand's binding site. Withaferin A interacts with most of the side chains in the active site except GLY219 (Table 2). Two hydrophobic interactions were found in the ILE35 and TRP93. It also forms polar interactions with HIS122, ASP124, HIS189, SER217, ASN220, and HIS250. Withaferin A forms aromatic (TRP93), acceptor (ASP124), and charged (ASP124) interaction with NDM-1 binding site. GLY219 and HIS250 form backbone interaction with withaferin A. In SIFt analysis, mangiferin shows side chain and polar interaction with most of the amino acids in the binding site in the NDM-1 (Table 3). It forms hydrophobic interaction with ILE35 and forms acceptor and charged interaction with

ASP124, GLU152, and ASP223. The backbone amino acid interaction between mangiferin is found in the HIS122, GLN123, and GLY219, respectively.

3.3. Validation of XP Docking Protocol.
The validity of the docking protocol was performed by redocking the X-ray crystal structure ligand (i.e., D-captopril) at the active site of NDM-1. RMSDs and amino acid interactions between the docked pose and the crystal structure pose of D-captopril are as shown in the suppl. Figure 3. We found that D-captopril redocked into the active site of NDM-1, which is similar to the crystal structure.

3.4. Binding Free Energy Calculation.
The MM-GBSA was used to determine the effect of solvent and free energy on the interaction between natural compounds and NDM-1 proteins. From Glide XP and QPLD docking, ligand-bound complexes were obtained, and MM-GBSA calculation was performed using surface area energy, solvation energy, and energy minimization of the protein-ligand complexes. The MM-GBSA of 4 natural compounds and known inhibitors are shown in Table 4. And for NDM-1 docked poses, Prime MM/GBSA (DGBind) ranges from -32.20 and -33.49 kcal·mol (withaferin A), -23.92 and -21.05 kcal mol (mangiferin), -15.74 and -13.92 kcal mol (mangostin), -24.32 and -27.18 kcal mol (rutin), and -11.93 and -18.57 kcal mol (sulbactam) in XP and QPLD docking. The results showed that nonsolvation terms (Glipo), van der Waals (GvdW), and covalent energy (Gcovalent) are more promising contributors for ligand binding. The binding free energies of these known inhibitors do not change significantly.

3.5. Determination of the Inhibitory Activity of Candidate Natural Compounds against NDM-1.
The IC_{50} values were calculated for natural compounds and known inhibitors under controlled experimental conditions. The percent inhibitory curves for the candidate natural compounds with efficacy for NDM-1 and β-lactamase enzyme are given in Figures 5(a) and 5(b). The natural compounds were incubated with NDM-1 enzyme, and the substrate, nitrocefin, and hydrolysis of the substrate were monitored at 490 nm OD.

3.5.1. NDM-1 Enzyme Inhibitory Activity Assay.
Of the eight natural compounds (at concentrations 10-100 μM)

TABLE 2: SIFt analysis of NDM-1 binding site amino acid interaction with withaferin A.

Amino acid	Side chain	Hydrophobic	Aromatic	Polar	Acceptor	Charged	Backbone
ILE35	1	1	0	0	0	0	0
TRP93	1	1	1	0	0	0	0
HIS122	1	0	0	1	0	0	0
ASP124	1	0	0	1	1	1	0
HIS189	1	0	0	1	0	0	0
SER217	1	0	0	1	0	0	0
GLY219	0	0	0	0	0	0	1
ASN220	1	0	0	1	0	0	1
HIS250	1	0	0	1	0	0	0

TABLE 3: SIFt analysis of NDM-1 binding site amino acids interaction with mangiferin.

Amino acids	Side chain	Hydrophobic	Polar	Acceptor	Charged	Backbone
ILE35	1	1	0	0	0	0
HIS122	1	0	1	0	0	1
GLN123	1	0	1	0	0	1
ASP124	1	0	1	1	1	0
GLU152	1	0	1	1	1	0
HIS189	1	0	1	0	0	0
LYN211	1	0	1	0	0	0
GLY219	0	0	0	0	0	1
ASN220	1	0	1	0	0	0
ASP223	1	0	1	1	1	0
HIS250	1	0	1	0	0	0

tested for the NDM-1 enzyme inhibitory activity assay, only four compounds showed 50% maximum inhibitory activity suggesting they could be potential inhibitors. The addition of withaferin A, mangiferin, rutin, and mangostin to the enzyme assay reduced the NDM-1 enzyme activity (reduction in the hydrolysis of nitrocefin) significantly with IC_{50} of $24.03 \pm 2.92 \mu M$ for withaferin A, mangiferin $30.6 \pm 4.41 \mu M$, and rutin $48.94 \pm 3.74 \mu M$ and minimal reduction with mangostin $97.48 \pm 5.59 \mu M$. The IC_{50} values of other compounds were more than $100 \mu M$, indicating that these compounds can have minimal or no inhibitory effect on NDM-1 and the IC_{50} of the known NDM-1 enzyme inhibitor EDTA was $2.081 \pm 0.296 \mu M$.

3.5.2. β-Lactamase Enzyme Inhibitory Activity Assay. The eight candidate natural compounds identified by *in silico* analysis against NDM-1 were also tested for β-lactamase inhibition assay. Of the eight, the addition of compounds withaferin A, mangiferin, rutin, and mangostin in the assay decreased β-lactamase activity significantly with IC_{50} of $32.83 \pm 2.59 \mu M$ for withaferin A and mangiferin $58.02 \pm 2.08 \mu M$. A very minimal inhibition of the enzyme activity was observed in the presence of rutin $127.4 \pm 15.9 \mu M$ and mangostin $136.1 \pm 37.1 \mu M$, while that of the known β-lacta-mase inhibitor sulbactam was $7.244 \pm 0.392 \mu M$.

3.5.3. Augmentation of Antimicrobial Effect of Imipenem by the Withaferin A and Mangiferin. Every new development in drug discovery is the challenge of resistance that competes equally. Making a comeback for the already available drugs differently is a more approachable method to combat the resistance development. Combination therapy is not a new avenue; combination drugs have been routinely used to treat life-threatening illnesses. Plant natural compounds are weak antimicrobials; however, as seen in *in vitro* studies, the synergizing effect has proven effective when used together.

The compounds, withaferin A and mangiferin, showed good enzyme inhibition activity against NDM-1 and were checked for their mechanism of action (potential augmenta-tion effect) with imipenem against the carbapenem-resistant *A. baumannii* strain. The subinhibitory concentrations of the natural compounds were used to test the synergy along with imipenem, and the results were given as fractional inhibitory concentration values.

The checkerboard method was used to design the dilu-tion panel, with twofold concentrations above the MIC of the antibiotics and MIC concentration and fivefold below the MIC. The 96-well microtitre plate was used for the above study, and the effects of the compounds on the MIC of imi-penem are classified as synergistic, indifferent, or additive based on the FIC index as given in Table 5. Four natural

TABLE 4: Binding free energy calculation of natural compounds and known inhibitor with NDM-1 protein.

Compounds ID	ΔG bind	ΔG bind Coulomb	Binding free energy (kcal/mol) (XP docking)			ΔG bind vdW	ΔG bind	ΔG bind Coulomb	Binding free energy (kcal/mol) (QPLD)			ΔG bind vdW
			ΔG bind Covalent	ΔG bind Hbond	ΔG bind Lipo	ΔG bind SolvGB			ΔG bind covalent	ΔG bind Hbond	ΔG bind Lipo	ΔG bind SolvGB
Withaferin A	-32.20	-42.92	6.82	-0.70	-14.07	78.07	-32.57	-33.49	-39.72	6.82	-0.88	-14.96	75.30	-33.21
Mangiferin	-23.92	-53.47	6.72	-2.91	-12.04	89.30	-40.44	-21.05	-29.32	7.27	-1.26	-12.79	88.86	-47.54
Mangostin	-15.74	-18.50	3.41	-0.91	-15.24	65.68	-42.97	-13.92	-32.57	3.27	-2.28	-15.42	63.13	-46.23
Rutin	-24.32	-50.66	3.41	-2.72	-10.54	104.10	-44.10	-27.18	-51.41	2.27	-5.48	-15.97	46.60	-48.59
D-captopril	-11.93	-67.53	5.68	-0.45	-4.93	83.25	-22.25	-18.57	-12.76	6.82	-0.35	-5.002	102.46	-22.91
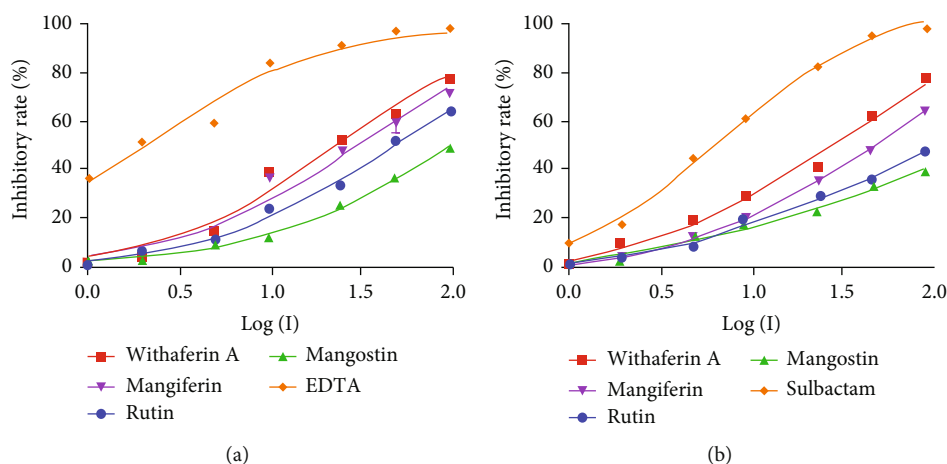
FIGURE 5: Effect of natural compounds and known inhibitors on (a) NDM-1 and (b) β-lactamase inhibition activity.

TABLE 5: Fractional inhibitory concentration (FIC) and FIC indices (FICIs) of combination of withaferin A and mangiferin with imipenem against *A. baumannii* MDR strain.

A. baumannii MDR strain	FIC	FIC index	Interpretation
Imipenem with withaferin	0.0625	0.3125	Synergy
Withaferin with imipenem	0.25		
Imipenem with mangiferin	0.125	0.625	Synergy
Mangiferin with imipenem	0.5		

compounds shortlisted from the enzyme inhibition assay were tested for synergy effect with imipenem, of which withaferin A and mangiferin had a potentiating effect on imipenem.

Withaferin A (128 mg/L) exhibited highly significant synergistic/potentiating effect with imipenem tested against carbapenem-resistant *A. baumannii* clinical strain (FIC index of 0.3125) followed by mangiferin, (128 mg/L) with an FIC index of 0.625. It is not surprising to see the synergistic potential of withaferin A, which has proven potentiating effect with anticancer drugs [36]. *Withania somnifera*, the source plant, has numerous therapeutic benefits. A previous structure-activity study by Moujir et al. has explored the antimicrobial properties and the functional groups involved in their potency [37]. Kannan and Kulandaivelu reported the antibacterial activity of Withaferin A activity towards both Gram-negative and Gram-positive bacteria, including *Bacillus subtilis*, *E. coli*, and *Staphylococcus aureus* [38]. *Anemarrhena asphodeloides*, a plant used in traditional Chinese medicine and whose main active component is mangiferin, has been found to have antiviral and antibacterial activities [39]. Mangiferin has many properties and is traditionally used in many countries; in Cuba, they are available with the brand name Vimang® and in Sri Lanka as Salaretin® [40]. Mangiferin has also been previously reported to be a good potentiator, along with many antibiotics proving to be effective for therapy [41]; this coincides with the findings from our current view of mangiferin in aiding the efficacy of available antibiotics. Mangiferin has been shown to have antibacterial activity against two *S. aureus* and *Salmonella*

typhi [42] [41]. Mangiferin and its derivatives showed antibacterial and antifungal action against *Bacillus pumilus*, *Bacillus cereus*, *Salmonella virchow*, and two fungal species, *Thermoascus aurantiacus* and *Aspergillus flavus* [43].

3.6. ADME. In silico predicted ADME (absorption, distribution, metabolism, and excretion) properties of four natural compounds were done using the QikProp (Table 6). Drug kinetics and tissue exposure, which are essentially determined by their ADME properties, affect a drug's pharmacological activity and efficacy. Natural compounds were predicted and analyzed for approximately 13 physically important descriptors and pharmacologically active properties. The analysis of predicted ADME properties shows QPlog QPlogPo/w QPpolrz, QPlogS, QPlogPw, QPlogPoct, QPlogKp, QPlogPC16, and Khsa in the allowed range. The physiochemical properties of the natural compounds were within the allowed ADME range. Molecular weights of these natural compounds range between 380 and 610 g/mol, and each comprises 1–6 H-bond donor groups, 2-10 H-bond acceptor groups, and 5-15 rotatable bonds. The identified compounds' total polar surface area (PSA) was within the 92-273 Å^2 range. And drug-like properties like QPpolrz, aqueous solubility (QPlogS), hexadecane/gas (QPlogPC16), octanol/gas (QPlogPoct), water/gas (QPlogPw), octanol/water (QPlogPo/w), skin permeability (QPlogKp), and Khsa serum protein binding (QPlogKhs) were shown to be in the allowed region. All the values for natural compounds come under the desirable range making it a suitable drug candidate.

TABLE 6: ADME properties of four natural compounds.

Compounds	#rotor	mol MW	donorHB	accptHB	QPpolrz	QPlogPC16	QPlogPoct	QPlogPw	QPlogPo/w	QPlogS	QPlogKp	QPlogKhsa	PSA
Accepted range	(1-15)	(130.0–725.0)	(0.0–6.0)	(2.0–20.0)	(13.0–70.0)	(4.0–18.0)	(8.0–35.0)	(4.0–45.0)	(−2.0–6.5)	(−6.5–0.5)	(−8.0–−1.0)	(−1.5–1.5)	(7.0–200.0)
Mangiferin	11	438.344	6	13.75	34.718	14.346	30.63	26.29	-1.82	-2.282	-6.727	-1.013	190.756
Withaferin A	5	470.605	1	9.4	47.967	13.214	23.019	12.717	3.117	-4.997	-3.993	0.385	114.741
Mangostin	8	380.44	2	3.75	39.477	12.498	18.024	8.63	4.449	-5.672	-2.54	0.779	92.69
Rutin	15	610.524	6	18	48.459	17.033	41.62	35.966	-2.558	-2.242	-7.331	-1.298	273.511

RMSD

(a)

RMSF

(b)

Radius of gyration

(c)
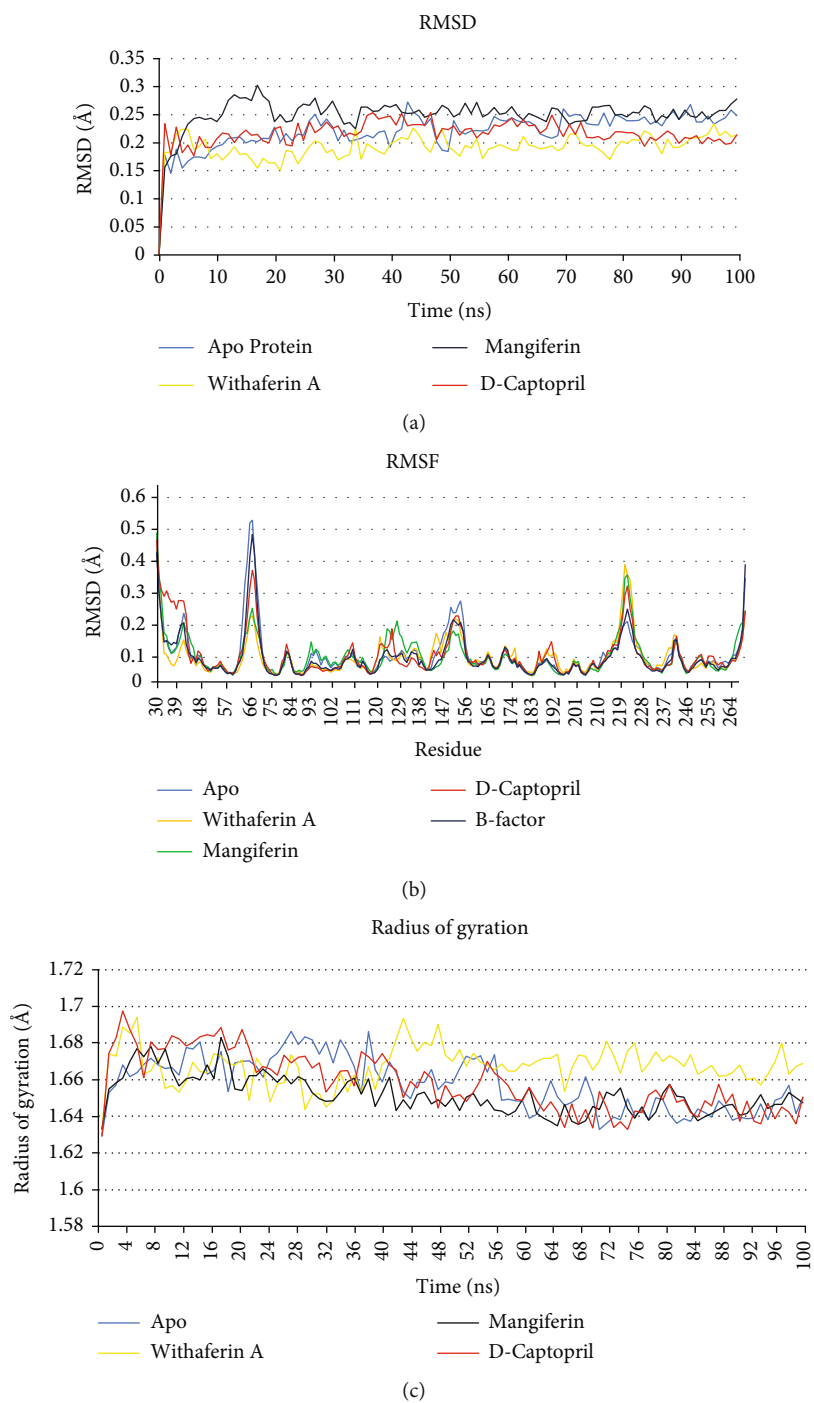
Figure 6: Continued.

(d)

(e)
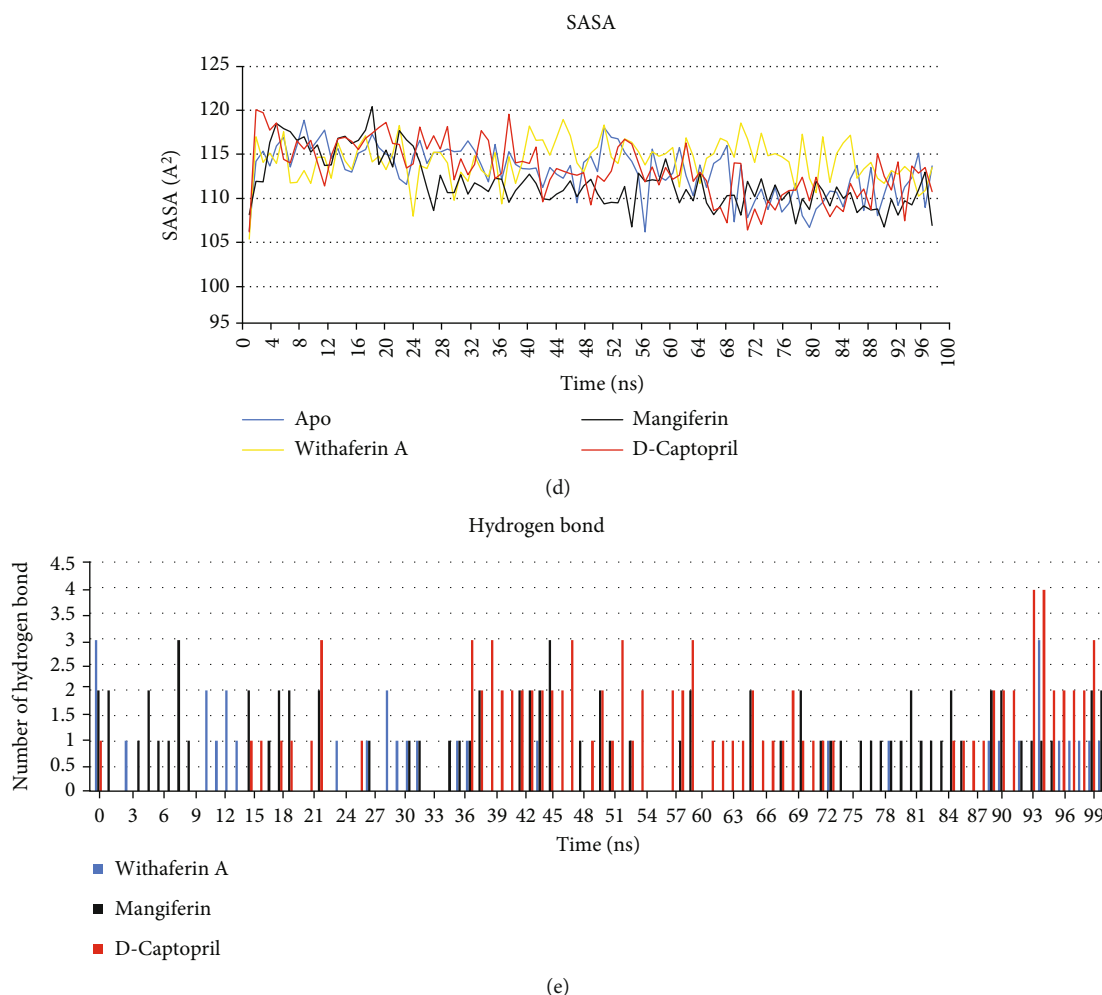
FIGURE 6: RMSD, RMSF, RG, SASA, and H-BOND of the backbone atom of the NDM-1 protein simulated over a time period of 100 ns.

TABLE 7: Binding free energy and interaction energy of NDM-1–ligand complexes calculated using the MM-PBSA approach.

Target	ID	Binding energy (kJ/mol)	Van der Waal energy (kJ/mol)	Electrostatic energy (kJ/mol)	Polar solvation energy (kJ/mol)	SASA energy (kJ/mol)
NDM-1	Withaferin A	-96.597 ± 56.626	-112.747 ± 67.710	-12.105 ± 12.260	39.594 ± 38.035	-11.339 ± 6.804
	Mangiferin	-168.570 ± 48.904	-97.906 ± 44.098	-114.624 ± 77.901	62.730 ± 31.574	-10.878 ± 5.269
	D-captopril	-132.842 ± 35.026	-60.775 ± 19.936	-99.864 ± 55.580	101.701 ± 66.646	-7.948 ± 2.811

3.7. Molecular Dynamic Simulation Results

3.7.1. RMSD.
After the QPLD docking study, molecular simulations of all the protein-ligand complexes and apoproteins were carried out for a period of 100 ns. The stability and conformational distribution of the ligands in the receptor protein were calculated using generated RMSD trajectories. For NDM-1, at the initial simulation phase, the backbone of all complexes was increased between 0 and 3 ns. In the apo NDM-1 protein, an increased fluctuation was observed at 43 ns, RMSD of 0.27 nm; after this, a stable deviation was observed throughout the simulation time, with an overall RMSD of 0.25 nm (Figure 6(a)). NDM-1 bound witha-

ferin and D-captopril had a maximum deviation at around 40 ns with RMSD of 0.2 nm and 0.25 nm, respectively, whereas mangiferin RMSD reached a maximum of 0.3 nm before 20 ns simulation. RMSD trajectories of NDM-1, when analyzed together with known inhibitors and natural compounds, showed that after an initial fluctuation, a successful steady confirmation with minimal deviation was maintained throughout the simulation.

3.7.2. RMSF.
The conformation and stability of Apo and protein-ligand complexes were determined by their amino acid residues. It was perceived from the RMSF plot that NDM-1 and ligand complex attained the overall low RMSF

TABLE 8: HOMO, LUMO, HELG, ESP, and solvation energy parameter of the withaferin A, mangiferin, and D-captopril.

S. no	Compound IDs	HOMO (eV)	LUMO (eV)	HLG (eV)	QM dipole (debye)	Solvation energy (kcal/mol)	ESP min kcal/mol	ESP max kcal/mol
1	Withaferin A	-0.25442	-0.06792	0.1865	8.9441	-23.82	-62.87	63.53
2	Mangiferin	-0.21798	-0.06246	0.1555	7.6612	-15.80	-74.91	79.73
3	D-captopril	-0.2394	-0.0058	0.2394	11.2215	-71.45	-79.28	76.73
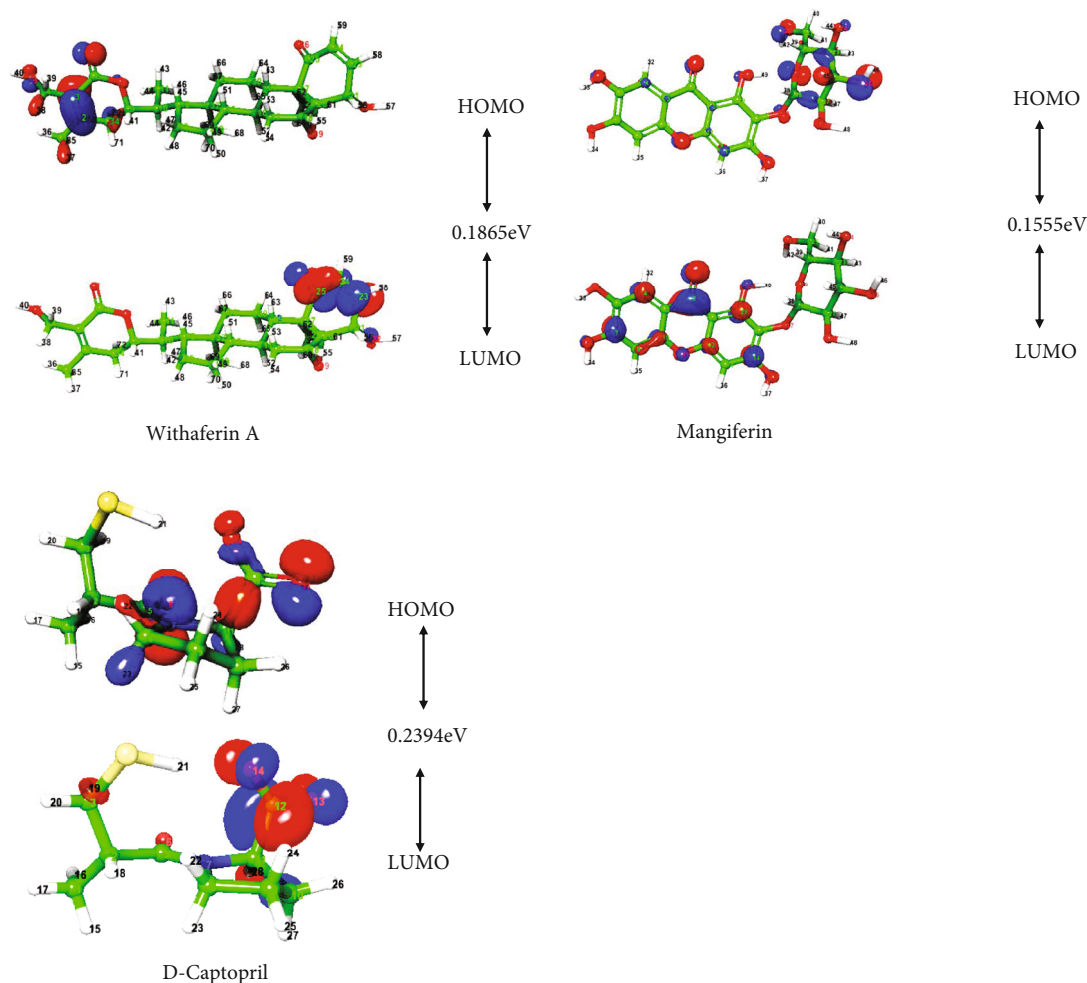
FIGURE 7: The highest occupied molecular orbital and the lowest unoccupied molecular orbital are plotted on a natural compound.

than apoprotein. The plot suggested the stable binding of all three ligands and residues interacting with all three ligands having low flexibility compared with apoprotein fluctuation data. The resultant RMSF profile of NDM-1 apo and ligand complex showed fluctuations in the range of 0.1 to 0.25 and 0.1 to 0.52 nm at the protein's catalytic site and noncatalytic sites. We have calculated the B-factor for Apo protein and compared it with RMSF of a protein-ligand complex.

In NDM-1, high fluctuation (0.3 to 0.52 nm) was observed in the loop region of GLU30, ILE31, MET39, ASP66, MET67, PRO68, GLY69, PHE70, and ARG270 in apo and ligand-bounded complexes of NDM-1. These regions belong to the loop region in the NDM-1 and had

fluctuations in both apo and ligand-bound complexes. In D-captopril–NDM-1 complex, high fluctuation was observed in the N-terminus loop region of GLU30, THR34, GLN37, and THR41 with RMSF around 0.25 to 0.46 nm. In ligand-bounded NDM-1 complex, slight fluctuations were observed in the loop region of ASN220, LEU221, GLY222, ASP223, ALA224, and ARG270 RMSF of 0.2 to 0.38 nm (Figure 6(b)). In this study, NDM-1 ligand-bounded complexes had no significant fluctuations at the ligand-binding site in the protein-ligand complexes compared with the Apo protein (Figure 6(b)). B-factor RMSF from the crystal structure and the simulated RMSF of NDM-1 were highly correlated throughout 100 ns.
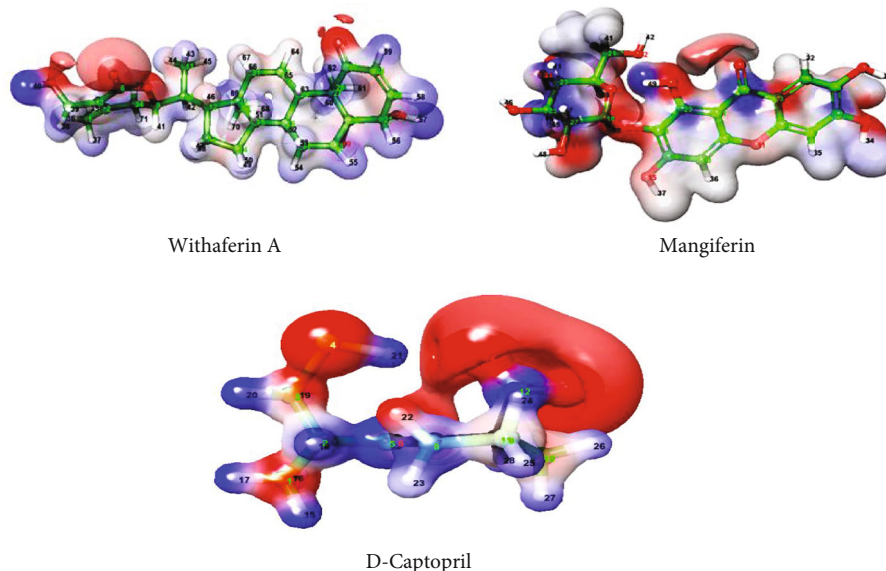
FIGURE 8: Electrostatic potential map generated for withaferin A and mangiferin, using the density functional theory (DFT) B3LYP/6-31G∗∗ method.

3.7.3. The Radius of Gyration (Rg). The radius of gyration (Rg) indicates the size and compactness of the protein. The Rg values of NDM-1 complexes were 1.7 nm at the initial state. The fluctuation of Rg of apo and ligand-bounded NDM-1 was observed initially, and it was stabilized after five ns. For apoprotein, Rg fluctuation was observed in 27 and 38 ns, and for withaferin A–NDM-1 complex, a slight increase in fluctuations was there at 43 and 48 ns, and the system was stable after that, still 100 ns. For D-captopril–NDM-1 complex, there was high fluctuation initially, and it was stabilized after 20 ns till 100 ns. For mangiferin–NDM-1 complex, overall, there was no fluctuation observed, and the system was stable till 100 ns (Figure 6(c)).

3.7.4. SASA. To better understand the impact of inhibitors on protein accessible surface area for solvent, we calculated solvent accessible surface area (SASA). The average SASA value of the NDM-1 ligand complex was calculated as 105-119 nm throughout 100 ns. The average SASA values of 118 ± 5 nm for withaferin A, 121 ± 10 nm for mangiferin, and 120 ± 9 nm for D-captopril were observed in 100 ns (Figure 6(d)). All the protein-ligand complexes and apoproteins showed minimum fluctuations during 100 ns. The SASA results showed that active site residues were well exposed to the solvent and readily accessible.

3.7.5. Hydrogen Bond. The number of hydrogen bonds was calculated during simulations for ligand-bound complexes of NDM-1. For NDM-1, an average of 2-3 hydrogen bonds in the NDM-1 ligand-bound complex were observed during 100 ns of simulations. For D-captopril–NDM-1 complex, 3-4 hydrogen bonds were observed in 90-95 ns. Overall, hydrogen bonds between the three ligands had stable interaction with the active site residues of NDM-1 (Figure 6(e)).

3.8. MMPBSA Analysis. The binding free energies were calculated using polar and nonpolar energy terms. During the 100 ns MD simulations, the energies associated with the binding of withaferin A, mangiferin, and D-captopril with NDM-1 were calculated. The following energies have been calculated: vdW interaction energy, electrostatic energy, polar solvation energy, SASA energy, and average binding energy (Table 7). NDM-1/ligand complexes and withaferin A/NDM-1 complex showed the lowest binding energy of -96.597 kcal/mol followed by mangiferin/NDM-1 and D-captopril/NDM-1 complexes -168.570 kcal/mol and -132.842 kcal/mol, respectively. The polar and nonpolar energies were distinct in each complex. The lowest polar solvation energy was observed in withaferin A–ligand complexes (39.594 kJ/mol), and the maximum energy was observed in the mangiferin–NDM-1 complex (62.730 kJ/mol). The withaferin A and mangiferin had good binding energies with NDM-1.

3.9. Density Functional Theory (DFT) Calculations

3.9.1. HOMO and LUMO Analysis. The properties of the molecular structure were explained using DFT calculations. DFT calculations at the level of B3LYP/6-31G∗∗ were optimized to produce these four molecules. In chemical reactivity, the molecules are sparkly, and the HOMO–LUMO distance increases charge transfer. The molecular orbital interactions with the other species and their energy difference (gap) assist in quantifying the chemical reactivity of the structure that participates in the chemical reactions. Naturally, the electron density is indicated by the intensity of the colour that would reflect the molecule's characteristic feature. The chemical reactivity of HOMO, LUMO, and MESP has been used to analyze molecule parameters. The LUMO is commonly used as an electron acceptor, while the HOMO is used as an electron donor. The stability of the structure

TABLE 9: The binding interactions of natural compounds in the active site residues of other β-lactamase enzymes.

Compounds	Beta-lactamase	Glide score	Glide energy	Glide EvdW	Glide Ecoul	Glide emodel	Amino acid interactions
Withaferin A	AMPC	-4.606	-38.022	-23.74	-14.282	-50.842	ARG204, GLN120, ASN289, and ASN346
	TEM-1	-2.791	-31.98	-17.237	-14.743	-34.431	GLU110, SER106, and VAL216
	VIM-2	-3.848	-35.208	-25.42	-9.788	-39.222	ASP97, ASN190
	SHV-1	-4.145	-31.208	-23.642	-7.566	-36.326	MET129
	KPC-2	-3.665	-32.831	-28.41	-4.422	-42.998	CYS238
	OXA 24/40	-5.68	-38.15	-35.609	-2.543	-37.991	SER128, SER81
	CTX-M-15	-4.1	-34.691	-25.794	-8.896	-41.456	GLY238
	ADC-7	-3.562	-30.258	-23.526	-6.732	-35.533	ASN204, GLN120, and PHE121
Mangiferin	AMPC	-7.848	-49.667	-30.064	-19.603	-62.404	ASN343, VAL121, and ASP123
	TEM-1	-4.079	-29.904	-20.442	-9.462	-40.812	ALA237, GLU104
	VIM-2	-6.117	-46.288	-20.793	-25.494	-56.383	TRP67, GLU126, and ASP43
	SHV-1	-7.653	-43.892	-28.665	-15.228	-57.531	TYR105, SER130, ASN276, and VAL216
	OXA 24/40	-10.05	-50.28	-34.581	-15.707	-69.695	ARG261, LEU127, and ALA126
	KPC-2	-6.293	-36.214	-25.905	-10.309	-47.456	TYR129, CYS238
	CTX-M-15	-6.117	-55.386	-26.468	-28.918	-84.69	ASN132
	ADC-7	-4.738	-33.168	-15.139	-18.029	-40.601	GLU289, ASN287, ASN343, and GLU344

was used to analyze the HOMO and LUMO energy gaps. Energy gap levels in the HOMO and LUMO elucidate the fragile essence of reactivity since electrons can be transferred quickly between the energy levels. In HOMO and LUMO, energy gaps of the natural compounds and known inhibitors are 0.1865 eV (withaferin A), 0.1530 eV (mangiferin), and 0.2394 eV (D-captopril), respectively (Table 8). The lesser the energy gap, the more energetically favourable the compound is for chemical reaction. As a result, the values indicate that the molecules have good chemical reactivity. The stability of the compounds was influenced by total energy, dipole moment, HOMO, LUMO, and energy distance. The natural compounds were plotted in the HOMO and LUMO energy gaps (Figure 7). The colour-coding area was red, which indicated the most negative potential region, and blue, which indicated the most positive potential region in the natural compounds.

In Figure 7, the frontier molecular orbital diagrams, the electrons are localized on 4-hydroxy-5,6-epoxy-22-en-1-one moiety in withaferin A and 2-hydroxymethyl-6methloxane-3,4,5-triol in mangiferin in the HOMO structures. The hydroxy groups in withaferin A and mangiferin are readily available to donate electrons to the interaction groups of amino acids at the binding site of NDM-1, based on the HOMO and LUMO structures. The DFT results agree well with the docking results, indicating that withaferin A and mangiferin are the study's best inhibitors. Both withaferin A and mangiferin have the smallest HOMO-LUMO gap among the ligands studied, indicating that the inhibitor's HOMO can transfer electrons to lower-energy LUMO of amino acid residues in the enzyme's active site.

3.9.2. Electrostatic Potential and Dipole Moment. Furthermore, the molecule's electrostatic potential and dipole moment have been proposed to determine the various inter-

molecular interaction properties and the most suitable regions between ligand and receptor [44]. Based on the electron density distribution on the respective molecular surface, the electrostatic map for withaferin A, mangiferin, and D-captopril is shown in Figure 8. The blue colour region on the electrostatic map indicates the strong electrophilic region of electrons in hydrogen atoms. This was observed for four natural compounds in this analysis. Similarly, the higher nucleophilic regions contributed by electron-rich molecules, such as hydroxy and carbonyl groups in the respective bioactive compounds, were coloured red on electrostatic maps. The measured electrostatic potential map for designated bioactive compounds indicated that highly electronegative atoms, such as oxygen, and highly electropositive atoms, such as carbon atoms bonded to oxygen in cyclic chains and hydrogen atoms, can introduce intermolecular interactions with the active residues of proteins in their vicinity during docking simulations [45]. The highly positive points were located at the hydroxy groups of oxygen atoms, and the highly negative points were located at the hydroxy group of hydrogen for the natural compounds (Figure 8). The natural compounds' high electropositive and electronegative atoms interacted with active site amino acids of NDM-1. The electrostatic potential maximum and minimum ranges for natural compounds and known inhibitors are shown in Table 8, respectively.

3.10. Molecular Docking Studies of Other Types of β-Lactamase with the Four Natural Compounds. The natural compounds withaferin A and mangiferin were also docked with other types of β-lactamases from different organisms to find their broad-spectrum β-lactamase activity. The β-lactamases, ADC-7 (PDB ID: 6PWL, *A. baumannii*), AmpC (PDB ID: 1KDW, *E. coli*), CTX-M-15 (PDB ID: 4HBT, *E. coli*), KPC-2 (PDB ID: 3RXX, *K. pneumoniae*), OXA-24/40

(PDB ID: 6MPQ, *A. baumannii*), SHV-1 (PDB ID: 3MXR, *K. pneumoniae*), TEM-1 (PDB ID: 1TEM, *E. coli*), and VIM-2 (PDB ID: 2YZ3 *P. putida*), were selected for the Glide docking studies. The previously used protein preparation and Glide protocol in Sections 2.1 and 2.7 were followed for this β-lactamase and four natural compounds.

Using XP Glide docking, the natural compounds were docked into their active site region of VIM-2, ADC-7, AmpC, CTX-M-15, KPC-2, SHV-1, and TEM-1 β-lactamase. The XP Glide score, Glide energy, and amino acid interactions are shown in Table 9. All four natural compounds had a good docking score and formed hydrogen bonds in the active site amino acids of all seven β-lactamases similar to NDM-1. These results indicate that withaferin A and mangiferin have good binding activity with the other types of β-lactamases.

4. Conclusions

Half of the global occurrence of infections due to *A. baumannii* is attributed to resistance to antibiotics of choice, including CRAB. *A. baumannii* has a solid shield of intrinsic factors and the acquisition of resistance mechanisms, together with working in unison against all known antibiotics of choice for treatment. CRAB is panresistant, often referred to as extensively drug-resistant (XDR). This study focused on identifying potential inhibitors targeting β-lactamases with carbapenem as substrate, using molecular docking, molecular dynamic modeling, *in silico* pharmacokinetics, and quantum chemical analysis on a collection of over two hundred phytochemical compounds. The *in silico* screening was done with D-captopril (known inhibitors) against NDM-1 target proteins, respectively, using a comparison of molecular docking scores and hydrogen bond interactions between the active site amino acids of the protein and phytochemicals. The top eight compounds were selected for *in vitro* NDM-1 inhibition assay; withaferin A, mangiferin, mangostin, and rutin showed inhibitory activity against β-lactamase and NDM-1 enzymes. Based on the IC_{50} values, withaferin A and mangiferin were subjected to fractional inhibitory concentration assay for ascertaining their mechanistic potential (synergy) with imipenem. The compounds had an FIC index in the range suggestive of possible synergistic mechanism of action potentiating the MIC of imipenem. Further refinement of the results was done using the *in silico* molecular dynamic simulation studies using GROMACS. The RMSD of NDM-1 and compounds and the RMSF and binding energy obtained from MD simulation trajectories strongly indicated that selected molecules have a good potential as β-lactamase inhibitors. Quantum chemical analyses revealed that the proposed molecules contain several reaction mechanisms to inhibit lactamase. According to pharmacokinetics analyses, all molecules have a strong absorption, distribution, metabolism, and distribution profile. As a result, it can be concluded that withaferin A and mangiferin could be safe natural potentiators and/or inhibitors substituting the available inhibitors against a wide spectrum β-lactamases contributing to carbapenem resistance with a possible use clinically.

Data Availability

Data are contained within the article.

Conflicts of Interest

The authors declare no conflict of interest.

Authors' Contributions

KD and VA designed the study, performed experiments and analyses, and helped to draft the manuscript. LW critically reviewed and edited the manuscript. ZS helped in drawing figures, and SW revised for its integrity and accuracy. MK helped in designing of *in vitro* studies. WH helped in analyzing computational studies. HX designed the study and approved the final version of this manuscript. Vasudevan Aparna and Kesavan Dinesh Kumar are co-first authors.

Acknowledgments

Supplementary Materials

Supplementary 1. Supplementary Figure 1: Ramachandran plots of the NDM-1 3D models. Ramachandran plots of the NDM-1 3D models built by homology modeling obtained by PROCHECK. 89.7%, residues in most favoured regions; 9.8%, residues in additional allowed regions; 0.0%, residues in generously allowed regions; and 0.5%, residues in disallowed regions.

Supplementary 2. Supplementary Figure 2: docking interaction fingerprints of natural compounds with active site residues of NDM-1 protein.

Supplementary 3. Supplementary Figure 3: validation of docking protocol by extracting and redocking the crystal structure bound inhibitor (D-captopril) at the active site of NDM-1 using XP docking. The redocked of D-captopril shows that it was docked into a similar position and amino acid interaction at the active site of NDM-1 in the docked conformations, as was present in the X-ray crystal structure.

References

[1] M. Asif, I. A. Alvi, S. U. J. I. Rehman, and D. Resistance, "Insight into Acinetobacter baumannii: pathogenesis, global resistance, mechanisms of resistance, treatment options, and alternative modalities," *Infect Drug Resist.*, vol. Volume 11, pp. 1249–1260, 2018.

[2] Y. Doi, G. L. Murray, and A. Y. Peleg, "Acinetobacter baumannii: evolution of antimicrobial resistance—treatment options. Seminars in respiratory and critical care medicine," *NIH Public Access*, vol. 36, p. 85, 2015.

[3] L. Poirel and P. Nordmann, "Carbapenem resistance in _Aci-netobacter baumannii_ : mechanisms and epidemiology," *Clinical Microbiology and Infection*, vol. 12, no. 9, pp. 826–836, 2006.

[4] K. Bush and G. A. Jacoby, "Updated functional classification of β-lactamases," *Antimicrobial Agents and Chemotherapy*, vol. 54, no. 3, pp. 969–976, 2010.

[5] D. Yong, M. A. Toleman, C. G. Giske et al., "Characterization of a new metallo-β-lactamase gene, blaNDM-1, and a novel erythromycin esterase gene carried on a unique genetic structure in Klebsiella pneumoniae sequence type 14 from India," *Antimicrobial Agents and Chemotherapy*, vol. 53, no. 12, pp. 5046–5054, 2009.

[6] K. Karthikeyan, M. Thirunarayan, and P. Krishnan, "Coexistence of blaOXA-23 with blaNDM-1 and armA in clinical isolates of Acinetobacter baumannii from India," *The Journal of Antimicrobial Chemotherapy*, vol. 65, no. 10, pp. 2253-2254, 2010.

[7] K. K. Kumarasamy, M. A. Toleman, T. R. Walsh et al., "Emergence of a new antibiotic resistance mechanism in India, Pakistan, and the UK: a molecular, biological, and epidemiological study," *The Lancet Infectious Diseases*, vol. 10, no. 9, pp. 597–602, 2010.

[8] Z. Liang, L. Li, Y. Wang et al., "Molecular basis of NDM-1, a new antibiotic resistance determinant," *PLoS One*, vol. 6, no. 8, article e23606, 2011.

[9] S. D. Lahiri, S. Mangani, T. Durand-Reville et al., "Structural insight into potent broad-spectrum inhibition with reversible recyclization mechanism: avibactam in complex with CTX-M-15 and Pseudomonas aeruginosa AmpC β-lactamases," *Antimicrobial Agents and Chemotherapy*, vol. 57, no. 6, pp. 2496–2505, 2013.

[10] M. J. Cheesman, A. Ilanko, B. Blonk, and I. E. Cock, "Developing new antimicrobial therapies: are synergistic combinations of plant extracts/compounds with conventional antibiotics the solution?," *Pharmacognosy Reviews*, vol. 11, p. 57, 2017.

[11] N. Guex, M. C. Peitsch, and T. Schwede, "Automated comparative protein structure modeling with SWISS-MODEL and Swiss-PdbViewer: a historical perspective," *Electrophoresis*, vol. 30, no. S1, pp. S162–S173, 2009.

[12] R. A. Laskowski, M. A. MW, D. S. Moss, and J. M. Thornton, "PROCHECK: a program to check the stereochemical quality of protein structures," *Journal of Applied Crystallography*, vol. 26, no. 2, pp. 283–291, 1993.

[13] C. Colovos and T. O. Yeates, "Verification of protein structures: patterns of nonbonded atomic interactions," *Protein Science*, vol. 2, no. 9, pp. 1511–1519, 1993.

[14] J. U. Bowie, R. Luthy, and D. J. S. Eisenberg, "A method to identify protein sequences that fold into a known three-dimensional structure," *Science*, vol. 253, no. 5016, pp. 164–170, 1991.

[15] US Department of Agriculture, ARS, *Dr. Duke's Phytochemical and Ethnobotanical Databases. Home Page*, 1992-2016.

[16] D. S. Raj, C. P. D. Kottaisamy, W. Hopper, and U. Sankaran, "Identification of immucillin analogue natural compounds to inhibit Helicobacter pylori MTAN through high throughput virtual screening and molecular dynamics simulation," *In Silico Pharmacology*, vol. 9, pp. 1–19, 2021.

[17] M. W. van der Kamp and A. J. Mulholland, "Combined quantum mechanics/molecular mechanics (QM/MM) methods in computational enzymology," *Biochemistry*, vol. 52, no. 16, pp. 2708–2728, 2013.

[18] K. D. Singh and K. Muthusamy, "Molecular modeling, quantum polarized ligand docking and structure-based 3D-QSAR analysis of the imidazole series as dual AT_1 and ET_A receptor antagonists," *Acta Pharmacologica Sinica*, vol. 34, no. 12, pp. 1592–1606, 2013.

[19] S. Chinnasamy, G. Selvaraj, A. C. Kaushik et al., *Identification of potent inhibitors against Aurora kinase A using molecular docking and molecular dynamics simulation studies*, 2019, http://Preprints.org.

[20] Q. Zhang, A. Khetan, and S. Er, "Comparison of computational chemistry methods for the discovery of quinone-based electroactive compounds for energy storage," *Scientific Reports*, vol. 10, pp. 1–13, 2020.

[21] M. A. Jordaan, O. Ebenezer, N. Damoyi, and M. Shapi, "Virtual screening, molecular docking studies and DFT calculations of FDA approved compounds similar to the non-nucleoside reverse transcriptase inhibitor (NNRTI) efavirenz," *Heliyon.*, vol. 6, no. 8, article e04642, 2020.

[22] C. A. Lipinski, "Drug-like properties and the causes of poor solubility and poor permeability," *Journal of Pharmacological and Toxicological Methods*, vol. 44, no. 1, pp. 235–249, 2000.

[23] P. Das, R. Majumder, M. Mandal, and P. Basak, "In-silico approach for identification of effective and stable inhibitors for COVID-19 main protease (Mpro) from flavonoid based phytochemical constituents of Calendula officinalis," *Journal of Biomolecular Structure & Dynamics*, vol. 39, pp. 6265–6280, 2020.

[24] R. Majumder and M. Mandal, "Screening of plant-based natural compounds as a potential COVID-19 main protease inhibitor: an in silico docking and molecular dynamics simulation approach," *Journal of Biomolecular Structure & Dynamics*, vol. 40, pp. 696–711, 2020.

[25] R. Kumari, R. Kumar, Open Source Drug Discovery Consortium, and A. Lynn, "g_mmpbsa—A GROMACS tool for high-throughput MM-PBSA calculations," *Journal of Chemical Information and Modeling*, vol. 54, no. 7, pp. 1951–1962, 2014.

[26] A. M. King, S. A. Reid-Yu, W. Wang et al., "Aspergillomarasmine A overcomes metallo-β-lactamase antibiotic resistance," *Nature*, vol. 510, no. 7506, pp. 503–506, 2014.

[27] N. Parvaiz, F. Ahmad, W. Yu, A. D. MacKerell Jr., and S. S. Azam, "Discovery of beta-lactamase CMY-10 inhibitors for combination therapy against multi-drug resistant Enterobacteriaceae," *PLoS One*, vol. 16, no. 1, article e0244967, 2021.

[28] V. Aparna, K. Dineshkumar, N. Mohanalakshmi, D. Velmurugan, and W. Hopper, "Identification of natural compound inhibitors for multidrug efflux pumps of Escherichia coli and Pseudomonas aeruginosa using in silico high-throughput virtual screening and in vitro validation," *PLoS One*, vol. 9, no. 7, article e101840, 2014.

[29] F. Aqil, R. Munagala, A. K. Agrawal, and R. Gupta, "Anticancer phytocompounds: experimental and clinical updates," *Journal of Virological Methods*, vol. 1, pp. 237–272, 2019.

[30] S. K. Yousuf, R. Majeed, M. Ahmad et al., "Ring A structural modified derivatives of withaferin A and the evaluation of their cytotoxic potential," *Steroids*, vol. 76, no. 10-11, pp. 1213–1222, 2011.

[31] G. Garg, A. Khandelwal, and B. S. Blagg, "Anticancer inhibitors of Hsp90 function: beyond the usual suspects," *Advances in Cancer Research*, vol. 129, pp. 51–88, 2016.

[32] M. Imran, M. S. Arshad, M. S. Butt, J.-H. Kwon, M. U. Arshad, and M. T. Sultan, "Mangiferin: a natural miracle bioactive compound against lifestyle related disorders," *Lipids in Health and Disease*, vol. 16, pp. 1–17, 2017.

[33] Y. Akao, Y. Nakagawa, and Y. Nozawa, "Anticancer effects of xanthones from pericarps of mangosteen," *International Journal of Molecular Sciences*, vol. 9, no. 3, pp. 355–370, 2008.

[34] R. Jadeja and R. Devkar, "Chapter 47 - polyphenols and flavonoids in controlling non-alcoholic steatohepatitis," in *Polyphenols in Human Health and Disease*, R. R. Watson, V. R. Preedy, and S. Zibadi, Eds., vol. 1, pp. 615–623, Academic Press, San Diego, CA, 2014.

[35] A. Ganeshpurkar and A. K. Saluja, "The pharmacological potential of rutin," *Saudi Pharm J.*, vol. 25, no. 2, pp. 149–164, 2017.

[36] F. A. Al Hassan Kyakulaga, R. Munagala, and R. C. J. O. Gupta, "Synergistic combinations of paclitaxel and withaferin A against human non-small cell lung cancer cells," *Oncotarget*, vol. 11, no. 16, pp. 1399–1416, 2020.

[37] L. Moujir, L. Araujo, G. Llanos, I. Jimenez, and I. Bazzocchi, "Evaluation of withaferin-A and analogues as antibacterial agents: structure-activity relationship study," *Planta Medica*, vol. 80, p. P2B29, 2014.

[38] N. Kannan and G. Kulandaivelu, "Novel method to isolate withaferin A from Withania somnifera roots and its bioactivity," *Allelopathy Journal*, vol. 20, pp. 213–220, 2007.

[39] T. Miura, H. Ichiki, N. Iwamoto et al., "Antidiabetic activity of the rhizoma of Anemarrhena asphodeloides and active components, mangiferin and its glucoside," *Biological and Pharmaceutical Bulletin*, vol. 24, no. 9, pp. 1009–1011, 2001.

[40] S. Singh, Y. Kumar, S. S. Kumar, V. Sharma, K. Dua, and A. Samad, "Antimicrobial evaluation of mangiferin analogues," *Indian Journal of Pharmaceutical Sciences*, vol. 71, no. 3, pp. 328–331, 2009.

[41] N. A. Mazlan, S. Azman, N. F. Ghazali et al., "Synergistic antibacterial activity of mangiferin with antibiotics against Staphylococcus aureus," *Drug Invention Today*, vol. 12, pp. 14–17, 2019.

[42] T. Biswas, A. Sen, R. Roy, S. Maji, and H. S. Maji, "Isolation of mangiferin from flowering buds of Mangifera indica L and its evaluation of in vitro antibacterial activity," *J Pharm Anal*, vol. 4, pp. 49–56, 2015.

[43] S. K. Singh, R. M. Tiwari, S. K. Sinha, C. C. Danta, and S. K. Prasad, "Antimicrobial evaluation of mangiferin and its synthesized analogues," *Asian Pacific Journal of Tropical Biomedicine*, vol. 2, no. 2, pp. S884–S887, 2012.

[44] E. J. Yearley, E. A. Zhurova, V. V. Zhurov, and A. A. Pinkerton, "Experimental electron density studies of non-steroidal synthetic estrogens: diethylstilbestrol and dienestrol," *Journal of Molecular Structure*, vol. 890, no. 1-3, pp. 240–248, 2008.

[45] K. E. Lee, S. Bharadwaj, U. Yadava, and S. G. Kang, "Computational and in vitro investigation of (-)-epicatechin and proanthocyanidin B2 as inhibitors of human matrix metalloproteinase 1," *Biomolecules*, vol. 10, no. 10, p. 1379, 2020.

Research Article

Molecular Mechanism of Gleditsiae Spina for the Treatment of High-Grade Serous Ovarian Cancer Based on Network Pharmacology and Pharmacological Experiments

Boran Zhang [iD],[1,2] **Wenchao Dan** [iD],[1] **Ganlin Zhang** [iD],[2] **and Xiaomin Wang** [iD][2]

[1]*Beijing University of Chinese Medicine, Beijing, China*
[2]*Oncology Department, Beijing Hospital of Traditional Chinese Medicine, Capital Medicine University, Beijing, China*

Correspondence should be addressed to Ganlin Zhang; kalinezhang@163.com
and Xiaomin Wang; wangxiaomin_bhtcm@126.com

Background. Gleditsiae Spina, widely used in traditional Chinese medicine, has a good curative effect on malignant tumors such as ovarian cancer, but the mechanism is not clear. So, we aimed to analyze the pharmacological mechanism of Gleditsiae Spina in the treatment of high-grade serous ovarian cancer (HGSC) based on network pharmacology and biological experiments. *Methods.* The main active ingredients of Gleditsiae Spina were identified by high performance liquid chromatography (HPLC) and mass spectrometry (MS), and the active ingredients were performed by ADME screening. The component targets of Gleditsiae Spina were screened using the PharmMapper platform, and differentially expressed genes in normal and HGSC tissues were identified through the GEO database. Thereafter, the network of "active ingredient-targets" was constructed by cytoscape 3.7.2 software. The protein-protein interaction network was established by the BioGenet database to mine the potential protein function. Biological processes and pathways were analyzed through Gene Ontology and Kyoto Encyclopedia of Genes and Genomes analysis. The binding ability of the core components of the Gleditsiae Spina and the core target of HGSC was verified by molecular docking and molecular dynamics simulation, and the therapeutic effect of Gleditsiae Spina was proved in vitro through cytotoxicity experiments. The effect of Gleditsiae Spina on the core pathway is obtained by western blotting. *Results.* Gleditsiae Spina had cytotoxicity on HGSC based on network pharmacology and biological experiments. Luteolin, genistein, D-(+)-tryptophan, ursolic acid, and berberine are the identified core active ingredients of Gleditsiae Spina for regulating HGSC, with HPSE, PI3KCA, AKT1, and CTNNB1as the ideal targets. The prediction results were verified by molecular docking, molecular dynamic simulation, cell viability, and western blot analysis. *Conclusion.* Gleditsiae Spina mainly downregulates the expression of heparanase and β-catenin to affect the composition of tumor cytoplasmic matrix and can regulate the PI3K-AKT pathway, integrating multiple targets and multiple pathways to play a therapeutic role. It also provides a theoretical basis for the prevention of ovarian cancer and its treatment using traditional Chinese medicine in the future.

1. Introduction

As one of the most serious diseases in women, ovarian cancer causes 152 000 deaths per year worldwide, ranking fourth among female tumor deaths [1–3]. The majority of patients are diagnosed at the advanced stage of ovarian cancer due to the lack of obvious symptoms and reliable diagnostic tools [4]. Therefore, improving ovarian cancer treatment, particularly highly serous ovarian cancer

(HGSC), has great clinical significance. As an aggressive cancer, HGSC often shows aneuploidy and mutations and is considered to be highly malignant, and their clinical prognosis is worse than other classifications [5]. Operative treatment includes total abdominal hysterectomy, bilateral salpingectomy, removal of pelvic and para-aortic lymph nodes, and omentum (such as appendectomy), combined with the usage of platinum drugs and taxane-like chemotherapy [6]. Traditional treatments such as cytoreductive

surgery and platinum-based chemotherapy, may cause 75-80% of relapses [7], and the overall survival of HGSC patients has not been noteworthy in the past 30 years.

Currently, traditional Chinese medicine (TCM) is being increasingly recognized due to its effectiveness in alleviating illnesses with minimal side effects [8]. The application of TCM in the treatment of tumors is increasing extensively in China and most Asian countries in the past decades. TCM plays an important role in the prevention and treatment of precancerous lesions, postoperative recurrence of tumors, reduction of toxic side effects of western medicine, and maintenance of advanced tumors [9]. In a previous meta-analysis, the combination of TCM treatments and western medicine significantly improved the KPS score, CA125 level, and 3-year survival rate in the postoperative adjuvant treatment of ovarian cancer [10]. The Chinese herbal medicine "Shenlinglan Capsule" can attenuate ovarian cancer migration by inhibiting the expression of glycogen synthase kinase 3 (GSK-3) in vitro [11]. Studies have shown that "Jianpi Huayu Decoction" can alleviate the progression of liver cancer by reducing the expression of reactive oxygen species (ROS) in myeloid-derived suppressor cells (MDSCs), attenuating inhibition of CD4 cell proliferation [12]. Bufalin in the TCM "Chan su" can regulate the cell cycle and inhibit receptor phosphorylation and tumor cell proliferation [13].

Gleditsiate Spina, as a widely used Chinese medicine, with its extensive activities has been proved, including detoxification, reduction of swelling and purulence, wound healing, and bloated dystocia [14]. Meanwhile, it is an alternative remedy in the treatment of ovarian cancer clinically. HPLC elucidated various flavonoids present in Gleditsiae Spina extracts, which confers anti-inflammatory, antibacterial, and antitumor effects [15]. It is reported that the ethanol extracts of Gleditsiae Spina can maintain tumor cells proliferation in G2/M phase, regulate phosphorylation of extracellular signal-regulated kinases (ERK), tumor necrosis factor-alpha (TNF-α), matrix metalloproteinase-9 (MMP-9) expression, and to inhibit tumor cell growth [16]. However, the main biologically active ingredients and the molecular mechanism of antiovarian cancer are not yet be elucidated.

With the development of network technology and bioinformatics, network pharmacology is gradually becoming a novel tool in elucidating molecular mechanisms and pharmacological effects [17]. It can effectively establish a "compound-protein/gene-disease" network and reveal the mechanism of small molecules through high-throughput methods [18]. Furthermore, networks can be constructed between various components to analyze their mutual relationships. Careful investigation of the key nodes in the network can systematically explain the material basis and mechanisms of Chinese medicines. So, this research predicts the mechanism of Gleditsiae Spina in the treatment of ovarian cancer by network pharmacology methods. Based on the results obtained, the experimental verification is carried out, revealing the mechanism of traditional Chinese medicine in the treatment of ovarian cancer.

Therefore, in this study, we hope to reveal the scientific connotation of the treatment of ovarian cancer by Gleditsiae Spina and provide new support for the expansion of clinical research and the development of new drugs to improve clinical efficacy.

2. Methods

2.1. Preparation of Gleditsiae Spina

2.1.1. Production of Freeze-Dried Powder. Gleditsiae Spina is administrated as medicine with dry spines of the leguminous Gleditsia sinensis Lam, and its Latin scientific name has been checked with the PlantList (http://www.theplantlist.org). In this study, Gleditsiae Spina was purchased as ready-to-use decoction pieces from Beijing Xinglin Pharmaceutical Co. (Beijing, China) and was identified by Professor Mao Ke-Chen according to the Chinese Pharmacopoeia standards.

Gleditsiae Spina decoction (450 mL) was prepared from 200 g Gleditsiae Spina pieces after twicely boiled in 1000 mL of distilled water 1 h and filtered through 200 mesh, and then the decoction was transferred to a vacuum freeze dryer (Epsilon 2-4LSC; Martin Christ Gefriertrocknungsanlagen, Harz, Germany) to obtain 18.72 g of freeze-dried powder, with a production rate of 9.36%. The powder was placed into a closed container containing silica gel to keep it dry. For subsequent experiments, the powder was dissolved in deionized water (100 mg/mL) and stored at −20°C.

2.1.2. Ingredient Identification Using High Performance Liquid Chromatography and Mass Spectrometry. Gleditsiae Spina freeze-dried powder (100 mg) was dissolved in 50% methanol and sonicated for 10 min. The solution was centrifuged at 3,000 r/min for 5 min (Beckman Coulter, Brea, CA, USA), and the supernatant was collected and filtered through a 0.22 μm filter (Millipore, Burlington, MA, USA). The filtered solution was subjected to mass spectrometry analysis using a Q-Exactive Orbitrap quadrupole-electrostatic field orbitrap mass spectrometer equipped with a thermal spray ion source and a Vanquish ultra-high performance liquid chromatography system (Thermo Fisher Scientific, Waltham, MA, USA).

2.2. Target Prediction

2.2.1. Prediction of Active Components in Gleditsiae Spina. Based on the mass spectrometry results, the active ingredients of Gleditsiae Spina were initially selected. The molecular structure of the active pharmaceutical ingredients and 3Dsdf was obtained on the PubChem platform, the latter was uploaded to the SwissADME platform, and then the pharmacokinetics and drug similarity were screened. The compound ingredients were required to have good gastrointestinal absorption, and the drug similarity received more than 3 positive evaluations. The potential targets of the ingredients were predicted on the PharmMapper platform [19]. We required the norm fit value to be greater than 0.75.

2.2.2. Construction of the Active Ingredient-Target Network of the Gleditsiae Spina. The "active ingredient-target" network of the Gleditsiae Spina was constructed and analyzed by Cytoscape 3.7.2 software [20]. "Node" was used to

indicate the component or target, and "edge" was used to indicate the relationship among them. The "Network Analyzer" analyzing tool built in Cytoscape 3.7.2 software was used to analyze the network characteristics, including degree, betweeness, and closeness, to study important components and target relationships of Gleditsiae Spina.

2.2.3. Ovarian Cancer-Related Targets. The differentially expressed genes of patients with ovarian cancer were obtained from the GEO database (series: GSE54388 and GSE14407, samples: normal tissue GSM1314222-GSM1314227, GSM360039-360049, and GSM359984, and tumor tissue GSM1314228-GSM1314243 and GSM359972-359983). Differential genes with an adj. P value <0.05 and |log2(fold change)| > 1 were considered to be of significantly differential expression and ovarian cancer-related targets.

2.2.4. Construction of Protein Interaction Network and Screening of Key Targets. The PPI were constructed by Biso-Genet3.0 [21]. The targets were related to the active ingredients of Gleditsiae Spina, and the targets of disease were introduced into BisoGenet, each generated a PPI network. The intersection network of the two PPI networks was extracted through the merge function in Cytoscape, and CytoNCA2.1 [22] was used to analyze the nodes of the intersection network. The targets were mapped and visualized by Cytoscape 3.7.2, and the protein-protein internetwork (PPI) of the shared genes was constructed through the String APP in Cytoscape.

2.2.5. Pathway Enrichment Analysis. The Metascape platform [23] was used to perform pathway enrichment analysis on the target. The platform integrates many authoritative functional databases such as GO and KEGG and supports batch genes or annotates, enriches and analyses proteins, and builds PPI networks. The platform is updated once a month to ensure data is reliable. Imported potential ovarian cancer targets were inserted into the Cytoscape platform for GO and KEGG analysis, and the results were saved and visualized with R software3.6.1.

2.2.6. Molecular Docking and Molecular Dynamic Simulation. In order to further determine the credibility of the relationship between the ovarian cancer target and the core components of Gleditsiae Spina, the top two compounds of traditional Chinese medicine compound target were selected as ligands genistein and luteolin, and four important targets were selected to analyze molecularly docking.

First, the crystal structure of the three proteins in pdb format from the RCSB database was downloaded, and the SDF was from the PubChem database. We also downloaded the 3D chemical structure of the candidate compound and used Open Babel 2.4 to convert to the pdb format file. Auto-Dock Tools 1.5.6 was used to delete the water molecules in the ligand, separate the ligand from the receptor, add nonpolar hydrogen, calculate the Gasteiger charge, and save the pdbqt format file. The selected potential core constituent ligands were subjected to energy minimization treatment, the ligand atom type was given, and the charge was calculated and stored in pdbqt format. Molecular docking opera-

tions were performed using Autodock Vina 1.1.2 and reflect the matching degree and docking activity between the target and the ligand through the docking score value, where we believe that a docking score > 4.25 means that the ligand and the target have binding activity, a score > 5.0 means good matching activity, and a score > 7.0 means strong docking activity [24].

The MD simulation of docked complexes was carried out using Desmond version 2020. Here, OPLS3e force field was used to initiate the MD simulation, and the system was solvated using the TIP3 water model. The neutralization of the system was performed by adding counter ions. Energy minimization of the entire system was performed using OPLS3e, as it is an all-atom type force field. The geometry of water molecules, the bond lengths, and the bond angles of heavy atoms was restrained using the SHAKE algorithm. Simulation of the continuous system was executed by applying periodic boundary conditions, and long-range electrostatics was maintained by the particle mesh Ewald method. The equilibration of the system was done using NPT ensemble with temperature at 300 k and pressure at 1.0 bar. The coupling of temperature-pressure parameters was done using the Berendsen coupling algorithm. On postpreparation of the system, the production run was performed for 200 ns with a time step of 1.2 fs, and trajectory recording was done for every 200 ps summing up to the recording of 10,00 frames. The calculation of the RMSD (Root mean square deviation) was done for the backbone atoms and was analyzed graphically to understand the nature of protein-ligand interactions. RMSF (root mean square fluctuation) for every residue was calculated to understand the major conformational changes in the residues in comparison between the initial state and dynamics state.

2.3. Verification In Vitro

2.3.1. Cells. Human ovarian cancer cell line A2780 purchased from ATCC was cultured in RPMI-1640 (Gibco Company, USA) with 10% foetal bovine serum (Gibco Company, USA) and 1% penicillin-streptomycin (10000 units/mL penicillin and 10000 μg/mL streptomycin, Gibco Company, USA). Human cancer cell line SKOV3 and HEY purchased from ATCC were cultured in DMEM (Gibco Company, USA) and cultured at 37°C in a humidified atmosphere under 5% CO_2. Human ovarian granulosa cell line SVOG and human ovarian epithelial cell line IOSE80 purchased from ATCC were cultured in RPMI-1640 (Gibco Company, USA) with foetal bovine serum and penicillin-streptomycin the same as the cell line A2780. Cells in the exponential growth phase were used in all experiments.

2.3.2. Cell Proliferation. The MTT was used to evaluate cell proliferation and viability. 2000 cells were seeded in each of the nonedge well of 96-well plates. Freeze-dried powder solution of the Gleditsiae Spina was diluted by multiples, from 0.25 to 8 mg/mL and added after the cells adhered to the wall. 24 hours and 48 hours after Gleditsiae Spina treatment, 20 μL of 3-(4,5-dimethylthiazol-2-yl)-2,5-diphenyltetrazolium bromide (MTT) (Sigma, St.
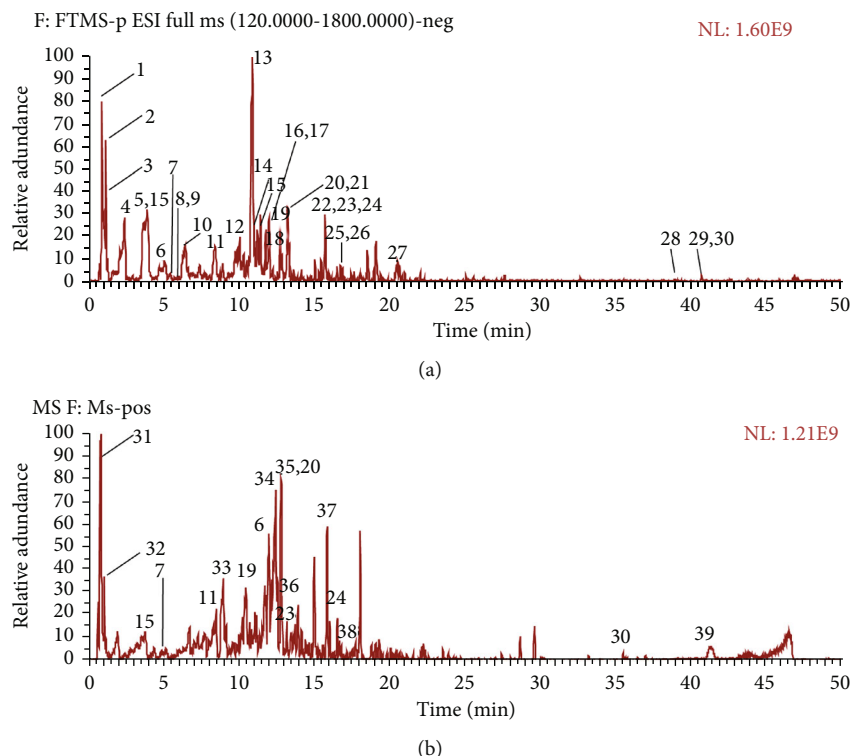
FIGURE 1: UHPLC-Q-Exactive Orbitrap MS identification results of the main chemical components in the extract of Gleditsiae Spina. (a) Total ion current graph in positive ion and negative ion mode. (b) Total ion current graph in negative ion and negative ion mode.

Louis, MO, USA) solution (5 mg/mL in phosphate-buffered saline (PBS)) was added to the culture medium in each well at a final concentration of 5 μg/mL, and the cells were incubated at 37°C for 4 hours. The supernatants were replaced with 150 μL of dimethyl sulfoxide (Sigma, St. Louis, MO, USA). Then, the 96-well plates were measured by microplate reader at 490 nm.

2.3.3. Western Blot. After exposure to the test compounds (1.25 mg/mL and 2.5 mg/mL freeze-dried powder of the Gleditsiae Spina) for 24 h, the A2780 cells were harvested and lysed with RIPA lysis buffer (Beyotime Biotechnology, Beijing, China) containing Protease Inhibitor Cocktail Set III (Calbiochem, San Diego, CA, USA). After centrifuged at 12,000 rpm for 15 min at 4°C, and the supernatants were collected, and the protein concentration was determined using the Pierce BCA Assay Kit (Thermo Scientific, Rockford, IL, USA). Equal amounts (30 μg/lane) of total protein were separated by 10% SDS-PAGE and transferred onto PVDF membranes. The membranes were blocked with 5% BSA (Amresco, Solon, OH, USA) at room temperature for 1 h and incubated overnight at 4°C with the following primary antibodies: anti-HPSE1 (1:1000, CST,USA), anti-MMP9 (1:1000, CST,USA), anti-β-catenin (1:1000, CST, USA), anti-N-cad (1:1000 CST, USA), anti-E-cad (1:1000 CST, USA),anti-PI3K/p-PI3K (1:1000, CST,USA), anti-AKT/p-AKT (1:1000, CST,USA), anti-YAP/TAZ (1:1000, CST,USA) and β-actin (1:10000, CST,USA). After washing the membranes in Tris-buffered saline with 0.1% Tween-20 (TBST),

the membranes were probed with secondary antibodies (1:10,000) for 1 h at room temperature. The signals were detected using an Odyssey Infrared Imaging System (Li-cor Biosciences, Lincoln, NE, USA). The relative density of the protein bands was measured by Odyssey version 3.0 software (LI-COR Biosciences). Each experiment was repeated three times. The ratios of the protein band intensities relative to that of β-actin were calculated for each sample using Image J.

2.3.4. AKT Kinase Dependency Validation. AKT kinase inhibitor, purchased from MedChemExpress (HY-10249, MCE), was added to A2780 cells at the dose from 1 nM to 8 nM, and the expression of AKT in the cells with or without inhibitor was tested by WB. The appropriate inhibitor concentration (2 nM) was selected for the efficacy experiment. 3000 cells with AKT kinase inhibitor were seeded in each of the nonedge well of 96-well plates and after 24 hours, Gleditsiae Spina was added. The MTT was used to evaluate cell proliferation and viability and the medicinal properties of Gleditsiae Spina.

3. Results

3.1. Mass Spectrometry Results. The extract of Gleditsiae Spina was analyzed according to the method in Section 2.1, and the total ion current diagram under the positive and negative ion mode was obtained (Figure 1). The height of the labels represents the relative content of ingredients. According to the retention time of each chemical

TABLE 1: UPLC-MS/MS analysis results of the main chemical components of Gleditsiae Spina.

Peak number	tR/min	Molecular formula	Accurate	Calculated	Error (ppm)	Identified compounds
1.	0.824	$C_6H_{12}O_6$	180.06339	180.0629	−2.48	D-(+)-Glucose
2.	1.018	$C_4H_6O_5$	134.02152	134.0211	−2.92	DL-malic acid
3.	1.229	$C_6H_6O_3$	126.03169	126.0312	−4	Pyrogallol
4.	2.201	$C_9H_{17}NO_5$	219.11067	219.1102	−2.14	Pantothenic acid
5.	3.265	$C_8H_8O_3$	152.04734	152.047	−2.3	2-Anisic acid
6.	4.062	$C_7H_6O_3$	138.03169	138.0313	−3.07	Salicylic acid
7.	5.626	$C_{15}H_{14}O_6$	290.07904	290.0787	−1.33	Catechin
8.	5.72	$C_6H_{10}O_4$	146.05791	146.0576	−2.4	Adipic acid
9.	5.763	$C_8H_8O_4$	168.04226	168.0419	−2.36	Vanillic acid
10.	6.578	$C_7H_6O_2$	122.03678	122.0365	−2.45	Benzoic acid
11.	8.569	$C_8H_8O_3$	152.04734	152.047	−2.15	Vanillin
12.	9.315	$C_{10}H_{10}O_4$	194.05791	194.0575	−2.29	Ferulic acid
13.	10.946	$C_{15}H_{12}O_7$	304.0583	304.0576	−2.21	Dihydrorobinetin
14.	10.953	$C_6H_6O_3$	126.03169	126.0309	−5.95	Phloroglucinol
15.	4.049	$C_{11}H_{12}N_2O_2$	204.08988	204.0894	−2.25	D-(+)-Tryptophan
16.	11.22	$C_{21}H_{20}O_{10}$	432.10565	432.1049	−1.85	Isovitexin
17.	11.275	$C_{21}H_{20}O_{12}$	464.09548	464.0949	−1.25	Quercetin-3-O-glucoside
18.	12.071	$C_9H_8O_2$	148.05243	148.0521	−2.07	trans-Cinnamic acid
19.	12.774	$C_{21}H_{20}O_{11}$	448.10056	448.0998	−1.67	Isoorientin
20.	12.895	$C_{15}H_{12}O_6$	288.06339	288.0629	−1.64	Fustin
21.	13.052	$C_9H_{10}O_2$	150.06808	150.0678	−2.18	Hydrocinnamic acid
22.	15.655	$C_8H_{11}NO$	137.08406	137.0837	−2.6	Tyramine
23.	15.736	$C_{15}H_{10}O_7$	302.04265	302.042	−2.3	Robinetin
24.	15.751	$C_{15}H_{10}O_6$	286.04774	286.0472	−2.06	Luteolin
25	17.106	$C_9H_{16}O_4$	188.10486	188.1044	−2.64	Azelaic acid
26.	17.631	$C_{15}H_{10}O_5$	270.05282	270.0525	−1.36	Genistein
27.	21.755	$C_{16}H_{30}O_4$	286.21441	286.2139	−1.63	Hexadecanedioic acid
28.	38.385	$C_{30}H_{46}O_4$	470.33961	470.3389	−1.43	18-β-Glycyrrhetinic acid
29.	40.138	$C_{30}H_{48}O_3$	456.36035	456.3597	−1.36	Ursolic acid
30.	41.117	$C_{30}H_{48}O_3$	456.36035	456.36	−0.83	Oleanolic acid
31.	0.753	$C_6H_{14}N_4O_2$	174.11168	174.11157	−0.58	L-(+)-Arginine
32.	1.118	$C_9H_{11}NO_3$	181.07389	181.07368	−1.17	L-tyrosine
33.	9.58	$C_{10}H_{10}O_2$	162.06808	162.0679	−1.1	Methyl cinnamate
34.	11.63	C_9H_7NO	145.05276	145.05256	−1.41	8-Hydroxyquinoline
35.	11.787	$C_{21}H_{20}O_{10}$	432.10565	432.10494	−1.64	Vitexin
36.	13.668	$C_{10}H_{16}O$	152.12012	152.12	−0.75	Citral
37.	16.6	$C_{20}H_{17}NO_4$	335.11576	335.11495	−2.42	Berberine
38.	17.966	$C_{16}H_{12}O_7$	316.0583	316.05771	−1.89	Rhamnetin
39.	43.089	$C_{29}H_{48}O_2$	428.36543	428.36437	−2.48	Stigmastane-3,6-dione

component, high-resolution precise molecular weight, MSn multilevel fragment information obtained by LC-MS detection, combined with the extracted ion current map and standard product information, Mzcloud database, and related literature, the composition was confirmed, and a total of 39 were identified. The results were shown in Table 1, and the mass spectra of 39 identified compounds were shown in Supplementary material 1. Among them, the number identified in the positive ion mode is 30, the number identified in the positive ion mode is 18, and the 9 compounds are the compounds identified by the positive and negative ions.

3.2. Network Construction and Target Prediction

3.2.1. Active Ingredients and Targets of Gleditsiae Spina. Thirty-nine Gleditsiae Spina components were observed in Section 3.1, screened according to the pharmacokinetics and drug similarity in SwissADME platform, and supplemented

TABLE 2: Candidate active components in Gleditsiae Spina.

ID	Mol name
GS1	Adipic acid
GS2	Azelaic acid
GS3	Berberine
GS4	Catechin
GS5	Citral
GS6	D-(+)-Glucose
GS7	D-(+)-Tryptophan
GS8	Ferulic acid
GS9	Fustin
GS10	Genistein
GS11	Hexadecanedioic acid
GS12	Hydrocinnamic acid
GS13	Luteolin
GS14	Methyl cinnamate
GS15	Oleanolic acid
GS16	Pantothenic acid
GS17	Phloroglucinol
GS18	Rhamnetin
GS19	Robinetin
GS20	Salicylic acid
GS21	Stigmastane-3,6-dione
GS22	trans-Cinnamic acid
GS23	Tyramine
GS24	Ursolic acid
GS25	Vanillic acid
GS26	Vanillin

FIGURE 2: Active component-target network map of Gleditsiae Spina. The purple labels represent the targets of the action of active components in the figure; the red labels represent 26 Gleditsiae Spina active components.

according to previous literature reports. This resulted in 26 active components. The SDF structure of 26 selected components were obtained from PubChem, and the PharmMapper target prediction model was used to predict the above 26 targets of active ingredients. The 26 medicinal active ingredients are shown by in Table 2. Relevant target prediction technology was used to predict the active targets, eliminating duplicate targets, and a total of 610 predicted targets were obtained, as shown in Figure 2.

3.2.2. Construction and Analysis of "Active Ingredient-Target" Network. Cytoscape 3.7.2 was used to draw and analyze the relationship network between the effective components of Gleditsiae Spina and its active targets, and a total of 635 nodes (including 609 targets and 26 active components) and 1090 relationships were obtained. The size represented the corresponding degree value. The larger the node area was, the larger the degree value, indicating that the more biological functions involved, the higher its biological importance (Figure 2).

3.2.3. Ovarian Cancer-Related Target Searching. Ovarian cancer-related targets (1483) were identified from the Gene Expression Omnibus (GEO) database. Figure 3 shows heat maps and volcano maps indicating the distribution of differ-

entially expressed genes, which are represented by red dots on the map.

3.2.4. Screening of Key Targets for Gleditsiae Spina Treatment in Ovarian Cancer. To obtain richer node-node connection information in PPI networks, the efficiency of node information transmission was optimized, the targets that play an important role in the network were identified, and the network topology characteristic attributed values of the abovementioned intersection PPI network graph was calculated. Through two screenings, a total of 87 key targets were obtained. The targets were shown in Figure 4(a), and the PPI network of the key genes was shown in Figure 4(b).

3.2.5. Pathway Enrichment Analysis and Visualization of Gleditsiae Spina Treatment for Ovarian Cancer. Metascape platform was used to perform gene enrichment analysis on the above 87 key nodes, including GO-BP (biological process), GO-CC (cellular component), GO-MF (molecular function), and KEGG pathway. R (version 6.1) was used to draw KEGG pathway a bubble chart (shown in Figure 5). The bubble color changed from red to purple to indicate that the log P value is from small to large. The smaller the log10 (P) value, the stronger the significance, and the larger the bubble, the larger the gene count (count value) of the pathway.

3.2.6. Molecular Docking and Molecular Dynamic Simulation Results. The two core potential compounds luteolin and genistein were molecularly docked with the four core targets PIK3CA, CTNNB1, HPSE, and AKT1 to obtain the group receptor-ligand docking results. Among the nine groups, the highest docking score is for luteolin-HPSE (-8.97 kcal/mol), and the lowest docking score is for genistein-HPSE (-7.35 kcal/mol). This indicates that the selected potential core compounds have better binding activity with the target. The docking affinity value is shown in Table 3, and a diagram depicting eight docking modes is shown in Figure 6. It can be seen from the figure that each ligand is embedded in the active pocket of the target and that it interacts with multiple residues of the target through hydrophobic interactions and hydrogen bond formation.

Next, genistein, luteolin, and berberine as the core components in the network were selected to perform molecular dynamics simulation tests with AKT1, HPSE, and PI3K.
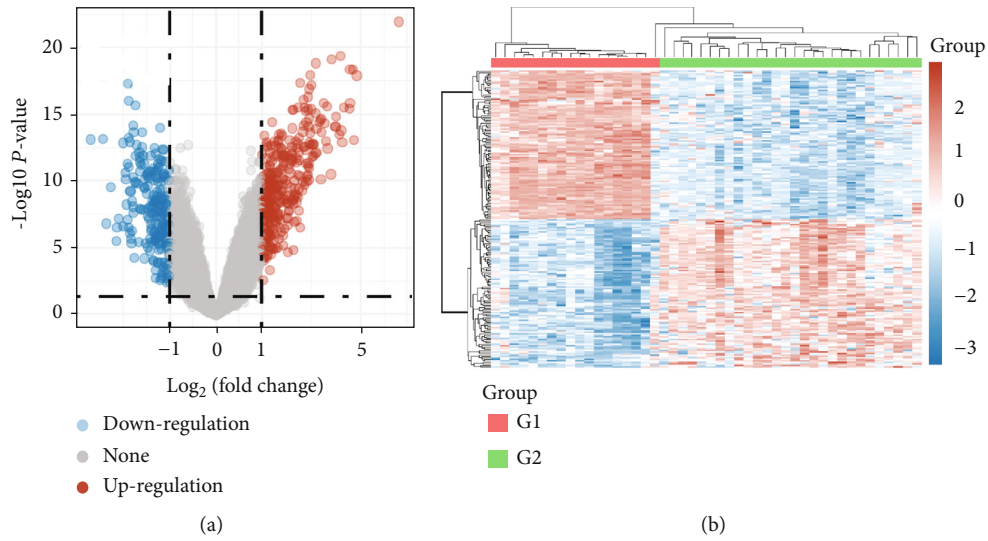
FIGURE 3: Volcano plot of differentially expressed genes. The abscissa represents the fold change in the gene expression, and the ordinate represents the statistical significance of the change in gene expression. Red dots represent genes with significantly increased expression, and blue dots represent genes with reduced expression (a). Heat map of differentially expressed genes. Heat map shows differentially expressed genes in normal ovarian tissue (G1) and HGSC (G2). Upregulated and downregulated genes are shown (b).
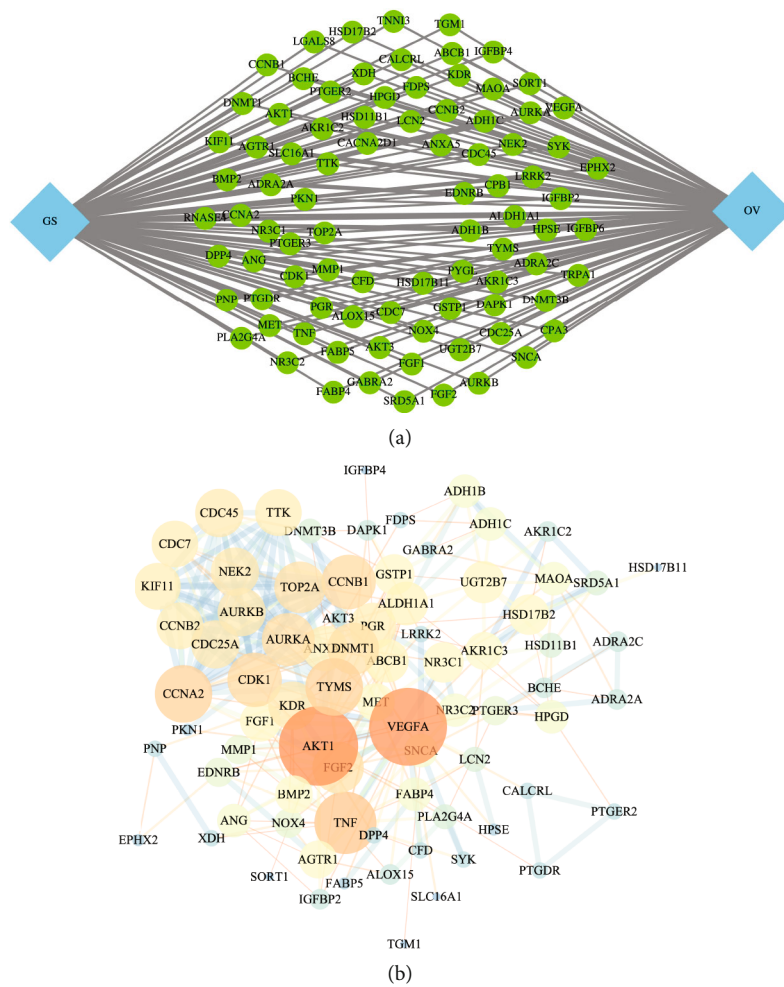
FIGURE 4: The key targets of the Gleditsiae Spina treating for ovarian cancer (a) and the PPI network (b).

(a)

(b)
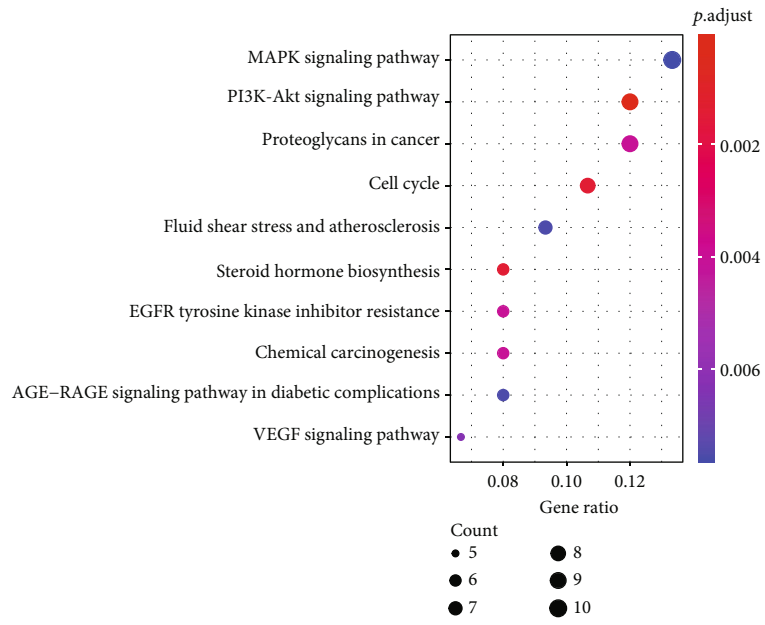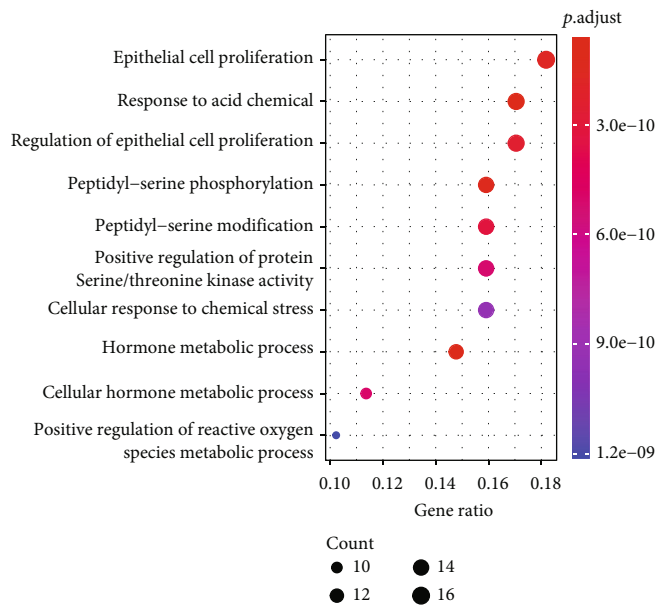
Figure 5: Continued.
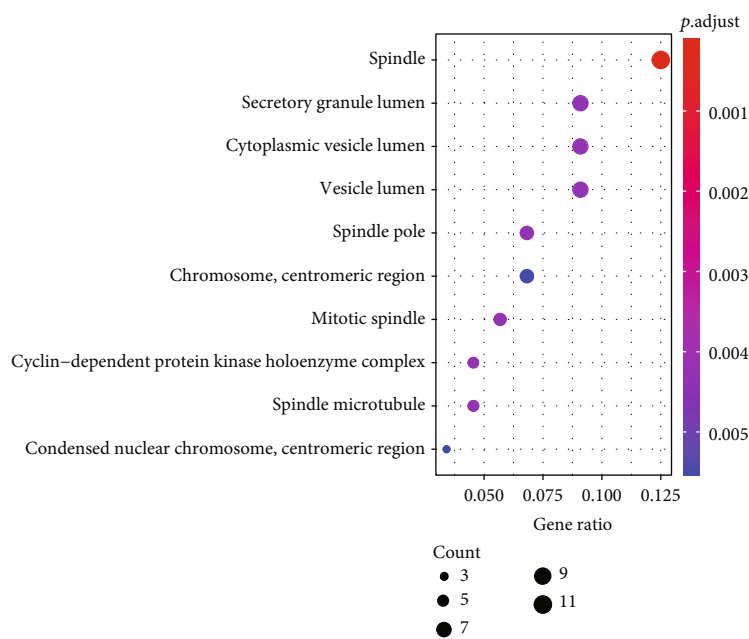
(c)
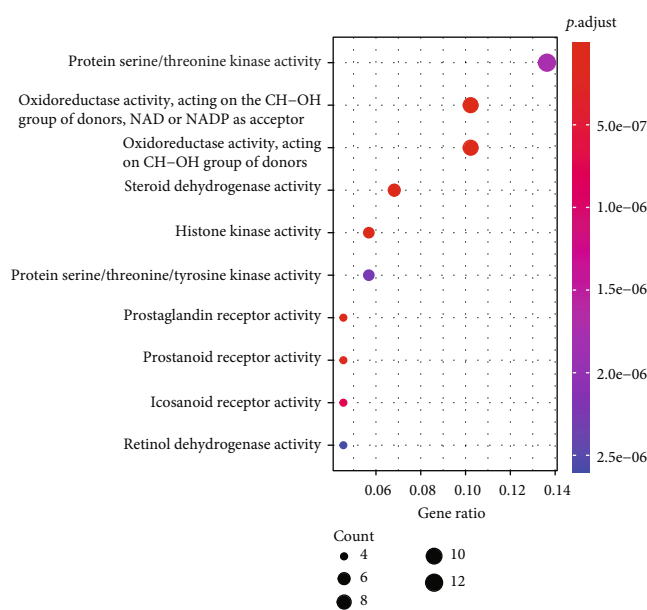
(d)

FIGURE 5: Bubble diagram of GO and KEGG enrichment of key targets for Gleditsiae Spina for treatment of HGSC. (a) KEGG analysis. (b) GO BP analysis. (c) GO CC analysis. (d) GO MF analysis. Pathways that had significant changes of log 10 $(P) < 0.05$ were identified. Size of the spot represents number of genes, and color represents log10 (P) value.

TABLE 3: The docking affinity value of compounds with core targets.

	Luteolin	Genistein
PIK3CA	-8.49	-8.59
CTNNB1	-8.47	-7.56
HSPE	-8.97	-7.35
AKT1	-8.22	-8.79

The binding of genistein and luteolin to the ligand quickly stabilized and continued to work and after a short period of fluctuation, the binding of berberine to the ligand also forms a stable state. The results were shown in Figure 7.

3.3. Verification of Therapeutic Effects of Gleditsiae Spina on Ovarian Cancer. Next, we conducted experiments in vitro to verify the potential therapeutic targets of Gleditsiae Spina. The MTT assay was performed to evaluate the viability of A2780, SKOV3, and HEY cancer cells and normal cells IOSE80 and SVOG as comparison treated with increasing
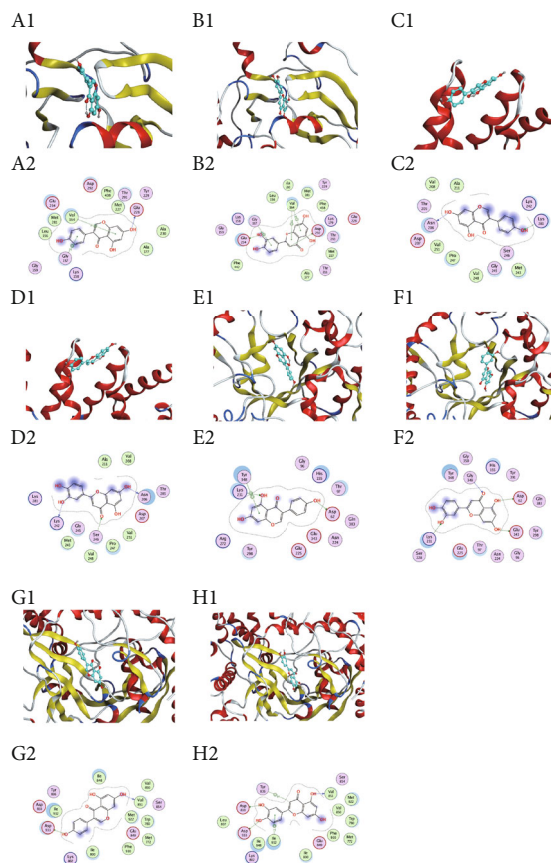
FIGURE 6: Molecular docking of compounds with core targets: (a) AKT1-genistein, (b) AKT1-luteolin, (c) CTNNB1-genistein, (d) CTNNB1-luteolin, (e) HPSE-genistein, (f) HPSE-luteolin, (g) PIK3CA-genistein, and (h) PIK3CA-luteolin.

concentrations of Gleditsiae Spina solution (0.25-8 mg/mL) for 24 and 48 h. Gleditsiae Spina decreased ovarian cancer cells viability in a dose-dependent way, but not the normal ovarian cells, and the normal cells only showed a large amount of died when above 8 mg/mL. The results showed that the Gleditsiae Spina has a certain killing effect on tumor cells but not on tissue cells (shown in Figures 8(a) and 8(b)). To further explore the therapeutic mechanisms of Gleditsiae Spina in combination with the above-described KEGG analysis data, A2780 cells were stimulated with 1.25 and 2.5 mg/ mL Gleditsiae Spina solution for 24 h, followed by protein extraction and analysis by western blotting, with heparinase as core (Figures 8(c) and 8(d)). Our results showed that the levels of heparinase 1, MMP9, β-catenin, and N-cadherin were significantly downregulated in ovarian cancer cells in response to Gleditsiae Spina treatment in a dose-dependent manner. However, the level of E-cadherin increased in the high-dose group; although, the increase was not statistically significant. Furthermore, treatment with Gleditsiae Spina inhibited the expression of proteins associated with the PI3K/AKT/mTOR pathway. However, the expression of these molecules increased at higher doses of Gleditsiae Spina compared to the low-dose group, though the higher doses of Gleditsiae Spina can also reduce the expression of PI3K/ AKT kinase and their phosphorylated proteins This may

be attributed to the interaction between the complex components of traditional Chinese medicine and the cells, which lead to cell death. At high Gleditsiae Spina concentrations, only a small number of cells survived for more than 48 h. Therefore, although the autocompensation mechanism of cells can be ruled out, the specific mechanism in vivo needs to be further explored. Next, we explored whether the antitumor effect of GS was AKT kinase-dependent. AKT kinase inhibitor was added to the cells at a concentration of 2 nM, and the expression of AKT kinase in ovarian cancer cells was shown in Figure 8(e). The antitumor effect of Gleditsiae Spina on A2780 cells after silencing AKT kinase expression is shown in Figure 8(f). After inhibiting the expression of AKT, the doubling time of cells increased from 26.3 hours to 30.2 hours, but the killing effect of Gleditsiae Spina on tumor cells also existed. The results showed that AKT is only one of the targets of Gleditsiae Spina, and the antitumor effect of Gleditsiae Spina partially depends on AKT kinase.

4. Discussion

Traditional Chinese medicine has a long history and has nurtured the Chinese nation for millennia. It protects human health through dialectical theory. Traditional Chinese medicine works against diseases through a single or compound prescription by multiple ingredients and targets. The cause of ovarian cancer is considered to be the accumulation of pathological products in TCM theory, and Gleditsiae Spina has the potential to clear these toxic metabolites. It is a summary of experience obtained in clinical practice of TCM and has obvious clinical effects based on clinical experience. The concept of network pharmacology and the theory of TCM have similar aspects, which can explore the unknown mechanism of action of Chinese herbal medicine from the perspective of overall composition and function [25]. Our experimental results also showed that Gleditsiae Spina has a selective therapeutic effect on ovarian cancer.

Based on the mass spectrometry results, along with previously reported data, we inferred that luteolin, genistein, D-(+)-tryptophan, ursolic acid, and berberine in the Gleditsiae Spina play a core role in the treatment of ovarian cancer. It was previously reported that D-(+)-tryptophan exhibits anticancer activity, which can stimulate mTORC1 and enhance the activity of T-cells within the tumor microenvironment [26]. Luteolin is a flavonoid compound that inhibits tumor cell proliferation, blocks cell cycle, and reverses tumor epithelial-mesenchymal transition [27]. Luteolin downregulates the expression of aromatase and consequently inhibits estrogen synthesis in ovarian cancer [28]. Genistein can modulate the cell cycle and regulate the ERK1/2, NF-κB, Wnt, β-catenin, and PI3K/Akt signaling pathways to exert its anticancer effects. Moreover, it can synergize with paclitaxel and other ovarian cancer drugs [29]. Ursolic acid can downregulate the expression of YAP1 of the hippo pathway in tumor treatment [30]. Studies have shown that berberine can induce apoptosis in various tumor cell lines. By inhibiting the transcriptional activity of β-catenin, berberine modulates the Wnt signaling pathway [31] and increases the expression of caspase-3 and -8; thus, it promotes apoptosis
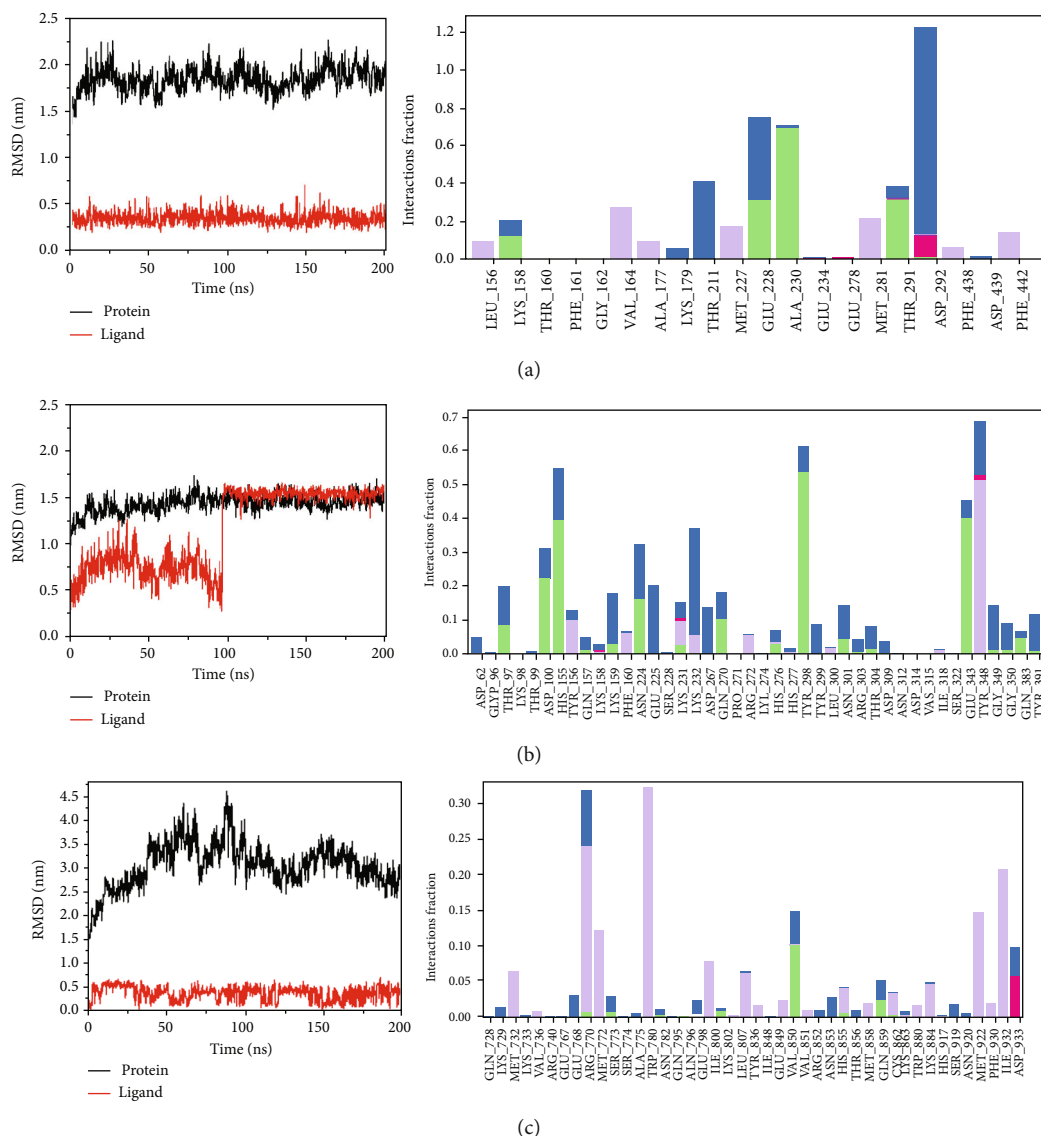
FIGURE 7: Molecular dynamic simulation of compounds with core targets: RMSD plot during molecular dynamic simulations of AKT1 with genistein (a), HPSE with luteolin (b), and PI3K with berberine (c).

of ovarian cancer cells, when used in combination with cisplatin [32].

The KEGG results showed that Gleditsiae Spina affects ovarian cancer development via multiple pathways and thus plays a therapeutic role. The expression levels of heparinase 1, MMP9, β-catenin, N-cadherin, and PI3K/AKT/mTOR, as well as their phosphorylation levels, which are involved in tumor progression, were reduced after treatment with Gleditsiae Spina.

Proteoglycans are widely distributed on the cell surface and in the cytoplasmic matrix; moreover, they play an important role in tumor development. Their glycosaminoglycan chains are modulated by heparinase, the only endoglycosidase in mammals; hence, heparinase plays an important role in regulating the function of proteoglycans [33]. Several studies have found that the expression of heparinase is positively correlated with malignancy, with heparinase overexpressing tumors being associated with a worse

prognosis compared with tumors in which heparinase is under expressed [34]. The extracellular matrix is mainly composed of keratan sulfate proteoglycans, chondroitin sulfate proteoglycans, and dermatan sulfate proteoglycans [35]; therefore, heparinase can accelerate the remodeling of tumor extracellular matrix and basement membrane [36] and contribute to tumor. Moreover, the cleaved heparan sulfate proteoglycans can bind to growth factors and increase the expression of VEGF by promoting p38 phosphorylation and Src kinase activity [37], thereby promoting angiogenesis and accelerating tumor metastasis and invasion [38]. Our in vitro experiments showed that Gleditsiae Spina can inhibit the tumor growth and downregulate heparinase expression in tumor cells. By reducing the expression of heparinase, Gleditsiae Spina can regulate signaling cascades within the tumors [39].

MMP9 plays an important role in tumor extracellular matrix remodeling and communication between tumor cells

(a)

(b)

(c)

(d)

(e)

(f)
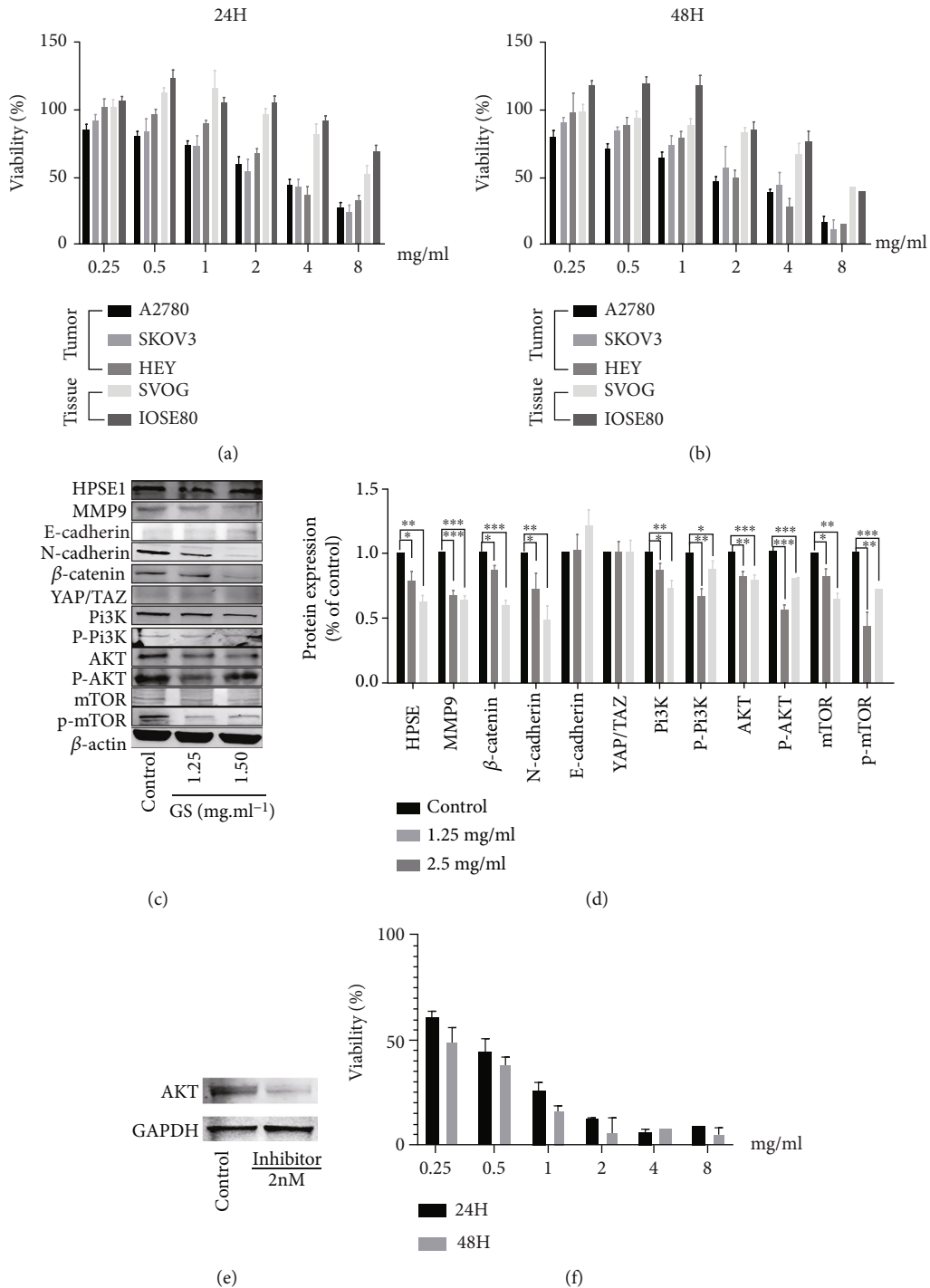
Figure 8: The cellular verification results. Gleditsiae Spina inhibited ovarian cancer cells proliferation in a dose-dependent way after incubation 24 h (a) and 48 h (b). (c) After exposure to the Gleditsiae Spina for 24 h, the total protein from each cell lysate was analyzed by Western blotting to measure the expression of proteins. (d) Data are presented as the mean ± SD and normalized to β-actin. (e) The AKT expression was decreased by AKT kinase inhibitor. (f) Dose-dependent inhibitory effect of Gleditsiae Spina on ovarian cancer cell proliferation under AKT kinase inhibitor of 2 nM ($^*P < 0.05$, $^{**}P < 0.01$, $^{***}P < 0.001$).

[40]. MMP9 is considered a potential biomarker for tumors, including ovarian cancer [41]. Our western blotting results showed that Gleditsiae Spina significantly inhibits the expression of MMP9 to reduce tumor cell activity. E-cadherin is a calcium ion-dependent transmembrane protein

closely related to cell adhesion. Adjacent cells interact via an extracellular domain of E-cadherin, which is connected to β-catenin and the cell cytoskeleton. Thus, the E-cadherin expression is negatively correlated with the degree of tumor invasion [42]. Numerous studies have shown that the

conversion of E-cadherin to N-cadherin often indicates the completion of the epithelial–mesenchymal transition process. Herein, although the expression of E-cadherin was low and changes in its expression could not be measured, the expression of N-cadherin was inhibited after treatment with Gleditsiae Spina, indicating that Gleditsiae Spina can reverse the expression of the two proteins, thereby inhibiting tumor development. β-Catenin is a cytoplasmic protein, and its nuclear expression plays a role in activating transcription factors. The abnormal expression of β-catenin is related to the hippo and HIF1 signaling pathways, and it can also activate the Wnt signaling pathway [43]. Moreover, its abnormal expression is closely related to colon cancer [44] and cervical cancer. Our western blotting results showed that Gleditsiae Spina inhibited the expression of β-catenin protein, which were consistent with the prediction results of the network pharmacology.

The PI3K/AKT/mTOR signaling pathway plays key role in cancer, as is related to cell proliferation, angiogenesis, chemotherapy resistance, and several other pathological conditions. Its downstream molecule mTOR can accelerate the formation of tumor stem cells [45], leading to tumor progression and relapse. The overexpression of PI3K can lead to RAS mutations and loss of PTEN and is associated with HIF1, hippo, and MAPK signaling pathways. Moreover, it activates the epidermal growth factor receptor, stimulates the expression of the vascular endothelial growth factor, and accelerates angiogenesis [46]. Approximately 70% of ovarian cancer patients present with overexpressed PI3K/AKT/mTOR cascade [47]; thus, using inhibitors to target this pathway is an important strategy to treat ovarian cancer. In our study, Gleditsiae Spina significantly inhibited the expression of PI3K and AKT; low-dose treatment with Gleditsiae Spina inhibited the phosphorylation of AKT and mTOR, whereas the remarkably increased phosphorylation in the high-dose-treated group suggested its own S6K1-IRS1 negative feedback. Additional experiments are warranted to elucidate the underlying mechanism of the regulatory effect exerted by Gleditsiae Spina. According to the WB results, when the cancer cells were exposed at the concentration of 2.5 mg/mL of Gleditsiae Spina, the levels of AKT and P-AKT kinase expressed in cells are downregulated, and the phosphorylated protein is not significantly decreased. The results indicated that Gleditsiae Spina did not mainly affect the phosphorylation of AKT pathway proteins, but its complex biological effects reduced the Pi3k/AKT and its phosphorylation kinase in cells. Later, we want to know whether the therapeutic effect of Gleditsiae Spina was dependent on the AKT pathway. We inhibited the expression of AKT in cells. In this case, Gleditsiae Spina still had an inhibitory effect, which also proves our prediction that PI3K/AKT signaling pathway is only one of the effects of Gleditsiae Spina. Traditional Chinese medicine has a complex mechanism in the treatment of ovarian cancer. The characteristics of multitarget and multipathway interaction need to be explored.

The molecular docking experiments can predict the binding ability of the ligand and the target at the molecular level. Using this approach, we determined that several components of Gleditsiae Spina have high binding ability to the ovarian cancer targets. Gleditsiae Spina can interfere with the activities of heparinase 1, β-catenin, PI3K, and AKT at the molecular level, thereby proving that Gleditsiae Spina can exert significant therapeutic effects on ovarian cancer. Molecular dynamic simulations, which can monitor time-resolved motions of molecules [48], further showed that the ingredients of Gleditsiae Spina stably interact with the disease-specific molecules in ovarian cancer, which indirectly provides a basis for verifying its therapeutic efficacy.

5. Conclusion

In this study, we firstly clarified the main components of Gleditsiae Spina and then predicted potential targets through network pharmacology and verified through molecular docking, molecular dynamic simulation, and experimental verification in vitro. We found that Gleditsiae Spina can regulate PI3K/AKT pathway and the composition of cytoplasmic matrix and proteoglycans in cancer. The regulatory mechanism of Gleditsiae Spina on ovarian cancer was partially revealed in this study, laying a foundation for future scientific research on TCM.

Abbreviation

ERK: Extracellular signal-regulated kinases
HGSC: High-grade serous ovarian cancer
HPLC: High performance liquid chromatography
MCE: MedChemExpress
MDSCs: Myeloid-derived suppressor cells
MMP9: Matrix metalloproteinase-9
MS: Mass spectrometry
MTT: 3-(4,5-Dimethylthiazol-2-yl)-2,5-diphenyltetrazoliumbromide
RMSD: Root mean square deviation
RMSF: Root mean square fluctuation
ROS: Reactive oxygen species
TCM: Traditional Chinese medicine
TNF-α: Tumor necrosis factor-alpha
WB: Western blot.

Data Availability

The data that support the findings of this study are available from the corresponding authors upon reasonable request.

Disclosure

The article was presented as a preprint in research square according to the following link "https://www.researchsquare.com/article/rs-744923/v1."

Conflicts of Interest

The authors declare that they have no conflicts of interest.

Authors' Contributions

Conceptualization was contributed by BZ and WD. Methodology was contributed by BZ. Software was contributed by

Acknowledgments

Supplementary Materials

Supplementary material 1: the mass spectra of 39 identified compounds was shown in supplementary material 1. Through the mass spectrum of each component, the structure of the compound could be speculated, and the type of compounds was indirectly determined. *(Supplementary Materials)*

References

[1] P. M. Webb and S. J. Jordan, "Epidemiology of epithelial ovarian cancer," *Best Practice & Research. Clinical Obstetrics & Gynaecology*, vol. 41, pp. 3–14, 2017.

[2] S. Siamakpour-Reihani, L. P. Cobb, C. Jiang et al., "Differential expression of immune related genes in high-grade ovarian serous carcinoma [published online ahead of print, 2020 Jan 7]," *Gynecologic Oncology*, vol. 19, article 8258, pp. 31840–31842, 2020.

[3] G. C. Jayson, E. C. Kohn, H. C. Kitchener, and J. A. Ledermann, "Ovarian cancer," *Lancet*, vol. 384, no. 9951, pp. 1376–1388, 2014.

[4] T. V. Gorodnova, A. P. Sokolenko, E. Kuligina, I. V. Berlev, and E. N. Imyanitov, "Principles of clinical management of ovarian cancer," *Chinese Clinical Oncology*, vol. 7, no. 6, p. 56, 2018.

[5] K. Lee, F. A. Tavassoli, J. Prat, and W. Böcker, "Tumors of the ovary and peritoneum," in *World Health Organization cassification of tumors: Pathology and genetics of tumors of the breast and female genital organs*, p. 117, IARC Press, Japan, 2003.

[6] L. Y. Han and R. L. Coleman, "Ovarian cancer staging," *Operative Techniques in General Surgery*, vol. 9, no. 2, pp. 53–60, 2007.

[7] R. Liu, R. Hu, Y. Zeng, W. Zhang, and H. H. Zhou, "Tumour immune cell infiltration and survival after platinum-based chemotherapy in high-grade serous ovarian cancer subtypes: a gene expression-based computational study," *eBioMedicine*, vol. 51, article 102602, 2020.

[8] K. Chan, "Progress in traditional Chinese medicine," *Trends in Pharmacological Sciences*, vol. 16, no. 6, pp. 182–187, 1995.

[9] J. Liu, S. Wang, Y. Zhang, H. T. Fan, and H. S. Lin, "Traditional Chinese medicine and cancer: history, present situation, and development," *Thoracic Cancer*, vol. 6, no. 5, pp. 561–569, 2015.

[10] R. Wang, Q. Sun, F. Wang et al., "Efficacy and safety of Chinese herbal medicine on ovarian cancer after reduction surgery and adjuvant chemotherapy: a systematic review and meta-analysis," *Frontiers in Oncology*, vol. 9, p. 730, 2019.

[11] S. Owen, F. Ruge, Y. Gao et al., "ShenLingLan influences the attachment and migration of ovarian cancer cells potentially through the GSK3 pathway," *Medicines*, vol. 4, no. 1, p. 10, 2017.

[12] Y. Xie, Y. Zhang, X. Wei et al., "Jianpi Huayu decoction attenuates the immunosuppressive status of H22 hepatocellular carcinoma-bearing mice: by targeting myeloid-derived suppressor cells," *Frontiers in Pharmacology*, vol. 11, no. 11, p. 16, 2020.

[13] Y. Jiang, Y. Zhang, J. Luan et al., "Effects of bufalin on the proliferation of human lung cancer cells and its molecular mechanisms of action," *Cytotechnology*, vol. 62, no. 6, pp. 573–583, 2010.

[14] J. N. M. College, *Dictionary of Chinese Medicine*, Shanghai Printing Factory, Shanghai, China, 1986.

[15] J. Li, K. Jiang, L. J. Wang et al., "HPLC–MS/MS determination of flavonoids in Gleditsiae Spina for its quality assessment," *Journal of Separation Science*, vol. 41, no. 8, pp. 1752–1763, 2018.

[16] S. J. Lee, Y. H. Cho, H. Kim et al., "Inhibitory effects of the ethanol extract of Gleditsia sinensis thorns on human colon cancer HCT116 cells in vitro and in vivo," *Oncology Reports*, vol. 22, no. 6, pp. 1505–1512, 2009.

[17] Y. Jiang, M. Zhong, F. Long, and R. Yang, "Deciphering the active ingredients and molecular mechanisms of Tripterygium hypoglaucum (Levl.) hutch against rheumatoid arthritis based on network pharmacology," *Evidence-based Complementary and Alternative Medicine*, vol. 2020, 9 pages, 2020.

[18] R. Z. Zhang, S. J. Yu, H. Bai, and K. Ning, "TCM-mesh: the database and analytical system for network pharmacology analysis for TCM preparations," *Scientific Reports*, vol. 7, no. 1, p. 2821, 2017.

[19] X. Wang, Y. Shen, S. Wang et al., "PharmMapper 2017 update: a web server for potential drug target identification with a comprehensive target pharmacophore database," *Nucleic Acids Research*, vol. 45, no. W1, pp. W356–W360, 2017.

[20] D. Otasek, J. H. Morris, J. Bouças, A. R. Pico, and B. Demchak, "Cytoscape automation: empowering workflow-based network analysis," *Genome Biology*, vol. 20, no. 1, p. 185, 2019.

[21] A. Martin, M. E. Ochagavia, L. C. Rabasa, J. Miranda, J. Fernandez-de-Cossio, and R. Bringas, "BisoGenet: a new tool for gene network building, visualization and analysis," *BMC Bioinformatics*, vol. 11, no. 1, p. 91, 2010.

[22] Y. Tang, M. Li, J. Wang, Y. Pan, and F.-X. Wu, "CytoNCA: A cytoscape plugin for centrality analysis and evaluation of protein interaction networks," *Biosystems*, vol. 127, pp. 67–72, 2015.

[23] Y. Zhou, B. Zhou, L. Pache et al., "Metascape provides a biologist-oriented resource for the analysis of systems-level datasets," *Nature Communications*, vol. 10, no. 1, p. 1523, 2019.

[24] K. Y. Hsin, S. Ghosh, and H. Kitano, "Combining machine learning systems and multiple docking simulation packages to improve docking prediction reliability for network pharmacology," *PLoS One*, vol. 8, no. 12, article e83922, 2013.

[25] Y. Jiang, N. Liu, S. Zhu, X. Hu, D. Chang, and J. Liu, "Elucidation of the mechanisms and molecular targets of Yiqi Shexue formula for treatment of primary immune thrombocytopenia based on network pharmacology," *Frontiers in Pharmacology*, vol. 10, p. 1136, 2019.

[26] E. Fox, T. Oliver, M. Rowe et al., "Indoximod: an immunometabolic adjuvant that empowers T cell activity in cancer," *Frontiers in Oncology*, vol. 8, no. 8, p. 370, 2018.

[27] Z. Tai, Y. Lin, Y. He et al., "Luteolin sensitizes the antiproliferative effect of interferon α/β by activation of Janus kinase/signal transducer and activator of transcription pathway signaling through protein kinase A-mediated inhibition of protein tyrosine phosphatase SHP-2 in cancer cells," *Cellular Signalling*, vol. 26, no. 3, pp. 619–628, 2014.

[28] Y. C. Ou, J. R. Li, Y. H. Kuan et al., "Luteolin sensitizes human 786-O renal cell carcinoma cells to TRAIL-induced apoptosis," *Life Sciences*, vol. 100, no. 2, pp. 110–117, 2014.

[29] C. Spagnuolo, G. L. Russo, I. E. Orhan et al., "Genistein and cancer: current status, challenges, and future directions," *Advances in Nutrition*, vol. 6, no. 4, pp. 408–419, 2015.

[30] S. H. Kim, H. Jin, R. Y. Meng et al., "Activating hippo pathway via Rassf1 by ursolic acid suppresses the tumorigenesis of gastric cancer," *International Journal of Molecular Sciences*, vol. 20, no. 19, p. 4709, 2019.

[31] K. F. Albring, J. Weidemüller, S. Mittag et al., "Berberine acts as a natural inhibitor of Wnt/β-catenin signaling-Identification of more active 13-arylalkyl derivatives," *BioFactors*, vol. 39, no. 6, pp. 652–662, 2013.

[32] L. Liu, J. Fan, G. Ai et al., "Berberine in combination with cisplatin induces necroptosis and apoptosis in ovarian cancer cells," *Biological Research*, vol. 52, no. 1, pp. 1–14, 2019.

[33] U. Barash, M. Lapidot, Y. Zohar et al., "Involvement of heparanase in the pathogenesis of mesothelioma: basic aspects and clinical applications," *Journal of the National Cancer Institute*, vol. 110, no. 10, pp. 1102–1114, 2018.

[34] X. Sun, G. Zhang, J. Nian et al., "Elevated heparanase expression is associated with poor prognosis in breast cancer: a study based on systematic review and TCGA data," *Oncotarget*, vol. 8, no. 26, pp. 43521–43535, 2017.

[35] R. V. Iozzo and L. Schaefer, "Proteoglycan form and function: a comprehensive nomenclature of proteoglycans," *Matrix Biology*, vol. 42, pp. 11–55, 2015.

[36] V. Masola, G. Bellin, G. Gambaro, and M. Onisto, "Heparanase: a multitasking protein involved in extracellular matrix (ECM) remodeling and intracellular events," *Cell*, vol. 7, no. 12, p. 236, 2018.

[37] L. M. Ellis, C. A. Staley, W. Liu et al., "Down-regulation of vascular endothelial growth factor in a human colon carcinoma cell line transfected with an antisense expression vector specific for c- src*," *The Journal of Biological Chemistry*, vol. 273, no. 2, pp. 1052–1057, 1998.

[38] V. C. Ramani, A. Purushothaman, M. D. Stewart et al., "The heparanase/syndecan-1 axis in cancer: mechanisms and therapies," *The FEBS Journal*, vol. 280, no. 10, pp. 2294–2306, 2013.

[39] G. L. Zhang, L. Gutter-Kapon, N. Ilan et al., "Significance of host heparanase in promoting tumor growth and metastasis," *Matrix Biology*, vol. 93, pp. 25–42, 2020.

[40] D. Xu, C. M. McKee, Y. Cao, Y. Ding, B. M. Kessler, and R. J. Muschel, "Matrix metalloproteinase-9 regulates tumor cell invasion through cleavage of protease nexin-1," *Cancer Research*, vol. 70, no. 17, pp. 6988–6998, 2010.

[41] R. Roy, J. Yang, and M. A. Moses, "Matrix metalloproteinases as novel biomarkers and potential therapeutic targets in human cancer," *Journal of Clinical Oncology*, vol. 27, no. 31, pp. 5287–5297, 2009.

[42] F. Van Roy and G. Berx, "The cell-cell adhesion molecule E-cadherin," *Cellular and Molecular Life Sciences*, vol. 65, no. 23, pp. 3756–3788, 2008.

[43] M. Katoh, "Multi-layered prevention and treatment of chronic inflammation, organ fibrosis and cancer associated with canonical WNT/β-catenin signaling activation (review)," *International Journal of Molecular Medicine*, vol. 42, no. 2, pp. 713–725, 2018.

[44] P. J. Morin, A. B. Sparks, V. Korinek et al., "Activation of β-catenin-Tcf signaling in colon cancer by mutations in β-catenin or APC," *Science*, vol. 275, no. 5307, pp. 1787–1790, 1997.

[45] P. Xia and X. Y. Xu, "PI3K/Akt/mTOR signaling pathway in cancer stem cells: from basic research to clinical application," *American Journal of Cancer Research*, vol. 5, no. 5, pp. 1602–1609, 2015.

[46] J. Karar and A. Maity, "PI3K/AKT/mTOR pathway in angiogenesis," *Frontiers in Molecular Neuroscience*, vol. 4, p. 51, 2011.

[47] Cancer Genome Atlas Research, "Network. Integrated genomic analyses of ovarian carcinoma [published correction appears in Nature. 2012 Oct 11;490(7419):298]," *Nature*, vol. 474, no. 7353, pp. 609–615, 2011.

[48] P. W. Hildebrand, A. S. Rose, and J. K. S. Tiemann, "Bringing molecular dynamics simulation data into view," *Trends in Biochemical Sciences*, vol. 44, no. 11, pp. 902–913, 2019.

Research Article

Network Pharmacology-Based Strategy for Predicting Therapy Targets of Citri Reticulatae Pericarpium on Myocardial Hypertrophy

Shisheng Jiang [ID],[1] **Chaoming Huang** [ID],[1] **Shulin Wang** [ID],[2] **Biyun Huang** [ID],[1] **Dan Wu** [ID],[1] **Guodong Zheng** [ID],[1] **and Yi Cai** [ID][1,2]

[1]*Key Laboratory of Molecular Target & Clinical Pharmacology and the State & NMPA Key Laboratory of Respiratory Disease, School of Pharmaceutical Sciences & The Fifth Affiliated Hospital, Guangzhou Medical University, Guangzhou 511436, China*
[2]*The Sixth Affiliated Hospital of Guangzhou Medical University, Qingyuan People's Hospital, Guangzhou Medical University, Guangzhou, Qingyuan 511500, China*

Correspondence should be addressed to Guodong Zheng; gd200237@126.com and Yi Cai; yicaisysu@163.com

Objective. Through a network pharmacology method, we screened the main active compounds of Citri Reticulatae Pericarpium (CRP), constructed a drug-ingredient-disease-target network, explored the molecular mechanism of its treatment of myocardial hypertrophy, and validated it by using molecular biology approach. *Methods.* Traditional Chinese Medicine Systems Pharmacology (TCMSP) and GeneCards were utilised to collect the effective component in CRP and the targets of CRP and myocardial hypertrophy. The STRING database constructed the protein interaction network. The drug-ingredient-disease-target network was outlined by the Cytoscape 3.9.0 software. The Gene Ontology (GO) and Kyoto Encyclopedia of Genes and Genomes (KEGG) pathway enrichment analyses were conducted using the Metascape database. Real-time PCR (RT-PCR) and Western blotting were utilised to determine the mRNA and protein level of the critical targets of CRP therapy for myocardial hypertrophy. *Results.* We found that five practical components of CRP exerted therapeutic effects on myocardial hypertrophy by modulating 41 targets. Further analysis revealed that naringenin was the essential active compound in CRP that regulated myocardial hypertrophy. In addition, we showed that the active compounds of CRP might exert antihypertrophy effects via regulating essential target proteins such as AKT1-, MAPK3-, PPARA-, PPARG-, and ESR1-mediated signaling pathways such as cell proliferation, nuclear receptor activation, and oxidative stress. The molecular biology experiments demonstrated that naringenin inhibited the mRNA level of NPPA and NPPB induced by Ang II and regulated related targets such as AKT1, MAPK3, PPARA, PPARG, and ESR1. *Conclusion.* CRP could inhibit myocardial hypertrophy through multitarget and multiapproach.

1. Introduction

Cardiovascular diseases (CVD) have become the "number one killer" threatening human health. Studies show that CVD is a primary cause of death in China, accounting for more than 40% of worldwide deaths, affecting hundreds of millions of people each year [1–3]. Myocardial hypertrophy is an everyday pathological basis and an independent risk factor for many CVD such as atherosclerosis, coronary artery disease, and valvular disease, mainly manifested by an increased surface area of cardiac myocytes, increased synthesis of cardiac proteins, and abnormal activation of embryonic genes. While early myocardial hypertrophy helps maintain average cardiac output and cardiac function, persistent pathological myocardial hypertrophy can trigger a decline in heart function and eventually lead to heart failure [4, 5]. The pathogenesis of myocardial hypertrophy is a complex multifactorial process that touches on several cellular and molecular systems. Several signaling pathways, including the CaMKII pathway, mitogen-activated protein
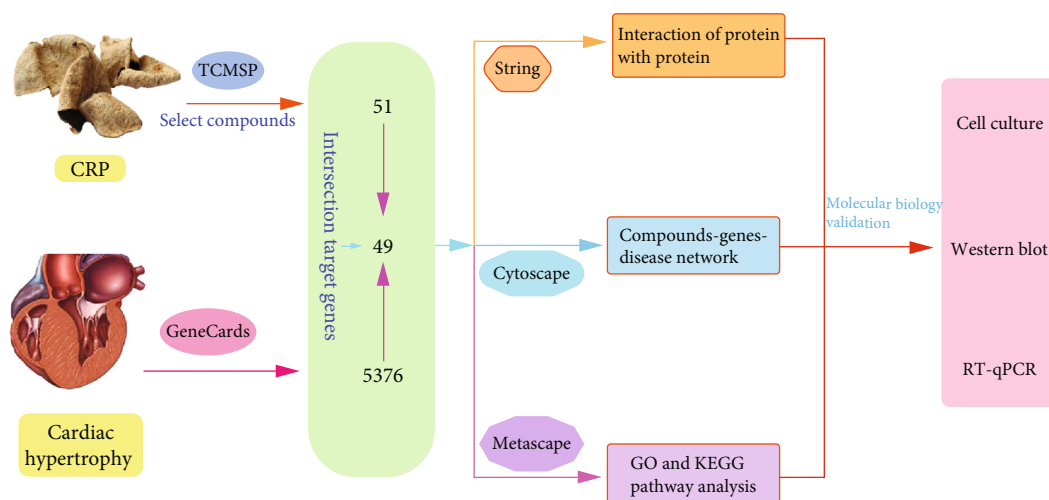
FIGURE 1: The workflow of key target gene prediction and validation of CRP therapy for myocardial hypertrophy.

TABLE 1: Primer sequences for qRT-PCR.

Primer	Sequences
NPPA	Forward:5′-GGAAGTCAACCCGTCTCA-3′
	Reverse:5′-AGCCCTCAGTTTGCTTTT-3′
NPPB	Forward:5′-TTTGGGCAGAAGATAGACCG-3′
	Reverse:5′-AGAAGAGCCGCAGGCAGAG-3′
PPARA	Forward:5′-TGAAAGATTCGGAAACTGC-3′
	Reverse:5′-TTCCTGCGAGTATGACCC-3′
PPARG	Forward:5′-TACCACGGTTGATTTCTC-3′
	Reverse:5′-TCTACTTTGATCGCACTTT-3′
ESR1	Forward: 5′ AGACTCGCTACTGTGCTGTG 3′
	Reverse:5′-CCTGGCAACTCTTCCTCC-3′
GAPDH	Forward:5′-AGGAGTAAGAAACCCTGGAC-3′
	Reverse:5′-CTGGGATGGAATTGTGAG-3′

TABLE 2: Characteristics of active ingredients in CRP.

No.	Molecule ID	Molecule name	Molecular weight	OB (%)	DL
1	MOL000359	Sitosterol	414.79	36.91	0.75
2	MOL004328	Naringenin	272.27	59.29	0.21
3	MOL005100	Hesperetin	302.3	47.74	0.27
4	MOL005815	Citromitin	404.45	86.9	0.51
5	MOL005828	Nobiletin	402.43	61.67	0.52

kinase (MAPK), peroxisome proliferator-activated receptor (PPAR), PI3K/AKT, and oxidative stress response pathway, are involved in the progression of myocardial hypertrophy [6–9]. Western drugs such as angiotensin-converting enzyme inhibitors (ACEI), aldosterone receptor antagonists, and β-blockers are mainly used in the clinical treatment of cardiac failure, which has not significantly reduced the mortality rate [10–12]. However, they have improved the clinical symptoms of patients to some extent. Chinese medicine emphasizes the treatment of both the symptoms and the root cause of the disease and identifying evidence. More and more studies have shown that traditional Chinese medicine (TCM) is widely valued for its stable efficacy and ability to act on multiple aspects of the development of myocardial hypertrophy [13].

Citri reticulatae pericarpium (CRP), commonly called Chenpi in Chinese, is the dried and ripe peel of Citrus reticulata Blanco and its cultivated varieties, aromatic, spicy, and bitter [14]. As one of the most commonly used TCM, CRP is rich in bioactive substances, such as flavonoids and volatile, volatile compounds, oils, and polysaccharides. These active ingredients have various biological activities and medicinal values, such as antioxidant, anti-inflammatory, antibacterial, anticancer, and cardiovascular protective functions [15]. In recent years, many components in CRP, especially flavonoid glycosides, such as naringenin and hesperidin, and polymethoxyflavonoids, such as nobiletin, are played in place of CVD which have become a hot research topic [16]. Several lines of evidence have proven that these flavonoids in CRP are significant in inhibiting atherosclerosis, regulating blood lipids, and improving myocardial hypertrophy [17]. Also, a previous study demonstrated the epidemiological association between the intake of foods containing citrus flavonoids and a reduction in CVD occurrence [18]. However, to date, studies on the role and mechanism of active ingredients in myocardial hypertrophy in CRP are still incomplete and deserve further investigation.

This present study constructs the interaction network between the active components of CRP, drug targets, and myocardial hypertrophy-related target genes, initially investigating the molecular mechanism of action of CRP in the treatment of myocardial hypertrophy. Moreover, we also investigate the effect of naringenin on myocardial hypertrophy and related targets predicted before. The workflow is shown in Figure 1.

TABLE 3: 41 potential target genes of CRP therapy for myocardial hypertrophy.

No.	Target	Symbol	Entrez ID
1	Progesterone receptor	PGR	5241
2	Nuclear receptor coactivator 2	NCOA2	10499
3	Nuclear receptor subfamily 3 group C member 2	NR3C2	4306
4	Prostaglandin-endoperoxide synthase 1	PTGS1	5742
5	Estrogen receptor 1	ESR1	2099
6	Prostaglandin-endoperoxide synthase 2	PTGS2	5743
7	Heat shock protein 90 alpha family class B member 1	HSP90AB1	3326
8	Metallo-beta-lactamase domain-containing 2	MBLAC2	153364
9	Protein kinase CAMP-activated catalytic subunit alpha	PRKACA	5566
10	Phosphatidylinositol-4,5-bisphosphate 3-kinase catalytic subunit gamma	PIK3CG	5294
11	RELA proto-oncogene, NF-KB subunit	RELA	5970
12	AKT serine/threonine kinase 1	AKT1	207
13	BCL2 apoptosis regulator	BCL2	596
14	Mitogen-activated protein kinase 3	MAPK3	5595
15	Mitogen-activated protein kinase 1	MAPK1	5594
16	Caspase 3	CASP3	836
17	Fatty acid synthase	FASN	2194
18	Low-density lipoprotein receptor	LDLR	3949
19	BCL2-associated agonist of cell death	BAD	572
20	Superoxide dismutase 1	SOD1	6647
21	Catalase	CAT	847
22	Peroxisome proliferator-activated receptor gamma	PPARG	5468
23	Apolipoprotein B	APOB	338
24	3-Hydroxy-3-methylglutaryl-CoA reductase	HMGCR	3156
25	Cytochrome P450 family 19 subfamily A member 1	CYP19A1	1588
26	Glutathione S-transferase pi 1	GSTP1	2950
27	UDP glucuronosyltransferase family 1 member A1	UGT1A1	54658
28	Peroxisome proliferator-activated receptor alpha	PPARA	5465
29	Sterol regulatory element-binding transcription factor 1	SREBF1	6720
30	Glutathione-disulfide reductase	GSR	2936
31	Adiponectin, C1Q and collagen domain containing	ADIPOQ	9370
32	4-Aminobutyrate aminotransferase	ABAT	18
33	Sterol O-acyltransferase 1	SOAT1	6646
34	Sodium voltage-gated Channel alpha subunit 5	SCN5A	6331
35	Potassium voltage-gated Channel subfamily H member 2	KCNH2	3757
36	Coagulation factor VII	F7	2155
37	Potassium calcium-activated channel subfamily M alpha 1	KCNMA1	3778
38	Nitric oxide synthase 2	NOS2	4843
39	Androgen receptor	AR	367
40	Estrogen receptor 2	ESR2	2100
41	Dipeptidyl peptidase 4	DPP4	1803

2. Materials and Methods

2.1. Reagents. Naringenin (purity >95%) was purchased from Aladdin Chemistry Co., Ltd. (Shanghai, China). Dulbecco's Modified Eagle Medium (DMEM) and fetal bovine serum (FBS) were purchased from Gibco (Logan, UT, USA). Real-time PCR kit was purchased from Takara Co., Ltd. (Dalian, China). Rabbit anti-ERK1/2 (#4695), anti-p-ERK1/2 (#8544), anti-AKT (#4691), and anti-p-AKT (#4060) antibodies were purchased from CST Company (Boston, MA, USA). The chemiluminescent substrate was purchased from Pierce (Rockford, IL, USA).

2.2. CRP Active Ingredients and Target Collection. The Traditional Chinese Medicine Systems Pharmacology Database and Analysis Platform (TCMSP) was applied to retrieve

(a)

(b)

Figure 2: Continued.

(c)
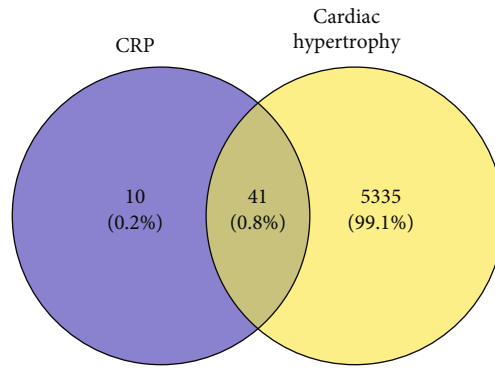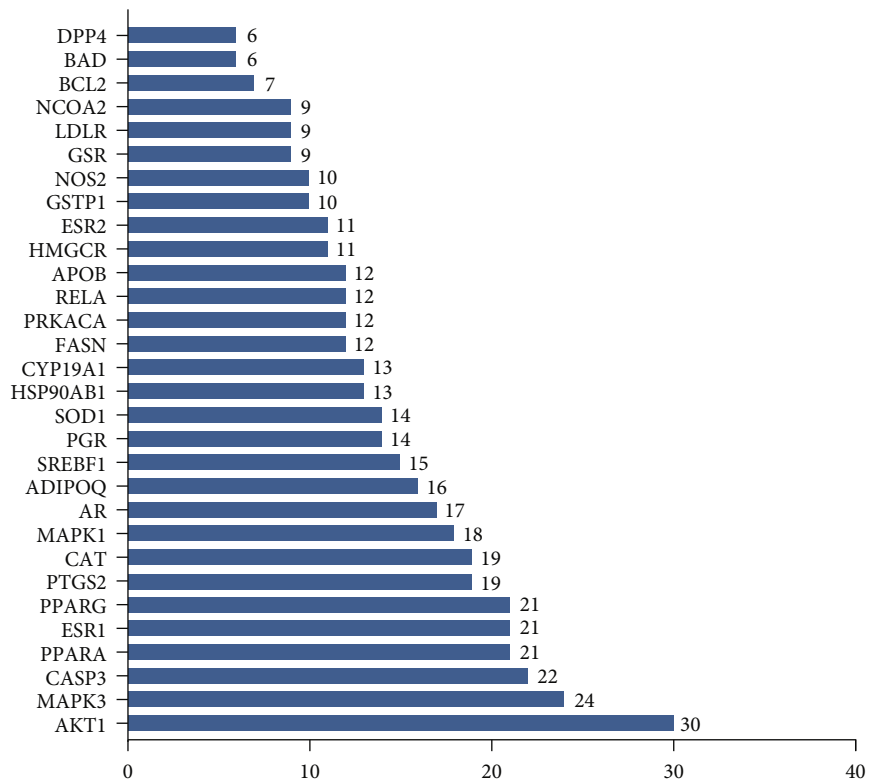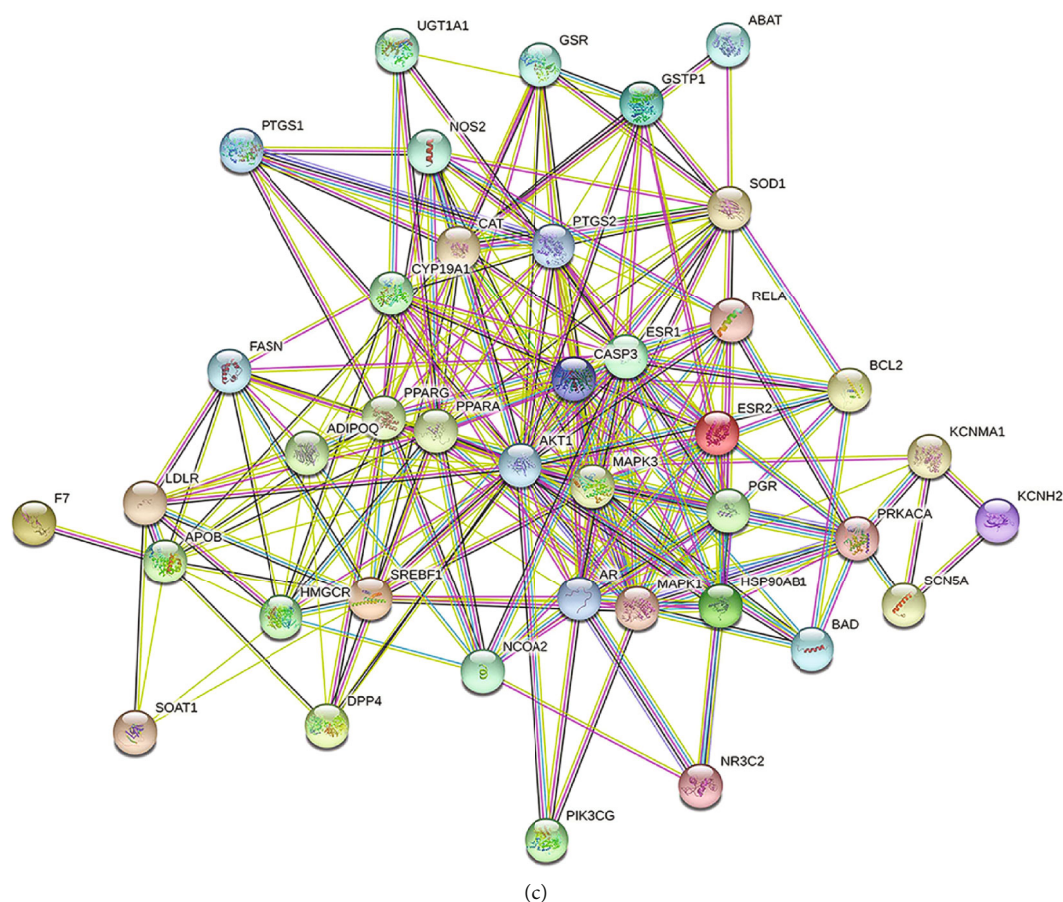
Figure 2: Potential target genes and PPI network map of CRP therapy for myocardial hypertrophy. (a) The Venny results of potential target genes of CRP therapy for myocardial hypertrophy. (b) The PPI network map of 41 target genes. (c) Count and list the top 30 genes of the PPI network map.

the active ingredients of CRP with the keywords of Citri reticulatae pericarpium. Oral bioavailability (OB) ≥ 30% and drug-likeness (DL) ≥ 0.18 were set as the screening criteria to screen out the active components of CRP. The active ingredients of CRP-related target genes were also obtained from the TCMSP database.

2.3. Disease-Target Network Construction. GeneCards (https://www.genecards.org/), an online tool, is a comprehensive resource of human genes, providing all known and predicted human-related genes in proteome, genome, genetics, transcription, and function. In this study, the GeneCards database was used to search for myocardial hypertrophy-related genes using the keyword of myocardial hypertrophy. The gene target names were corrected using Perl's computer programming language (https://www.perl.org/).

2.4. Clustering of CRP- and Myocardial Hypertrophy-Related Target Genes. Based on the Venn Diagram program running R statistical programming language, gene mapping was carried out on the online Venny 2.1.0 platform to find the intersection of drug targets and genes related to myocardial hypertrophy, namely drug-disease coacting target genes. And then, the target information of the active component

compounds of CRP and the target information of myocardial hypertrophy were classified and stored, and a Venny diagram was drawn.

2.5. Protein-Protein Interaction (PPI) Network Construction and Analysis. The information of active ingredients of CRP and myocardial hypertrophy targets was imported into the network visualization software Cytoscape 3.9.0 (https://cytoscape.org/), and an optical network topology diagram of CRP-active ingredient-myocardial hypertrophy was constructed based on the Cytoscape software. The network described the relationship between the active components of CRP and myocardial hypertrophy. The active ingredients, drugs, and disease genes were nodes of the web, and the line between each node represented the relationship between the three.

2.6. Data Processing and Analysis. With the intersection gene of CRP-myocardial hypertrophy entered on the STRING database (https://string-db.org/), the species selected was human. Then, the protein interaction network relationships were mapped, and the data were analyzed by Cytoscape 3.9.0 to filter out the core components of the protein interaction network. Then, the intersection target genes were placed into
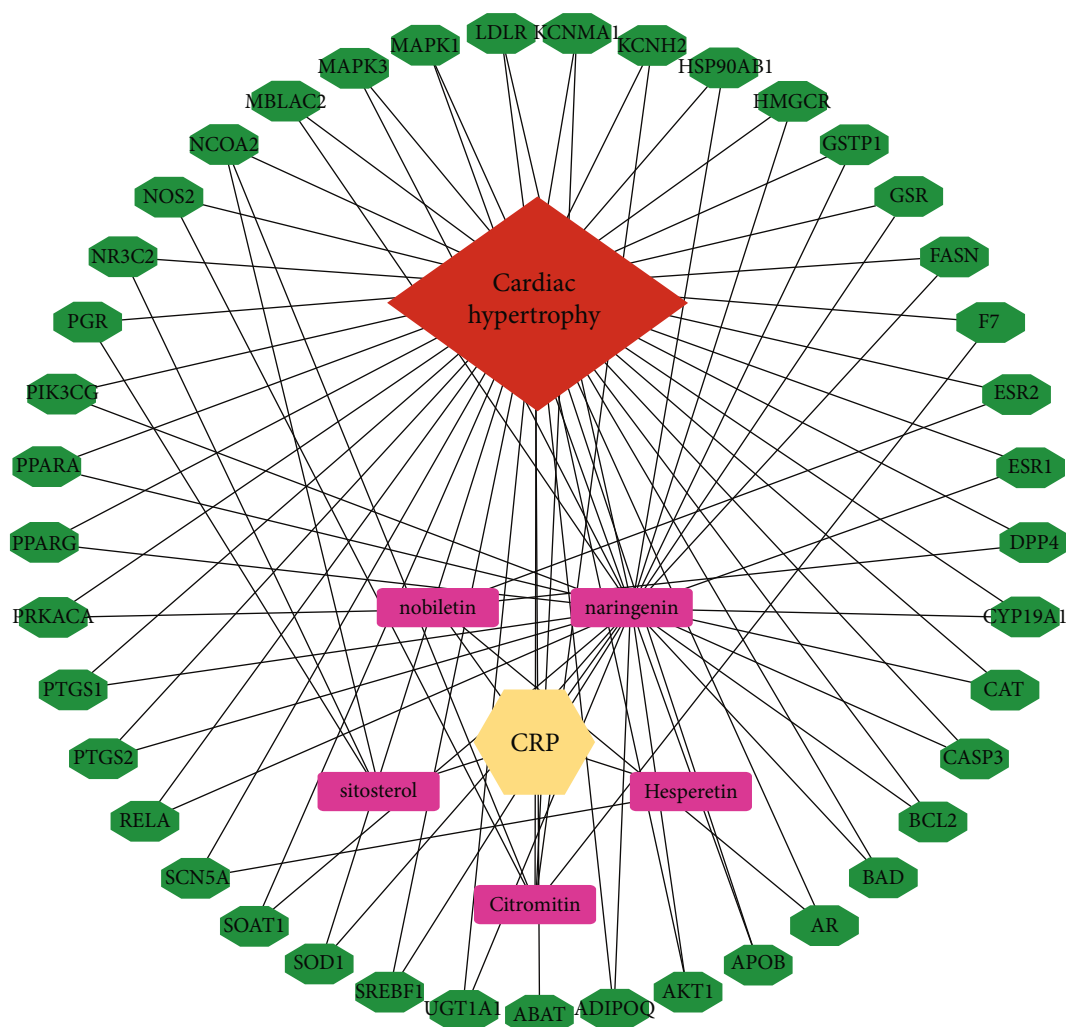
Figure 3: The CRP-myocardial hypertrophy-potential target gene network.

Table 4: The list of key active components in CRP dependent on the centrality of a node.

No	Molecule name	Degree	Closeness unDir	Betweenness unDir
1	Naringenin	30	0.013157895	534.495935
2	Citromitin	6	0.008064516	30.08565434
3	Nobiletin	4	0.0078125	14.99268293
4	Sitosterol	4	0.0078125	13.7000562
5	Hesperetin	2	0.007575758	3.497560976

the Metascape database, and species were selected as "Homo sapiens," and $P < 0.01$ were set for gene ontology (GO) and Kyoto Encyclopedia of Genes and Genomes (KEGG) analysis.

2.7. *Cell Culture.* H9C2 cardiomyocytes were grown in DMEM supplemented with 10% fetal bovine serum (FBS) and maintained at 37°C in a humidified atmosphere of 95% air-5% CO_2. The cells were digested by trypsin-EDTA (0.25%, Sigma) when they reached 80%-90% fusion and then

passaged. Before treatment, the cells were treated with DMEM medium containing 0.1% FBS for 12 h to treatment to synchronize the cells, and then, subsequent experiments were performed.

2.8. *Real-Time PCR.* After H9C2 cardiomyocytes were treated with naringenin and Ang II, the culture medium was discarded, and the total RNA of cardiomyocytes was extracted with TRIzol. The mRNA concentration was detected by Bio-Rad quantitative PCR kit. PCR primers were designed using the sequences shown in Table 1, and GAPDH was utilised as an endogenous control. Three replicate wells were set up for each group of samples to ensure the validity of the experimental data.

2.9. *Western Blotting.* The extracted total cell protein was added to 2× SDS buffer, followed by SDS-PAGE gel electrophoresis, membrane transfer, blocking, the addition of primary antibody (anti-AKT, anti-p-AKT, anti-ERK1/2, and anti-p-ERK1/2), incubation at 4°C overnight, incubation at room temperature for one h on the next day with secondary antibody, detection of target protein expression by

(a)

(b)

Figure 4: Continued.

(c)
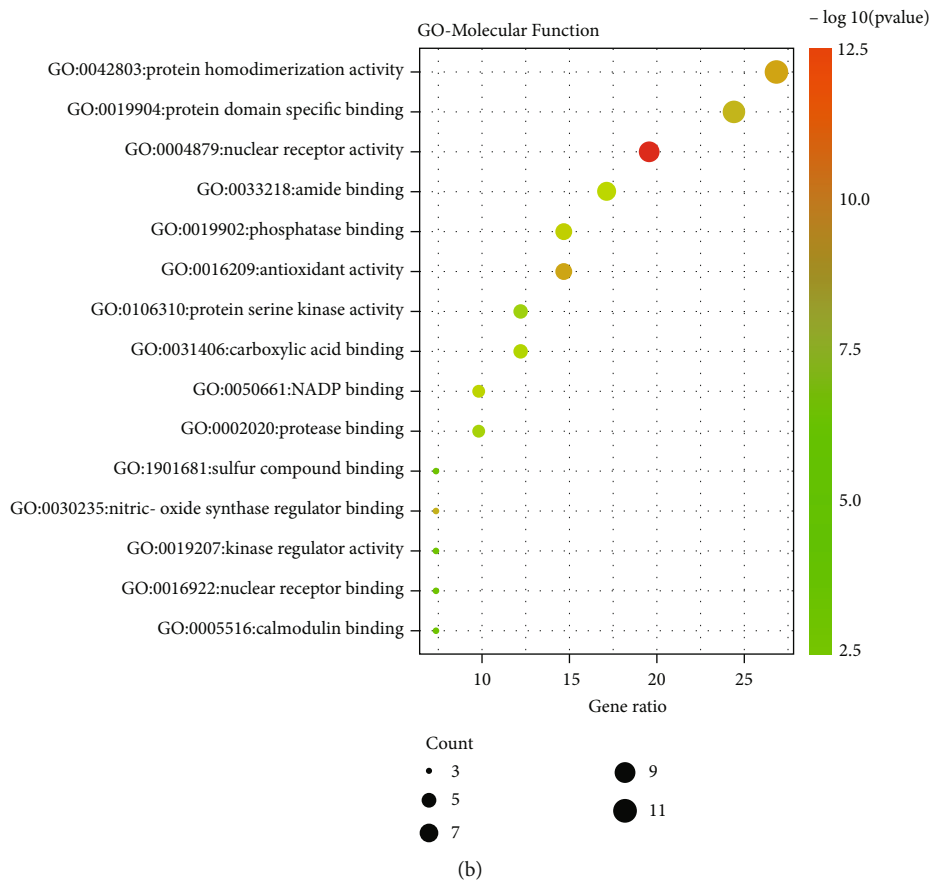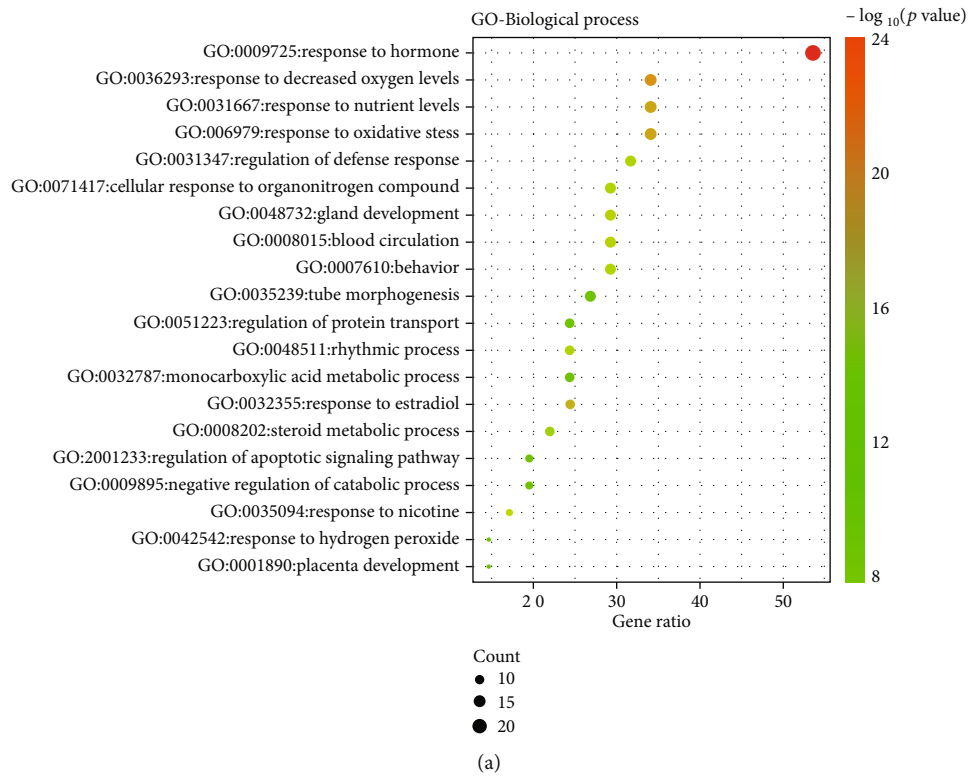
(d)
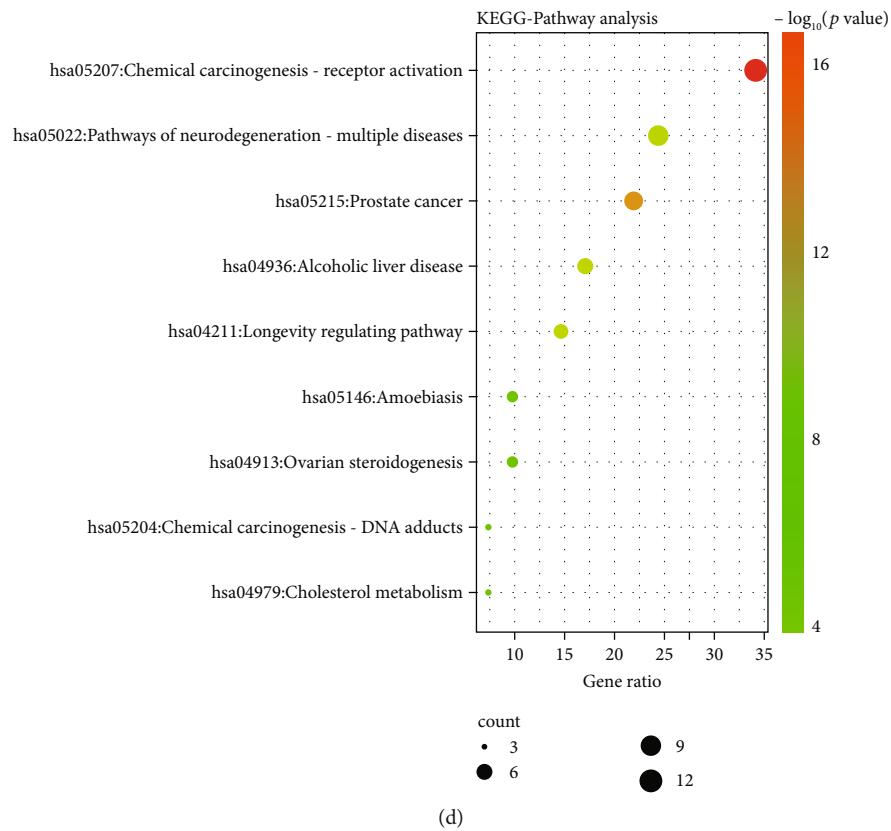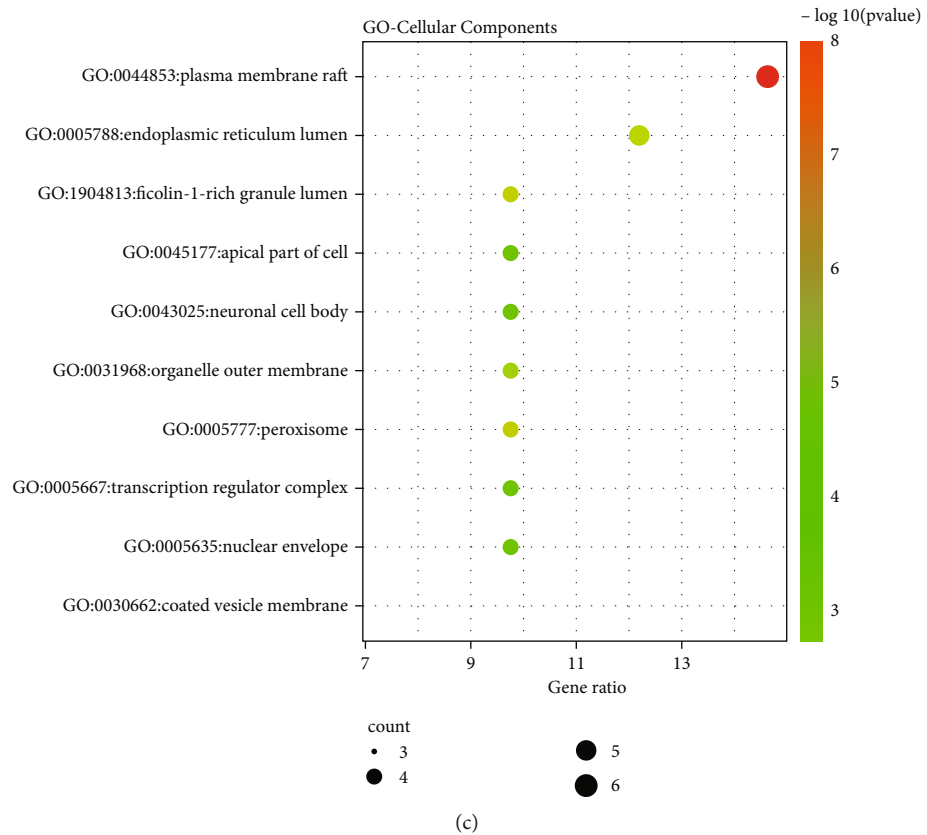
FIGURE 4: GO and KEGG analyses of potential target genes of CRP in myocardial hypertrophy. The GO analysis for biological process (a), molecular function (b), and cellular components (c) of potential target genes of CRP in myocardial hypertrophy. (d) The top 9 remarkably enriched KEGG analysis for the signaling pathway of potential target genes of CRP in myocardial hypertrophy.
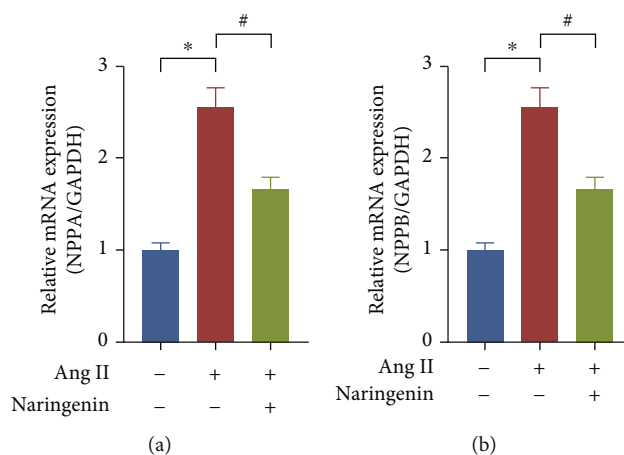
FIGURE 5: Effect of naringenin on the mRNA expression of NPPA and NPPB. H9C2 cells were treated with $20\,\mu$M naringenin for 1 h followed by stimulation with Ang II for 24 h. The mRNA expressions of NPPA (a) and NPPB (b) were detected by real-time PCR. $^*P <$ 0.05 vs. the group without treatment, $^\#P < 0.05$ vs. the group treated with Ang II, $n = 5$.

chemiluminescence, and grayscale analysis of bands by the ImageJ software.

2.10. Statistical Analysis. We use the SPSS 13.0 software for statistical analysis. The data of each group were presented as mean ± SD. One-way ANOVA was used for comparison between multiple groups. In all cases, differences were considered statistically significant with $P < 0.05$.

3. Results

3.1. CRP Active Ingredient Database Establishment. Based on the TCMSP search results, 63 active ingredients of CRP were collected. Each component's chemical information was standardized by molecular ID, molecular name, molecular weight, OB value, and DL value to establish the chemical composition information database of the drug. Subsequently, with OB ≥ 30% and DL ≥ 0.18 as criteria, five compounds with high activity were obtained by further screening, as shown in Table 2. Based on TCMSP, the active ingredient targets of CRP were obtained, the computer programming language Perl was used for name correction, and 51 marks of CRP action were obtained. The GeneCards database was used to query 5376 targets of myocardial hypertrophy disease. Based on the Venn Diagram program running R language, a total of 41 intersecting genes of CRP and myocardial hypertrophy were analyzed (Table 3 and Figure 2(a)).

OB: oral bioavailability; DL: drug-likeness.

3.2. Analysis of Protein-Protein Interaction Network. With the intersection targets of CRP and myocardial hypertrophy being imported into the STRING database, the free nodes outside the network being hidden, and the self-defined confidence score value > 0.4, the protein-protein interaction network of CRP-myocardial hypertrophy was carried out (Figure 2(b)). The whole network contained 233 edges, 40 nodes, and an average node degree value of 11.6. The nodes in the network represent the targets, and the edges represent the interaction between the marks. The nodes with more edges indicate that they are more critical in the network. The interaction between the nodes is supported by relevant literature evidence, with black edges representing coexpression, yellow edges representing evidence from text mining, and light blue edges representing protein homology, orange for gene fusion, etc. The cytoHubba plug-in in Cytoscape3.9.0 is used to analyze the data, calculate the nodes in the network, and draw the information histogram (Figure 2(c)). The results showed that the node degree values of target proteins such as AKT1, MAPK3, CASP3, PPARA, ESR1, and PPARG were high, indicating that these targets were in a critical position in the protein interaction network.

3.3. Construction and Analysis of the Drug-Component-Disease-Target Network. The intersections of active ingredient targets of CRP and myocardial hypertrophy disease targets were placed into Cytoscape 3.9.0, and the network of CRP-active ingredient-disease-intersection targets was mapped to elucidate the connection between the four targets (Figure 3). A total of 42 interrelationships between active ingredients of CRP and myocardial hypertrophy targets were obtained, and the critical components of CRP to inhibit myocardial hypertrophy were selected according to the parameters of Betweenness Centrality (BC), Closeness Centrality (CC), and Degree Centrality (DC). The results showed that the nodal degree value of naringenin was much higher than that of the other four compounds and was an important node in this network, suggesting that the naringenin in CRP might be a key component in the inhibition of myocardial hypertrophy (Table 4).

3.4. Enrichment Analysis of Biological Process and KEGG Pathway. Based on the annotated database of biological information, Metascape, GO bioprocess enrichment analysis, and KEGG pathway analysis of CRP-myocardial hypertrophy disease were established. The results of GO analysis obtained 20 biological processes ($P < 0.05$), 15 molecular functions (MF), and 10 cell composition (CC)
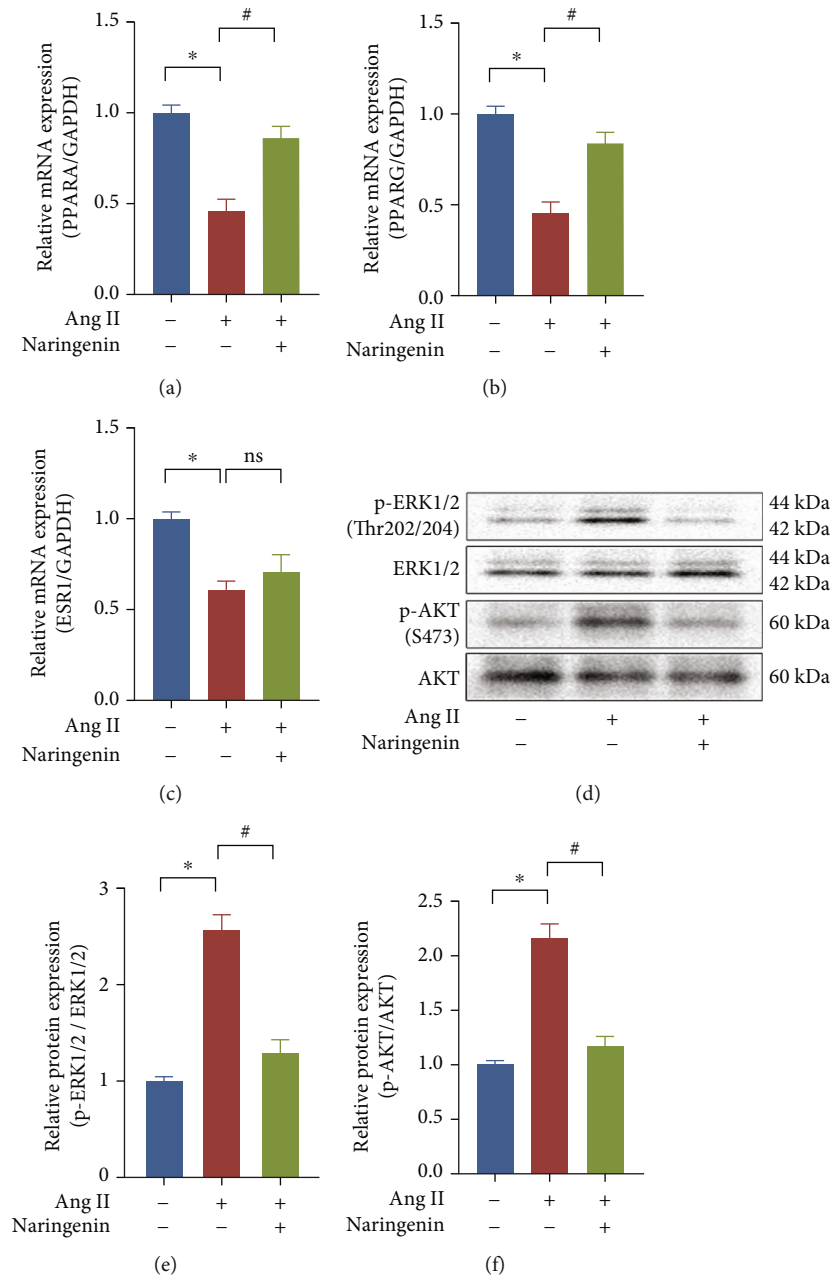
FIGURE 6: Effect of naringenin on the expression of essential target genes (AKT, PPARA, PPARG, ESR1, and ERK1/2). H9C2 cells were treated with 20 μM naringenin for 1 h followed by stimulation with Ang II for 24 h. The mRNA expression of PPARA (a), PPARG (b), and ESR1 (c) were detected by real-time PCR. (d–f) The protein expression of ERK and AKT were checked by Western blotting. $^{*}P <$ 0.05 vs. the group without treatment, $^{\#}P < 0.05$ vs. the group treated with Ang II, $n = 5$.

corresponding to the target of the practical components of CRP for treating myocardial hypertrophy (Figures 4(a)–4(c)). Hormone (target number 22), decreased oxygen content (target number 14), oxidative stress (target number 14), and nutrient level (target number 14) were significantly enriched in the treatment of myocardial hypertrophy by CRP, suggesting that CRP could treat myocardial hypertrophy by regulating multiple complex biological processes. 138 pathways were obtained through KEGG pathway enrichment analysis ($P < 0.01$), and the top 9 pathways with higher enrichment were screened (Figure 4(d)). The results

showed that the practical components of CRP could treat myocardial hypertrophy through multiple signaling pathways such as tumor-related signaling pathway (target number 16), receptor activation signaling pathway (target number 14), and nerve regeneration signaling pathway (target number 10).

3.5. Effects of Naringenin on Myocardial Hypertrophy Induced by Ang II. To clarify the effect of naringenin on cardiomyocyte hypertrophy, H9C2 cells were pretreated with naringenin for 1 h and then treated with Ang II for 24 h.

The mRNA expressions of hypertrophy-related genes NPPA and NPPB were detected. Ang II was able to induce increased mRNA level of NPPA and NPPB, while naringenin pretreatment inhibited the mRNA expression of NPPA and NPPB (Figures 5(a) and 5(b)), which suggested that naringenin could inhibit Ang II-induced cardiomyocyte hypertrophy in vitro.

3.6. Effects of Naringenin on the Critical Targets of CRP Therapy for Myocardial Hypertrophy. To clarify the effect of naringenin on the screened cardiac hypertrophic targets, we gave H9C2 cardiomyocytes naringenin pretreatment for 1 h, followed by Ang II treatment for 24 h. Real-time PCR detected the mRNA expression of PPARA, PPARG, and ESR1. The phosphorylation levels of AKT and ERK1/2 were detected by Western blotting. The results showed that naringenin pretreatment could inhibit the Ang II-induced decrease in mRNA expression of PPARA, PPARG, and ESR1 (Figures 6(a)–6(c)). At the same time, the administration of Ang II alone could increase the protein levels of p-AKT and p-ERK, and naringenin could inhibit the phosphorylation of AKT and ERK (Figures 6(d)–6(f)).

4. Discussion

Cyberpharmacology provides new ideas for Chinese medicine research by searching databases such as proteomics, genomics, and bioinformatics to perform a systematic analysis of Chinese medicine at the molecular and holistic levels to obtain the core chemical components and protein targets of TCM and to clarify the mechanism of action of TCM [19, 20]. As a traditional Chinese medicine, the role and mechanism of CRP and its various active ingredients in myocardial hypertrophy have been reported more frequently. It was found that CRP could inhibit Ang II-induced myocardial hypertrophy in mice through upregulation of PPARG [21]. Important active constituents of CRP, such as nobiletin, hesperidin, and naringenin, were also able to inhibit the development of myocardial hypertrophy. It was shown that nobiletin ameliorated pressure overload-induced myocardial hypertrophy by inhibiting oxidative stress-related signaling pathways [22]. In contrast, hesperidin may exert antimyocardial hypertrophy effects through anti-inflammatory and antioxidant pathways [8]. In addition, naringenin was also reported to inhibit diabetes-induced myocardial hypertrophy through modulation of PPAR-related pathways [23]. The above results suggested that CRP-related active components are potential candidate compounds for preventing and treating cardiovascular diseases. In this study, we collected five potent compounds of CRP, 51 targets, and 5376 disease targets of myocardial hypertrophy for gene mapping and obtained 41 intersecting genes. The critical compound naringenin and five key targets: AKT1, MAPK3, PPARA, PPARG, and ESR1, which affect myocardial hypertrophy in CRP, were obtained by analyzing the protein-protein interaction network and combining the enrichment analysis results. GO functional analysis showed that the main targets of the active ingredients of CRP in regulating myocardial hypertrophy were focused on hormone-related receptor genes, nutrition-related genes, and oxidative stress-related genes. KEGG signaling pathway enrichment analysis revealed that the active ingredients of CRP inhibited myocardial hypertrophy through tumor-related signaling pathways, receptor-activated signaling pathways, and neurodegenerative signaling pathways.

Numerous extracellular and intracellular signals synergistically regulate the onset and progression of myocardial hypertrophy [24]. Myocardial hypertrophy occurs due to an imbalance between pro and antihypertrophy factors. Several cells' signaling nodes are continuously activated during myocardial hypertrophy, and PI3K/AKT and MAPK-dependent signaling are two critical signaling pathways in the progression of myocardial hypertrophy [7, 9]. Studies have shown that various pathological stimuli, such as infarction, hypertension, and neuroendocrine factors, can activate the PI3K/AKT signaling pathway, inducing myocardial hypertrophy development. After PI3K signaling is activated, it can phosphorylate and activate Akt [25, 26]. AKT protein further regulates the transcriptional activity of myocardial hypertrophy-related transcription factors through GSK-3β and mTOR to initiate the expression of myocardial hypertrophy marker genes such as NPPA and NPPB [7, 27]. MAPK family, a group of serine-threonine protein kinases, plays an important role in cell proliferation, transformation, development, and inflammation [9]. MAPK-dependent signaling pathway is widely present in various cells and is involved in multiple physiopathological processes such as cell growth, proliferation, oxidative stress, inflammation, drug resistance, and autophagy [28]. The MAPK subfamily includes extracellular signal-regulated kinases (ERKs), c-Jun amino-terminal kinase (JNK), and p38 mitogen-activated protein kinase (p38-MAPK) [29]. In cardiomyocytes, in response to continuous mechanical or chemical stimulation, transforming growth factor-beta activated kinase 1 and apoptosis signal-regulating kinase 1 are activated and mediate the downstream MAPK signaling pathways ERKs, JNK, and p38-MAPK phosphorylation and shift from the cytoplasm to the nucleus [30]. ASK1 activation triggers the downstream MAPK signaling pathways ERKs, JNK, and p38-MAPK phosphorylation, which further regulates the development of myocardial hypertrophy [31]. ERK1 (MAPK3) was the first MAPK identified in mammals [32]. Previous studies have shown that G protein-coupled receptors were activated upon stimulation by extracellular hypertrophic signals, which triggered the RAS-RAF-MEK-ERK1/2 cascade signaling system, causing ERK1/2 to undergo phosphorylation translocation into the nucleus, thereby increasing the expression of hypertrophy-associated transcription factors [33]. In this present study, we predicted that AKT1 and MAPK3 might be the key targets of the active compound naringenin in Chenopodium during the prescreening process to regulate myocardial hypertrophy. Therefore, we detected the effect of naringenin on AKT and ERK phosphorylation levels in myocardial hypertrophy induced by Ang II. We showed naringenin could significantly inhibit the phosphorylation levels of AKT and ERK.

As one of the high energy-consuming tissues in the body, cardiac mitochondrial energy metabolism dysfunction is closely associated with many CVD [34]. The PPAR is highly expressed in myocardial tissues with increased mitochondrial fatty acid oxidation rates, is closely related to the homeostasis of myocardial mitochondrial energy metabolism, and is involved in processes such as cardiomyocyte differentiation and development [35]. Studies have shown that PPARA and PPARG are closely associated with the development of myocardial hypertrophy. The expression of PPARA and PPARG significantly downregulated in myocardial hypertrophy, and activation of either PPARA or PPARG was able to inhibit the hypertrophic response [35, 36]. Through some molecular experiments, we also found that naringenin significantly inhibited the Ang II-induced decrease in the expression of PPARA and PPARG, which is consistent with our predicted results.

In summary, we found that naringenin may be the critical active component in CRP that regulates myocardial hypertrophy. Moreover, we also showed that naringenin could exert inhibitory effects on myocardial hypertrophy through AKT1, MAPK3, PPARA, PPARG, and other essential target proteins mediating cell proliferation, receptor activation, oxidative stress, and different signaling pathways. Further molecular biology experiments also verified this prediction. The present study provides a scientific basis for further research on the mechanism of action of CRP against myocardial hypertrophy.

Data Availability

All the data used to support the findings of this study are included in the paper.

Conflicts of Interest

The authors declare that they have no conflicts of interest.

Authors' Contributions

Shisheng Jiang and Chaoming Huang contributed equally to this study.

Acknowledgments

References

[1] H. Gu, B. Lu, Y. Gao et al., "Prognostic value of atherosclerosis progression for prediction of cardiovascular events in patients with nonobstructive coronary artery disease," *Academic Radiology*, vol. 28, no. 7, pp. 980–987, 2021.

[2] H. Marshall, S. Mullany, A. Qassim et al., "Cardiovascular disease predicts structural and functional progression in early glaucoma," *Ophthalmology*, vol. 128, no. 1, pp. 58–69, 2021.

[3] C. E. Vlad, L. Foia, M. Pavel-Tanasa et al., "Evaluation of cardiovascular events and progression to end-stage renal disease in patients with dyslipidemia and chronic kidney disease from the North-Eastern area of Romania," *International Urology and Nephrology*, vol. 54, pp. 647–659, 2021.

[4] X. Tang, P. Wang, R. Zhang et al., "KLF2 regulates neutrophil activation and thrombosis in cardiac hypertrophy and heart failure progression," *The Journal of clinical investigation*, vol. 132, no. 3, 2021.

[5] H. Kerp, G. S. Hones, E. Tolstik et al., "Protective effects of thyroid hormone deprivation on progression of maladaptive cardiac hypertrophy and heart failure," *Frontiers in Cardiovascular Medicine*, vol. 8, article 683522, 2021.

[6] Y. Yang, W. W. Yu, W. Yan, and Q. Xia, "Decorin induces cardiac hypertrophy by regulating the CaMKII/MEF-2 signaling pathway in vivo," *Current Medical Science*, vol. 41, no. 5, pp. 857–862, 2021.

[7] R. R. Magaye, F. Savira, Y. Hua et al., "Attenuating PI3K/Akt-mTOR pathway reduces dihydrosphingosine 1 phosphate mediated collagen synthesis and hypertrophy in primary cardiac cells," *The International Journal of Biochemistry & Cell Biology*, vol. 134, article 105952, 2021.

[8] P. Bhargava, V. K. Verma, S. Malik, S. I. Khan, J. Bhatia, and D. S. Arya, "Hesperidin regresses cardiac hypertrophy by virtue of PPAR-γ agonistic, anti-inflammatory, antiapoptotic, and antioxidant properties," *Journal of Biochemical and Molecular Toxicology*, vol. 33, no. 5, article e22283, 2019.

[9] Y. Zhang, Y. Cui, S. Dai et al., "Isorhynchophylline enhances Nrf2 and inhibits MAPK pathway in cardiac hypertrophy," *Naunyn-Schmiedeberg's Archives of Pharmacology*, vol. 393, no. 2, pp. 203–212, 2020.

[10] S. Takai, D. Jin, M. Sakaguchi, and M. Miyazaki, "Significant target organs for hypertension and cardiac hypertrophy by angiotensin-converting enzyme inhibitors," *Hypertension Research*, vol. 27, no. 3, pp. 213–219, 2004.

[11] K. Nagata, K. Obata, J. Xu et al., "Mineralocorticoid receptor antagonism attenuates cardiac hypertrophy and failure in low-aldosterone hypertensive rats," *Hypertension*, vol. 47, no. 4, pp. 656–664, 2006.

[12] T. Igawa, K. Ikezono, K. Watanabe, and Y. Kimura, "Dose-related inhibitory effects of the β-adrenoceptor blocking drugs carteolol and propranolol on cardiac hypertrophy in spontaneously hypertensive rats," *European Journal of Pharmacology*, vol. 104, no. 1-2, pp. 93–99, 1984.

[13] R. R. Gao, X. D. Wu, H. M. Jiang et al., "Traditional Chinese medicine Qiliqiangxin attenuates phenylephrine-induced cardiac hypertrophy via upregulating PPARγ and PGC-1α," *Annals of Translational Medicine*, vol. 6, no. 8, p. 153, 2018.

[14] G. D. Zheng, P. J. Hu, Y. X. Chao et al., "Nobiletin induces growth inhibition and apoptosis in human nasopharyngeal carcinoma C666-1 cells through regulating PARP-2/SIRT1/AMPK signaling pathway," *Food Science & Nutrition*, vol. 7, no. 3, pp. 1104–1112, 2019.

[15] X. Yu, S. Sun, Y. Guo et al., "Citri Reticulatae Pericarpium (Chenpi): botany, ethnopharmacology, phytochemistry, and pharmacology of a frequently used traditional Chinese medicine," *Journal of Ethnopharmacology*, vol. 220, p. 265, 2018.

[16] D. Barreca, G. Gattuso, E. Bellocco et al., "Flavanones: citrus phytochemical with health-promoting properties," *BioFactors*, vol. 43, no. 4, pp. 495–506, 2017.

[17] J. M. Assini, E. E. Mulvihill, and M. W. Huff, "Citrus flavonoids and lipid metabolism," *Current Opinion in Lipidology*, vol. 24, no. 1, pp. 34–40, 2013.

[18] P. M. Kris-Etherton, K. D. Hecker, A. Bonanome et al., "Bioactive compounds in foods: their role in the prevention of cardiovascular disease and cancer," *The American Journal of Medicine*, vol. 113, no. 9, pp. 71–88, 2002.

[19] W. H. Niu, F. Wu, W. Y. Cao, Z. G. Wu, Y. C. Chao, and C. Liang, "Network pharmacology for the identification of phytochemicals in traditional Chinese medicine for COVID-19 that may regulate interleukin-6," *Bioscience Reports*, vol. 41, no. 1, 2021.

[20] Y. Fang, X. Liu, and J. Su, "Network pharmacology analysis of traditional Chinese medicine formula Shuang Di Shou Zhen tablets treating nonexudative age-related macular degeneration," *Evidence-Based Complementary and Alternative Medicine*, vol. 2021, Article ID 6657521, 14 pages, 2021.

[21] G. Ni, K. Wang, Y. Zhou et al., "Citri Reticulatae Pericarpium attenuates Ang II-induced pathological cardiac hypertrophy via upregulating peroxisome proliferator-activated receptors gamma," *Annals of Translational Medicine*, vol. 8, no. 17, p. 1064, 2020.

[22] N. Zhang, W. Y. Wei, Z. Yang et al., "Nobiletin, a polymethoxy flavonoid, protects against cardiac hypertrophy induced by pressure-overload via inhibition of NAPDH oxidases and endoplasmic reticulum stress," *Cellular Physiology and Biochemistry*, vol. 42, no. 4, pp. 1313–1325, 2017.

[23] J. Zhang, H. Qiu, J. Huang et al., "Naringenin exhibits the protective effect on cardiac hypertrophy _via_ EETs- PPARs activation in streptozocin-induced diabetic mice," *Biochemical and Biophysical Research Communications*, vol. 502, no. 1, pp. 55–61, 2018.

[24] Y. Cai, S. S. Yu, Y. He et al., "EGCG inhibits pressure overload-induced cardiac hypertrophy via the PSMB5/Nmnat2/SIRT6-dependent signalling pathways," *Acta Physiologica (Oxford, England)*, vol. 231, no. 4, article e13602, 2021.

[25] S. Cheng, X. Zhang, Q. Feng et al., "Astragaloside IV exerts angiogenesis and cardioprotection after myocardial infarction via regulating PTEN/PI3K/Akt signaling pathway," *Life Sciences*, vol. 227, p. 82, 2019.

[26] F. Briest and P. Grabowski, "PI3K-AKT-mTOR-signaling and beyond: the complex network in gastroenteropancreatic neuroendocrine neoplasms," *Theranostics*, vol. 4, no. 4, pp. 336–365, 2014.

[27] L. Ba, J. Gao, Y. Chen et al., "Allicin attenuates pathological cardiac hypertrophy by inhibiting autophagy via activation of PI3K/Akt/mTOR and MAPK/ERK/mTOR signaling pathways," *Phytomedicine*, vol. 58, article 152765, 2019.

[28] J. Y. Fang and B. C. Richardson, "The MAPK signalling pathways and colorectal cancer," *The Lancet Oncology*, vol. 6, no. 5, pp. 322–327, 2005.

[29] E. F. Wagner and A. R. Nebreda, "Signal integration by JNK and p38 MAPK pathways in cancer development," *Nature Reviews. Cancer*, vol. 9, no. 8, pp. 537–549, 2009.

[30] F. Donohoe, M. Wilkinson, E. Baxter, and D. J. Brennan, "Mitogen-activated protein kinase (MAPK) and obesity-related cancer," *International Journal of Molecular Sciences*, vol. 21, no. 4, 2020.

[31] H. Feng, J. Cao, G. Zhang, and Y. Wang, "Kaempferol attenuates cardiac hypertrophy via regulation of ASK1/MAPK signaling pathway and oxidative stress," *Planta Medica*, vol. 83, no. 10, pp. 837–845, 2017.

[32] G. Maik-Rachline, I. Wortzel, and R. Seger, "Alternative splicing of MAPKs in the regulation of signaling specificity," *Cells*, vol. 10, no. 12, 2021.

[33] Y. Li, X. H. Tang, X. H. Li et al., "Regulator of G protein signalling 14 attenuates cardiac remodelling through the MEK-ERK1/2 signalling pathway," *Basic Research in Cardiology*, vol. 111, no. 4, p. 47, 2016.

[34] S. Wu and M. H. Zou, "AMPK, mitochondrial function, and cardiovascular disease," *International Journal of Molecular Sciences*, vol. 21, no. 14, 2020.

[35] E. Legchenko, P. Chouvarine, P. Borchert et al., "PPARgamma agonist pioglitazone reverses pulmonary hypertension and prevents right heart failure via fatty acid oxidation," *Science Translational Medicine*, vol. 10, no. 438, 2018.

[36] S. C. Xu, Z. G. Ma, W. Y. Wei, Y. P. Yuan, and Q. Z. Tang, "Bezafibrate attenuates pressure overload-induced cardiac hypertrophy and fibrosis," *PPAR Research*, vol. 2017, Article ID 5789714, 12 pages, 2017.

Research Article

Protective Effects of the Wenfei Buqi Tongluo Formula on the Inflammation in Idiopathic Pulmonary Fibrosis through Inhibiting the TLR4/MyD88/NF-κB Pathway

Siyu Song,[1] **Jing Wang,**[2] **Guanwen Liu,**[3] **Lu Ding,**[4] **Yaxin Li,**[1] **Hongyu Qi,**[4] **Lai Wei,**[5] **Jiachao Zhao,**[1] **Tian Chen,**[1] **Meiru Zhao,**[1] **Ziyuan Wang,**[5] **Yingying Yang,**[6] **Daqing Zhao** ⓘ,[4] **Xiangyan Li** ⓘ,[4] **and Zeyu Wang** ⓘ[7]

[1]*College of Integrated Traditional Chinese and Western Medicine, Changchun University of Chinese Medicine, Changchun, China*
[2]*Department of Respiration, Affiliated Hospital of Changchun University of Chinese Medicine, Changchun, China*
[3]*GCP, Affiliated Hospital of Changchun University of Chinese Medicine, Changchun, China*
[4]*Jilin Ginseng Academy, Key Laboratory of Active Substances and Biological Mechanisms of Ginseng Efficacy, Ministry of Education, Jilin Provincial Key Laboratory of Bio-Macromolecules of Chinese Medicine, Changchun University of Chinese Medicine, Changchun, China*
[5]*College of Traditional Chinese Medicine, Changchun University of Chinese Medicine, Changchun, China*
[6]*Graduate College, Beijing University of Chinese Medicine, Beijing, China*
[7]*Department of Scientific Research, Changchun University of Chinese Medicine, Changchun, China*

Correspondence should be addressed to Xiangyan Li; xiangyan_li1981@163.com and Zeyu Wang; zeyu781022@163.com

Background. Idiopathic pulmonary fibrosis (IPF) is a progressive disease with high mortality and poor prognosis. The prognostic signatures related to conventional therapy response remain limited. The Wenfei Buqi Tongluo (WBT) formula, a traditional Chinese medicine (TCM) formula, has been widely utilized to treat respiratory diseases in China, which is particularly effective in promoting inflammatory absorption. In this study, we aim to explore the mechanism of the WBT formula in the inhibition of inflammatory response during IPF, based on network pharmacology and *in vivo* experiments. *Methods*. Network pharmacology was applied to predict the changes of biological processes and potential pathways for the WBT formula against IPF. Histopathological changes, inflammatory factors (IL-6, IL-1β, and TNF-α), and the proteins of the TLR4/MyD88/NF-κB pathway in bleomycin- (BLM-) induced mice model were examined by hematoxylin-eosin (H&E), Masson or immunohistochemistry staining, Western blot, and enzyme-linked immunosorbent assay analysis. *Results*. A total of 163 possible components and 167 potential targets between the WBT formula and IPF were obtained. The enrichments of network pharmacology showed that inflammation response, TNF, and NF-κB pathways were involved in the treatment of WBT against IPF. The *in vivo* experiments indicated that the WBT formula could ameliorate inflammatory exudation and collagen deposition at a histopathology level in the BLM-induced mice model. The levels of IL-6, IL-1β, and TNF-α were reduced after the WBT formula treatment. Moreover, the expressions of phosphorylated-NF-κB p65, TLR4, and MyD88 were significantly downregulated by the WBT formula, compared with the BLM-induced group. *Conclusion*. These results indicated that the WBT formula can suppress BLM-induced IPF in a mouse model by inhibiting the inflammation via the TLR4/MyD88/NF-κB pathway. This study provides a new insight into the molecular mechanisms of the WBT formula in the application at the clinic.

1. Introduction

Idiopathic pulmonary fibrosis (IPF) is a chronic, progressive disease with a median survival time of three to five years since diagnosis [1]. IPF, the most common interstitial lung disease, is characterized by interstitial inflammation, fibrocyte proliferation of the alveolar wall, and fibrosis [2, 3]. Inflammatory and oxidative injuries, shortened telomeres, epithelial-mesenchymal transition (EMT), and endoplasmic reticulum stress lead to increased secretion of fibrotic factors [4]. Repeated inflammation and lung tissue injury appear to be an early-stage phenotype of pulmonary fibrosis (PF). The aberrant repair of inflammatory cells subsequently leads to the cross talk among epithelial cells, the extracellular matrix, and nearby mesenchymal cells [1]. Chronic inflammation triggered the secretion of transforming growth factor-β (TGF-β) in the alveolar compartments, which was the primary mechanism driving fibroblast activation and proliferation [5]. Inflammatory response, wounding, and oxidative stress play important roles in the prior phase of IPF [6]. It has been proven that mice deficient for the toll-like receptor 4 (TLR4) developed worse fibrosis phenotype and downregulation of cell surface hyaluronan, which has been evidenced in patients with IPF [7]. TLR4 activates the canonical NF-κB pathway through MyD88 as an innate immune response, which is related to IPF [8, 9]. Importantly, the NF-κB pathway as a key mediator for inflammatory response modulates the secretion of numerous cytokines and plays a key role in the inflammatory stage of PF [10, 11]. Therefore, the suppression of inflammation through the TLR4/MyD88/NF-κB pathway in an early stage of the fibrosis process can effectively improve lung fibrosis.

The Wenfei Buqi Tongluo (WBT) formula is an effective prescription for treating IPF, based on a traditional and classical Chinese medicine formula, Buyang Huanwu decoction, including *Astragalus membranaceus* (Fisch.) Bunge (Huang qi), *Angelica sinensis* (Oliv.) Diels (Dang gui), *Prunus persica* (L.) Batsch (Tao ren), *Pheretima aspergillum* (E. Perrier) (Di long), *Ligusticum striatum* DC. (Chuan xiong), *Carthamus tinctorius* L. (Hong hua), and *Radix Paeoniae Rubra* (Chi shao), which was created by Qing-Ren Wang for hundreds of years during the Qing Dynasty. Buyang Huanwu decoction ameliorates PF through inhibiting the PI3K/Akt signaling pathway [12, 13]. The WBT formula is composed of 13 Chinese medicines, containing the five medicines in Buyang Huanwu decoction and other eight herbs, such as *Scutellaria baicalensis* Georgi (Huang qin), *Salvia miltiorrhiza* Bunge (Dan shen), *Polygonum cuspidatum* Siebold & Zucc (Hu zhang), *Aster tataricus* L.f. (Zi wan), *Tussilago farfara* L. (Kuan donghua), *Pinellia ternata* (Thunb.) Makino (Ban xia), *Clematis chinensis* Osbeck (Wei lingxian), and *Siegesbeckia orientalis* L. (Xi xiancao) (Table 1). As we previously reported, the WBT formula inhibited cell proliferation, morphology, and EMT in the TGF-β1-induced A549 cell model [14]. Multiple components in the WBT formula have been proven that they are effective in the prevention and treatment of main pathological progresses of IPF. Isorhamnetin and kaempferol are bioactive compounds from *Tussilago farfara* L. and *Pinellia ternata* (Thunb.) Makino, which

reduces inflammatory cytokines and oxidative stress to protect acute lung injury in mice model by regulating the NF-κB pathway [15–17]. A bioactive compound from *Ligusticum striatum* DC., ligustilide, can suppress oxidative stress and inflammation to avoid BLM-induced PF in rat model through the inhibition of the TLR4/MyD88/NF-κB pathway [18]. However, the protective effects and possible mechanisms of the WBT formula in the early phase of IPF, especially the inflammatory process, have not been thoroughly explored. In this study, we first screened out IPF-related targets and potential chemical components of the WBT formula by network pharmacology, according to several common databases. Based on the prediction data, the pathway enrichment analysis was performed to elucidate the possible mechanisms of the WBT formula against IPF. Furthermore, the mice model after BLM induction for 7 days was employed to validate the anti-inflammatory effects of the WBT formula and investigate its regulatory roles on the TLR4/MyD88/NF-κB pathway. Our study might provide new insights into the molecular mechanism of the WBT formula for inhibiting inflammatory response during IPF.

2. Materials and Methods

2.1. Reagents. BLM and pirfenidone (PFD) were purchased from MedChemExpress (Monmouth Junction, NJ, USA). Antibodies against TLR4 (95/120 kDa, sc-293072), MyD88 (33 kDa, sc-74532), p-NF-κB p65 (65 kDa, sc-166748), and fibronectin (FN, 220 kDa, sc-8422) were purchased from Santa Cruz Biotechnology (Rosemont, IL, USA). IκBα (39 kDa, #4814) and NF-κB p65 (65 kDa, #8242) were obtained from Cell Signaling Technology (Beverly, MA, USA). Tubulin (50 kDa, 11224-1-AP) was purchased from ProteinTech (Rosemont, IL, USA).

2.2. Network Pharmacology Analysis for the WBT Formula and IPF. The potential gene targets of the 13 Chinese medicines in the WBT formula were identified via network pharmacology analysis. The monomer chemicals in the WBT formula were retrieved from Traditional Chinese Medicine databases (TCMSP, http://tcmspw.com/tcmsp.php) [19] and Traditional Chinese Medicine Information Database (TCMID, http://www.megabionet.org/tcmid/) [20]. In the TCMSP database, oral bioavailability ≥30% and drug-likeness ≥0.18 were conditioned to the absorption parameters for the compound screening. To collect the potential gene targets of these components of the WBT formula, the following two databases, TCMSP and SwissTargetPrediction Database (STPD, http://old.swisstargetprediction.ch/), were used [21]. Then, the Universal Protein Resource Knowledgebase (UniProt Knowledgebase, http://www.uniprot.org/, entering at Jan 2021) was applied to unify the official gene symbol, which was a collection from the candidates above. The IPF-associated target genes were acquired from GeneCards (https://www.genecards.org/) [22], the screening parameter was "relevance score ≥ 4.56." Protein-protein interaction (PPI) data were obtained from STRING (https://cn.string-db.org/) with parameter conditions filtered by "*Homo sapiens*" (confidence score > 0.9) and visualized

TABLE 1: The compositions of the WBT formula.

Chinese name	Latin name	Family	Weight (g)	Part used	Voucher specimen
Huang qi	*Astragalus membranaceus* (Fisch.) Bunge	Leguminosae	40	Root	201213-1
Huang qin	*Scutellaria baicalensis* Georgi	Lamiaceae	20	Root	201213-2
Dan shen	*Salvia miltiorrhiza* Bunge	Lamiaceae	20	Root	201213-3
Hu zhang	*Polygonum cuspidatum* Siebold & Zucc	Polygonaceae	15	Rhizome	201213-4
Dang gui	*Angelica sinensis* (Oliv.) Diels	Apiaceae	15	Root	201213-5
Chuan xiong	*Ligusticum striatum* DC.	Umbelliferae	15	Root	201213-6
Tao ren	*Prunus persica* (L.) Batsch	Rosaceae	10	Seed	201213-7
Di long	*Pheretima aspergillum* (E. Perrier)	Megascolecidae	10	Whole animal	201213-8
Zi wan	*Aster tataricus* L.f.	Compositae	15	Rhizome and root	201213-9
Kuan donghua	*Tussilago farfara* L.	Compositae	15	Flower bud	201213-10
Ban xia	*Pinellia ternata* (Thunb.) Makino	Araceae	9	Tuber	201213-11
Wei lingxian	*Clematis chinensis* Osbeck	Ranunculaceae	15	Root	201213-12
Xi xiancao	*Siegesbeckia orientalis* L.	Asteraceae	15	Above ground part	201213-13

TABLE 2: The possible components of the WBT formula were predicted by network pharmacology.

Chinese medicines	Number	Components
Astragalus membranaceus (Fisch.) Bunge	20	Mairin, jaranol, hederagenin, quercetin, isorhamnetin, 3,9-di-O-methylnissolin, $5'$-hydroxyiso-muronulatol-$2'$,$5'$-di-O-glucoside, 7-O-methylisomucronulatol, 9,10-dimethoxyp-terocarpan-3-O-β-D-glucoside, bifendate, etc.
Scutellaria baicalensis Georgi	36	Diop, panicolin, skullcapflavone II, baicalein, supraene, carthamidin, norwogonin, salvigenin, ent-epicatechin, sitosterol, etc.
Salvia miltiorrhiza Bunge	65	Salvilenone, salviolone, sugiol, luteolin, miltipolone, miltirone, baicalin, manool, digallate, sugiol, etc.
Polygonum cuspidatum Siebold & Zucc	10	6,8-Dihydroxy-7-methoxyxanthoneluteolin, beta-sitosterol, physciondiglucoside, torachrysone-8-O-beta-D-($6'$-oxayl)-glucoside, quercetin, rhein, (+)-catechin, picralinal, physovenine, etc.
Angelica sinensis (Oliv.) Diels	2	Stigmasterol, beta-sitosterol
Ligusticum striatum DC.	7	Mandenol, myricanone, perlolyrine, senkyunone, wallichilide, sitosterol, FA
Prunus persica (L.) Batsch	23	Hederagenin, beta-sitosterol, campesterol, 3-O-p-coumaroylquinic acid, sitosterol alpha1, gibberellin 7, gibberellin 17, 2,3-didehydro GA70, gibberellin A44, populoside_qt, etc.
Pheretima aspergillum (E. Perrier)	10	4-Guanidino-1-butanol, cholesterol, cholesteryl ferulate, guanidine, guanine(1,7-dihydro-form), guanosine, hypoxanthine, hyrcanoside, xanthine, xanthinin, etc.
Aster tataricus L.f.	19	Rabdosinatol, shionone, galangin, isorhamnetin, beta-sitosterol, epifriedelanol acetate, kaempferol, spinasterol, luteolin, quercetin, etc.
Tussilago farfara L.	22	Tussilagolactone, beta-sitosterol, taraxanthin, kaempferol, quercetin, senkirkine, tussilagin, femara, methyl 3-o-caffeoylquinate, alpha-Carotene-5,6-epoxide, etc.
Pinellia ternata (Thunb.) Makino	13	Cavidine, gondoic acid, coniferin, baicalein, beta-sitosterol, cycloartenol, baicalin, stigmasterol, 24-ethylcholest-4-en-3-one, 10,13-eicosadienoic, etc.
Clematis chinensis Osbeck	7	(4aS,6aR,6aS,6bR,8aR,10R,12aR,14bS)-10-hydroxy-2,2,6a,6b,9,9,12aheptamethyl-1,3,4,5,6,6a,7,8,8a,10,11,12,13,14b-tetradecahydropicene-4a-carboxylic acid, (6Z,10E,14E,18E)-2,6,10,15,19,23-hexamethyltetracosa-2,6,10,14,18,22-hexaene, beta-sitosterol, stigmasterol, clematosideA'_qt, embinin, heptyl phthalate
Siegesbeckia orientalis L.	9	Stigmasterol, hederagenin, beta-sitosterol, 15alpha-Hydroxy-ent-kaur-16-en-19-oic acid, vernolic acid, coronaridine, siegesesteric acid II, siegesmethyletheric acid, (1R)-1-[(2S,4aR,4bS,7R,8aS)-7-hydroxy-2,4b,8,8-tetramethyl-4,4a,5,6,7,8a,9,10-octahydro-3H-phenanthren-2-yl]ethane-1,2-diol

using Cytoscape. Finally, Gene Ontology (GO) and Kyoto Encyclopedia of Genes and Genomes (KEGG) pathways were enriched by using the Metascape (http://metascape.org/) tool.

2.3. Preparation of the WBT Formula. The 13 Chinese medicines present in the WBT formula were purchased from the Hongjian Pharmacy (Changchun, China), which were deposited in the Jilin Ginseng Academy, Changchun

WBT target genes   IPF-related target genes

(a)

(b)
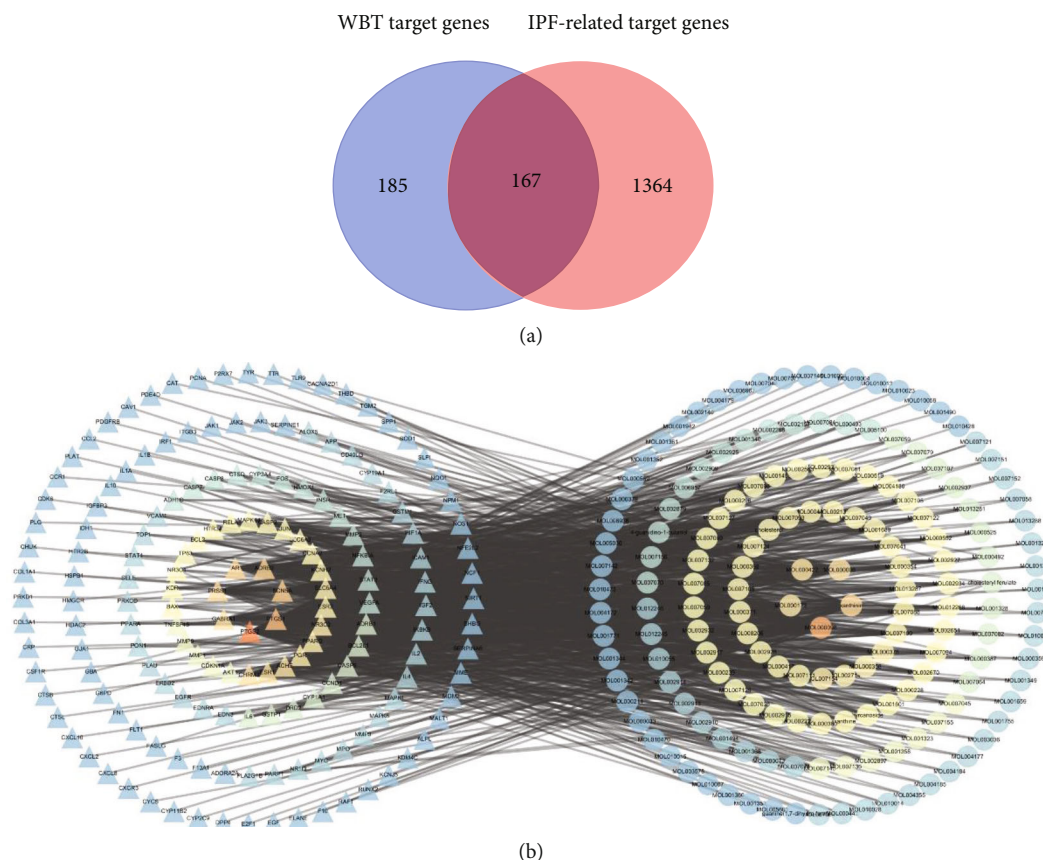
FIGURE 1: Screening of potential targets and the compound-target-disease network. (a) Venn chart of potential target genes between the WBT formula and IPF. A total of 352 genes of the components from the WBT formula and 1,531 disease genes of IPF were predicted and contributed to 167 shared targets, as potential targets of the WBT formula treating IPF. (b) Bioactive components of the WBT formula-potential targets network. The left triangles represent treatment targets of the WBT formula for IPF, the right circles represent the bioavailable components of the WBT formula.

University of Chinese Medicine (Changchun, China). Raw materials of the WBT formula were codecocted in the distilled water for 1 h twice using 10 times of the total weight of the medicine mixture to obtain the aqueous extract. After filtering and centrifuging at 3,500 rpm for 15 min, the supernatants of WBT were subjected to vacuum to obtain the powder for further experiments.

2.4. Establishment of BLM-Induced Pulmonary Inflammation and Fibrosis and Drug Treatment. All mice (the Vital River Laboratory Animal Technology Co. Ltd, Beijing, China) were housed under standard conditions at the Experimental Animal Center, Changchun University of Chinese Medicine (Changchun, China). All experiments were approved by the Experimental Animal Administration Committee of Changchun University of Chinese Medicine (Approval No. 2021230). After three days of acclimatization, a total of 60 male C57BL/6N mice with body weight about 20 ± 2 g, aged 6–8 weeks, were randomly divided into six groups ($n = 10$): sham, BLM (3 mg/kg), WBT (3, 6, and 12 g/kg), and PFD (200 mg/kg) groups. The pulmonary inflammation and fibrosis model was established by intratracheal injection with BLM (3 mg/kg) under anesthesia by 0.3% pentobarbital sodium on day 0. The sham group was

instilled with an equal volume of normal saline only. After BLM administration, mice were intragastrically administered with different doses of the WBT formula or PFD once a day for 7 consecutive days. On day 8, all the mice were sacrificed to collect serum, bronchoalveolar lavage fluid (BALF), and lung tissues for further analysis.

2.5. Interleukin-6 (IL-6), TNF-α, and Interleukin-1β (IL-1β) Measurement. According to the instructions, the IL-6 level in the serum and TNF-α and IL-1β in BALF from the mice of different groups were determined by the enzyme-linked immunosorbent assay kit (Sinobest Bio, Shanghai, China).

2.6. Histopathological Analysis. The mouse lung tissue was fixed using 4% formaldehyde, was embedded in paraffin, and then was cut into the slices at 4 μm thickness. The lung sections were deparaffinized with xylene after being rehydrated in water by graded concentrations of ethanol solution. The sections were stained to estimate lung inflammation and fibrotic changes using H&E and Masson's trichrome stainings. For immunohistochemical (IHC) staining, the slides were submerged with a citric acid solution (pH 6.0, 0.01 mol/L; Servicebio, Wuhan, China) for 10 min for antigen retrieval. After incubation with 3% hydrogen

(a)

(b)

Figure 2: Continued.

(c)

(d)

FIGURE 2: The GO and KEGG pathway enrichment analysis of the key targets for the WBT formula. GO enrichment analysis showing the top 20 biological processes (a) and KEGG pathway analysis (b) for 167 shared targets from the WBT formula and IPF-related target genes. (c) The PPI network of targets for the WBT formula against IPF was constructed by the Cytoscape software. (d) The PPI network of an NF-κB pathway-related gene from (c) is shown. The size and color depth of nodes are positively correlated with their degrees, respectively.

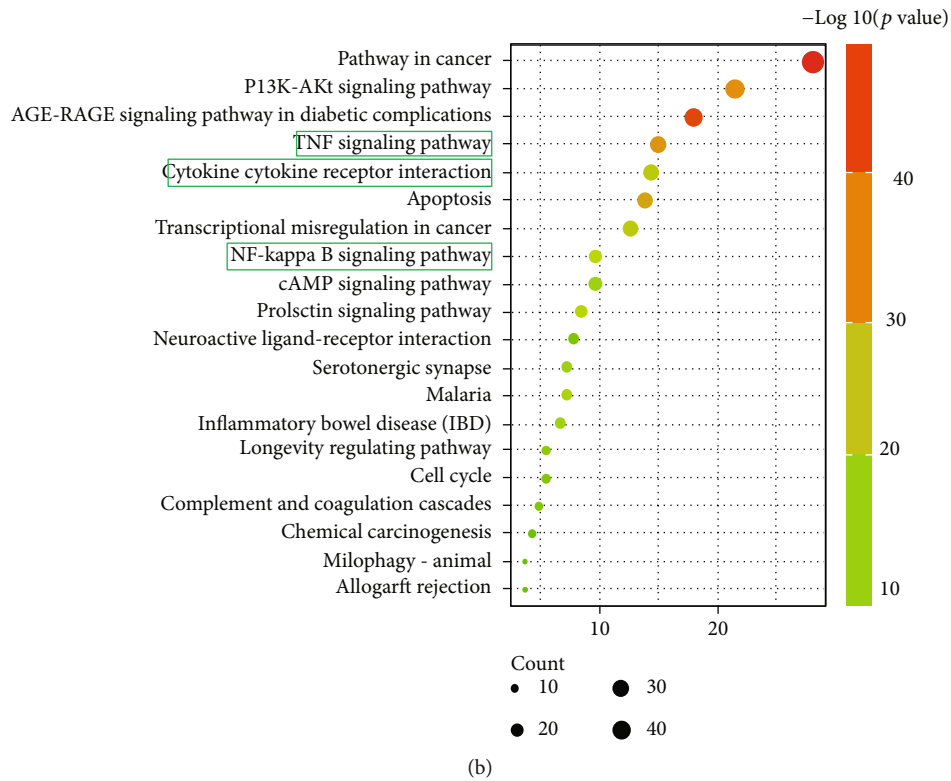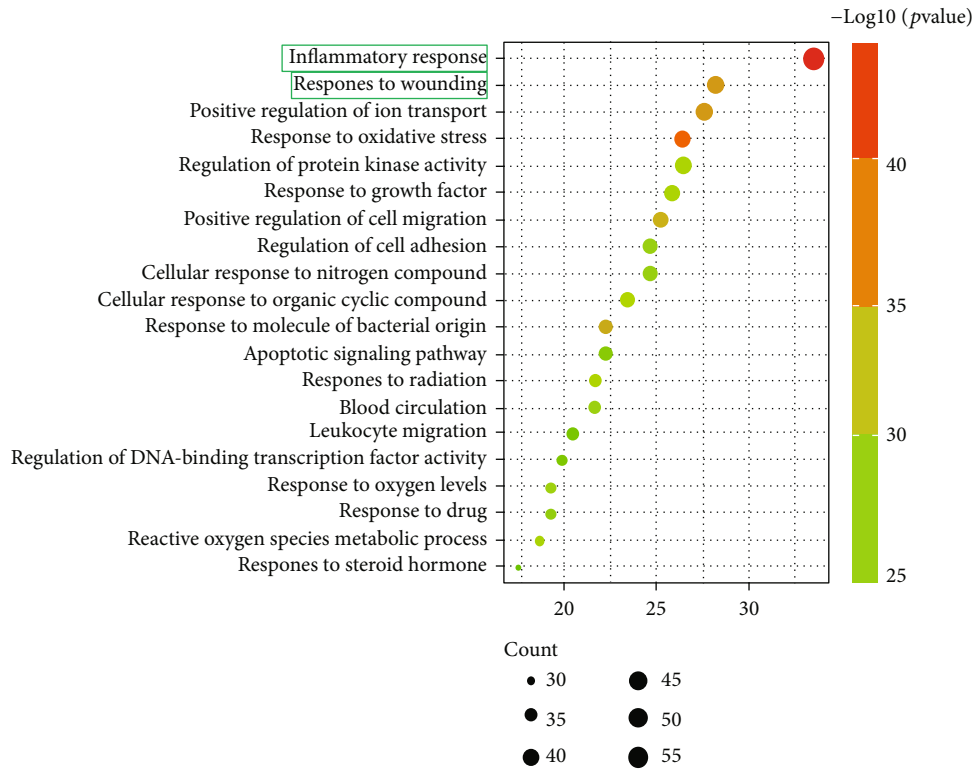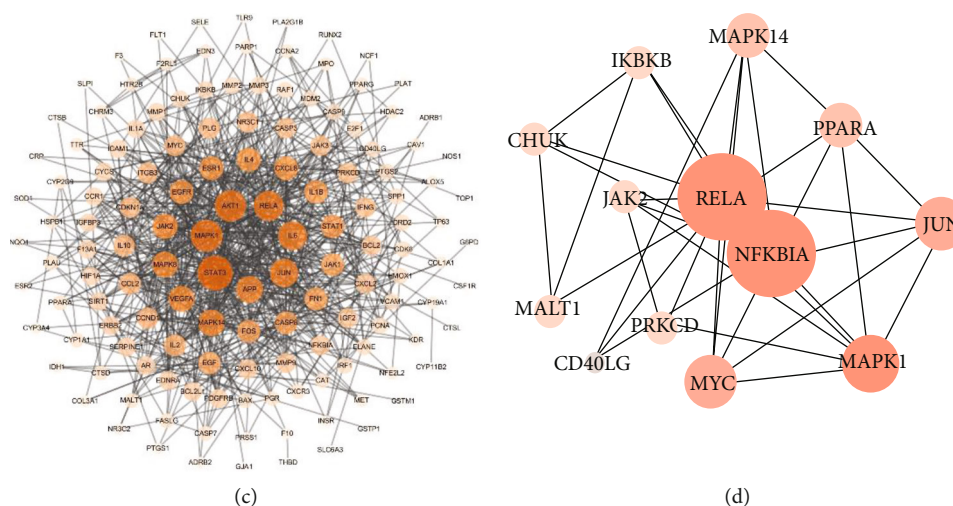peroxide for 25 min, the slides were incubated with primary antibodies against TLR4, MyD88, and p-NF-κB overnight at 4°C and secondary antibody for 1 h. The positive staining was determined with a 3,3′-diaminobenzidine substrate and counterstained with hematoxylin. Histological images were acquired using an M8 microscope (PreciPoint, Thüringen, Germany).

2.7. Western Blot Analysis. Proteins from mouse lung tissues were extracted, separated on 12% SDS-PAGE gels, and transferred to the PVDF membranes (Roche, Basel, Switzerland). After blocking with 5% BSA or nonfat milk for 1.5 h, the membranes were incubated with primary antibodies against TLR4, MyD88, IκBα, NF-κB p65, p-NF-κB p65, and Tubulin overnight at 4°C. After the incubation with HRP-conjugated secondary antibody (ProteinTech, IL, USA) for 1 h at room temperature, the membranes were washed three times with Tris-buffered saline with 0.1% Tween 20. The protein brands were visualized and detected using the ECL Moon kit (Beyotime Biotechnology, Shanghai, China) by a chemiluminescence detection system (ChemiDoc XRS, Bio-Rad, CA, USA). The quantification of the bands was performed using the ImageJ software (National Institutes of Health, Bethesda, MD, USA).

2.8. Statistical Analysis. Data were analyzed on the Prism software version 8 (GraphPad, San Diego, CA, USA). All values are expressed as the mean ± SEM. The significant differences among the groups were evaluated by one-way ANOVA with Tukey's post hoc test. The results are accepted as the level of significance was set at P value of < 0.05.

3. Results

3.1. The Activated Compounds and Potential Targets of the WBT Formula against IPF Are Predicted by Network Pharmacology. Using the TCMSP and TCMID databases,

243 candidate compounds were found in the WBT formula. Among these components, 20, 36, 65, 10, 2, 7, 23, 10, 19, 22, 13, 7, and 9 compounds were identified in *Astragalus membranaceus* (Fisch.) Bunge, *Scutellaria baicalensis* Georgi, *Bunge Salvia miltiorrhiza* Bunge, *Polygonum cuspidatum* Siebold & Zucc, *Angelica sinensis* (Oliv.) Diels, *Ligusticum striatum* DC., *Prunus persica* (L.) Batsch, *Pheretima aspergillum* (E. Perrier), *Aster tataricus* L.f., *Tussilago farfara* L., *Pinellia ternata* (Thunb.) Makino, *Clematis chinensis* Osbeck, and *Siegesbeckia orientalis* L., respectively (Table 2). Among these compounds, 40 compounds with the repeated names and 38 compounds without targets were deleted to obtain 165 compounds for further analysis. In the WBT formula, 352 targets of these 165 components (Supplementary Table 1) were predicted at TCMID and STPD websites. Then, we input 352 targets into the UniProt Knowledgebase website to unify the standard nomenclature. Meanwhile, 1,531 pathogenic genes-related with IPF were collected from the databases mentioned above (Supplementary Table 2). After the overlapping analysis, 167 intersection targets, as the potential targets of the WBT formula for treating IPF, were acquired and shown in a Venn diagram (Figure 1(a)). Furthermore, two compounds not for 167 targets of IPF were screened out to obtain 163 candidate compounds. In addition, those intersection targets were used to build the network diagram of the components of the WBT formula and their targets, which were composed of 330 nodes and 999 edges (Figure 1(b) and Supplementary Table 3). Collectively, 163 candidate compounds and 167 potential targets of the WBT formula against IPF were predicted by a network pharmacology-based method.

3.2. Potential Pathways and Gene Functional Enrichments for the WBT Formula against IPF. The GO annotation and KEGG pathway enrichments for 167 overlapping targets showed the top 20 significantly enriched terms in the
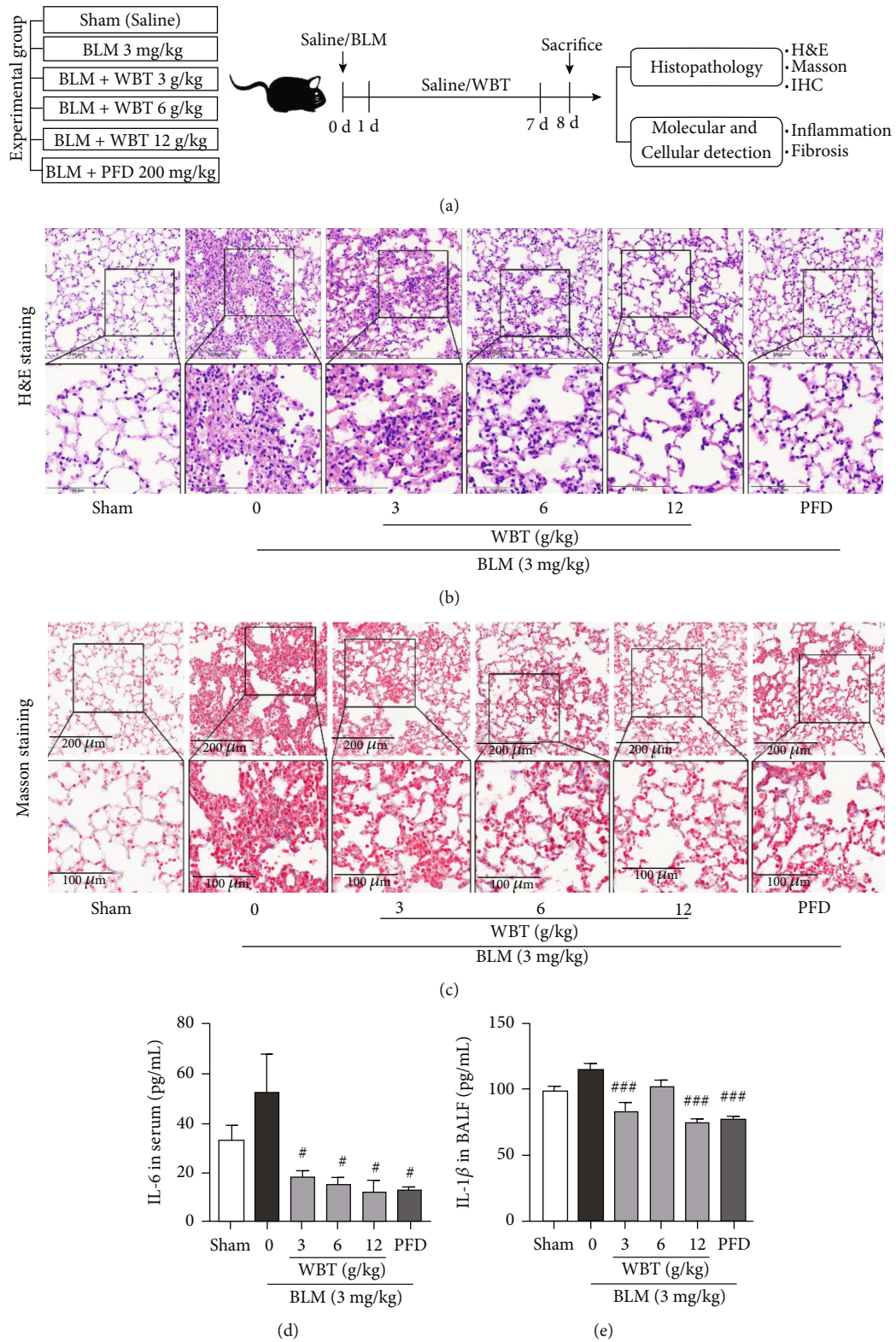
(a)

(b)

(c)

(d)

(e)

FIGURE 3: Continued.

(f)   (g)   (h)
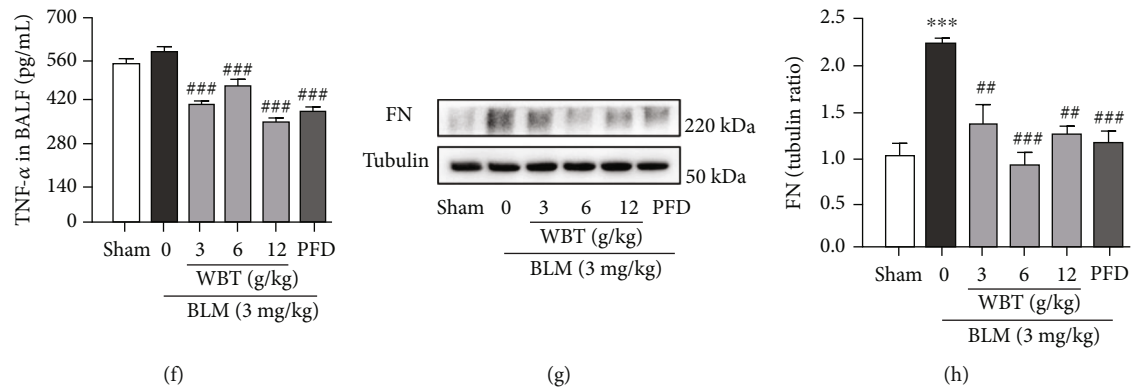
FIGURE 3: The WBT formula alleviates inflammation and fibrosis in a mouse model induced by BLM. (a) Diagram describing the protocol of animal experiment ($n = 10$ mice in each group). (b) H&E staining for observing inflammatory cell infiltration of lung tissues. (c) Masson's trichrome staining for detecting collagen fibers. (d–f) Serum IL-6 level and IL-1β, and TNF-α in BALF in different groups was measured by ELISA commercial kits. (g, h) The level of FN in lung tissues was measured by Western blot analysis. The bands from three independent experiments were semiquantitatively analyzed by using the ImageJ software, normalized to Tubulin density. Sham: sham surgery with intratracheal administration of normal saline (NS) + oral NS for 7 days; BLM (intratracheal administration of BLM (3 mg/kg) + oral NS); BLM induction and WBT/PFD treatment: BLM + WBT (3, 6, or 12 g/kg)/PFD (pirfenidone 200 mg/kg) for 7 days. Scale bar = 200 μ m (upper image), 100 μm (lower image). ***$P < 0.001$, compared to the sham group; #$P < 0.05$, ##$P < 0.01$, and ###$P < 0.001$ compared with the BLM group. All data were analyzed using one-way ANOVA followed by Tukey's test.

biological process (BP), and cell component (CC) and molecular function (MF) categories are shown in Figure 2(a) and Supplementary Figure 1. As suggested from the results, 167 key targets showed tight relations to the major BP, such as inflammatory response, response to wounding, response to oxidative stress, and regulation of cell adhesion. The WBT formula was reported for integrating multiple signaling pathways in the fibrosis process, inflammatory response, and cancers. The enrichment of target-pathway was built to delve into the mechanisms of potential targets acting on their corresponding signal pathways (Figure 2(b)). The PPI network for therapeutic targets of the WBT formula against IPF was constructed (Figure 2(c)). Furthermore, the therapeutic effect of the WBT formula on IPF was most likely achieved through modulating multiple pathways such as the PI3K-Akt, TNF, and NF-κB pathways. Among these pathways, the NF-κB pathway might be the core potential pathway of the WBT formula for inhibiting the inflammatory response, wounding response, and subsequent fibrosis. The targets of the NF-κB pathway subnetwork were built and are shown in Figure 2(d). Based on the results of the network pharmacology enrichment analysis, we further examined whether the protective effect of the WBT formula against inflammation and subsequent fibrosis were dependent on the regulation of the NF-κB-mediated inflammatory pathways.

3.3. Anti-Inflammatory and Fibrotic Effects of the WBT Formula on BLM-Induced Mice. To further validate the mechanism of the WBT formula for preventing inflammatory response during lung fibrosis, the protocol for animal group, drug administration, and mechanism experiment were designed and are visualized in Figure 3(a). As shown in Figures 3(b) and 3(c), histopathological changes with inflammatory and fibrotic responses due to BLM induction

showed the gathering of multiple inflammatory cells and collagen fibrogenesis in alveolar spaces after 7 days. Alveolar infiltration in the model group was suppressed in a dose-dependent manner after treatment with the WBT formula (Figure 3(b)). Masson's trichrome staining reflected collagen accumulation, as an indicator for lung fibrosis. The newly formed collagen fibers were decreased by the treatment of the WBT formula and PFD. The WBT formula at the dose of 12 g/kg and PFD effectively inhibited the formation of collagen fiber in the alveoli (Figure 3(c)), compared to the BLM-induced group. Subsequently, we examined the content of the IL-6 level in the serum and the levels of IL-1β and TNF-α in BALF from different groups. We found that WBT or PFD treatment significantly inhibited serum IL-6 level, compared with the BLM-induced group (Figure 3(d)). Importantly, the contents of IL-1β and TNF-α in BALF induced by BLM were lower than that of WBT or PFD treatment (Figures 3(e) and 3(f)). In addition, Western blot analysis showed that the expression of FN, a key molecule involved in fibrosis, was upregulated by BLM induction, which was obviously suppressed by WBT or PFD treatment (Figures 3(g) and 3(h)). Together, these data indicated that the WBT formula can inhibit inflammatory and fibrotic responses in the BLM-induced mouse model.

3.4. The WBT Formula Attenuates BLM-Induced Inflammatory Response by Inhibiting the TLR4/MyD88/NF-κB Pathway to Protect Lung Tissue from Fibrosis. To further validate the mechanism of the WBT formula for inflammatory response from the prediction, Western blot and IHC staining methods were used to analyze the NF-κB inflammatory pathway for clarifying the mechanism of the WBT formula. Western blotting revealed that IκBα was reduced by BLM, while NF-κB p-p65/p65 was upregulated in the BLM-induced lung tissues (Figures 4(a)–4(c)). WBT treatment promoted the expression of IκBα and inhibited the

(a)

(b)

(c)

(d)
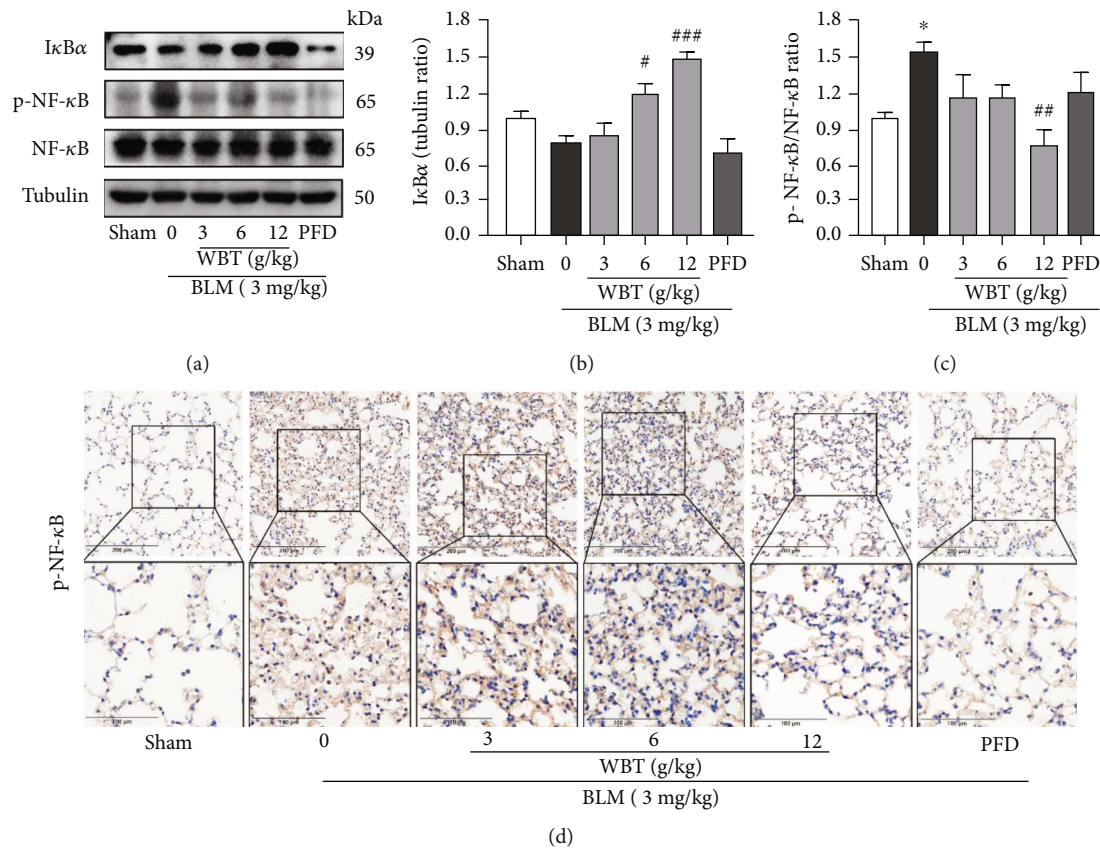
Figure 4: The WBT formula alleviated the NF-κB signaling pathway in BLM-induced mouse model. (a) Protein levels of phosphorylated-NF-κB p65 (p-NF-κB p65), total p65, and IκBα were measured with Western blotting. Tubulin was a loading control. (b, c) The bands of IκBα, p-NF-κB p65, and p65 were semiquantitatively analyzed by using the ImageJ software, normalized to Tubulin density, and calculated relative IκBα expression and the ratio of p-NF-κB p65 and p65. (d) The p-NF-κB p65 expression in lung tissues from different groups was determined by IHC staining. Scale bar: 200 μm (upper image), 100 μm (lower image). BLM: bleomycin. Sham: sham surgery with intratracheal administration of normal saline (NS) + oral NS for 7 days; BLM (intratracheal administration of BLM (3 mg/kg) + oral NS); BLM induction and WBT/PFD treatment: BLM (3 mg/kg) + WBT (3, 6, or 12 g/kg)/PFD (pirfenidone, 200 mg/kg) for 7 days, n = 10. $^{*}P < 0.001$, compared to the sham group; $^{#}P < 0.05$, $^{##}P < 0.01$, and $^{###}P < 0.001$ compared with the BLM group.

phosphorylation of NF-κB p65, compared with the BLM group (Figures 4(a)–4(c)). Similarly, the increased phosphorylation of NF-κB p65 induced by BLM in lung tissues was inhibited by the WBT formula according to IHC staining (Figure 4(d)). Recent studies have shown that TLR4 activity is crucial for inflammation and PF [23], which is upstream of the NF-κB pathway. MyD88 can be recruited to mediate the release of proinflammatory cytokines when the TLR4 pathway is activated [24, 25]. Therefore, we used Western blot and IHC staining to further investigate the effect of the WBT formula on the levels of TLR4 and MyD88 in the BLM-induced lung tissues. As shown in Figures 5(a)–5(c), Western blot analysis showed that BLM increased the expressions of TLR4 and MyD88 in the lung tissues, which were significantly downregulated after WBT formula intervention. For the IHC staining shown in Figure 5(d), similar results were found that WBT treatment significantly suppressed the BLM-induced increases of TLR4 and MyD88. Taken together, the WBT formula can inhibit the TLR4/MyD88/NF-κB signaling pathway to reduce inflammatory response in a BLM-induced mouse model with IPF.

4. Discussion

In the early stages following inflammation, fibroblasts and myofibroblasts provide a tissue scaffold for repairing the injured alveolar epithelial cell [26]. The inflammatory response is the initial pathogenesis of IPF, which stimulates the secretion of profibrotic cytokines to initiate fibroblast activation. Hence, the suppression of inflammation could slow down the IPF process [27]. The potential targets of the WBT formula for inhibiting inflammatory response were predicted using a network pharmacology approach. The WBT formula is a TCM and has extensively achieved efficacy in the Affiliated Hospital of Changchun University of Chinese Medicine (Changchun, China) for the prevention and treatment of IPF. However, its exact mechanism of anti-inflammatory action on IPF is still unclear. This study provides experimental evidence for the inhibitory effect of the WBT formula against inflammatory response by inactivating the TLR4/MyD88/NF-κB pathway, which could be a potential mechanism of the WBT formula treatment for IPF patients (Figure 6).

(a)   (b)   (c)

(d)

(e)
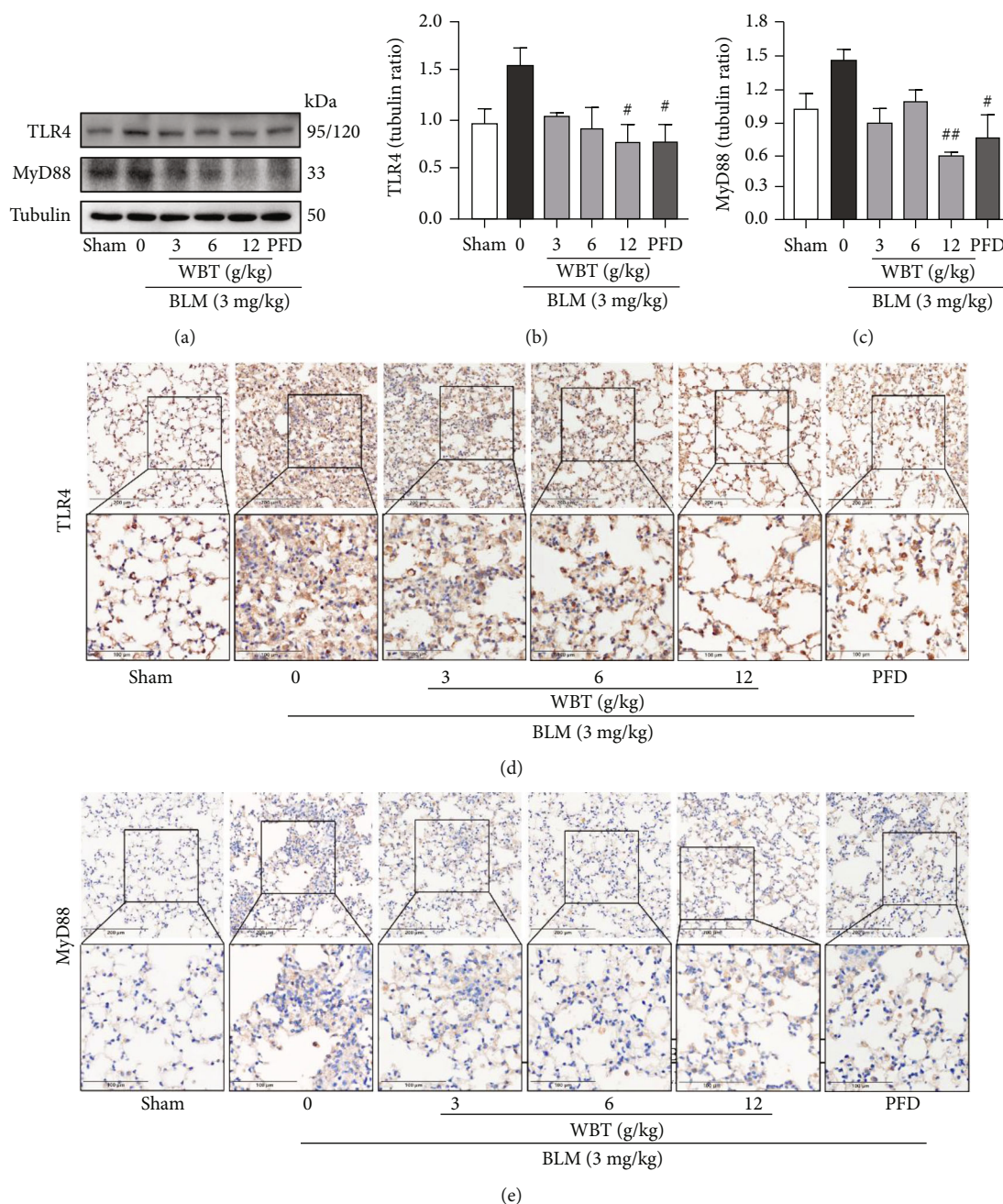
FIGURE 5: The WBT formula decreased the protein expression of the TLR4/MyD88 pathway in mouse lung tissues induced by BLM. (a) Protein levels of TLR4 and MyD88 were measured by Western blot analysis. (b, c) Quantification of relative expression of TLR4 or MyD88 was performed by densitometric analysis after the normalization of Tubulin. Tubulin was a loading control. (d, e) The levels of TLR4 and MyD88 were detected by immunohistochemical staining in lung tissues from sham (sham surgery with intratracheal administration of normal saline (NS) + oral NS), BLM (intratracheal administration of BLM (3 mg/kg) + oral NS), and WBT (intratracheal administration of BLM (3 mg/kg) + 3, 6, or 12 g/kg WBT) or PFD (intratracheal administration of BLM (3 mg/kg) + pirfenidone 200 mg/kg) for 7 days, $n = 10$. BLM: bleomycin. Scale bar: 200 μm (upper image), 100 μm (lower image). $^{\#}P < 0.05$ and $^{\#\#}P < 0.01$ compared with the BLM group.

Some herbs and bioactive components have been shown to possess pharmacologic activities for the treatment of IPF. *Astragalus membranaceus* (Fisch.) Bunge is a kind of the most widely used traditional Chinese herbal medicines for antioxidant and anti-inflammatory effects [28]. Extracts of *Scutellaria baicalensis* Georgi and its major chemical constituents have been reported to possess antioxidant and anti-

inflammatory functions [29], which promoted wound healing by suppressing the secretion of inflammatory cytokines [28]. After the prediction by network pharmacology, the degrees representing the connections of the nodes with direct neighbors were calculated to estimate the significance of the nodes in a network between the compounds and the targets [30]. In the present study, some targets with higher
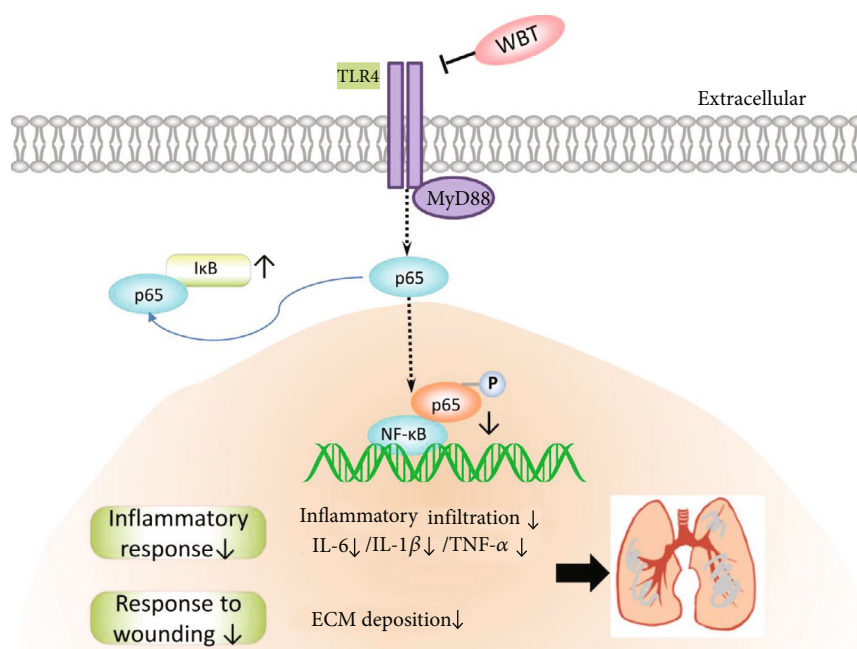
FIGURE 6: The potential mechanism of the WBT formula for inhibiting the TLR4/MyD88/NF-κB pathway-mediated inflammation against IPF.

degree values are important for the network. The top ten degree-ranked compounds are quercetin (MOL000098), xanthinin, luteolin (MOL000006), kaempferol (MOL000422), wogonin (MOL000173), tanshinone IIA (MOL007154), baicalein (MOL002714), beta-sitosterol (MOL000358), 7-O-methylisomucronulatol (MOL000378), and dihydrotanshinlactone (MOL007100), indicating their essential roles of these compounds for the target network of the inflammatory response during IPF. Certainly, those components in the WBT formula need to require LC-MS methods to identify the active compounds in further experiments.

The early stage of IPF is manifested inflammation, especially in the mouse model after BLM for 7 days. According to recent studies and our results, the TLR4/MyD88/NF-κB p65 signaling pathway appears to have potential functions in IPF [18, 31]. In our study, some compounds in the WBT formula have been shown to inhibit the TLR4/MyD88/NF-κB pathway. Researchers have found that quercetin has anti-inflammatory effects and can reduce the inflammatory response in a variety of diseases and inhibit inflammation-related signaling pathways [32–34]. Luteolin can inhibit TLR4 activation in multiple diseases [35–37]. To be of worth, PI3K/Akt, AGE-RAGE, and other pathways were also predicted by network pharmacology, which is important in the multiple stages of IPF progression and requires further experimental validation.

5. Conclusion

This research is aimed at exploring the mechanism of the WBT formula using a network pharmacology analysis in the early stage of IPF. After the prediction, 163 candidate compounds and 167 key targets of the WBT formula against IPF were identified. The inflammatory response, TNF, and NF-κB pathways were considered the potential pathway of the WBT formula, which was validated using a mouse model of IPF. The results indicated that the WBT formula can suppress IPF progression by inhibiting the TLR4/MyD88/NF-κB pathway-mediated inflammation. This study provides a new insight to the molecular mechanisms of the WBT formula in the application at the clinic.

Data Availability

The datasets used and/or investigated during the current study are available from the corresponding authors upon reasonable request.

Ethical Approval

All animal experiments were approved by the Experimental Animal Administration Committee of Changchun University of Chinese Medicine (Approval No. 2021230) and carried out in accordance with the institutional guidelines.

Conflicts of Interest

The authors declare that they have no competing interests.

Authors' Contributions

ZeW, XL, and DZ conceptualized the research topic and supervised its implementation; SS, JW, GL, LD, YL, HQ, LW, JZ, TC, MZ, ZiW, and YY designed the method, conducted the experiments, analyzed the data, and prepared figures/tables; SS and JW wrote the manuscript; XL and ZeW revised the manuscript. All authors have read and approved

the final manuscript. SS and JW contributed equally to this work.

Supplementary Materials

Supplementary Figure 1: GO analysis for the 167 shared targets from WBT formula and IPF-related target genes. (a) Molecular function. (b) Cell component. Supplementary Table 1: the possible targets of 165 compounds from the WBT formula. Supplementary Table 2: the target genes of idiopathic pulmonary fibrosis. Supplementary Table 3: a total of 167 potential targets of 163 candidate compounds in the WBT formula were obtained by network pharmacology. *(Supplementary Materials)*

References

[1] J. C. Hewlett, J. A. Kropski, and T. S. Blackwell, "Idiopathic pulmonary fibrosis: epithelial-mesenchymal interactions and emerging therapeutic targets," *Matrix Biology*, vol. 71-72, pp. 112–127, 2018.

[2] D. J. Lederer and F. J. Martinez, "Idiopathic pulmonary fibrosis," *The New England Journal of Medicine*, vol. 378, no. 19, pp. 1811–1823, 2018.

[3] J. A. Kropski and T. S. Blackwell, "Progress in understanding and treating idiopathic pulmonary fibrosis," *Annual Review of Medicine*, vol. 70, pp. 211–224, 2019.

[4] F. J. Martinez, H. R. Collard, A. Pardo et al., "Idiopathic pulmonary fibrosis," *Nature Reviews Disease Primers*, vol. 3, no. 1, 2017.

[5] P. W. Noble and R. J. Homer, "Back to the future: historical perspective on the pathogenesis of idiopathic pulmonary fibrosis," *American Journal of Respiratory Cell and Molecular Biology*, vol. 33, no. 2, pp. 113–120, 2005.

[6] W. H. Ma, M. Li, H. F. Ma et al., "Protective effects of GHK-Cu in bleomycin-induced pulmonary fibrosis via anti-oxidative stress and anti-inflammation pathways," *Life Sciences*, vol. 241, p. 117139, 2020.

[7] J. Liang, Y. Zhang, T. Xie et al., "Hyaluronan and TLR4 promote surfactant-protein-C-positive alveolar progenitor cell renewal and prevent severe pulmonary fibrosis in mice," *Nature Medicine*, vol. 22, no. 11, pp. 1285–1293, 2016.

[8] H. Yu, L. Lin, Z. Zhang, H. Zhang, and H. Hu, "Targeting NF-κB pathway for the therapy of diseases: mechanism and clinical study," *Signal Transduction and Targeted Therapy*, vol. 5, no. 1, p. 209, 2020.

[9] L. Richeldi, H. R. Collard, and M. G. Jones, "Idiopathic pulmonary fibrosis," *The Lancet*, vol. 389, no. 10082, pp. 1941–1952, 2017.

[10] Y. Tian, H. Li, T. Qiu et al., "Loss of PTEN induces lung fibrosis via alveolar epithelial cell senescence depending on NF-κB activation," *Aging Cell*, vol. 18, no. 1, p. e12858, 2019.

[11] X. H. Li, T. Xiao, J. H. Yang et al., "Parthenolide attenuated bleomycin-induced pulmonary fibrosis via the NF-κB/Snail signaling pathway," *Respiratory Research*, vol. 19, no. 1, p. 111, 2018.

[12] X. Wang, X. Li, L. N. Wang, J. J. Pan, X. Yang, and Y. L. Wei, "Buyang Huanwu decoction ameliorates bleomycin-induced pulmonary fibrosis in rats via downregulation of related protein and gene expression," *Evidence-based Complementary and Alternative Medicine*, vol. 2018, Article ID 9185485, 8 pages, 2018.

[13] Z. F. Yin, Y. L. Wei, X. Wang, L. N. Wang, and X. Li, "Buyang Huanwu Tang inhibits cellular epithelial-to-mesenchymal transition by inhibiting TGF-β1 activation of PI3K/Akt signaling pathway in pulmonary fibrosis model in vitro," *BMC complementary medicine and therapies*, vol. 20, no. 1, p. 13, 2020.

[14] L. Ding, S. Y. Song, S. Y. X. Li, X. Y. Li, and Z. Y. Wang, "Effect of Wenfei Buqi Tongluo prescription on the cell proliferation, morphology, and epithelial-mesenchymal transition in the TGF-β1-induced A549 cells," *Chinese Journal of Gerontology*, vol. 41, no. 8, pp. 1686–1690, 2021.

[15] X. Ren, L. Han, Y. Li et al., "Isorhamnetin attenuates TNF-α-induced inflammation, proliferation, and migration in human bronchial epithelial cells via MAPK and NF-κB pathways," *The Anatomical Record*, vol. 304, no. 4, pp. 901–913, 2021.

[16] J. Qian, X. Chen, X. Chen et al., "Kaempferol reduces K63-linked polyubiquitination to inhibit nuclear factor-κB and inflammatory responses in acute lung injury in mice," *Toxicology letters*, vol. 306, pp. 53–60, 2019.

[17] Y. Liu, Z. Li, X. Xue, Y. Wang, Y. Zhang, and J. Wang, "Apigenin reverses lung injury and immunotoxicity in paraquat-treated mice," *International immunopharmacology*, vol. 65, pp. 531–538, 2018.

[18] S. Luo, J. Gong, X. Cao, and S. Liu, "Ligustilide modulates oxidative stress, apoptosis, and immunity to avoid pathological damages in bleomycin induced pulmonary fibrosis rats via inactivating TLR4/MyD88/NF-KB P65," *Annals of Translational Medicine*, vol. 8, no. 15, p. 931, 2020.

[19] J. Ru, P. Li, J. Wang et al., "TCMSP: A database of systems pharmacology for drug discovery from herbal medicines," *Journal of cheminformatics*, vol. 6, p. 13, 2014.

[20] L. Huang, D. Xie, Y. Yu et al., "TCMID 2.0: a comprehensive resource for TCM," *Nucleic acids research*, vol. 46, pp. D1117–D1120, 2018.

[21] A. Daina, O. Michielin, and V. Zoete, "SwissTargetPrediction: updated data and new features for efficient prediction of protein targets of small molecules," *Nucleic acids research*, vol. 47, pp. W357–W364, 2019.

[22] M. Safran, I. Dalah, J. Alexander et al., "GeneCards Version 3: the human gene integrator," *Database*, vol. 2010, 2010.

[23] H. Z. Yang, J. P. Wang, S. Mi et al., "TLR4 activity is required in the resolution of pulmonary inflammation and fibrosis after acute and chronic lung injury," *The American Journal of Pathology*, vol. 180, no. 1, pp. 275–292, 2012.

[24] A. Roy, M. Srivastava, U. Saqib et al., "Potential therapeutic targets for inflammation in toll-like receptor 4 (TLR4)-mediated signaling pathways," *International immunopharmacology*, vol. 40, pp. 79–89, 2016.

[25] K. Takeda and S. Akira, "TLR signaling pathways," in *Seminars in immunology*, vol. 16, no. 1pp. 3–9, Academic Press, 2004.

[26] V. J. Craig, L. Zhang, J. S. Hagood, and C. A. Owen, "Matrix metalloproteinases as therapeutic targets for idiopathic pulmonary fibrosis," *American Journal of Respiratory Cell and Molecular Biology*, vol. 53, no. 5, pp. 585–600, 2015.

[27] S. Andugulapati, K. Gourishetti, S. K. Tirunavalli, T. B. Shaikh, and R. Sistla, "Biochanin-A ameliorates pulmonary fibrosis by suppressing the TGF-β mediated EMT, myofibroblasts differentiation and collagen deposition in in vitro and in vivo systems," *Phytomedicine*, vol. 78, p. 153298, 2020.

[28] Y. Cui, Q. Wang, R. Sun et al., "Astragalus membranaceus (Fisch.) Bunge repairs intestinal mucosal injury induced by LPS in mice," *BMC complementary and alternative medicine*, vol. 18, no. 1, p. 230, 2018.

[29] Z. Wang, S. Wang, Y. Kuang, Z. M. Hu, X. Qiao, and M. Ye, "A comprehensive review on phytochemistry, pharmacology, and flavonoid biosynthesis of Scutellaria baicalensis," *Pharmaceutical biology*, vol. 56, no. 1, pp. 465–484, 2018.

[30] W. Liu, W. H. Lin, A. J. Davis, F. Jordán, H. T. Yang, and M. J. Hwang, "A network perspective on the topological importance of enzymes and their phylogenetic conservation," *BMC bioinformatics*, vol. 8, pp. 1–21, 2007.

[31] J. Wang, H. Wang, F. Fang et al., "Danggui Buxue Tang ameliorates bleomycin-induced pulmonary fibrosis by suppressing the TLR4/NLRP3 signaling pathway in rats," *Evidence-Based Complementary and Alternative Medicine*, vol. 2021, Article ID 8030143, 2021.

[32] K. R. Manjeet and B. J. I. J. O. I. Ghosh, "Quercetin inhibits LPS-induced nitric oxide and tumor necrosis factor-alpha production in murine macrophages," *International journal of immunopharmacology*, vol. 21, no. 7, pp. 435–443, 1999.

[33] J. Tan, J. He, W. Qin, and L. Zhao, "Quercetin alleviates lipopolysaccharide-induced acute kidney injury in mice by suppressing TLR4/NF-κB pathway," *Nan Fang yi ke da xue xue bao= Journal of Southern Medical University*, vol. 39, no. 5, pp. 598–602, 2019.

[34] L. Geraets, H. J. Moonen, K. Brauers, E. F. Wouters, A. Bast, and G. J. Hageman, "Dietary flavones and flavonoles are inhibitors of poly(ADP-ribose)polymerase-1 in pulmonary epithelial cells," *The Journal of nutrition*, vol. 137, no. 10, pp. 2190–2195, 2007.

[35] R. Shen, L. Ma, and Y. Zheng, "Antiinflammatory effects of luteolin on acute gouty arthritis rats via TLR/MyD88/NFκB pathway," *Yi xue ban= Journal of Central South University. Medical sciences*, vol. 45, no. 2, pp. 115–122, 2020.

[36] C. Chen, C. Kao, and C. M. Liu, "The cancer prevention, anti-inflammatory and anti-oxidation of bioactive phytochemicals targeting the TLR4 signaling pathway," *International journal of molecular sciences*, vol. 19, no. 9, 2018.

[37] E. Kwon and M. J. N. Choi, "Luteolin targets the toll-like receptor signaling pathway in prevention of hepatic and adipocyte fibrosis and insulin resistance in diet-induced obese mice," *Nutrients*, vol. 10, p. 10, 2018.

Research Article

Mechanism of Sanhua Decoction in the Treatment of Ischemic Stroke Based on Network Pharmacology Methods and Experimental Verification

YingHuang,[1] **Shan-shan Gao,**[2] **Zi-han Gong,**[3] **Wen-jie Li,**[1] **Xiao-junGou** [ID],[2] **Ji-jia Sun** [ID],[4] **and Ming-jie Sun** [ID][1]

[1]*Experimental Research Center, China Academy of Chinese Medical Sciences, Beijing Key Laboratory of Research of Chinese Medicine on Prevention and Treatment for Major Diseases, Beijing 100700, China*
[2]*Central Laboratory, Baoshan District Hospital of Integrated Traditional Chinese and Western Medicine of Shanghai, Shanghai University of Traditional Chinese Medicine, Shanghai 201999, China*
[3]*Institute of Basic Theory for Chinese Medicine, China Academy of Chinese Medical Sciences, Beijing 100700, China*
[4]*Mathematics and Physics Teaching and Research Section, School of Pharmacy, Shanghai University of Traditional Chinese Medicine, Shanghai 201203, China*

Correspondence should be addressed to Xiao-junGou; gouxiaojun1975@163.com, Ji-jia Sun; jijiasun@163.com, and Ming-jie Sun; sunmj62@tom.com

Objective. The mechanism of action of Sanhua Decoction (SHD) in the treatment of ischemic stroke (IS) was analyzed based on the network pharmacology technology, and the pharmacodynamics and key targets were verified using the rat middle cerebral artery occlusion (MCAO) model. *Methods.* The GEO database was used to collect IS-related gene set S_D, and DrugBank and TTD databases were used to obtain the therapeutic drug target set S_T. IS disease gene set S_I was collected from DisGeNET, GeneCards, and OMIM databases. These three different gene sets obtained from various sources were merged, duplicates were removed, and the resulting IS disease gene set S_{IS} was imported into the STRING database to establish the protein-protein interaction (PPI) network. Two methods were used to screen the key targets of IS disease based on the PPI network analysis. The TCMSP database and PubChem were applied to retrieve the main chemical components of SHD, and the ACD/Labs software and the SwissADME online system were utilized for ADMET screening. HitPick, SEA, and SwissTarget Prediction online systems were used to predict the set of potential targets for SHD to treat IS. The predicted set of potential targets and the IS disease gene set were intersected. Subsequently, the set of potential targets for SHD treatment of IS was identified, the target information was confirmed through the UniProt database, and finally, the component-target data set for SHD treatment of IS was obtained. clusterProfiler was used for GO function annotation and KEGG pathway enrichment analysis on the target set of SHD active ingredients. A rat MCAO model was established to evaluate the pharmacodynamics of SHD in the treatment of IS, and Western blot analysis assessed the level of proteins in the related pathways. *Results.* This study obtained 1,009 IS disease gene sets. PPI network analysis identified 12 key targets: AGT, SAA1, KNG1, APP, GNB3, C3, CXCR4, CXCL12, CXCL8, CXCL1, F2, and EDN1. Database analyses retrieved 40 active ingredients and 47 target genes in SHD. The network proximity algorithm was used to optimize the six key components in SHD. KEGG enrichment showed that the signaling pathways related to IS were endocrine resistance, estrogen, TNF signal pathway, and AGEs/RAGE. Compound-disease-target regulatory network analysis showed that AKT1, IL-6, TNF-α, TP53, VEGFA, and APP were related to the treatment of IS with SHD. Animal experiments demonstrated that SHD significantly reduces the neurological function of rat defect symptoms ($P < 0.05$), the area of cerebral avascular necrosis, and neuronal necrosis while increasing the levels of IL-6 and APP proteins ($P < 0.05$) and reducing the levels of AKT1 and VEGFA proteins ($P < 0.05$). *Conclusion.* The effective components of SHD

may regulate multiple signaling pathways through IL-6, APP, AKT1, and VEGFA to reduce brain damage and inflammatory damage and exert a neuroprotective role in the treatment of IS diseases. Thus, this study provides a feasible method to study the pharmacological mechanism of traditional Chinese medicine compound prescriptions and a theoretical basis for the development of SHD into a new drug for IS treatment.

1. Introduction

Stroke is the second leading cause of death worldwide and is becoming a serious medical problem in developing countries [1, 2]. In China, approximately 1.3 million people suffer from stroke each year, and about 80% are related to ischemia [3]. Ischemic stroke (IS) is a common type of cerebrovascular disease with high morbidity and disability [4]. It is the first of the three major causes of death in China, accounting for about 50–70% of cerebrovascular accident diseases. Most surviving patients have severe disabilities, which casts a heavy economic burden on the family and society [5]. IS refers to the stenosis or occlusion of cerebral blood vessels, leading to the blockage of cerebral blood flow, which in turn causes ischemia, hypoxia, softening, and even necrosis of brain tissue, thereby resulting in cerebrovascular dysfunction and irreversible brain damage [6, 7]. Presently, the accepted theories about the pathogenesis of IS include energy exhaustion, depolarization of the penumbra around the infarct focus, excitatory amino acid (EAA) toxic effects, nitric oxide, inflammatory cytokines, free radical damage and cell damage, and apoptosis [8]. Therefore, adopting active and effective methods to start the protective program of cerebral ischemia injury in the early stage to reduce the neurological deficit and restore and reconstruct the cerebral neurological function is the current hotspot for research [9]. Clinically, patients with IS are treated with platelet aggregation inhibitors, statins, antihypertensive drugs, cerebrovascular nutrients, and other drugs [10]. Although progress has been made in treating IS in the clinic, the prevention and rehabilitation of IS are still a challenge.

Traditional Chinese medicine (TCM) has a history of thousands of years in the treatment of IS [11, 12]. SHD is a representative TCM prescription for IS [13] that comes from Liu Wansu's book "Su Tong Diseases, Qi Yi Bao Ming Ji." It is composed of *Magnolia officinalis*, *Citrus aurantium*, *Rhubarb*, and *Notopterygium* and is used for the treatment of stroke [14] even today in the modern world [15]. Previous studies have confirmed that this prescription is an optimal treatment of IS. It reduces the blood viscosity and the risk of thrombosis recurrence and increases the cerebral infarction area in patients [16]. Although the curative effect is definite, the pharmacological mechanism underlying SHD in the treatment of IS is unclear. Network pharmacology is a novel discipline based on the theory of system biology to conduct network analysis of biological systems and select specific signal nodes for multitarget drug molecular design [17]. The research field is aimed at revealing the synergy of multimolecular drugs by analyzing their regulatory effect on the disease network [18]. Network pharmacology combines system biology, omics, and computational biology to clarify the mechanism of drug action from a holistic perspective. It has the characteristics of completeness, synergy, and dynamics [19]. These characteristics are similar to those of TCM holism [20]. This method provides a new perspective for Chinese medicine's multicomponent and multitargeted therapy [21]. This method provides a system-level understanding of the effects of drugs and the complexity of diseases through network mapping and analysis. The network pharmacology method explains the mechanism of action of Chinese medicine in various diseases [22]. Therefore, the present study used network pharmacology to explore the mechanism of SHD on the effectiveness of IS treatment. A total of 40 representative compounds of SHD's four herbal medicines were screened. Subsequently, key targets were discovered using public databases and mathematical modeling calculations, and a protein-protein interaction (PPI) network was established. GO function and KEGG pathway enrichment analyses were performed. Finally, the signal pathway was verified by animal experiments. The results showed that SHD is an effective IS treatment, significantly reducing the symptoms of neurological deficits in rats, the area of avascular necrosis of brain tissue, and the amount of neuronal necrosis. Furthermore, SHD promotes the level of IL-6 and APP proteins in rats after ischemic brain injury and reduces the level of AKT1 and VEGFA proteins. These results provide a new perspective and further research direction for SHD treatment of IS. In addition, network pharmacology strategies can help researchers simplify the complex prescription system and provide novel avenues to elucidate the mechanisms underlying TCM prescriptions.

2. Materials and Methods

2.1. IS Disease Gene Collection

2.1.1. IS Differential Gene Analysis Based on Gene Expression Omnibus (GEO). In the GEO database (https://www.ncbi.nlm.nih.gov/geo/), "Ischemic Stroke" was entered to query and collect IS-related gene expression profiling chip to obtain the IS-related expression profiling data GSE22255. The data platform was GPL570 [HG-U133_Plus_2] Affymetrix Human Genome U133 Plus 2.0 Array, consisting of 20 normal and 20 IS samples.

The GSE22255 expression profile chip data file was downloaded from GEO, and the original data were preprocessed sequentially by standardization, correction, and gene name annotation using the limma package (version 3.42.2) based on the R language (version 3.6.3). Then, differentially expressed genes (DEGs) were analyzed. The IS DEG set was also screened according to p.value < 0.05 and $|\log_2 FC| > 0.5$, and ultimately, the IS gene set S_D was obtained based on the GEO differential gene analysis.

2.1.2. Collection and Collation of Data on Known IS Therapeutic Drug Targets. "Ischemic Stroke" was entered into the DrugBank (https://www.drugbank.ca/) to search

for existing small-molecule drugs for the treatment of IS and obtain target information of these drugs. Similarly, "Ischemic Stroke" was entered into the Therapeutic Target Database (TTD) (http://db.idrblab.net/ttd/) to identify IS-related targets. All targets from the two databases were merged, the points sorted, and the IS target set S_T was queried based on the database of the known therapeutic IS drug targets.

2.1.3. Collection and Sorting of IS Disease-Related Genes. Genes related to IS diseases were collected from DisGeNET (http://disgenet.org/home/), GeneCards (https://www.genecards.org/), and OMIM (https://omim.org/) databases. The IS-related genes were entered into "Ischemic Stroke," respectively, and searched in DisGeNET, GeneCards, and OMIM. Then, the intersection was obtained using the Venny Venn diagram tool (version 2.1.0, https://bioinfogp.cnb.csic.es/tools/venny/index.html). Subsequently, the genes overlapping in two or more databases were considered as IS disease candidate genes, and thus, the IS disease gene set S_I based on the query of the disease database was obtained. Finally, the three different gene sets S_D, S_T, and S_I obtained from three different sources were merged, duplicated removed, and the IS disease gene set S_{IS} obtained for further analysis.

2.2. IS Disease PPI Network Construction and Key Target Discovery

2.2.1. Construction of PPI Disease Network. The IS disease gene set obtained in Section 2.1 was imported into the STRING database (version 11.0, https://string-db.org/), the parameter organization was set to *Homo sapiens*, the combined score threshold was set to 0.7, and the IS disease PPI was obtained. The Gephi (version 0.9.2) software (https://gephi.org/) was used to visualize the IS disease PPI network.

2.2.2. Key Target Discovery Based on PPI Network Analysis. Typically, the critical targets in the PPI network play a key role in the disease; however, several methods are used to measure the importance of the nodes in the network. In order to elucidate and explore the key targets in the IS disease network, two methods were used to screen the key IS disease targets from different perspectives in this study.

(1) Method 1: Comprehensive Evaluation of Node Importance Based on Information Entropy Method. Generally, the parameter indicators in the PPI network, such as degree, closeness, betweenness, eccentricity, and page rank value, can be used to evaluate the importance of the target point from different angles in the network.

Entropy was first introduced into information theory by Shannon and since then has been widely used in engineering technology, social economy, and other fields. The evaluation method based on information entropy is that the objective weight is determined according to the size of the variability of the indicator. In the present study, an improved information entropy method (IIEM) was used to comprehensively

evaluate the importance value Z of each target on the PPI network. The computation is as follows:

(1) The network index value x_{ij} of each protein target in the PPI network is standardized and preprocessed using the following equation (1):

$$y_{ij} = \frac{x_{ij} - \min\left(x_{ij}\right)}{\max\left(x_{ij}\right) - \min\left(x_{ij}\right)}. \tag{1}$$

(2) The information entropy value H_j of each network index is calculated using the following equation (2):

$$H_j = -\frac{1}{\ln m} \sum_{i=1}^{m} b_{ij} \times \ln b_{ij}. \tag{2}$$

Among them, $b_{ij} = (y_{ij} + \varepsilon)/(\sum_{i=1}^{m}(y_{ij} + \varepsilon))$, $\varepsilon = 10^{-4}$.

(3) The weight value ω_j of each network index is calculated using the following equation (3):

$$\omega_j = \frac{1 - H_j + 0.1 \times \sum_{j=1}^{n}\left(1 - H_j\right)}{\sum_{j=1}^{n}\left[1 - H_j + 0.1 \times \sum_{j=1}^{n}\left(1 - H_j\right)\right]}. \tag{3}$$

(4) The importance value Z_i of the i protein target in the PPI network is calculated using the following equation (4):

$$Z_i = \left[\sum_{j=1}^{n} w_j\left(y_{ij} - f_j\right)\right]^2, \tag{4}$$

where m is the number of protein targets in the network and n is the number of network indicators at $f_j = 0$. Herein, we first calculated the five indicators of each protein target in the IS disease PPI network, including degree, closeness, betweenness, eccentricity, and page rank. Then, according to the magnitude of the importance value Z_i, the importance of the targets in the PPI network was sorted using IIEM, and the key IS target genes were screened out.

(2) Method 2: Screening of Key Targets Based on Network Modules. From the perspective of network modules, the critical targets in the PPI network were analyzed and screened. The CytoHubba tool in the Cytoscape (version 3.7.1) software (https://cytoscape.org/) based on the Maximal Clique Centrality (MCC) algorithm was employed, and the crucial nodes in the network were discovered from the mining perspective of the largest group of network modules.

2.3. Collection of the Main Ingredients and Screening of ADMET in SHD. SHD is mainly composed of four TCMs, including *Rhubarb* (DH), *Magnolia officinalis* (HP), *Citrus aurantium* (ZS), and *Notopterygium* (QH). First, we collected all the ingredients of these medicines from our TCMID database (http://www.megabionet.org/tcmid/). Then, according to the PubChem database (https://pubchem.ncbi.nlm.nih.gov), the compound name, molecular formula, PubChem CID, Canonical SMILES, and other information on each component were collected and confirmed to establish the SHD component database.

In this study, we used two ADMET prediction systems, the ACD/Labs software and SwissADME online system (http://www.swissadme.ch/), to screen the active ingredients according to the molecular weight (MW), Lipinski, solubility, bioavailability (dose = 50 mg), Ames, hERG, synthetic accessibility, and other indicators. Among these, the evaluation result of MW and Lipinski was "Good" or "Moderate," that of solubility removal was considered as "Highly Insoluble," the oral availability bioavailability was ≥60%, Ames and hERG were genotoxicity and cardiotoxicity indicators, respectively, the clear toxic components were removed during screening, and synthetic accessibility was ≤5.

2.4. Prediction and Identification of Potential Targets of Active Ingredients. Canonical SMILES corresponding to the SHD active ingredients filtered by ADMET were imported into HitPick (http://mips.helmholtz-muenchen.de/proj/hitpick), SEA (http://sea.bkslab.org/), and SwissTargetPrediction (http://www.swisstargetprediction.ch/) to predict the potential target points of all components. Among these, the screening threshold precision predicted by HitPick was 70%, the screening threshold max Tc predicted by SEA was 0.7, and the SwissTarget Prediction threshold probability was 0.6.

Next, the predicted potential target set and IS disease gene set were intersected, and the potential target set of SHD treatment of IS was identified. The target information was confirmed through the UniProt database (https://www.uniprot.org/). Finally, the component-target data of the treatment of IS by SHD was obtained. The Cytoscape software was used to draw the effective component-target network diagram of the SHD treatment of IS. This network was termed as the SHD active component direct action target network for subsequent analysis.

2.5. GO Function of the Target and the Enrichment Analysis of the KEGG Pathway. Cluster Profiler (version 3.14.3) was used to perform GO function annotation and KEGG pathway enrichment analysis of the target set of SHD active ingredients. The gene annotation and the signaling pathway catalogs were selected according to the P value < 0.05 and q value < 0.05 criteria. A data file was created based on the results of KEGG pathway enrichment analysis, and the target-enrichment pathway network was constructed using the Cytoscape software.

2.6. Regulation Analysis of Key Targets of SHD Intervention Based on the Proximity of Human PPI Networks. Next, we investigated whether the active ingredients of SHD have direct or indirect regulatory effects on the key targets in Section 2.2. Although some ingredients do not directly affect, they may influence and regulate the key targets through adjacent intervention targets. Therefore, we proposed an in-depth analysis of the effective ingredients in SHD based on the calculation method of the network proximity of the human PPI background network using equations (5) and (6):

$$S_{AB} = \langle d_{AB} \rangle - \frac{\langle d_{AA} \rangle + \langle d_{BB} \rangle}{2}, \tag{5}$$

$$\langle d_{AB} \rangle = \frac{1}{\|A\| \times \|B\|} \sum_{a \in A, b \in B} d(a, b). \tag{6}$$

A is the component action target set, $\|A\|$ is the number of the target set, B is the key gene set, $\|B\|$ is the number of the target in the key gene set, $d(a, b)$ is the shortest path distance between two nodes in the human PPI background network, $\langle d_{AA} \rangle$ represents the average distance between the target points of the component action, $\langle d_{BB} \rangle$ represents the average distance between key genes, and $\langle d_{AB} \rangle$ represents the average distance between the target set and the key target set of the component action on the background network; the network distance is calculated using the igraph package (version 1.2.5).

The human PPI background network used in the calculation integrated 15 commonly used databases and focused on high-quality PPI with five types of evidence. The PPI network consisted of 16,677 proteins and 243,603 interaction correlations. This network was used as the background network to evaluate the overall regulation of the effective components of SHD decoction on the key gene set.

Typically, when $S_{AB} < 0$, it means that the target set A and the key gene set B of the component's action are close in the network topology, indicating that the component can regulate the key gene set B by intervening in the target set A. When $S_{AB} \geq 0$, the target set A and the key gene set B of the component action are separated in the network topology, indicating that the component has no significant regulatory intervention related to the key gene set B. Therefore, we can further judge the presence of certain components in SHD by calculating the value of S_{AB} that might interfere with the key target set via specific target proteins in order to improve or treat the diseases.

2.7. Experimental Verification

2.7.1. Experimental Animals. Male Sprague–Dawley (SD) rats (8-weeks-old, bodyweight 230–250 g, clean grade) were purchased from Beijing Huafukang Biotechnology Co., Ltd., license number, SCXK (Beijing) 2019-0008. All rats were bred routinely, with free water, at a room temperature of 22–24°C.

2.7.2. Establishment of Animal Model. The rat middle cerebral artery occlusion model (MCAO model) was established using the thread plug method. Rats were anesthetized by

intraperitoneal injection of 1% pentobarbital (35 mg/kg body weight). The limbs of the rats were fixed on the operating table, the neck skin was prepared, the drape was routinely disinfected, and a median neck incision was made. The right common carotid artery (CCA) was exposed layer-by-layer separation, and the right CCA, internal carotid artery (ICA), and external carotid artery (ECA) were carefully separated to avoid stimulating the vagus nerve. A silk thread was placed on CCA, ICA, and ECA, respectively. At 5 mm from the bifurcation of ICA and ECA, CCA was tied, ECA was ligated at the root of CCA, and the preset silk thread was pulled to block the blood flow of ICA. Then, a small cut was made at the bifurcation of ICA and CCA, the end of the threaded bolt was inserted along the incision, and the lifting line was loosened and slowly advanced 18–20 mm; the advancing was stopped when it encountered slight resistance. The ICA was ligated, and the silk thread was left to prevent the embolus from falling off. At 90 min postoperatively, the threaded plug was withdrawn from the ICA, and reperfusion was performed. In the sham operation group, the tether was inserted only 10 mm, such that it was placed in the ICA without entering the middle cerebral artery (MCA); the rest of the steps were the same as before. After the operation, the rat MCAO model was scored according to Zea-Longa's standard scoring method [4], and the animals that met the model success criteria were included in this study.

2.7.3. Grouping and Administration. After the MCAO model was successfully prepared, the rats were randomly divided into the model and SHD groups ($n = 6$ rats in each group). In addition, a blank control group and a sham operation group were set up ($n = 6$ in each group). The blank control, sham operation, and model groups were given purified water, while the SHD group was given SHD water decoction consisting of 20 g of *Rhubarb* (HD), 20 g of *Magnolia officinalis* (HP), 20 g of *Citrus aurantium* (ZS), and 20 g of *Notopterygium* (QH). It was decocted in water at a concentration of 0.864 g/mL of the crude drug. The dosage for rats was converted according to the daily clinical dosage of the patient and administered at 10 a.m. daily; each rat was administered 7.2 g/kg for 5 consecutive days.

2.7.4. Neurological Deficit Score (NDS) to Detect the Recovery of the Neurological Function. Zea-Longa scoring method was used to evaluate the NDS: 0 points to without neurological deficits and normal activity, 1 point to those who could not fully extend the contralateral front paw, 2 points to those who turn to the left while crawling, 3 points to those who fall to the hemiplegic side while walking, 4 points to those who cannot walk spontaneously and have a consciousness disorder.

2.7.5. 2,3,5-Triphenyltetrazolium Chloride (TTC) Staining to Detect the Cerebral Infarction Rate. At 24 h after the last administration, the rats were anesthetized with 1% pentobarbital (35 mg/kg body weight) by intraperitoneal injection to perform a craniotomy. The brain tissue was excised, and the coronal sections were cut into six slices, each about 2 mm thick. The sections were immersed in 2% TTC solution for staining. The Image-Pro Plus image analysis software was used to calculate the percentage of the white part (this is the stroke infarct part) in the cerebral hemisphere after staining. Cerebral infarction rate = (volume of the contralateral ischemic hemisphere − volume of noninfarcted ischemic side)/volume of contralateral ischemic hemisphere × 100%.

2.7.6. Effect of SHD on the Pathomorphology of Cerebral Ischemia-Reperfusion Rats. The brain tissue was fixed in 4% paraformaldehyde, routinely dehydrated, paraffin-embedded, sectioned, hematoxylin-eosin (HE) stained, mounted, and placed under a Leica optical microscope to observe the morphological changes.

2.7.7. Western Blot Detection. An equivalent of 100 mg of the tissue was homogenized in 1 mL of RIPA buffer using a tissue grinder (60HZ, 90S). The supernatant was collected by centrifugation of the lysate at 12000 rpm 4°C for 10 min. The total protein concentration was estimated using the BCA method. An equivalent of protein was resolved on SDS-PAGE and transferred to membrane. After blocking in TBST, the membrane was probed with AKT1, IL-6, TP53, TNF-α, VEGFA, and APP primary antibodies at 4°C, overnight, followed by incubation with secondary antibody at room temperature for 1 h. Subsequently, the immunoreactive bands were developed using the ECL reagent, and the protein expression level was analyzed by the Quantity One software.

2.7.8. Statistical Analysis. The experimental data are expressed as mean ± standard deviation ($\bar{x} \pm sd$) and analyzed using the SPSS 19 statistical software. One-way analysis of variance (ANOVA) is used to compare the mean values of samples in multiple groups. The measurement data of the two groups were evaluated by t-test, and $P < 0.05$ indicated statistical significance.

3. Results

3.1. Gene Collection of IS Disease. A total of 55 DEGs related to IS disease were screened based on GEO differential gene analysis. Among these, 1 upregulated gene and 54 downregulated genes comprised the IS gene set S_D. Subsequently, 86 small-molecule drugs for the treatment of IS and 110 targets of their effects were collected from DrugBank, and 15 related targets were obtained from TTD. Thus, a total of 123 therapeutic drug targets for IS were obtained from the combination of the two, namely, the IS target point set S_T, based on a database of known therapeutic IS drug targets. Finally, 1159, 3350, and 182 related genes were collected from DisGeNET, GeneCards, and OMIM, respectively. All genes that overlapped in the two databases were included, and a total of 898 genes were obtained, which comprised the IS disease gene set S_I based on the disease data queries. Finally, the three sets of genes were merged to obtain a total of 1009 IS disease genes, i.e., the IS disease gene set S_{IS}. The result is shown in Figure 1.
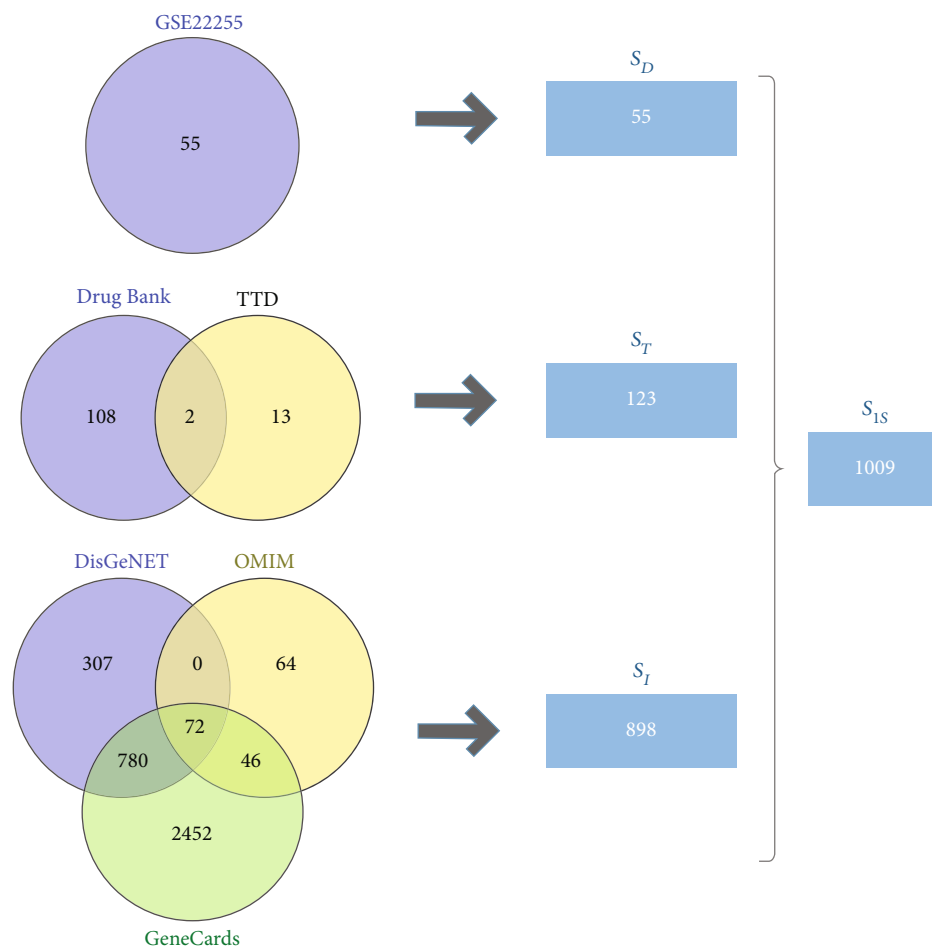
FIGURE 1: (a) 55 differentially expressed genes obtained from the GSE22255 chip GEO differential gene analysis. 123 drug treatment targets based on the query and combination of DrugBank and TTD databases. 898 genes based on the query and combination of DisGeNET, GeneCards, and OMIM databases. A total of 1009 IS disease genes were obtained by three methods.

3.2. IS Disease PPI Network Construction and Key Target Discovery.

All 1009 genes of the IS gene set were imported into STRING, and the PPI network of IS disease was generated using Gephi (Figure 2). Next, we calculated the importance of all nodes in the PPI network (Supplementary materials 1) based on the IIEM method. In this study, we stipulated that nodes with an evaluation score of $Z_i \geq 0.4$ were included as the key targets, and 39 IS disease targets were obtained. We also screened and ranked the top 50 targets based on the MCC algorithm of CytoHubba. Finally, the intersection of the two methods revealed 12 key targets (AGT, SAA1, KNG1, APP, GNB3, C3, CXCR4, CXCL12, CXCL8, CXCL1, F2, and EDN1) (Table 1).

3.3. Collection of SHD and ADMET Screening.

A total of 328 components were collected from TCMID, of which 84 were Rhubarb (DH), 20 were *Magnolia officinalis* (HP), 193 were *Notopterygium* (QH), and 31 were *Citrus aurantium* (ZS). Furthermore, the chemical information of all small molecules was collected and confirmed from the PubChem database. In addition, for the convenience of follow-up analysis, we sequentially numbered the components MOL001–MOL328. The ACD/Labs software and the SwissADME were used for ADMET

screening, and 147 active ingredients meeting ADMET conditions were obtained (Supplementary materials 2).

3.4. Prediction and Identification of Effective Component Targets.

HitPick, SEA, and SwissTarget prediction databases were used to predict and filter the 147 active ingredients of SHD based on the threshold; consequently, 72 active ingredients and 137 potential targets of their effects were intersected with the IS disease gene set S_{IS}, and it was found that the 40 active ingredients in SHD directly acted on the 47 IS targets. The information of these 47 targets is listed in Table 2. Finally, Cytoscape was used to construct the active ingredient-target direct action network of SHD (Figure 3).

3.5. GO Functional Annotation and KEGG Pathway Enrichment Analysis of SHD Targets.

GO functional annotation and KEGG pathway enrichment analyses of 47 IS disease targets affected by SHD were performed, and the results are shown in Figures 4(a) and 4(b).

GO function annotation and KEGG pathway enrichment analyses revealed that the 47 targets are involved in 683 biological process (BP) functions, such as response to metal ion (GO: 0010038), icosanoid metabolic process

(a)

(b)

Figure 2: Continued.

(c)
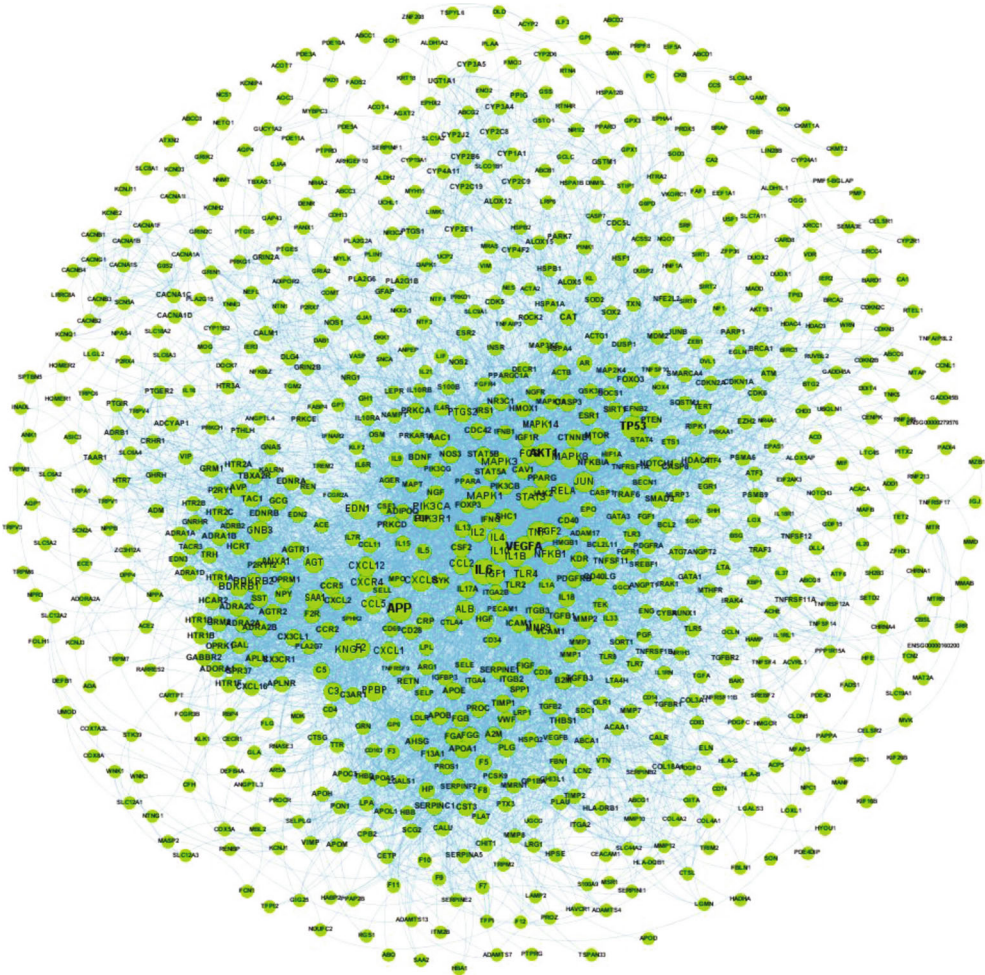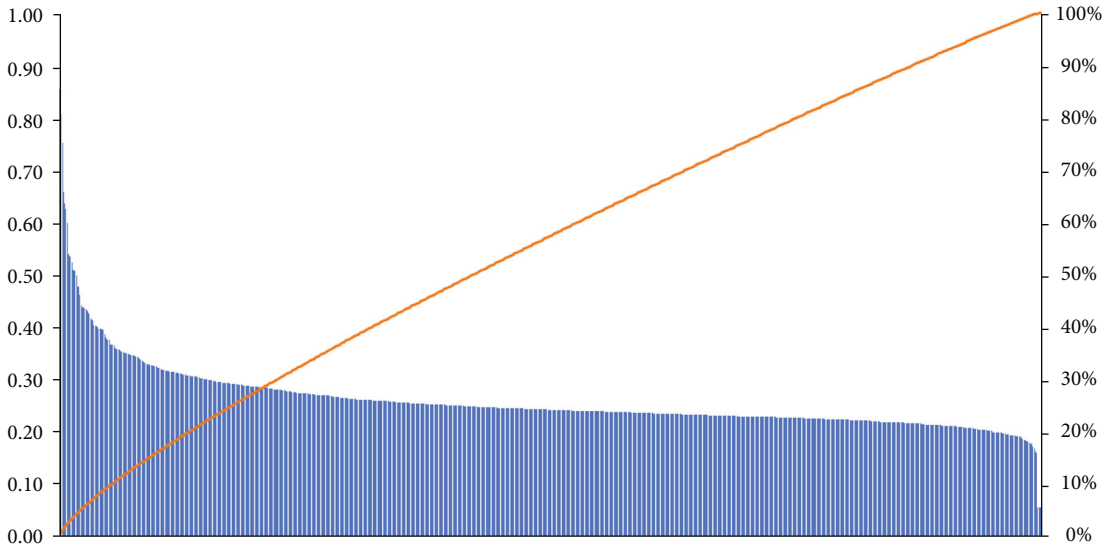
(d)
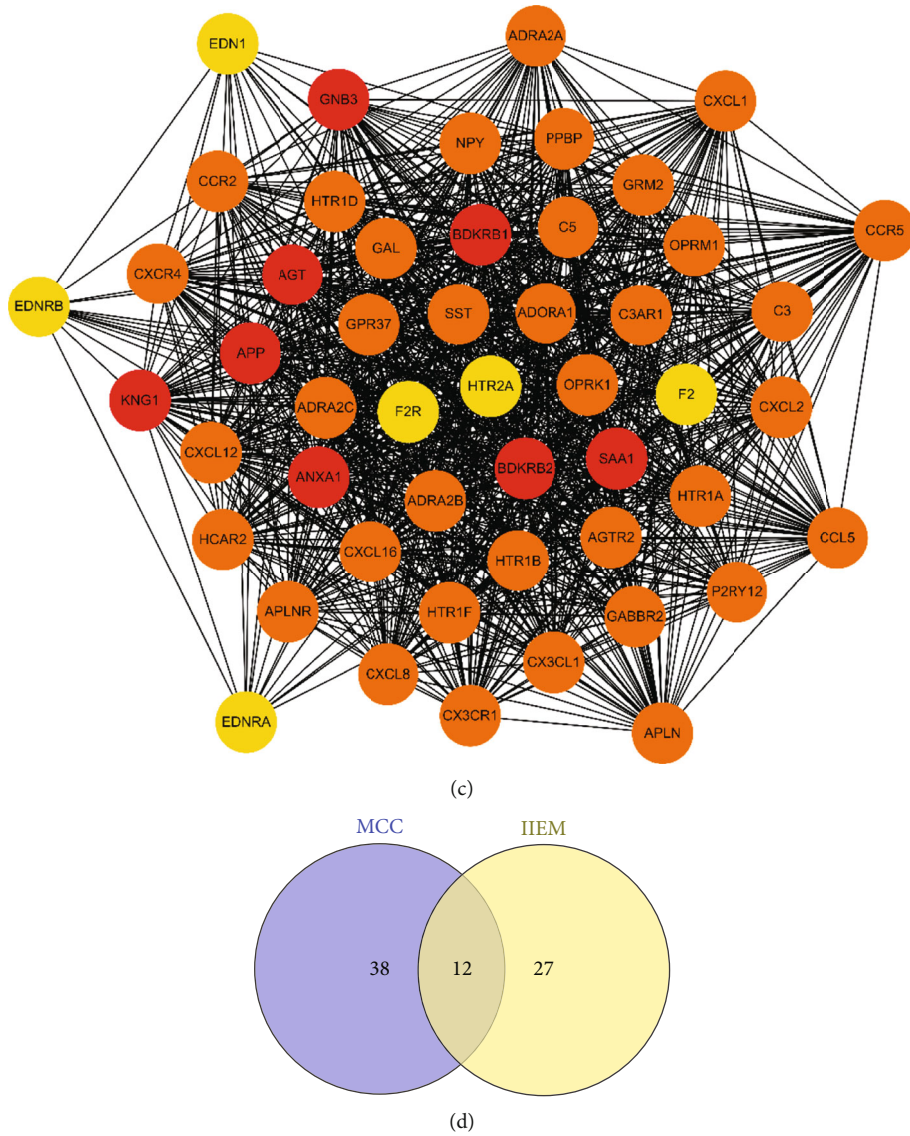
Figure 2: (a) PPI network of IS disease genes by STRING. (b) Pareto distribution diagram of the scores of important nodes in the PPI network based on the IIEM. (c) The results of the top 40 important targets of the PPI network based on MCC. (d) 12 key genes of IS obtained through MCC and IIEM.

Table 1: Information table of 12 key genes.

Genes	Protein names	UniProt ID
AGT	Angiotensinogen	P01019
APP	Amyloid-beta precursor protein	P05067
C3	Complement C3	P01024
CXCL1	Growth-regulated alpha protein	P09341
CXCL12	Stromal cell-derived factor 1	P48061
CXCL8	Interleukin-8	P10145
CXCR4	C-X-C chemokine receptor type 4	P61073
EDN1	Endothelin-1	P05305
F2	Prothrombin	P00734
GNB3	Guanine nucleotide-binding protein G(I)/G(S)/G(T) subunit beta-3	P16520
KNG1	Kininogen-1	P01042
SAA1	Serum amyloid A-1 protein	P0DJI8

TABLE 2: Information table of SHD targets.

| Targets	Protein names	UniProt ID
ABCB1	ATP-dependent translocase ABCB1	P08183
ABCC1	Multidrug resistance-associated protein 1	P33527
ABCG2	Broad substrate specificity ATP-binding cassette transporter ABCG2	Q9UNQ0
ALB	Albumin	P02768
ALDH2	Aldehyde dehydrogenase	P05091
ALOX15	Polyunsaturated fatty acid lipoxygenase ALOX15	P16050
ALOX5	Polyunsaturated fatty acid 5-lipoxygenase	P09917
APP	Amyloid-beta precursor protein	P05067
BCL2	Apoptosis regulator Bcl-2	P10415
CA1	Carbonic anhydrase 1	P00915
CA2	Carbonic anhydrase 2	P00918
CYP19A1	Aromatase	P11511
CYP1A1	Cytochrome P450 1A1	P04798
CYP3A4	Cytochrome P450 3A4	P08684
DLG4	Disks large homolog 4	P78352
EPHX2	Bifunctional epoxide hydrolase 2	P34913
ESR1	Estrogen receptor	P03372
ESR2	Estrogen receptor beta	Q92731
F3	Tissue factor	P13726
FABP4	Fatty acid-binding protein	P15090
FOS	Proto-oncogene c-Fos	P01100
GAMT	Guanidinoacetate N-methyltransferase	Q14353
HMGCR	3-Hydroxy-3-methylglutaryl-coenzyme A reductase	P04035
JUN	Transcription factor AP-1	P05412
KCND3	Potassium voltage-gated channel subfamily D member 3	Q9UK17
KCNH2	Potassium voltage-gated channel subfamily H member 2	Q12809
LCN2	Neutrophil gelatinase-associated lipocalin	P80188
MAPK14	Mitogen-activated protein kinase 14	Q16539
MAPT	Microtubule-associated protein tau	P10636
MMP2	Matrix metalloproteinase-2	P08253
MMP9	Matrix metalloproteinase-9	P14780
NFE2L2	Nuclear factor erythroid 2-related factor 2	Q16236
NFKB1	Nuclear factor NF-kappa-B p105 subunit	P19838
NOX4	NADPH oxidase 4	Q9NPH5
OPRM1	Mu-type opioid receptor	P35372
PPARA	Peroxisome proliferator-activated receptor alpha	Q07869
PPARD	Peroxisome proliferator-activated receptor delta	Q03181
PPARG	Peroxisome proliferator-activated receptor gamma	P37231
PRKCA	Protein kinase C alpha type	P17252
PTGES	Prostaglandin E synthase	O14684
PTGS1	Prostaglandin G/H synthase 1	P23219
PTGS2	Prostaglandin G/H synthase 2	P35354
SLC18A2	Synaptic vesicular amine transporter	Q05940
TERT	Telomerase reverse transcriptase	O14746
TLR2	Toll-like receptor 2	O60603
TNKS	Poly [ADP-ribose] polymerase tankyrase-1	O95271
TTR	Transthyretin	P02766

(a)

(b)
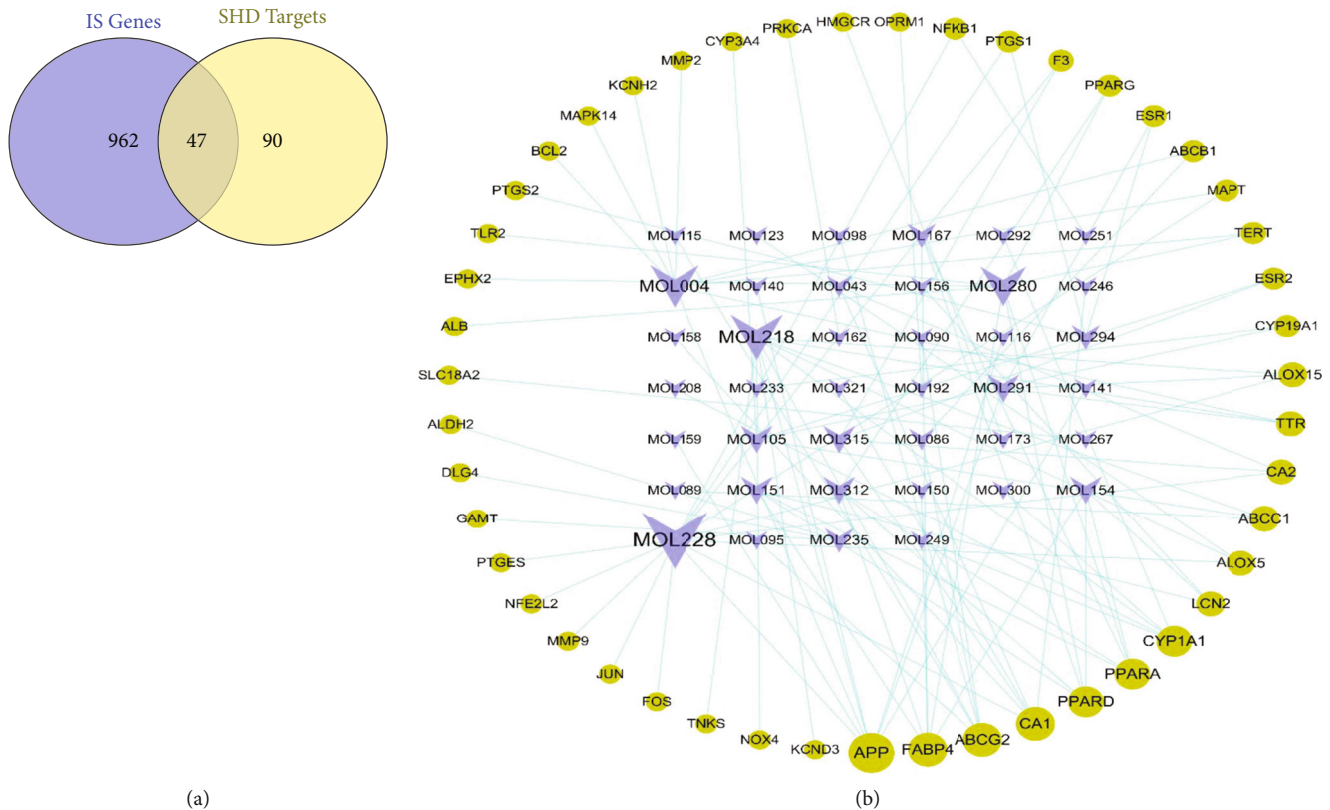
Figure 3: (a) Venn diagram of target prediction and recognition results of SHD. (b) SHD ingredients-direct acting target network diagram, where the yellow nodes represent the target and the V-shaped nodes represent the ingredients. The larger the node, the greater the degree value of the node in the network.

(GO: 0006690), response to lipopolysaccharide (GO: 0032496), cellular response to metal ion (GO:0071248), and response to molecule of bacterial origin (GO: 0002237); 67 molecular function (MF) functions, such as fatty acid binding (GO: 0005504), oxygen binding (GO: 0019825), nuclear receptor activity (GO: 0004879), transcription factor activity, direct ligand regulated sequence-specific DNA binding (GO: 0098531), and RNA polymerase II transcription factor binding (GO: 0001085); and 21 cellular component (CC) functions, such as secretory granule lumen (GO: 0034774), cytoplasmic vesicle lumen (GO: 0060205), vesicle lumen (GO: 0031983), RNA polymerase II transcription factor complex (GO: 0090575), and nuclear transcription factor complex (GO: 0044798).

The KEGG pathway was mainly enriched in 61 signaling pathways, such as endocrine resistance (hsa01522), AGE-RAGE in diabetic complications (hsa04933), estrogen signaling pathway (hsa04915), fluid shear stress and atherosclerosis (hsa05418), Hepatitis B (hsa05161), IL-17 (hsa04657), serotonergic synapse (hsa04726), relaxin signaling pathway (hsa04926), human immunodeficiency virus 1 infection (hsa05170), and microRNAs (miRNAs) in cancer (hsa05206). The pathways with the number of enrichment targets ≥ 5 were selected, and the target-enrichment pathway network was constructed using Cytoscape (Figure 4(c)).

3.6. Analysis of the Regulation of Key Target Genes by Small Molecules. According to the results in Section 2.2, we identi-

fied 12 key genes in the IS disease. Among the 47 targets directly affected by the 40 active ingredients of SHD, only APP belonged to these 12 key genes. Therefore, we further used the calculation method based on the network proximity to further explore whether these 40 active ingredients have an indirect regulatory effect on the key IS targets. The results are shown in Figure 5.

40/72 active ingredients of SHD had a network proximity of $S_{AB} < 0$ to the key target set and network proximity of $S_{AB} < 0$ to the key target set, indicating that these small molecules regulate these 12 key targets by intervening with specific targets. Interestingly, six components (MOL040, MOL064, MOL239, MOL247, MOL279, and MOL298) did not directly affect the 47 targets of IS but could directly interfere with the 12 key targets in the PPI network, which promoted the anti-IS disease.

3.7. Effect of SHD on Neurological Function Score and Cerebral Infarction Rate of MCAO Rats. The neurological function score results showed that the rats in the blank control and the sham-operated groups had no signs of neurological damage after the operation, and the neurological deficit score was 0. The rats in the model group showed severe symptoms of neurological impairment ($P < 0.01$). Compared to the model group, the SHD group showed significantly reduced symptoms of neurological deficit in rats ($P < 0.05$). TTC staining of nonischemic brain tissue was red, and the ischemic area was white (Figure 6). The results of TTC
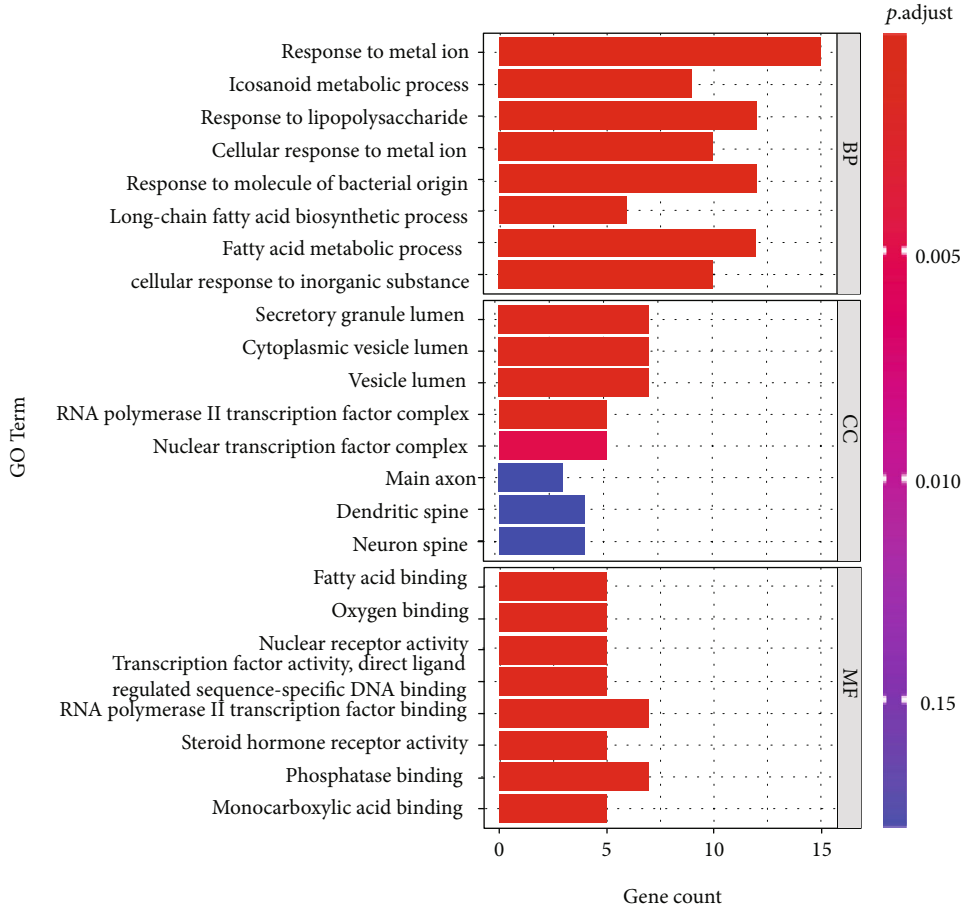
Figure 4: Continued.

(b)

Figure 4: Continued.

(c)
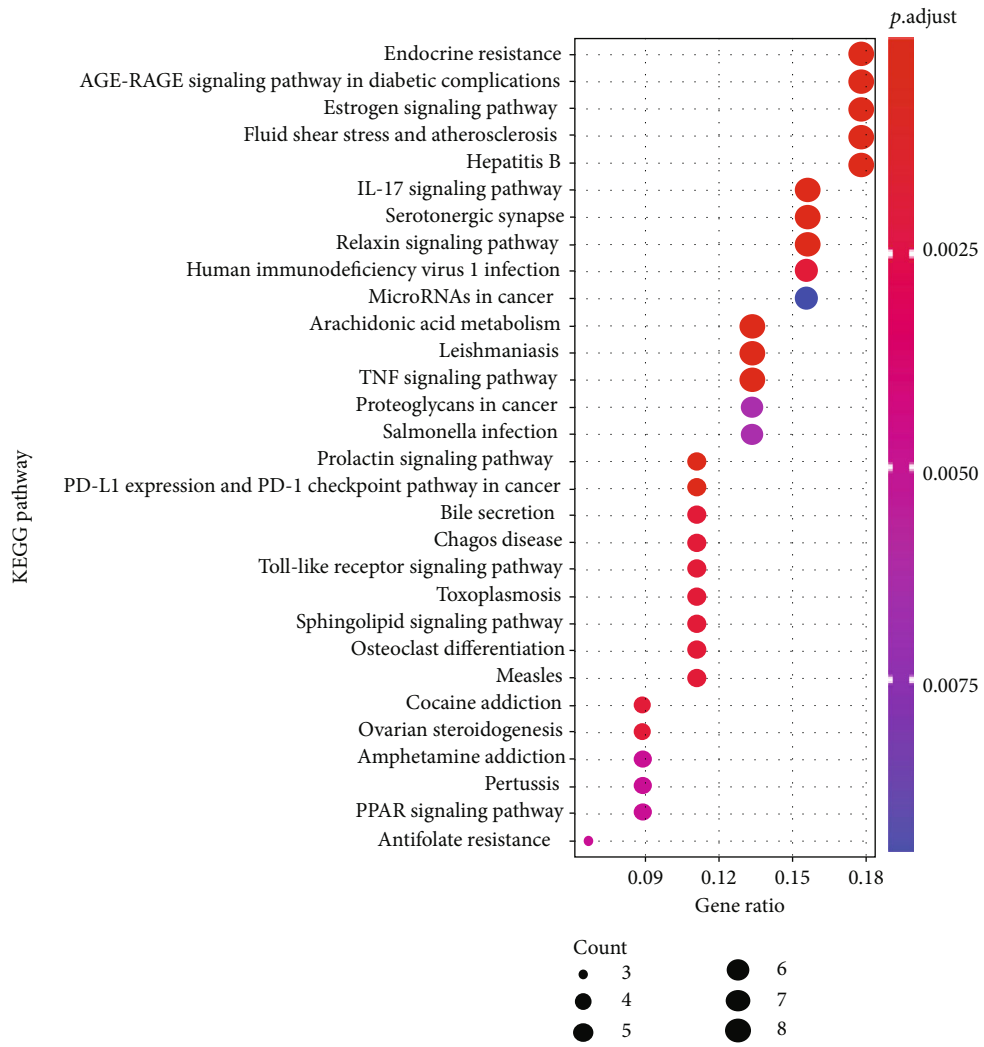
Figure 4: (a) GO function annotation results for the active ingredients of SHD acting on IS targets. (b) KEGG pathway enrichment analysis results for the active ingredients of SHD acting on IS targets. (c) Target-pathway enrichment network; dots represent protein targets, and squares represent pathways. The greater the degree of the node, the larger the node.
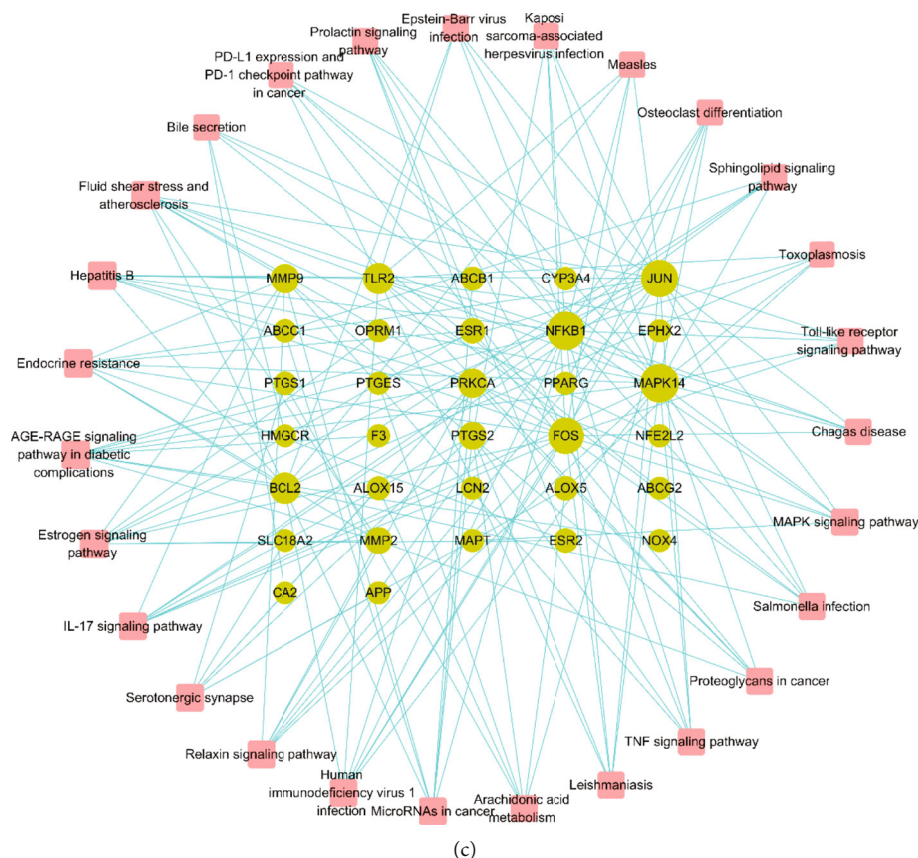
staining showed brain tissue infarction in the brain tissue of the model group ($P < 0.01$). Compared to the model group, the infarct area of the brain tissue in the SHD group was significantly reduced ($P < 0.05$). These results indicated that SHD reduces the neurological score of MCAO rats and the scope of cerebral infarction. The specific results are shown in Table 3.

3.8. Effect of IS on the Pathological Morphology of Brain Tissue in MCAO Rats.
The brain tissue of the blank and the sham operation groups was normal, the cell structure was complete, the cells were arranged neatly, the nucleus was centered, the nucleolus was clear, and the cytoplasm was not red stained. Large areas of brain tissue showed necrosis in the ischemic area of the model group, a part of the cortex showed a highly loose mesh structure, the cell structure was unclear, the number of brain tissue cells was significantly reduced, the neurons showed degeneration, necrosis, and nuclear pyknosis, nucleoli disappeared, and the cytoplasm stained red. Compared to the model group, the number of necrotic foci in the SHD group was significantly reduced, the cell arrangement was more orderly, the brain tissue structure on the ischemic side was significantly improved, and the inflammatory cell infiltration was lighter (Figure 7).

3.9. Western Blot Results of Brain Tissue AKT1, IL-6, TP53, TNF-α, VEGFA, and APP Proteins.
Western blot results showed no significant difference in the brain tissue protein levels between the blank and the sham operation groups ($P > 0.01$). Compared to the sham operation group, the protein levels of the brain tissue in the model group increased except for AKT1, while the levels of other protein levels decreased ($P < 0.01$). Compared to the model group, the expression levels of TP53 and TNF-α proteins in the SHD group differed significantly ($P > 0.01$), the expression levels of AKT1 and VEGFA proteins decreased, and the expression levels of IL-6 and APP proteins increased ($P < 0.05$). The above results suggested that SHT drugs can promote the levels of IL-6 and APP proteins in rats after ischemic brain injury and reduce the levels of AKT1 and VEGFA proteins (Table 4 and Figure 8).

4. Discussion

IS is one of the leading causes of death and disability worldwide; however, currently, there is a lack of effective treatment methods [23]. The rise in alternative medicine has provided new strategies for IS treatment, especially in developing countries, where cheap and easily available Chinese herbal medicines are a major choice for patients [24]. TCM represented by compound prescriptions has
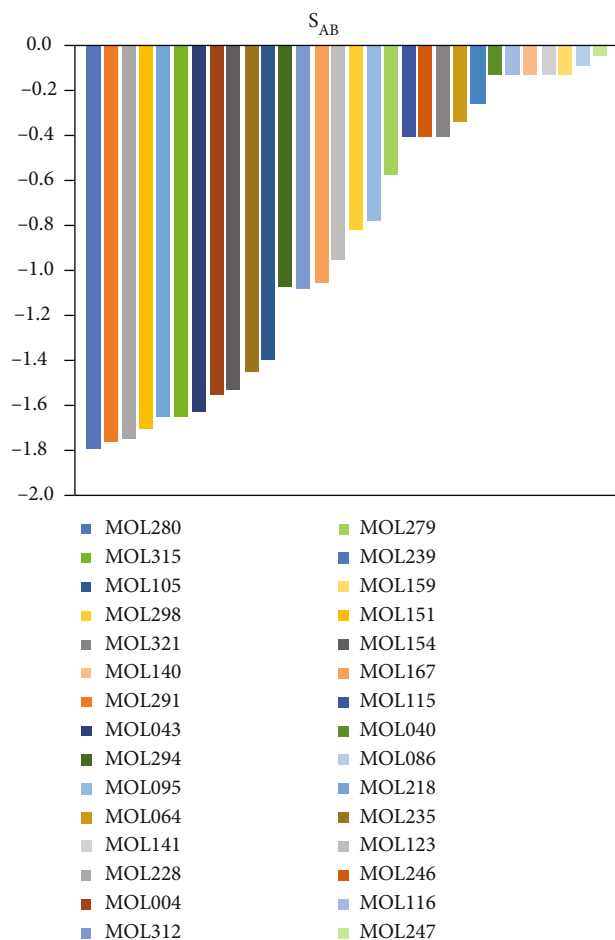
FIGURE 5: Analysis results of SHD intervention on key targets of IS based on network proximity.
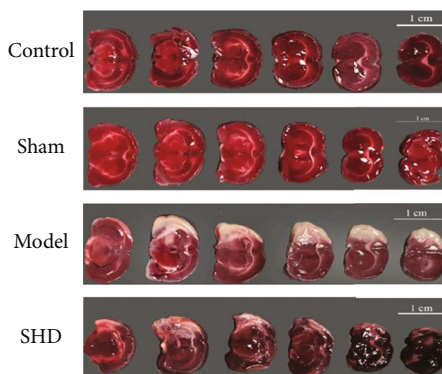

FIGURE 6: TTC brain tissue staining image.

TABLE 3: Effect of SHD on the neurological function score and cerebral infarction rate in MCAO rats ($\bar{x} \pm$ sd, $n = 6$).

Group	Group neurological score	Cerebral infarction rate (%)
Control	0	0
Sham	0	0
Model	1.75 ± 0.42[##]	53.67 ± 0.19[##]
SHD	1.25 ± 0.42[**]	34.26 ± 0.18[**]

[##]Compared to the sham operation group, $P < 0.01$. [**]Compared to the model group, $P < 0.01$.

patients [27] and reduces the cerebral infarction volume of focal I/R rats [28], significantly reducing and improving cerebral edema in focal cerebral I/R rats with nervous system defects [29]. However, the exact pharmacological mechanism of SHD in the treatment of IS remains unclear. The present study used network pharmacology methods to describe the correlation between active compounds, compound targets, and signaling pathways and in vivo experimental verification to reveal the mechanism underlying SHD.

In this study, 40 active compounds and 47 direct-acting target genes in SHD were identified, indicating that SHD plays a pharmacological role in treating IS through multiple targets. Emodin anthrone, Isoimperatorin, and Scopoletin have been identified as critical active compounds in SHD. Dyslipidemia plays a critical role in the pathogenesis of IS. The elevated cholesterol and reduced HDL levels are related to the increased risk of IS [30]. The anthraquinone derivative Emodin has a significant cholesterol-lowering effect. When Emodin enters the animal's body, it reduces the body's absorption of exogenous cholesterol, and on the other hand, it inhibits the synthesis of endogenous cholesterol in the body, thereby reducing total cholesterol and triglycerides [31]. Therefore, Emodin anthrone could be utilized to treat IS by regulating blood lipids. Emodin inhibits the activation of the MAPK-ERK pathway by downregulating ROS expression and reducing the expression of the nuclear transcription factor c-Myc and the proliferation protein Ki67. These effects inhibit the excessive proliferation of vascular smooth muscle cells (VSMCs) in the neointima and reduce the neointima membrane formation after carotid artery injury in rats, ultimately improving carotid artery stenosis, preventing and treating atherosclerosis and cardio-cerebrovascular diseases caused by carotid artery stenosis [32]. Isoperatorin is the active ingredient of notopterygium in SHD [33]. The protective effect of notopterygium extract (water extract and alcohol extract) on the brain has been verified in various cerebral ischemia and hypoxia animal models. In the hypoxia tolerance test, both extracts can improve tissue damage, reduce oxygen consumption, and prolong the survival time of mice [34]. The alcohol extract of notopterygium inhibits platelet aggregation, antithrombosis, and cerebral blood flow, which exerts a specific influence on hemorheology indexes [35]. Scopoletin has a significant protective effect on glutamate-induced neurotoxicity in HT22 cells [36]. In addition, the drug has neuron protection, reduces neuronal apoptosis, and improves neuronal autophagy, which could be attributed to the trigger of the AMPK/mTOR signaling

accumulated a large amount of clinical practice in the treatment of IS and formed effective prescriptions [25].

SHD is a classic Chinese herbal medicine for the treatment of stroke. It is mainly composed of four TCMs, including *Rhubarb* (DH), *Magnolia officinalis* (HP), *Citrus aurantium* (ZS), and *Notopterygium* (QH), and has the functions of dispersing qi, moving blood, dredging the fu-organs, and opening up nodules, regulating qi movement and unblocking sweat pores [26]. SHD improves the NIHSS score and Glasgow score of IS
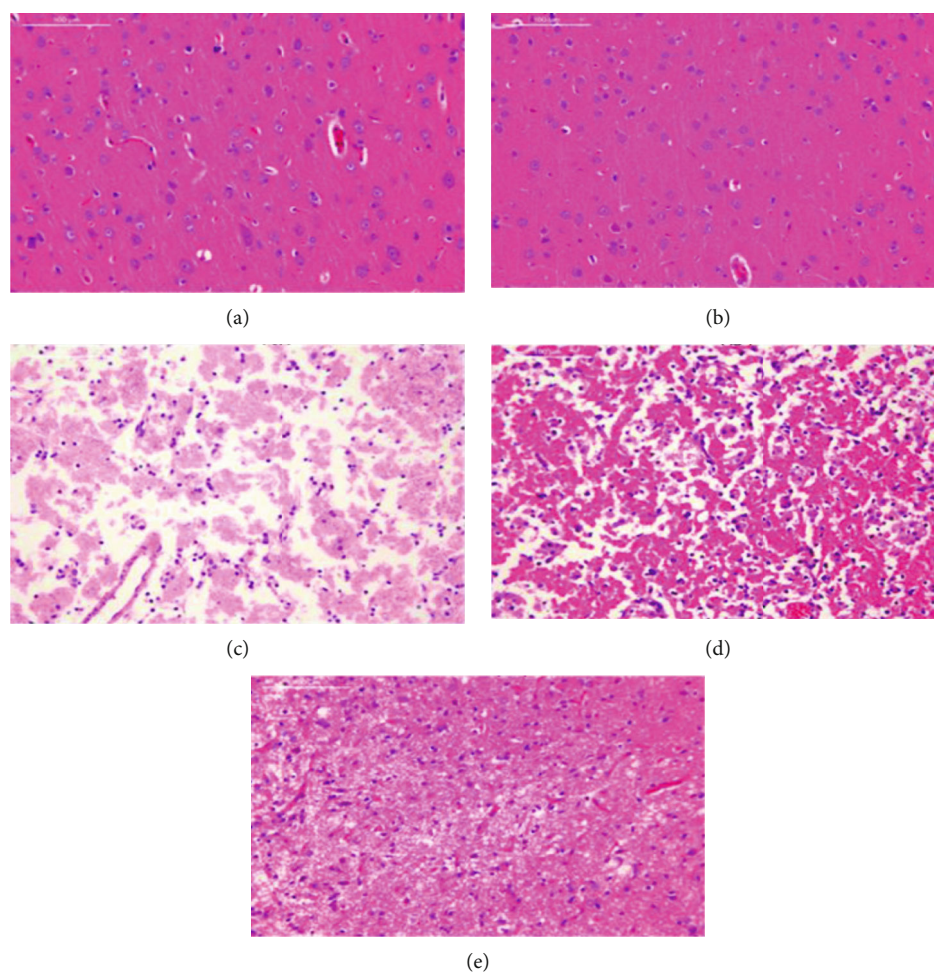
FIGURE 7: (a) Control group; (b) sham operation group; (c) model group 1; (d) model group 2; (e) SHT group.

TABLE 4: Protein levels in the brain tissue samples of rats in each group ($\bar{x} \pm$ sd, $n = 6$).

Group	AKT1	IL-6	TP53	TNF-α	VEGFA	APP
Control	1.68 ± 0.22##	1.96 ± 0.19##	1.85 ± 0.18	2.00 ± 0.19##	2.16 ± 0.21##	1.48 ± 0.12##
Sham	1.63 ± 0.16##	1.90 ± 0.18**	1.83 ± 0.18	2.04 ± 0.19##	2.10 ± 0.20##	1.57 ± 0.13##
Model	2.01 ± 0.19**	1.41 ± 0.12**	1.68 ± 0.16	1.57 ± 0.15**	1.54 ± 0.16**	1.16 ± 0.10**
SHD	1.53 ± 0.13##	1.58 ± 0.12**,#	1.72 ± 0.14	1.59 ± 0.13**	1.35 ± 0.13**	1.45 ± 0.10##

**Compared to the blank, $P < 0.01$. ##Compared to the model group, $P < 0.01$. #Compared to the model group, $P < 0.05$.

pathway by stimulating the autophagy of the rat model induced by spinal cord injury (SCI) and improving the functional recovery of rats induced by SCI [37]. Thus, it is speculated that SHD is a multicomponent formula with multitarget therapeutic effects, and the correlation between these active compounds and IS should be studied in depth.

In this study, AKT1, IL-6, TNF-α, TP53, VEGFA, and APP were identified as six key protein targets related to IS. Isoimperatorin has pharmacological effects, such as analgesia, anti-inflammatory, and vasodilation [38]. Isoimperatorin inhibits the TNF-α-induced ROS/PI3K/Akt/NF-κB signaling pathway and exerts an anti-inflammatory effect [39]. Scopoletin is a natural coumarin [40] that prevents the phosphorylation of PI3K and AKT proteins [41]. Tabana et al. [42] found that Scopoletin exerts an antiangiogenic effect by regulating VEGFA signaling. IL-6 is a proinflammatory cytokine with a low level in the central nervous system under normal conditions [43]. When brain tissue is damaged, the level of some proinflammatory cytokine TNF-α increases, which promotes the production of IL-6 by other inflammatory cytokines [44]. IL-6 has various proinflammatory effects that might increase the stimulation and development of early inflammatory damage in the brain and its vasculature [45]. The results of the Akhter et al. [46] study showed that IL-6 levels increased after IS, which in turn elevated the rate of cerebral infarction and worsened the clinical results.
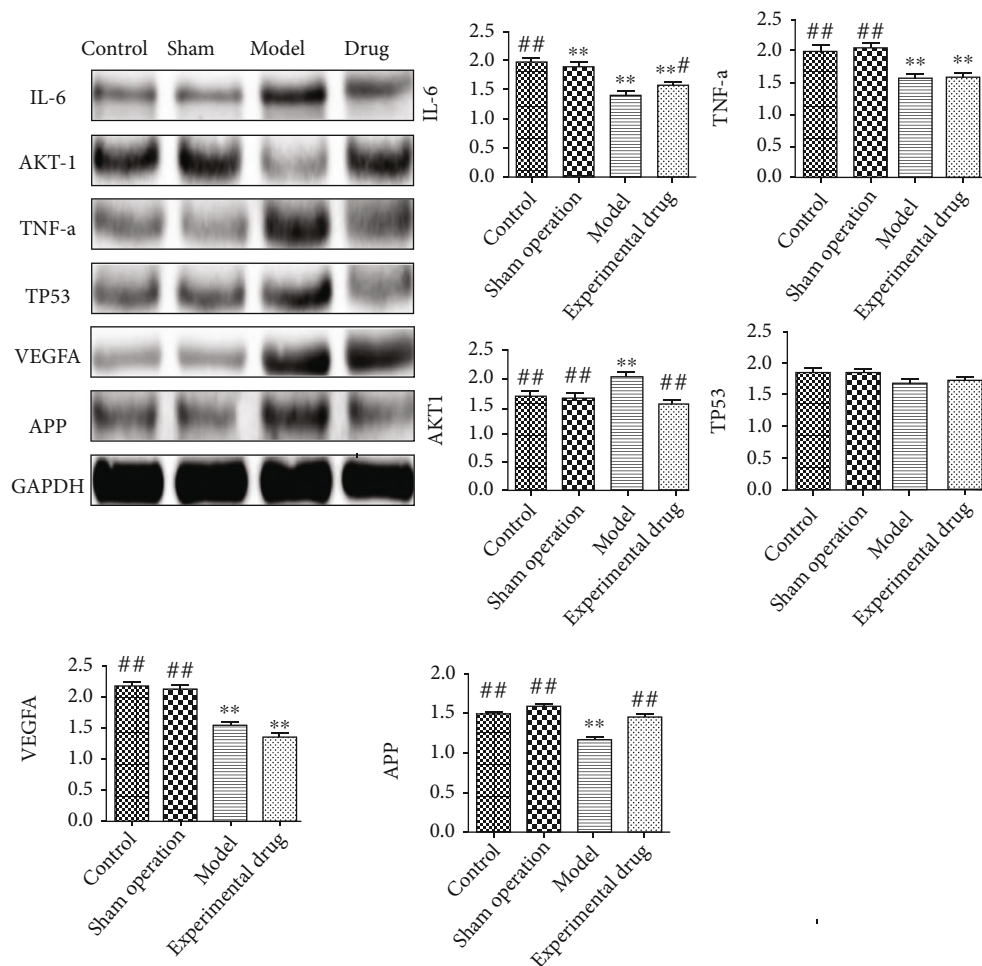
FIGURE 8: Comparison of protein expression levels in brain tissue of rats in each group.

Accumulating evidence showed that the membrane protein APP has a neuroprotective effect under metabolic stress. When acute (stroke and cardiac arrest) or chronic (cerebrovascular disease) hypoxic-ischemic disease occurs, APP will be upregulated [47]. Blumenau et al. [48] showed that APP-Aß catabolism genes are significantly upregulated in the event of insufficient cerebral blood supply. Previous studies on network pharmacology predictions and animal model verification confirmed that SHD could treat IS diseases by promoting the expression of IL-6 and APP proteins. Animal experiments have shown that SHD significantly increases the levels of IL-6 and APP proteins and reduces the levels of AKT1 and VEGFA proteins. Therefore, we can infer that SHD achieves anti-inflammatory effects by inhibiting the expression of TNF-α and then inhibits the expression of AKT1 and VEGFA and effectuates IS treatment.

The results of GO enrichment analysis showed that SHD is related to major biological processes (for example, the reaction of metal ions, the metabolic process of eicosanic acid, the reaction of lipopolysaccharide, and the reaction of bacteria-derived molecules). KEGG pathway enrichment analysis showed that SHD has a therapeutic effect on IS through regulatory pathways (such as endocrine resistance signaling pathway, estrogen signaling pathway, TNF signal-ing pathway, AGEs/RAGE signaling pathway, and miRNAs in cancer). Metal homeostasis disorder (BMD) in the brain is considered a plausible cause of various neurodegenerative diseases [49]. The excessive concentration of divalent metal ions is a known mediator of acute IS injury [50]. Decanoic acid is a saturated fatty acid. Usually, the saturated fatty acid is a "bad" fatty acid. Saturated fatty acids increase the level of serum LDL-C, leading to cholesterol deposition in the inner arterial walls, which makes the human body susceptible to various cardiovascular diseases [51]. Lipopolysaccharide (LPS) is the main component of the cell wall of Gram-negative bacteria that mediates severe inflammation [52]. Several studies have identified four bacterial metabolic pathways, and LPS synthesis is significantly enriched in patients with IS [53]. After a stroke, the intestinal flora is disordered, and the LPS metabolite of the flora increases [54]. The LPS-mediated inflammatory response damages the intestinal barrier, and the leakage of the intestinal wall causes excessive pathogenic bacteria and LPS circulation into the blood. Subsequently, pathogenic bacteria and LPS enter the brain tissue through the damaged blood-brain barrier, aggravating brain tissue damage [55, 56]. Estrogen has neuroprotective effects in the central nervous system injuries, such as spinal cord injury, traumatic brain injury, and ischemic brain injury.

Animal experiments have also shown the potential neuroprotective effects of estrogen, inhibiting the secretion of proinflammatory cytokines by microglia and astrocytes, reducing the neuroinflammatory response after cerebral ischemia through the estrogen receptor signaling pathway, and reducing neuronal death after cerebral ischemia through PI3K-Akt-GSK3 and MAPK/ERK signaling pathways [57].TNF-α activates microglia, promotes the adhesion and chemokine expression, and improves the migration ability of inflammatory-related cells, which is one of the key reasons for neuronal damage after IS [58]. In addition, animal studies demonstrated that the cerebral infarction volume and the degree of brain damage after cerebral ischemia in mice lacking the TNF receptor gene are significantly higher than those in wild-type mice, suggesting the neuroprotective role of TNF [59]. RAGE is a member of the immunoglobulin superfamily of cell surface molecules [60] and acts as a proinflammatory mediator in the inflammatory response [61]. AGEs are critical ligands of RAGE. They activate the microglia by acting on the receptor RAGE, induce the release of IL-1β and TNF-α, and mediate immunoinflammatory response [62]. These studies have shown that IL-1β and TNF-α play a critical role in nerve injury [63]. IS involves various BPs, including hypoxia, neuronal necrosis, and a strong inflammatory response [64, 65]. miRNAs, long noncoding RNAs (lncRNAs), and circular RNAs (circRNAs) participate in RNA-mediated networks through complex mechanisms, and these networks are related to IS [66].

The current results confirmed the neuroprotective effect of SHD in MCAO rats. Specifically, SHD reduces the neurological function score of MCAO rats, the scope of cerebral infarction, and brain tissue necrosis, followed by orderly arrangement of brain cells, improvement in the brain tissue structure of the ischemic side, and decreased infiltration of the inflammatory cells. Aquaporin-4 (AQP4) is an abundant aquaporin in the brain that regulates water transport to maintain homeostasis. Cerebral edema caused by AQP4 overexpression is the main determinant of progressive neuronal damage during cerebral ischemia [67]. SHD alleviates the neurological deficit of rats with I/R injury, reduces brain water content, and downregulates the expression of AQP4. It also has a neuroprotective effect on focal brain I/R injury in rats by targeting AQP4 [29], promoting IL-6 and APP protein expression level in rats after ischemic brain injury, and reducing the level of AKT1 and VEGFA proteins. Emodin inhibits the synthesis of inflammatory factors downstream of the NF-κB pathway (TNF-α, IL-1, and IL-6), mediated by TLR-2 and PPARγ, thereby reducing the infiltration of inflammatory cells and alleviating the inflammatory response [68]. Jiang et al. [69] found that notopterygium extract reduces the secretion of amyloidβ-protein-40 (Aβ-40) and Aβ-42 in APPswe293T cells and inhibits the phosphorylation of GSK3β/tau in AKT/PKC N2a cells. In addition, chronic oral administration of notopterygium extract improves the cognitive ability of APP/PS1 mice. Many coumarin compounds in notopterygium have specific effects on the central nervous system [70]. These findings indicated that the mechanism of SHD on IS is related to the pivotal targets of IL-6, APP, AKT1, and VEGFA. Therefore, we can speculate that SHD exerts a therapeutic effect on IS through these active compounds, target genes, and signaling pathways.

5. Conclusion

In this study, Emodin anthrone, Isoimperatorin, and Scopoletin were identified as critical active compounds, and IL-6, APP, AKT1, and VEGFA were considered as the main targets. SHD may treat IS through signaling pathways, including endocrine resistance, estrogen, TNF, and AGEs/RAGE and microRNAs in cancer. Some studies have shown that SHD reduces the symptoms of neurological deficits in rats, the area of cerebral avascular necrosis, and the number of neuronal necrosis and has a therapeutic effect on IS, and the mechanism lies in the regulation of related target proteins. This study proves the potential pharmacological mechanism of SHD on IS and provides a reference for the clinical application of SHD.

Data Availability

The data used to support the findings of this study are available from the corresponding author upon request.

Conflicts of Interest

The authors declare that they have no conflicts of interest.

Authors' Contributions

Ying Huang, Zi-han Gong, and Wen-jie Li participated in the study design and carried out the experiments. Ji-jia Sun and Shan-shan Gao analyzed the data. Xiao-jun Gou and Ming-jie Sun reviewed the manuscript. All authors read and approved the final manuscript. Shan-shan Gao and Ying Huang contributed to this work equally and should be considered co-first authors. Xiao-jun Gou, Ji-Jia Sun, and Mingjie Sun contributed equally to this work and should be considered corresponding authors.

Acknowledgments

Supplementary Materials

Supplementary materials 1. According to the steps described in Method 1 in Section 1.2, the importance values of all nodes in the PPI network of IS disease are calculated. Supplementary materials 2 Supporting material 2 is the data of 147 active ingredients in the TCM compound obtained after screening by ADMET. (Supplementary Materials)

References

[1] T. Yamashita and K. Abe, "Recent progress in therapeutic strategies for ischemic stroke," Cell Transplantation, vol. 25, no. 5, pp. 893–898, 2016.

[2] J. Gairolla, R. Kler, M. Modi, and D. Khurana, "Leptin and adiponectin: pathophysiological role and possible therapeutic target of inflammation in ischemic stroke," *Reviews in the Neurosciences*, vol. 28, no. 3, pp. 295–306, 2017.

[3] P. F. Liu, R. Li, A. A. Antonov et al., "Discovery of metabolite biomarkers for acute ischemic stroke progression," *Journal of Proteome Research*, vol. 16, no. 2, pp. 773–779, 2017.

[4] A.-M. Yu, X.-L. Yan, H.-Z. Zheng, Y.-Y. He, N.-J. Zhong, and L.-S. Wang, "Effect of Buyang Huanwu Decotion on axon regeneration after ischemic stroke injury in rats," *Chinese Journal of Experimental Traditional Medical Formulae*, vol. 26, no. 21, pp. 15–20, 2020.

[5] J. L. Peng and M. Z. Zhu, "Research overview of traditional Chinese medicine in the treatment of ischemic stroke," *Hunan Journal of Traditional Chinese Medicine*, vol. 35, no. 6, pp. 145–147, 2019.

[6] W. Xue, "Treatment of 33 cases of ischemic stroke with Yiqi HuoxueTongluoDecoction," *Henan Traditional Chinese Medicine*, vol. 39, no. 10, pp. 1563–1566, 2019.

[7] M. H. An, "Analysis of the effect of Shuxuetong combined acupuncture on neurological deficits in patients with ischemic stroke at the recovery stage," *Cardiovascular Disease Journal of Integrated Traditional Chinese and Western Medicine*, vol. 6, no. 35, p. 168, 2018.

[8] E. V. Spudis and M. G. Netsky, "Pathogenesis, diagnosis, and treatment of intermittent cerebral ischemia," *North Carolina Medical Journal*, vol. 20, pp. 449–457, 1959.

[9] Z.-M. Qin, X.-M. Liu, Z.-X. Zeng, X.-Y. Zhang, X.-H. Liu, and Y.-L. Zhang, "Progress of study on traditional Chinese medicine in protecting neuro vascular unit after ischemic stroke," *World Chinese Medicine*, vol. 18, no. 3, pp. 2084–2089, 2019.

[10] Y. L. Han, "The effect of standardized nursing care for patients with ischemic stroke," *Contemporary Medicine Forum*, vol. 17, no. 1, pp. 222-223, 2019.

[11] S. W. Seto, D. Chang, A. Jenkins, A. Bensoussan, and H. Kiat, "Angiogenesis in ischemic stroke and angiogenic effects of Chinese herbal medicine," *Journal of clinical medicine*, vol. 5, no. 6, p. 56, 2016.

[12] J. H. Li, Z. X. Chen, X. G. Zhang et al., "Bioactive components of Chinese herbal medicine enhance endogenous neurogenesis in animal models of ischemic stroke," *Medicine (Baltimore)*, vol. 95, no. 40, p. e4904, 2016.

[13] D. L. Fu, J. H. Li, Y. H. Shi, X. L. Zhang, Y. Lin, and G. Q. Zheng, "Sanhua decoction, a classic herbal prescription, exerts neuroprotection through regulating phosphorylated tau level and promoting adult endogenous neurogenesis after cerebral ischemia/reperfusion injury," *Frontiers in Physiology*, vol. 11, p. 57, 2020.

[14] X. H. Qi and J. Q. Xi, "Compatibility characteristics and enlightenment of Sanhua decoction," *Journal of Shandong University of Traditional Chinese Medicine*, vol. 20, no. 6, pp. 370-371, 1996.

[15] Z. Z. Yang, Y. K. Sun, and M. D. Tian, "Clinical study on integrative medicine in treatment of 40 cases of acute cerebral infarction," *Jiangsu Journal of Traditional Chinese Medicine*, vol. 41, no. 7, pp. 33-34, 2009.

[16] J. H. Liu, "Sanhua decoction for 28 cases of acute ischemic stroke," *Western Journal of Traditional Chinese Medicine*, vol. 24, no. 7, pp. 61–63, 2011.

[17] A. I. Casas, A. A. Hassan, S. J. Larsen et al., "From single drug targets to synergistic network pharmacology in ischemic stroke," *Proc Natl AcadSci U S A*, vol. 116, no. 14, pp. 7129–7136, 2019.

[18] M. Kibble, N. Saarinen, J. Tang, K. Wennerberg, S. Mäkelä, and T. Aittokallio, "Network pharmacology applications to map the unexplored target space and therapeutic potential of natural products," *Natural product reports*, vol. 32, no. 8, pp. 1249–1266, 2015.

[19] A. L. Hopkins, "Network pharmacology: the next paradigm in drug discovery," *Nature Chemical Biology*, vol. 4, no. 11, pp. 682–690, 2008.

[20] S. J. Sheng, J. X. Wang, L. R. Wang et al., "Network pharmacology analyses of the antithrombotic pharmacological mechanism of FufangXueshuantong Capsule with experimental support using disseminated intravascular coagulation rats," *Journal of ethnopharmacology*, vol. 154, no. 3, pp. 735–744, 2014.

[21] L. D. Chen, Y. Cao, H. Zhang et al., "Network pharmacology-based strategy for predicting active ingredients and potential targets of Yangxinshi tablet for treating heart failure," *Journal of Ethnopharmacology*, vol. 219, pp. 359–368, 2018.

[22] C. Zhang, T. Su, D. Yu, F. Wang, C. Yue, and H. Q. Wang, "Revealing active ingredients, potential targets, and action mechanism of Ermiao fang for treating endometritis based on network pharmacology strategy," *Journal of Ethnopharmacology*, vol. 260, p. 113051, 2020.

[23] C. T. Jiang, W. F. Wu, Y. H. Deng, and J. W. Ge, "Modulators of microglia activation and polarization in ischemic stroke (review)," *Molecular Medicine Reports*, vol. 21, no. 5, pp. 2006–2018, 2020.

[24] B. P. Gaire, "Herbal medicine in ischemic stroke: challenges and prospective," *Chinese Journal of Integrative Medicine*, vol. 24, no. 4, pp. 243–246, 2018.

[25] X. Q. Li, R. Q. Lin, B. L. Yang, J. F. Lu, and Y. Q. Hu, "New progress in traditional chinese medicine treatment of ischemic stroke," *Journal of Liaoning University of TCM*, vol. 21, no. 11, pp. 145–147, 2019.

[26] K. Fan, X. Li, X. Liang, and Y. Tang, "The protectiv effect of Sanhua Tang on blood brain barrier injury in cerebral ischemia-reperfusion rat," *Chinese Journal of Experimental Traditional Medical Formulae*, vol. 18, no. 76, pp. 182–184, 2012.

[27] L. Lu, H. Q. Li, D. L. Fu, G. Q. Zheng, and J. P. Fan, "Rhubarb root and rhizome-based Chinese herbal prescriptions for acute ischemic stroke: a systematic review and meta-analysis," *Complementary Therapies in Medicine*, vol. 22, no. 6, pp. 1060–1070, 2014.

[28] Y. Y. Dai, H. J. Huang, X. T. Wang, and G. Q. Zheng, "Effects of sanhua decotion on expression of sodium ion channel in cerebral infarct zone in rats," *Chinese Journal Clinicians*, vol. 5, no. 14, pp. 4079–4083, 2011.

[29] L. Lu, H. Q. Li, J. H. Li, A. J. Liu, and G. Q. Zheng, "Neuroprotection of Sanhua decoction against focal cerebral ischemia/reperfusion injury in rats through a mechanism targeting aquaporin 4," *Evidence-based Complementary and Alternative Medicine*, vol. 2015, no. 2015, p. 7, 2015.

[30] D. L. Tirschwell, N. L. Smith, S. R. Heckbert, R. N. Lemaitre, W. T. Longstreth, and B. M. Psaty, "Association of cholesterol with stroke risk varies in stroke subtypes and patient subgroups," *Neurology*, vol. 63, no. 10, pp. 1868–1875, 2004.

[31] L. Jin, L. Jin, Z. Luan, C. Liu, and C. Pan, "Research progress on chemical constituents and pharmacology of rhubarb,"

Information on Traditional Chinese Medicine, vol. 37, no. 1, pp. 121–126, 2020.

[32] Y. Zhang, K. Li, J. Yang et al., "Effect and mechanism of emodin on carotid stenosis in rats after balloon injury," *Journal of Third Military Medical University*, vol. 39, no. 1, pp. 48–53, 2017.

[33] L. M. Ma and J. L. Yang, "Research progress on chemical constituents and pharmacological activities of Notopterygii Rhizoma et Radix," *Chinese Traditional and Herbal Drugs*, vol. 52, no. 19, pp. 6111–6119, 2021.

[34] L. Zhang and Y. K. Guo, "Mechanism of Xinglou Chengqi decoction in the treatment of acute ischemic stroke research progress," *Chinese Journal of Integrative Medicine on Cardio-Cerebrovascular Disease*, vol. 18, no. 18, pp. 3017–3020, 2020.

[35] B. Shi and J. J. Shi, "Textual research on application of the drug properties of notopterygium root and its effect," *Acta Chinese Medicine*, vol. 32, no. 7, pp. 1239–1241, 2017.

[36] B. Lee, J. B. Weon, M. R. Eom, Y. S. Jung, and C. J. Ma, "Neuroprotective compounds of Tilia amurensis," *Pharmacognosy Magazine*, vol. 11, Supplement 2, pp. S303–S307, 2015.

[37] R. J. Zhou, S. F. Kan, S. Cai, R. Sun, H. Yuan, and B. Yu, "Scopoletin activates adenosine monophosphate-activated protein kinase/mammalian target of rapamycin signaling pathway and improves functional recovery after spinal cord injury in rats," *Pharmacology*, vol. 105, no. 5-6, pp. 349–359, 2020.

[38] L. Ke, X. Feng, P. Huang, and Y. Liu, "Simultaneous determination of imperatorin and isoimperatorin blood concentration by LC-MS/MS," *Chinese Journal of Clinical Laboratory Science*, vol. 37, no. 12, pp. 885–888, 2019.

[39] X. Q. Li, Y. Q. Tan, H. J. Li, L. F. Zhao, and F. Sui, "Research progress on the pharmacological effects and mechanisms of imperatorin," *Chinese Journal of Experimental Traditional Medical Formulae*, vol. 26, no. 18, pp. 196–201, 2020.

[40] V. Pandy and K. Vijeepallam, "Antipsychotic-like activity of scopoletin and rutin against the positive symptoms of schizophrenia in mouse models," *Experimental Animals*, vol. 66, no. 4, pp. 417–423, 2017.

[41] Q. Tian, L. Y. Wang, X. Sun, F. Zeng, Q. Pan, and M. Xue, "Scopoletin exerts anticancer effects on human cervical cancer cell lines by triggering apoptosis, cell cycle arrest, inhibition of cell invasion and PI3K/AKT signalling pathway," *JBUON*, vol. 24, no. 3, pp. 997–1002, 2019.

[42] Y. M. Tabana, L. E. Hassan, M. B. Ahamed et al., "Scopoletin, an active principle of tree tobacco (Nicotianaglauca) inhibits human tumor vascularization in xenograft models and modulates ERK1, VEGF-A, and FGF-2 in computer model," *Microvascular Research*, vol. 107, pp. 17–33, 2016.

[43] Q. Jia, F. Jiang, D. L. Ma, J. Li, F. Wang, and Z. Wang, "Association between IL-6 and seizure recurrence in patients with the first post-ischemic stroke seizure," *Neuropsychiatric Disease and Treatment*, vol. Volume 16, pp. 1955–1963, 2020.

[44] T. Liu, K. Q. Yang, G. S. Li et al., "Experimental evidence and network pharmacology identify the molecular targets of Tong Sheng tablets in cerebral ischemia reperfusion injury," *American journal of translational research*, vol. 11, no. 6, pp. 3301–3316, 2019.

[45] I. M. Cojocaru, M. Cojocaru, R. Tănăsescu, I. Iliescu, L. Dumitrescu, and I. Silosi, "Expression of IL-6 activity in patients with acute ischemic stroke," *Romanian Journal of Internal Medicine*, vol. 47, no. 4, pp. 393–396, 2009.

[46] M. S. Akhter, A. Biswas, S. M. Abdullah et al., "Influence of interleukin-6 (IL-6) promoter gene polymorphisms (-174G>C, -572G>C, and -597G>a) on IL-6 plasma levels and their impact in the development of acute ischemic stroke in young Indians," *Clinical and Applied Thrombosis/Hemostasis*, vol. 25, 2019.

[47] D. Hefter and A. Draguhn, "APP as a protective factor in acute neuronal insults," *Frontiers in Molecular Neuroscience*, vol. 10, p. 22, 2017.

[48] S. Blumenau, M. Foddis, S. Müller et al., "Investigating APOE, APP-Aβ metabolism genes and Alzheimer's disease GWAS hits in brain small vessel ischemic disease," *Scientific Reports*, vol. 10, no. 1, p. 7103, 2020.

[49] S. Bolognin, L. Messori, and P. Zatta, "Metal ion physiopathology in neurodegenerative disorders," *Neuromolecular Medicine*, vol. 11, no. 4, pp. 223–238, 2009.

[50] J. M. Lee, G. J. Zipfel, and D. W. Choi, "The changing landscape of ischaemic brain injury mechanisms," *Nature*, vol. 399, no. 6738, pp. A7–A14, 1999.

[51] Y. J. Chen, X. R. Ju, and G. H. Zhou, "Classification and physiological function of saturated fatty acid," *China Oils and Fats*, vol. 33, no. 3, pp. 35–39, 2008.

[52] D. L. Long, M. Liu, H. Y. Li et al., "Dysbacteriosis induces abnormal neurogenesis via LPS in a pathway requiring NF-κB/IL-6," *Pharmacological Research*, vol. 167, p. 105543, 2021.

[53] L. Huang, T. Wang, Q. Wu et al., "Analysis of microbiota in elderly patients with acute cerebral infarction," *Peer J*, vol. 7, p. e6928, 2019.

[54] R. Huo, J. Tian, M. Zhao, F. Li, K. Sun, and Y. Han, "Effect of Huazhuo Jiedu HuoxueTongluo Decoction on LPS and TLR4/NF-kB signalingpathway of cerebral ischemia-reperfusion injury rats," *Chinese Journal of Immunology*https://kns.cnki.net/kcms/detail/22.1126.R.20210728.1301.002.html.

[55] A. Grylls, K. Seidler, and J. Neil, "Link between microbiota and hypertension: focus on LPS/TLR4 pathway in endothelial dysfunction and vascular inflammation, and therapeutic implication of probiotics," *Biomedicine & Pharmacotherapy*, vol. 137, p. 111334, 2021.

[56] E. Patterson, J. F. Cryan, G. F. Fitzgerald, R. P. Ross, T. G. Dinan, and C. Stanton, "Gut microbiota, the pharmabiotics they produce and host health," *Proceedings of the Nutrition Society*, vol. 73, no. 4, pp. 477–489, 2014.

[57] D. Luan, C. J. Chen, Y. Xu, and S. Zhao, "Neuroprotective effects fo selective estrogen receptor modulators in cerebral ischemia," *International Journal of Cerebrovascular Diseases*, vol. 26, no. 5, pp. 368–372, 2018.

[58] A. Tuttolomondo, R. Pecoraro, and A. Pinto, "Studies of selective TNF inhibitors in the treatment of brain injury from strokeand trauma: a review of the evidence to date," *Drug Design, Development and Therapy*, vol. 8, pp. 2221–2238, 2014.

[59] A. J. Bruce, W. Boling, M. S. Kindy et al., "Altered neuronal and microglial responses to excitotoxic and ischemic brain injury in mice lacking TNF receptors," *Nature Medicine*, vol. 2, no. 7, pp. 788–794, 1996.

[60] F. Li, F. Li, J. Zhang, L. Zhu, S. Zhu, and B. Sun, "Influence of Huoluoyuyinfang decoction upon rage receptor expressionin rat brain tissue with diabetes and cerebral embolis," *Chinese Journal of Experimental Traditional Medical Formulae*, vol. 15, no. 4, pp. 50–53, 2009.

[61] M. T. Win, Y. Yamamoto, S. Munesue et al., "Regulation of RAGE for attenuating progression of diabetic Vascular

Complications," *Experimental Diabetes Research*, vol. 2012, Article ID 894605, 8 pages, 2012.

[62] M. X. Wang, X. P. Liu, S. Xu, C. F. DONG, L. HOU, and S. H. YUAN, "Effect of advanced glycationend products on interleukin-1β and tumor necrosis factor-α secretion from microglialcells," *Journal of Shandong University (Health Sciences)*, vol. 49, no. 2, pp. 34–38, 2011.

[63] X. L. Li, Z. G. Lu, M. Chen, and Z. P. Cai, "Protective effects of extract from Polygonumcuspidatum on focal cerebral ischemia-reperfusion injury in rats," *Chinese Journal of Experimental Traditional Medical Formulae*, vol. 17, no. 18, pp. 226–228, 2011.

[64] N. Mitsios, J. Gaffney, P. Kumar, J. Krupinski, S. Kumar, and M. Slevin, "Pathophysiology of acute ischaemic stroke: an analysis of common signalling mechanisms and identification of new molecular targets," *Pathobiology*, vol. 73, no. 4, pp. 159–175, 2006.

[65] P. Deb, S. Sharma, and K. M. Hassan, "Pathophysiologic mechanisms of acute ischemic stroke: an overview with emphasis on therapeutic significance beyond thrombolysis," *Pathophysiology*, vol. 17, no. 3, pp. 197–218, 2010.

[66] X. C. Duan, L. Han, D. Y. Peng, L. Xiao, Q. Bao, and H. Peng, "Bioinformatics analysis of a long non-coding RNA and mRNA regulation network in rats with middle cerebral artery occlusion based on RNA sequencing," *Molecular Medicine Reports*, vol. 20, no. 1, pp. 417–432, 2019.

[67] P. Bhattacharya, A. K. Pandey, S. Paul, R. Patnaik, and D. R. Yavagal, "Aquaporin-4 inhibition mediates piroxicam-induced neuroprotection against focal cerebral ischemia/reperfusion injury in rodents," *PLoS One*, vol. 8, no. 9, p. e73481, 2013.

[68] H. H. Gao and J. H. Zhou, "Advances in research on antiinflamatory activity and related mechanisms of emodin," *Journal of Jining Medical University*, vol. 398, no. 5, pp. 348–352, 2016.

[69] X. W. Jiang, W. W. Liu, Y. T. Wu et al., "Notopterygium incisum extract (NRE) rescues cognitive deficits in APP/PS1 Alzheimer's disease mice by attenuating amyloid-beta, tau, and neuroinflammation pathology," *Journal of Ethnopharmacology*, vol. 249, p. 112433, 2020.

[70] K. Skalicka-Woźniak, I. E. Orhan, G. A. Cordell, S. M. Nabavi, and B. Budzyńska, "Implication of coumarins towards central nervous system disorders," *Pharmacological Research*, vol. 103, pp. 188–203, 2016.

Research Article

In Silico Screening of Marine Compounds as an Emerging and Promising Approach against Estrogen Receptor Alpha-Positive Breast Cancer

Abdulwahab Alamri [1], Abdur Rauf [2], Anees Ahmed Khalil [3], Adel Alghamdi [4], Ahmed Alafnan [1], Abdulrahman Alshammari,[5] Farhan Alshammari [6], Jonaid Ahmed Malik,[7] and Sirajudheen Anwar [1]

[1] *Department of Pharmacology and Toxicology, College of Pharmacy, University of Hail, Hail, Saudi Arabia*
[2] *Department of Chemistry, University of Swabi, Anbar, Swabi, Khyber Pakhtunkhwa (KP), Pakistan*
[3] *University Institute of Diet and Nutritional Sciences, Faculty of Allied Health Sciences, The University of Lahore, Pakistan*
[4] *Department of Pharmaceutical Chemistry, Faculty of Clinical Pharmacy, Al Baha University, Al Baha, Saudi Arabia*
[5] *Department of Pharmacology and Toxicology, College of Pharmacy, King Saud University, Riyadh, Saudi Arabia*
[6] *Department of Pharmaceutics, College of Pharmacy, University of Hail, Hail, Saudi Arabia*
[7] *Department of Pharmacology and Toxicology, National Institute of Pharmaceutical Education and Research, Guwahati, India*

Correspondence should be addressed to Sirajudheen Anwar; si.anwar@uoh.edu.sa

Presently, the majority of breast tumors are estrogen receptor (ER) positive. Breast cancer (BC) is defined by uncontrolled cell proliferation (CP) in breast tissue. BCs are caused by the overexpression of genes that promote CP in breast cells. The discovery of effective inhibitors is an excellent chemopreventive method. Our *in silico* approach analysis offers a pharmacoinformatics methodology for identifying lead molecules targeting cochaperone HSP90 and the epidermal growth factor receptors (EGFR) and human epidermal growth factor receptor 2 (HER2)/neu receptor. BC has been associated with the high expression of these targets. The use of drug-likeness filters aided in determining the therapeutic properties of possible lead compounds. In this study, docking-based virtual screening (VS) was performed. Database of about 450 cancer marine compounds was used. The X-ray-assisted structure of ERα with 4-OHT (PDB code: 3ERT) was chosen for 4-OHT. A docking-based virtual screening was performed on the dataset supplied using the molecular operating environment (MOE) dock application. The binding energy (BE) and explanation of the protein inhibitor interaction (PII) are crucial findings for future both in terms of dry or wet lab research. The GBVI/WAS binding-free energy assessment (in kcal/mol) scores were used to grade the compounds. Compounds with a BE of less than -9.500 kcal/mol were deemed to be the most effective inhibitors. For further analysis, the top seven structurally diverse scaffolds were selected. Seven marine compounds exhibited the best docking score, which validates them to be potent anti-BC compounds. These compounds' bioactive potential and prospective drug-likeness profile make them promising leads for further experimental research.

1. Introduction

Breast cancer (BC) is responsible for around half million deaths and 1.2 million new cases every year. It is the primary cause of female mortality (cancer accounts for 23 percent of all cancer cases and 14 percent of cancer deaths) [1]. In 2012, mortality rates in women due to this cancer were reported to be 15.5 percent in developed economies (189,000 deaths) and 12.7 percent in emerging economies (269,000 deaths), respectively [2]. According to the Saudi

Cancer Registry of the King Faisal Specialist Hospital and Research Centre (KFSH), around 930 new BC patients are diagnosed each year in Saudi Arabia. BC was the most frequently newly diagnosed cancer among Saudi women in 2010, contributing to 27.4 percent of all malignancies diagnosed [3].

Estrogen levels are associated with the genesis of osteoporosis and, breast and uterine cancers. The estrogen receptor (ER) is found in the endometrium, BC, and ovarian stromal cells, and also the hypothalamic, and promotes cell proliferation (CP) [4]. Tamoxifen, a selective ER modulator, is a widely used antiestrogen adjuvant medication for ER-positive (ER+) premenopausal women selective estrogen receptor modulators (SERM). Tamoxifen's active metabolite is 4-hydroxytamoxifen (4-OHT) [5]. Tamoxifen is also commonly used to treat postmenopausal women with ER+ malignancies. In ER+ BC cells, it acts as an ER antagonist, blocking the ER signalling pathway. As a result, tamoxifen medication dramatically lowers the chance of recurrence of BC. In addition, the tamoxifen-bound ER complex prevents estrogen from turning on genes, hence preventing the estrogenic actions that cause cancer cell growth [6].

Tamoxifen has a clear advantage in the treatment of BC, but it also has significant side effects. Because of its agonistic impact in the uterus, for instance, the threat of endometrial cancer (EC) and hyperplasia increases 1.5- to 6.9-fold [7] following cumulative and long-term use [8] because of its agonistic effect in the uterus. Furthermore, the risk of EC increased considerably in overweight postmenopausal females. To complicate matters further, many ER+ women, regardless of ER levels, showed intrinsic resistance to hormonal treatments. As a result, alternative therapies are required.

BC is among the most perilous and often diagnosed cancers in women [9]. BC, with a prevalence of 21.8 percent, is a widespread malignancy among Saudi women [10]. According to the most recent cancer-related mortality study, breast cancer is the leading cause of mortality among Saudi women. Resistance to therapeutic agents is a significant issue in the treatment of cancer disorders, and it is thought to impair the efficacy of selective therapies as well as the prognosis of cancer patients [11]. BC is a heterogeneous illness on the molecular level, with molecular features such as activation of human epidermal growth factor receptor 2 (HER2), activation of hormone receptors like ER and progesterone (PR), and/or breast cancer gene (BRCA) mutations [12].

BC, defined as uncontrolled CP, causes a hard, pain-free lump in the breast tissue, most commonly in the milk ducts or lobules that supply milk [13, 14]. The most popular method for classifying BCs is based on the state of three distinct cell surface receptors: the ER, PR, and EGF (epidermal growth factor receptor) HER2/neu receptor [15]. Many biological problems have been solved using *in silico* techniques [16, 17], resulting in novel inhibitors against a wide range of diseases [15].

Marine pharmacology is a modern area that investigates the marine ecosystem in pursuit of possible medicinal drugs. Marine natural products (MNPs) are untapped resources with potential pharmacological properties. The harsh environmental conditions and competition within the biological systems make marine flora and fauna produce structurally distinct metabolites. To date, a significant number of MNPs have been identified as potential anticancer drugs. Furthermore, these MNPs play a vital role in inhibiting human tumor cells under laboratory conditions and in cancer clinical trials. To mention a few, glembatumumab vedotin derived from *Dolabella auricularia*-associated *Symploca* sp. is currently being tested for advanced or metastatic breast cancer in a phase I/II clinical trial [18]. Keeping in this mind, this study was aimed at exploring the potential of MNPs for the potential anti-BC drugs. The MarinLit database was used to extract the compounds for the study.

2. Materials and Methods

2.1. Protein Preparation. The study's key treatment targets for BC were ER-alpha. In addition, the 3DS of the following BC target protein (PDB code: 3ERT) was obtained from the protein data bank.

2.2. Dataset Preparation. The compounds were selected based on their reported activity against BC both in *in vitro* and *in vivo* studies. Thirteen one (31) compounds from the MarinLit database (RSC) and 176 compounds from Natural Product Updates (RSC) were used to analyze against the BC targets. The Ligand.mdb database of compounds was built from a SMILES format. Our previously disclosed methods were applied for ligand preparation, enzyme downloading, energy minimization, 3D protonation, and binding site determination. The MOE Builder tool was utilized to create the ligand structures. The compound database Ligand.mdb was made. The compounds were then energy-reduced up to 0.001 Gradient using the MMFF94X force field.

2.3. Docking-Based VS. Docking experiments were carried out using the MOE 2016.08. The MOE window was opened to view the enzyme structure. Water molecules were eliminated (if present). All atoms were 3D protonated in an implicit solubilized environment at 300 K temperature, pH = 7, and salt concentration of 0.1. The entire structure was energy minimized using the MMFF94X force field, and all chemicals were docked into the binding sites of the produced enzymes. Default docking settings were defined, and ten alternative conformations were constructed for each chemical. MOE ligand interaction module was utilized to evaluate low binding energy ligand enzyme complexes, while the Discovery Studio visualizer was employed for 3D interaction plots.

2.4. Drug Likeness Evaluation. To determine whether the active compounds had the potential to be developed as medication, we used Lipinski's "Rule of Five" [19] to predict oral bioavailability using the Molinspiration WebME editor 1.16 (http://www.molinspiration.com). The large percentage of orally administered medications have an MW of less than 500, an average log P of less than 5, five or fewer HB donation sites, and ten or fewer HB acceptor sites. Furthermore, bioavailability was determined using the TPSA analysis (http://www.molinspiration.com).
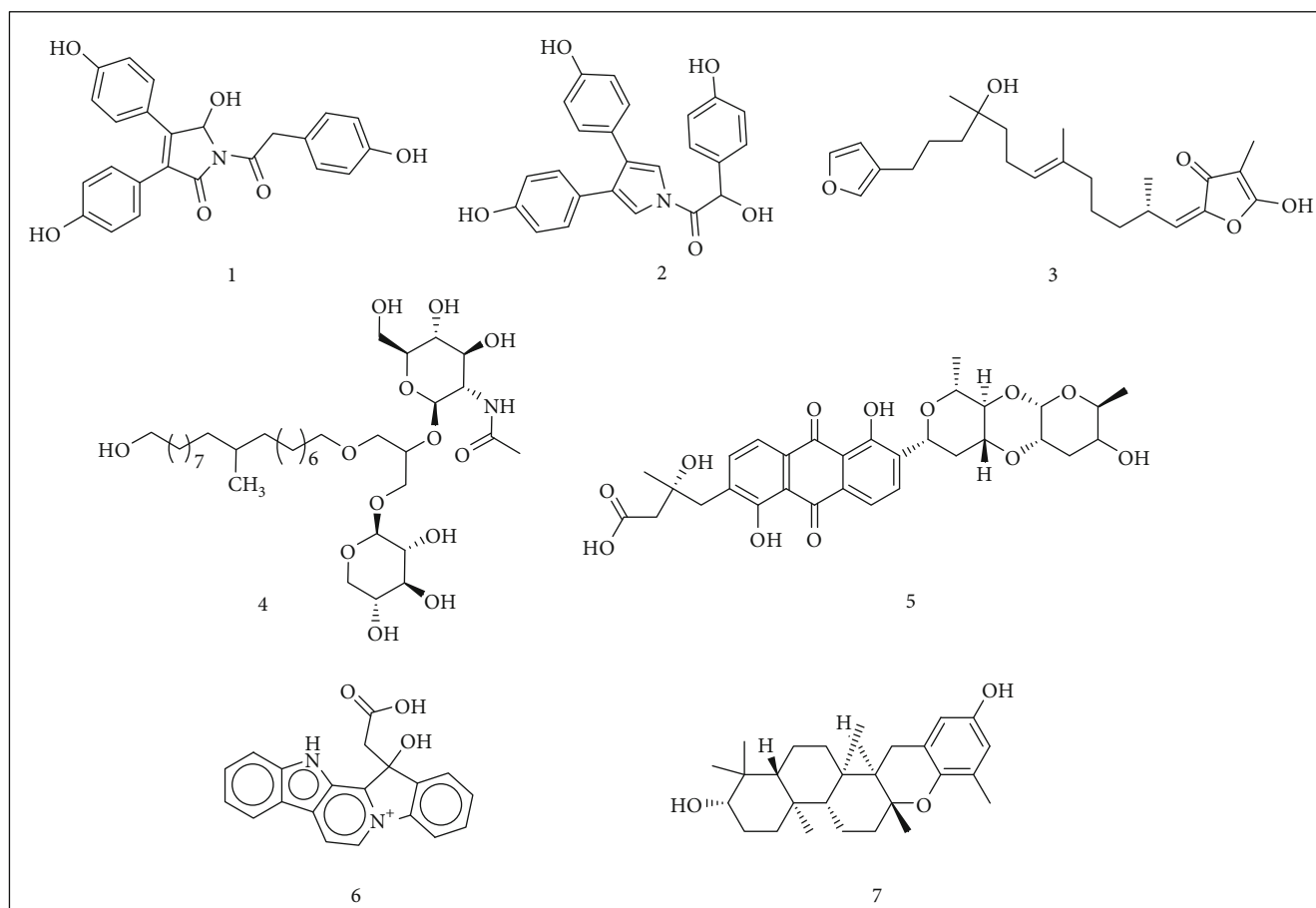
FIGURE 1: Structures of Top 7 structurally diverse scaffolds from SBVS experiment.

TABLE 1: BEs, RMSD, and key interacting amino acid residues (H binding and hydrophobic binding).

No.	Binding energy (kcal/mol)	RMSD (Å)	Interacting residues	
			HB interactions	Hydrophobic interactions
1	-10.2389	0.95	Arg394, Leu87	His524 ($\pi - \pi$), Met343(π-S), Leu391 ($\pi - \sigma$)
2	-9.8315	1.33	Thr347, Glu419	Met343 ($\pi - $S)
3	-9.5103	0.79	Arg394, Cys530	Leu391 ($\pi - \sigma$)
4	-10.5086	1.075	Met343, Arg394, Val534	Met343 (π-S), Met421 (π-S)
5	-9.8805	1.33	Thr347, Asp351	Met343 (π-S)
6	-9.5830	0.92	Leu387, Arg394, Met421	Leu391 ($\pi - \sigma$)
7	-9.5440	1.146	Glu353, Arg394, Cys530	—

3. Results and Discussion

3.1. In Silico Docking Results. BC is a prevalent malignancy and has become the second leading cause of cancer death among women globally. Several medications for the treatment of breast cancer have been licensed by the US Food and Drug Administration. However, these treatments are costly and can have a variety of side effects. Patients frequently report fatigue, headaches, musculoskeletal problems, blood clots, lymphedema, fertility problems, loss of memory, and other side effects, which become necessary to seek alternative medicines from marine sources [20]. Some of these challenges can be addressed with new anticancer agents

derived from marine sources. Several well-known marine compounds have been discovered [18]. However, only a few marine compounds and derivatives have been licensed for commercial usage, while many are now undergoing preclinical and clinical testing [18]. The current study is aimed at identifying alternative compounds from natural origin against BC target ERα. Today, the majority of breast tumors are ERα-positive. Chemotherapy is less effective in ERα-positive BC than in ERα-negative disease [21]. The binding energy and explanation of the PII are significant findings for future experimental and theoretical research.

SBVS on the database of about 450 cancer marine compounds was performed using MOE docking suite. The
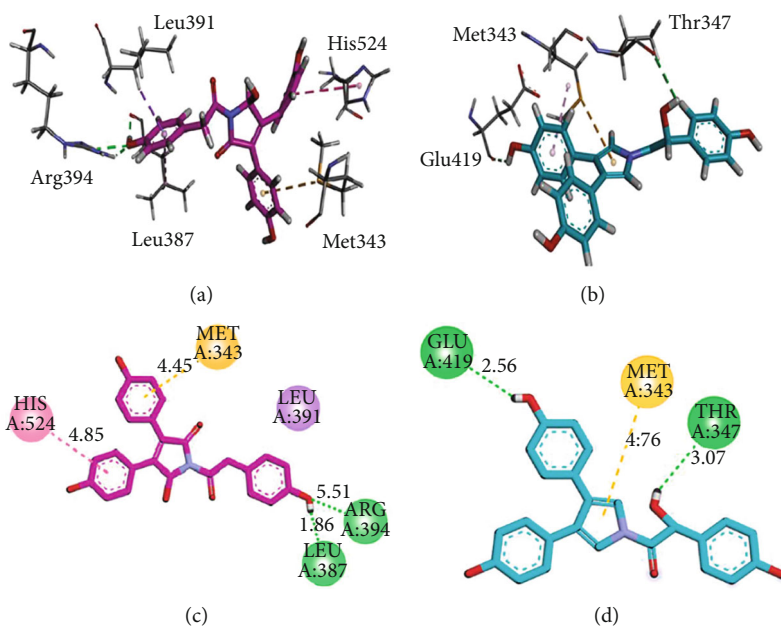
FIGURE 2: 3D (a, b) and 2D (c, d) interaction plots of (a) 5-hydroxyneolamellarin B (1) and (b) 7-hydroxylamellarin A (2), into the binding site of 3ERT.
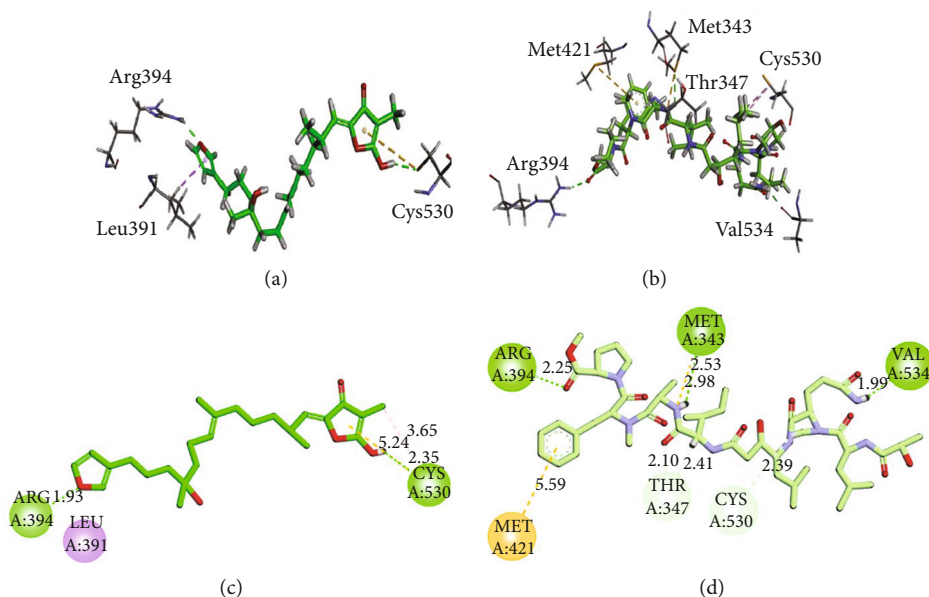

FIGURE 3: 3D (a, b) and 2D (c, d) interaction plots of (a) 8-hydroxyisovariabilin (3) and 5 and (b) 7 myrmekioside E-1 (4) into the binding site of 3ERT.

X-ray-derived structure of ERα in complex with 4-OHT (PDB code: 3ERT) was selected for VS.

3.2. Validation of Docking Protocol. Before the docking-based VS of the dataset, we performed a comprehensive validation of MOE docking protocol. For this purpose, cocrystallized ligand 4-OHT was extracted and redocked into the active site of 3ERT, and RMSD was calculated. For a prediction of ligand-target conformations, an RMSD cut-off value less than 2 Å is considered good [22]. Starting with the Triangle Matcher as placement stage algorithm and

London dG scoring function, and GBVI/WSAdG final scoring function, we tried the alpha triangle (placement stage), while two other scoring functions, ASE and affinity dG, were also attempted for docking validation. Best performance in terms of 133 computed RMSD value, conformation, position, and pose (orientation) was obtained with Triangle Matcher and London dG scoring function.

3.3. Structure-Based Virtual Screening. After docking protocol validation, SBVS of the dataset of compounds was carried out. The compounds were ranked by the scores by
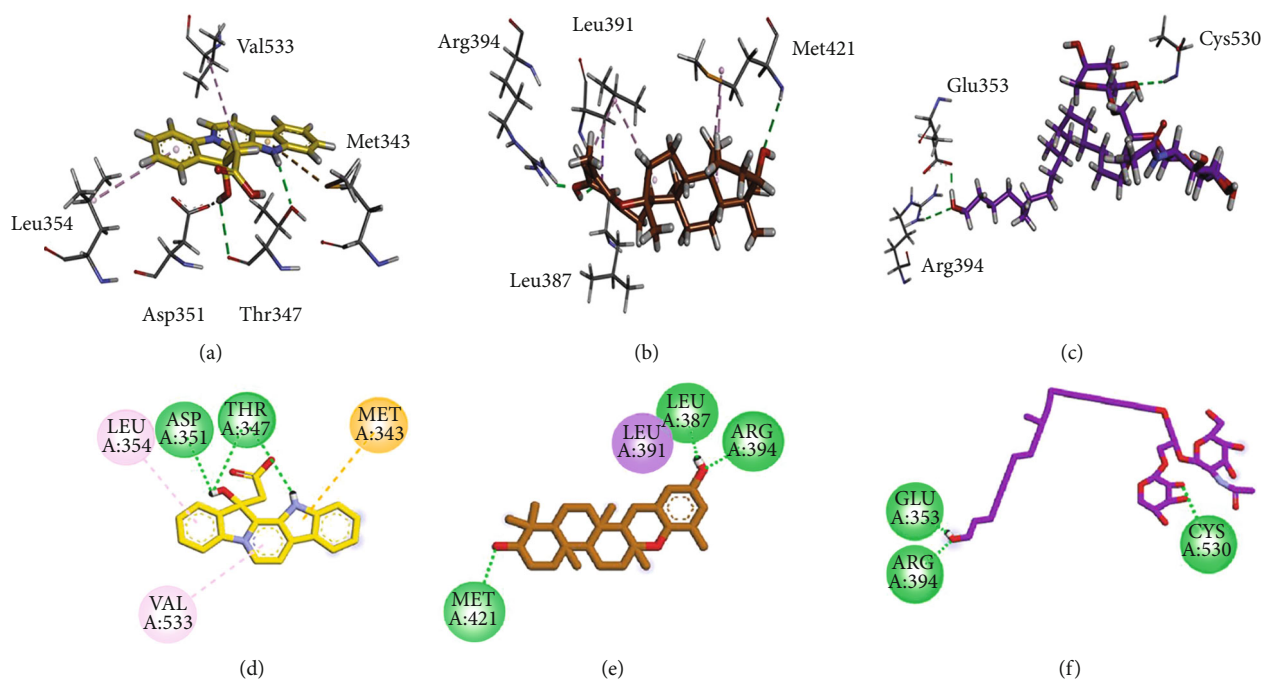
FIGURE 4: 3D (a–c) and 2D (d–f) interaction plots of (a) vineomycin E (5) (b) homofascaplysate A (6) and isoepitaondiol (7) into the binding site of 3ERT.

TABLE 2: *In silico* pharmacokinetic prediction of identified compounds.

Compounds	Human intestinal absorption	Blood-brain barrier	Carcinogenicity (binary)
5-Hydroxyneolamellarin B	0.9804	0.9675	No
7-Hydroxylamellarin A	0.9675	0.9688	No
8-Hydroxyisovariabilin	0.9475	0.9562	No
Myrmekioside E-1	-0.9349	-0.5458	No
Vineomycin E	0.9245	-0.4254	No
Homofascaplysate A	0.6659	0.9618	No
Isoepitaondiol	0.9936	0.9189	No

the GBVI/WAS binding free energy calculation (in kcal/mol). Compounds with binding energy values less than -9.500 kcal/mol were considered best for inhibition. Top 7 structurally diverse scaffolds were selected for further analysis (Figure 1).

5-Hydroxyneolamellarin B (1) was found to demonstrate the best docking conformation with the BE value of -10.2389 kcal/mol followed by 7-hydroxylamellarin A (2), 8-hydroxyisovariabilin (3), myrmekioside E-1 (4), vineomycin E (5), homofascaplysate A (6), and isoepitaondiol (7) (Figure 1). Computed BE values and RMSD refine (the root mean square deviation between the pose before refinement and the pose after refinement) are shown in Table 1.

Next, we analyzed the binding orientation of the identified seven compounds into the binding site of 3ERT. ERα possesses six functional domains A-F. Among them, three main functional domains are A/B domain, C domain, E domain, i.e., N-terminus, DNA binding domain, and LBD, respectively. Analysis of the 3ERT revealed that the key

amino acid residues' lining active sites are Met343, Leu346, Thr347, Ala350, Asp351, Glu353, Trp383. Arp394, Glu419, Gly420, Met421, Gly521, and Leu525. Tamoxifen, a marketed ERα antagonist binds with Arg394 and thus inhibits and blocks the ER function.

Three/two-dimensional (3D/2D) binding interaction plots of the identified compounds are shown in Figures 2–4. The important interacting amino acid residues showing HB and hydrophobic interactions are listed in Table 1. Structures shown in Figure 1 revealed that all the identified compounds contain hydroxyl groups. These hydroxyl groups establish HB interactions with important residues Thr347, Glu353, Arg394, and Leu387. Phenyl rings form $\pi - \pi$ stacking interaction (His524) and $\pi - \sigma$ (Leu391) types of interactions. Met343 forms π-sulfur interactions.

3.4. In Silico Pharmacokinetic Prediction. Using online server AdmetSAR, we predicted the pharmacokinetic properties of the identified compounds. All the compounds, except

myrmekioside E-1, showed excellent human intestinal absorption. Similarly, all compounds, except myrmekioside E-1 and vineomycin E, showed blood-brain barrier penetration. All the identified compounds were found noncarcinogen. Findings of in silico pharmacokinetic properties of identified compounds are listed in Table 2.

4. Conclusion

BC is one of the most common cancers in women worldwide. Computational techniques have been broadly used in drug discovery and the finding of multitargeted inhibitors of numerous upregulated proteins in BC. This research identifies five multitargeted drugs with strong BEs against the most prevalent target proteins involved in BC. Following in vitro and in vivo testing, these virtual hits with excellent PK and PD features may be considered for early therapeutic development against BC. The seven marine compounds exhibited the best docking score, which valid them to be potent anti-BC compounds. These compounds' bioactive potential and prospective drug-likeness profile make them promising leads for further experimental research. The chemicals investigated show that they could be employed as pharmaceuticals or as functional food additives with a promising role in creating medicines and nutritional supplements. Development of new functional ingredients/foods was mechanistically proven efficacy through in vivo screening, lead optimization, and bioavailability.

Abbreviations

3DS: 3-Dimensional structure
4-OHT: 4-Hydroxytamoxifen
BE: Binding energy
BC: Breast cancer
BRCA: Breast cancer gene
EGF: Epidermal growth factor
CP: Cell proliferation
HB: Hydrogen bond
HER2:   Human epidermal growth factor receptor 2
EC: Endometrial cancer
ER: Estrogen receptor
EGFR: Epidermal growth factor receptors
LBD: Ligand binding domain
MW: Molecular weight
MOE: Molecular operating environment
PR: Progesterone receptor
PII: Protein inhibitor interactions
RMSD: Root square mean deviation
TSA: Topological surface area
SBVS: Structure-based virtual screening
VS: Virtual screening.

Data Availability

The docking data used to support the findings of this study are available from the corresponding author.

Conflicts of Interest

The authors declare that the research was conducted in the absence of any commercial or financial relationships that could be construed as a potential conflict of interest upon request.

Acknowledgments

References

[1] A. Jemal, F. Bray, M. M. Center, J. Ferlay, E. Ward, and D. Forman, "Global cancer statistics," CA: a cancer journal for clinicians, vol. 61, no. 2, pp. 69–90, 2011.

[2] F. Cardoso, N. Harbeck, L. Fallowfield, S. Kyriakides, and E. Senkus, "Locally recurrent or metastatic breast cancer: ESMO Clinical Practice Guidelines for diagnosis, treatment and follow-up," Annals of oncology., vol. 23, pp. vii11–vii19, 2012.

[3] E. M. Ibrahim, A. A. Zeeneldin, B. B. Sadiq, and A. A. Ezzat, "The present and the future of breast cancer burden in the Kingdom of Saudi Arabia," Medical Oncology, vol. 25, no. 4, pp. 387–393, 2008.

[4] E. R. Levin, "Integration of the extranuclear and nuclear actions of estrogen," Molecular endocrinology, vol. 19, no. 8, pp. 1951–1959, 2005.

[5] S. Sanyakamdhorn, D. Agudelo, L. Bekale, and H. Tajmir-Riahi, "Targeted conjugation of breast anticancer drug tamoxifen and its metabolites with synthetic polymers," Colloids and Surfaces B: Biointerfaces., vol. 145, pp. 55–63, 2016.

[6] M. Chang, "Tamoxifen resistance in breast cancer," Biomolecules & Therapeutics, vol. 20, no. 3, pp. 256–267, 2012.

[7] A. Subarnas, A. Diantini, R. Abdulah et al., "Apoptosis induced in MCF-7 human breast cancer cells by $2',4'$-dihydroxy-6-methoxy-3,5-dimethylchalcone isolated from Eugenia aquea Burm f. leaves," Oncology letters, vol. 9, no. 5, pp. 2303–2306, 2015.

[8] L. H. Cohen, M. J. Remley, D. Raunig, and A. D. Vaz, "In vitro drug interactions of cytochrome p450: an evaluation of fluorogenic to conventional substrates," Drug Metabolism and Disposition., vol. 31, no. 8, pp. 1005–1015, 2003.

[9] Society AC, Cancer Facts & Figures, American Cancer Society, 2016.

[10] N. Elkum, S. Dermime, D. Ajarim et al., "Being 40 or younger is an independent risk factor for relapse in operable breast cancer patients: the Saudi Arabia experience," BMC cancer, vol. 7, no. 1, pp. 1–8, 2007.

[11] A. H. Mokdad, S. Jaber, M. I. A. Aziz et al., "The state of health in the Arab world, 1990-2010: an analysis of the burden of diseases, injuries, and risk factors," The Lancet., vol. 383, no. 9914, pp. 309–320, 2014.

[12] R. Lozano, M. Naghavi, K. Foreman et al., "Global and regional mortality from 235 causes of death for 20 age groups in 1990 and 2010: a systematic analysis for the Global Burden of Disease Study 2010," The lancet, vol. 380, no. 9859, pp. 2095–2128, 2012.

[13] Y. B. Goldsmith, N. Roistacher, and M. S. Baum, "Capecitabine-Induced coronary vasospasm," *Journal of clinical oncology*, vol. 26, no. 22, pp. 3802–3804, 2008.

[14] D. S. Salomon, R. Brandt, F. Ciardiello, and N. Normanno, "Epidermal growth factor-related peptides and their receptors in human malignancies," *Critical reviews in oncology/hematology*, vol. 19, no. 3, pp. 183–232, 1995.

[15] Z. Yousuf, K. Iman, N. Iftikhar, and M. U. Mirza, "Structure-based virtual screening and molecular docking for the identification of potential multi-targeted inhibitors against breast cancer," *Breast Cancer: Targets and Therapy.*, vol. Volume 9, pp. 447–459, 2017.

[16] M. U. Mirza and N. Ikram, "Integrated computational approach for virtual hit identification against ebola viral proteins VP35 and VP40," *International journal of molecular sciences.*, vol. 17, no. 11, p. 1748, 2016.

[17] M. U. Mirza, N. I. Noor-Ul-Huda Ghori, A. R. Adil, and S. Manzoor, "Pharmacoinformatics approach for investigation of alternative potential hepatitis C virus nonstructural protein 5B inhibitors," *Drug design, development and therapy*, vol. 9, p. 1825, 2015.

[18] A. Rauf, A. A. Khalil, M. Khan et al., "Can be marine bioactive peptides (MBAs) lead the future of foodomics for human health?," *Critical Reviews in Food Science and Nutrition*, vol. 10, pp. 1–79, 2021.

[19] C. A. Lipinski, L. Lombardo, B. W. Dominy, and P. J. Feeney, "Experimental and computational approaches to estimate solubility and permeability in drug discovery and development settings[1]," *Advanced Drug Delivery Reviews*, vol. 46, no. 1-3, pp. 3–26, 2001.

[20] A. G. Waks and E. P. Winer, "Breast cancer treatment: a review," *Journal of the American Medical Association*, vol. 321, no. 3, pp. 288–300, 2019.

[21] J. TilakVijay, K. Vivek Babu, and A. Uma, "Virtual screening of novel compounds as potential ER-alpha inhibitors," *Bioinformation*, vol. 15, no. 5, pp. 321–332, 2019.

[22] M. J. García-Godoy, E. López-Camacho, J. García-Nieto, A. J. Nebro, and J. F. Aldana-Montes, "Molecular docking optimization in the context of multi-drug resistant and sensitive EGFR mutants," *Molecules*, vol. 21, no. 11, p. 1575, 2016.

Hindawi

Research Article

3D-QSAR Studies of 1,2,4-Oxadiazole Derivatives as Sortase A Inhibitors

Neda Shakour,[1,2] Farzin Hadizadeh ©,[1,3] Prashant Kesharwani,[4]
and Amirhossein Sahebkar ©[3,5,6]

[1]Department of Medicinal Chemistry, School of Pharmacy, Mashhad University of Medical Sciences, Mashhad, Iran
[2]Student Research Committee, Faculty of Medicine, Mashhad University of Medical Sciences, Mashhad, Iran
[3]Biotechnology Research Center, Pharmaceutical Technology Institute, Mashhad University of Medical Sciences, Mashhad, Iran
[4]Department of Pharmaceutics, School of Pharmaceutical Education and Research, Jamia Hamdard, New Delhi 110062, India
[5]Applied Biomedical Research Center, Mashhad University of Medical Sciences, Mashhad, Iran
[6]Department of Biotechnology, School of Pharmacy, Mashhad University of Medical Sciences, Mashhad, Iran

Correspondence should be addressed to Farzin Hadizadeh; hadizadehf@mums.ac.ir
and Amirhossein Sahebkar; amir_saheb2000@yahoo.com

Sortase A (SrtA) is an enzyme that catalyzes the attachment of proteins to the cell wall of Gram-positive bacterial membrane, preventing the spread of pathogenic bacterial strains. Here, one class of oxadiazole compounds was distinguished as an efficient inhibitor of SrtA via the "S. aureus Sortase A" substrate-based virtual screening. The current study on 3D-QSAR was done by utilizing preparation of the structure in the Schrödinger software suite and an assessment of 120 derivatives with the crystal structure of 1,2,4-oxadiazole which was extracted from the PDB data bank. The docking operation of the best compound in terms of pMIC (pMIC = 2.77) was done to determine the drug likeliness and binding form of 1,2,4-oxadiazole derivatives as antibiotics in the active site. Using the kNN-MFA way, seven models of 3D-QSAR were created and amongst them, and one model was selected as the best. The chosen model based on q^2 (pred_r^2) and R^2 values related to the sixth factor of PLS illustrates better and more acceptable external and internal predictions. Values of crossvalidation (pred_r^2), validation (q^2), and F were observed 0.5479, 0.6319, and 179.0, respectively, for a test group including 24 molecules and the training group including 96 molecules. The external reliability outcomes showed that the acceptable and the selective 3D-QSAR model had a high predictive potential ($R^2 = 0.9235$) which was confirmed by the Y-randomization test. Besides, the model applicability domain was described successfully to validate the estimation of the model.

1. Introduction

Sortase A (SrtA) is a polypeptide containing 206 amino acids. This enzyme speeds up two consecutive reactions: (a) transpeptidation and (b) thioesterification. SrtA is involved in the bacterial adhesion process and acts by attaching proteins holding LPXTG to lipid II [1–11]. SrtA inhibitors do not influence bacterial growth, but instead, they prevent the emergence of the virulence of pathogenic bacterial strains, thereby hindering infections produced by Staphylococcus aureus (S. aureus) or other bacteria of

Gram-positive strain. To the surface membrane protein of S. aureus, sortase is attached which links it to the cell wall via transpeptidation [6, 10, 12], and needing a C-terminal regulates signal through a protected LPXTG motif [13–15]. S. aureus mutations with a deficiency of the srtA gene cannot display and bind some surface proteins which results in a disorder/disease such as animal infection [13, 16]. S. aureus is an important anthropological bacterial pathogen of Gram-positive strain that leads to common infections in society. Regarding the resistance to antibiotics, and the report of the Centers for Disease Control and Prevention

(CDC) about resistance to methicillin of S. aureus (MRSA) in 2013, S. aureus was distinguished as a critical and a persistent threat [17–19].

The Gram-positive bacteria S. aureus is communal to humans and exists on the mucosa and skin of 30% of the population [20, 21]. It is a chief reason for hospital infections, the most common and serious of which are endocarditis and bacteremia endocarditis in hospitalized patients [22–25]. This organism has created resistance to a broad range of antibiotic medicine types [26]. Principal commercial compounds of the antimicrobial class (such as ciprofloxacin, ampicillin, and posaconazole) have limited performance against resistance microorganisms strains [27–30]. The erratic usage of antibiotics is known as one of the primary reasons for the increase in resistance of bacteria. The growth of bacterial resistance has resulted in a significant rise in mortality rates of individuals around the world [31]. On this path, there is a serious necessity to discover novel molecules with more effective antibacterial features, as well as obvious synthetic routes. This led to widespread research such as designing heterocyclic derivatives (like 1,2,4-oxadiazoles) with antimicrobial properties to treat S. aureus infections [32–36]. These discovered antibiotics are active and exhibit grampositive activity, particularly against Staphylococcus aureus, including vancomycin-resistant, methicillinresistant (MRSA), and linezolid-resistant by inhibiting srtA [24, 35, 37]. 1,2,4-Oxadiazole heterocycle was first manufactured in 1884. They showed remarkable action in vitro and in vivo and are orally bioavailable. The medicinal chemistry literatures report diverse structures for the 1,2,4-oxadiazoles (Figure 1) [38, 39]. In the present article, we represent 3D-QSAR investigations concerning 120 molecules of 1,2,4-oxadiazoles with antibacterial healing properties. This class of compounds (oxadiazoles) targets SrtA of the cell wall and inhibits it [40]. The advancement of antibiotics, especially of those that target cells of bacteria and have a desirable characteristic of toleration and safety, has largely helped population growth and has improved the quality of life in the last 75 years.

2. Materials and Methods

2.1. Data Set.
A collection containing 120 compounds having 1,2,4-oxadiazole as antimicrobials was taken from the available literature [24] and was employed in the present study. All structures were extracted from Chembl (https://www.ebi.ac.uk/chembldb). The chosen compounds for the set of data shared a similar evaluation method with notable changes in their strength profiles and their structures. The compounds incorporated in the collection of datasets have antibiotics potencies with MIC values varying from 2 to 500 μg/ml which were changed to M (molar). These were then converted to pMICs according to the following equation [41–44].

pMIC = −log$_{10}$ [MIC].

The ligand 3D-formula of compounds was produced utilizing the Maestro v2015-2 and afterwards corrected using the LigPrep. Partial charges of atoms were attrib-

uted, and potential ionization was calculated at a neutral medium. The force field of OPLS_2005 was utilized for minimization to the conformer creation with the low energy of ligand. The minimization of energy was done for every compound (ligand) to reach an RMSD cutoff of 0.01 Å. Then, the final structures were used for modeling investigation. Additionally, all the 120 molecules were aligned in the method of alignment (Figure 2) relying on Maestro through choosing a common structure minimum as "template" and the most efficient one (compound **89**) as the "Reference Molecule" (Figure 3). Of the 120 molecules recognized in this investigation, a training group, including 96 molecules and a test group, including 24 molecules was created in Maestro [45–48].

2.2. Model Validation and Statistical Analysis.
A high q^2 only indicates a good internal validation in the training group, but it does not show a high prediction capability of the created models; hence, an external validation was necessary. The proved capability from generated models of 3D-QSAR was confirmed by computing the biological activities of compounds that applied as a test set and not inserted in the training set (Suppl. Table 1). In the present investigation, eighty percent of the molecules from the data set was accidentally chosen as training set models based on the atom field which were created of PLS factors (one until seven), and the obtained models were approved after predicting the activity of the test group ligand. The value of the model's prediction was assessed through the leaveone-out (LOO). The q^2 (predictive correlation coefficient) was determined by utilizing Equation (1) [49].

$$q^2 = 1 - \frac{\sum \left(Y_{\text{predicted}} - Y_{\text{observed}}\right)^2}{\sum \left(Y_{\text{observed}} - Y_{\text{mean}}\right)^2}. \tag{1}$$

In the above equation, each of the three indices including Y_{mean}, $Y_{\text{predicted}}$, and Y_{observed}, demonstrates the mean values predicted and observed of the pMIC feature, respectively. The $\left(Y_{\text{predicted}} - Y_{\text{observed}}\right)^2$ index displays PRESS (the predictive residual sum of squares). The r_pred^2 index related to the predictive correlation coefficient ($r\_\text{pred}^2 > 0.6$) [50] is calculated for the test group and is characterized through Equation (2).

$$r^2_{\text{pred}} = \left(\frac{\text{SD} - \text{PRESS}}{\text{SD}}\right) \tag{2}$$

In Equation (2), the SD index shows the squared deviation sum for molecules amongst the test group biological activities and training group mean activities [51]. Also, the PRESS index indicates the squared deviation summation amongst actual and predicted activity values for molecules individually in the test group. Based on previous studies [52], If R^2 is bigger than 0.6, and R^2cv (Q^2) is bigger than 0.5, 3D-QSAR models are acceptable. The regression model action composed was assessed using the RMSE index. For the data group, RMSE is computed as
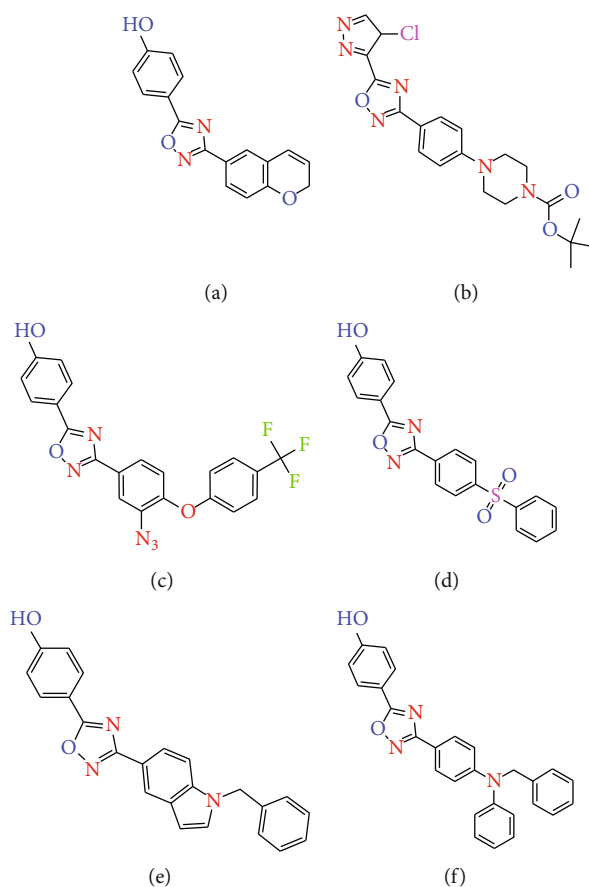
(a)   (b)

(c)   (d)

(e)   (f)

Figure 1: Examples of diverse structure for the 1,2,4-oxadiazole compounds.
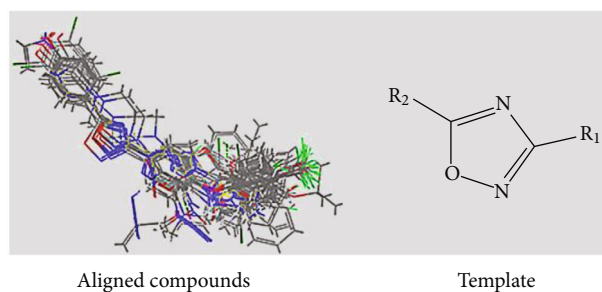

Aligned compounds   Template

Figure 2: 3D-QSAR structure superposition and alignment of the series (Strick model).

Equation (3) [53].

$$RMSE = \sqrt{\frac{\Sigma_{i=1}^{n}(y_i - y\wedge_l)^2}{n}}.$$ (3)

The 3D-QSAR model with the sixth component of the PLS factor was considered as the best for 1,2,4-oxadiazole derivatives. This model was approved for its precision in the ligand activity estimate in the training group [51]. Scatter plots for experimental and predicted activities of ligands showed a notable linear correlation. In Figures 4(a) and 4(b), the average difference of values of predicted and experimental for training and test groups is exposed, respectively.

2.3. Applicability Domain. APD can be determined using resemblance measures relying on the Euclidean distances between the entire compounds test and training. A comparison between the distance of the test compounds and their nearest neighbor to a predefined threshold in the training group is done, and the prediction is considered inaccurate when the interval is higher than that. The determination of APD was done based on the displayed formula, as follows.

$$APD = (d) + Z\delta.$$ (4)

δ and d were calculated in a series of steps: first, the mean of Euclidean distances among all training compound pairs was estimated. Then, the collection of distances lower than the median was determined. δ and d were finally measured as the standard deviation and mean of distances that included in this set. The value equals 0.5 was selected for Z, which was the experimental cutoff in this study. For the applicability domain calculation, we utilized "AD using standardization approach" in DTC Lab (https://dtclab.webs.com/software-tools) [54–56].

Y-Randomization Test

The procedure of *Y*-randomization guarantees the validity of a 3D-QSAR model [57]. The dependent changeable
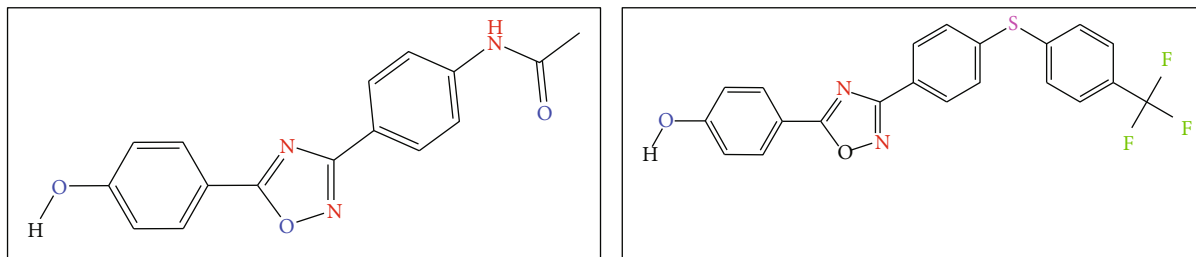
FIGURE 3: (b) Structure of compound **89** with the best active. (a) Structure of compound **120** with the lowest active.
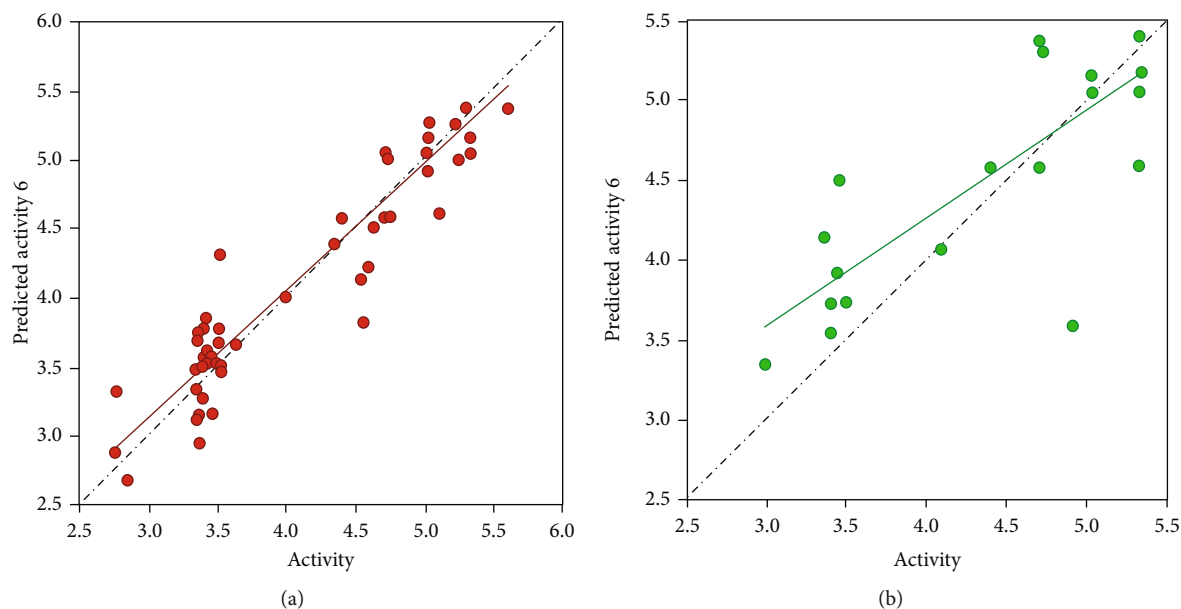

(a)

(b)

FIGURE 4: Scatter plot of the observed activity versus predicted activity of (a) training group compounds ($y = 0.92x + 0.34$, $R^2 = 0.92$) and (b) test group compounds with the best fit line ($y = 0.68x + 1.54$, $R^2 = 0.65$).

vector is altered accidentally, and a novel 3D-QSAR model is produced. The strategy is repeated several times and if the recently produced 3D-QSAR models show low R^2 and Q^2 values, the accurateness of the original model is confirmed [58].

2.4. Docking Studies. One most frequent tool for drug design is molecular docking, which employs a mode of association between binding sites of a suitable target with small molecules. Polypeptide structure, SrtA (accession number: 2KID), was acquired from the PDB data bank. Here, small-molecule docking in its active site and its analysis was done via Molecular Operation Environment (MOE) software (http://www.chemcomp.com) for selecting out the most active compound in terms of pMIC (pMIC = 2.77) with SrtA polypeptide. Before docking, the preparation of the ligand was done, and the 2D structure of ligand was set up by Chemoffice 12.0 which was further changed to 3D format by Hyper Chem7 software and was optimized employing PM3 semiempirical tool. Also, removal of crystallographic water molecules was done followed by association with pH 7 (for suitable ionization for both alkaline and acidic amino acids) and finally, hydrogen bonds were added. Utilizing the man-

ual recommended parameters of the MOE energy minimization with a gradient of 0.05 and MMFF94X ff (force field), the energy of the retrieved protein molecule was calculated. The docking was done with force field as a filtration method via the triangle matcher placement, and the scoring function of the London DG algorithm in combination and the best conformation was analyzed in more details with the LigX module in MOE software. Docking was accomplished for the best compound (compound **89**) with the lowest MIC (Figure 5(a)) utilizing the default setting of MOE-Dock [12]. In the last section of the docking process, the selected ligand conformation was further investigated for its interactions of binding. The hydrophilic and hydrophobic field map for compound 89 was also formed (Figure 6(a)). The 2D pictures of the docked conformation of compound 89 are exhibited in Figure 6(b). The compound position in the protein active site is illustrated in Figure 6(c) [59–65].

3. Results and Discussion

3.1. 3D-QSAR Model. The 3D-QSAR model was created utilizing PLS regression statistics with the grid spacing 1 Å. The seven PLS factors were requested from the program, and the
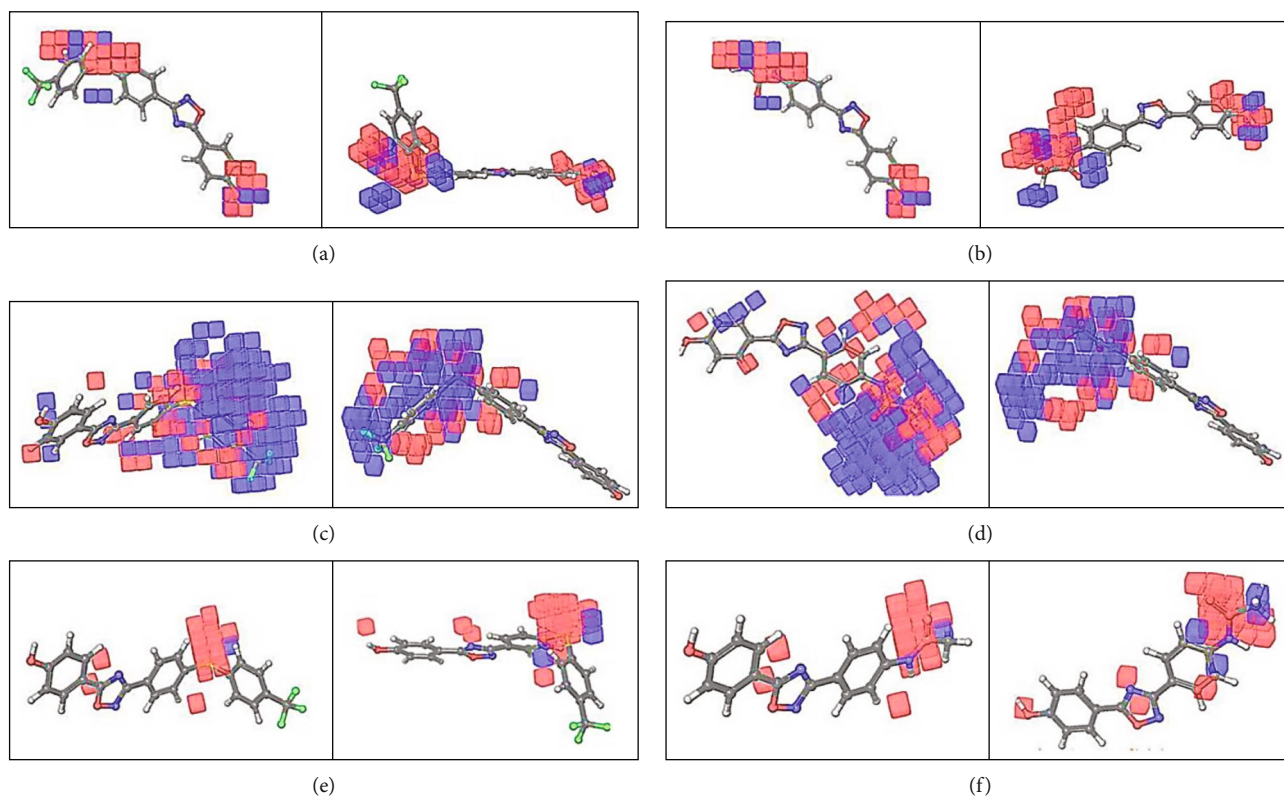
(a)

(b)

(c)

(d)

(e)

(f)

FIGURE 5: The visualizing of the 3D-QSAR model in the field of unfavorable and favorable effects of hydrogen bond donor (HBD) in: (a) ligand **89** and (b) ligand **120**. The visualizing of the 3D-QSAR model in the field of unfavorable and favorable effects of interaction in (c) ligand **89** and (d) ligand **120**. The visualizing of the 3D-QSAR model in the field of unfavorable and favorable effects of electron-withdrawing groups in (e) ligand **89** and (f) ligand **120** in two different dimensions, (positive coefficient color: dark blue, negative coefficient color: red, most active compound is **89** (pMIC = 5.617), and least active compound is **120** (pMIC = 2.771)).

best model was observed for the sixth PLS factor owing to its high statistical importance and predictability. (Table 1) The fractions of field and parameters of statistical measured in QSAR-based Gaussian are organized in Table 2.

3.2. Model Validation. Validation of a common pharmacophore model and its prediction relying on active compounds were distinguished by $Q_{cv}^2 = 0.5479$ (Table 1). The training group R^2 was 0.9235, which revealed the importance of this model. The produced model stability differs from 0.994 to 0.674. The value of F was observed to be 179.0. Moreover, a P value equal to 1.95e-047 and Pearson r equals 0.8050 showed an assurance of a higher degree in the model. The standard deviation and the root-mean-square error were equal to 0.2291 and 0.48, respectively, which depicts the strength of the created model in the test for the estimation of the unrecognized compounds. The values of measured pMIC related to the ligands which were included in the predicted group are summarized in Suppl. Table 1. R^2 values greater than 0.5 as seen amongst the experimental and predicted values produced in the suitable model could show the inhibitory activity that was not included in the progression procedure. [66, 67]. These outcomes suggest that this method can analyze the QSAR model and the ligand-receptor interactions and could be employed in the design of new imidazole inhibitors. Scatter plots, given in Figures 3(a) and 3(b), showed a moderate distinction

between the values of two groups, experimental and predicted, and striking linear correlation.

3.3. Applicability Domain. Reports of model constraints by the APD are critical. This shows an important aspect because the user can not only creatively and easily design new compounds but also they can be warned for the estimation validity as to when the structure features cannot be provided via the model. Therefore, after selecting the best model, the ADP of the model showed that the predicted model was valid. In the applicability domain, the compound was completely put inside the range. Indeed, all ligands were in the applicability domain and hence can be assumed as acceptable.

Y-Randomization Test

Further confirmation of the model was done via *Y*-randomization. Ten accidental changes of the *Y* vector were done, and the low values of R^2 and Q^2 were calculated. The range of the R^2 and Q^2 values were 0.34 to 0.57 and -0.45 to -0.65, respectively. It needs to be mentioned that every *Y* vector random stage was followed by the perfect training method to improve the new QSAR model, involving the choice of the most proper descriptors [68].

3.4. 3D-QSAR Contour Map Analysis. Contour plot interpretation was done to detect the influence of spatial arrangement on the structural characteristics like hydrophobic,
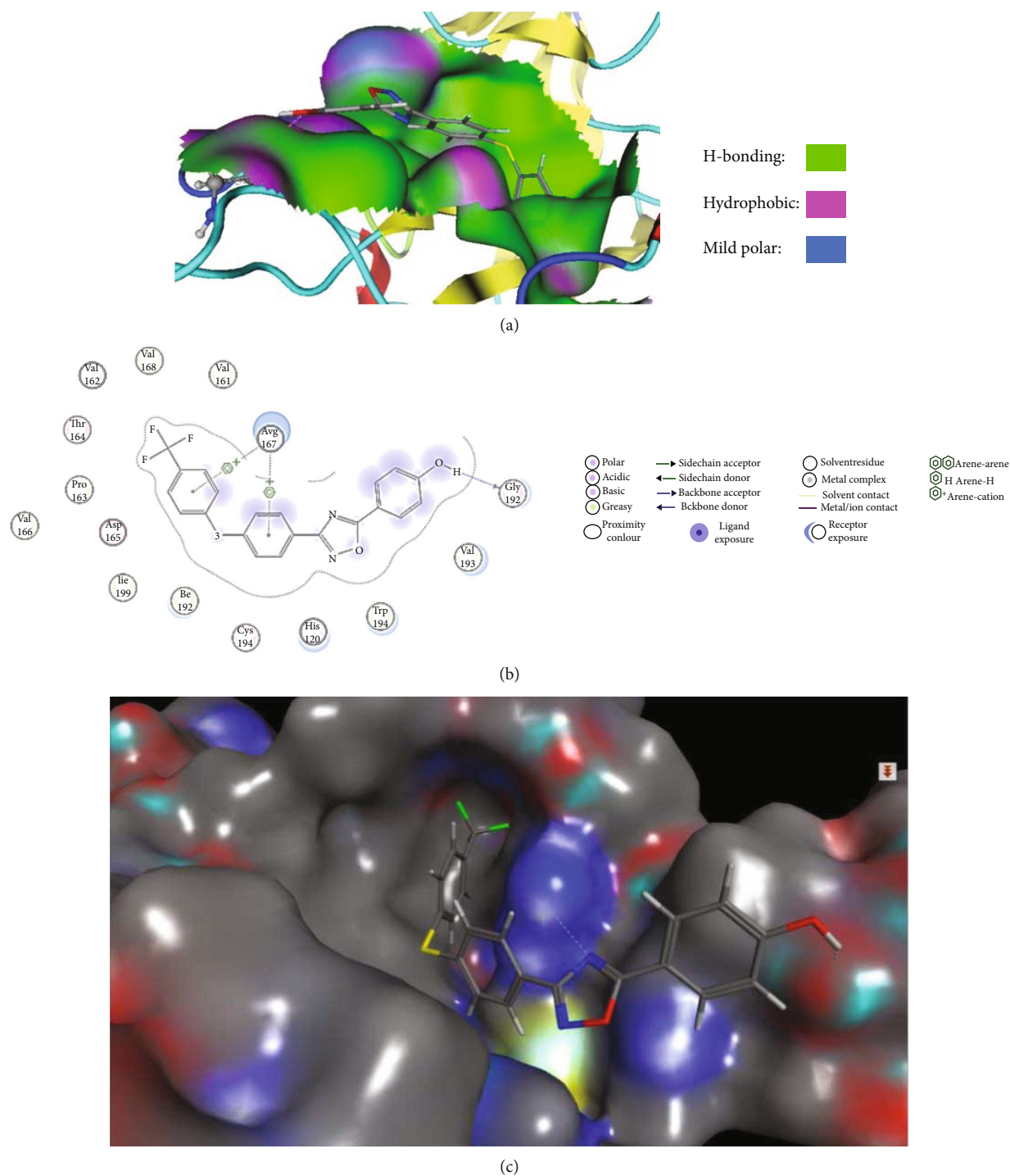
(a)

(b)

(c)

FIGURE 6: (a) The display of the image related to hydrophobic and hydrophilic fields for compound **89** into the active site (2KID). (b) The 2D pictures of the docked conformation of compound **89**. (c) The positioning of the compound **89** in the protein active site.

ionic, electrostatic, H-bond acceptor, and H-bond donor locations on oxadiazole inhibitory effects. The positive contribution appeared in blue-colored cubes, and the negative contribution was visible in red. Figures 5(a)–5(f) are shown for the identification of the acceptable and unacceptable important interactions in two different dimensions, which resulted in the use of the QSAR model. HBD nature comparison of compound 89 (the best activity, Figure 5(a)) and the

compound **120** (the least activity, Figure 5(b)) displays unacceptable and acceptable regions as red and blue cubes, respectively. Hydrogen bond donor maps showed that unfavorable locations placed next to the nitrogen atom of amide present on one side of the oxadiazole (Figure 5(a)) are an HBD group which is in the inappropriate place, whereas for the most active molecule, unfavorable regions lay near the sulfur atom which is not an HBD group (Figure 5(b)).

TABLE 1: PLS statistical parameters of the model QSAR model.

PLS	SD	R^2	F	P	Stability	RMSE	Q^2	Pearson-R
1	0.4285	0.7171	238.3	1.62e-027	0.994	0.45	0.6744	0.8302
2	0.3774	0.7830	167.8	1.41e-031	0.971	0.48	0.6323	0.8012
3	0.3254	0.8403	161.4	1.57e-036	0.907	0.44	0.6900	0.8342
4	0.2808	0.8824	170.7	2.1e-041	0.835	0.43	0.7056	0.8462
5	0.2503	0.9076	176.8	5.91e-045	0.773	0.45	0.6772	0.8314
6	0.2291	0.9235	179.0	1.95e-047	0.722	0.48	0.6319	0.8050
7	0.2070	0.9382	190.9	2.31e-050	0.674	0.49	0.6134	0.7970

SD: standard deviation of regression; R^2: regression coefficient; F: variance ratio (ratio of the model variance to the observed activity variance); P: significance level of variance ratio; Q^2: Crossvalidated correlation coefficient for the test group; RMSE: the RMS error in the test group predictions; Pearson-R: correlation among the predicted and observed activity for the test group.

TABLE 2: Seven factors of PLS were calculated for the QSAR model.

# factors	H-bond donor	Hydrophobic/nonpolar	Negative ionic	Positive ionic	Electron-withdrawing
1	0.028420	0.709533	0.030517	0.031581	0.156872
2	0.029319	0.646792	0.039072	0.039833	0.190441
3	0.028610	0.647774	0.045189	0.045139	0.200709
4	0.029662	0.668252	0.038533	0.037152	0.195964
5	0.029213	0.666539	0.039458	0.037827	0.195301
6	0.029931	0.669972	0.037575	0.035876	0.194004
7	0.032992	0.677689	0.033050	0.032073	0.191071

Also, the hydrogen of the hydroxyl group on p-hydroxyphenyl, present on the other side of the oxadiazole near the desirable region, is available for two compounds—categorized as active and the least active.

Compounds such as ligand **89** with p-CF$_3$-phenylthio hydrophobic substituent had higher potency values than compounds without substitute mentioned such as ligand **120**, because of the presence of favorable hydrophobic regions in that position (Figures 5(c) and 5(d)), which was confirmed by the results obtained from previous CoMFA studies [69]. For less active ligands such as compound **120**, the hydrophilic group (amid) fell into the favorable hydrophobic envelope that is not suitable for the hydrophilic groups. Comparison between the effects of the electron-withdrawing moieties of the best compound **89** with an electron p-CF3-phenylthio group and the least active compound **120** with the acetamido group was shown in Figures 5(f) and 5(e).

3.5. Docking Studies. The MOE-Dock program was utilized to check the stability of the models created in this study with the sortase A polypeptide receiver (PDB code 2KID). Studies of docking showed that interactions were commanded by aromaticity and hydrophobicity due to the position of phenol moiety (Figures 6(a)–6(c)). The best compound (pMIC = 5.617) was connected into the binding cavity of polypeptide SrtA with high affinity and created interactions in association with the oxygen of phenol with the Gly192 residue in one side of the ligand, while two rings on the other side of the oxadiazole have two interactions arene-cation with Arg 197 residue. The scores of docking studies of the best compound were -11.12 kcal/mol. Therefore, the compound **89** had a three-point attachment with the protein binding cavity. The interactions were present in the region containing Gly 192 and Arg 197 residues (Figure 6(b)). In general, oxygen is bound to hydrogen of hydroxyl in the acidic part of Gly 192 residue that showed only one hydrogen bond. This subject is visible by analyzing the hydrophilic and hydrophobic regions of compound 89 (Figure 6(a)). 3D-QSAR contour map analysis studies confirm this and showed that the compounds like ligand 89 are placed in a hydrophobic envelope (Figure 6(c)).

4. Conclusions

Using model prediction by 3D-QSAR studies of 120 analogs of 1,2,4-oxadiazoles and docking, we provided insights into the critical features needed for the design of inhibitors of SrtA. 3D-QSAR modeling was performed to provide a structural network for the comprehension of structure-activity relationships of the ligands present in the study. Studies of molecular docking were done to create desirable poses that bind to these compounds. The gets scores in VS (virtual screening) of compounds gave us chemically important points for the design and improvement of novel oxadiazoles as sortase inhibitors. The most active compound (**89**) of 1,2,4-oxadiazoles used in this study had four rings, named A, B, C, and D. HBD moieties in the A ring were essential for antibacterial activity. The aniline, phenol, and some heterocyclic compounds with hydrogen-bonding ability, such as pyrazoles, were allowed. These findings are in line with previous results. In line with previous explanations on the 3D-QSAR map analysis section, a hydrophobic substituent

was seen essential for the activity in the D ring region [24, 69]. In general, by 3D-QSAR, we attempted to study the structural diversity in the ring D antibacterial activity in a 1,2,4-oxadiazoles region (Figure 1). Finally, our findings suggest that the 1,2,4-oxadiazoles are inhibitors of sortase A and act against *S. aureus*, further holding great promising potential as future therapeutics for treating hospital infections.

Abbreviations

R^2:   Regression coefficient
Q^2:   Crossvalidation correlation coefficient
APD: Applicability domain
PLS: Partial least square
SD: Standard deviation
RMSD: Root mean square deviation
RMSE: Root mean squared error
HBD: Hydrogen-bond donor.

Data Availability

The data about this original article are available upon reasonable request.

Conflicts of Interest

The authors confirm they have no conflict of interest.

Supplementary Materials

Supplementary Table 1: molecular view, assay-organism and assay-strain, the experimental, and predicted corresponding values of pMIC gained via QSAR models. (*Supplementary Materials*)

References

[1] L. Si, P. Li, X. Liu, and L. Luo, "Chinese herb medicine against sortase a catalyzed transformations, a key role in gram-positive bacterial infection progress," *Journal of Enzyme Inhibition and Medicinal Chemistry.*, vol. 31, supplement 1, pp. 184–196, 2016.

[2] C. Garandeau, H. Réglier-Poupet, I. Dubail, J.-L. Beretti, P. Berche, and A. Charbit, "The sortase SrtA of listeria monocytogenes is involved in processing of internalin and in virulence," *Infection and Immunity.*, vol. 70, no. 3, pp. 1382–1390, 2002.

[3] Y. Zong, T. W. Bice, H. Ton-That, O. Schneewind, and S. V. Narayana, "Crystal structures of _Staphylococcus aureus_ sortase A and its substrate complex," *Journal of Biological Chemistry.*, vol. 279, no. 30, pp. 31383–31389, 2004.

[4] A. Grigoletto, K. Maso, and G. Pasut, *Enzymatic Approaches to New Protein Conjugates*, Elsevier, Polymer-Protein Conjugates, 2020.

[5] H. M. Burke, L. McSweeney, and E. M. Scanlan, "Exploring chemoselective _S_ -to- _N_ acyl transfer reactions in synthesis and chemical biology," *Nature Communications*, vol. 8, no. 1, pp. 1–16, 2017.

[6] S. Cascioferro, D. Raffa, B. Maggio, M. V. Raimondi, D. Schillaci, and G. Daidone, "Sortase a inhibitors: recent

advances and future perspectives," *Journal of Medicinal Chemistry.*, vol. 58, no. 23, 2015.

[7] J. Wang, H. Li, J. Pan et al., "Oligopeptide targeting Sortase a as potential anti-infective therapy for Staphylococcus aureus," *Frontiers in Microbiology.*, vol. 9, p. 245, 2018.

[8] M. V. Raimondi, R. Listro, M. G. Cusimano et al., "Novel sortase A inhibitors to counteract gram-positive bacterial biofilms," *Multidisciplinary Digital Publishing Institute Proceedings.*, vol. 22, no. 1, 2019.

[9] B. T. Russo, Y. A. Ayinuola, D. Singh et al., "The M protein of streptococcus pyogenes strain AP53 retains cell surface functional plasminogen binding after inactivation of the sortase A Gene," *Journal of Bacteriology.*, vol. 202, no. 10, 2020.

[10] L. A. Marraffini, A. C. DeDent, and O. Schneewind, "Sortases and the art of anchoring proteins to the envelopes of gram-positive bacteria," *Microbiology and Molecular Biology Reviews*, vol. 70, no. 1, pp. 192–221, 2006.

[11] Y. Zong, S. K. Mazmanian, O. Schneewind, and S. V. Narayana, "The structure of sortase B, a cysteine transpeptidase that tethers surface protein to the _Staphylococcus aureus_ Cell Wall," *Structure*, vol. 12, no. 1, pp. 105–112, 2004.

[12] Y. Guo, S. Cai, G. Gu, Z. Guo, and Z. Long, "Recent progress in the development of sortase A inhibitors as novel anti-bacterial virulence agents," *RSC Advances.*, vol. 5, no. 62, pp. 49880–49889, 2015.

[13] C.-Y. Kang, I.-H. Huang, C.-C. Chou et al., "Functional analysis of _Clostridium difficile_ sortase B reveals key residues for catalytic activity and substrate specificity," *Journal of Biological Chemistry.*, vol. 295, no. 11, pp. 3734–3745, 2020.

[14] T. Huang, Z. Peng, M. Hu et al., "Interactions between _Lactobacillus plantarum_ NCU116 and its environments based on extracellular proteins and polysaccharides prediction by comparative analysis," *Genomics*, vol. 112, no. 5, pp. 3579–3587, 2020.

[15] H. Bierne and P. Cossart, "Listeria monocytogenes surface proteins: from genome predictions to function," *Microbiology and Molecular Biology Reviews*, vol. 71, no. 2, pp. 377–397, 2007.

[16] S. K. Mazmanian, H. Ton-That, and O. Schneewind, "Sortase-catalysed anchoring of surface proteins to the cell wall of Staphylococcus aureus," *Molecular Microbiology.*, vol. 40, no. 5, pp. 1049–1057, 2001.

[17] T. Hampton, "Report reveals scope of US antibiotic resistance threat," *Journal of the American Medical Association*, vol. 310, no. 16, pp. 1661–1663, 2013.

[18] J.-Y. Maillard, S. F. Bloomfield, P. Courvalin et al., "Reducing antibiotic prescribing and addressing the global problem of antibiotic resistance by targeted hygiene in the home and everyday life settings: a position paper," *American Journal of Infection Control.*, vol. 48, no. 9, pp. 1090–1099, 2020.

[19] Z. M. Burcham, C. J. Schmidt, J. L. Pechal et al., "Detection of critical antibiotic resistance genes through routine microbiome surveillance," *PLoS One*, vol. 14, no. 3, article e0213280, 2019.

[20] F. Cunha, J. Nogueira, and A. de Aguiar, "Synthesis and antibacterial evaluation of 3, 5-diaryl-1, 2, 4-oxadiazole derivatives," *Journal of the Brazilian Chemical Society*, vol. 29, no. 11, pp. 2405–2416, 2018.

[21] J. Lee, S. Cho, and M.-h. Kim, "Discovery of CNS-like D3R-selective antagonists using 3D pharmacophore guided virtual screening," *Molecules*, vol. 23, no. 10, p. 2452, 2018.

[22] R. R. Watkins, M. Z. David, and R. A. Salata, "Current concepts on the virulence mechanisms of meticillin-resistant Staphylococcus aureus," *Journal of Medical Microbiology.*, vol. 61, no. 9, pp. 1179–1193, 2012.

[23] L. García-Álvarez, M. T. G. Holden, H. Lindsay et al., "Meticillin-resistant _Staphylococcus aureus_ with a novel _mecA_ homologue in human and bovine populations in the UK and Denmark: a descriptive study," *The Lancet Infectious Diseases.*, vol. 11, no. 8, pp. 595–603, 2011.

[24] D. Ding, M. A. Boudreau, E. Leemans et al., "Exploration of the structure-activity relationship of 1,2,4-oxadiazole antibiotics," *Bioorganic & Medicinal Chemistry Letters.*, vol. 25, no. 21, pp. 4854–4857, 2015.

[25] I. Gould, J. Reilly, D. Bunyan, and A. Walker, "Costs of healthcare-associated methicillin-resistant _Staphylococcus aureus_ and its control," *Clinical Microbiology and Infection.*, vol. 16, no. 12, pp. 1721–1728, 2010.

[26] Z. Tavajjohi, R. Moniri, and A. Khorshidi, "Detection and characterization of multidrug resistance and extended-spectrum-beta-lactamase-producing (ESBLS) Pseudomonas aeruginosa isolates in teaching hospital," *African Journal of Microbiology Research.*, vol. 5, no. 20, pp. 3223–3228, 2011.

[27] A. S. Kaka, A. M. Rueda, S. A. Shelburne III, K. Hulten, R. J. Hamill, and D. M. Musher, "Bactericidal activity of orally available agents against methicillin-resistant Staphylococcus aureus," *Journal of Antimicrobial Chemotherapy.*, vol. 58, no. 3, pp. 680–683, 2006.

[28] J. Janardhanan, J. E. Meisel, D. Ding et al., "In vitro and in vivo synergy of the oxadiazole class of antibacterials with β-lactams," *Antimicrobial Agents and Chemotherapy.*, vol. 60, no. 9, pp. 5581–5588, 2016.

[29] R. McCool, I. M. Gould, J. Eales et al., "Systematic review and network meta-analysis of tedizolid for the treatment of acute bacterial skin and skin structure infections caused by MRSA," *BMC Infectious Diseases.*, vol. 17, no. 1, p. 39, 2017.

[30] S. Ningaiah, U. K. Bhadraiah, S. Keshavamurthy, and C. Javarasetty, "Novel pyrazoline amidoxime and their 1,2,4-oxadiazole analogues: Synthesis and pharmacological screening," *Bioorganic & Medicinal Chemistry Letters.*, vol. 23, no. 16, pp. 4532–4539, 2013.

[31] P. Dadgostar, "Antimicrobial resistance: implications and costs," *Infection and Drug Resistance.*, vol. Volume 12, pp. 3903–3910, 2019.

[32] R. J. Loureiro, F. Roque, A. T. Rodrigues, M. T. Herdeiro, and E. Ramalheira, "Use of antibiotics and bacterial resistances: brief notes on its evolution," *Revista Portuguesa de Saúde Pública.*, vol. 34, no. 1, pp. 77–84, 2016.

[33] R. Musumeci, C. E. A. Cocuzza, C. G. Fortuna, P. Andrea, and A. P. PICCIONELLO, "4-Oxadiazol compounds active against gram-positive pathogens," *Google Patents*, vol. 1, 2018.

[34] C. G. Fortuna, C. Bonaccorso, A. Bulbarelli et al., "New linezolid-like 1,2,4-oxadiazoles active against Gram-positive multiresistant pathogens," *European Journal of Medicinal Chemistry.*, vol. 65, pp. 533–545, 2013.

[35] E. Spink, D. Ding, Z. Peng et al., "Structure–activity relationship for the oxadiazole class of antibiotics," *Journal of Medicinal Chemistry.*, vol. 58, no. 3, pp. 1380–1389, 2015.

[36] M. A. Boudreau, D. Ding, J. E. Meisel et al., "Structure–activity relationship for the oxadiazole class of antibacterials," *ACS Medicinal Chemistry Letters.*, vol. 11, no. 3, pp. 322–326, 2020.

[37] E. A. Hall, *Fighting Bacterial Drug Resistance by Targeting Peptidoglycan Biosynthesis: Depsipeptide Antibiotics and Biological Probes*, Indiana University, 2014.

[38] S. Yatam, R. Gundla, S. S. Jadav et al., "Focused library design and synthesis of 2-mercapto benzothiazole linked 1,2,4-oxadiazoles as COX-2/5-LOX inhibitors," *Journal of Molecular Structure.*, vol. 1159, pp. 193–204, 2018.

[39] P. Zhang, J.-H. Chen, X. Dong et al., "6r, a novel oxadiazole analogue of ethacrynic acid, exhibits antitumor activity both in vitro and in vivo by induction of cell apoptosis and S-phase arrest," *Biomedicine & Pharmacotherapy.*, vol. 67, no. 1, pp. 58–65, 2013.

[40] S. Cascioferro and D. Schillaci, "The future of antibiotic: from the magic bullet to the smart Bullet," *Technology*, vol. 6, no. 5, 2014.

[41] S. E. Adeniji, S. Uba, and A. Uzairu, "Theoretical modeling and molecular docking simulation for investigating and evaluating some active compounds as potent anti-tubercular agents against MTB CYP121 receptor," *Future Journal of Pharmaceutical Sciences.*, vol. 4, no. 2, pp. 284–295, 2018.

[42] A. Khatkar, A. Nanda, P. Kumar, and B. Narasimhan, "Synthesis, antimicrobial evaluation and QSAR studies of _p-_ coumaric acid derivatives," *Arabian Journal of Chemistry.*, vol. 10, pp. S3804–S3815, 2017.

[43] J. J. van Zanden, H. M. Wortelboer, S. Bijlsma et al., "Quantitative structure activity relationship studies on the flavonoid mediated inhibition of multidrug resistance proteins 1 and 2," *Biochemical Pharmacology*, vol. 69, no. 4, pp. 699–708, 2005.

[44] K. E. Hevener, D. M. Ball, J. K. Buolamwini, and R. E. Lee, "Quantitative structure-activity relationship studies on nitrofuranyl anti- tubercular agents," *Bioorganic & Medicinal Chemistry.*, vol. 16, no. 17, pp. 8042–8053, 2008.

[45] M. F. Khan, G. Verma, W. Akhtar et al., "Pharmacophore modeling, 3D-QSAR, docking study and ADME prediction of acyl 1,3,4-thiadiazole amides and sulfonamides as antitubulin agents," *Arabian Journal of Chemistry.*, vol. 12, no. 8, pp. 5000–5018, 2019.

[46] B. Rasulev, "Recent developments in 3D QSAR and molecular docking studies of organic and Nanostructures," *Chemistry*, vol. 2133, 2017.

[47] N. Shakour, R. Cabezas, J. G. Santos et al., "Curcumin can bind and interact with CRP: an in silico study," *Pharmacological Properties of Plant-Derived Natural Products and Implications for Human Health.*, vol. 1308, pp. 91–100, 2021.

[48] N. Shakour, A. Sahebkar, G. Karimi et al., "Design, synthesis and biological evaluation of novel 5-(imidazolyl-methyl) thiazolidinediones as antidiabetic agents," *Bioorganic Chemistry*, vol. 115, article 105162, 2021.

[49] N. Chirico and P. Gramatica, "Real external predictivity of QSAR models: how to evaluate it? Comparison of different validation criteria and proposal of using the concordance correlation coefficient," *Journal of Chemical Information and Modeling.*, vol. 51, no. 9, pp. 2320–2335, 2011.

[50] A. I. Foudah, A. A. Sallam, M. R. Akl, and K. A. El Sayed, "Optimization, pharmacophore modeling and 3D-QSAR studies of sipholanes as breast cancer migration and proliferation inhibitors," *European Journal of Medicinal Chemistry.*, vol. 73, pp. 310–324, 2014.

[51] Y. Xu, Z. He, H. Liu et al., "3D-QSAR, molecular docking, and molecular dynamics simulation study of thieno [3, 2-b]

pyrrole-5-carboxamide derivatives as LSD1 inhibitors," *RSC Advances.*, vol. 10, no. 12, pp. 6927–6943, 2020.

[52] S. Norouzia, M. Farahania, and S. N. Ebrahimi, "The integration of pharmacophore-based 3D QSAR modeling and virtual screening in identification of natural product inhibitors against SARS-CoV-2," *Pharmaceutical Sciences.*, vol. 27, pp. S94–S108, 2021.

[53] A. Rácz, D. Bajusz, and K. Héberger, "Consistency of QSAR models: correct split of training and test sets, ranking of models and performance parameters," *SAR and QSAR in Environmental Research.*, vol. 26, no. 7-9, pp. 683–700, 2015.

[54] K. Roy, S. Kar, and P. Ambure, "On a simple approach for determining applicability domain of QSAR models," *Chemometrics and Intelligent Laboratory Systems*, vol. 145, pp. 22–29, 2015.

[55] H. Hadni and M. Elhallaoui, "3D-QSAR, docking and ADMET properties of aurone analogues as antimalarial agents," *Heliyon.*, vol. 6, no. 4, article e03580, 2020.

[56] A. A. Alizadeh, B. Jafari, and S. Dastmalchi, "Alignment independent 3D-QSAR studies and molecular dynamics simulations for the identification of potent and selective $S1P_1$ receptor agonists," *Journal of Molecular Graphics and Modelling.*, vol. 94, article 107459, 2020.

[57] M. Shen, C. Béguin, A. Golbraikh, J. P. Stables, H. Kohn, and A. Tropsha, "Application of predictive QSAR models to database mining: identification and experimental validation of novel anticonvulsant compounds," *Journal of Medicinal Chemistry.*, vol. 47, no. 9, pp. 2356–2364, 2004.

[58] Z. Ul-Haq, U. Mahmood, and S. Reza, "A combined 3D-QSAR and molecular docking strategy to understand the binding mechanism of V600E B-RAF inhibitors," *Molecular Diversity.*, vol. 16, no. 4, pp. 771–785, 2012.

[59] N. K. Salam, R. Nuti, and W. Sherman, "Novel method for generating structure-based pharmacophores using energetic analysis," *Journal of Chemical Information and Modeling.*, vol. 49, no. 10, pp. 2356–2368, 2009.

[60] V. Sharma, H. Kumar, and S. Wakode, "Pharmacophore generation and atom based 3D-QSAR of quinoline derivatives as selective phosphodiesterase 4B inhibitors," *RSC Advances.*, vol. 6, no. 79, pp. 75805–75819, 2016.

[61] M. Athar, M. Y. Lone, V. M. Khedkar, and P. C. Jha, "Pharmacophore model prediction, 3D-QSAR and molecular docking studies on vinyl sulfones targeting Nrf2-mediated gene transcription intended for anti-Parkinson drug design," *Journal of Biomolecular Structure and Dynamics.*, vol. 34, no. 6, pp. 1282–1297, 2016.

[62] D. Panigrahi, A. Mishra, and S. K. Sahu, "Pharmacophore modelling, QSAR study, molecular docking and insilico ADME prediction of 1, 2, 3-triazole and pyrazolopyridones as DprE1 inhibitor antitubercular agents," *SN Applied Sciences.*, vol. 2, no. 5, pp. 1–28, 2020.

[63] C. N. Cavasotto and M. G. Aucar, "High-throughput docking using quantum mechanical Scoring," *Chemistry*, vol. 8, 2020.

[64] W.-L. Ye, C. Shen, G.-L. Xiong et al., "Improving docking-based virtual screening ability by integrating multiple energy auxiliary terms from molecular docking scoring," *Journal of Chemical Information and Modeling.*, vol. 60, no. 9, pp. 4216–4230, 2020.

[65] S. Mirzaei, F. Hadizadeh, F. Eisvand, F. Mosaffa, and R. Ghodsi, "Synthesis, structure-activity relationship and molecular docking studies of novel quinoline-chalcone hybrids as potential anticancer agents and tubulin inhibitors," *Journal of Molecular Structure.*, vol. 1202, article 127310, 2020.

[66] G. Verma, M. F. Khan, W. Akhtar et al., "Pharmacophore modeling, 3D-QSAR, docking and ADME prediction of quinazoline based EGFR inhibitors," *Arabian Journal of Chemistry.*, vol. 12, no. 8, pp. 4815–4839, 2019.

[67] A. Golbraikh and A. Tropsha, "Beware of q2!," *Journal of Molecular Graphics and Modelling.*, vol. 20, no. 4, pp. 269–276, 2002.

[68] A. B. Umar, A. Uzairu, G. A. Shallangwa, and S. Uba, "Design of potential anti-melanoma agents against SK-MEL-5 cell line using QSAR modeling and molecular docking methods," *SN Applied Sciences.*, vol. 2, no. 5, pp. 1–18, 2020.

[69] E. Leemans, K. V. Mahasenan, M. Kumarasiri et al., "Three-dimensional QSAR analysis and design of new 1,2,4-oxadiazole antibacterials," *Bioorganic & Medicinal Chemistry Letters.*, vol. 26, no. 3, pp. 1011–1015, 2016.

Research Article

Research on the Mechanism of Guizhi to Treat Nephrotic Syndrome Based on Network Pharmacology and Molecular Docking Technology

Dan He,[1] Qiang Li,[2] Guangli Du,[1] Jijia Sun,[2] Guofeng Meng,[3] and Shaoli Chen [1]

[1]*School of Basic Medicine, Shanghai University of Traditional Chinese Medicine, Shanghai 201203, China*
[2]*School of Pharmacy, Shanghai University of Traditional Chinese Medicine, Shanghai 201203, China*
[3]*Institute of Interdisciplinary Integrative Medicine Research, Shanghai University of Traditional Chinese Medicine, Shanghai 201203, China*

Correspondence should be addressed to Shaoli Chen; shaolichen2020@163.com

Objective. Nephrotic syndrome (NS) is a common glomerular disease caused by a variety of causes and is the second most common kidney disease. Guizhi is the key drug of Wulingsan in the treatment of NS. However, the action mechanism remains unclear. In this study, network pharmacology and molecular docking were used to explore the underlying molecular mechanism of Guizhi in treating NS. *Methods*. The active components and targets of Guizhi were screened by the Traditional Chinese Medicine Systems Pharmacology Database and Analysis Platform (TCMSP), Hitpick, SEA, and Swiss Target Prediction database. The targets related to NS were obtained from the DisGeNET, GeneCards, and OMIM database, and the intersected targets were obtained by Venny2.1.0. Then, active component-target network was constructed using Cytoscape software. And the protein-protein interaction (PPI) network was drawn through the String database and Cytoscape software. Next, Gene Ontology (GO) and pathway enrichment analyses of Kyoto Encyclopedia of Genes and Genomes (KEGG) enrichment analyses were performed by DAVID database. And overall network was constructed through Cytoscape. Finally, molecular docking was conducted using Autodock Vina. *Results*. According to the screening criteria, a total of 8 active compounds and 317 potential targets of Guizhi were chosen. Through the online database, 2125 NS-related targets were identified, and 93 overlapping targets were obtained. In active component-target network, beta-sitosterol, sitosterol, cinnamaldehyde, and peroxyergosterol were the important active components. In PPI network, VEGFA, MAPK3, SRC, PTGS2, and MAPK8 were the core targets. GO and KEGG analyses showed that the main pathways of Guizhi in treating NS involved VEGF, Toll-like receptor, and MAPK signaling pathway. In molecular docking, the active compounds of Guizhi had good affinity with the core targets. *Conclusions*. In this study, we preliminarily predicted the main active components, targets, and signaling pathways of Guizhi to treat NS, which could provide new ideas for further research on the protective mechanism and clinical application of Guizhi against NS.

1. Introduction

Nephrotic syndrome (NS) is a clinical syndrome defined as massive proteinuria, hypoalbuminemia, hyperlipidemia, and edema [1]. According to the epidemiological survey, the incidence of NS is about 2-10/100000, and it mostly occurs in male children [2]. NS greatly affects people's health and life quality with poor prognosis and high recurrence rate [3]. At present, the etiopathogenesis of NS is incompletely

understood, but relevant reports have shown that it is related to inflammatory response and immune suppression.

According to traditional Chinese medicine (TCM), NS belongs to "edema," and the pathogenesis of NS lies in the dysfunction of the lung, spleen, and kidney [4]. TCM has been used to treat kidney disease and its complications, for that it can protect the kidney from dysfunction and delay the renal failure [5]. Guizhi is a Chinese herbal medicine that is commonly used to treat edema [6]. Currently, there are
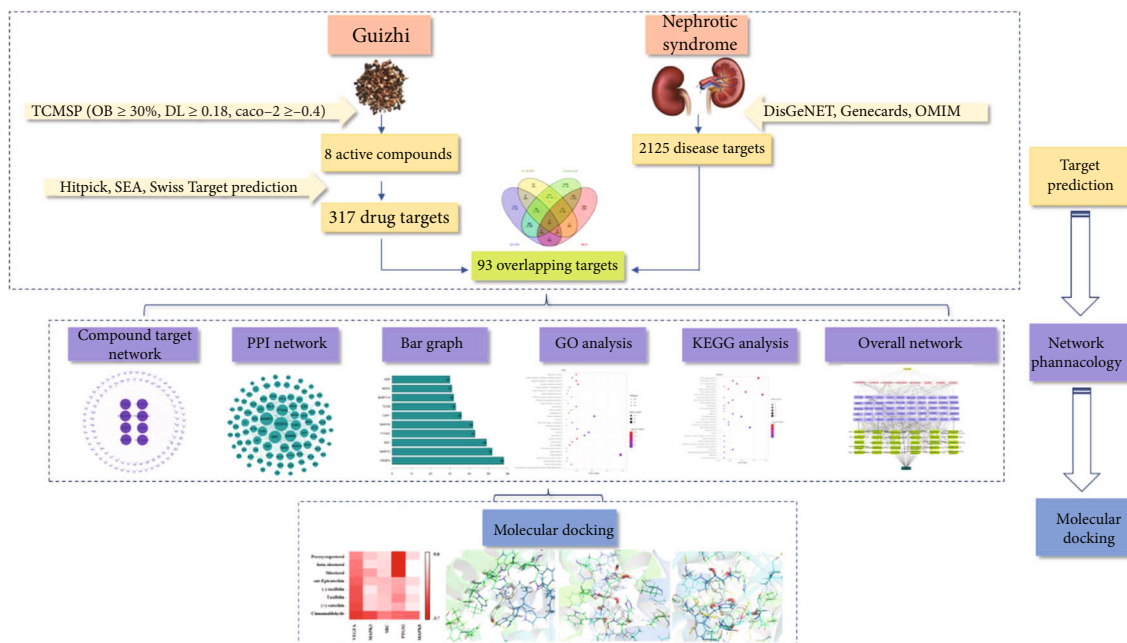
FIGURE 1: A flow diagram based on a cohesive integration strategy of network pharmacology and molecular docking.

many reports on the pharmacological effects of Guizhi, but it is not comprehensive and systematic in the mechanism studies of Guizhi to treat NS.

Network pharmacology integrates diseases and drugs into the biomolecular network, to predict the active components and the action mechanism [7]. As a new idea approach of TCM research, network pharmacology has been widely applied in the research of the complex network relationship between TCM and disease [8–10].

In the present study, network pharmacology and molecular docking were used to explore the potential action mechanism of Guizhi to treat NS. It is hoped to provide theoretical foundation and scientific evidence for the clinical treatment of NS, and the workflow of our study is shown in Figure 1.

2. Materials and Methods

2.1. Screening of Active Compounds. The active compounds of Guizhi were searched by TCMSP database (https://tcmspw.com/tcmsp.php). The PubChem ID, molecular formula, and canonical SMILES of each component were collected through PubChem database (https://pubchem.ncbi.nlm.nih.gov/). And the main active components were obtained by the screening criteria of oral bioavailability (OB) $\geq 30\%$, drug – like (DL) ≥ 0.18, and cell permeability (Caco – 2) ≥ -0.4.

2.2. Predicting Drug Targets. The targets of active compounds of Guizhi were predicted by Hitpick (http://mips.helmholtz-muenchen.de/hitpick/cgi-bin/index.cgi?content=help.html), SEA (http://sea.bkslab.org/), and Swiss Target Prediction database (http://swisstargetprediction.ch/). The

TABLE 1: The main active compounds of Guizhi.

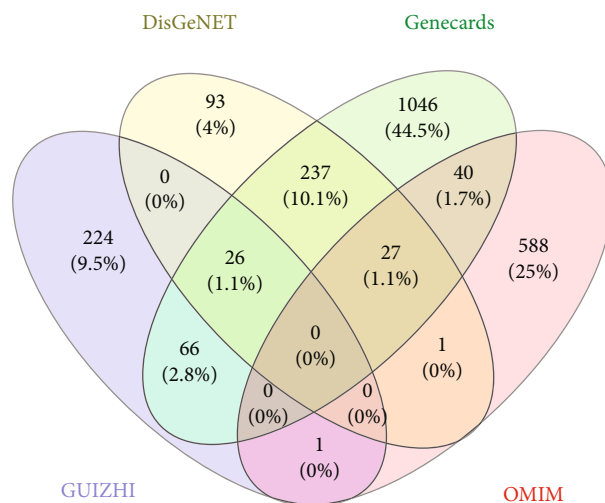| Mol ID	Molecule name	OB (%)	DL	Caco-2
MOL000073	Ent-Epicatechin	48.96	0.24	0.02
MOL000358	Beta-sitosterol	36.91	0.75	1.32
MOL000359	Sitosterol	36.91	0.75	1.32
MOL000492	(+)-catechin	54.83	0.24	-0.03
MOL000991	Cinnamaldehyde	31.99	0.02	1.35
MOL001736	(-)-taxifolin	60.51	0.27	-0.24
MOL004576	Taxifolin	57.84	0.27	-0.23
MOL011169	Peroxyergosterol	44.39	0.82	0.86

FIGURE 2: The Venny plot of 93 potential targets.

TABLE 2: 93 potential targets and UniProt information.

No.	Gene names	Protein names	UniProt ID
1	ABCB1	ATP-dependent translocase ABCB1	P08183
2	ABCC2	ATP-binding cassette subfamily C member 2	Q92887
3	ABCG2	Broad substrate specificity ATP-binding cassette transporter ABCG2	Q9UNQ0
4	ACE	Angiotensin-converting enzyme	P12821
5	ACHE	Acetylcholinesterase	P22303
6	ACP1	Low molecular weight phosphotyrosine protein phosphatase	P24666
7	AKR1B1	Aldo-keto reductase family 1 member B1	P15121
8	AKR1B10	Aldo-keto reductase family 1 member B10	O60218
9	ALK	ALK tyrosine kinase receptor	Q9UM73
10	APP	Amyloid-beta precursor protein	P05067
11	AR	Androgen receptor	P10275
12	AVPR1A	Vasopressin V1a receptor	P37288
13	CASR	Extracellular calcium-sensing receptor	P41180
14	CCR1	C-C chemokine receptor type 1	P32246
15	CD4	T-cell surface glycoprotein CD4	P01730
16	CDK4	Cyclin-dependent kinase 4	P11802
17	CTSB	Cathepsin B	P07858
18	CTSL	Procathepsin L	P07711
19	CYP11B2	Cytochrome P450 11B2	P19099
20	CYP19A1	Cytochrome P450 19A1	P11511
21	CYP1A1	Cytochrome P450 1A1	P04798
22	CYP1B1	Cytochrome P450 1B1	Q16678
23	CYP2A6	Cytochrome P450 2A6	P11509
24	CYP2C19	Cytochrome P450 2C19	P33261
25	CYP3A4	Cytochrome P450 3A4	P08684
26	DNMT1	DNA (cytosine-5)-methyltransferase 1	P26358
27	DUSP1	Dual specificity protein phosphatase 1	P28562
28	ELANE	Neutrophil elastase	P08246
29	ELAVL1	ELAV-like protein 1	Q15717
30	ESR1	Estrogen receptor	P03372
31	ESR2	Estrogen receptor beta	Q92731
32	F10	Coagulation factor X	P00742
33	F2	Coagulation factor II	P00734
34	F2R	Coagulation factor II receptor	P25116
35	F3	Coagulation factor III	P13726
36	FABP1	Fatty acid-binding protein 1	P07148
37	G6PD	Glucose-6-phosphate 1-dehydrogenase	P11413
38	GC	Group-specific component	P02774
39	GLO1	Glyoxalase I	Q04760
40	HDAC2	Histone deacetylase 2	Q92769
41	HIF1A	Hypoxia-inducible factor 1-alpha	Q16665
42	HMGCR	3-Hydroxy-3-methylglutaryl-coenzyme A reductase	P04035
43	HSD11B1	Corticosteroid 11-beta-dehydrogenase isozyme 1	P28845
44	HSD11B2	Corticosteroid 11-beta-dehydrogenase isozyme 2	P80365
45	HTR2B	5-Hydroxytryptamine receptor 2B	P41595
46	ICAM1	Intercellular adhesion molecule 1	P05362
47	IGF1R	Insulin-like growth factor 1 receptor	P08069
48	ITGAL	Integrin alpha-L	P20701

TABLE 2: Continued.

| No.	Gene names	Protein names	UniProt ID
49	ITGB2	Integrin beta-2	P05107
50	KAT2B	Histone acetyltransferase KAT2B	Q92831
51	KCNH2	Potassium voltage-gated channel subfamily H member 2	Q12809
52	KDR	Kinase insert domain receptor	P35968
53	MAP2K1	Dual specificity mitogen-activated protein kinase kinase 1	Q02750
54	MAPK14	Mitogen-activated protein kinase 14	Q16539
55	MAPK3	Mitogen-activated protein kinase 3	P27361
56	MAPK8	Mitogen-activated protein kinase 8	P45983
57	MAPT	Microtubule-associated protein tau	P10636
58	MCL1	Induced myeloid leukemia cell differentiation protein Mcl-1	Q07820
59	MDM2	E3 ubiquitin-protein ligase Mdm2	Q00987
60	MET	Hepatocyte growth factor receptor	P08581
61	MMP12	Matrix metalloproteinase-12	P39900
62	MPO	Myeloperoxidase	P05164
63	NFE2L2	Nuclear factor erythroid 2-related factor 2	Q16236
64	NOS1	Peptidyl-cysteine S-nitrosylase NOS1	P29475
65	NOS2	Peptidyl-cysteine S-nitrosylase NOS2	P35228
66	NOS3	NOS type III	P29474
67	NR1I2	Nuclear receptor subfamily 1 group I member 2	O75469
68	NR3C1	Nuclear receptor subfamily 3 group C member 1	P04150
69	PARP1	Poly [ADP-ribose] polymerase 1	P09874
70	PLA2G1B	Phosphatidylcholine 2-acylhydrolase 1B	P04054
71	PLA2G7	Platelet-activating factor acetylhydrolase	Q13093
72	PPARA	Peroxisome proliferator-activated receptor alpha	Q07869
73	PRKCB	Protein kinase C beta type	P05771
74	PRKCD	Protein kinase C delta type	Q05655
75	PSEN1	Presenilin-1	P49768
76	PTGS2	Prostaglandin G/H synthase 2	P35354
77	PTK2B	Protein-tyrosine kinase 2-beta	Q14289
78	PTPN11	Tyrosine-protein phosphatase nonreceptor type 11	Q06124
79	PTPN2	Tyrosine-protein phosphatase nonreceptor type 2	P17706
80	PTPRC	Receptor-type tyrosine-protein phosphatase C	P08575
81	RELA	Transcription factor p65	Q04206
82	SLC6A2	Sodium-dependent noradrenaline transporter	P23975
83	SNCA	Alpha-synuclein	P37840
84	SRC	Protooncogene tyrosine-protein kinase Src	P12931
85	TGM2	Protein-glutamine gamma-glutamyltransferase 2	P21980
86	TLR4	Toll-like receptor 4	O00206
87	TOP1	DNA topoisomerase 1	P11387
88	TRPA1	Transient receptor potential cation channel subfamily A member 1	O75762
89	TYMP	Thymidine phosphorylase	P19971
90	TYMS	Thymidylate synthase	P04818
91	VDR	Vitamin D3 receptor	P11473
92	VEGFA	Vascular endothelial growth factor A	P15692
93	XDH	Xanthine dehydrogenase/oxidase	P47989
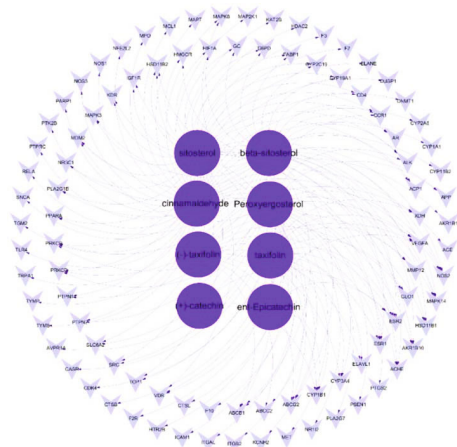
FIGURE 3: The active component-target network. The network formed with 101 nodes and 169 edges. The dark purple circles represented active compounds; the light purple inverted triangles represented intersecting targets. The edges represented the connection between active component and targets.

TABLE 3: Degree value of 8 main active components of Guizhi.

Mol ID	Molecule name	Degree
MOL000358	Beta-sitosterol	37
MOL000359	Sitosterol	37
MOL000991	Cinnamaldehyde	36
MOL011169	Peroxyergosterol	29
MOL001736	(-)-taxifolin	12
MOL004576	Taxifolin	12
MOL000492	(+)-catechin	3
MOL000073	Ent-Epicatechin	3

duplicates were deleted after the predicted targets of the 3 databases were merged.

2.3. Screening of Disease Targets. Using "Nephrotic syndrome" and "Adriamycin Nephropathy" as the keywords, the NS-related targets were collected from DisGeNET, GeneCards, and OMIM databases. After the removal of repeated targets, Venny2.1.0 was used to screening the intersection of drug targets and disease targets to obtain the potential targets of Guizhi in the treatment of NS.

2.4. Construction of Active Component-Target Network. The potential targets were imported into Cytoscape to construct the components-target-network.

2.5. Construction of PPI Network. The PPI network was constructed using the String database and Cytoscape software. In this process, the potential targets were input into the String database to obtain the protein interactions, and the interactions were visualized by Cytoscape software in a form of PPI network.

(a)

(b)
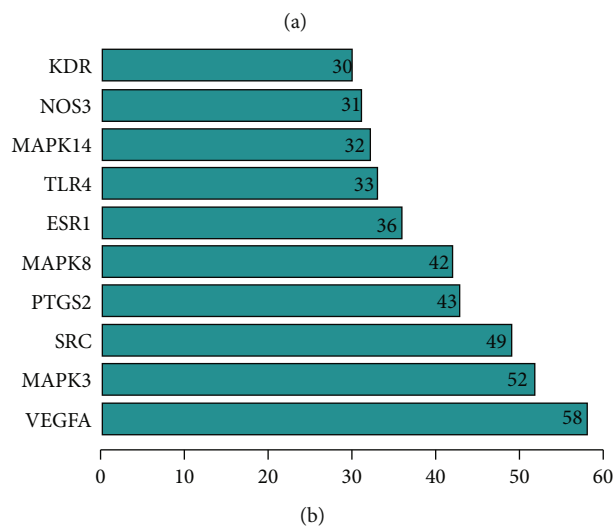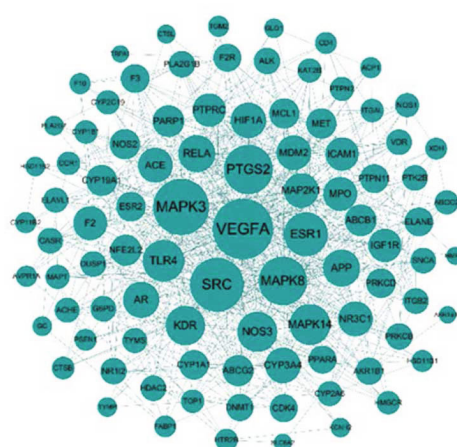
FIGURE 4: The PPI network diagram (a) and the bar graph of the top 10 intersecting targets with degree values in PPI network (b). In PPI network, nodes represented intersecting targets, and edges represented interactions between targets, and the size reflected the value of degree. In the bar graph, the top 10 targets were selected according to the degree value.

2.6. GO and KEGG Pathway Enrichment Analysis. DAVID database was used for GO and KEGG pathway enrichment analysis. The GO and KEGG enriched terms were collected for biological process (BP), cell component (CC), and molecular function (MF), at a cutoff of $P < 0.05$, and the corresponding bubble diagram were drawn.

2.7. Construction of Overall Network. The active compounds of Guizhi, the top 30 KEGG signaling pathways, and the corresponding targets were used to construct the drug-compound-target-pathway-disease network through Cytoscape.

2.8. Molecular Docking. The top 5 important targets with high network connection degrees were selected for molecular docking analysis using Autodock Vina. The smaller the binding energy (affinity) was, the more stable the interaction between the target protein and the active ingredient was.
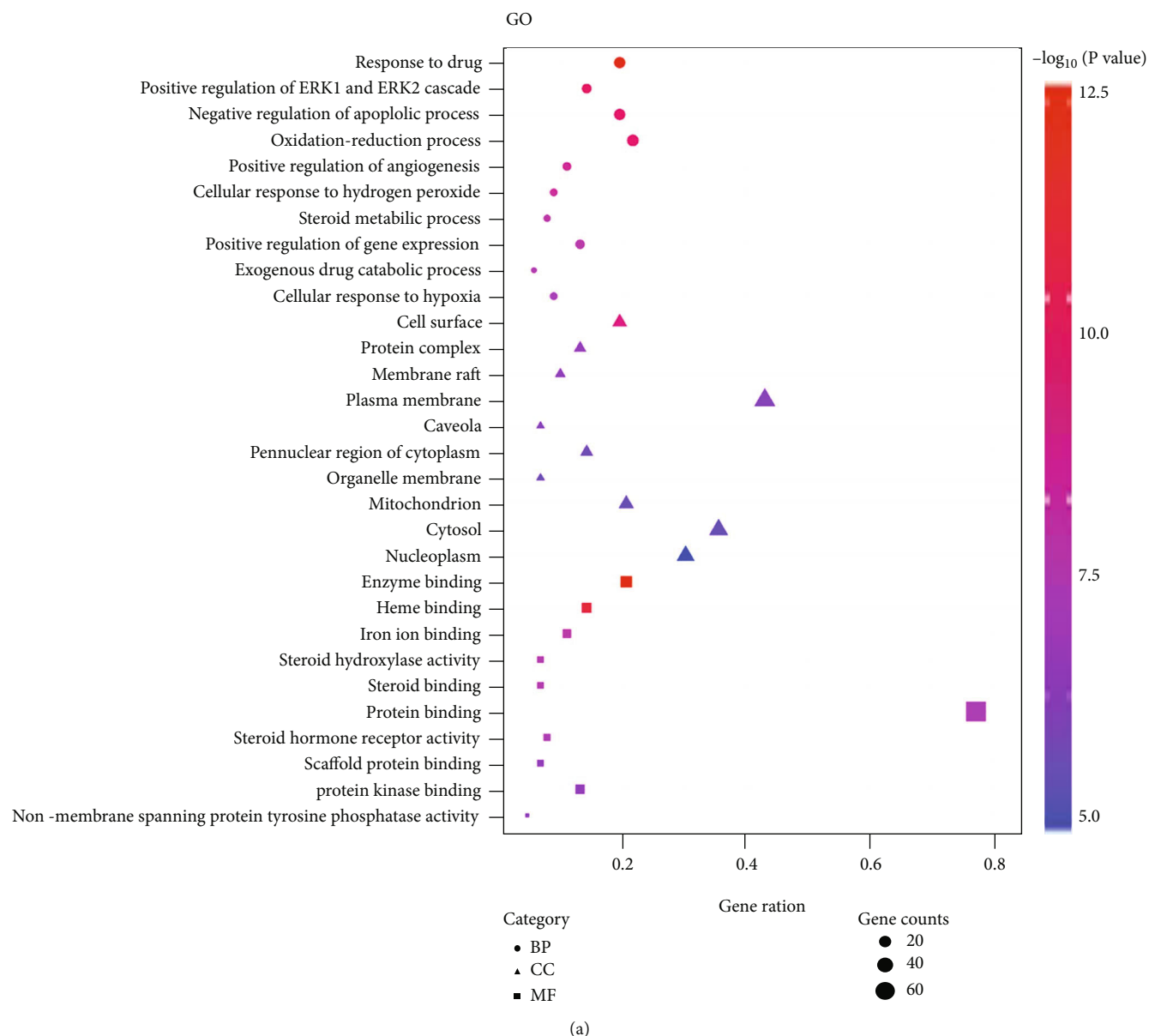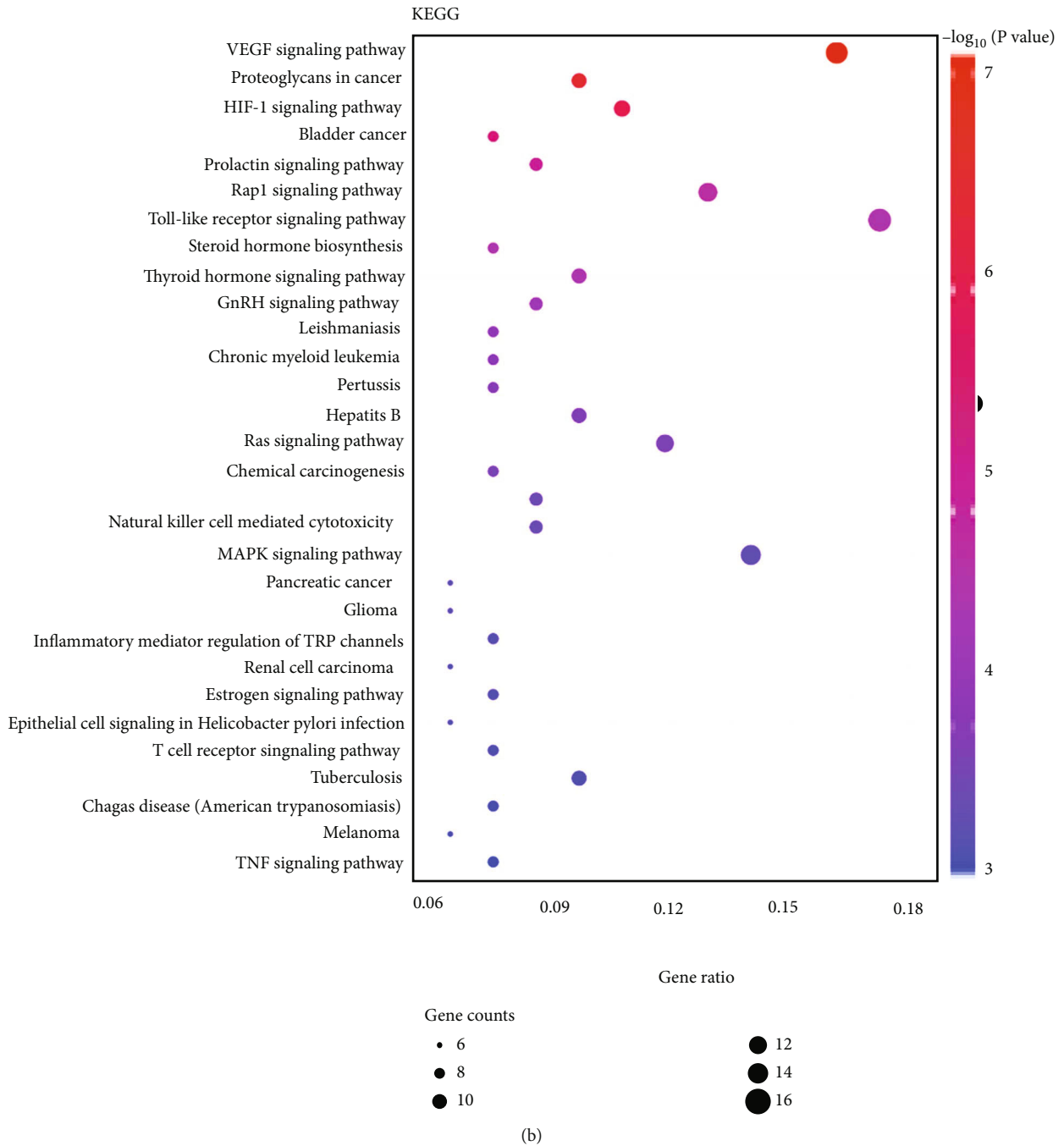
GO

(a)

FIGURE 5: Continued.

FIGURE 5: Go (a) and KEGG enrichment analysis (b). The top 10 items of BP, CC, and MF and the top 30 KEGG signal pathways were selected according to the P value to draw the GO and KEGG bubble diagram. The color of the bubbles changes from purple to red indicating that the P value decreases from large to small. Gene ratio is the number of targets that located in the pathway. The higher the gene ratio is, the more targets were enriched.

3. Results

3.1. Active Compounds of Guizhi. A total of 220 compounds were collected from the TCMSP database, with OB ≥ 30%, DL ≥ 0.18, and Caco − 2 ≥ −0.4, and 7 active compounds were identified. Cinnamaldehyde, OB = 31.99%, DL = 0.02, and Caco − 2 = 1.35, was not included in the results of TCMSP screening. However, our previous study found that cinnamaldehyde might be an important active compound of Guizhi [11]. Therefore, cinnamaldehyde was selected as a candidate active component in this study, as shown in Table 1.

3.2. Drug Target Prediction. 8 active components of Guizhi were input into Hitpick, SEA, and Swiss Target Prediction databases. After combining the predicted targets from the 3 databases, the duplicates were deleted, and a total of 317 potential targets were selected.

3.3. Disease Target Prediction. The keywords "Nephrotic syndrome" and "Adriamycin Nephropathy" were searched in DisGeNET, GeneCards, and OMIM databases. A total of 2125 targets were identified. Venny 2.1.0 was used to intersect disease targets with drug targets. Finally, 93 potential targets (Figure 2) were selected and further confirmed by UniProt database, as shown in Table 2.

3.4. Analysis of Active Component-Target Network. The 93 potential targets were analyzed by Cytoscape to construct the active component-target interaction network (Figure 3). The result included 101 nodes and 169 edges. And different components indicated different targets. Among them, the degree values of beta-sitosterol, sitosterol, cinnamaldehyde, and peroxyergosterol were 37, 37, 36, and 29, respectively (Table 3), which might be the important active components in the network.

3.5. PPI Network Analysis. A total of 93 nodes and 1478 edges were involved in the PPI network (Figure 4(a)). The bar chart of the top 10 target proteins was drawn based on the degree value (Figure 4(b)). Among them, VEGFA, MAPK3, SRC, PTGS2, and MAPK8 degree values were 58, 52, 49, 43, and 42, respectively, which were the core nodes of the network, suggesting that Guizhi might play a significance role in the protection of NS through them.

3.6. GO and KEGG Analysis. 93 potential targets were analyzed using DAVID 6.8, and the GO terms (BP, CC, and MF) and KEGG signaling pathway were selected. Targets in the BP were closely related to response to organic substance and positive regulation of molecular function and response to hormone stimulus. In the CC, Guizhi had great effect on cell surface, cell fraction, and plasma membrane part. At the MF level, drug components of Guizhi were mainly related to steroid binding, heme binding, and tetrapyrrole binding (Figure 5(a)). A total of 71 KEGG pathways were mainly involved, including VEGF, Toll-like receptor, and MAPK signaling pathway (Figure 5(b)).

3.7. Overall Network Analysis. To further investigate the molecular mechanism of Guizhi against NS, overall network
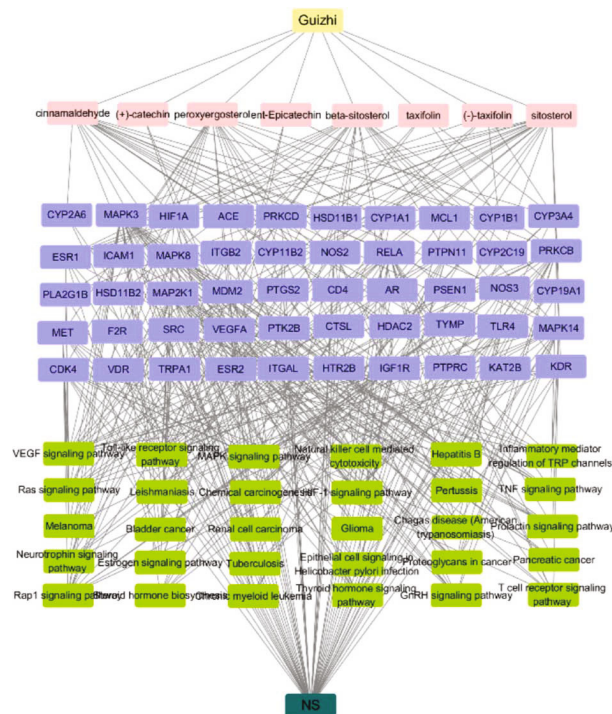

FIGURE 6: The overall network of the top 30 significant KEGG signaling pathways with their corresponding targets. The yellow represents Guizhi, pink represents active compounds, purple represents core targets, green represents signaling pathways, and dark green represents NS.

TABLE 4: The top 5 targets in PPI network.

No.	Target name	PDB ID	Degree
1	VEGFA	6BFT	58
2	MAPK3	2ZOQ	52
3	SRC	6HTY	49
4	PTGS2	5IKV	43
5	MAPK8	4L7F	42

was constructed based on the top 30 significant KEGG signaling pathways and their corresponding targets (Figure 6). 90 nodes (1 drug, 8 compound, 50 targets, 30 pathways, and 1disease) were contained in this network. Among these targets, MAPK3, MAPK8, MAPK14, VEGFA, and TLR4 were identified as high-degree targets, and in these pathways, Toll-like receptor, VEGF, and MAPK signaling pathways were the most important signaling pathways. Therefore, the network analysis suggests that the action mechanism of Guizhi to treat NS might be related to Toll-like receptor, VEGF, and MAPK signaling pathways.

3.8. Molecular Docking. The top 5 targets, including VEGFA, MAPK3, SRC, PTGS2, and MAPK8 (Table 4) in the PPI network were analyzed for the molecular docking with the active compounds of Guizhi. It was found that the top 5 targets had good binding affinity with the active components of Guizhi (Table 5; Figure 7). And the binding site of compounds-targets are shown in Figure 8.

TABLE 5: Molecular docking results of targets and active components.

Target name	PDB ID	Molecule name	Affinity (kcal/Mol)
VEGFA	6BFT	Peroxyergosterol	-6.8
		Beta-sitosterol	-6.4
		Sitosterol	-6.3
		Ent-Epicatechin	-5.9
		(-)-taxifolin	-5.7
		Taxifolin	-5.6
		(+)-catechin	-5.4
		Cinnamaldehyde	-4.9
MAPK3	2ZOQ	(-)-taxifolin	-9.0
		Beta-sitosterol	-8.7
		Taxifolin	-8.5
		(+)-catechin	-8.4
		Peroxyergosterol	-8.1
		Ent-Epicatechin	-7.9
		Sitosterol	-7.3
		Cinnamaldehyde	-5.4
SRC	6HTY	Peroxyergosterol	-8.7
		Beta-sitosterol	-8.5
		Sitosterol	-8.4
		(+)-catechin	-8.1
		Taxifolin	-8.1
		(-)-taxifolin	-7.9
		Ent-Epicatechin	-7.8
		Cinnamaldehyde	-6.6
PTGS2	5IKV	(+)-catechin	-7.6
		Ent-Epicatechin	-7.5
		(-)-taxifolin	-7.3
		Taxifolin	-6.8
		Cinnamaldehyde	-6.1
		Peroxyergosterol	-3.8
		Beta-sitosterol	-3.7
		Sitosterol	-3.7
MAPK8	4L7F	Beta-sitosterol	-9.8
		Sitosterol	-9.8
		(-)-taxifolin	-9.3
		(+)-catechin	-9.1
		Taxifolin	-8.7
		Ent-Epicatechin	-8.5
		Peroxyergosterol	-8.5
		Cinnamaldehyde	-6.0

4. Discussion

NS is a common glomerular disease caused by various etiologies and is the second most common kidney disease after acute glomerulonephritis. At present, Western medicine mainly focuses on glucocorticoids, cytotoxic drugs, and immunosuppressants for NS [1], such as glucocorticoids,
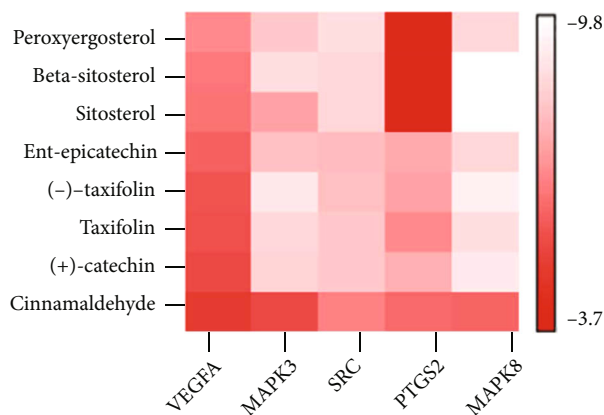
FIGURE 7: The binding energy of the main active components of Guizhi and core targets.

cyclophosphamide, and cyclosporine, which can achieve certain efficacy. However, hormone therapy is prone to infection, hormone resistance [12], withdrawal, and relapse [3], which eventually lead to chronic terminal renal failure [13, 14]. Therefore, to explore the pathogenesis of NS and to find safe and effective treatment drugs are urgent problems [15].

Wulingsan is a classic prescription for NS, which has obvious advantages in improving urinary system diseases. Guizhi is an important component of Wulingsan, which has the pharmacological activities of diuresis, improving blood circulation and dilating blood vessels. Our preliminary study found that Guizhi is indeed an important drug of Wulingsan with the protective effect on rats with adriamycin-induced nephropathy [11]. However, the action mechanism remains unknown.

In order to further explore the potential mechanism of Guizhi in treating NS and provide more evidence for clinical treatment, the main active components and targets of Guizhi, as well as the possible signaling pathways of Guizhi to treat NS, were predicted through network pharmacology and molecular docking.

In the active component-target network, the degree values of beta-sitosterol, sitosterol, cinnamaldehyde, and peroxyergosterol were much higher than those of other components, which were 37, 37, 36, and 29, respectively, suggesting that they were the key active components in the treatment of NS.

Among them, beta-sitosterol and sitosterol belong to plant sterols. Studies have found that beta-sitosterol has antihyperlipemia, anti-inflammatory, and immunomodulatory effects and can treat cholesterol, proteinuria, and edema [16]. Cinnamaldehyde is an organic compound of olefine aldehyde, and it is the main component of Guizhi that plays a diuretic role. Pharmacological studies have shown that cinnamaldehyde has a variety of pharmacological activity of anti-inflammatory [17], antitumor [18], hypotensive [19], lipid-lowering [20], hypoglycemic [21], and vascular endothelial protection [22], that is playing a protective role on kidney in various aspects. Our previous study also found that cinnamaldehyde had a protective effect on renal function in adriamycin nephropathy rat [11]. Peroxyergosterol is a kind of relatively rare sterol, with antioxidant [23],
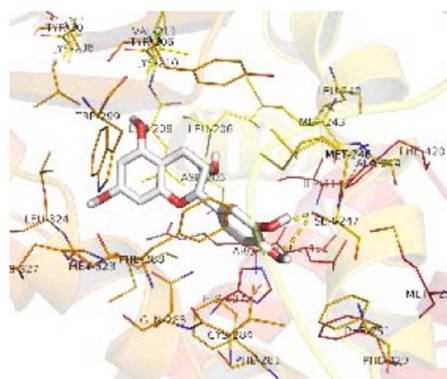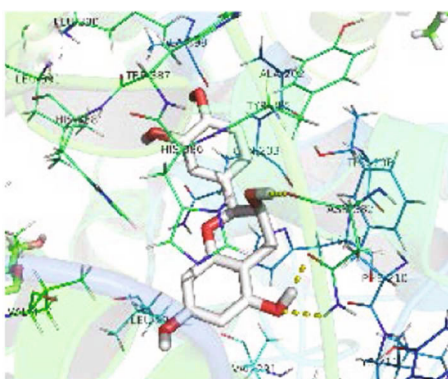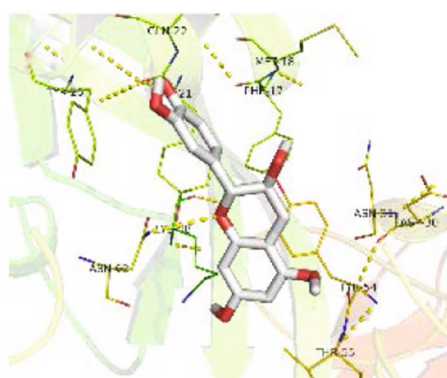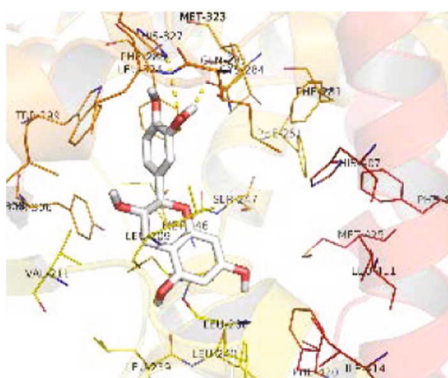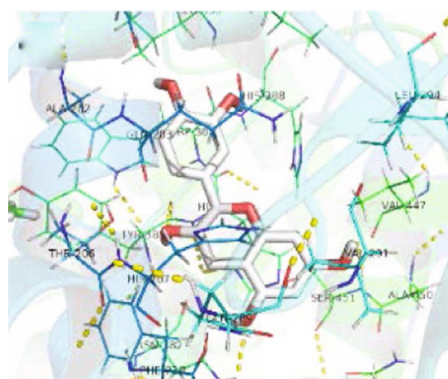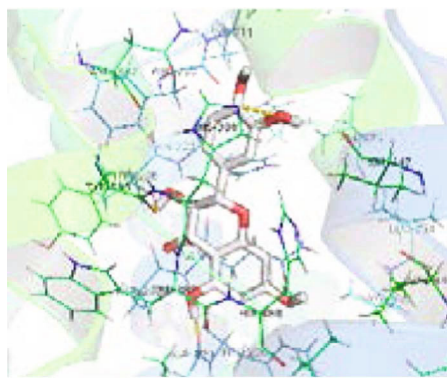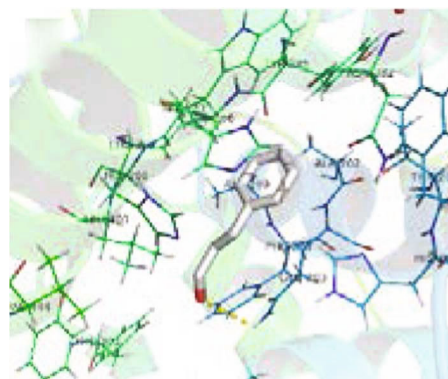
(a)

(b)

(c)

(d)

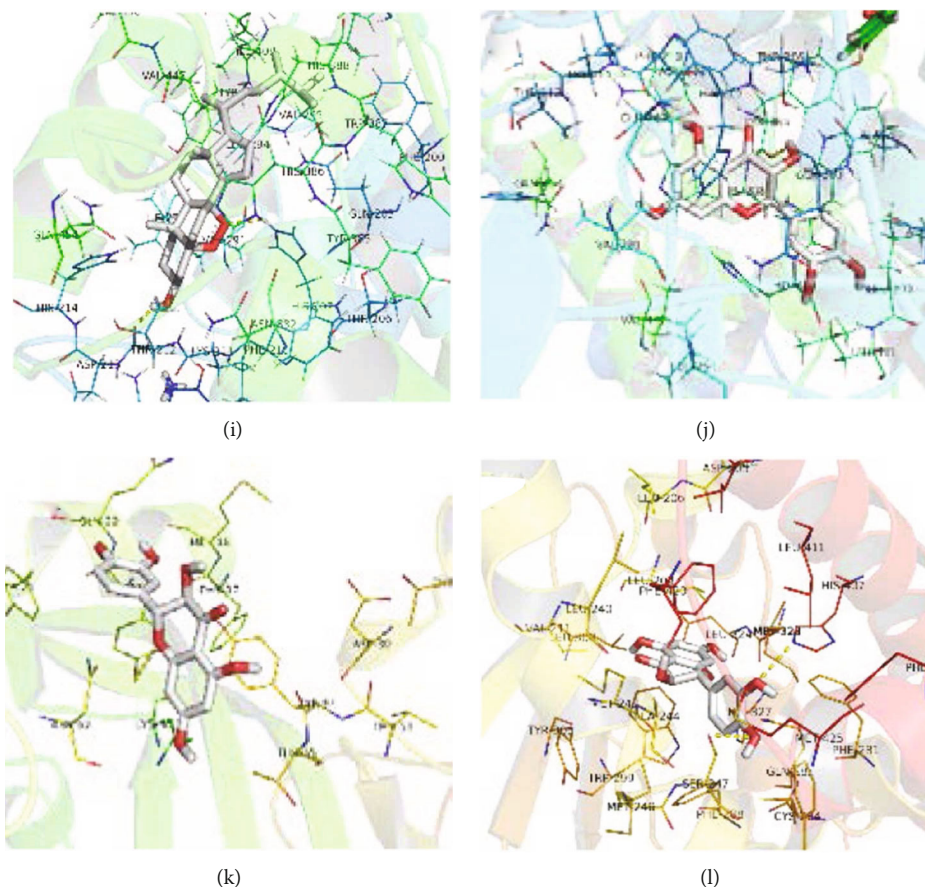

(e)

(f)

(g)

(h)
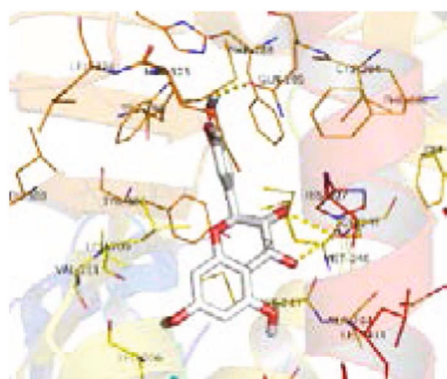
Figure 8: Continued.

FIGURE 8: The molecular docking of active compounds and core targets: (a) cinnamaldehyde-PTGS2, (b) (-)-taxifolin-PTGS2, (c) (+)-catechin-PTGS2, (d) (-)-taxifolin-VEGFA, (e) (+)-catechin-SRC, (f) (+)-catechin-VEGFA, (g) ent-Epicatechin-PTGS2, (h) ent-Epicatechin-SRC, (i) peroxyergosterol-PTGS2, (j) taxifolin-PTGS2, (k) taxifolin-VEGFA, and (l) taxifolin-SRC.

antibacterial [24], immunosuppressive [25], antitumor [26], and other activities and can repair damaged kidney cells through antioxidant action. In conclusion, beta-sitosterol, sitosterol, cinnamaldehyde, and peroxyergosterol might be the main pharmacodynamic basis of Guizhi against NS.

In the PPI network, VEGFA, MAPK3, SRC, PTGS2, and MAPK8 had higher degrees than others, indicating that Guizhi might achieve the protective effect on the kidney through the above targets.

VEGFA is a receptor in vascular endothelial cells that can induce endothelial cell differentiation and proliferation [27]. It is an important molecule that maintains the function of the glomerular filtration barrier and plays an important role in renal microangiogenesis. The study has shown that the upregulation of VEGF expression is closely related to the occurrence of proteinuria [28]. Its signal conduction runs through the whole life process of podocytes and glomerular vascular endothelial cells. MAPK3 and MAPK8 are both mitogen-activated protein kinases that can mediate the progress of differentiation, proliferation, and apoptosis [29, 30]. SRC is a nonreceptor protein with tyrosine protein kinase activity and plays an important role in mitosis and proliferation in normal cell [31, 32]. SRC can participate in the process of cell differentiation, proliferation, and apoptosis through the MAPK signaling pathway and plays a crucial

role in the inflammation and autoimmune diseases. PTGS2 is significant in inhibiting the development of excessive fibrosis and inflammatory response. When cells are stimulated, the expression of PTGS2 is rapidly upregulated, which catalyzes arachidonic acid to produce a variety of prostaglandins and produces anti-inflammatory and antifibrotic effects, thus achieving the protective effect on the kidney [33]. Therefore, the targets of VEGFA, MAPK3, SRC, PTGS2, and MAPK8 might play an essential role in the protective effect of Guizhi against NS.

In KEGG and overall network analysis, the key targets were mainly involved in VEGF, Toll-like receptor, and MAPK signaling pathway, which were highly correlated with renal disease, suggesting that the action mechanism of Guizhi to treat NS might be related to VEGF, Toll-like receptor, and MAPK signaling pathways.

VEGF signaling pathway plays an irreplaceable role in the whole process of angiogenesis and is directly related to the occurrence of hypertension. When the endothelial function of patients with hypertensive is impaired, blood pressure will significantly increase, and proteinuria is aggravated. Studies have found that the inhibition of VEGF signaling pathway can lead to large amounts of proteinuria accompanied by irreversible renal impairment [34]. In recent years, the role of the innate immune Toll-like receptor

(TLR) in kidney disease has attracted more and more attention [35] and is involved in the innate immune and inflammatory response [36]. Studies have shown that TLR can be expressed in a small amount in renal mesangial cells, renal tubular epithelial cells, and podocytes [37]. The increase of TLR expression can cause the pathophysiological changes such as the upregulation of inflammatory factors and cell apoptosis [38]. MAPK signaling pathway is a stress pathway of cellular functional activities, plays a vital role in acute and chronic inflammation, and participates in physiological processes such as cell growth, development, differentiation, and apoptosis [39]. Activation of MAPK signaling pathway can not only trigger renal inflammation [40] but also lead to podocyte injury [41]. Studies have shown that MAPK signaling pathway can cause proteinuria and glomerulosclerosis through oxidative stress, triggering inflammatory factors and activating inflammatory pathways [42]. Munkonda et al. found that MAPK can also promote proximal tubule fibrosis, thus mediating the development of renal disease [43].

Based on the network pharmacology results, molecular docking was performed to verify the interactions between the 8 active components of Guizhi and the key targets. The docking results showed that all the compounds had good binding activities with the targets, indicating that they may play an important role in Guizhi to treat NS.

5. Conclusion

In conclusion, the potential mechanism of Guizhi to treat NS was predicted based on the network pharmacology and molecular docking. The results indicated that the underlying mechanism of Guizhi in treating NS may be related to VEGF, Toll-like receptor, and MAPK signaling pathway. However, the transmission of each signal pathway is complicated, and the final mechanism needs to be further verified by subsequent experiments.

Data Availability

The data used to support the findings of this study are included within the article.

Conflicts of Interest

The authors declare that there is no conflict of interests.

Authors' Contributions

Dan He designed the study. Dan He, Qiang Li, and Jijia Sun performed the data analysis. Guangli Du, Guofeng Meng, and Shaoli Chen modified the manuscript. All authors have read and approved the final manuscript.

Acknowledgments

References

[1] R. G. Krishnan, "Nephrotic syndrome," *Paediatrics and Child Health*, vol. 22, no. 8, pp. 337–340, 2012.

[2] S. S. Shah, N. Akhtar, F. Sunbleen, M. F. ur Rehman, and T. Ahmed, "Histopathological patterns in paediatric idiopathic steroid resistant nephrotic syndrome," *Journal of Ayub Medical College, Abbottabad: JAMC*, vol. 27, no. 3, pp. 633–636, 2015.

[3] S. Aaltonen and E. Honkanen, "Outcome of idiopathic membranous nephropathy using targeted stepwise immunosuppressive treatment strategy," *Nephrology, Dialysis, Transplantation*, vol. 26, no. 9, pp. 2871–2877, 2011.

[4] Y. X. Gao, P. Q. Zhang, and Q. Zhang, "Professor Zhang Qi's experience in treating refractory nephrotic syndrome edema with "tong"," *Chinese Journal of Integrated Traditional and Western Nephrology*, vol. 5, no. 8, pp. 663-664, 2014.

[5] X. L. Zhang, C. H. Liu, H. J. Li, M. Tian, L. J. Wu, and G. H. Cao, "Effect of Guizhifuling Decoction combined with hormone on primary nephrotic syndrome in children and its effect on serum inflammatory factors," *Shaanxi Journal of Traditional Chinese Medicine*, vol. 39, no. 11, pp. 1609–1612, 2018.

[6] R. Z. Jin, R. H. Yu, H. Gao, C. X. Yang, F. Fang, and J. N. Wang, "Clinical control study of Wuling SAN and Wuling Tang in treating nephrotic syndrome with internal stasis of water and dampness," *Journal of Traditional Chinese Medicine*, vol. 53, no. 7, pp. 572-573, 2012.

[7] S. Li and B. Zhang, "Traditional Chinese medicine network pharmacology: theory, methodology and application," *Chinese Journal of Natural Medicines*, vol. 11, no. 2, pp. 110–120, 2013.

[8] D. J. Barlow, A. Buriani, T. Ehrman, E. Bosisio, I. Eberini, and P. J. Hylands, "In-silico studies in Chinese herbal medicines ' research: evaluation of in- silico methodologies and phytochemical data sources, and a review of research to date," *Journal of Ethnopharmacology*, vol. 140, no. 3, pp. 526–534, 2012.

[9] W. Dai, J. X. Chen, P. Lu et al., "Pathway pattern-based prediction of active drug components and gene targets from H1N1 influenza's treatment with maxingshigan-yinqiaosan formula," *Molecular BioSystems*, vol. 9, no. 3, pp. 375–385, 2013.

[10] J. J. Sun, T. Han, T. Yang, Y. Chen, and J. Huang, "Interpreting the molecular mechanisms of Yinchenhao decoction on hepatocellular carcinoma through absorbed components based on network pharmacology," *BioMed Research International*, vol. 2021, Article ID 6616908, 22 pages, 2021.

[11] Q. X. Zhang, S. L. Chen, X. P. Wen, and G. L. Du, "Effect of Guizhi, the main drug of Wulingsan, on the renal protection of rats with adriamycin nephropathy," *Journal of Traditional Chinese Medicine*, vol. 60, no. 2, pp. 65–69, 2019.

[12] T. Saito, "Treatment and prognosis of idiopathic membranous nephropathy in guidelines for nephrotic syndrome," *Nihon Jinzo Gakkai Shi*, vol. 53, no. 5, pp. 708–712, 2011.

[13] R. M. Lombel, D. S. Gipson, and E. M. Hodson, "Treatment of steroid-sensitive nephrotic syndrome: new guidelines from KDIGO," *Pediatric Nephrology*, vol. 28, no. 3, pp. 415–426, 2013.

[14] W. Wong, "Idiopathic nephrotic syndrome in New Zealand children, demographic, clinical features, initial management and outcome after twelve-month follow-up: results of a three-year national surveillance study," *Journal of Paediatrics and Child Health*, vol. 43, no. 5, pp. 337–341, 2007.

[15] K. U. Eckardt, J. Coresh, O. Devuyst et al., "Evolving importance of kidney disease: from subspecialty to global health burden," *Lancet*, vol. 382, no. 9887, pp. 158–169, 2013.

[16] P. J. Jones, F. Y. Ntanios, M. Raeini-Sarjaz, and C. A. Vanstone, "Cholesterol-lowering efficacy of a sitostanol-containing phytosterol mixture with a prudent diet in hyperlipidemic men," *The American Journal of Clinical Nutrition*, vol. 69, no. 6, pp. 1144–1150, 1999.

[17] B. H. Kim, Y. G. Lee, J. Lee, J. Y. Lee, and J. Y. Cho, "Regulatory effect of cinnamaldehyde on monocyte/macrophage-mediated inflammatory responses," *Mediators of Inflammation*, vol. 2010, Article ID 529359, 9 pages, 2010.

[18] L. T. Lin, C. J. Tai, S. P. Chang, J. L. Chen, S. J. Wu, and C. C. Lin, "Cinnamaldehyde-induced apoptosis in human hepatoma PLC/PRF/5 cells involves the mitochondrial death pathway and is sensitive to inhibition by cyclosporin A and z-VAD-fmk," *Anti-Cancer Agents in Medicinal Chemistry*, vol. 13, no. 10, pp. 1565–1574, 2013.

[19] Y. Yao, H. Y. Huang, Y. X. Yang, and J. Y. Guo, "Cinnamic aldehyde treatment alleviates chronic unexpected stress-induced depressive-like behaviors via targeting cyclooxygenase-2 in mid-aged rats," *Journal of Ethnopharmacology*, vol. 162, pp. 97–103, 2015.

[20] B. Huang, H. D. Yuan, D. Y. Kim, H. Y. Quan, and S. H. Chung, "Cinnamaldehyde prevents adipocyte differentiation and adipogenesis via regulation of peroxisome proliferator-activated receptor-γ (PPARγ) and AMP-activated protein kinase (AMPK) pathways," *Journal of Agricultural and Food Chemistry*, vol. 59, no. 8, pp. 3666–3673, 2011.

[21] A. Nikzamir, A. Palangi, A. Kheirollaha et al., "Expression of glucose transporter 4 (GLUT4) is increased by cinnamaldehyde in C2C12 mouse muscle cells," *Iranian Red Crescent Medical Journal*, vol. 16, no. 2, pp. 1–5, 2014.

[22] F. Wang, C. H. Pu, P. Zhou et al., "Cinnamaldehyde prevents endothelial dysfunction induced by high glucose by activating nrf2," *Cellular Physiology and Biochemistry*, vol. 36, no. 1, pp. 315–324, 2015.

[23] S. W. Kim, S. S. Park, T. J. Min, and K. H. Yu, "Antioxidant activity of ergosterol peroxide (5,8-epidioxy-5a,8a-ergosta-6,22E-dien-3bo1) in Armillariella mellea," *Bulletin of the Korean Chemical Society*, vol. 20, no. 7, pp. 819–823, 1999.

[24] T. Akihisa, S. G. Franzblau, H. Tokuda et al., "Antitubercular activity and inhibitory effect on Epstein-Barr virus activation of sterols and polyisoprenepolyols from an edible mushroom, Hypsizigus marmoreus," *Biological and Pharmaceutical Bulletin*, vol. 28, no. 6, pp. 1117–1119, 2005.

[25] Y. C. Kuo, S. C. Weng, C. J. Chou, T. T. Chang, and W. J. Tsai, "Activation and proliferation signals in primary human T lymphocytes inhibited by ergosterol peroxide isolated fromCordyceps cicadae," *British Journal of Pharmacology*, vol. 140, no. 5, pp. 895–906, 2003.

[26] T. Takei, M. Yoshida, M. Ohnishi-Kameyama, and M. Kobori, "Ergosterol peroxide, an apoptosis-inducing component isolated fromSarcodon aspratus(Berk.) S. Ito," *Bioscience, Biotechnology, and Biochemistry*, vol. 69, no. 1, pp. 212–215, 2005.

[27] Y. Hirata, D. Nagata, E. Suzuki, H. Nishimatsu, J. I. Suzuki, and R. Nagai, "Diagnosis and treatment of endothelial dysfunction in cardiovascular disease a review," *International Heart Journal*, vol. 51, no. 1, pp. 1–6, 2010.

[28] V. Eremina, M. Sood, J. Haigh et al., "Glomerular-specific alterations of VEGF-A expression lead to distinct congenital and acquired renal diseases," *Journal of Clinical Investigation*, vol. 111, no. 5, pp. 707–716, 2003.

[29] J. V. Michael, J. G. Wurtzel, and L. E. Goldfinger, "Regulation of H-Ras-driven MAPK signaling, transformation and tumorigenesis, but not PI3K signaling and tumor progression, by plasma membrane microdomains," *Oncogene*, vol. 5, no. 5, pp. e228–e228, 2016.

[30] A. Plotnikov, E. Zehorai, S. Procaccia, and R. Seger, "The MAPK cascades: signaling components, nuclear roles and mechanisms of nuclear translocation," *Biochimica et Biophysica Acta*, vol. 1813, no. 9, pp. 1619–1633, 2011.

[31] M. Warmuth, R. Damoiseaux, Y. Liu, D. Fabbro, and N. Gray, "Src family kinases: potential targets for the treatment of human cancer and leukemia," *Current Pharmaceutical Design*, vol. 9, no. 25, pp. 2043–2059, 2003.

[32] J. B. Cordero, R. A. Ridgway, N. Valeri et al., "c-Src drives intestinal regeneration and transformation," *The EMBO Journal*, vol. 33, no. 13, pp. 1474–1491, 2014.

[33] K. A. Bauman, S. H. Wettlaufer, K. Okunishi et al., "The antifibrotic effects of plasminogen activation occur via prostaglandin E2 synthesis in humans and mice," *The Journal of Clinical Investigation*, vol. 120, no. 6, pp. 1950–1960, 2010.

[34] D. Takahashi, K. Nagahama, Y. Tsuura, H. Tanaka, and T. Tamura, "Sunitinib-induced nephrotic syndrome and irreversible renal dysfunction," *Clinical and Experimental Nephrology*, vol. 16, no. 2, pp. 310–315, 2012.

[35] B. Z. Zhang, G. Ramesh, S. Uematsu, S. Akira, and W. B. Reeves, "TLR4 signaling mediates inflammation and tissue injury in nephrotoxicity," *Journal of the American Society of Nephrology*, vol. 19, no. 5, pp. 923–932, 2008.

[36] S. Khakpour, K. Wilhelmsen, and J. Hellman, "Vascular endothelial cell toll-like receptor pathways in sepsis," *Innate Immunity*, vol. 21, no. 8, pp. 827–846, 2015.

[37] A. Gluba, M. Banach, S. Hannam, D. P. Mikhailidis, A. Sakowicz, and J. Rysz, "The role of Toll-like receptors in renal diseases," *Nature Reviews. Nephrology*, vol. 6, no. 4, pp. 224–235, 2010.

[38] H. Kaur, A. Chien, and I. Jialal, "Hyperglycemia induced toll like receptor 4 expression and activity in mesangial cells: relevance to diabetic nephropathy," *American Journal of Physiology. Renal Physiology*, vol. 303, no. 8, pp. 1145–1150, 2012.

[39] K. C. Wu, K. S. Cheng, Y. W. Wang et al., "Perturbation of Akt signaling, mitochondrial potential, and ADP/ATP ratio in acidosis-challenged rat cortical astrocytes," *Journal of Cellular Biochemistry*, vol. 118, no. 5, pp. 1108–1117, 2017.

[40] E. J. Park, S. W. Park, H. J. Kim, J. H. Kwak, D. U. Lee, and K. C. Chang, "Dehydrocostuslactone inhibits LPS-induced inflammation by p38MAPK-dependent induction of hemeoxygenase-1 in vitro and improves survival of mice in CLP- induced sepsis in vivo," *International Immunopharmacology*, vol. 22, no. 2, pp. 332–340, 2014.

[41] S. Yoshida, M. Nagase, S. Shibata, and T. Fujita, "Podocyte injury induced by albumin overload in vivo and in vitro: involvement of TGF-beta and p38 MAPK," *Nephron. Experimental Nephrology*, vol. 108, no. 3, pp. e57–e68, 2008.

[42] F. A. Hakim and A. Pflueger, "Role of oxidative stress in diabetic kidney disease," *Medical Science Monitor*, vol. 16, no. 2, pp. 37–48, 2010.

[43] M. N. Munkonda, S. Akbari, C. Landry et al., "Podocyte-derived microparticles promote proximal tubule fibrotic signaling via p38 MAPK and CD36," *Journal of Extracellular Vesicles*, vol. 7, no. 1, pp. 1–12, 2018.

Research Article

Green Biosynthesis, Antioxidant, Antibacterial, and Anticancer Activities of Silver Nanoparticles of *Luffa acutangula* Leaf Extract

Devi Nallappan [ID],[1,2] Agustine Nengsih Fauzi [ID],[3] Balam Satheesh Krishna [ID],[4] Basivi Praveen Kumar [ID],[5] Avula Vijaya Kumar Reddy [ID],[6] Tasqeeruddin Syed [ID],[7] Cirandur Suresh Reddy [ID],[4] Nik Soriani Yaacob [ID],[3] and Pasupuleti Visweswara Rao [ID][1,8,9,10]

[1]*Bioindustrial Technology Program, Faculty of Agro-Based Industry, Universiti Malaysia Kelantan, Campus Jeli, 17600 Jeli, Malaysia*
[2]*Department of Biomedical Science, Faculty of Medicine, University of Malaya, 50603 Kuala Lumpur, Malaysia*
[3]*Department of Chemical Pathology, School of Medical Sciences, Universiti Sains Malaysia, 16150 Kubang Kerian, Kelantan, Malaysia*
[4]*Department of Chemistry, Sri Venkateswara University, -517502, Tirupati, Andhra Pradesh, India*
[5]*Department of Biochemistry, Sri Kadiri Babu Rao College of Agriculture, C.S. Puram, Andhra Pradesh-523112, India*
[6]*Centre for Chemical Sciences and Technology, Institute of Science & Technology, Jawaharlal Nehru Technological University Hyderabad, -500085, Hyderabad, Telangana, India*
[7]*Department of Pharmaceutical Chemistry, College of Pharmacy, King Khalid University, Abha-61421, Saudi Arabia*
[8]*Department of Biomedical Science and Therapeutics, Faculty of Medicine and Health Sciences, Universiti Malaysia Sabah, Kota Kinabalu 88400, Malaysia*
[9]*Department of Biochemistry, Faculty of Medicine and Health Sciences, Abdurrab University, Jl Riau Ujung No. 73, Pekanbaru, 28292 Riau, Indonesia*
[10]*Centre for Excellence in Biomaterials Engineering (CoEBE), AIMST University, 08100 Bedong, Kedah, Malaysia*

Correspondence should be addressed to Nik Soriani Yaacob; niksoriani@usm.my
and Pasupuleti Visweswara Rao; pvrao@ums.edu.my

Studies on green biosynthesis of newly engineered nanoparticles for their prominent medicinal applications are being the torch-bearing concerns of the state-of-the-art research strategies. In this concern, we have engineered the biosynthesized *Luffa acutangula* silver nanoparticles of flavonoid *O*-glycosides in the anisotropic form isolated from aqueous leave extracts of *Luffa acutangula*, a popular traditional and ayurvedic plant in south-east Asian countries. These were structurally confirmed by Ultraviolet-visible (UV-Vis), Fourier transform infrared spectroscopy accessed with attenuated total reflection (FTIR-ATR) spectral analyses followed by the scanning electron microscopic (SEM) and the X-ray diffraction (XRD) crystallographic studies and found them with the face-centered cubic (*fcc*) structure. Medicinally, we have explored their significant antioxidant (DPPH and ABTS assays), antibacterial (disc diffusion assay on *E. coli*, *S. aureus*, *B. subtilis*, *S. fecilis*, and *S. boydii*), and anticancer (MTT assay on MCF-7, MDA-MB-231, U87, and DBTRG cell lines) potentialities which augmented the present investigation. The molecular docking analysis of title compounds against 3NM8 (DPPH) and 1DNU (ABTS) proteins for antioxidant activity; 5FGK (Gram-Positive Bacteria) and 1AB4 (Gram-Negative Bacteria) proteins for antibacterial activity; and 4GBD (MCF-7), 5FI2 (MDA-MB-231), 1D5R (U87), and 5TIJ (DBTRG) proteins for anticancer activity has affirmed the promising ligand-protein binding interactions among the hydroxy groups of the title compounds and aspartic acid of the concerned enzymatic proteins. The binding energy varying from -9.1645 to -7.7955 for Cosmosioside (1, Apigenin-7-glucoside) and from -9.2690 to -7.8306 for Cynaroside (2, Luteolin-7-glucoside) implies the isolated compounds as potential bioactive compounds. In addition, the performed studies like QSAR, ADMET, bioactivity properties, drug scores, and toxicity risks confirmed them as potential drug candidates and aspartic acid receptor antagonists. This research auxiliary augmented the existing array of phytological nanomedicines with new drug candidates that are credible with multiple bioactivities.

1. Introduction

Phytological origin is the main source for many flavonoids and corresponding flavonoid O-glycosides (FOGs) [1]; these FOGs are proven antioxidant [2], antimicrobial [3], anticancer [4], antiobesity [5], and medicinal agents [6]. The collective advances of FOGs concerning nanotechnology have emerged as a new arena that captivating medicinal researchers to pursue research in it [7, 8]. As acclaimed *in vivo* oxidation being identified as a vital process that spawns the ample energy for the proper execution of biological processes in all organisms, often, it causes the overproduction of free radicals in turn for the cell damage and in turn for the metabolic diseases like diabetes, cardiovascular diseases, cancers, and neurological disorders [9, 10]. In its counter administration, antioxidants inhibit the reactive free radicals by neutralizing and arrest the structural disruption of biomolecules in cells [11].

During so, the distinguished biosynthesized phytological nanoparticles (NPs) are identified more remarkable than their plant extracts in exhibiting potential activity [12]. This has fascinated nanotechnology in embodiment with scientific results that abridged the gap between with atomic/molecular structures and bulk materials and accelerated the chemotherapeutic potency in treating various diseases [13, 14]. Structurally, the surface-to-volume ratio of NPs is contrarily proportional to their sizes, [15] more precisely the inherent potential of silver nanoparticles (AgNPs) grows reciprocally with an escalation in the specific surface area owing to high surface energy and catalytic reactivity [16]. The preference and advancement of green chemistry over conventional are due to eco-friendliness, cost-effectiveness, and feasibility for large-scale synthesis [16, 17]. The extensive array of AgNPs with medicinal efficacies like anticancer, [18, 19], antioxidants [20], and antimicrobial [21] abilities is derived from various plant origins like *Rhinacanthus nasutus* [22], *Trigonella foenum-graecum* [23], *Ocimum bacillicum* [24], *Vitex negundo L* [25], *Hypnea musciformis (Wulfen) JV lamouroux* [26], *Terminalia chebula* [27], *Raphanus sativus* var. *aegyptiacus* [28], *Citrus sinensis* [29], *Cassia roxburghii* [30], *Eurocyma longifolia* [31], *Annona muricata* [32], and *Eriobotrya japonica* [33].

It is profound that excessive usage of antibiotics results in dissemination and emergence of multidrug-resistant strains of several types of microorganisms [31, 34]. In this scenario, the needs and demands to discover new medicinal agents are increasing, and nanotechnology paves ways to synthesize NPs to substitute current antibiotics and other synthetic agents. In such, *Luffa acutangula* (*LA*), a traditional perennial flowering climber plant, ordinarily stated as ridge gourd regards to *Cucurbitaceae* family and is enriched with medicinal properties [35] like antioxidant, antidiabetic, antiproliferative, antiangiogenic, anticataleptic, analgesic, antiulcer, and antimicrobial activities [36, 37].

As LA plant parts are enriched with a large number of pharmacologically active phytochemicals like flavonoids, proteins, saponin triterpene, anthraquinones, fatty acids, and other phytoconstituents, it is ethnopharmacologically used to treat hemorrhoids, leprosy, splenitis, and ringworm infections by topical administration of pulverized leaves of LA [38]. Hence, we synthesised LAAgNPs from the leaf extract of LA and succeeded in synthesising AgNPs. The flavonoids present in leaves *viz.*, Cosmosioside (1, Apigenin-7-glucoside), Cynaroside (2, Luteolin-7-glucoside) with potential antioxidant, antibacterial, and anticancer activities are FOGs originated from O-glycosidic linkage of (2ξ)-β-D-arabino-Hexopyranose with 7-OH group of Apigenin and O-glycosidic linkage of β-D-glucopyranose with 7-OH group of Luteolin (Figure 1).

2. Materials and Methods

2.1. Chemistry. Silver nitrate ($AgNO_3$) and 2, 2-diphenyl-1-picrylhydrazyl (DPPH) were procured from Sigma (St. Louis, Missouri MO, United States). All the other chemicals were of analytical grade. Human glioma cells (DBTRG and U87) and human breast adenocarcinoma cells (MCF-7 and MDA-MB-231) were procured from the American Type Cell Culture (ATCC). The media, serum, and antibiotics were procured from Gibco™ (Melbourne, Australia).

2.2. Collection of Plant Materials. Fresh leaves of LA were collected from the botanical garden, Department of Botany, Universiti Malaysia Kelantan, Campus Jeli, Malaysia. The collected plant material was rinsed under running tap water to remove all attached materials. The plants and its components have been collected according to the guidelines.

2.3. Preparation of Plant Extract and Synthesis of LAAgNPs. The leaves were shade dried and powdered. Three different concentrations of leaf extracts were prepared (1.0, 2.5, and 5.0%). The mixture was boiled in water bath continuously for 30 min at 100°C and filtered through Whatman No. 1 filter paper, and the same filtrate was used as reducing agent during the nanoparticle synthesis. A stock solution of 1 mM $AgNO_3$ was prepared. LA leaf extracts (25 mL) were added to 25 mL of $AgNO_3$ solution in 1 : 1 ratio in the dark conditions. The colour changes and was observed from light colour to dark colour, and the synthesis of nanoparticle was confirmed by using UV-Vis spectroscopy. The solution was centrifuged at 8000 rpm for 10 min. The pellets of formed silver nanoparticles were dried and powdered for further use.

2.4. Characterization of LAAgNPs. The solution that contained colloidal silver nanoparticles was diluted 10 fold using into distilled water. The reduction of pure silver ions was monitored in the range of 200-700 nm in the visible region by measuring the UV-Vis spectrum of the colloidal solution obtained at different functional time. The crystallization nature of the silver nanoparticles was analysed by using XRD crystallography. The functional groups associated with silver nanoparticles analysis were done by FTIR-ATR spectroscopy. The FTIR spectrum was measured at the adsorption range of 500-4000 cm^{-1}. The particle size was determined by using scanning electron microscope (SEM). The thin layer of synthesised silver nanoparticles was mounted on a copper grid coated with carbon. The extra solution was removed by using blotting paper. Lastly, the

Cosmosioside (1, Apigenin-7-glucoside)

Cynaroside (2, Luteolin-7-glucoside)

FIGURE 1: Potential natural FOGs (1 and 2) identified in *Luffa acutangula* (LA) leaves.

Formation of silver nanoparticles

AgNO₃

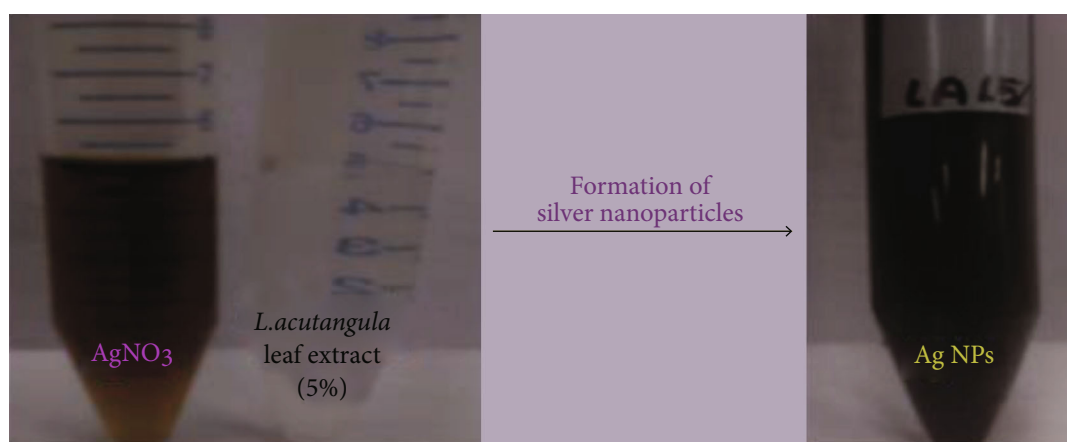*L.acutangula* leaf extract (5%)

Ag NPs

FIGURE 2: Formation of silver nanoparticles using 5% of *LA* leaf extract.

thin film on the SEM grid was placed under mercury lamp for 5 min for complete drying purpose.

2.5. Antioxidant Activity

2.5.1. DPPH Antioxidant Assay. Different concentrations (50, 100, 150, 200, 250, and 300 μg/mL) of LAAgNPs and plant extracts were prepared from the stock solution through serial dilution (1 mg/mL). The mixture was incubated for 30 min at rt. The decrease in absorbance reading was measured at 517 nm using spectrophotometer. Ascorbic acid (3), which is known as an antioxidant was used as reference standard. The assay was performed in triplicate. The free radical scavenging activity was calculated as the percentage inhibition.

$$\text{Free radical scavenging activity\%} = \frac{\left[\left(A_{\text{Control}} - A_{\text{Sample}}\right)\right]}{\left(A_{\text{Control}}\right)} \times 100.$$

(1)

2.5.2. ABTS Antioxidant Assay. The final reaction mixture (1 mL) of standard and extracts comprised of 950 μL of ABTS solution and 50 μL of the sample. This reaction solution was vortexed for 10 sec. The UV-Vis readings were taken at 734 nm to measure absorbance, the result was compared with control ABTS solution, ascorbic acid (3) was used as reference standard, and the percentage inhibition was calculated (Equation (1)).

2.6. Antibacterial Activity. *In vitro* antibacterial activity of synthesised nanoparticles and leaf extracts was analysed by Kirby-Bauer technique. Here, three Gram-positive bacteria (*Bacillus subtilis*, *Staphylococcus aureus*, and *Streptococcus*) and two Gram-negative bacteria (*Escherichia coli* and *Shigella boydii*) were used for antibacterial assay. Initially, 20 μL of both plant extracts and silver nanoparticles was pipetted into 6 mm of sterile antibacterial discs. The impregnated discs were left to dry at 30°C for 30 min. Prepared bacterial suspension solution was spread on NA agar by using sterile cotton swab, then dried the infused sterile discs with plant extracts; and silver nanoparticles were placed on NA agar. The plates were left to incubate at rt for 24 h, and ampicillin (4) was used as standard.

2.7. Anticancer Activity

2.7.1. Cell Culture Condition. Dulbecco's modified Eagle's medium (DMEM) was used to propagate the cells which is supplemented with 10% fetal bovine serum and 1 unit/mL antibiotic penicillin/streptomycin. LAAgNP extract-mediated silver nanoparticles stock (10 mg/mL) was prepared in dimethyl sulfoxide (DMSO). Different types of concentrations were prepared which are of 10, 25, 50, 75, and 100 μg/mL in culture medium for experimental purposes.

2.7.2. Determination of Cell Viability by MTT Assay. Human glioma cells (DBTRG and U87) and human breast adenocarcinoma cells (MCF-7 and MDA-MB-231) with $0.5 - 1.0 \times 10^4$ concentration were cultured with LAAgNPs for 24 h and were maintained at 37°C in 5%CO₂ humidified atmosphere. The number of viable cells in both the samples was determined by MTT assay. The absorbance was recorded at 570 nm wavelength and the cell viability percentage
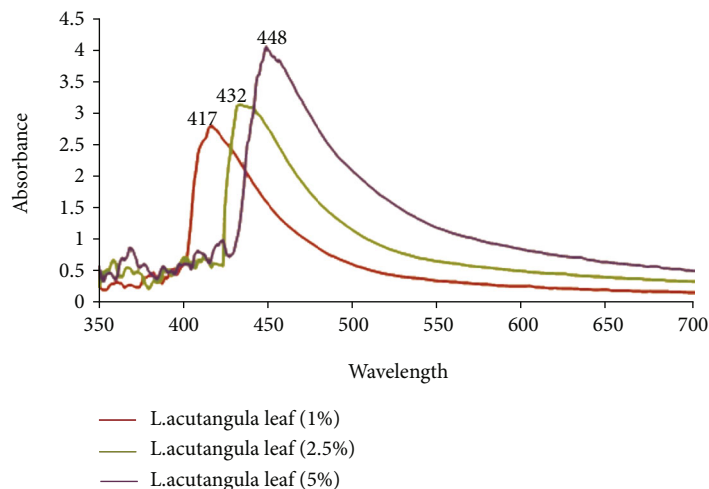
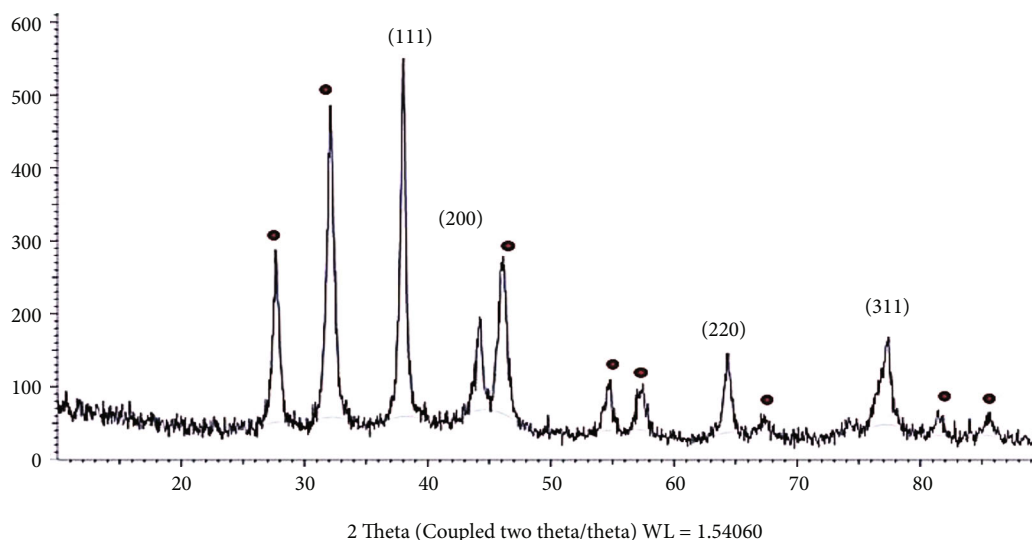Figure 3: UV-Vis spectrum of LAAgNPs at various concentrations.

Figure 4: XRD graph of synthesised LAAgNPs (5%).

against LAAgNPs concentrations were determined in the form of IC_{50}, tamoxifen (5) was used as reference standard for activity against DBTRG and U87cell lines, and gefitinib (6) was used as reference standard for activity against MCF-7 and MDA-MB-231 cell lines.

2.8. Molecular Docking Studies. The potential bioactivity of the two FOG ligands (Cosmosioside and Cynaroside) has been mechanistically investigated from the molecular docking studies by predicting effective interactions against selected proteins. In execution, the protein crystal structures are obtained in PDB form from protein data bank repository and removed the unnecessary bound ligands, cofactors, and water molecules from their vicinity. The .mol2 and .pdb files of the corresponding FOG ligands were generated from ChemBioOffice 14.0 (Chem3D Pro) software and performed docking on SwissDock software [39]. The best outfit interactions optimized with energy minima at a gradient of 0.100 of

root mean standard deviation were captured on UCSF Chimera by envisaging the best binding modes [40]. The binding energies of two FOG ligands interacted with the corresponding target protein receptors in chain A of 3NM8 (oxidoreductase, tyrosinase complex) for DPPH antioxidant activity, chain A of 1DNU (oxidoreductase, myeloperoxidase-thiocyanate complex) for ABTS antioxidant activity, chain A of 5FGK (transferase, cyclin-dependent kinase 8 associated with cyclin C) for gram positive bacteria (B. subtilis, S. aureus, and S. felicis in the current study), chain A of 1AB4 (topoisomerase, the N-terminal 59 kDa fragment of Gyrase A) from gram negative bacteria (E. coli and S. boydii in the current study), chain A of 4GBD (lyase, adenosine deaminase complex) for MCF-7 anticancer activity, chain C of 5FI2 (hydrolase, kidney glutaminase isoform C complex of UPGL 00009 inhibitor) for MDA-MB-231 anticancer activity, chain A of 1D5R (hydrolase, PTEN tumor suppressor) for U87
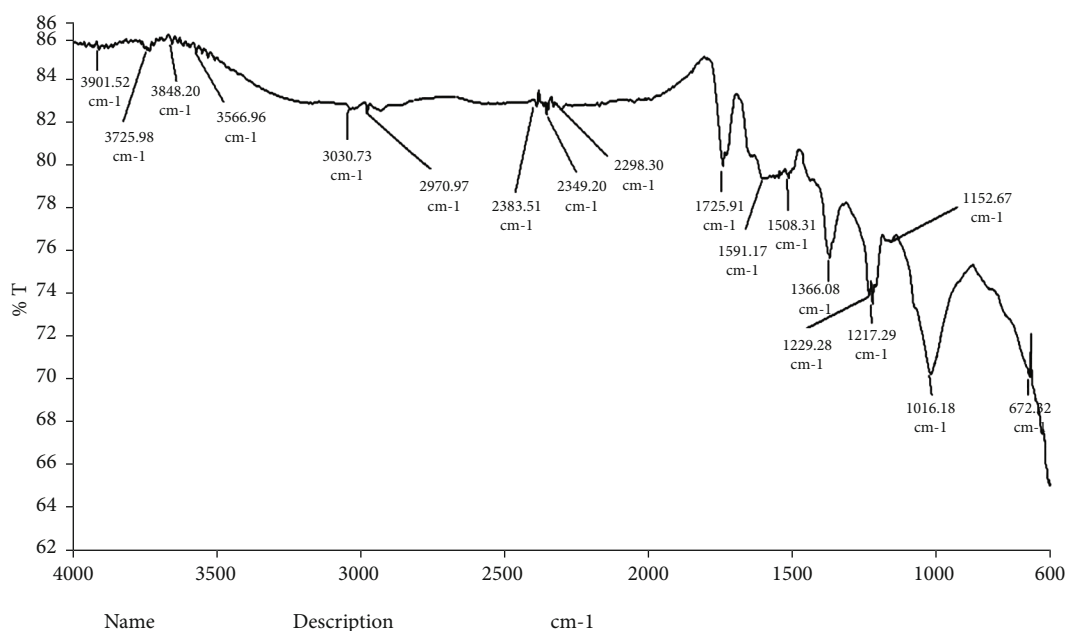
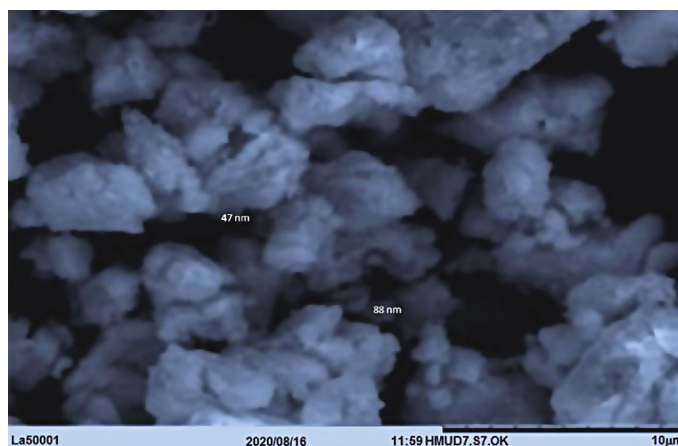FIGURE 5: FTIR–ATR graph of synthesised LAAgNPs.

FIGURE 6: The SEM micrograph of synthesised LAAgNPs (5%).

anticancer activity; and chain B of 5TIJ (lyase, human enolase 2 complex) for DBTRG anticancer activity have predicted in the macromolecular environment and also compared with their reference standards viz., ascorbic acid, ampicillin, tamoxifen, and gefetinib.

2.9. ADMET Properties. [41] The ADMET properties of 1 and 2 have been predicted from preADMET online server [42] to comprehend their biocapabilities like *in vitro* Caco-2 cell permeability, *in vivo* blood-brain barrier (BBB) penetration, *in vitro* Maden Darby Canine Kidney (MDCK) cell permeability, human intestinal absorption (%HIA), and *in vitro* plasma protein binding (PPB) properties. In extension mutagenic, tumarogenic, reproductive, and irritant effects have also been predicted to establish the detailed toxicity analysis for Cosmosioside and Cynaroside. The BBB

deals with the intensely bound endothelial cells which oblige a compound's proficiency to be passed into the bloodstream through the administered route. The analysis of BBB penetration rate (BBB = [Brain]/[Blood]) helps to examine the capability of a compound to penetrate over blood-brain barrier, which is vital in allocating central nervous system (CNS) activity to the biological properties of a compound. The compounds with BBB penetration rate > 0.40 are passable through the BBB and are denoted as CNS active; on contrary, the compounds with BBB penetration rate < 0.40 are unable to pass through the BBB and are denoted as CNS inactive. Likewise, human colon adenocarcinoma-based Caco-2 cells that are associated with intestinal epithelium system in multiple drug transportation pathways like transcellular, paracellular, and active efflux transports are assessed by in vitro Caco-2 permeability value as the value
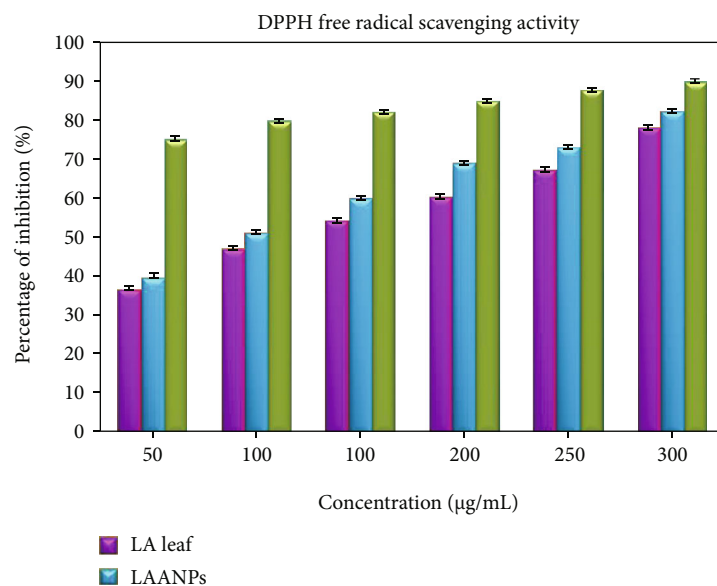
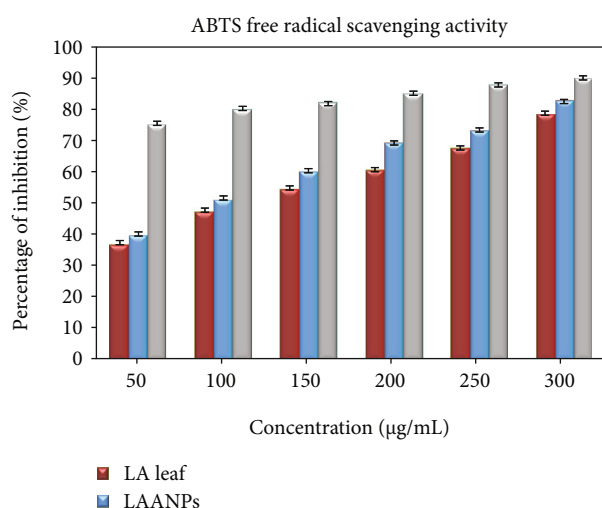Figure 7: The DPPH free radical scavenging activity.

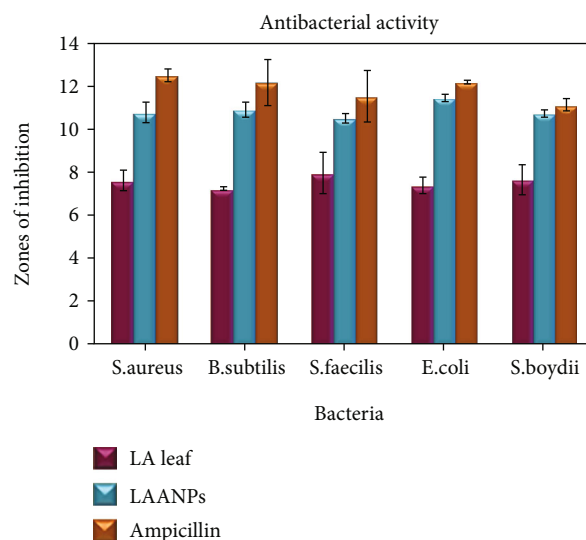Figure 8: The ABTS free radical scavenging activity.

Figure 9: The results of antibacterial activity with zones of inhibition.

is <4 is poor permeable, value in the range of 4-70 is moderately permeable, and value >70 is extremely permeable and is certainly transported to cellular cite in the biochemical processes. Furthermore, the degree of plasma protein binding (PPB) influences the level of distribution of compound unbound in body tissues and infers about unbound quantity of the compound that has been distributed in the active cellular sites and then stimulated further to metabolize and then excreted from the system. The in vitro PPB percentage > 90% classifies the compounds under study as strongly bound and *in vitro* PPB percentage < 90% classifies the compounds under study as weakly bound and eventually replicates its action as well as proficiency. In addition, the MDCK cell system is considered as a sensible tool to predict the prompt permeable compounds and determine their capability as greater the life span of Caco-2 cells than the cellular life span consequences for its high correspondence.

Here, the compounds with *in vitro* MDCK permeability value < 25 are poor permeable, and compounds with in vitro MDCK permeability value in the range of 25-500 are good permeable. In addition, the percentage of HIA is considered as the percentage of an orally administered compound with significant bioavailability into the hepatic portal vein by absorption in relation to total content that excreted through bile, urine, and feces. Compounds with the percentage of HIA in the range of 0-20 are of identified with poor absorbance, 20-70 are of identified with moderate absorbance, and 70-100 are of identified with good absorbance. The consideration of toxicology properties of a compound with its structure greatly helps to design them with bioactivity. The negative toxicology value of a compound affords it as a safer drug works against mutagenicity, carcinogenicity,
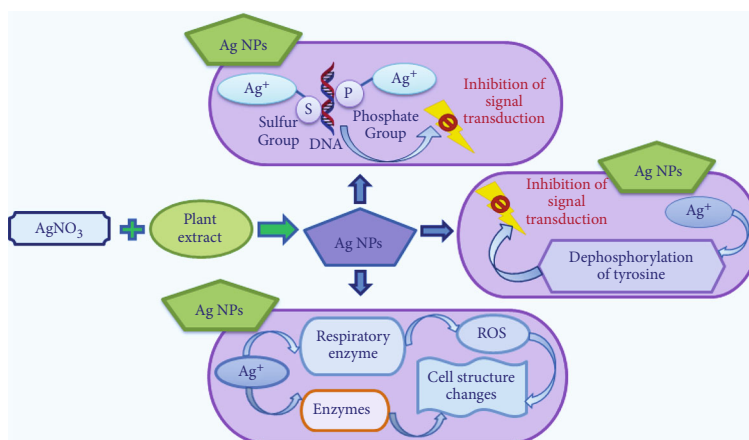
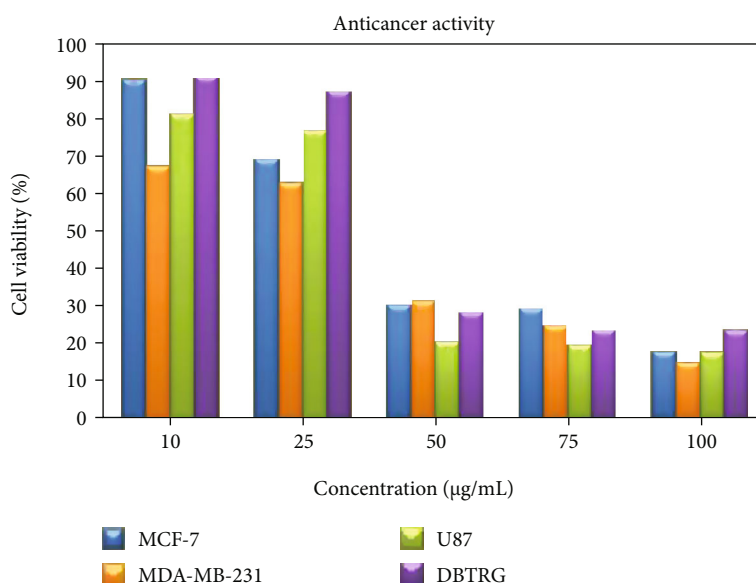FIGURE 10: Different modes of antibacterial mechanisms induced by AgNPs in microbial cells.

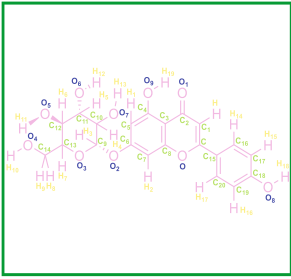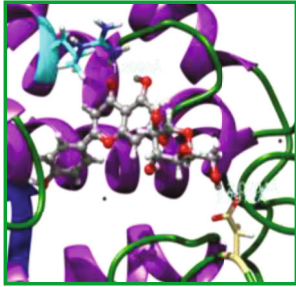FIGURE 11: Cytotoxic activity of LAAgNPs against MCF-7, MDA-MB-231, U87, and DBTRG cell lines.
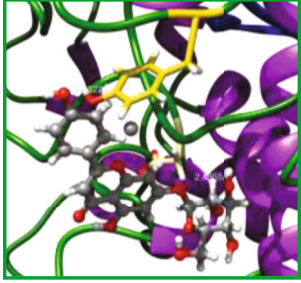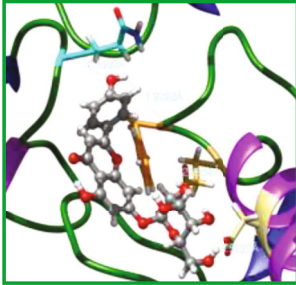
and human ether-a-go-go-related gene (HERG) channel inhibition.
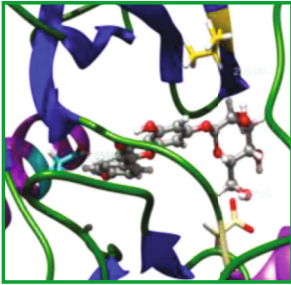
2.10. QSAR Studies. Many drug candidates suffer to clear the clinical trials stage due to their inadequate absorption, distribution, metabolism, excretion, and toxic potentialities, where the worthy oral bioavailability made them as potential with right poise of partitioning and solubility. Computationally, Lipinski's rule of five [43] helps to screen newer molecules to affirm their potentiality based on the parameters like (i) molecular weight ≤ 500 da, (ii) number of hydrogen bond donors ≤ 5, (iii) number of hydrogen bond acceptors ≤ 10, (iv) logP (octanol/water partition coefficient) ≤ 5, and (v) molar refractivity f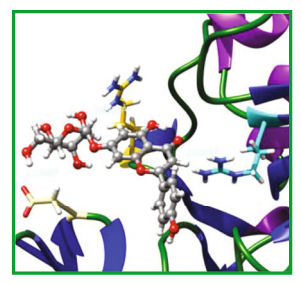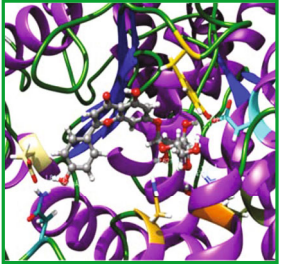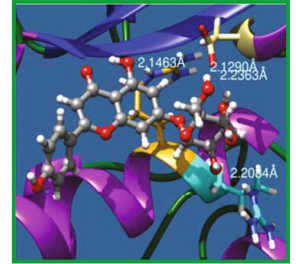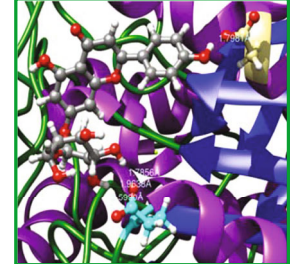rom 40 to 130. Likely the Lipinski parameters, Molinspiration [44] helps to predict Veber parameters (number of rotatable bonds and total polar surface area in addition to Lipinski parameters) and other parameters like Van der Waals volume, number of hydrophobic atoms, solubility,

density, percentage of absorption, and octanol to water partition coefficient, which help to testify the structural sensitivity of the compound under study.

2.11. Bioactivity and Toxicity Risk Studies. The bioactivity and toxicity risk studies of compounds under study have been assessed on molinspiration online server [44] where physico-chemical properties were explored on molinspiration v2018.10 engine, and biochemical properties were explored on molinspiration v2018.03 engine. This exploration revealed bioactivity properties like G protein-coupled receptor (GPCR) ligand property, kinase inhibition (KI) property, ion channel modulator (ICM) capability, nuclear receptor ligand (NRL) interactions, enzyme inhibitor (EI) properties, and protease inhibitor (PI) properties. Similarly explored the drug-likeness and drug scores along with the toxicity risks like tumorigenic, mutagenic, reproductive and irritant effects and proved that the compound 1 and 2 (Cosmosioside (1, Apigenin-7-glucoside) Cynaroside (2, Luteolin-7-glucoside) as safer drugs as predicted the results

TABLE 1: Potential ligand-protein molecular docking bindings of Cosmosioside (1) with identified proteins.

Cosmosioside (1, Apigenin-7-glucoside, $C_{21}H_{20}O_{10}$)

3NM8 (chain A)-oxidoreductase-tyrosinase

1DNU (chain A)-oxidoreductase-myeloperoxidase-thiocyanate complex

5FGK (chain A)-*A Transferase Enzymatic Protein*-CDK8-associated CycC

1AB4 (chain A)-*A Topoisomerase Enzymatic Protein*-59 KDA fragment of gyrase A

4GBD (chain A)–Lyase-adenosine deaminase

5FI2 (chain C)-*Hydrolase* Inhibitor Enzymatic Protein -GAC in complex UPGL 00009 inhibitor

1D5R (chain A)-*A Hydrolase Enzymatic Protein*-PTEN tumor suppressor

5TIJ (chain B)-A *Lyase* Enzymatic Protein-human enolase 2

with Osiris online property explorer toolkit [45]. These predictions helped to understand physicochemical interactions of the compounds under study against their targets and ultimately helped to defining their drug properties.

2.12. Statistical Analysis. The results were expressed as the mean ± standard deviation of triplicates. Statistical analysis was performed using one-way analysis of variance (ANOVA) followed by Tukey's test. $P < 0.05$ was considered statistically significant.

3. Results and Discussion

3.1. Chemistry

3.1.1. Observation of Colour Changes of Silver Nanoparticles. The colour of LA leaf extract was changed from light colour to brown colour (Figure 2), indicating the synthesis of silver nanoparticles. The noticeable colour change in LA leaf extract was mainly due to the reduction of Ag^+ ions to Ag^0

atoms (Equation (2)). Bounteous biomolecules present in the leaf extracts act as natural reducing agents and the reduction reaction can be summarised as follows.

$$\text{Plant Extract} + \text{AgNO3} \longrightarrow \text{Ag nanoparticles.} \quad (2)$$
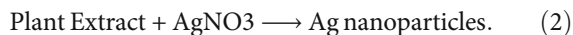
In this connection, previous studies showed similar colour changes to form dark brown colour [21, 46, 47]. It was confirmed that concentrations of plant extracts are one of the significant aspects that influence the rate of synthesis of silver nanoparticles. Higher intensity of colour was spotted as the concentrations increased from 1.0, 2.5, and 5.0%. This could be a result of higher content of the biomolecules that reacted as reducing agents in silver reduction process. Uniform results had also been noticed in the leaves of *Luffa acutangula* in synthesising silver nanoparticles [22].

3.1.2. UV-Vis Spectral Studies of LA Silver Nanoparticles. Time interval to measure the absorption peak was 30-

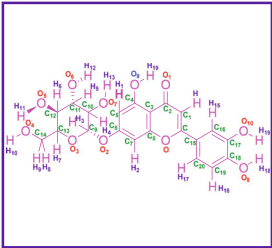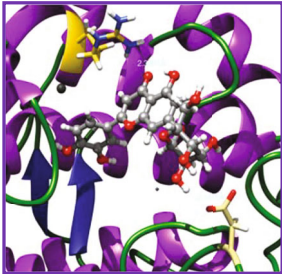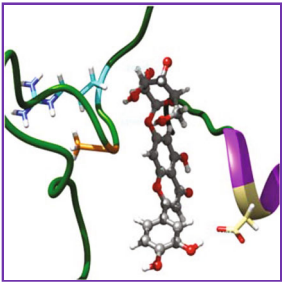TABLE 2: Potential ligand-protein molecular docking interactions of Cosmosioside (1) with identified proteins.
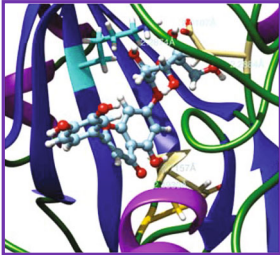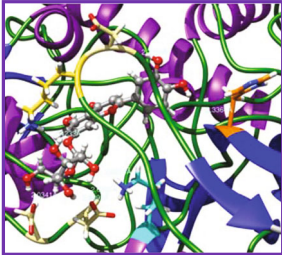
Enzymatic protein	Cluster number	Cluster element	BE (KCal/mol)	HB	HBL atoms	HBR atoms	Binding interactions	BL (A°)	BA (°)	H.B. type
3NM8 (chain A) - *oxidoreductase* - tyrosinase	0	7	-8.2618	3	2	3	Ligand[$O_{(4)}$-$H_{(10)}$]——ASP55(OCOH)	2.0704		Acceptor
							Ligand[$O_{(4)}$-$H_{(10)}$]——ASP55[O(H)CO]	2.2912	54.6126[##]	Acceptor
							Ligand[$C_{(2)}$-]——$O_{(1)}$——ARG209(HN)	2.8998	—	Donor
1DNU (chain A) - *oxidoreductase* - myeloperoxidase-thiocyanate complex	30	7	-7.9463	2	2	2	Ligand[$O_{(7)}$-]——$H_{(13)}$——ASP172(OC)	2.4855	—	Acceptor
							Ligand[$O_{(8)}$-$H_{(18)}$]——TYR316(OH)	2.2322	—	Acceptor
5FGK (chain A) - *transferase* - CDK8 associated CycC	0	0	-9.1645	3	3	3	Ligand[$O_{(4)}$-$H_{(10)}$]——ASP103(OCOH)	1.9270	—	Acceptor
							Ligand[$O_{(6)}$-]——$H_{(12)}$——VAL27(OC)	2.4636	—	Acceptor
							Ligand[$O_{(8)}$-$H_{(18)}$]——GLU66(OCOH)	2.0588	—	Acceptor
1AB4 (chain A) - *topoisomerase* -59KDA fragment of gyrase A	0	0	-8.2294	4	4	4	Ligand[$O_{(4)}$-$H_{(10)}$]——ASP87(OCOH)	2.5627	—	Acceptor
							Ligand[$O_{(7)}$-$H_{(13)}$]——GLN94(OCNH$_2$)	2.2952	—	Acceptor
							Ligand[$O_{(8)}$-]——$H_{(18)}$——PHE96(OC)	1.9022	—	Acceptor
							Ligand[$H_{(18)}$-$O_{(8)}$]——GLN267(HN)	2.1500	—	Donor
4GBD (chain A) - *Lyase* - adenosine deaminase	8	1	-7.7955	3	3	3	Ligand[$O_{(4)}$-$H_{(10)}$]——ASP36(OCOH)	2.1348	—	Acceptor
							Ligand[$H_{(13)}$-$O_{(7)}$]——ARG411(HN)	2.0486	—	Donor
							Ligand[$C_{(2)}$-]——$O_{(1)}$——ARG149(HN)	2.5263	—	Donor

TABLE 2: Continued.

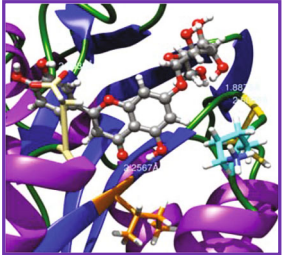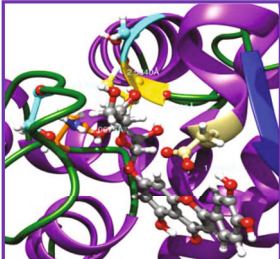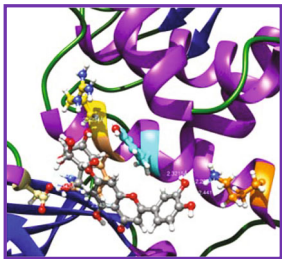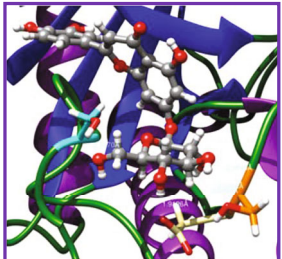| Enzymatic protein	Cluster number	Cluster element	BE (KCal/mol)	HB	HBL atoms	HBR atoms	Binding interactions	BL (A°)	BA (°)	H.B. type
5FI2 (chain C) - *hydrolase* - GAC in complex UPGL 00009 inhibitor	0	0	-8.8921	7	6	7	Ligand[$O_{(8)}$-$H_{(18)}$]——ASP446(OCOH)	1.8467	—	Acceptor
							Ligand[$O_{(4)}$-$H_{(10)}$]——TYR248(OH)	2.1513	—	Acceptor
							Ligand[$O_{(6)}$-$H_{(12)}$]——GLU380(OH)	1.7125	—	Acceptor
							Ligand[$H_{(18)}$-$O_{(8)}$]——ASN318(HNOC)	2.2940	—	Donor
							Ligand[$C_{(9)}$-$O_{(3)}$-$C_{(13)}$]-ASN334(HNOC)	2.6215	—	Donor
							Ligand[$H_{(11)}$-$O_{(5)}$]——ASN387(HN)	2.1575	—	Donor
							Ligand[$H_{(11)}$-$O_{(5)}$]——TYR413(HO)	2.4479	106.6382[@]	Donor
1D5R (chain A) - *hydrolase* - PTEN tumor suppressor	0	0	-8.7975	4	4	3	Ligand[$O_{(4)}$-$H_{(10)}$]——ASP324(OCOH)	2.2363	—	Acceptor
							Ligand[$O_{(6)}$-$H_{(12)}$]——ASP324(OCOH)	2.1290	102.4531[$]	Acceptor
							Ligand[$H_{(13)}$-$O_{(7)}$]——ARG172(HN)	2.2084	—	Donor
							Ligand[$H_{(19)}$-$O_{(9)}$]——ARG173(HN)	2.1463	—	Donor
5TIJ (chain B) - *lyase* - human enolase 2	5	7	-7.9044	4	3	3	Ligand[$O_{(8)}$-$H_{(18)}$]——ASP282(OCOH)	1.7981	—	Acceptor
							Ligand[$O_{(7)}$-$H_{(13)}$]—GLU219(O(H)OC)	2.5990	56.2469[#]	Acceptor
							Ligand[$O_{(7)}$-$H_{(13)}$]——GLU219(OCOH)	1.9638	69.7145[*]	Acceptor
							Ligand[$O_{(6)}$-$H_{(12)}$]——GLU219(OCOH)	1.7856	—	Acceptor

[$]Ligand $H_{(10)}$-ASP324(OCOH)-Ligand $H_{(12)}$; [*]Ligand $H_{(12)}$; [@]ASN387(NH)-Ligand $O_{(5)}$-TYR413(HO); [##]ASP55[OC(H)O]-Ligand $H_{(10)}$-ASP55(OCOH); HBL atoms: number of hydrogen bond ligand atoms; [#]GLU219(HOCO)-Ligand $H_{(13)}$-GLU219(O(H)OC); HB: number of hydrogen bonds; HBR Atoms: number of hydrogen bond receptor atoms; BE: binding energy; BL: bond length; BA: bond angle.

TABLE 3: Potential ligand-protein molecular docking bindings of Cynaroside (2) with identified proteins.

Cynaroside (2, luteolin-7-glucoside), C21H20O11)

3NM8 (chain A) - oxidoreductase - tyrosinase

1DNU (chain A) - oxidoreductase - myeloperoxiase-thiocyanate complex

5FGK (chain A) - A Transferase Enzymatic Protein - CDK8 associated CycC

1AB4 (chain A) - A Topoisomerase Enzymatic Protein -59KDA fragment of gyrase A

4GBD (chain A) – lyase - adenosine deaminase

5FI2 (chain C) - Hydrolase Inhibitor Enzymatic Protein - GAC in complex UPGL 00009 inhibitor

1D5R (chain A) - A Hydrolase Enzymatic Protein - PTEN tumor suppressor

5TIJ (chain B) - A Lyase Enzymatic Protein -human enolase 2

150 sec. At 150 sec, the highest peak was observed for all the different concentrations, and all the high adsorption peaks were in the range of standard adsorption of silver nanoparticles. The spectral peaks were recorded at 417, 432, and 448 nm for different concentrations of biologically synthesised nanoparticles at 1.0, 2.5, and 5.0%, respectively (Figure 3).

There are no qualms that silver nanoparticles achieved the highest peak as cause of Surface Plasmon Resonance (SPR) adsorption band. Free electrons of biologically synthesised silver nanoparticles promote the generation of SPR band through coalescing the vibrations of electrons in resonance with the light wave [48]. The aspects like size and shape of the nanoparticles, type of biomolecules existing in the plant extracts, silver nitrate concentration, and amount of extracts have influenced the SPR banding patterns.

3.1.3. XRD Analysis. X-ray diffraction analysis is an advanced method to figure out the crystalline nature of metallic nanoparticles. As shown in Figure 4, the peaks at 2θ values of 38°, 44°, 64°, and 77° are reflecting (111),

(200), (220), and (311) lattice plans for silver, respectively. The present result clearly illustrates that the biologically synthesised silver nanoparticles are in crystalline nature and face-centered cubic (fcc) shape. The studies on carob and olive leaf extract confirmed the shape of the synthesised nanoparticles as fcc [49, 50]. Debye Scherrer's equation (Equation (3)) was used to calculate the average particular size of the silver nanoparticles synthesised by present biological method, where β is the full width at half maximum of the diffraction peak, t is the mean crystalline size, θ is the centre angle of the peak, and λ is the wavelength of X-ray source. The recognized crystalline size of LAAgNPs is 44 nm. This clearly illustrates that LAAgNPs is nanocrystalline shape. Similar results have been reported on the biologically synthesised AgNPs using *Pulicaria glutinosa* plant extract showed average crystalline size of 42 nm [13].

$$t = \frac{0.89\lambda}{\beta cos\theta} \qquad (3)$$

TABLE 4: Potential ligand-protein molecular docking interactions of Cynaroside (2) with identified proteins.

Enzymatic protein	Cluster number	Cluster element	BE (KCal/mol)	HB	HBL atoms	HBR atoms	Binding interactions	BL(A°)	BA (°)	HB type
3NM8 (chain A) - *oxidoreductase* - tyrosinase	19	3	-7.9386	2	2	2	Ligand[$O_{(7)}$-$H_{(13)}$]———ASP324(OCOH)	2.1516	—	Acceptor
							Ligand[$C_{(2)}$-$O_{(1)}$]———ARG209(HN)	2.3601	—	Donor
1DNU (chain A) - *oxidoreductase* - myeloperoxidase-thiocyanate complex	0	3	-8.3238	3	3	3	Ligand[$O_{(10)}$-$H_{(19)}$]—ASP324(OCOH)	1.9449	—	Acceptor
							Ligand[$O_{(7)}$-$H_{(13)}$]———ARG27(HN)	2.0962	—	Acceptor
							Ligand[$O_{(6)}$-$H_{(12)}$]———ALA24(OC)	2.2144	—	Acceptor
5FGK (chain A) - *transferase* - CDK8 associated CycC	18	12	-8.8514	5	5	5	Ligand[$O_{(5)}$-$H_{(11)}$]———ASP173(OCOH)	2.0107	—	Acceptor
							Ligand[$C_{(14)}$-$O_{(4)}$]———ASP173(HN)	2.2884	—	Donor
							Ligand[$C_{(10)}$-$O_{(7)}$]———LYS52(HN)	2.2874	—	Donor
							Ligand[$H_{(14)}$-$O_{(8)}$]———LYS52(HN)	2.4930	—	Donor
							Ligand[$O_{(8)}$-$H_{(14)}$]———ASP98(OC)	2.7157	—	Acceptor
1AB4 (chain A) - *topoisomerase* -59KDA fragment of gyrase A	1	3	-8.2753	7	7	6	Ligand[$O_{(5)}$-$H_{(11)}$]———ASP113(OCOH)	2.0095	49.2269*	Acceptor
							Ligand[$O_{(7)}$-$H_{(13)}$]--ASP113(OCOH)	2.6325	—	Acceptor
							Ligand[$O_{(4)}$-$H_{(10)}$]———ASP115(OCOH)	2.0341	—	Acceptor
							Ligand[$O_{(10)}$-$H_{(19)}$]———ASP299(OC)	2.7050	—	Acceptor
							Ligand[$C_{(10)}$-$O_{(7)}$]———LYS270(HN)	2.0314	—	Donor
							Ligand[$C_{(6)}$-$O_{(2)}$]———LYS298(HN)	2.4233	—	Donor
							Ligand[$O_{(9)}$-$H_{(18)}$]———HSD262(OC)	2.3361	—	Acceptor

TABLE 4: Continued.

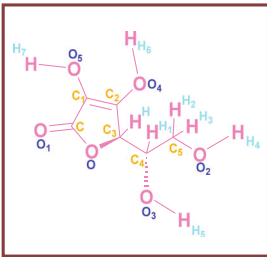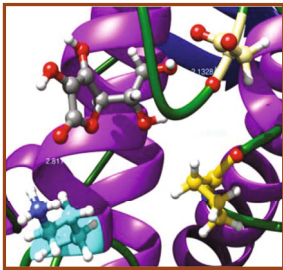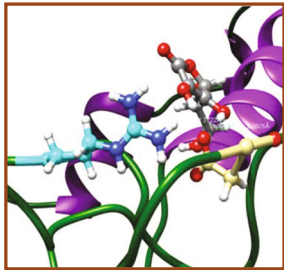| Enzymatic protein	Cluster number	Cluster element	BE (KCal/mol)	HB	HBL atoms	HBR atoms	Binding interactions	BL(A°)	BA (°)	HB type
4GBD (chain A) – *lyase* - adenosine deaminase	4	4	-7.8306	4	4	4	Ligand[$O_{(10)}$-$H_{(19)}$]–ASP215(OCOH)	2.1032	—	Acceptor
							Ligand[$O_{(6)}$-$H_{(12)}$]——LYS182(OC)	2.5865	—	Acceptor
							Ligand[$O_{(4)}$-$H_{(10)}$]——LYS184(OC)	1.8875	—	Acceptor
							Ligand[$H_{(19)}$-$O_{(9)}$]——ILE189(HN)	2.2567	—	Donor
5FI2 (Chain C) - *hydrolase inhibitor* - GAC in complex UPGL 00009 inhibitor	0	0	-9.1290	5	5	5	Ligand[$O_{(10)}$-$H_{(19)}$]–ASP446(OCOH)	1.9065	—	Acceptor
							Ligand[$C_{(11)}$-$O_{(6)}$]——ASN330(HN)	2.0675	—	Donor
							Ligand[$O_{(5)}$-$H_{(11)}$]——CYS462(O'C)	2.5840	—	Acceptor
							Ligand[$O_{(7)}$-$H_{(13)}$]——CYS462(OC)	1.9953	—	Acceptor
							Ligand[$O_{(4)}$-$H_{(10)}$]——SER313(OC)	2.5769	—	Acceptor
1D5R (chain A) - *hydrolase* - PTEN tumor suppressor	0	0	-9.2690	7	7	5	Ligand[$O_{(4)}$-$H_{(10)}$]——ASP324(OCOH)	1.9343	—	Acceptor
							Ligand[$O_{(6)}$-$H_{(12)}$]——ASP324(OCOH)	1.8831	90.6238[$]	Acceptor
							Ligand[$C_{(18)}$-$O_{(9)}$]——LYS183(HN)	2.4417	—	Donor
							Ligand[$C_{(17)}$-$O_{(10)}$]——LYS183(HN)	2.2624	74.4086[#]	Donor
							Ligand[$O_{(10)}$-$H_{(19)}$]——TYR176(HN)	2.3215	—	Acceptor
							Ligand[$C_{(4)}$-$O_{(8)}$]——ARG173(HN)	2.2435	—	Donor
							Ligand[$O_{(7)}$-$H_{(13)}$]——ARG172(HN)	2.2234	—	Donor

TABLE 4: Continued.

Enzymatic protein	Cluster number	Cluster element	BE (KCal/mol)	HB	HBL atoms	HBR atoms	Binding interactions	BL(A°)	BA (°)	HB type
							Ligand[O$_{(5)}$-H$_{(11)}$]——ASP142(OCOH)	1.9126	—	Acceptor
							Ligand[O$_{(7)}$-H$_{(13)}$]————ASP142(OC)	2.4464	—	Acceptor
5TIJ (chain B) -*lyase* - human enolase 2	24	1	-8.7736	5	4	5	Ligand[C$_{(10)}$-O$_{(7)}$]————ASP142(HN)	2.1296		Donor
							Ligand[C$_{(10)}$-O$_{(7)}$]————SER141(HN)	2.3549	48.5632[@]	Donor
							Ligand[C$_{(14)}$-O$_{(4)}$]————SER432(HO)	2.2870	—	Donor

TABLE 5: Potential ligand-protein molecular docking bindings of ascorbic acid (3) with identified proteins.

| Ascorbic acid (3, hex-1-enofuranos-3-ulose, $C_6H_8O_6$) | 3NM8 (chain A) - oxidoreductase - tyrosinase | 1DNU (chain A) - oxidoreductase - myeloperoxidase-thiocyanate complex |

3.1.4. FTIR-ATR Analysis. The interaction between biologically synthesised nanoparticles and biological molecules of aqueous leaf extracts of *LA* can be understood from the FTIR-ATR spectrum. In Figure 5, the absorption peaks at 3030.73 and 2970.97 cm^{-1} represent the O-H groups in alcohols, phenols, and C-H stretching of alkenes amide I or proteins [26]. Band appearing at 2383.51 and 2349.20 cm^{-1} denotes C-O groups. Further, the adsorption peaks at 2298.3 and 1508.31 cm^{-1} reflect the functional groups of –C=C- group and C=C of amide II groups, respectively [12]. Specific IR bands at 1366.08, 1152.67, 1229.28, and 1217.29 cm^{-1} attribute to C-H alkenes and C-N stretching vibration of aliphatic amines, respectively [26]. Absorption peaks at 1016.18 and 672.32 cm^{-1} assign the presence of ether linkage and aromatic hydrocarbon [51, 52]. A similar result was reported for phenols, flavonoids, alkaloids, and proteins in plant extracts lead to stabilization and synthesis of AgNPs [50]. In the present study, the stretching vibrations of silver nanoparticles of *LA* indicated different proteins and terpenoids in aqueous extracts and enhanced the bioreduction of Ag ions. A previous study reported that *LA* leaves possess numerous molecules such as alkaloids, flavonoids, saponins, and glycosides [53]. These functional groups in aqueous leaf extracts of *LA* facilitate capping and reduction process of Ag ions. In the present study, the stretching vibrations of green mediated synthesised silver nanoparticles using *LA* indicated different proteins and terpenoids in aqueous extracts and enhanced the bioreduction of Ag ions. A previous study reported that *LA* leaves possess numerous molecules such as alkaloids, flavonoids, saponins, and glycosides [53]. These functional groups in aqueous leaf extracts of *LA* facilitate capping and reduction process of Ag ions.

3.1.5. SEM Analysis. The biosynthesised LAAgNPs were morphologically visualized on scanning electron microscopy (SEM) and identified as uniform and spherical in shape with 10 μm size under 7000× magnification (Figure 6). However, the structure of all the AgNPs could be observed more clearly at higher magnification. Further, the overall SEM image is attributed due to electrostatic interaction between bioorganic capping molecules attached on the AgNPs surface. Several factors such as aggregation of the smaller ones and SEM measurements could influence the formation of larger AgNPs [11].

3.2. Antioxidant Activity

3.2.1. DPPH Antioxidant Assay. DPPH (1,1-diphenyl-2-picrylhydrazyl) free radical scavenging activity [54] was studied on leaf extracts and AgNPs from *LA* in this study. AA was chosen as positive control for comparison purposes. The *LA* leaf extract revealed free radical scavenging action by 37.1% to 79.1% at 50 μg/mL to 300 μg/mL concentrations, respectively. Further, biologically synthesised LAAgNPs demonstrated free radical scavenging activity from 39.9% to 83.2% at 50 μg/mL to 300 μg/mL concentrations (Figure 7). A similar result was reported for the biosynthesised AgNPs from *Syzygium cumini* (L.) seed extract exhibited high DPPH free radical scavenging activity [11] compared to *Argemone mexicana* and *Turnera ulmifolia* seed extracts [55].

The present data is in accordance with the result reported for the biosynthesised AgNPs from aqueous leaf extracts of *Terminalia mellueri*, *Terminalia catappa*, *Terminalia bellerica*, and *Terminalia bentazoe* showed high DPPH free radical scavenging activity (more than 80%) compared to leaf extracts in the range of 60%-70% [56]. The values represented are the mean ± S.D of triplicate sample significant level at ($P < 0.05$). The IC$_{50}$ values of *LA* and LAAgNPs were 126.29 μg/mL and 96.89 μg/mL. The lower IC$_{50}$ values indicate the greater tendency for antioxidant activity of the extracts. Similar activity was reported for the lower IC$_{50}$ value of *Psidium guajava* extract and AgNPs from *Psidium guajava* was 110 μg/mL and 80 μg/mL, respectively [57].
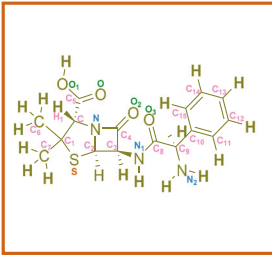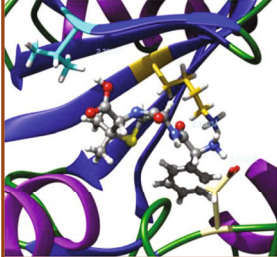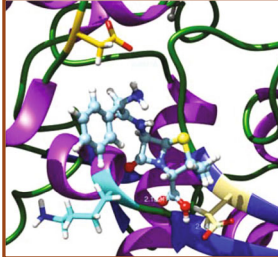
3.2.2. ABTS Antioxidant Assay. In the present study, ABTS free scavenging test was analysed on AgNPs and leaf extract of *LA*. ABTS^{+} is considered as protonated radical which could readily accept electron from antioxidant compound and transfer its colour from blue to pink which was detected at 734 nm [58]. The leaf extract of *LA* showed the potential to scavenge the free radicals was found to be 43.8-82.9% at concentrations from 50-300 μg/mL, respectively, whereas biologically synthesised AgNPs showed the activity as 47.9-85.2% at different concentrations from 50-300 μg/mL, respectively (Figure 8). The values represented are the

TABLE 6: Potential ligand-protein molecular docking interactions of ascorbic acid (3) with identified proteins.

Enzymatic protein	Cluster number	Cluster element	BE (KCal/mol)	No. of HB	No. of HBL atoms	No. of HBR atoms	Binding interactions	BL (A°)	BA (°)	HB type
3NM8 (chain A) - *oxidoreductase* - tyrosinase	1	4	-6.4837	3	3	3	Ligand[$O_{(2)}$-$H_{(4)}$]—ASP140(C=O)	2.1328	—	Acceptor
							Ligand[C-$O_{(1)}$]—LYS47(NH)	2.8116	—	Donor
							Ligand[$O_{(5)}$-$H_{(3)}$]—PRO219(C=O)	1.9298	—	Acceptor
1DNU (chain A) - *oxidoreductase* - myeloperoxidase-thiocyanate complex	31	2	-6.6112	4	3	3	Ligand[$O_{(4)}$-$H_{(6)}$]———ASP5(O=C)	2.3826	78.7795*	Acceptor
							Ligand[$O_{(4)}$-$H_{(6)}$]———ASP5(OCOH)	1.9709	61.7009#	Acceptor
							Ligand[$O_{(5)}$-$H_{(7)}$]—ASP5(OCOH)	1.7722	—	Acceptor
							Ligand[$H_{(7)}$-$O_{(5)}$]———ARG17(NH)	2.7187	—	Donor

*ASP5(CO)-Ligand $H_{(6)}$-ASP5(OCOH); #Ligand $H_{(6)}$-ASP5(OCOH)-Ligand $H_{(7)}$.

TABLE 7: Potential ligand-protein molecular docking bindings of ampicillin (4) with identified proteins.

Ampicillin (4, aminobenzylpenicillin, $C_{16}H_{19}N_3O_4S$)

5FGK (chain A) - *A Transferase Enzymatic Protein* - CDK8 associated CycC

1AB4 (chain A) - *A Topoisomerase Enzymatic Protein* -59KDA fragment of gyrase A

mean ± S.D of triplicate sample significant level at ($P < 0.05$). The IC_{50} value of standard AA is $31.42 \mu g/mL$ which has proven that AA had higher scavenging activity with the lowest IC_{50} ($\mu g/mL$). The IC_{50} values of *LA* and LAAgNPs were found as 100.96 and 76.0 $\mu g/mL$, respectively. Similar activity was reported for the IC_{50} value of *Psidium guajava* extract (105 $\mu g/mL$) and found higher than AgNPs from *Psidium guajava* (70 $\mu g/mL$), respectively [57]. Similar ABTS radical scavenging action of biologically synthesised AgNPs was found in previous studies [59, 60].

3.3. *Antibacterial Activity*. There are no qualms that silver and silver-based compounds are the potential antibacterial or antimicrobial agents [61]. It has become compulsory to produce the safer substitutes for the currently available antimicrobial agents and also the antibiotics due to the high multidrug resistance problems [62]. The synthesis of metallic nanoparticles from the biological sources with potential antibacterial or antimicrobial properties has opened up a new avenue against multidrug resistance bacteria.

In the current study, human pathogenic microorganisms such as *B. subtilis*, *S. aureus*, *S. faecilis*, *E. coli*, and *S. boydii* were chosen to study the antibacterial efficacy of biologically synthesised silver nanoparticles. *LA* leaf aqueous extracts expressed potential antibacterial effect against both Gram-positive and Gram-negative bacterium. *LA* leaf extract expressed the highest inhibition which was seen in *S. faecilis* with 7.9 mm diameter, followed by *S. boydii* (7.6 mm), *S. aureus* (7.6 mm), *E. coli* (7.4 mm), and *B. subtilis* (7.2 mm). Moreover, biologically synthesised AgNPs revealed that the antibacterial efficacy of *LA* leaf extract was enhanced by inducing a higher zone of inhibition against the tested microorganisms. The silver nanoparticles from *LA* showed the highest inhibition against *E. coli*, Gram-negative bacteria. The zone of inhibition was recorded as 11.5 mm. Similarly, *LA* leaf-mediated silver nanoparticles did express high anticidal property by suppressing the growth of other microorganisms, *B. subtilis* (10.9 mm), *S. aurus* (10.8 mm), *S. boydii* (10.7 mm), and *S. faecilis* (10.5 mm) (Figure 9). Ampicillin was chosen as standard and positive control in this study. Ampicillin performed the highest inhibitory effect against all tested microorganisms compared to *LA* leaf extract and synthesised AgNPs.
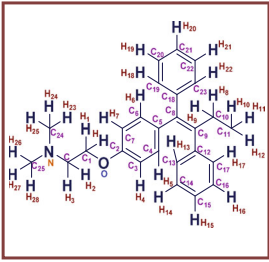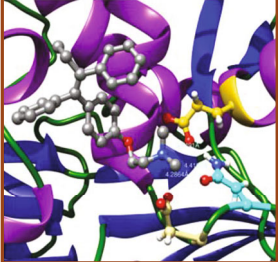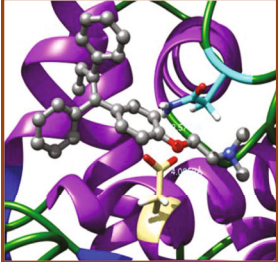
The present study proved that gram-negative bacteria, *E. coli*, were more sensitive to the action of biologically synthesised silver nanoparticles compared to gram-positive bacteria. This is in accordance with the result stated by Kim and the coworkers [63]. Literature denoted the inhibitory effects of silver nanoparticles could be associated with characteristics of specific bacterial species. Naturally, gram-positive and gram-positive grouped bacteria have dissimilar membrane structure, especially the difference in thickness of peptidoglycan layer. The mild antibacterial features of synthesised silver nanoparticles in contradiction of gram-positive bacteria could be due to membrane structure [63]. The antibacterial mechanism of action of metallic nanoparticles is still not exactly explained and being unverified. However, several theories and possible mechanism(s) of actions of biologically and chemically synthesised silver nanoparticles have been reported with basic information [64]. The graphic representation (Figure 10) depicts the penetration of silver nanoparticles (AgNPs) into the cell and their different mode of antibacterial mechanisms. The reactivity begins with synthesis of silver nanoparticles using silver nitrate and selected plant extracts.

3.4. *Anticancer Activity*. Plants contain several types of bioactive compounds that are ideally favorable for the drug development in anticancer therapy. Nowadays, researchers found that the plant-based medicines or drugs are safer and cost-effective when compared to the synthetic drugs [65]. *LA* is one of the herbal plants which belongs to a family of Cucurbitaceae and widely cultivated in Asia, India, Brazil, and USA [66]. Previously, itself isolated five major components of *LA*, a bioactive component among them named 1,8 dihydroxy-4-methylanthracene 9,10-dione (DHMA) was reported as potential antiproliferative agent against nonsmall cell lung cancer cells (NCI-H460). DHMA showed promising anticancer activities through inhibition of cell growth, generation of reactive oxygen species (ROS), and induction of p53-mediated apoptotic pathway against human nonsmall cell lung cancer cell line (NCI-H460) [67, 68]. Another study reported on the potential anticancer effect of *LA* on human colon cancer cell line HT29 cells [69]. *LA* seeds consist of ribosome inactivating proteins which were reported, and the study revealed the potential

TABLE 8: Potential ligand-protein molecular docking interactions of ampicillin (4) with identified proteins.

Enzymatic protein	Cluster number	Cluster element	BE (KCal/mol)	No. of HB	No. of HBL atoms	No. of HBR atoms	Binding interactions	BL (A°)	BA (°)	HB type
5FGK (chain A) - *transferase* - CDK8 associated CycC	5	0	-8.4767	3	3	3	Ligand[$N_{(2)}$-$H_{(17)}$]—ASP173(OCOH)	2.1290	—	Acceptor
							Ligand[$C_{(8)}$-$O_{(3)}$]——LYS52($HNCH_2$)	2.1803	—	Donor
							Ligand[$O_{(1)}$-$H_{(3)}$]————VAL27(OC)	2.3334	—	Acceptor
1AB4 (chain A) - *topoisomerase* -59KDA fragment of gyrase A	1	4	-7.8486	3	3	3	Ligand[$O_{(1)}$-$H_{(3)}$]—ASP104(OCOH)	2.1401	—	Acceptor
							Ligand[$N_{(2)}$-$H_{(18)}$]—ASP515(OCOH)	2.4497	—	Acceptor
							Ligand[$C_{(5)}$-O]————LYS129(HN)	2.1821	—	Donor

TABLE 9: Potential ligand-protein molecular docking bindings of tamoxifen (5) with identified proteins.

Tamoxifen (5, 1-*p*-*β*-dimethylaminoethoxyphenyl-trans-1,2-diphenylbut-1-ene, $C_{26}H_{29}NO$)	4GBD (chain A) – lyase - adenosine deaminase	5FI2 (chain C) - *Hydrolase* Inhibitor Enzymatic Protein -GAC in complex UPGL 00009 inhibitor

anticancer activity of luffaculin 1 and luffaculinin in human leukemia K562 cells [70]. Anticancer effects of AgNPs have been demonstrated in various cell models. It observed a dose-dependent cytotoxic effect of biosynthesized AgNPs from *Piper longum* extract in MCF-7 breast cancer cells [71]. Cytotoxic effects of AgNPs from other plant extracts such as *Iresine herbstii* and *Vitex negundo Linn* were demonstrated in HeLa (cervical) and HCT15 (colorectal) cancer cells, respectively [9, 25]. In the present study, LAAgNPs were tested against four human cancer cell lines, MCF-7, MDA-MB-231, DBTRG, and U87. The synthesised silver nanoparticles by *LA* leaf extract triggered a dose-dependent reduction in the cell proliferation with IC_{50} values ranging from 35-42 μg/ml (Figure 11). There are several anticancer mechanisms that have been suggested based on previous studies. AgNPs tend to generate reactive oxidative species (ROS) intracellularly that results excess oxidative stress [72]. High oxidative stress inhibits chromosome inhibition and eventually damage cell cycle of tumor cells [73, 74]. Size independent property of AgNPs enhances cytotoxic effect against drug-resistant cancer cells [75]. In addition, cytotoxic effect can be as the result of poor angiogenesis and programmed cell death by AgNPs [76]. Further studies are needed to interpret the anticancer mechanism(s) of the biosynthesized AgNPs.

3.5. Molecular Docking Studies. The obtained *in vitro* antioxidant, antibacterial, and anticancer activity of FOGs have been additionally supported by investigating of ligand-protein binding interactions against the selected enzymatic proteins *viz.*, 3NM8-Chain A (DPPH radical scavenging activity), 1DNU-Chain A (ABTS radical scavenging activity), 5FGK-Chain A (gram-positive bacterial activity), 1AB4-Chain A (gram-negative bacterial activity), 4GBD-Chain A (MCF-7 anticancer activity), 5FI2-Chain C (MDA-MB-231 anticancer activity), 1D5R-Chain A (U87 anticancer activity), and 5TIJ-Chain B (DBTRG anticancer activity); and docking postures and binding interactions were bestowed in Tables 1–12.

In view of antioxidant activity, the hydroxy groups (-OH) of FOGs bound with carbonyl groups (O=C) of aspartic acid and amino groups (-NH) of arginine in 3NM8 (Chain A) are responsible for DPPH radical scav-

enging activity; and binding of -OH of FOGs bound with O=C of aspartic acid and alanine, -NH of arginine, and -OH of tyrosine in 1DNU (Chain A) is responsible for ABTS radical scavenging activity. Concerning the antibacterial activity, the -OH of FOGs bound with C=O of aspartic acid, valine and glutamic acid, and -NH of aspartic acid and lysine in 5FGK (Chain A) is responsible for gram-positive bacterial activity; and binding of -OH in FOGs with C=O of aspartic acid, glutamine, histidine and phenyl alanine, and -NH of glutamine and lysine in 1AB4 (Chain A) is responsible for gram-negative bacterial activity. In relation to MCF-7 anticancer inhibition, the -OH of FOGs bound with C=O of aspartic acid and lysine, and -NH of arginine and isoleucine in 4GBD (Chain A) were identified as responsible. Coming to MDA-MB-231 anticancer inhibition, the -OH of FOGs bound with C=O of aspartic acid, cysteine and serine, -OH of tyrosine and glutamic acid, and -NH of asparagine in 5FI2 (Chain C) was identified as responsible.

Concerning the U87 anticancer inhibition, the -OH of FOGs bound with C=O of aspartic acid, and -NH of lysine, and tyrosine and arginine in 1D5R (chain A was identified as responsible). In aspects of DBTRG anticancer inhibition, the -OH of FOGs bound with C=O of aspartic acid and glutamic acid, -OH of glutamic acid and serine, and -NH of aspartic acid and serine in 5TIJ (chain B) was identified as responsible. The binding specificity studies have affirmed the promising ligand-protein binding interactions in between the hydroxy groups of the FOGs and aspartic acid of the concerned enzymatic proteins with a binding energy in the range of -9.2690 to -7.7955 KCal/mol.
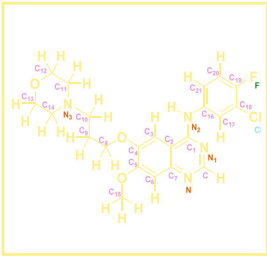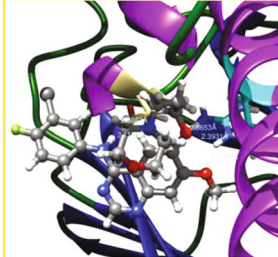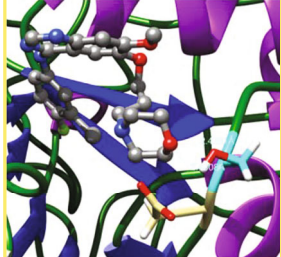
3.6. ADMET Properties. The study of ADMET properties of the interested analytes under investigation helps to realize their physicochemical interactions [77]. The potentiality of a drug depends on its degree of absorption and in turn on its inherent bioavailability properties. Once a potential drug be absorbed and self-distributed in to muscles and organs by circulation through extracellular sites and hence lowers its plasma concentration individually, therefore, metabolizes *in vivo*, then, such metabolites will be distributed by the action of reduction and oxidation reactions by the enzymatic action and work potentially on cellular systems, and

TABLE 10: Potential ligand-protein molecular docking interactions of tamoxifen (5) with identified proteins.

Enzymatic protein	Cluster number	Cluster element	BE (KCal/mol)	HB	HBL atoms	HBR atoms	Binding interactions	BL (A°)	BA (°)	HB type
4GBD (chain A) - *lyase* - adenosine deaminase	0	3	-7.7235	3	1	3	Ligand[C-N]————ASP316(OCOH)	4.2864	39.9133*	Acceptor
							Ligand[C-N]————ASN314(O=C)	4.4192		Acceptor
							Ligand[C-N]————GLU282(OCOH)	3.2491	40.7597$	Acceptor
5FI2 (Chain C) - *hydrolase inhibitor* - GAC in complex UPGL 00009 inhibitor	4	0	-7.5313	2	2	2	Ligand[C_{(2)Ph}-O]————ASP466(HN)	4.0253	104.	Donor
							Ligand[C_{(2)Ph}-O]————ASN318(HN)	3.5771	5635#	Donor

*ASP316(HOCO)-Ligand[CN]-ASN314(OC); $ASN314(CO)-Ligand[CN]-GLU282(OCOH); #ASP466(NH)-Ligand[O]-ASN318(HN).

TABLE 11: Potential ligand-protein molecular docking bindings of gefitinib (6) with identified proteins.

Gefitinib (6, N-(3-chloro-4-fluorophenyl)-7-methoxy-6-(3-morpholinopropoxy) quinazolin-4-amine, $C_{22}H_{24}ClFN_4O_3$)

1D5R (chain A) - *A Hydrolase Enzymatic Protein* - PTEN tumor suppressor

5TIJ (chain B) - *A Lyase Enzymatic Protein* - human enolase 2

ultimately the inert metabolites will be automatically excreted from kidneys. Such analysis of ADMET properties (Table 13) inferred us that the two FOGs are with 0.0373 and 0.0336 of BBB penetration potentiality confirms their CNS significance and esteems their superior permeability and their *in vivo* distribution. Further, it is supported on the ground of the *in vitro* Caco-2 cell permeability held with 7.2167 and 4.8722 nm/sec, respectively, which enables their robust permeability to bind to plasma proteins and to penetrate in to the BBB system. The *in vitro* PPB efficiency with 73.43 and 73.27 respective percentages approves their robust binding capability to plasma proteins. The *in vitro* MDCK cell permeability with 0.6424 and 0.7567 nm/sec empowers their strong permeability. The %HIA with 47.1059 and 25.1651 supports their interactions with targeted domains of the cells. The negative magnitudes of the toxicity calculations that designate FOGs are nontoxic and with safer drug properties. In ultimate, ADMET analysis of the two FOGs has greatly manifested their potential physicochemical interactions and drug-likeness.

3.7. QSAR Studies. QSAR results (Table 14) indicate that FOGs under study with molecular weights 432.38 and 448.38 (less than 500 Daltons) have confirmed their greater permeability *via* cell membranes with log *P* values of 0.68 and 0.19 (less than 5). Correspondingly, the numbers of hydrogen bond acceptors and donors have also obeyed the limitations. The molecular refractivity values with 107.46 and 109.27 cm³/mol have aligned in the standard range (40-130 cm³/mol) and confirmed that the two FOGs are obeying the Lipinski rule of five and are designated as significant oral active drugs. On the other hand, the total polar surface area bankrolled by the addition of polar surface area of the atoms like oxygen, nitrogen, and hydrogen [78], for the two FOGs are with 170.05 and 190.28 A°² obeying the limitations; and the number of total rotatable bonds in FOGs are 4 in number and obeying its potential boundaries; in complementary to obeying of the Lipinski rule, these two accounts for the validation of the Veber's rule pertaining to the two FOGs of the study. Henceforth, these FOGs are admired to be absorbed, diffused, and transported certainly

and ascertained as oral administrable drugs. The TPSA is greatly correlated with the hydrogen bonding of a molecule and is complemented with transport properties of a drug through the membranes, and hence, also accounts for the BBB penetrability [79]. Furthermore, density with 1.642 and 1.713 gm/cc, solubility with -2.74 and -2.45, and *Van der Waals* volume with 356.17 and 364.19Å³, respectively, ascertain the safer and potential drug-likeness of the FOGs. In ultimate, this study greatly helped in accepting the physicochemical interactions of FOGs with the anticipated targets; and in defining their drug properties by complementing with bioactivity and toxicity risks studies, where the ligand interactions and enzyme inhibition properties along with the like drug-likeness and drug scores will be evaluated.

3.8. Bioactivity and Toxicity Risk Studies. The bioactivity and toxicity risk exploration studies of the FOGs have shown their bioactivity properties *viz.,* GPCR ligand property, ion channel modulator, kinase inhibitor, nuclear receptor ligand interactions, protease inhibitor, and enzyme inhibitor interactions; and the drug properties like drug-likeness and drug score and established as potential nontoxic drugs (Table 15). This molinspiration exploration comprehensively assists us to explore the cheminformatics of the molecules under investigation by correlating with the *in vitro* and *in vivo* results database of the recognized drugs basing on the functional group similarities in mutual. The drug property exploration of the two FOGs has evidenced for their safer drug properties as they are with no risks of tumorigenicity, irritant effects, mutagenicity, and shown no effect on reproductive system. The positive magnitude of the drug-likeness value represents that the scrutinized molecule comprises the significant fragments that are present in the established commercial drugs [45]. Drug-likeness is an significant factor which helps in understanding the kinesis of a molecule from the site of administration to the bloodstream, hence, its good solubility accounts for good absorption and assures the drug-likeness [80]. Similarly, drug score is also a complementary parameter of the drug-likeness and helps to assure to decide molecule's drug potentiality. Hence, the present investigation reveals that all the properties of the bioactivity

TABLE 12: Potential ligand-protein molecular docking interactions of gefitinib (6) with identified proteins.

Enzymatic protein	Cluster number	Cluster element	BE (KCal/mol)	HB	HBL atoms	HBR atoms	Binding interactions	BL (A°)	BA (°)	HB type
1D5R (chain A) - *hydrolase* - PTEN tumor suppressor	0	0	-8.0338	5	3	4	Ligand[$N_{(2)}$-$H_{(3)}$]——ASP324(OCOH)	2.3863	54.6314$	Acceptor
							Ligand[$N_{(2)}$-$H_{(3)}$]——ASP324(OCOH)	2.1188		Acceptor
							Ligand[$C_{(5)}$-$O_{(2)}$]——ARG173(HN=C)	2.2728	71.0798#	Donor
							Ligand[$C_{(4)}$-O]——ARG173(HN=C)	2.3931		Donor
							Ligand[$C_{(4)}$-O]——ARG173(HN-CH)	2.8653	50.4066*	Donor
5TIJ (chain B) - *lyase* - human enolase 2	13	3	-7.8985	2	1	2	Ligand[$C_{(12)}$-$O_{(1)}$]——ASP142(HN)	2.4308	52.5638$	Donor
							Ligand[$C_{(12)}$-$O_{(1)}$]——SER141(HN)	2.4781		Donor

$ASP324(HOCO)-Ligand [$H_{(3)}$]-ASP324(O(H)OC); *ARG173(C = HN)-Ligand[O]-ARG173(HN=CH); #Ligand[$O_{(2)}$]-ARG173(HN=C)-Ligand[O]; ASP142(NH)-Ligand[$O_{(1)}$]-SER141(HN).

TABLE 13: ADMET properties the compounds 1-6.

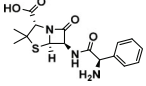| Compounds	In vivo blood-brain barrier penetration (C. brain/C. blood)[a]	In vitro Caco-2 cell permeability (nm/sec)[b]	In vitro plasma protein binding (%)[c]	In vitro MDCK cell permeability (nm/sec)[d]	Human intestinal absorption (HIA, %)[e]	Toxicity[f]
Apigenin-7-glucoside (1)	0.0373	7.2167	73.4332	0.6424	47.1059	Negative
Luteolin-7-glucoside (2)	0.0336	4.8722	73.2796	0.7567	25.1651	Negative
Ampicillin (3)	0.0588	0.6307	36.1547	0.9376	81.4785	Negative
Ascorbic acid (4)	0.1173	2.4836	5.3035	0.8819	33.1572	Negative
Gefitinib (5)	0.0476	54.1474	80.7309	0.07737	96.6375	Negative
Tamoxifen (6)	14.1639	49.5448	94.7448	69.8462	100	Negative
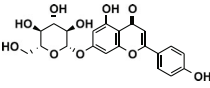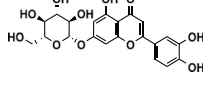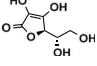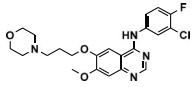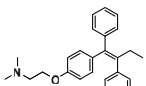
[a]Blood – brain barrier (BBB) penetration = [brain]/[blood]; [b]Caco-2 cells are derived from human colon adenocarcinoma and possess multiple drug transport pathways through intestinal epithelium; [c]% of drug binds to plasma protein; [d]MDCK cell system used as tool for rapid permeability screening; [e]human intestinal absorption is the sum of bioavailability and absorption evaluated from ratio of excretion or cumulative excretion in urine, bile, and feces; [f]in vitro Ames test by metabolic and nonmetabolic activated TA100 and TA1535 strains collected from rat liver homogenate.

TABLE 14: QSAR properties of the compounds 1-6.

| Entry | Lipinski parameters | | | | | | Veber parameters | | | | Other parameters | | |
	MW	HB Don	HB Acc	logP (o/w)	MR	Lip. Vio.	TPSA	No. of RB	Veb. Vio.	No. of H	V. Volume	ρ	Solubility
Apigenin-7-glucoside (1)	432.38	10	6	0.68	107.46	0	170.05	4	0	20	356.17	1.642	-2.74
Luteolin-7-glucoside (2)	448.38	11	7	0.19	109.27	0	190.28	4	0	20	364.19	1.713	-2.45
Ampicillin (3)	349.41	7	4	-0.87	89.37	0	112.73	4	0	19	298.87	1.453	-1.57
Ascorbic acid (4)	176.12	6	4	-1.40	36.61	0	107.22	2	0	8	139.71	1.954	-0.35
Gefitinib (5)	446.91	7	1	4.19	118.38	0	68.75	8	0	24	385.07	1.322	-5.06
Tamoxifen (6)	371.52	2	0	6.06	119.87	0	12.47	8	0	29	376.13	1.042	-4.40

MW: molecular weight; HB Don: hydrogen bond donors; HB Acc: hydrogen bond acceptors; logP: octanol to water partition coefficient; MR: molecular refractivity (cm^3/mol); Lip Vio: Lipinski violations; TPSA: total polar surface area; No. of RB: number of rotatable bonds; Veb Vio: Veber violations; No. of "H": number of hydrophobic atoms; V. Volume: *Van der Waals* volume; ρ: density (gm/cc).

TABLE 15: Bioactivity scores, drug properties, and toxicity risks of the compounds 1-6.

Compounds	Structure	Bioactivity						Drug properties	
		GPCRL	ICM	KI	NRL	PI	EI	Drug-likeness	Toxicity risks
Apigenin-7-glucoside (1)		0.10	-0.01	0.14	0.31	0.02	0.43	2.29	0.44
Luteolin-7-glucoside (2)		0.09	-0.02	0.15	0.27	-0.01	0.42	1.79	0.45
Ampicillin (3)		0.04	-0.47	-0.71	-0.61	0.87	0.25	10.72	0.91
Ascorbic acid (4)		-0.53	-0.24	-1.09	-1.01	-0.81	0.20	0.02	0.74
Gefitinib (5)		0.12	-0.04	0.66	-0.21	0.30	0.03	-2.62	0.28
Tamoxifen (6)		0.30	0.002	-0.01	0.57	0.04	0.32	6.3	0.35

GPCRL: G protein-coupled receptor ligand; ICM: ion channel modulator; KI: kinase inhibitor; NRL: nuclear receptor ligand; PI: protease inhibitor; EI: enzyme inhibitor.

and toxicity risk studies are up to the potential limits of the safe drugs and ascertains the FOGs as the drug-like compounds.

4. Conclusions

Luffa acutangula is one of the regularly used plants with various secondary metabolites such as polyphenols and flavonoids, which possesses biological and pharmacological activities. Here in this study, the aim is to test the biogenically synthesised nanoparticles for their biological activities including antibacterial, antioxidant, and anticancer activities. The results revealed that the silver nanoparticles of *Luffa acutangula* leaf extract enriched with its inherent flavonoid *O*-glycosides (FOGs, *viz.*, Cosmosioside (1, Apigenin-7-glucoside) and from -9.2690 to -7.8306 for Cynaroside (2, Luteolin-7-glucoside)) prepared by green biosynthetic approach. The biogenically synthesised silver nanoparticles found to be significant against bacteria and cancer cell lines which clearly show antibacterial and anticancer activities. Antioxidants play an important in reducing the oxidative stress and diminishing the growth of the cancerous cell. The results showed that AgNPs showed potential antioxidant activity. The profound studies performed based on the molecular docking analysis have revealed that the FOGs are identified as antagonists of aspartic acid receptor of enzymatic proteins referenced based on the microorganisms, cell lines, and oxidizing agents considered for the *in vitro* studies. Furthermore, QSAR, ADMET properties showed them as prospective drugs. The results validated that AgNPs could be potential agents to treat various types of cancers and boosting the immune system functions. Never-theless, future studies with *in vivo* toxicological studies with clear mechanism of action and the pharmacodynamics studies of LAAgNPs would shed the light more thoroughly to show the possible mechanisms for anticancer activities.

Data Availability

The data has been included in the manuscript.

Conflicts of Interest

The authors declare that there are no conflicts of interest.

Acknowledgments

References

[1] E. Corradini, P. Foglia, P. Giansanti, R. Gubbiotti, R. Samperi, and A. Laganà, "Flavonoids: chemical properties and analytical methodologies of identification and quantitation in foods and

plants," *Natural Product Research*, vol. 25, no. 5, pp. 469–495, 2011.

[2] P. G. Pietta, "Flavonoids as antioxidants," *Journal of Natural Products*, vol. 63, no. 7, pp. 1035–1042, 2000.

[3] T. P. T. Cushnie and A. J. Lamb, "Antimicrobial activity of flavonoids," *International Journal of Antimicrobial Agents*, vol. 26, no. 5, pp. 343–356, 2005.

[4] H. Khan, M. Saeedi, S. M. Nabavi, M. S. Mubarak, and A. Bishayee, "Glycosides from medicinal plants as potential anticancer agents: emerging trends towards future drugs," *Current Medicinal Chemistry*, vol. 26, no. 13, pp. 2389–2406, 2019.

[5] J. Y. Park, C. S. Kim, K. M. Park, and P. S. Chang, "Inhibitory characteristics of flavonol-3-O-glycosides from *Polygonum aviculare* L. (common knotgrass) against porcine pancreatic lipase," *Scientific Reports*, vol. 9, no. 1, article 18080, 2019.

[6] K. Niaz and F. Khan, "Analysis of polyphenolics," in *Recent Advances in Natural Products Analysis*, A. S. Silva, S. F. Nabavi, and M. Saeedi, Eds., Elsevier, Netherlands, 2nd ed. edition, 2020.

[7] F. J. Osonga, A. Akgul, I. Yazgan et al., "Flavonoid-derived anisotropic silver nanoparticles inhibit growth and change the expression of virulence genes inEscherichia coliSM10," *RSC Advances*, vol. 8, no. 9, pp. 4649–4661, 2018.

[8] J. Kurepa, R. Nakabayashi, T. Paunesku et al., "Direct isolation of flavonoids from plants using ultra-small anatase-TiO2nanoparticles," *The Plant Journal*, vol. 77, no. 3, pp. 443–453, 2014.

[9] C. Dipankar and S. Murugan, "The green synthesis, characterization and evaluation of the biological activities of silver nanoparticles synthesized from *Iresine herbstii* leaf aqueous extracts," *Colloids and Surfaces B: Biointerfaces*, vol. 98, no. 9, pp. 112–119, 2012.

[10] P. V. Rao, D. Nallappan, K. Madhavi, S. Rahman, L. Jun Wei, and S. H. Gan, "Phytochemicals and biogenic metallic nanoparticles as anticancer agents," *Oxidative Medicine and Cellular Longevity*, vol. 2016, Article ID 3685671, 15 pages, 2016.

[11] C. A. Santos, F. A. Almeida, B. X. V. Quecán et al., "Bioactive properties of *Syzygium cumini* (L.) skeels pulp and seed phenolic extracts," *Frontiers in Microbiology*, vol. 11, p. 990, 2020.

[12] A. Singh, P. K. Gautam, A. Verma et al., "Green synthesis of metallic nanoparticles as effective alternatives to treat antibiotics resistant bacterial infections: a review," *Biotechnology Reports*, vol. 25, article e00427, 2020.

[13] M. R. Siddiqui, M. Khan, Khan et al., "Green synthesis of silver nanoparticles mediated by *Pulicaria glutinosa* extract," *International Journal of Nanomedicine*, vol. 8, no. 1, pp. 1507–1616, 2013.

[14] G. Z. Kyzas and K. A. Matis, "Nanoadsorbents for pollutants removal: a review," *Journal of Molecular Liquids*, vol. 203, pp. 159–168, 2015.

[15] P. J. Shiny, A. Mukherjee, and N. Chandrasekaran, "DNA damage and mitochondria-mediated apoptosis of A549 lung carcinoma cells induced by biosynthesised silver and platinum nanoparticles," *RSC Advances*, vol. 6, no. 33, pp. 27775–27787, 2016.

[16] S. Das, A. Das, A. Maji, M. Beg, A. Singha, and M. Hossain, "A compact study on impact of multiplicative *Streblus asper* inspired biogenic silver nanoparticles as effective photocatalyst, good antibacterial agent and interplay upon interaction

[17] A. Niaz, A. Bibi, Huma, M. I. Zaman, M. Khan, and A. Rahim, "Highly selective and ecofriendly colorimetric method for the detection of iodide using green tea synthesized silver nanoparticles," *Journal of Molecular Liquids*, vol. 249, pp. 1047–1051, 2018.

[18] L. Wei, J. Lu, H. Xu, A. Patel, Z. S. Chen, and G. Chen, "Silver nanoparticles: synthesis, properties, and therapeutic applications," *Drug Discovery Today*, vol. 20, no. 5, pp. 595–601, 2015.

[19] D. Ghosh, S. Dhibar, A. Dey et al., "Graphene oxide dispersed supramolecular hydrogel capped benign green silver nanoparticles for anticancer, antimicrobial, cell attachment and intracellular imaging applications," *Journal of Molecular Liquids*, vol. 282, pp. 1–12, 2019.

[20] M. S. Abdel-Aziz, M. S. Shaheen, A. A. el-Nekeety, and M. A. Abdel-Wahhab, "Antioxidant and antibacterial activity of silver nanoparticles biosynthesized using _Chenopodium murale_ leaf extract," *Journal of Saudi Chemical Society*, vol. 18, no. 4, pp. 356–363, 2014.

[21] P. Banerjee, M. Satapathy, A. Mukhopahayay, and P. Das, "Leaf extract mediated green synthesis of silver nanoparticles from widely available Indian plants: synthesis, characterization, antimicrobial property and toxicity analysis," *Bioresources and Bioprocessing*, vol. 1, no. 1, article 3, 2014.

[22] V. R. Pasupuleti, T. N. V. K. V. Prasad, R. A. Sheikh et al., "Biogenic silver nanoparticles using Rhinacanthus nasutus leaf extract: synthesis, spectral analysis, and antimicrobial studies," *International Journal of Nanomedicine*, vol. 8, no. 1, pp. 3355–3564, 2013.

[23] V. K. Vidhu and D. Philip, "Catalytic degradation of organic dyes using biosynthesized silver nanoparticles," *Micron*, vol. 56, pp. 54–62, 2014.

[24] S. Pirtarighat, M. Ghannadnia, and S. Baghshahi, "Biosynthesis of silver nanoparticles using _Ocimum basilicum_ cultured under controlled conditions for bactericidal application," *Materials Science and Engineering: C Materials for Biological Applications*, vol. 98, pp. 250–255, 2019.

[25] D. Prabhu, C. Arulvasu, G. Babu, R. Manikandan, and P. Srinivasan, "Biologically synthesized green silver nanoparticles from leaf extract of *Vitex negundo* L. induce growth-inhibitory effect on human colon cancer cell line HCT15," *Process Biochemistry*, vol. 48, no. 2, pp. 317–324, 2013.

[26] G. Ganapathy Selvam and K. Sivakumar, "Phycosynthesis of silver nanoparticles and photocatalytic degradation of methyl orange dye using silver (Ag) nanoparticles synthesized from Hypnea musciformis (Wulfen) J.V. Lamouroux," *Applied Nanoscience*, vol. 5, no. 5, pp. 617–622, 2015.

[27] K. Mohan Kumar, M. Sinha, B. K. Mandal, A. R. Ghosh, K. Siva Kumar, and P. Sreedhara Reddy, "Green synthesis of silver nanoparticles using *Terminalia chebula* extract at room temperature and their antimicrobial studies," *Spectrochimica Acta Part A: Molecular and Biomolecular Spectroscopy*, vol. 91, pp. 228–233, 2012.

[28] S. M. Ali, N. M. H. Yousef, and N. A. Nafady, "Application of biosynthesized silver nanoparticles for the control of land snail eobania vermiculata and some plant pathogenic fungi," *Journal of Nanomaterials*, vol. 2015, Article ID 218904, 10 pages, 2015.

[29] S. Kaviya, J. Santhanalakshmi, B. Viswanathan, J. Muthumary, and K. Srinivasan, "Biosynthesis of silver nanoparticles using

citrus sinensis peel extract and its antibacterial activity," *Spectrochimica Acta, Part A: Molecular and Biomolecular Spectroscopy*, vol. 79, no. 3, pp. 594–598, 2011.

[30] P. Moteriya, H. Padalia, and S. Chanda, "Characterization, synergistic antibacterial and free radical scavenging efficacy of silver nanoparticles synthesized using *Cassia roxburghii* leaf extract," *Journal of Genetic Engineering and Biotechnology*, vol. 15, no. 2, pp. 505–513, 2017.

[31] D. Nallappan, N. V. K. V. P. Tollamadugu, A. N. Fauzi, N. S. Yaacob, and V. R. Pasupuleti, "Biomimetic synthesis and anticancer activity ofEurycoma longifoliabranch extract-mediated silver nanoparticles," *IET Nanobiotechnology*, vol. 11, no. 7, pp. 889–897, 2017.

[32] M. S. Jabir, Y. M. Saleh, G. M. Sulaiman et al., "Green synthesis of silver nanoparticles using *Annona muricata* extract as an inducer of apoptosis in cancer cells and inhibitor for NLRP3 inflammasome *via* enhanced autophagy," *Nanomaterials*, vol. 11, no. 2, article 384, 2021.

[33] M. S. Jabir, A. A. Hussien, G. M. Sulaiman et al., "Green synthesis of silver nanoparticles fromEriobotrya japonicaextract: a promising approach against cancer cells proliferation, inflammation, allergic disorders and phagocytosis induction," *Artificial Cells, Nanomedicine, and Biotechnology*, vol. 49, no. 1, pp. 48–60, 2021.

[34] H. Harbottle, S. Thakur, S. Zhao, and D. G. White, "Genetics of antimicrobial resistance," *Animal Biotechnology*, vol. 17, no. 2, pp. 111–124, 2006.

[35] M. J. Firdhouse and P. Lalitha, "Biosynthesis of silver nanoparticles and its applications," *Journal of Nanotechnology*, vol. 2015, Article ID 829526, 18 pages, 2015.

[36] B. P. Pimple, P. V. Kadam, and M. J. Patil, "Protective effect of *Luffa acutangula* extracts on gastric ulceration in NIDDM rats: Role of gastric mucosal glycoproteins and antioxidants," *Asian Pacific Journal of Tropical Medicine*, vol. 5, no. 8, pp. 610–615, 2012.

[37] J. Taruna, J. B. Kaushal, J. Bhatti, and P. Kumar, "Green synthesis and physico-chemical study of silver nanoparticles extracted from a natural source *Luffa acutangula*," *Journal of Molecular Liquids*, vol. 224, no. A, pp. 991–998, 2016.

[38] P. N. Shendge and S. Belemkar, "Therapeutic potential of Luffa acutangula: a review on its traditional uses, phytochemistry, pharmacology and toxicological aspects," *Frontiers in Pharmacology*, vol. 9, article 1177, 2018.

[39] July 2021, http://www.swissdock.ch/docking.

[40] E. F. Pettersen, T. D. Goddard, C. C. Huang et al., "UCSF Chimera - a visualization system for exploratory research and analysis," *Journal of Computational Chemistry*, vol. 25, no. 13, pp. 1605–1612, 2004.

[41] M. A. Bakht, M. S. Yar, S. G. Abdel-Hamid, S. I. al Qasoumi, and A. Samad, "Molecular properties prediction, synthesis and antimicrobial activity of some newer oxadiazole derivatives," *European Journal of Medicinal Chemistry*, vol. 45, no. 12, pp. 5862–5869, 2010.

[42] July 2021, http://preadmet.bmdrc.kr/.

[43] C. A. Lipinski, F. Lombardo, B. W. Dominy, and P. J. Feeney, "Experimental and computational approaches to estimate solubility and permeability in drug discovery and development settings[1]," *Advanced Drug Delivery Reviews*, vol. 46, no. 1-3, pp. 3–26, 2001.

[44] July 2021, http://www.molinspiration.com/cgi-bin/properties.

[45] July 2021, https://www.organic-chemistry.org/prog/peo/druglikeness.html.

[46] S. Ahmed, M. Saifullah, M. Ahmad, B. L. Swami, and S. Ikram, "Green synthesis of silver nanoparticles usingAzadirachta indicaaqueous leaf extract," *Journal of Radiation Research and Applied Sciences*, vol. 9, no. 1, pp. 1–7, 2016.

[47] H. Padalia, P. Moteriya, and S. Chanda, "Green synthesis of silver nanoparticles from marigold flower and its synergistic antimicrobial potential," *Arabian Journal of Chemistry*, vol. 8, no. 5, pp. 732–741, 2015.

[48] N. G. Mlalila, H. S. Swai, A. Hilonga, and D. Kadam, "Antimicrobial dependence of silver nanoparticles on surface plasmon resonance bands against *Escherichia coli*," *Nanotechnology, Science and Applications*, vol. Volume 10, pp. 1–9, 2017.

[49] A. M. Awwad, N. M. Salem, and A. O. Abdeen, "Green synthesis of silver nanoparticles using carob leaf extract and its antibacterial activity," *International Journal of Industrial Chemistry*, vol. 4, no. 1, p. 29, 2013.

[50] M. M. H. Khalil, E. H. Ismail, K. Z. el-Baghdady, and D. Mohamed, "Green synthesis of silver nanoparticles using olive leaf extract and its antibacterial activity," *Arabian Journal of Chemistry*, vol. 7, no. 6, pp. 1131–1139, 2014.

[51] C. Ramteke, T. Chakrabarti, B. K. Sarangi, and R. A. Pandey, "Synthesis of silver nanoparticles from the aqueous extract of leaves of Ocimum sanctum for enhanced antibacterial activity," *Journal of Chemistry*, vol. 2013, Article ID 278925, 7 pages, 2013.

[52] P. Kumar, M. Govindaraju, S. Senthamilselvi, and K. Premkumar, "Photocatalytic degradation of methyl orange dye using silver (Ag) nanoparticles synthesized from *Ulva lactuca*," *Colloids and Surfaces B: Biointerfaces*, vol. 103, pp. 658–661, 2013.

[53] T. Nagao, R. Tanaka, Y. Iwase, H. Hanazono, and H. Okabe, "Studies on the constituents of Luffa acutangula Roxb. I. Structures of acutosides A–G, oleanane-type triterpene saponins isolated from the herb," *Chemical and Pharmaceutical Bulletin*, vol. 39, no. 3, pp. 599–606, 1991.

[54] M. V. K. Reddy, K. Y. Rao, G. Anusha et al., "*In-vitro* evaluation of antioxidant and anticholinesterase activities of novel pyridine, quinoxaline and *s*-triazine derivatives," *Environmental Research*, vol. 199, article 111320, 2021.

[55] N. Chandrasekhar and S. P. Vinay, "Yellow colored blooms of Argemone mexicana and Turnera ulmifolia mediated synthesis of silver nanoparticles and study of their antibacterial and antioxidant activity," *Applied Nanoscience*, vol. 7, no. 8, pp. 851–861, 2017.

[56] H. Mohamed el-Rafie and M. Abdel-Aziz Hamed, "Antioxidant and anti-inflammatory activities of silver nanoparticles biosynthesized from aqueous leaves extracts of fourTerminaliaspecies," *Advances in Natural Sciences: Nanoscience and Nanotechnology*, vol. 5, no. 3, article 035008, 2014.

[57] D. Bose and S. Chatterjee, "Biogenic synthesis of silver nanoparticles using guava (Psidium guajava) leaf extract and its antibacterial activity against Pseudomonas aeruginosa," *Applied Nanoscience*, vol. 6, no. 6, pp. 895–901, 2016.

[58] M. Gangwar, M. K. Gautam, A. K. Sharma, Y. B. Tripathi, R. K. Goel, and G. Nath, "Antioxidant capacity and radical scavenging effect of polyphenol rich *Mallotus philippenensis* fruit extract on human erythrocytes: an *in vitro* study," *Scientific World Journal*, vol. 2014, article 279451, pp. 1–12, 2014.

[59] P. Dauthal and M. Mukhopadhyay, "*In-vitro* free radical scavenging activity of biosynthesized gold and silver nanoparticles

using *Prunus armeniaca* (apricot) fruit extract," *The Journal of Nanoparticle Research*, vol. 15, no. 1, article 1366, 2013.

[60] A. K. Mittal, J. Bhaumik, S. Kumar, and U. C. Banerjee, "Biosynthesis of silver nanoparticles: elucidation of prospective mechanism and therapeutic potential," *Journal of Colloid and Interface Science*, vol. 415, pp. 39–47, 2014.

[61] R. Geethalakshmi and D. V. Sarada, "Gold and silver nanoparticles from Trianthema decandra: synthesis, characterization, and antimicrobial properties," *International Journal of Nanomedicine*, vol. 7, pp. 5375–5384, 2012.

[62] F. C. Tenover, "Mechanisms of antimicrobial resistance in bacteria," *The American Journal of Medicine*, vol. 119, no. 6, pp. S3–S10, 2006.

[63] J. S. Kim, E. Kuk, K. N. Yu et al., "Antimicrobial effects of silver nanoparticles," *Nanomedicine: Nanotechnology, Biology and Medicine*, vol. 3, no. 1, pp. 95–101, 2007.

[64] H. Soliman, A. Elsayed, and A. Dyaa, "Antimicrobial activity of silver nanoparticles biosynthesised byRhodotorulasp.strain ATL72," *Egyptian Journal of Basic and Applied Sciences*, vol. 5, no. 3, pp. 228–233, 2018.

[65] G. M. Sulaiman, E. H. Ali, I. I. Jabbar, and A. H. Saleem, "Synthesis, characterization, antibacterial and cytotoxic effects of silver nanoparticles," *Digest Journal of Nanomaterials and Biostructures*, vol. 9, no. 2, pp. 787–796, 2014.

[66] G. Chomicki, H. Schaefer, and S. S. Renner, "Origin and domestication of *Cucurbitaceae* crops: insights from phylogenies, genomics and archaeology," *New Phytologist*, vol. 226, no. 5, pp. 1240–1255, 2020.

[67] R. Vanajothi and P. Srinivasan, "An anthraquinone derivative fromLuffa acutangulainduces apoptosis in human lung cancer cell line NCI-H460 through p53-dependent pathway," *Journal of Receptor and Signal Transduction Research*, vol. 36, no. 3, pp. 292–302, 2016.

[68] R. Vanajothi and P. Srinivasan, "Bioassay-guided isolation and identification of bioactive compound from aerial parts ofLuffa acutangulaagainst lung cancer cell line NCI-H460," *Journal of Receptor and Signal Transduction Research*, vol. 35, no. 4, pp. 295–302, 2015.

[69] M. Mahadi, A. Jamil, H. B. Mamman, and S. Ganeson, "Investigation of anti-cancer proliferation properties of Luffa acutangula on HT-29 using electroporation method," in *8th International Conference on Biomedical Engineering and Technology (ICBET) Bali Indonesia*, pp. 108–111, New York, NY, United States, 2018.

[70] L. Junkai, M. Chen, X. Jieming et al., "Purification and characterization of two luffaculins, ribosome-inactivating proteins from seeds of *Luffa acutangula*," *Chinese Journal of Biochemistry and Molecular Biology*, vol. 18, no. 5, pp. 609–613, 2002.

[71] K. Venugopal, H. A. Rather, K. Rajagopal et al., "Synthesis of silver nanoparticles (Ag NPs) for anticancer activities (MCF 7 breast and A549 lung cell lines) of the crude extract of *Syzygium aromaticum*," *Journal of Photochemistry and Photobiology B: Biology*, vol. 167, pp. 282–289, 2017.

[72] Z. Yu, Q. Li, J. Wang et al., "Reactive oxygen species-related nanoparticle toxicity in the biomedical field," *Nanoscale Research Letters*, vol. 15, no. 1, p. 115, 2020.

[73] P. D. Nallathamby and X. H. N. Xu, "Study of cytotoxic and therapeutic effects of stable and purified silver nanoparticles on tumor cells," *Nanoscale*, vol. 2, no. 6, pp. 942–952, 2010.

[74] M. I. Sriram, S. B. M. Kanth, K. Kalishwaralal et al., "Antitumor activity of silver nanoparticles in Dalton’s lymphoma ascites tumor model," *International Journal of Nanomedicine*, vol. 5, no. 5, pp. 753–762, 2010.

[75] J. Liu, Y. Zhao, Q. Guo et al., "TAT-modified nanosilver for combating multidrug-resistant cancer," *Biomaterials*, vol. 33, no. 26, pp. 6155–6161, 2012.

[76] P. Sanpui, A. Chattopadhyay, and S. S. Ghosh, "Induction of apoptosis in cancer cells at low silver nanoparticle concentrations using chitosan nanocarrier," *ACS Applied Materials & Interfaces*, vol. 3, no. 2, pp. 218–228, 2011.

[77] T. I. Oprea and H. Matter, "Integrating virtual screening in lead discovery," *Current Opinion in Chemical Biology*, vol. 8, no. 4, pp. 349–358, 2004.

[78] P. Ertl, B. Rohde, and P. Selzer, "Fast calculation of molecular polar surface area as a sum of fragment-based contributions and its application to the prediction of drug transport properties," *Journal of Medicinal Chemistry*, vol. 43, no. 20, pp. 3714–3717, 2000.

[79] M. Maximo da Silva, M. Comin, T. Santos Duarte et al., "Synthesis, antiproliferative activity and molecular properties predictions of galloyl derivatives," *Molecules*, vol. 20, no. 4, pp. 5360–5373, 2015.

[80] A. M. Alafeefy, S. I. Alqasoumi, A. E. Ashour et al., "Quinazoline-tyrphostin as a new class of antitumor agents, molecular properties prediction, synthesis and biological testing," *European Journal of Medicinal Chemistry*, vol. 53, pp. 133–140, 2012.